CHAPTER

ELEVEN

Atmospheric equations of motion

In vector form, the equations of motion are valid in any coordinate system. However, those equations do not lend themselves to application and standard methods of solution. To be useful, the governing equations must be expressed in scalar form. They then depend on the coordinate system.

We develop the scalar equations of motion within the general framework of curvilinear coordinates. In addition to accounting for geometric distortions inherent to spherical coordinates, that framework allows a straightforward development of the equations in thermodynamic coordinates, which afford a number of simplifications.

11.1 CURVILINEAR COORDINATES

Consider the *Cartesian coordinates*

$$\boldsymbol{x} = (x_1, x_2, x_3). \tag{11.1.1}$$

They are measured from planar coordinate surfaces: $x_i = \text{const}$. If those planes are perpendicular, (x_1, x_2, x_3) are referred to as *rectangular Cartesian coordinates*. More generally, consider the *curvilinear coordinates*

$$\hat{\boldsymbol{x}} = (\hat{x}_1, \hat{x}_2, \hat{x}_3). \tag{11.1.2}$$

They are measured from coordinate surfaces that need not be planar nor mutually orthogonal (Fig. 11.1). Insofar as $\boldsymbol{x}$ and $\hat{\boldsymbol{x}}$ are both valid coordinate systems, there exists a transformation

$$\hat{\boldsymbol{x}} = \hat{\boldsymbol{x}}(\boldsymbol{x}) \tag{11.2}$$

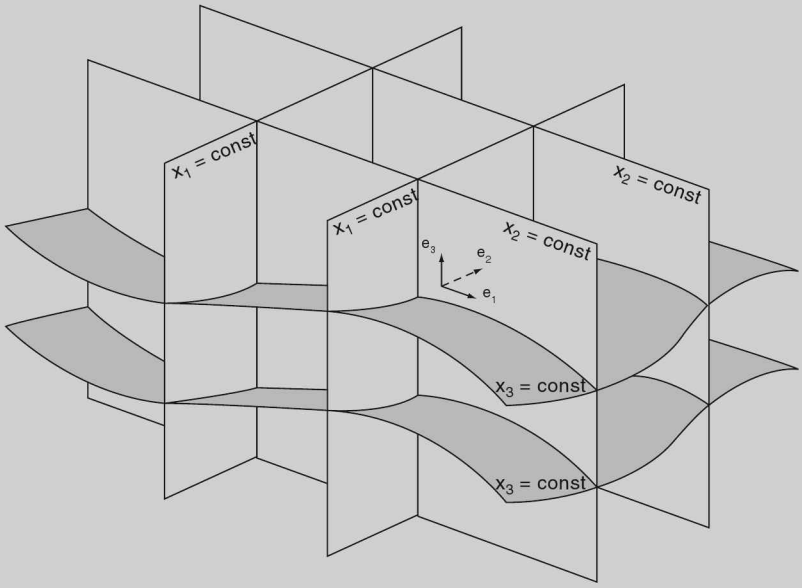

Figure 11.1 Coordinate surfaces $x_i = \text{const}$ for curvilinear coordinates. Coordinate vectors $\boldsymbol{e}_i$ point in the directions of increasing $\boldsymbol{x}_i$.

from one representation to the other. It constitutes a mapping between all coordinates $\boldsymbol{x}$ in the original system and coordinates $\hat{\boldsymbol{x}}$ in the curvilinear coordinate system.

The mapping (11.2) is unique and therefore invertible, provided that the *Jacobian* of the transformation

$$J(\boldsymbol{x}, \hat{\boldsymbol{x}}) = \left| \frac{\partial \hat{x}_i}{\partial x_j} \right| \tag{11.3}$$

is nonzero for all $\boldsymbol{x}$. The Jacobian applies irrespective of whether the original coordinate system is Cartesian. It has the reciprocal property

$$J(\boldsymbol{x}, \hat{\boldsymbol{x}}) \cdot J(\hat{\boldsymbol{x}}, \boldsymbol{x}) = 1. \tag{11.4}$$

Unlike Cartesian coordinates, the curvilinear coordinates $\hat{x}_i$ need not represent length. For example, the spherical coordinates, longitude λ and latitude ϕ, represent angular displacements. The physical length ds_i corresponding to an increment of the curvilinear coordinate $\hat{x}_i$ is accounted for in the *metric scale factor* h_i:

$$ds_i = h_i d\hat{x}_i \tag{11.5.1}$$

$$h_i^{-1} = |\nabla \hat{x}_i|, \tag{11.5.2}$$

where the summation convention is suspended and ∇ refers to differentiation with respect to the original coordinates x_i. Similarly, the physical volume corresponding to the incremental element $dV_{\hat{x}} = d\hat{x}_1 d\hat{x}_2 d\hat{x}_3$ in the curvilinear coordinate system is

described by

$$\begin{aligned} dV_x &= J(\hat{\boldsymbol{x}}, \boldsymbol{x}) dV_{\hat{x}} \\ &= \frac{1}{J(\boldsymbol{x}, \hat{\boldsymbol{x}})} dV_{\hat{x}}. \end{aligned} \tag{11.6}$$

The curvilinear coordinate system is *orthogonal* if coordinate surfaces are mutually perpendicular. Coordinate vectors $\hat{\boldsymbol{e}}_i$, which point in the directions of increasing $\hat{x}_i$ (Fig. 11.1), are then likewise mutually perpendicular

$$\hat{\boldsymbol{e}}_i \cdot \hat{\boldsymbol{e}}_j = \delta_{ij}.$$

Under those circumstances, the Jacobian reduces to

$$J(\hat{\boldsymbol{x}}, \boldsymbol{x}) = h_1 h_2 h_3 \tag{11.7}$$

(Prob. 11.10). Similarly, the physical volume corresponding to the element $d\hat{x}_1\, d\hat{x}_2\, d\hat{x}_3$ in the curvilinear system is just the product of the corresponding physical lengths (11.5).

The Jacobian accounts for distortions of physical length in all three curvilinear coordinates. A special case arise when only the third coordinate is transformed

$$\hat{\boldsymbol{x}}(\boldsymbol{x}) = (x_1, x_2, \hat{x}_3). \tag{11.8}$$

Such is the case when surfaces of constant height are replaced by isobaric surfaces. The Jacobian is then given by

$$\begin{aligned} J(\boldsymbol{x}, \hat{\boldsymbol{x}}) &= \begin{vmatrix} 1 & 0 & 0 \\ 0 & 1 & 0 \\ \frac{\partial \hat{x}_3}{\partial x_1} & \frac{\partial \hat{x}_3}{\partial x_2} & \frac{\partial \hat{x}_3}{\partial x_3} \end{vmatrix} \\ &= \frac{\partial \hat{x}_3}{\partial x_3}. \end{aligned} \tag{11.9}$$

For this special class of transformations, (11.4) reduces to the simple reciprocal property

$$\frac{\partial \hat{x}_3}{\partial x_3} = \left(\frac{\partial x_3}{\partial \hat{x}_3} \right)^{-1}, \tag{11.10}$$

which is not true in general.

Vector operations in arbitrary curvilinear coordinates can now be expressed in terms of the corresponding metric scale factors:

$$\nabla \psi = \frac{1}{h_1} \frac{\partial \psi}{\partial \hat{x}_1} \hat{\boldsymbol{e}}_1 + \frac{1}{h_2} \frac{\partial \psi}{\partial \hat{x}_2} \hat{\boldsymbol{e}}_2 = \frac{1}{h_3} \frac{\partial \psi}{\partial \hat{x}_3} \hat{\boldsymbol{e}}_3 \tag{11.11.1}$$

$$\nabla \cdot \boldsymbol{A} = \frac{1}{h_1 h_2 h_3} \left[\frac{\partial}{\partial \hat{x}_1} (h_2 h_3 A_1) + \frac{\partial}{\partial \hat{x}_2} (h_1 h_3 A_2) + \frac{\partial}{\partial \hat{x}_3} (h_1 h_2 A_3) \right] \tag{11.11.2}$$

$$\nabla \times \boldsymbol{A} = \begin{vmatrix} h_1 \hat{\boldsymbol{e}}_1 & h_2 \hat{\boldsymbol{e}}_2 & h_3 \hat{\boldsymbol{e}}_3 \\ \frac{\partial}{\partial \hat{x}_1} & \frac{\partial}{\partial \hat{x}_2} & \frac{\partial}{\partial \hat{x}_3} \\ h_1 A_1 & h_2 A_2 & h_3 A_3 \end{vmatrix} \tag{11.11.3}$$

$$\nabla^2 \psi = \frac{1}{h_1 h_2 h_3} \left[\frac{\partial}{\partial \hat{x}_1} \left(\frac{h_2 h_3}{h_1} \frac{\partial \psi}{\partial \hat{x}_1} \right) + \frac{\partial}{\partial \hat{x}_2} \left(\frac{h_1 h_3}{h_2} \frac{\partial \psi}{\partial \hat{x}_2} \right) \frac{\partial}{\partial \hat{x}_3} \left(\frac{h_1 h_2}{h_3} \frac{\partial \psi}{\partial \hat{x}_3} \right) \right]. \tag{11.11.4}$$

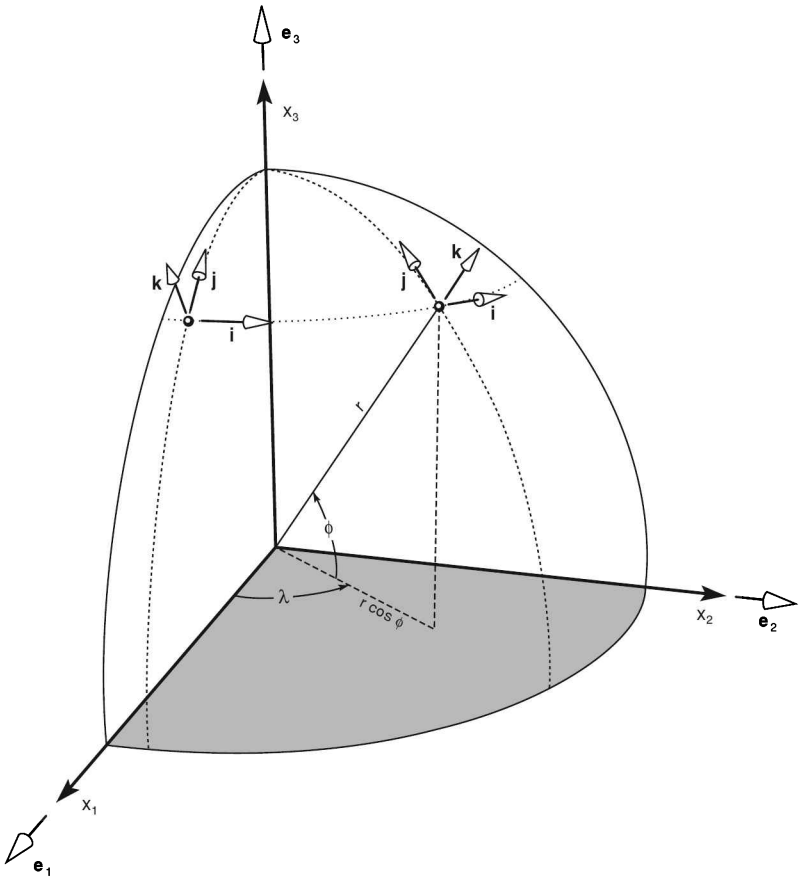

Figure 11.2 Spherical coordinates: longitude λ, latitude ϕ, and radial distance r. Coordinate vectors $\boldsymbol{e}_\lambda = \boldsymbol{i}$, $\boldsymbol{e}_\phi = \boldsymbol{j}$, and $\boldsymbol{e}_r = \boldsymbol{k}$ change with position (e.g., relative to fixed coordinate vectors $\boldsymbol{e}_1$, $\boldsymbol{e}_2$, and $\boldsymbol{e}_3$ of rectangular Cartesian coordinates).

11.2 SPHERICAL COORDINATES

Consider the rectangular Cartesian coordinates $\boldsymbol{x} = (x_1, x_2, x_3)$ having origin at the center of the Earth and the spherical coordinates

$$\hat{\boldsymbol{x}} = (\lambda, \phi, r),$$

both fixed with respect to the Earth (Fig. 11.2). Spherical coordinate surfaces, $\lambda = \text{const}$, $\phi = \text{const}$, and $r = \text{const}$, are then: (1) vertical planes intersecting the Cartesian x_3 axis, (2) conical shells with apex at the origin $\boldsymbol{x} = 0$, and (3) concentric spherical shells, respectively. The corresponding unit vectors

$$\begin{aligned} \boldsymbol{e}_\lambda &= \boldsymbol{i} \\ \boldsymbol{e}_\phi &= \boldsymbol{j} \\ \boldsymbol{e}_r &= \boldsymbol{k} \end{aligned} \tag{11.12}$$

are everywhere perpendicular to those coordinate surfaces. Because coordinate surfaces are mutually perpendicular, so are the unit vectors. The spherical coordinates (λ, ϕ, r) constitute an orthogonal coordinate system.

The rectangular Cartesian coordinates can be expressed in terms of the spherical coordinates as

$$\begin{aligned} x_1 &= r\ cos\phi\ cos\lambda \\ x_2 &= r\ cos\phi\ sin\lambda \\ x_3 &= r\ sin\phi. \end{aligned} \tag{11.13.1}$$

The latter may be inverted for the spherical coordinates:

$$\begin{aligned} \lambda &= tan^{-1}\left(\frac{x_2}{x_1}\right) \\ \phi &= tan^{-1}\left[\frac{x_3}{x_1^2 + x_2^2}\right] \\ r &= \sqrt{x_1^2 + x_2^2 + x_3^2}. \end{aligned} \tag{11.13.2}$$

Metric scale factors for the spherical coordinates then follow as

$$\begin{aligned} h_1 &= r cos\phi \\ h_2 &= r \\ h_3 &= 1 \end{aligned} \tag{11.14}$$

(Prob. 11.2). Because $\hat{\boldsymbol{x}}$ constitutes an orthogonal coordinate system, the Jacobian of the transformation follows from (11.7) as

$$J(\hat{\boldsymbol{x}}, \boldsymbol{x}) = r^2 cos\phi, \tag{11.15}$$

which is nonzero except at the poles. At $\phi = \pm 90°$, coordinate surfaces $\phi =$ const converge onto the x_3 axis. The incremental volume encased by two such surfaces vanishes there, so the transformation is singular. Vector operations follow from (11.11) as

$$\nabla\psi = \frac{1}{r\,cos\phi}\frac{\partial\psi}{\partial\lambda}\boldsymbol{i} + \frac{1}{r}\frac{\partial\psi}{\partial\phi}\boldsymbol{j} + \frac{\partial\psi}{\partial r}\boldsymbol{k} \tag{11.16.1}$$

$$\nabla\cdot\boldsymbol{A} = \frac{1}{r\,cos\phi}\frac{\partial A_\lambda}{\partial\phi} + \frac{1}{r\,cos\phi}\frac{\partial}{\partial\phi}\left(cos\phi A_\phi\right) + \frac{1}{r^2}\frac{\partial}{\partial r}\left(r^2 A_r\right) \tag{11.16.2}$$

$$\nabla\times\boldsymbol{A} = \frac{1}{r^2\,cos\phi}\begin{vmatrix} r\,cos\phi\,\boldsymbol{i} & r\boldsymbol{j} & \boldsymbol{k} \\ \frac{\partial}{\partial\lambda} & \frac{\partial}{\partial\phi} & \frac{\partial}{\partial r} \\ r\,cos\phi A_\lambda & rA_\phi & A_r \end{vmatrix} \tag{11.16.3}$$

$$\nabla^2\psi = \frac{1}{r^2\,cos^2\phi}\frac{\partial^2\psi}{\partial\lambda^2} + \frac{1}{r^2\,cos\phi}\left[cos\phi\frac{\partial\psi}{\partial\phi}\right] + \frac{1}{r^2}\frac{\partial}{\partial r}\left(r^2\frac{\partial\psi}{\partial r}\right). \tag{11.16.4}$$

From (11.14), physical displacements in the directions of increasing longitude, latitude, and radial distance are described by

$$\begin{aligned} dx &= r\cos\phi\, d\lambda \\ dy &= r\, d\phi \\ dz &= dr, \end{aligned} \tag{11.17.1}$$

in which vertical distance is measured by height

$$z = r - a, \tag{11.17.2}$$

where a denotes the mean radius of the Earth.[1] Physical velocities in the spherical coordinate system are then expressed by

$$\begin{aligned} u &= \frac{dx}{dt} = r\cos\phi \frac{d\lambda}{dt} \\ v &= \frac{dy}{dt} = r\frac{d\phi}{dt} \\ w &= \frac{dz}{dt} = \frac{dr}{dt}. \end{aligned} \tag{11.18}$$

The vector equations of motion may now be cast in terms of spherical coordinates. With the above expressions, derivatives of scalar quantities transform directly. However, Lagrangian derivatives of vector quantities are complicated by the dependence on position of the coordinate vectors $\boldsymbol{i}, \boldsymbol{j}$, and $\boldsymbol{k}$. Each rotates in physical space under a displacement of longitude or latitude. For example, an air parcel moving along a latitude circle at a constant speed u has velocity $\boldsymbol{v} = u\boldsymbol{i}$. The latter appears constant in the spherical coordinate representation. However, in physical space, it actually rotates (Fig. 11.2). The parcel therefore experiences an acceleration, which must be accounted for in the equations of motion.

Consider the velocity

$$\boldsymbol{v} = u\boldsymbol{i} + v\boldsymbol{j} + w\boldsymbol{k}.$$

The spherical coordinate vectors $\boldsymbol{i}, \boldsymbol{j}$, and $\boldsymbol{k}$ are functions of position $\hat{\boldsymbol{x}}$. Therefore, the material acceleration is actually

$$\begin{aligned} \frac{d\boldsymbol{v}}{dt} &= \frac{du}{dt}\boldsymbol{i} + \frac{dv}{dt}\boldsymbol{j} + \frac{dw}{dt}\boldsymbol{k} + u\frac{d\boldsymbol{i}}{dt} + v\frac{d\boldsymbol{j}}{dt} + w\frac{d\boldsymbol{k}}{dt} \\ &= \left(\frac{d\boldsymbol{v}}{dt}\right)_C + u\frac{d\boldsymbol{i}}{dt} + v\frac{d\boldsymbol{j}}{dt} + w\frac{d\boldsymbol{k}}{dt}, \end{aligned} \tag{11.19.1}$$

where the subscript refers to the basic form of the material derivative in Cartesian geometry

$$\left(\frac{d}{dt}\right)_C = \frac{\partial}{\partial t} + \boldsymbol{v}\cdot\nabla. \tag{11.19.2}$$

To evaluate corrections on the right hand side of (11.19), the spherical coordinate vectors are expressed in terms of the fixed rectangular Cartesian coordinate

[1] This representation is only approximate, because it ignores departures from sphericity of height surfaces (Sec. 6.2).

vectors e_1, e_2, e_3

$$\begin{aligned} \boldsymbol{i} &= -sin\lambda \boldsymbol{e}_1 + cos\lambda \boldsymbol{e}_2 \\ \boldsymbol{j} &= -sin\phi cos\lambda \boldsymbol{e}_1 - sin\phi sin\lambda \boldsymbol{e}_2 + cos\phi \boldsymbol{e}_3 \\ \boldsymbol{k} &= cos\phi cos\lambda \boldsymbol{e}_1 + cos\phi sin\lambda \boldsymbol{e}_2 + sin\phi \boldsymbol{e}_3, \end{aligned} \tag{11.20}$$

demonstration of which is left as an exercise. From these and reciprocal expressions for e_1, e_2, and e_3 in terms of $\boldsymbol{i}, \boldsymbol{j}$, and $\boldsymbol{k}$, Lagrangian derivatives of the spherical coordinate vectors follow as

$$\begin{aligned} \frac{d\boldsymbol{i}}{dt} &= u\left(\frac{tan\phi}{r}\boldsymbol{j} - \frac{1}{r}\boldsymbol{k}\right) \\ \frac{d\boldsymbol{j}}{dt} &= -u\frac{tan\phi}{r}\boldsymbol{i} - \frac{v}{r}\boldsymbol{k} \\ \frac{d\boldsymbol{k}}{dt} &= \frac{u}{r}\boldsymbol{i} + \frac{v}{r}\boldsymbol{j} \end{aligned} \tag{11.21}$$

(see Prob. 11.11). Then material accelerations in the spherical coordinate directions become

$$\frac{du}{dt} = \left(\frac{du}{dt}\right)_C - \frac{uvtan\phi}{r} + \frac{uw}{r} \tag{11.22.1}$$

$$\frac{dv}{dt} = \left(\frac{dv}{dt}\right)_C + \frac{u^2 tan\phi}{r} + \frac{vw}{r} \tag{11.22.2}$$

$$\frac{dw}{dt} = \left(\frac{dw}{dt}\right)_C - \left(\frac{u^2+v^2}{r}\right). \tag{11.22.3}$$

Corrections appearing on the right-hand sides of (11.22) are referred to as *metric terms*. They describe accelerations that result from curvature of the coordinate system.

Because the atmosphere occupies a thin shell, it is customary to simplify the radial dependence by neglecting small fractional changes of r in (11.16)–(11.22). The *shallow atmosphere approximation* makes use of the fact that $z \ll a$. It takes $r = a$ and ignores the geometric divergence associated with vertical displacements. The vector operations (11.16) then reduce to

$$\nabla\psi = \frac{1}{acos\phi}\frac{\partial\psi}{\partial\lambda}\boldsymbol{i} + \frac{1}{a}\frac{\partial\psi}{\partial\phi}\boldsymbol{j} = \frac{\partial\psi}{\partial z}\boldsymbol{k} \tag{11.23.1}$$

$$\nabla\cdot\boldsymbol{A} = \frac{1}{acos\phi}\frac{\partial A_\lambda}{\partial\phi} + \frac{1}{acos\phi}\frac{\partial}{\partial\phi}\left(cos\phi A_\phi\right) + \frac{\partial A_z}{\partial z} \tag{11.23.2}$$

$$\nabla\times\boldsymbol{A} = \frac{1}{a^2 cos\phi}\begin{vmatrix} acos\phi\boldsymbol{i} & a\boldsymbol{j} & \boldsymbol{k} \\ \frac{\partial}{\partial\lambda} & \frac{\partial}{\partial\phi} & \frac{\partial}{\partial z} \\ acos\phi A_\lambda & aA_\phi & A_z \end{vmatrix} \tag{11.23.3}$$

$$\nabla^2\psi = \frac{1}{a^2 cos^2\phi}\frac{\partial^2\psi}{\partial\lambda^2} + \frac{1}{a^2 cos\phi}\left[cos\phi\frac{\partial\psi}{\partial\phi}\right] + \frac{\partial^2\psi}{\partial z^2}, \tag{11.23.4}$$

in which height is formally adopted as the vertical coordinate.

With this approximation and material accelerations (11.22), the equations of motion can be cast into component form. The planetary vorticity (Sec. 10.6.2) can be expressed

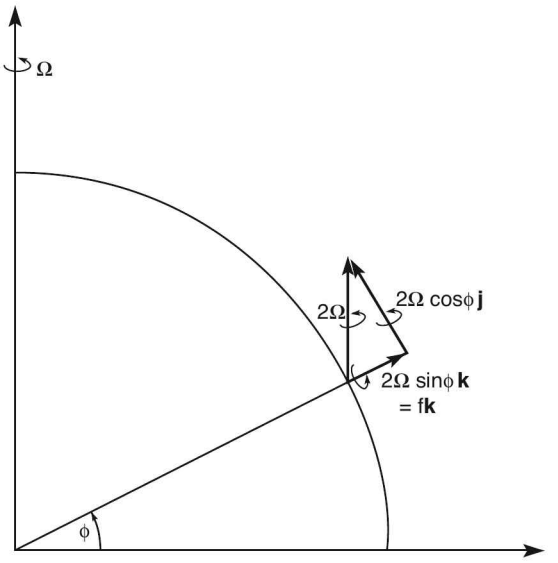

Figure 11.3 Planetary vorticity $2\boldsymbol{\Omega}$ decomposed into horizontal and vertical components.

in terms of horizontal and vertical components of the Earth's rotation

$$2\boldsymbol{\Omega} = 2\Omega(cos\phi \boldsymbol{j} + sin\phi \boldsymbol{k}) \tag{11.24}$$

(Fig. 11.3). The scalar equations of motion in spherical coordinates then become:

$$\frac{du}{dt} - 2\Omega(vsin\phi - wcos\phi) = -\frac{1}{\rho acos\phi}\frac{\partial p}{\partial \lambda} + uv\frac{tan\phi}{a} - \frac{uw}{a} - D_{\lambda} \tag{11.25.1}$$

$$\frac{dv}{dt} + 2\Omega usin\phi = -\frac{1}{\rho a}\frac{\partial p}{\partial \phi} - \frac{u^2 tan\phi}{a} - \frac{uw}{a} - D_{\phi} \tag{11.25.2}$$

$$\frac{dw}{dt} - 2\Omega ucos\phi = -\frac{1}{\rho}\frac{\partial p}{\partial z} - g + \frac{u^2 + v^2}{a} - D_z \tag{11.25.3}$$

$$\frac{d\rho}{dt} + \rho\nabla \cdot \boldsymbol{v} = 0 \tag{11.25.4}$$

$$\rho c_v \frac{dT}{dt} + p\nabla \cdot \boldsymbol{v} = \dot{q}_{net}, \tag{11.25.5}$$

where

$$\frac{d}{dt} = \frac{\partial}{\partial t} + \frac{u}{acos\phi}\frac{\partial}{\partial \lambda} + \frac{v}{a}\frac{\partial}{\partial \phi} + w\frac{\partial}{\partial z} \tag{11.25.6}$$

and

$$\dot{q}_{net} = -\nabla \cdot \boldsymbol{F} + \nabla \cdot (k\nabla T) + \rho\dot{q} \tag{11.25.7}$$

denotes the net heating rate from all diabatic sources.

11.2.1 The traditional approximation

Although it simplifies the mathematics, using height as the vertical coordinate with r replaced by the constant value a has an important drawback: the resulting equations do not possess an angular momentum principle, like the one satisfied by the equations in full spherical geometry (Prob. 11.12). On conceptual grounds alone, this is an important deficiency because much of atmospheric dynamics concerns how angular momentum is concentrated into strong jets that characterize the general circulation. The failure of (11.25) to properly represent the angular momentum of individual air parcels follows from an inconsistency in the treatment of horizontal and vertical displacements. Geometric variations in the radial direction are neglected. However, Coriolis and metric terms proportional to $cos\phi$, which accompany radial displacements, are retained.

Terms proportional to $2\Omega cos\phi$ in (11.25) are associated with the horizontal component of planetary vorticity (11.24) and vertical motion. They are much smaller than other terms, so they are often neglected on the basis of scaling arguments (Sec. 11.4). Known as the *traditional approximation* (Eckart, 1960), the neglect of terms proportional to $2\Omega cos\phi$ is formally valid in the limit of strong stratification, wherein

$$\frac{N^2}{\Omega^2} \to \infty. \tag{11.26}$$

Air is then constrained to move quasi-horizontally. This makes the vertical component of planetary vorticity $2\Omega sin\phi$ dominant in the Coriolis acceleration $2\boldsymbol{\Omega} \times \boldsymbol{v}$. For a lapse rate of $\Gamma = 6.5$ K km^{-1}, (7.10) gives N^2 of order 10^{-4} s^{-2} and $\Omega^2 \cong 5\ 10^{-9}$ s^{-2}. Hence $\frac{N^2}{\Omega^2} \cong 2\ 10^4$ is in good agreement with (11.26). On the other hand, weak or unstable stratification is controlled by convection. The latter operates on time scales short enough to render both components of the Coriolis acceleration unimportant.

An alternate derivation of the equations of motion (Phillips, 1966) provides a rationale for neglecting the aforementioned terms. The component equations assume a simpler form if derived from the momentum equations in vector-invariant form. In an inertial reference frame, the vector equations of motion can be expressed

$$\left(\frac{\partial \boldsymbol{v}_i}{\partial t}\right)_i + \nabla\left(\frac{\boldsymbol{v}_i \cdot \boldsymbol{v}_i}{2}\right) + (\nabla \times \boldsymbol{v}_i) \times \boldsymbol{v}_i = -\frac{1}{\rho}\nabla p - g\boldsymbol{k} - \boldsymbol{D}, \tag{11.27.1}$$

where the subscript refers to the velocity and local time rate of change apparent in the inertial frame (Prob. 11.13). Evaluating metric scale factors at $r = a$ before derivatives are applied recovers the vector operations (11.23). Expressing the velocity and time derivative in terms of those apparent in the rotating frame of the Earth gives

$$\boldsymbol{v}_i = \boldsymbol{v} + \Omega a cos\phi \boldsymbol{i} \tag{11.27.2}$$

$$\left(\frac{\partial}{\partial t}\right)_i = \frac{\partial}{\partial t} - \Omega\frac{\partial}{\partial \lambda}. \tag{11.27.3}$$

Then incorporating (11.23) yields the simplified momentum equations

$$\frac{du}{dt} - \left(f + \frac{utan\phi}{a}\right)v = -\frac{1}{\rho a cos\phi}\frac{\partial p}{\partial \lambda} - D_\lambda \tag{11.28.1}$$

$$\frac{dv}{dt} + \left(f + \frac{utan\phi}{a}\right)u = -\frac{1}{\rho a}\frac{\partial p}{\partial \phi} - D_\phi \tag{11.28.2}$$

$$\frac{dw}{dt} = -\frac{1}{\rho}\frac{\partial p}{\partial z} - g - D_z, \tag{11.28.3}$$

where the *Coriolis parameter*

$$f = 2\Omega sin\phi \tag{11.28.4}$$

represents the vertical component of planetary vorticity (Fig. 11.3).

In (11.28), the horizontal momentum equations are free of metric and Coriolis terms proportional to w. The vertical momentum equation is free of all such terms. The preceding system possesses the conservation principle

$$\frac{d}{dt}[(u + \Omega acos\phi)acos\phi] = -acos\phi\left(\frac{1}{\rho acos\phi}\frac{\partial p}{\partial \lambda} + D_{\lambda}\right). \tag{11.29}$$

According to (11.29), the angular momentum of an air parcel changes through the torque about the axis of rotation exerted on it by longitudinal forces (Prob. 11.14). Consistent with the shallow atmosphere approximation, angular momentum is treated as though the air parcel remains at $r = a$.

11.3 SPECIAL FORMS OF MOTION

Certain conditions simplify the governing equations. For *incompressible motion*, the specific volume of an individual air parcel is conserved, so

$$\frac{d\rho}{dt} = 0.$$

Then the continuity equation (11.25.4) reduces to

$$\nabla \cdot \boldsymbol{v} = 0. \tag{11.30}$$

Because ρ is conserved, an air parcel that coincides initially with a particular isochoric surface: ρ = const, remains on that surface – despite movement of that surface. Thus isochoric surfaces are material surfaces (viz. they are comprised of a fixed collection of matter). If the motion is steady, ρ surfaces are also stream surfaces, to which the motion is tangential. These conditions hold automatically for an incompressible fluid like water. They also hold for a compressible fluid like air if the velocity is steady and everywhere orthogonal to the gradient of density. Because large-scale motion is quasi-horizontal, the latter condition is approximately satisfied by the atmospheric circulation.

For *adiabatic motion*, individual air parcels experience no heat transfer with their surroundings (Sec. 3.6.1). The thermodynamic equation (10.38) then reduces to

$$\frac{d\theta}{dt} = 0, \tag{11.31}$$

which asserts that the potential temperature of an air parcel is conserved. Thus an air parcel that coincides initially with an isentropic surface, θ = const, remains on that surface (cf. Fig. 2.9). Isentropic surfaces are material surfaces.

The above are particular examples of a conserved property, which behaves as a material tracer. More generally, a property r that is conserved for individual air parcels obeys the continuity equation

$$\frac{dr}{dt} = 0. \tag{11.32}$$

Mixing ratios of long-lived chemical species approximately satisfy (11.32). The rates of production and destruction of such species formally appear on the right-hand side

of (11.32). However, those processes are much slower than advective changes in the Lagrangian derivative, which are represented on the left-hand side. Water vapor, which is conserved away from cloud and the Earth's surface, behaves in this manner (cf. Fig. 1.18). So does ozone, which, in the lower stratosphere, has a photochemical lifetime of several weeks. Hence, to leading approximation, particular values of mixing ratio track the movement of individual bodies of air. To the same degree of approximation, surfaces $r = \text{const}$ are material surfaces.

11.4 PREVAILING BALANCES

The preceding equations govern motion in a compressible, stratified, and rotating atmosphere. Consequently, they describe a wide range of phenomena. While describing planetary-scale circulations that involve times scales of days and longer, the equations of motion also describe small-scale acoustic waves that have time scales of only fractions of a second. This generality needlessly complicates the description of phenomena that comprise the general circulation. To elucidate essential balances that control large-scale motion, it is useful to examine the relative sizes of various terms.

11.4.1 Motion-related stratification

Stratification is represented in the distributions of pressure and density. It involves two components: (1) a basic component associated with static conditions and (2) a small departure from it that is related exclusively to motion:

$$\begin{aligned} p_{tot} &= p_0(z) + p(\boldsymbol{x}, t) \\ \rho_{tot} &= \rho_0(z) + \rho(\boldsymbol{x}, t), \end{aligned} \tag{11.33}$$

where $\boldsymbol{x} = (x, y, z)$ follows from (11.17). The static components p_0 and ρ_0 are functions of height alone. They are symbolized by global-mean pressure and density. Those components overshadow vertical variations associated with motion. It is therefore useful to eliminate them from the governing equations. What remains is then discriminated to variations that are related directly to motion.

Incorporating (11.33) into the horizontal momentum equation transforms the pressure gradient force into

$$\begin{aligned} -\frac{1}{(\rho_0 + \rho)} \nabla_h (p_0 + p) &\cong -\frac{1}{\rho_0} \left(1 - \frac{\rho}{\rho_0}\right) \nabla_h p \\ &\cong -\frac{1}{\rho_0} \nabla_h p, \end{aligned} \tag{11.34}$$

where ∇_h denotes the horizontal gradient. In (11.34), $\frac{\rho}{\rho_0} \ll 1$ and $\frac{p}{p_0} \ll 1$ have been used, in combination with the binomial expansion, to ignore higher order terms. Because $p_0(z)$ depends on height alone, it drops out of (11.34). The horizontal momentum equations are therefore left in their original form (11.28).

In the vertical momentum equation, the basic components of stratification introduce vertical gradients that cannot be ignored. The right-hand side of (11.28.3) contains the net buoyancy force acting on an air parcel (7.2). Incorporating (11.33) transforms

the buoyancy force into

$$f_b = -\frac{1}{(\rho_0+\rho)}\frac{\partial}{\partial z}(p_0+p) - g \cong -\frac{1}{\rho_0}\left(1-\frac{\rho}{\rho_0}\right)\left(\frac{\partial p_0}{\partial z}+\frac{\partial p}{\partial z}\right) - g$$
$$\cong -\frac{1}{\rho_0}\left(\frac{\partial p}{\partial z}+\rho g\right), \tag{11.35}$$

wherein the basic stratification automatically satisfies hydrostatic equilibrium. The vertical momentum equation then becomes

$$\frac{dw}{dt} = -\frac{1}{\rho_0}\frac{\partial p}{\partial z} - \frac{\rho}{\rho_0}g - D_z. \tag{11.36}$$

11.4.2 Scale analysis

With dependent variables discriminated to motion, terms in the momentum equations may now be evaluated for relative importance. Away from the Earth's surface and regions of organized convection, the frictional drag $\boldsymbol{D}$ is small enough to be ignored. Large-scale atmospheric motion is then characterized by the scales

$$\begin{array}{lll} U = 10\ \text{m s}^{-1} & L = 10^3\ \text{km} & P = 10\ \text{mb} = 10^3\ \text{Pa} \\ W = 10^{-2}\ \text{m s}^{-1} & H = 10\ \text{km} & f_0 = 10^{-4}\ \text{s}^{-1}, \end{array}$$

where U and W refer to horizontal and vertical motion, respectively, L and H are horizontal and vertical length scales that characterize the motion field, and $f_0 = 2\Omega sin\phi_0$ is the planetary vorticity at a representative latitude ϕ_0. The pressure scale P characterizes the departure from static conditions, namely the pressure variation associated directly with motion. If the Lagrangian derivative is dominated by advective changes (e.g., by $\boldsymbol{v}\cdot\nabla$), then $\frac{L}{U}$ represents a time scale for advection that may be used to characterize $\frac{d}{dt}$.

Scaling velocities, lengths, and the Lagrangian derivative by the above (e.g., $u \to Uu$, $x \to Lx$, $\frac{d}{dt} \to \frac{U}{L}\frac{d}{dt}$, with u, x, and $\frac{d}{dt}$ then nondimensional) transforms the horizontal momentum equations (11.28.1) and (11.28.2) into the dimensionless forms

$$Ro\frac{du}{dt} - sin\phi v - Ro\left(\frac{L}{a}\right)tan\phi uv = -\frac{P}{f_0\rho_{00}UL}\cdot\frac{1}{\rho_0}\frac{\partial p}{\partial x} \tag{11.37.1}$$

$$Ro\frac{dv}{dt} + sin\phi u + Ro\left(\frac{L}{a}\right)tan\phi u^2 = -\frac{P}{f_0\rho_{00}UL}\cdot\frac{1}{\rho_0}\frac{\partial p}{\partial y}, \tag{11.37.2}$$

where $\rho_{00} = \rho_0(0)$ and $Ro = U/f_0L$. In (11.37), all variables are nondimensional, of order unity, and are related to their dimensional counterparts through multiplication by the preceding scale factors. The *Rossby number*

$$Ro = \frac{U}{f_0 L} \tag{11.38}$$

is a dimensionless parameter that represents the ratio of the rotational time scale f_0^{-1} to the advective time scale $\frac{L}{U}$.

With the preceding scales, dimensionless factors in (11.37) are characterized by the following orders of magnitude:

$$Ro = 10^{-1} \qquad Ro\left(\frac{L}{a}\right) = 10^{-2} \qquad \frac{P}{f_0\rho_{00}UL} = 1.$$

The horizontal momentum equations are seen to be dominated by a balance between the Coriolis acceleration associated with the vertical component of planetary vorticity and the horizontal pressure-gradient force. Both are of order unity. The material acceleration, which is of order *Ro*, is comparatively small – because advection is slow compared with rotation. It follows that the horizontal motion of air is strongly influenced by rotation. Accelerations associated with metric terms and with vertical advection of momentum in $\frac{d}{dt}$ are even smaller. Those proportional to w that were eliminated in the derivation of (11.28) are much smaller.

Similar treatment transforms the vertical momentum equation (11.36) into the dimensionless form

$$Ro\left(\frac{W}{U}\right)\frac{dw}{dt} = -\left(\frac{L}{H}\right)\frac{P}{f_0\rho_{00}UL}\cdot\frac{1}{\rho_0}\frac{\partial p}{\partial z} - \left(\frac{P}{p_{00}}\right)\frac{g}{f_0U}\cdot\frac{\rho}{\rho_0}, \tag{11.39}$$

where $p_{00} = p_0(0)$. The preceding scales imply the orders of magnitude

$$Ro\left(\frac{W}{U}\right) = 10^{-3} \qquad \left(\frac{L}{H}\right)\frac{P}{f_0\rho_{00}UL} = 10^2 \qquad \left(\frac{P}{p_{00}}\right)\frac{g}{f_0U} = 10^2.$$

For large-scale motion, the vertical momentum equation is dominated by a balance between the vertical pressure-gradient and gravitational forces. Hence, like basic fields, the motion-related component of stratification is in hydrostatic equilibrium. Other vertical forces are much smaller. Vertical forces that balance in hydrostatic equilibrium are also two orders of magnitude stronger than those appearing in the horizontal momentum equations. The disparate magnitudes of those forces reflect the comparative influences of gravity and rotation (11.26).

The preceding analysis allows the equations of motion to be simplified. Inclusive of the basic stratification, the dimensional equations governing large-scale atmospheric motion in spherical coordinates then become

$$\frac{du}{dt} - \left(f + \frac{utan\phi}{a}\right)v = -\frac{1}{\rho acos\phi}\frac{\partial p}{\partial \lambda} - D_\lambda \tag{11.40.1}$$

$$\frac{dv}{dt} + \left(f + \frac{utan\phi}{a}\right)u = -\frac{1}{\rho a}\frac{\partial p}{\partial \phi} - D_\phi \tag{11.40.2}$$

$$\frac{1}{\rho}\frac{\partial p}{\partial z} = -g, \tag{11.40.3}$$

$$\frac{d\rho}{dt} + \rho\nabla\cdot\boldsymbol{v} = 0 \tag{11.40.4}$$

$$\rho c_v\frac{dT}{dt} + p\nabla\cdot\boldsymbol{v} = \dot{q}_{net}. \tag{11.40.5}$$

Known as the *primitive equations*, (11.24) represent the starting point for descriptions of large-scale atmospheric motion. Metric terms proportional to $tan\phi$ and horizontal drag have been retained in (11.40). However, although often included in numerical integrations, they are small enough to be ignored for many applications. In chemical considerations, the primitive equations are augmented by continuity equations of the form

$$\frac{dr_i}{dt} = \dot{P}_i - \dot{D}_i \tag{11.40.6}$$

for the mixing ratio of the ith species, where $\dot{P}_i$ and $\dot{D}_i$ denote the local rates of production and destruction of that species.

The governing equations must be closed with boundary conditions. Spherical geometry is periodic, so cyclic continuity suffices for horizontal boundary conditions. Vertical boundary conditions constrain the vertical velocity. At the ground, air motion must be tangential to the Earth's surface, which has elevation $z_s(\lambda, \phi, t)$.[2] This is equivalent to requiring an air parcel that is initially in contact with the Earth's surface to track along that elevation:

$$\begin{aligned} w &= \frac{dz}{dt} \\ &= \frac{dz_s}{dt}, \end{aligned} \tag{11.41}$$

where $\frac{d}{dt}$ is given by (11.25.6).[3] In the presence of viscosity, air motion must also satisfy the *no-slip condition*, which requires all components of the velocity at the surface to vanish. Upper boundary conditions are more difficult to apply because the atmosphere is unbounded. Nevertheless, similar constraints are often imposed at a finite height.

11.5 THERMODYNAMIC COORDINATES

11.5.1 Isobaric coordinates

Because they involve hydrostatic equilibrium, the primitive equations simplify when formulated with pressure as the vertical coordinate. Hence we consider a transformation from the standard spherical coordinates $\boldsymbol{x} = (x, y, z)$ given by (11.17) to the modified coordinates $\boldsymbol{x}_p = (x, y, p)$. Isobaric surfaces $p = \text{const}$ then replace constant height surfaces $z = \text{const}$ as coordinate surfaces. Horizontal derivatives must therefore be evaluated along isobaric surfaces. Using p as a vertical coordinate is possible because hydrostatic equilibrium (11.40.3) ensures that pressure decreases upward monotonically. p is therefore a single-valued function of z.

In casting the equations into isobaric coordinates, the variables p and z are interchanged. Pressure then becomes the independent variable and z becomes the dependent variable. For a specified pressure, $z(p)$ represents the height of an isobaric surface. It is contoured in Fig. 1.9. Isobaric surfaces are not perpendicular to other coordinate surfaces. Therefore, this representation is not an orthogonal coordinate system.

Consider a scalar quantity

$$\psi(x, y, z, t) = \hat{\psi}\Big(x, y, p(x, y, z, t), t\Big). \tag{11.42}$$

Hereafter, the caret will be omitted with the pressure dependence understood. By the chain rule, the vertical derivative can be expressed

$$\left(\frac{\partial \psi}{\partial z}\right)_{xyt} = \left(\frac{\partial \psi}{\partial p}\right)_{xyt} \left(\frac{\partial p}{\partial z}\right)_{xyt}, \tag{11.43}$$

[2] The lower boundary condition may be applied on a surface internal to the atmosphere, in which case the elevation is time-dependent.

[3] Even though an air parcel at the ground must remain in contact with that boundary, neighboring parcels can undergo large vertical displacements through deformation of finite bodies of air (e.g., in convection; cf. Fig. 5.4).

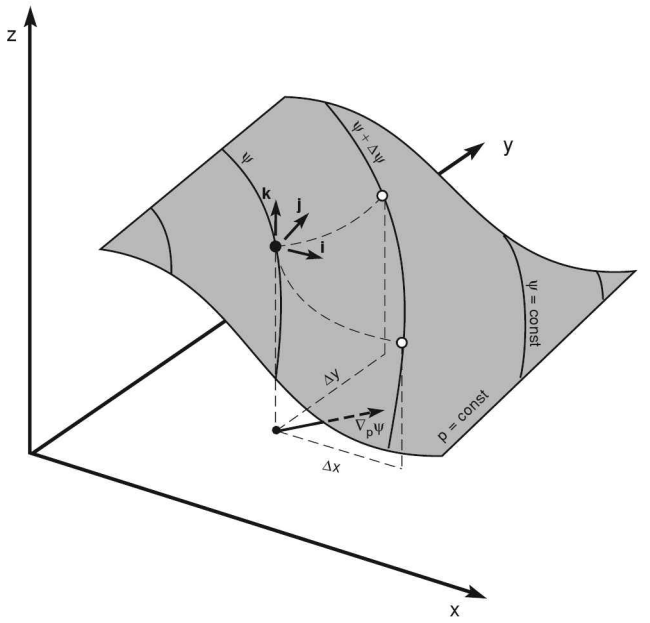

Figure 11.4 Variation of property ψ along an isobaric surface. Horizontal derivatives $(\frac{\partial\psi}{\partial x})_{ypt} = \lim_{\Delta x\to 0} \frac{\Delta\psi}{\Delta x}$ and $(\frac{\partial\psi}{\partial y})_{xpt} = \lim_{\Delta y\to 0} \frac{\Delta\psi}{\Delta y}$ are evaluated with changes of ψ along the isobaric surface $p = \text{const}$. (For clarity, Δx and Δy have been chosen to place the incremented values of ψ on the same contour.) Those derivatives define the horizontal gradient evaluated along the isobaric surface $\nabla_p\psi = (\frac{\partial\psi}{\partial x})_{ypt}\boldsymbol{i} + (\frac{\partial\psi}{\partial y})_{xpt}\boldsymbol{j}$, which lies in the horizontal plane but reflects how ψ varies along the isobaric surface.

where subscripts denote variables that are held fixed. Likewise, differentiation with respect to x becomes

$$\left(\frac{\partial\psi}{\partial x}\right)_{yzt} = \left(\frac{\partial\psi}{\partial x}\right)_{ypt} + \left(\frac{\partial\psi}{\partial p}\right)_{xyt}\left(\frac{\partial p}{\partial x}\right)_{yzt}$$

and similarly for differentiation with respect to y. Thus, the horizontal gradient evaluated on surfaces of constant height, ∇_z, translates into

$$\nabla_z\psi = \nabla_p\psi + \left(\frac{\partial\psi}{\partial p}\right)_{xyt}\nabla_z p, \tag{11.44.1}$$

where

$$\nabla_p = \left(\frac{\partial}{\partial x}\right)_{ypt}\boldsymbol{i} + \left(\frac{\partial}{\partial y}\right)_{xpt}\boldsymbol{j} \tag{11.44.2}$$

denotes the horizontal gradient evaluated on an isobaric surface (Fig. 11.4). The local time derivative becomes

$$\left(\frac{\partial\psi}{\partial t}\right)_{xyz} = \left(\frac{\partial\psi}{\partial t}\right)_{xyp} + \left(\frac{\partial\psi}{\partial p}\right)_{xyt}\left(\frac{\partial p}{\partial t}\right)_{xyz}. \tag{11.45}$$

Incorporating the above expressions transforms the Lagrangian derivative into

$$\begin{aligned}\frac{d\psi}{dt} &= \left(\frac{\partial\psi}{\partial t}\right)_{xyp} + \boldsymbol{v}_h\cdot\nabla_p\psi + \left(\frac{\partial\psi}{\partial p}\right)_{xyt}\left[\left(\frac{\partial p}{\partial t}\right)_{xyz} + \boldsymbol{v}_h\cdot\nabla_z p + w\left(\frac{\partial p}{\partial z}\right)_{xyt}\right] \\ &= \left(\frac{\partial\psi}{\partial t}\right)_{xyp} + \boldsymbol{v}_h\cdot\nabla_p\psi + \frac{dp}{dt}\left(\frac{\partial\psi}{\partial p}\right)_{xyt},\end{aligned} \tag{11.46}$$

where

$$\boldsymbol{v}_h = u\boldsymbol{i} + v\boldsymbol{j} \tag{11.47}$$

denotes horizontal velocity. From (11.44.2), the second term in (11.46) represents horizontal advective changes evaluated on an isobaric surface.[4] The third term has the form of vertical advection if

$$\omega = \frac{dp}{dt} \tag{11.48}$$

is identified as the vertical velocity in pressure coordinates. With p as the vertical coordinate, ω denotes the Lagrangian derivative of vertical position. It is positive in the direction of increasing p (i.e., *downward*). In isolation, ω does not have dimensions of velocity. Nonetheless, the product $\omega\frac{\partial\psi}{\partial p}$ has dimensions of vertical advection of the property ψ. The material derivative may then be expressed

$$\begin{aligned}\frac{d\psi}{dt} &= \frac{\partial\psi}{\partial t} + (\boldsymbol{v}\cdot\nabla\psi)_p \\ &= \frac{\partial\psi}{\partial t} + \boldsymbol{v}_h\cdot\nabla_p\psi + \omega\frac{\partial\psi}{\partial p},\end{aligned} \tag{11.49}$$

in which p is held fixed unless otherwise noted and $(\boldsymbol{v}\cdot\nabla\psi)_p$ denotes 3-dimensional advection of ψ in pressure coordinates.

Letting $\psi = z(x, y, p, t)$ in (11.43) and (11.44), which for fixed p represents the height of an isobaric surface, obtains

$$\frac{\partial z}{\partial z} = 1$$

$$\nabla_z z = \left(\frac{\partial z}{\partial x}\right)_{yzt}\boldsymbol{i} + \left(\frac{\partial z}{\partial y}\right)_{xzt}\boldsymbol{j} = 0.$$

Then (11.43) reduces to the simple reciprocal property

$$\begin{aligned}\left(\frac{\partial z}{\partial p}\right)^{-1} &= \frac{\partial p}{\partial z} \\ &= -\rho g.\end{aligned} \tag{11.50.1}$$

This relationship was foreshadowed earlier by the Jacobian (11.10) for transformations that involve the vertical coordinate alone. Similarly, (11.44) reduces to

$$\begin{aligned}\nabla_z p &= -\left(\frac{\partial z}{\partial p}\right)^{-1}\nabla_p z \\ &= \rho g\nabla_p z.\end{aligned} \tag{11.50.2}$$

[4] Not to be confused with advective changes introduced by motion along that surface.

Incorporating (11.50.2) into the horizontal momentum equation transforms the pressure gradient force into

$$\begin{aligned} -\frac{1}{\rho}\nabla_z p &= -g\nabla_p z \\ &= -\nabla_p \Phi, \end{aligned} \tag{11.51}$$

where the geopotential Φ is given by (6.7). Then, with (11.49), the horizontal momentum equations become

$$\frac{\partial \boldsymbol{v}_h}{\partial t} + (\boldsymbol{v}\cdot\nabla\boldsymbol{v}_h)_p + \left(f + u\frac{tan\phi}{a}\right)\boldsymbol{k}\times\boldsymbol{v}_h = -\nabla_p\Phi - \boldsymbol{D}_h, \tag{11.52}$$

where $\boldsymbol{D}_h$ denotes the horizontal component of drag. Simple substitution transforms the hydrostatic equation into

$$\begin{aligned} \frac{\partial \Phi}{\partial p} &= -\alpha \\ &= -\frac{RT}{p}. \end{aligned} \tag{11.53}$$

The continuity equation follows from its expression in terms of specific volume. In isobaric coordinates, (10.31) becomes

$$\frac{d\alpha_p}{dt} = \alpha_p(\nabla\cdot\boldsymbol{v})_p, \tag{11.54.1}$$

where α_p refers to the incremental material volume between isobaric surfaces, dV_p, and

$$(\nabla\cdot\boldsymbol{v})_p = \nabla_p\cdot\boldsymbol{v}_h + \frac{\partial\omega}{\partial p}. \tag{11.54.2}$$

Then (11.6) implies

$$\alpha_p = J(\boldsymbol{x},\boldsymbol{x}_p)\alpha. \tag{11.55}$$

According to (11.9),

$$\begin{aligned} J(\boldsymbol{x},\boldsymbol{x}_p) &= \left|\frac{\partial p}{\partial z}\right| \\ &= \rho g. \end{aligned} \tag{11.56}$$

Hence,

$$\begin{aligned} \alpha_p &= \rho\alpha\cdot g \\ &= g. \end{aligned} \tag{11.57}$$

It follows that

$$\frac{d\alpha_p}{dt} = 0, \tag{11.58}$$

which asserts that the material volume in isobaric coordinates is conserved. The continuity equation (11.54) then reduces to

$$\nabla_p\cdot\boldsymbol{v}_h + \frac{\partial\omega}{\partial p} = 0. \tag{11.59}$$

In isobaric coordinates, the continuity equation has the same form as that for incompressible motion (11.30).

The thermodynamic equation can be developed from the First Law for an individual air parcel (2.22), which implies

$$c_p \frac{dT}{dt} - \alpha \frac{dp}{dt} = \dot{q}_{net}. \tag{11.60}$$

With (11.49), this becomes

$$\frac{\partial T}{\partial t} + (\boldsymbol{v}_h \cdot \nabla T)_p - \frac{\alpha\omega}{c_p} = \frac{\dot{q}_{net}}{c_p}. \tag{11.61.1}$$

Expansion work is seen to be proportional to the velocity across isobaric surfaces. As before, the thermodynamic equation assumes a more compact form when expressed in terms of potential temperature:

$$\frac{\partial \theta}{\partial t} + (\boldsymbol{v}_h \cdot \nabla \theta)_p = \frac{\theta}{c_p T} \dot{q}_{net}, \tag{11.61.2}$$

derivation of which is left as an exercise. Expansion work is thus absorbed into θ.

Collectively, the equations of motion in isobaric coordinates are then given by

$$\frac{d\boldsymbol{v}_h}{dt} + \left(f + u\frac{tan\phi}{a} \right) \boldsymbol{k} \times \boldsymbol{v}_h = -\nabla_p \Phi - \boldsymbol{D}_h \tag{11.62.1}$$

$$-\frac{\partial \Phi}{\partial ln p} = RT \tag{11.62.2}$$

$$(\nabla \cdot \boldsymbol{v})_p = 0 \tag{11.62.3}$$

$$\frac{d\theta}{dt} = \frac{\theta}{c_p T} \dot{q}_{net}, \tag{11.62.4}$$

with

$$\frac{d}{dt} = \frac{\partial}{\partial t} + \boldsymbol{v}_h \cdot \nabla_p + \omega \frac{\partial}{\partial p}. \tag{11.62.5}$$

The lower boundary condition requires air to maintain the surface elevation z_s, so

$$\frac{d\Phi}{dt} = g\frac{dz_s}{dt} \tag{11.63}$$

at $p = p_s(x, y, t)$.

Transforming the equations into this coordinate system yields the following simplifications:

(1) The pressure gradient force has been linearized through elimination of ρ.

(2) The continuity equation has reduced to a statement of 3-dimensional nondivergence. In addition to being linear, it is now "diagnostic" (i.e., it involves no time derivatives).

These simplifications are not acquired without a price. Coordinate surfaces $p =$ const are now time dependent. Their positions evolve with the circulation. Further, isobaric surfaces need not coincide with the Earth's surface. The lower boundary condition

(11.63) then involves different values of the vertical coordinate $p = p_s(x, y, t)$, complicating its application.

Complications in the lower boundary condition can be averted by introducing the modified pressure coordinate

$$\sigma = \frac{p}{p_s}. \tag{11.64}$$

Unlike p, σ preserves a constant value at the Earth's surface. Transforming to *σ-coordinates* passes the complication of the lower boundary condition into the governing equations. Nevertheless, σ-coordinates offer computational advantages. They are relied upon in GCMs; see Haltiner and Williams (1980) for a formal development.

11.5.2 Log-pressure coordinates

Combining some of the benefits of height and pressure is the modified vertical coordinate

$$z^* = -H ln\left(\frac{p}{p_{00}}\right), \tag{11.65.1}$$

where

$$H = \frac{RT_0}{g} \tag{11.65.2}$$

is treated as constant. At this level of approximation, the basic pressure and density that correspond to static conditions reduce to

$$\begin{aligned} p_0(z^*) &= p_0(0)e^{-\frac{z^*}{H}} \\ \rho_0(z^*) &= \rho_0(0)e^{-\frac{z^*}{H}}. \end{aligned} \tag{11.66}$$

Log-pressure height is formally constant on isobaric surfaces. It is based on the stratification under static conditions, namely on global-mean properties that vary only with height. For this reason, log-pressure height is an approximation to geopotential height. Because variations of H are comparatively small, so are discrepancies between z^* and z. Under isothermal conditions, the two measures of elevation are identical.

In terms of z^*, the hydrostatic equation becomes

$$\frac{\partial \Phi}{\partial z^*} = \frac{RT}{H}. \tag{11.67}$$

The vertical velocity in log-pressure coordinates is given by

$$\begin{aligned} w^* &= \frac{dz^*}{dt} \\ &= -\frac{H}{p}\frac{dp}{dt} = -\frac{H}{p}\omega. \end{aligned} \tag{11.68}$$

Then the Lagrangian derivative translates into

$$\frac{d}{dt} = \frac{\partial}{\partial t} + \boldsymbol{v}_h \cdot \nabla_{z^*} + w^*\frac{\partial}{\partial z^*}, \tag{11.69}$$

where ∇_{z^*} reflects the horizontal gradient evaluated on an isobaric surface. Likewise, vertical divergence in pressure coordinates becomes

$$\begin{aligned}\frac{\partial \omega}{\partial p} &= \frac{\partial w^*}{\partial z^*} - \frac{w^*}{H} \\ &= \frac{1}{\rho_0}\frac{\partial}{\partial z^*}\left(\rho_0 w^*\right).\end{aligned} \tag{11.70}$$

It transforms the continuity equation into

$$\nabla_{z^*} \cdot \boldsymbol{v}_h + \frac{1}{\rho_0}\frac{\partial}{\partial z^*}\left(\rho_0 w^*\right) = 0. \tag{11.71}$$

The thermodynamic equation is transformed in similar fashion and is left as an exercise.

With the foregoing expressions, the equations of motion in log-pressure coordinates become

$$\frac{d\boldsymbol{v}_h}{dt} + \left(f + u\frac{tan\phi}{a}\right)\boldsymbol{k} \times \boldsymbol{v}_h = -\nabla_{z^*}\Phi - \boldsymbol{D}_h \tag{11.72.1}$$

$$\frac{\partial \Phi}{\partial z^*} = \frac{RT}{H} \tag{11.72.2}$$

$$\nabla_{z^*} \cdot \boldsymbol{v}_h + \frac{1}{\rho_0}\frac{\partial}{\partial z^*}\left(\rho_0 w^*\right) = 0 \tag{11.72.3}$$

$$\left(\frac{\partial}{\partial t} + \boldsymbol{v}_h \cdot \nabla_{z^*}\right)\left(\frac{\partial \Phi}{\partial z^*}\right) + N^{*^2} w^* = \frac{\kappa}{H}\dot{q}_{net}, \tag{11.72.4}$$

where

$$\frac{d}{dt} = \frac{\partial}{\partial t} + \boldsymbol{v}_h \cdot \nabla_{z^*} + w^*\frac{\partial}{\partial z^*} \tag{11.72.5}$$

and

$$N^{*^2} = \frac{R}{H}\left(\frac{\partial T}{\partial z^*} + \frac{\kappa}{H}T\right) \tag{11.72.6}$$

represents the static stability in log-pressure coordinates. In the troposphere, N^{*^2} varies with height only weakly. To leading order, it can therefore be treated as constant. The lower boundary condition requires geometric vertical velocity to be specified (11.63). It becomes

$$\frac{\partial \Phi}{\partial t} + \boldsymbol{v}_h \cdot \nabla_{z^*}\Phi + \frac{RT}{H}w^* = g\frac{dz_s}{dt}. \tag{11.73}$$

At the level of approximation inherent to log-pressure coordinates, this may be evaluated at the constant elevation $z^* = z_s^*$, but with variations of z_s^* accounted for in the right-hand side of (11.73).

The equations in log-pressure coordinates have several advantages. Variables are analogous to those in physical coordinates, so they are easily interpreted. Yet, the pressure-gradient force, hydrostatic equation, and continuity equation retain nearly the same simplified forms as in isobaric coordinates. In addition, mathematical complications surrounding comparatively small variations of temperature are ignored.

11.5.3 Isentropic coordinates

The nearly adiabatic nature of air motion simplifies the governing equations when θ is treated as the vertical coordinate. Isentropic surfaces are then coordinate surfaces. Large-scale air motion is nearly tangential to them (Fig. 2.9).

We consider a transformation from the standard spherical coordinates $\boldsymbol{x} = (x, y, z)$ to the modified coordinates $\boldsymbol{x}_\theta = (x, y, \theta)$. For it to serve as a vertical coordinate, potential temperature must vary monotonically with altitude. Hydrostatic stability requires $\frac{\partial\theta}{\partial z} > 0$. The relationship between potential temperature and height is then single valued – so long as the stratification remains stable. As is true for isobaric coordinates, using isentropic surfaces as coordinate surfaces leads to a coordinate system that is nonorthogonal.

Consider the scalar variable

$$\psi = \hat{\psi}\Big(x, y, \theta(x, y, z, t), t\Big). \tag{11.74}$$

Proceeding as in the development of (11.43) and (11.44) transforms vertical and horizontal derivatives into

$$\frac{\partial\psi}{\partial z} = \frac{\partial\psi}{\partial\theta}\frac{\partial\theta}{\partial z} \tag{11.75.1}$$

$$\nabla_z\psi = \nabla_\theta\psi + \frac{\partial\psi}{\partial\theta}\nabla_z\theta, \tag{11.75.2}$$

where θ is held fixed unless otherwise noted and

$$\nabla_\theta = \left(\frac{\partial}{\partial x}\right)_{y\theta t}\boldsymbol{i} + \left(\frac{\partial}{\partial y}\right)_{x\theta t}\boldsymbol{j} \tag{11.75.3}$$

represents the horizontal gradient evaluated on an isentropic surface. Then the Lagrangian derivative becomes

$$\begin{aligned}\frac{d\psi}{dt} &= \frac{\partial\psi}{\partial t} + (\boldsymbol{v}\cdot\nabla\psi)_\theta \\ &= \frac{\partial\psi}{\partial t} + \boldsymbol{v}_h\cdot\nabla_\theta\psi + \frac{d\theta}{dt}\frac{\partial\psi}{\partial\theta}.\end{aligned} \tag{11.76}$$

As before, we identify

$$\omega_\theta = \frac{d\theta}{dt} \tag{11.77}$$

as the vertical velocity in potential temperature coordinates. Positive upwards, ω_θ represents the Lagrangian derivative of vertical position in this coordinate system.

Letting $\psi = z(x, y, \theta, t)$ in (11.75), which for fixed θ represents the height of an isentropic surface, leads to the identities

$$\frac{\partial\theta}{\partial z} = \left(\frac{\partial z}{\partial\theta}\right)^{-1} \tag{11.78.1}$$

$$\nabla_\theta z = -\frac{\partial z}{\partial\theta}\nabla_z\theta. \tag{11.78.2}$$

Then substituting (11.78.2) transforms (11.75.2) into

$$\nabla_z\psi = \nabla_\theta\psi - \frac{\partial\psi}{\partial z}\nabla_\theta z. \tag{11.79}$$

Taking $\psi = p$ and incorporating (11.79) transforms the pressure-gradient force in the horizontal momentum equations into

$$\begin{aligned} -\frac{1}{\rho}\nabla_z p &= -\frac{1}{\rho}\nabla_\theta p + \frac{1}{\rho}\frac{\partial p}{\partial z}\nabla_\theta z \\ &= -\frac{1}{\rho}\nabla_\theta p - g\nabla_\theta z. \end{aligned} \tag{11.80}$$

Now Poisson's relationship for potential temperature (2.31) implies the identity

$$ln\theta = lnT - \kappa(lnp - lnp_0).$$

Applying the horizontal gradient evaluated on an isentropic surface obtains

$$\begin{aligned} c_p\nabla_\theta T &= \frac{RT}{p}\nabla_\theta p \\ &= \frac{1}{\rho}\nabla_\theta p. \end{aligned} \tag{11.81}$$

Then the pressure gradient force (11.80) reduces to

$$\begin{aligned} -\frac{1}{\rho}\nabla_z p &= -c_p\nabla_\theta T - g\nabla_\theta z \\ &= -\nabla_\theta \Psi. \end{aligned} \tag{11.82}$$

The *Montgomery streamfunction*

$$\begin{aligned} \Psi &= c_p T + gz \\ &= c_p T + \Phi \end{aligned} \tag{11.83}$$

plays a role in isentropic coordinates analogous to the role in isobaric coordinates played by geopotential. With (11.82) and (11.76), the horizontal momentum equations become

$$\frac{\partial \boldsymbol{v}_h}{\partial t} + (\boldsymbol{v}\cdot\nabla\boldsymbol{v}_h)_\theta + \left(f + u\frac{tan\phi}{a}\right)\boldsymbol{k}\times\boldsymbol{v}_h = -\nabla_\theta\Psi - \boldsymbol{D}_h. \tag{11.84}$$

To transform the hydrostatic equation, we consider (11.75.1) with $\psi = p$, which gives

$$-\rho g\frac{\partial z}{\partial\theta} = \frac{\partial p}{\partial\theta}. \tag{11.85}$$

Poisson's relationship implies

$$\frac{1}{\theta} = \frac{1}{T}\frac{\partial T}{\partial\theta} - \frac{\kappa}{p}\frac{\partial p}{\partial\theta}.$$

Then substituting into (11.85) obtains

$$c_p\frac{\partial T}{\partial\theta} + g\frac{\partial z}{\partial\theta} = \frac{c_p T}{\theta}$$

or

$$\frac{\partial\Psi}{\partial\theta} = c_p\left(\frac{p}{p_0}\right)^\kappa, \tag{11.86}$$

which serves as the hydrostatic equation in isentropic coordinates.

The continuity equation follows from its expression in terms of specific volume. In isentropic coordinates, this becomes

$$\frac{d\alpha_\theta}{dt} = \alpha_\theta (\nabla \cdot \boldsymbol{v})_\theta, \tag{11.87.1}$$

where α_θ refers to the incremental material volume between isentropic surfaces, dV_θ, and

$$(\nabla \cdot \boldsymbol{v})_\theta = \nabla_\theta \cdot \boldsymbol{v}_h + \frac{\partial \omega_\theta}{\partial \theta}. \tag{11.87.2}$$

According to (11.6),

$$\alpha_\theta = J(\boldsymbol{x}, \boldsymbol{x}_\theta)\alpha, \tag{11.88}$$

where

$$J(\boldsymbol{x}, \boldsymbol{x}_\theta) = \left| \frac{\partial \theta}{\partial z} \right|. \tag{11.89}$$

Incorporating (11.85), with (11.78.1), obtains

$$\begin{aligned} \alpha_\theta &= \rho\alpha \cdot g \left(\frac{\partial p}{\partial \theta} \right)^{-1} \\ &= g \left(\frac{\partial p}{\partial \theta} \right)^{-1}. \end{aligned} \tag{11.90}$$

Then the continuity equation (11.87) reduces to

$$\frac{d}{dt} \left(\frac{\partial p}{\partial \theta} \right)^{-1} = \left(\frac{\partial p}{\partial \theta} \right)^{-1} (\nabla \cdot \boldsymbol{v})_\theta,$$

or

$$\frac{d}{dt} \left(\frac{\partial p}{\partial \theta} \right) + \left(\frac{\partial p}{\partial \theta} \right) (\nabla \cdot \boldsymbol{v})_\theta = 0. \tag{11.91}$$

If $(\frac{\partial p}{\partial \theta})$ is identified with density, then (11.91) has the same form as the continuity equation in physical coordinates (11.25). The thermodynamic equation also has the same form as earlier.

Collectively, the equations of motion in isentropic coordinates are then given by

$$\frac{d\boldsymbol{v}_h}{dt} + \left(f + u\frac{tan\phi}{a} \right) \boldsymbol{k} \times \boldsymbol{v}_h = -\nabla_\theta \Psi - \boldsymbol{D}_h \tag{11.92.1}$$

$$\frac{\partial \Psi}{\partial \theta} = c_p \left(\frac{p}{p_0} \right)^\kappa \tag{11.92.2}$$

$$\frac{d}{dt} \left(\frac{\partial p}{\partial \theta} \right) + \left(\frac{\partial p}{\partial \theta} \right) (\nabla \cdot \boldsymbol{v})_\theta = 0 \tag{11.92.3}$$

$$\omega_\theta = \frac{\theta}{c_p T} \dot{q}_{net}, \tag{11.92.4}$$

with

$$\frac{d}{dt} = \frac{\partial}{\partial t} + \boldsymbol{v}_h \cdot \nabla_\theta + \omega_\theta \frac{\partial}{\partial \theta}. \tag{11.92.5}$$

The lower boundary condition becomes

$$\frac{d\Psi}{dt} - \frac{d}{dt}\left(\theta \frac{\partial \Psi}{\partial \theta}\right) = g\frac{dz_s}{dt}. \tag{11.93}$$

These equations simplify the description of vertical motion, which is related directly to the rate at which heat is absorbed by an air parcel (11.92.4). Under adiabatic conditions, air motion is tangential to coordinate surfaces. ω_θ and vertical advection then vanish. Under diabatic conditions, the system is still advantageous because it relates vertical motion (difficult to measure because of its smallness) to quantities that are determined more reliably.

Another advantage of isentropic coordinates is enhanced resolution in regions of strong temperature gradient, as typify frontal zones. Figure 11.5 displays a frontal zone, represented in isobaric and isentropic coordinates. In the isobaric representation (Fig. 11.5a), motion and potential temperature vary sharply across the frontal zone. Representing those properties numerically therefore requires high resolution. The fine computational mesh, in turn, requires a short time step. Together, these requirements sharply magnify the computational burden necessary to treat such behavior. The sharp gradients in Fig. 11.5 develop through flow deformation (Sec. 10.2). During the amplification of synoptic weather systems (Chap. 16), it concentrates θ surfaces into a narrow zone. Such deformation, however, proceeds under nearly adiabatic conditions. It is therefore absorbed into the representation in isentropic coordinates. In that representation, θ surfaces maintain a fixed separation. This feature of isentropic coordinates magnifies the region of sharp behavior (Fig. 11.5b). Properties therefore vary smoothly, limiting the computational burden necessary to treat such behavior. Although offering these advantages, isentropic coordinates make the continuity equation more complex. They also suffer from variations of θ along the Earth's surface, which complicate the lower boundary condition.

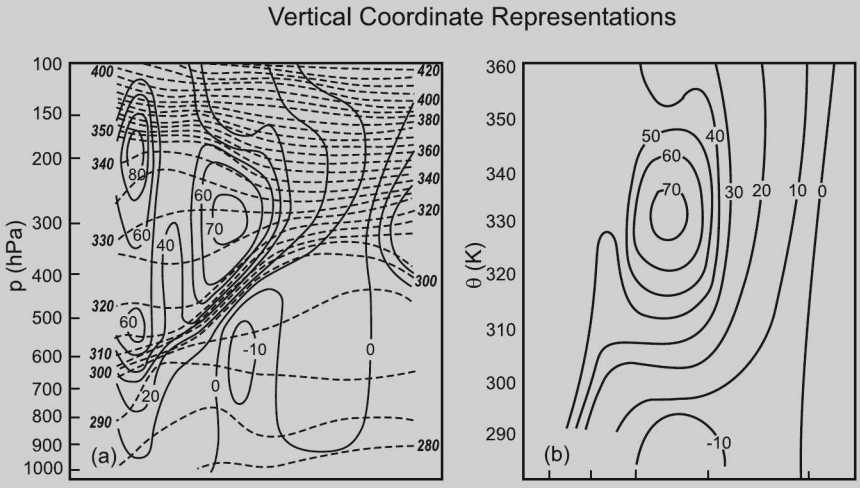

Figure 11.5 Cross section of isotachs (solid) and isentropes (dashed) through a frontal zone represented in (a) isobaric coordinates and (b) isentropic coordinates. *Sources*: Shapiro and Hastings (1973) and R. Bleck (U. Miami), personal communication.

SUGGESTED REFERENCES

Vectors, Tensors, and the Basic Equations of Fluid Mechanics (1962) by Aris provides a complete treatment of curvilinear coordinates.

A treatment of generalized vertical coordinates is given in *The Ceaseless Wind* (1986) by Dutton. Their advantages in numerical applications are developed in Bleck (1978a,b).

Numerical Prediction and Dynamic Meteorology (1980) by Haltiner and Williams describes σ coordinates and their application in large-scale simulations.

PROBLEMS

1. Show that spherical coordinates are expressed in terms of the rectangular Cartesian coordinates by (11.13).
2. Show that metric scale factors for spherical coordinates are given by (11.14).
3. In isobaric coordinates, (a) derive the thermodynamic equation in terms of potential temperature (11.61.2), (b) express the vertical velocity ω in terms of the geometric vertical velocity w, and (c) for $\omega = 100$ hPa day^{-1} at 500 hPa, estimate w.
4. Show that isochoric surfaces are material if the motion is steady and $\boldsymbol{v}$ is everywhere orthogonal to $\nabla\rho$.
5. (a) For a characteristic velocity of 10 m s^{-1}, at what horizontal scale does the Earth's rotation become important? (b) How will the Earth's rotation be manifested in the streamlines of steady flow?
6. The *geostrophic wind* $\boldsymbol{v}_g$ is the horizontal velocity that follows from a balance between the Coriolis and pressure-gradient forces. Provide expressions for u_g and v_g in (a) isobaric coordinates and (b) isentropic coordinates. (c) How does $\boldsymbol{v}_g$ behave as the equator is approached?
7. Use the result in Prob. 11.6, along with the hydrostatic equation, to derive an expression in isobaric coordinates for the vertical variation of geostrophic wind.
8. Isentropic surfaces slope meridionally more steeply than isobaric surfaces. Use the surface temperature in Fig. 10.1b and a uniform lapse rate of 6.5 K km^{-1} to estimate the heights over the equator and pole of (a) the 300 K isentropic surface and (b) the 700 mb isobaric surface.
9. Derive the thermodynamic equation in log-pressure coordinates (11.72.4).
10. Show that the Jacobian reduces to the product of the metric scale factors (11.7) if the curvilinear coordinate system is orthogonal.
11. (a) Show that the spherical coordinate vectors are expressed in terms of the Cartesian coordinate vectors by (11.20). (b) Then show that the spherical coordinate vectors have spatial derivatives

$$\frac{\partial \boldsymbol{i}}{\partial \lambda} = \sin\phi\,\boldsymbol{j} - \cos\phi\,\boldsymbol{k} \qquad \frac{\partial \boldsymbol{i}}{\partial \phi} = 0 \qquad \frac{\partial \boldsymbol{i}}{\partial z} = 0$$

$$\frac{\partial \boldsymbol{j}}{\partial \lambda} = -\sin\phi\,\boldsymbol{i} \qquad \frac{\partial \boldsymbol{j}}{\partial \phi} = -\boldsymbol{k} \qquad \frac{\partial \boldsymbol{j}}{\partial z} = 0$$

$$\frac{\partial \boldsymbol{k}}{\partial \lambda} = \cos\phi\,\boldsymbol{i} \qquad \frac{\partial \boldsymbol{k}}{\partial \phi} = \boldsymbol{j} \qquad \frac{\partial \boldsymbol{k}}{\partial z} = 0.$$

(Hint: Obtain reciprocal identities for $\boldsymbol{e}_1$, $\boldsymbol{e}_2$, and $\boldsymbol{e}_3$ in terms of $\boldsymbol{i}$, $\boldsymbol{j}$, and $\boldsymbol{k}$.) (c) Evaluate the Lagrangian derivatives of the spherical coordinate vectors to obtain (11.21).

12. Derive the angular momentum principle implied by the vector equations of motion in full spherical geometry.
13. Show that the equations of motion in an inertial reference frame are expressed by (11.27). (Hint: See Prob. 10.9).
14. Show that the approximate system (11.28) has the angular momentum principle (11.29).
15. The equations of motion are expressed conveniently in terms of the *Exner function* $\pi = c_p(\frac{p}{p_0})^\kappa$ as the vertical coordinate, where $p_0 = 1000$ hPa. Transform the equations from isobaric coordinates to Exner coordinates.
16. Frictional drag beneath a cyclone produces horizontal convergence, which varies with height inside the planetary boundary layer as

$$-\nabla \cdot \boldsymbol{v}_h = \zeta e^{-\frac{z^*}{h}},$$

where $\zeta = (\nabla \times \boldsymbol{v}_g) \cdot \boldsymbol{k}$ is the (constant) vorticity of the geostrophic wind above the boundary layer and z^* is log-pressure height (Prob 11.6). (a) Determine the vertical motion as a function of height if $\frac{h}{H} \ll 1$. (b) Describe the divergent component of motion which must exist above the boundary layer ($z^* \gg h$) if, at sufficient height, vertical motion eventually vanishes.

CHAPTER

TWELVE

Large-scale motion

Scale analysis indicates that large-scale motion is dominated by a balance between the Coriolis acceleration and the pressure-gradient force (11.37). Material acceleration is of order Rossby number, denoted $O(Ro)$. It is an order of magnitude smaller than the dominant terms. Metric terms are even smaller. The horizontal momentum equations can therefore be expressed in terms of the horizontal velocity v_h

$$\frac{d\boldsymbol{v}_h}{dt} + f\boldsymbol{k}\times\boldsymbol{v}_h = -\nabla_p\Phi - \boldsymbol{D}. \tag{12.1}$$

We use the prevalence of certain terms in (12.1) to illustrate the essential balances that control large-scale motion. In the framework of asymptotic series representation, dependent variables in (12.1) can be expanded in a power series in the small parameter Ro. The momentum equations can then be balanced with the expansion in Ro truncated to the gravest terms. In principle, this procedure can be carried out recursively: The momentum balance can be obtained at successively higher order in Ro, based on the balance at lower order. However, $Ro \ll 1$ makes terms omitted much smaller than those retained in the approximate momentum balance. Retaining only the gravest terms therefore often provides sufficient accuracy.

12.1 GEOSTROPHIC EQUILIBRIUM

To zero order in Ro, the momentum equations reduce to

$$f\boldsymbol{k}\times\boldsymbol{v}_g = -\nabla_p\Phi \tag{12.2.1}$$

where frictional drag $\boldsymbol{D}$ is presumed to be $O(Ro)$ or smaller. Reflecting a balance between the Coriolis acceleration and the horizontal pressure-gradient force, (12.2.1) defines *geostrophic equilibrium* (*geo* referring to Earth and *strophic* to turning). The

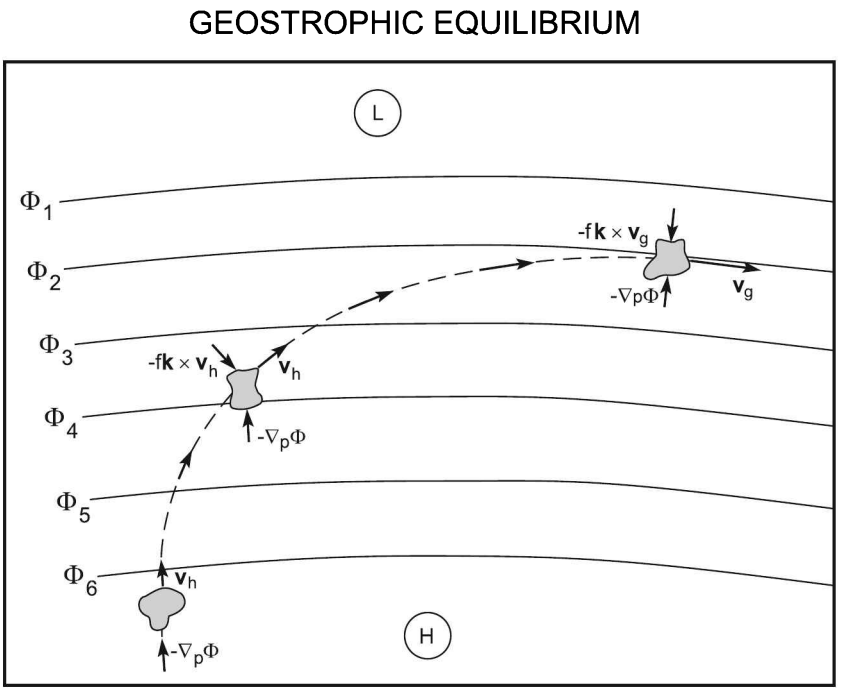

Figure 12.1 Evolution of a hypothetical air parcel that is initially motionless in the Northern Hemisphere and in stratification wherein contours of isobaric height $z = \frac{1}{g}\Phi$ are nearly straight, uniformly spaced, and, for the sake of illustration, fixed.

horizontal velocity that satisfies (12.2.1) is the *geostrophic velocity*

$$\begin{aligned} \boldsymbol{v}_g &= \frac{1}{f}\boldsymbol{k}\times\nabla_p\Phi \\ &= \frac{1}{f}\left(-\frac{\partial\Phi}{\partial y}, \frac{\partial\Phi}{\partial x}\right). \end{aligned} \tag{12.2.2}$$

Similar expressions follow in isentropic coordinates with the Montgomery streamfunction.

According to (12.2.2), the geostrophic velocity is tangential to contours of height, $z = \frac{1}{g}\Phi$, with low height on the left (right) in the Northern (Southern) Hemisphere. This is equivalent to motion being along isobars on a constant height surface (Sec. 6.3). Such motion is apparent in the observed circulation (Fig. 1.9). It is just perpendicular to air motion that is normally observed in an inertial reference frame, namely, from high toward low pressure and, hence, perpendicular to isobars. This peculiarity of large-scale atmospheric motion (one of several related features) is referred to as the "geostrophic paradox." Derived from the Coriolis force, which acts orthogonal to motion, it was not resolved until the Earth's rotation was accounted for.

To illustrate how geostrophic equilibrium is established, consider a hypothetical initial value problem: An atmosphere, initially at rest, is characterized by contours of isobaric height that are nearly straight, uniformly spaced, and, for the sake of illustration, fixed (Fig. 12.1). At $t = 0$, an air parcel has $\boldsymbol{v}_h = 0$. The Coriolis force acting

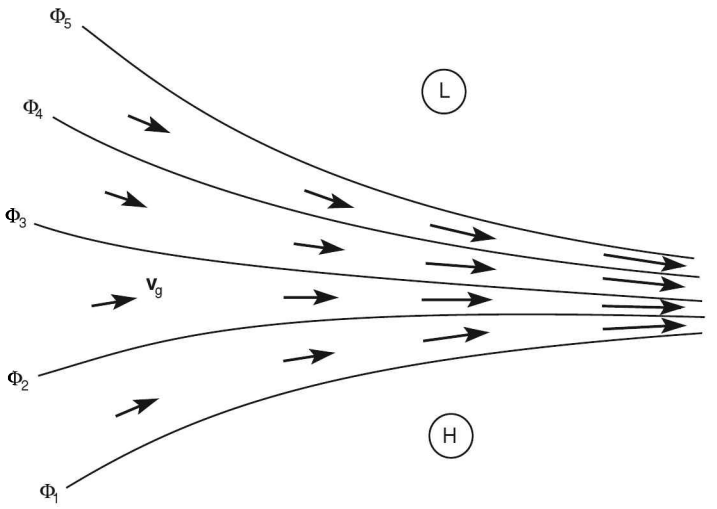

Figure 12.2 Variation of geostrophic velocity with changes of isobaric height.

on it therefore vanishes. In response to the pressure gradient force, the parcel accelerates in the direction of $-\nabla_p\Phi$, toward low height. As soon as motion develops, the Coriolis force $-f\boldsymbol{k}\times\boldsymbol{v}_h$ acts perpendicular to the horizontal velocity. In the Northern Hemisphere, where $f = 2\Omega sin\phi$ is positive, the Coriolis force deflects the parcel's motion toward the right. Were it in the Southern Hemisphere, the parcel would be deflected to the left. In either event, the Coriolis force performs no work on the parcel – because it acts orthogonal to the instantaneous motion. While the parcel's trajectory veers to the right, the pressure gradient force remains unchanged because, under the foregoing conditions, $\nabla_p\Phi$ is invariant of position. However, the Coriolis force changes continually, remaining proportional and orthogonal to $\boldsymbol{v}_h$. As the parcel accelerates under the pressure-gradient force, its trajectory veers increasingly to the right. Eventually, $\boldsymbol{v}_h$ has been deflected tangential to contours of Φ. At that point, the Coriolis force acts in direct opposition to the pressure gradient force. Both are perpendicular to the parcel's velocity. If $\boldsymbol{v}_h$ satisfies (12.2), the forces are in balance. The motion is then in geostrophic equilibrium. Consequently, the parcel experiences no further acceleration.[1]

Once this mechanical equilibrium is established, the parcel's motion is steady – except for gradual adjustments allowed for in contours of Φ. According to (12.2.2), geostrophic wind speed v_g is proportional to $\nabla_p\Phi$. It is therefore inversely proportional to the spacing of height contours (Fig. 12.2). Geostrophic wind speed increases into a region where height contours converge. It decreases into a region where they diverge. For either case, $\boldsymbol{v}_g$ remains tangential to height contours. In the absence of vertical motion, such behavior automatically satisfies conservation of mass: It is nondivergent, $\nabla\cdot\boldsymbol{v} = 0$. This feature of geostrophic motion makes height contours streamlines.

[1] If the Coriolis and pressure-gradient forces do not balance exactly, the motion will undergo an oscillation about contours of Φ, which, upon being damped out, leaves the parcel in geostrophic equilibrium.

The balance (12.2) is valid for curved motion, so long as an anomaly's horizontal scale is large enough and its velocity is slow enough for the material acceleration to be negligible relative to the pressure-gradient and Coriolis forces. (These conditions maintain $Ro \ll 1$). Geostrophic equilibrium then implies circular motion about a closed center of height. Low height lies to the left (right) in the Northern (Southern) Hemisphere. Therefore, geostrophic flow about a closed low is counterclockwise in the Northern Hemisphere. It is clockwise in the Southern Hemisphere. In each hemisphere, motion about a closed low has the same sense of rotation as the planetary vorticity $f\boldsymbol{k}$. Such motion is termed *cyclonic*. About a closed high, geostrophic motion is clockwise in the Northern Hemisphere. It is counterclockwise in the Southern Hemisphere. In each hemisphere, such motion has a sense of rotation opposite to the planetary vorticity. Motion about a closed high is termed *anticyclonic*.

Geostrophic motion is apparent in the 500-hPa circulation (Fig. 1.9a). Punctuating the jet stream are anomalies of low height. Motion about them is counterclockwise. In fact, the circumpolar flow itself may be regarded as a cyclonic vortex. It is implied by the hypsometric relationship (6.12). Poleward-decreasing temperature in the troposphere produces low isobaric height over the pole (Fig. 6.2). Geostrophic equilibrium then establishes a cyclonic circulation about the pole, manifest in the subtropical jet (Fig. 1.9b). The circulation at 10 hPa is also cyclonic, but intensified (Fig. 1.10b). Ozone heating at low latitude and LW cooling at high latitude (Fig. 8.27) produce poleward-decreasing temperature across the winter stratosphere. Through the hypsometric relationship, this establishes the polar-night vortex. Outside the vortex is the *Aleutian high*. It is accompanied by anticyclonic motion. Even though the instantaneous circulation can be highly disturbed from zonal symmetry (Figs. 1.9a, 1.10a), motion remains nearly tangential to contours of height.

12.1.1 Motion on an f plane

Consider motion in which meridional displacements of air are sufficiently narrow to ignore variations of f. Expanding f in a Taylor series about the reference latitude ϕ_0 and truncating to zeroth order gives the constant Coriolis parameter

$$f_0 = 2\Omega sin\phi_0. \tag{12.3.1}$$

In the same framework, it is convenient to neglect spherical curvature in favor of simple Cartesian geometry. A Cartesian plane tangent to the Earth at latitude ϕ_0 (Fig. 12.3) describes horizontal position in terms of the distances

$$\begin{aligned} x &= acos\phi_0 \cdot \lambda \\ y &= a \cdot (\phi - \phi_0), \end{aligned} \tag{12.3.2}$$

but with the Earth's sphericity ignored. Together, these simplifications comprise the *f-plane* description of atmospheric motion.

On an f plane, the geostrophic velocity defines a nondivergent vector field. Tangential paths of $\boldsymbol{v}_g$, which coincide with height contours, then serve as streamlines. These and other implications of nondivergence follow from the general representation of a vector field.

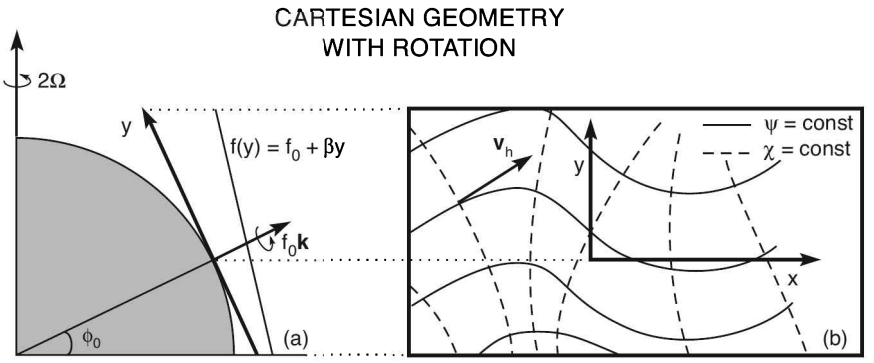

Figure 12.3 Approximation of the rotating spherical Earth by Cartesian geometry. On a plane tangent to the Earth at latitude ϕ_0, distance is measured by the coordinates $x = a\cos\phi_0 \cdot \lambda$ and $y = a \cdot (\phi - \phi_0)$, which increase to the east and north, respectively. (a) Approximating the Coriolis parameter by its zeroth order variation: $f(y) = f_0 = 2\Omega\sin\phi_0$, yields the *f-plane* description of atmospheric motion. Approximating it to first order: $f(y) = f_0 + \beta y$, where $\beta = \frac{df}{dy}|_{y=0}$, yields the *β-plane* description of atmospheric motion. (b) The horizontal motion field at any instant $\boldsymbol{v}_h(x, y, t)$ can be expressed in terms of a *streamfunction* $\psi(x, y, t)$ and a *velocity potential* $\chi(x, y, t)$: $\boldsymbol{v}_h = \boldsymbol{k} \times \nabla\psi + \nabla\chi$, which represent the rotational and divergent components of $\boldsymbol{v}_h$, respectively.

The Helmholtz Theorem

Any vector field $\boldsymbol{v}$ can be represented in terms of a *divergent* or irrotational component and a *solenoidal* or rotational component:

$$\boldsymbol{v} = \nabla\chi + \nabla \times \boldsymbol{\psi}, \tag{12.4}$$

where χ is a *scalar potential* (analogous to the potential function in Chap. 2) and $\boldsymbol{\psi}$ is a *vector potential*. The divergent component

$$\boldsymbol{v}_d = \nabla\chi \tag{12.5.1}$$

possesses zero vorticity

$$\nabla \times \boldsymbol{v}_d = 0. \tag{12.5.2}$$

The solenoidal component

$$\boldsymbol{v}_s = \nabla \times \boldsymbol{\psi} \tag{12.6.1}$$

possesses zero divergence

$$\nabla \cdot \boldsymbol{v}_s = 0. \tag{12.6.2}$$

For the 2-dimensional field of horizontal velocity, (12.4) reduces to

$$\boldsymbol{v}_h = \nabla\chi + \boldsymbol{k} \times \nabla\psi, \tag{12.7.1}$$

where χ is the *velocity potential* and ψ is the *streamfunction*. The horizontal velocity field then has divergence

$$\nabla \cdot \boldsymbol{v}_h = \nabla^2\chi \tag{12.7.2}$$

and vorticity

$$\nabla \times \boldsymbol{v}_h = \nabla^2 \psi \boldsymbol{k}. \tag{12.7.3}$$

The divergent component of motion $\boldsymbol{v}_d$ is orthogonal to contours of χ. The solenoidal component $\boldsymbol{v}_s$ is tangential to contours of ψ.

According to (12.2.2), geostrophic motion on an f plane has the form of a solenoidal vector field. It is characterized by the *geostrophic streamfunction*

$$\psi = \frac{1}{f_0}\Phi. \tag{12.8}$$

Because the divergence of $\boldsymbol{v}_g$ vanishes, the continuity equation implies little or no vertical motion.[2] If pressure variations along the Earth's surface can be ignored, integrating (11.54.2) upward to some isobaric surface obtains

$$\omega(x, y, p, t) = -\int_p^{p_s} \nabla \cdot \boldsymbol{v}_h dp. \tag{12.9}$$

As $\nabla \cdot \boldsymbol{v}_g = 0$ (12.6.2), geostrophic equilibrium implies zero vertical motion. Air parcels then simply exchange horizontal positions with no vertical rearrangement. The solenoidal character of large-scale motion follows from the Earth's rotation, which maintains the circulation close to geostrophic equilibrium. Vertical motion does occur in the large-scale circulation. However, it is higher order in *Ro* and therefore small. Such motion enters through the *ageostrophic* or divergent component of horizontal velocity $\boldsymbol{v}_d$.

Owing to its rotational character, geostrophic motion involves substantial deformation. Horizontal shear associated with vorticity (10.5) distorts finite bodies of air into complex forms. Figure 12.4 displays the evolution of a material volume as it is advected though a 2-dimensional cyclone. Shear strains the body into an elongated shape. Through this distortion, the transverse separation of boundaries collapses to small scales. Accompanying gradients therefore steepen. On those scales, turbulence and nonconservative processes act efficiently (Chap. 13). They homogenize sharp contrasts that have developed through shear strain. This consequence of rotational motion is tantamount to mixing. It is analogous to cream being stirred into a cup of coffee. Shear strains exaggerate fluid gradients until, eventually, they are dissolved by small-scale turbulence and molecular diffusion. In the atmosphere, such mixing is accomplished by horizontal eddy motions and by vertical motions in convection (cf. Figs. 1.18, 1.28).

12.2 VERTICAL SHEAR OF THE GEOSTROPHIC WIND

Geostrophic balance determines the horizontal structure of motion. Together with hydrostatic balance, it also determines the vertical structure. A fundamental principle of rotating fluid mechanics is the *Taylor-Proudman theorem*. It asserts that the motion

[2] Hereafter, the term *divergence* will be understood to refer to the divergence of the horizontal velocity.

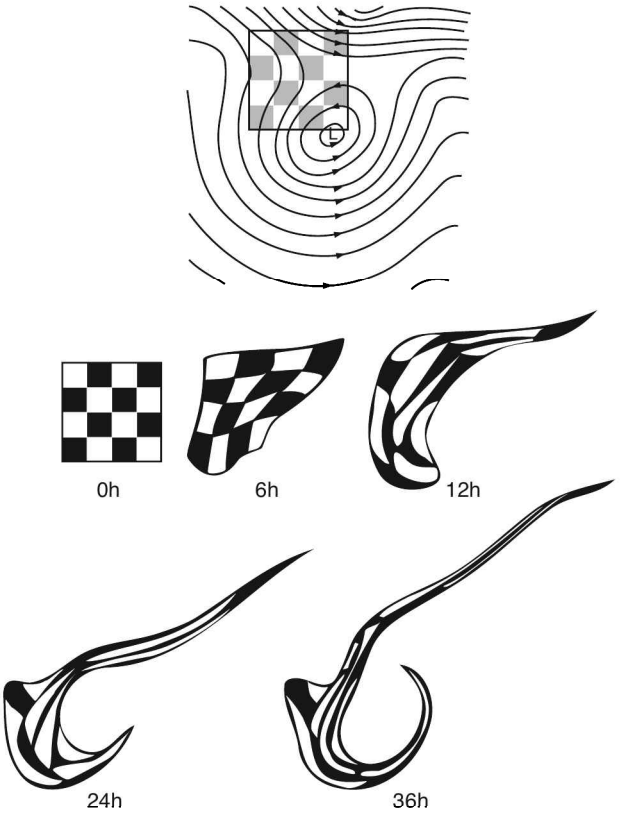

Figure 12.4 Deformation of a material volume at successive times inside a 2-dimensional cyclone, obtained by integrating the barotropic nondivergent vorticity equation. Adapted from Welander (1955). Copyright (1955) Munksgaard International Publishers Ltd., Copenhagen Denmark.

of a homogeneous incompressible fluid cannot vary along the axis of rotation. Motion then occurs in so-called *Taylor-Proudman columns.*[3] The atmosphere is not homogeneous nor incompressible. Nevertheless, it obeys an analogue of the Taylor-Proudman theorem, which relates horizontal motion to stratification.

12.2.1 Classes of stratification

Stratification is represented in the distributions of thermodynamic properties. For dry air, only two such properties are independent (Sec. 2.1.4). Therefore, any two families of thermodynamic surfaces uniquely describe the stratification (Fig. 12.5). Mathematically, this is expressed by $\theta = \theta(p, T)$, where p and T are functions of space and time.

[3] See Greenspan (1968) for a laboratory demonstration.

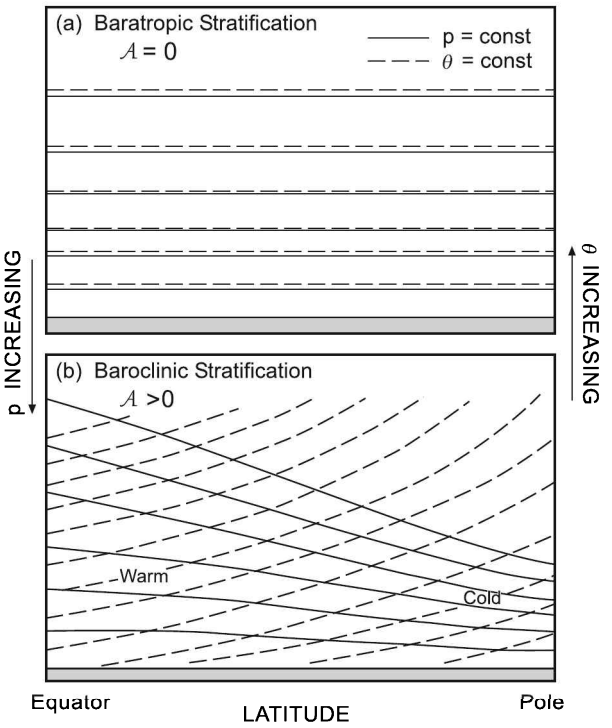

Figure 12.5 Thermal structure corresponding to (a) barotropic stratification, wherein isentropic surfaces coincide with isobaric surfaces and available potential energy $\mathcal{A}$ is zero (Sec. 15.1.3), and (b) baroclinic stratification, wherein isentropic surfaces do not coincide with isobaric surfaces and $\mathcal{A}$ is positive. The rotation of isobaric and isentropic surfaces from their positions under barotropic stratification is symbolic of atmospheric heating at low latitude and cooling at middle and high latitudes (cf. Figs. 1.34c and 9.41b).

Should isentropic surfaces coincide with isobaric surfaces (Fig. 12.5a), $\theta = \theta(p)$. The stratification is then said to be *barotropic*. Under barotropic stratification, the circulation possesses only one thermodynamic degree of freedom. It is represented in the single independent family of thermodynamic surfaces. Because other thermodynamic surfaces coincide with that family, specifying p uniquely determines θ. Jointly, they determine the thermodynamic state and all other thermodynamic properties. Under these circumstances, the geostrophic velocity will be seen to be invariant with height. Air motion then occurs in columns.

More generally, two families of thermodynamic surfaces do not coincide (Fig. 12.5b), so $\theta = \theta(p, T)$. The stratification is then said to be *baroclinic*. Under baroclinic stratification, the circulation possesses two thermodynamic degrees of freedom. Consequently, along any thermodynamic surface, other thermodynamic properties vary. The geostrophic velocity then varies with height. However, it does so in direct proportion to the variation of temperature along isobaric surfaces.

12.2.2 Thermal wind balance

Under barotropic stratification, temperature does not vary along isobaric surfaces. Integrating the hypsometric relationship (6.12) upward from the ground then gives Φ. The latter has a contribution from the lower boundary, which may vary horizontally, plus a function of pressure alone. The horizontal distribution of height therefore does not change from one isobaric surface to another. It follows that the geostrophic velocity (12.1.2) is independent of elevation. The motion is columnar. Under barotropic stratification (wherein density is uniform along isobaric surfaces), geostrophic motion is invariant in the direction of $f\boldsymbol{k}$. The behavior is analogous to Taylor-Proudman flow for a homogeneous incompressible fluid.

Under baroclinic stratification, T varies along isobaric surfaces. Differentiating (12.1.2) with respect to p obtains

$$\frac{\partial \boldsymbol{v}_g}{\partial p} = \frac{1}{f}\boldsymbol{k} \times \nabla_p \frac{\partial \Phi}{\partial p}. \tag{12.10}$$

Incorporating the hydrostatic equation (11.62.2) then yields the vertical gradient of geostrophic velocity

$$\frac{\partial \boldsymbol{v}_g}{\partial ln p} = \frac{R}{f}\boldsymbol{k} \times \nabla_p T \tag{12.11.1}$$

or, in terms of log-pressure height z,

$$\frac{\partial \boldsymbol{v}_g}{\partial z} = \frac{R}{Hf}\boldsymbol{k} \times \nabla_z T. \tag{12.11.2}$$

Known as *thermal wind balance*, (12.11) asserts that vertical shear of the geostrophic velocity is proportional to the horizontal temperature gradient along isobaric surfaces. The term *thermal wind* describes the incremental velocity $\Delta \boldsymbol{v}_g$ across a layer bounded by two isobaric surfaces and of thickness $-H\Delta ln p$. According to (12.11), thermal wind is proportional to the horizontal gradient of temperature in that layer. Vertical shear is thus a measure of the departure from barotropic stratification.

From (12.11), an equatorward temperature gradient is accompanied by positive (westerly) shear of the zonal wind. Westerlies then intensify upward. Examples are found in the troposphere and winter stratosphere (Figs. 1.7, 1.8). Radiative heating at low latitude, supported by transfer of latent heat, and radiative cooling at middle and high latitudes establish an equatorward temperature gradient in the troposphere (Figs. 1.34c; 9.41b). The latter prevails in both hemispheres. Thermal wind balance then implies westerlies that intensify upward. They form the subtropical jets, which maximize near the tropopause (Fig. 1.8). In the stratosphere, ozone heating prevails at low latitude, whereas LW cooling to space prevails at high latitude of the winter hemisphere, e.g., inside polar night (Fig. 8.27). They establish an equatorward temperature gradient over a deep layer. Westerlies therefore intensify upward, forming the polar-night jet. Opposite behavior occurs in the summer stratosphere. There, solar insolation is greatest at high latitude (Fig. 1.33), producing a poleward temperature gradient. Zonal wind, which is westerly in the troposphere, therefore experiences easterly shear. It reverses not far above the tropopause. Easterlies then intensify upward, forming the summer easterly jet.

These features can also be inferred directly from geostrophic equilibrium and the hypsometric relationship (a consequence of hydrostatic balance). In the presence of a horizontal temperature gradient, the vertical spacing of isobaric surfaces is expanded

in warm air (e.g., at tropical latitudes) but compressed in cold air (e.g., at polar latitudes); cf. Fig. 6.2. An equatorward gradient of isobaric height is produced. The gradient of height steepens with increasing elevation. Geostrophic equilibrium then requires westerlies to intensify upward. They form the jet stream, which coincides with the steep temperature gradient at mid-latitude. Separating warm tropical air from cold polar air (Fig. 6.3), that gradient marks the polar front. The steeper the temperature gradient, the sharper is the polar front and the stronger is the jet stream.

The distribution of net radiation (Fig. 1.34c), in concert with geostrophic equilibrium, thus favors strong westerlies at mid-latitude. Such motion transfers no heat poleward, as is required to offset radiative heating at low latitude and radiative cooling at middle and high latitudes. The same applies to water vapor and chemical constituents that have sources in the tropics. Consequently, the Earth's rotation tends to stratify properties meridionally, just as gravity tends to stratify them vertically.

Thermal wind balance also applies to zonally asymmetric motion. The polar front and jet stream are disturbed by synoptic weather systems, which prevail at mid-latitude (Fig. 1.9a). Those disturbances are typified by a cold-core low (Prob. 6.4). According to (12.11), such thermal structure produces cyclonic vertical shear. It reinforces cyclonic motion. A cold-core low therefore intensifies upward, achieving maximum wind near the tropopause. The reverse occurs inside a warm-core low, as typifies tropical cyclones (Prob. 6.6). That thermal structure produces anticyclonic shear. It opposes cyclonic motion. A warm-core low therefore weakens upward, achieving maximum wind at the surface.

Geostrophic equilibrium applies to motion that is sufficiently steady, slow, and weakly curved for material acceleration to be negligible relative to the Coriolis and pressure-gradient forces (i.e., for it to satisfy $Ro \ll 1$). Frictional drag must also be negligible. These conditions are well-satisfied by large-scale extratropical motion away from the Earth's surface. v_h is then approximately nondivergent. However, the conditions for geostrophic equilibrium break down near the equator. They are also invalidated if the horizontal scale of advection becomes small. Either renders terms in (12.1) that are $O(Ro)$ nonnegligible. These effects introduce an ageostrophic component to $\boldsymbol{v}_h$. The latter is accompanied by divergence and hence by vertical motion (12.9).

12.3 FRICTIONAL GEOSTROPHIC MOTION

Inside the planetary boundary layer, frictional drag is no longer negligible. It is large enough to invalidate geostrophic equilibrium. Turbulent eddy motion within a kilometer of the surface is produced by strong vertical shear (see Fig. 13.3). It mixes momentum between bodies of air. The accompanying momentum flux exerts a shear stress on individual air parcels, making $\boldsymbol{D}$ in (12.1) of the same order as the Coriolis and pressure-gradient forces (Sec. 10.6).

Drag can be represented as *Rayleigh friction*, with linear drag coefficient K:

$$\boldsymbol{D} = K\boldsymbol{v}_h. \tag{12.12}$$

Mechanical equilibrium then requires

$$f\boldsymbol{k} \times \boldsymbol{v}_h = -\nabla_p \Phi - K\boldsymbol{v}_h. \tag{12.13}$$

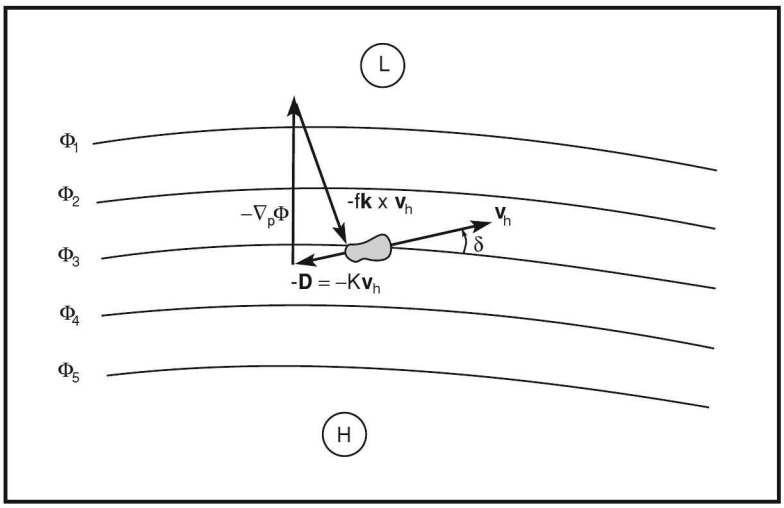

Figure 12.6 Frictional geostrophic balance in a flow characterized by nearly-straight contours of height and in the presence of Rayleigh friction.

Defining *frictional geostrophic equilibrium*, (12.13) may be solved for the components of horizontal motion (Prob. 12.11). Friction modifies both the magnitude and the direction of $\boldsymbol{v}_h$. The ensuing mechanical equilibrium can be motivated by introducing drag into the geostrophic balance in Fig. 12.1. $\boldsymbol{D}$ reduces the the velocity of the air parcel, which reduces the Coriolis force $-f\boldsymbol{k} \times \boldsymbol{v}_h$ acting on it. That, in turn, allows the pressure-gradient force to drive the parcel's motion across isobars toward low pressure (Fig. 12.6). Eventually, the motion achieves an angle δ from isobars such that the resultant of the three forces acting on the parcel vanishes. The air parcel is then in mechanical equilibrium.

Unlike simple geostrophic motion, frictional geostrophic motion is not solenoidal. The divergent component of $\boldsymbol{v}_h$ introduces vertical motion via continuity (12.9). Friction produces convergence into a center of low surface pressure (Fig. 12.7a). The convergence must be compensated overhead by rising motion. Frictional convergence into a cyclone organizes moisture near the surface, while forcing upward motion. Simultaneously, it reduces vertical stability (Sec. 7.4.4). These features of cyclonic motion encourage convection and cloud formation. Conversely, friction produces divergence out of a center of high surface pressure (Fig. 12.7b). It must be compensated overhead by subsidence. Frictional divergence out of an anticyclone leads to surface air being replaced by dry air from overhead. The accompanying subsidence opposes upward motion. It also produces a subsidence inversion, which traps water vapor and pollutants near the surface. These features of anticyclonic motion inhibit convection and cloud formation, while favoring the accumulation of pollutants.

The foregoing behavior is a consequence of vertical motion, which develops through the small departure from geostrophic equilibrium. The divergent component of motion under frictional geostrophic equilibrium is inversely proportional to f (Prob. 12.12). For this reason, vertical motion is favored in the tropics, where small f allows large departures from geostrophic equilibrium. The latter support thermally-direct

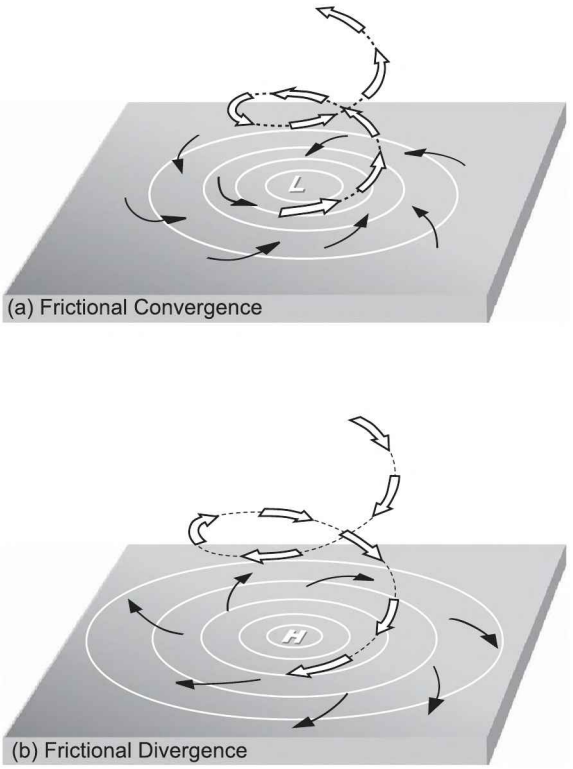

Figure 12.7 Vertical motion introduced by (a) frictional convergence into surface low pressure and (b) frictional divergence out of surface high pressure.

circulations, wherein air ascends over low pressure and descends over high pressure (Figs. 1.35, 1.36).

12.4 CURVILINEAR MOTION

The other factor driving the circulation out of geostrophic equilibrium is material acceleration. If the trajectory of an air parcel is sufficiently curved, it experiences a centripetal acceleration. Embodied in the advective contribution, $\boldsymbol{v}_h \cdot \nabla_p \boldsymbol{v}_h$, that acceleration makes Ro nonnegligible. Unsteadiness can have the same effect through the local time derivative $\frac{\partial \boldsymbol{v}_h}{\partial t}$. However, this contribution is typically less important than advective acceleration.

Consider steady motion in which an air parcel moves along a curved trajectory, characterized by the local radius of curvature R. The parcel trajectory then coincides with a streamline. It is convenient to introduce the *trajectory coordinates* $\boldsymbol{s}$ and $\boldsymbol{n}$, which increase along and orthogonal to the path of an individual parcel (Fig. 12.8). Coordinate vectors $\boldsymbol{s}$ and $\boldsymbol{n}$ are tangential and orthogonal to the local velocity $\boldsymbol{v}_h$, with $\boldsymbol{n}$ pointing to the left of $\boldsymbol{s}$. R is defined to be positive if the center of curvature lies in the positive $\boldsymbol{n}$ direction (i.e., to the left of $\boldsymbol{s}$). Curvature is then cyclonic if R is of the same sign as f ($fR > 0$) and anticyclonic if it is of opposite sign ($fR < 0$).

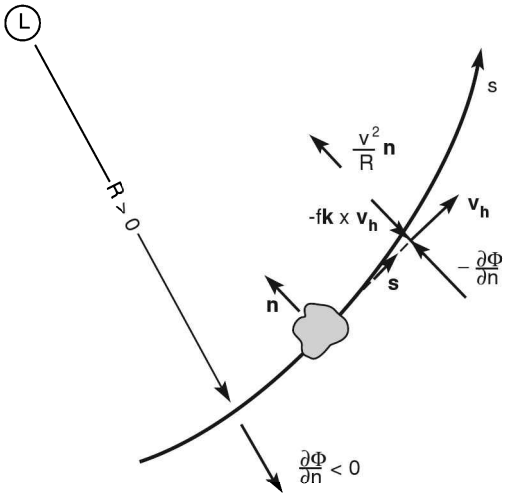

Figure 12.8 Trajectory coordinates s and n, which increase along and orthogonal to the path of an individual parcel. The coordinate vectors $\boldsymbol{s}$ and $\boldsymbol{n}$ are then tangential and orthogonal to the local velocity $\boldsymbol{v}_h$, with $\boldsymbol{n}$ pointing to the left of $\boldsymbol{s}$ to form a right-handed coordinate system: $\boldsymbol{s} \times \boldsymbol{n} = \boldsymbol{k}$. The trajectory's curvature is represented in the radius of curvature R, which is defined to be positive (negative) if the center of curvature lies in the positive (negative) n direction. The local velocity is then described by $\boldsymbol{v}_h = v\boldsymbol{s}$, with speed $v = \frac{ds}{dt}$. Centripetal acceleration $\frac{v^2}{R}\boldsymbol{n}$ follows from an imbalance between the pressure gradient force $-\frac{\partial\Phi}{\partial n}$ and the Coriolis force $-f\boldsymbol{k} \times \boldsymbol{v}_h$.

In this coordinate system, the horizontal velocity is described by

$$\boldsymbol{v}_h = v\boldsymbol{s}, \tag{12.14.1}$$

where the speed is simply

$$v = \frac{ds}{dt}. \tag{12.14.2}$$

The material acceleration of an individual parcel follows as

$$\frac{d\boldsymbol{v}_h}{dt} = \frac{dv}{dt}\boldsymbol{s} + v\frac{d\boldsymbol{s}}{dt}. \tag{12.15}$$

The first term on the right hand side represents longitudinal acceleration along the parcel's trajectory. The second represents centripetal acceleration. It acts transverse to the parcel's motion, following from curvature of its trajectory.

By the chain rule,

$$\begin{aligned} \frac{d\boldsymbol{s}}{dt} &= \frac{d\boldsymbol{s}}{ds}\frac{ds}{dt} \\ &= v\frac{d\boldsymbol{s}}{ds}. \end{aligned} \tag{12.16}$$

Analysis similar to that in Sec. 10.6.2 shows that the unit vector $\boldsymbol{s}$ changes at the rate

$$\frac{d\boldsymbol{s}}{dt} = \frac{v}{R}\boldsymbol{n}. \tag{12.17}$$

Substituting (12.16) then obtains

$$\frac{d\boldsymbol{v}_h}{dt} = \frac{dv}{dt}\boldsymbol{s} + \frac{v^2}{R}\boldsymbol{n}, \tag{12.18}$$

which describes the material acceleration in terms of components longitudinal and transverse to the motion. As $R \to \infty$, the centripetal acceleration approaches zero and the parcel's motion becomes rectilinear.

Incorporating (12.18) transforms the horizontal momentum equation (12.1) into

$$\frac{dv}{dt}\boldsymbol{s} + \frac{v^2}{R}\boldsymbol{n} = -fv\boldsymbol{n} - \frac{\partial\Phi}{\partial s}\boldsymbol{s} - \frac{\partial\Phi}{\partial n}\boldsymbol{n}. \tag{12.19}$$

The component equations in the $\boldsymbol{s}$ and $\boldsymbol{n}$ directions are thus:

$$\frac{dv}{dt} = -\frac{\partial\Phi}{\partial s} \tag{12.20.1}$$

$$\frac{v^2}{R} + fv = -\frac{\partial\Phi}{\partial n}. \tag{12.20.2}$$

Consider now motion that is tangential to contours of height, which serve as streamlines. Then $\frac{\partial\Phi}{\partial s}$ vanishes and (12.20.1) implies that $v = \text{const}$ along an individual streamline. Accordingly, we focus on the momentum budget in the normal direction. The centripetal acceleration $\frac{v^2}{R}$ represents the material acceleration in (11.37). It is $O(Ro)$, where the Rossby number

$$Ro = \frac{U}{fR}$$

is based on the length scale R. According to (12.20.2), centripetal acceleration follows from an imbalance between the Coriolis and pressure-gradient forces.

12.4.1 Inertial motion

If the centripetal and Coriolis accelerations are in balance,

$$\frac{v^2}{R} + fv = 0. \tag{12.21.1}$$

This balance applies in the absence of pressure gradient. The radius of curvature follows as

$$R = -\frac{v}{f}. \tag{12.21.2}$$

On an f plane, $R = \text{const}$. Streamlines then form circular orbits that are anticyclonic ($fR < 0$). The period of revolution is given by

$$\tau = \frac{\pi}{\Omega sin\phi}. \tag{12.22}$$

τ equals half a *sidereal day*: the time for a Foucalt pendulum to sweep through 180° of azimuth. The motion (12.21) describes an *inertial oscillation*. Parcels revolve opposite to the vertical component of planetary vorticity. Inertial oscillations have been observed in the oceans. However, they do not play a major role in the atmospheric circulation.

12.4.2 Cyclostrophic motion

If either R or f approaches zero, $Ro \to \infty$. These circumstances apply for small horizontal scale or near the equator. The material acceleration then dominates the Coriolis acceleration. Under these conditions, (12.20.2) reduces to the balance

$$\frac{v^2}{R} = -\frac{\partial \Phi}{\partial n}, \tag{12.23.1}$$

which defines *cyclostrophic equilibrium*. The *cyclostrophic wind speed*

$$v_c = \sqrt{-R\frac{\partial \Phi}{\partial n}} \tag{12.23.2}$$

may be either cyclonic or anticyclonic. However, it is always about low pressure (e.g., $\frac{\partial \Phi}{\partial n}$ has sign opposite to R).

Cyclostrophic equilibrium applies to motion (1) with strong curvature, wherein the advective acceleration is large, or (2) in the presence of slow planetary rotation f, wherein the Coriolis force is weak. The former is typical of small-scale vortices like tornadoes. The latter is important in tropical cyclones. Slow planetary rotation is also a feature of the Venusian atmosphere. Unlike the Earth's atmosphere, the circulation of Venus is governed by cyclostrophic equilibrium.

12.4.3 Gradient motion

To first order in Ro, all three terms in (12.20.2) are retained. The resulting balance defines *gradient equilibrium*. Gradient wind balance describes horizontal motion when no two of the terms dominate. This often applies to tropical motions, for which fR is small.

Equation (12.20.2) is quadratic in v. It can be solved for the *gradient wind speed*

$$v_{gr} = -\frac{fR}{2} \pm \sqrt{\frac{f^2R^2}{4} - R\frac{\partial \Phi}{\partial n}}. \tag{12.24}$$

Not all roots of (12.24) are physically meaningful. Real wind speed requires

$$\frac{\partial \Phi}{\partial n} \begin{cases} < \frac{f^2R}{4} & (R > 0) \\ > \frac{f^2R}{4} & (R < 0)\,. \end{cases} \tag{12.25}$$

Subsequent analysis is restricted to regular cyclonic or anticyclonic motion in the Northern Hemisphere, for which $\frac{\partial \Phi}{\partial n} < 0$ (Fig. 12.8). This corresponds to cyclonic motion about a low and anticyclonic motion about a high, as prevails under geostrophic equilibrium (i.e., to zero order in Ro). The second inequality in (12.25) limits the pressure gradient that can be sustained by anticyclonic motion. Under these conditions, $\frac{\partial \Phi}{\partial n} < 0$ and $R < 0$. $\frac{\partial \Phi}{\partial n}$ is then sandwiched between $\frac{f^2R}{4}$ and 0. Near the center of an anticyclone, $R \to 0$. The height distribution must therefore become flat and the accompanying motion weak (12.24). For cyclonic motion, no corresponding limitation applies. With $R > 0$, $\frac{\partial \Phi}{\partial n} < 0$ automatically satisfies the first inequality in (12.25). Hence, cyclones are free to intensify, whereas the amplification of anticyclones is limited. This distinction explains why wind inside an anticyclone is comparatively weak. It follows from the fact that the pressure-gradient force $(-\frac{\partial \Phi}{\partial n})$ reinforces the centripetal acceleration in a cyclone but opposes it in an anticyclone; cf. Fig. 12.8.

Letting $R \to \infty$ ($Ro \to 0$) in (12.20.2) recovers geostrophic equilibrium. Conversely, letting $R \to 0$ ($Ro \to \infty$) recovers cyclostrophic equilibrium. Intermediate to those extremes is the gradient wind. It is only approximated by the geostrophic wind. Eliminating the pressure gradient in favor of the geostrophic wind speed

$$v_g = -\frac{1}{f}\frac{\partial \Phi}{\partial n}$$

transforms (12.20.2) into

$$\frac{v_g}{v_{gr}} = 1 + \frac{v_{gr}}{fR}. \tag{12.26}$$

The geostrophic wind speed overestimates the gradient wind speed in cyclonic motion ($fR > 0$). It underestimates it in anticyclonic motion ($fR < 0$). The discrepancy from gradient wind (e.g., the error) is proportional to Ro. For large-scale extratropical motion, the discrepancy is of order 10–20%. However, discrepancies as large as 50–100% can occur inside intense cyclones and in tropical systems characterized by small fR.

12.5 WEAKLY DIVERGENT MOTION

The idealized balances considered in the preceding section are useful for describing the structure of large-scale motion. However, they provide no information on how the circulation evolves. Free of time derivatives, such equations are termed *diagnostic*. Unsteadiness and divergence are comparatively small. Nevertheless, they enable the circulation to evolve from one state to another. Equations that describe such changes are termed *prognostic*. A simple framework for describing how the circulation evolves may be developed in the absence of vertical motion.

12.5.1 Barotropic nondivergent motion

Consider motion that is horizontally nondivergent and under barotropic stratification. Continuity then implies that vertical motion vanishes (12.9). Thermal wind balance (12.11) implies that $\boldsymbol{v}_h$ is independent of height. Consequently, the motion is 2-dimensional or columnar. The governing equations in physical coordinates then reduce to

$$\frac{d\boldsymbol{v}_h}{dt} + f\boldsymbol{k} \times \boldsymbol{v}_h = -\alpha \nabla p \tag{12.27.1}$$

$$\nabla \cdot \boldsymbol{v}_h = 0, \tag{12.27.2}$$

where friction is ignored and ∇ is understood to refer to the horizontal gradient. Vector identity (D.14) in Appendix D enables (12.27.1) to be written

$$\frac{\partial \boldsymbol{v}_h}{\partial t} + \frac{1}{2}\nabla(\boldsymbol{v}_h \cdot \boldsymbol{v}_h) + (\zeta + f)\boldsymbol{k} \times \boldsymbol{v}_h = -\alpha \nabla p, \tag{12.28.1}$$

where

$$\begin{aligned} \zeta &= (\nabla \times \boldsymbol{v}_h) \cdot \boldsymbol{k} \\ &= \frac{\partial v}{\partial x} - \frac{\partial u}{\partial y} \end{aligned} \tag{12.28.2}$$

is the vertical component of *relative vorticity*. Consistent with prior convention, relative vorticity is cyclonic if it has the same sign as the planetary vorticity f and anticyclonic otherwise. Applying the curl to (12.28.1) and making use of other vector identities in Appendix D yields the vorticity budget for an air parcel

$$\frac{\partial \zeta}{\partial t} + \boldsymbol{v}_h \cdot \nabla \zeta + \boldsymbol{v}_h \cdot \nabla f = (\nabla p \times \nabla \alpha) \cdot \boldsymbol{k}.$$

Because $\alpha = \alpha(p)$ under barotropic stratification and $f = f(y)$, this reduces to

$$\frac{d\zeta}{dt} + v\frac{\partial f}{\partial y} = 0. \tag{12.29}$$

Because

$$v\frac{\partial f}{\partial y} = \frac{df}{dt},$$

the vorticity budget can be expressed

$$\frac{d(\zeta + f)}{dt} = 0. \tag{12.30}$$

$(\zeta + f)$ represents the *absolute vorticity* of air, namely, that apparent to an observer in an inertial reference frame. According to (12.30), $(\zeta + f)$ is conserved for an individual air parcel. Thus, under barotropic nondivergent conditions, absolute vorticity behaves as a tracer of horizontal air motion. It is simply rearranged by the circulation. Air moving equatorward experiences decreasing f. It must compensate by spinning up cyclonically, increasing its relative vorticity ζ (cf. the outbreak of cold polar air in the cyclone west of Africa in Figs. 1.28 and 1.29). Air moving poleward must evolve in the opposite manner, decreasing its relative vorticity. On large scales, the circulation tends to remain close to barotropic stratification. For this reason, absolute vorticity is approximately conserved.

Because it is nondivergent, the preceding motion may be represented in terms of a streamfunction (12.6), which automatically satisfies the continuity equation (12.27.2). Incorporating the vorticity (12.7.3) then transforms (12.30) into

$$\left(\frac{\partial}{\partial t} - \frac{\partial \psi}{\partial y}\frac{\partial}{\partial x} + \frac{\partial \psi}{\partial x}\frac{\partial}{\partial y}\right)\left\{\nabla^2 \psi + f\right\} = 0, \tag{12.31}$$

where ψ is the geostrophic streamfunction, e.g., (12.8). Known as the *barotropic nondivergent vorticity equation*, (12.31) provides a closed prognostic system for the single unknown ψ. It governs the structure of motion and how it evolves. Advective terms in the material derivative make (12.31) quadratically nonlinear in the dependent variable ψ. With suitable initial conditions and boundary conditions, the barotropic nondivergent vorticity equation can be integrated for the motion at some later time. It was applied to perform seminal experiments in numerical weather prediction (e.g., Charney et al., 1950).

12.5.2 Vorticity budget under baroclinic stratification

Under more general circumstances, absolute vorticity is not conserved. However, the governing equations still possess a conservation principle, albeit more complex. Baroclinic stratification renders the motion 3-dimensional. Vorticity is then a

3-dimensional vector quantity. Despite this complication, the quasi-horizontal nature of large-scale motion makes the vertical component of vorticity dominant.

Exclusive of friction, the horizontal momentum equations in physical coordinates are

$$\frac{\partial u}{\partial t} + \boldsymbol{v}\cdot\nabla u - fv = -\alpha\frac{\partial p}{\partial x} \tag{12.32.1}$$

$$\frac{\partial v}{\partial t} + \boldsymbol{v}\cdot\nabla v + fu = -\alpha\frac{\partial p}{\partial y}, \tag{12.32.2}$$

where $\boldsymbol{v}$ and ∇ denote the full 3-dimensional velocity and gradient. Cross differentiating (12.32) with respect to x and y and subtracting obtains

$$\left(\frac{\partial}{\partial t} + \boldsymbol{v}\cdot\nabla\right)\left(\frac{\partial v}{\partial x} - \frac{\partial u}{\partial y}\right) + \frac{\partial \boldsymbol{v}}{\partial x}\cdot\nabla v - \frac{\partial \boldsymbol{v}}{\partial y}\cdot\nabla u + f\left(\frac{\partial u}{\partial x} + \frac{\partial v}{\partial y}\right) + v\frac{\partial f}{\partial y} = \frac{\partial p}{\partial x}\frac{\partial \alpha}{\partial y} - \frac{\partial p}{\partial y}\frac{\partial \alpha}{\partial x}.$$

This may be consolidated into

$$\frac{d(\zeta + f)}{dt} + f\nabla_z\cdot\boldsymbol{v}_h + \left(\frac{\partial \boldsymbol{v}}{\partial x}\cdot\nabla v - \frac{\partial \boldsymbol{v}}{\partial y}\cdot\nabla u\right) = \left(\nabla_z p\times\nabla_z\alpha\right)\cdot\boldsymbol{k}. \tag{12.33}$$

The third term in (12.33) may be written

$$\begin{aligned}\frac{\partial \boldsymbol{v}_h}{\partial x}\cdot\nabla v - \frac{\partial \boldsymbol{v}}{\partial y}\cdot\nabla u &= \frac{\partial u}{\partial x}\left(\frac{\partial v}{\partial x} - \frac{\partial u}{\partial y}\right) + \frac{\partial v}{\partial y}\left(\frac{\partial v}{\partial x} - \frac{\partial u}{\partial y}\right) + \frac{\partial w}{\partial x}\frac{\partial v}{\partial z} - \frac{\partial w}{\partial y}\frac{\partial u}{\partial z}\\ &= \zeta\nabla_z\cdot\boldsymbol{v}_h + \frac{\partial w}{\partial x}\frac{\partial v}{\partial z} - \frac{\partial w}{\partial y}\frac{\partial u}{\partial z}.\end{aligned} \tag{12.34}$$

Similarly, the last term in (12.34) may be expressed

$$\frac{\partial w}{\partial x}\frac{\partial v}{\partial z} - \frac{\partial w}{\partial y}\frac{\partial u}{\partial z} = -\left(\xi\frac{\partial w}{\partial x} + \eta\frac{\partial w}{\partial y}\right), \tag{12.35.1}$$

where

$$\xi = \frac{\partial w}{\partial y} - \frac{\partial v}{\partial z} \tag{12.35.2}$$

$$\eta = \frac{\partial u}{\partial z} - \frac{\partial w}{\partial x} \tag{12.35.3}$$

represent the horizontal components of vector vorticity $\boldsymbol{\zeta} = (\xi, \eta, \zeta)$. Then the budget for the vertical component of vorticity becomes

$$\frac{d(\zeta + f)}{dt} = -(\zeta + f)\nabla_z\cdot\boldsymbol{v}_h + \left(\xi\frac{\partial w}{\partial x} + \eta\frac{\partial w}{\partial y}\right) + \left(\nabla_z p\times\nabla_z\alpha\right)\cdot\boldsymbol{k}, \tag{12.36}$$

wherein the Lagrangian derivative includes full 3-dimensional advection.

According to (12.36), the absolute vorticity of an air parcel can change through three mechanisms (Fig. 12.9):

Vertical stretching: By continuity, horizontal convergence $-\nabla_z\cdot\boldsymbol{v}_h$ is compensated by vertical stretching an air parcel (Fig. 12.9a). The reduced moment of inertia then leads to that material element spinning up to conserve angular momentum (in the same sense as its absolute vorticity). Horizontal divergence leads to the material element spinning down to conserve angular momentum.

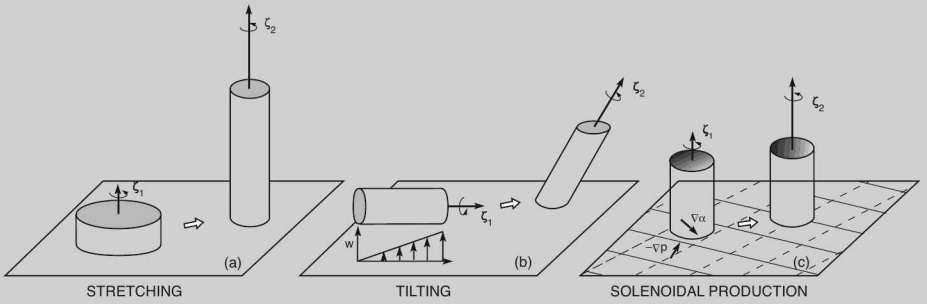

Figure 12.9 Forcing of the absolute vorticity $(f+\zeta)$ of an air parcel by (a) vertical stretching, which is compensated by horizontal convergence, (b) tilting, which exchanges horizontal and vertical vorticity, and (c) solenoidal production, which results from variation of density (stipled) across the pressure gradient force. The latter exerts a torque on the air parcel that is located inside a *solenoid* defined by two intersecting isobars (solid) and isochores (dashed).

Tilting: Horizontal shear of the vertical velocity $\nabla_z w$ deflects an air parcel, along with its vector angular momentum (Fig. 12.9b). This process transfers vorticity from horizontal components into the vertical component. A sharp horizontal temperature gradient is accompanied by strong vertical shear of the horizontal velocity (12.11). That shear magnifies the horizontal components of vorticity ξ and η, making tilting an important source of vertical vorticity.

Solenoidal production: Under baroclinic stratification, isobars on a surface of constant height do not coincide with isochores. Two sets of intersecting isobars and isochores then define a *solenoid* (Fig. 12.9c). Across it, pressure varies in one direction, but density varies in another. Variation of density across the pressure-gradient force then introduces a torque. The latter changes the angular momentum of the air parcel occupying a solenoid. Under barotropic stratification, density is uniform across the pressure gradient. The torque and solenoidal production of vorticity $\nabla_z p \times \nabla_z \alpha$ then vanish.

These forcing mechanisms reflect rearrangements of angular momentum – not its dissipation, which has been excluded by considering adiabatic and inviscid conditions. Scale analysis indicates that, in large-scale motion, vertical stretching dominates the forcing of absolute vorticity. Other mechanisms, which are generally smaller, derive from baroclinic stratification. The dominance of vertical stretching is a reflection of the nearly barotropic nature of large-scale motion.

If the vorticity budget is expressed in isentropic coordinates, tilting and solenoidal production disappear under adiabatic conditions. Vector identities in Appendix D enable the horizontal momentum equation (11.92.1) to be expressed

$$\frac{\partial \boldsymbol{v}_h}{\partial t} + \frac{1}{2}\nabla_\theta \left(\boldsymbol{v}_h \cdot \boldsymbol{v}_h\right) + \left(\zeta_\theta + f\right)\boldsymbol{k} \times \boldsymbol{v}_h + \omega_\theta \frac{\partial \boldsymbol{v}_h}{\partial \theta} = -\nabla_\theta \Psi, \tag{12.37}$$

where $\zeta_\theta = (\nabla_\theta \times \boldsymbol{v}_h) \cdot \boldsymbol{k}$ is the relative vorticity evaluated on an isentropic surface. Under adiabatic conditions, the term representing vertical advection disappears.

Applying $\boldsymbol{k} \cdot \nabla_\theta \times$ to (12.37) then obtains the vorticity budget

$$\frac{\partial(\zeta_\theta + f)}{\partial t} + \boldsymbol{v}_h \cdot \nabla_\theta(\zeta_\theta + f) = -(\zeta_\theta + f)\nabla_\theta \cdot \boldsymbol{v}_h$$

or

$$\frac{d(\zeta_\theta + f)}{dt} = -(\zeta_\theta + f)\nabla_\theta \cdot \boldsymbol{v}_h. \tag{12.38}$$

The Lagrangian derivative now involves only horizontal advection. Because vertical motion vanishes identically, so does the tilting that appears in physical coordinates (12.36). Likewise, solenoidal production vanishes because the vertical vorticity ζ_θ is evaluated on an isentropic surface. Absolute vorticity then changes only through vertical stretching. Because of the simple balance in (12.38), horizontal velocity can be treated through the scalar properties, vorticity and divergence. This enables motion to be integrated in numerical frameworks more effectively than can velocity directly (Bourke, 1974). For this reason, such treatment is widely adopted in GCMs (see, e.g., Williamson et al., 1987).

Under adiabatic conditions, the continuity equation in isentropic coordinates (11.92.3) reduces to

$$\frac{d}{dt}\left(\frac{\partial p}{\partial \theta}\right) + \left(\frac{\partial p}{\partial \theta}\right)\nabla_\theta \cdot \boldsymbol{v}_h = 0. \tag{12.39}$$

Combining this with (12.38) yields

$$\frac{1}{(\zeta_\theta + f)}\frac{d(\zeta_\theta + f)}{dt} = \frac{1}{\left(\frac{\partial p}{\partial \theta}\right)}\frac{d}{dt}\left(\frac{\partial p}{\partial \theta}\right).$$

The vorticity budget may then be expressed

$$\frac{dQ}{dt} = 0, \tag{12.40.1}$$

where

$$Q = \frac{\zeta_\theta + f}{-\frac{1}{g}\left(\frac{\partial p}{\partial \theta}\right)} \tag{12.40.2}$$

is one of several equivalent definitions of the *potential vorticity*, also called the *Ertel potential vorticity* (Ertel, 1942) and the *isentropic potential vorticity*.

Equation (12.40) is a generalization of the conservation principle for barotropic nondivergent motion. It asserts that, under inviscid adiabatic conditions, the potential vorticity of an air parcel is conserved. The parcel's absolute vorticity $(\zeta_\theta + f)$ can change. However, it does so in direct proportion to the change in vertical spacing $-\frac{1}{g}\left(\frac{\partial p}{\partial \theta}\right)$ of isentropic surfaces (11.85), which, under adiabatic conditions, are material surfaces. Despite its name, the conserved property Q does not have dimensions of vorticity; the denominator in (12.40.2) introduces other dimensions.

Potential vorticity is a dynamical tracer of horizontal motion. Under the same conditions that Q is conserved, vertical motion is determined by variations in the elevation of an isentropic surface, on which Q is evaluated. Unlike chemical tracers, potential vorticity is not a passive tracer: It is not advected "passively." Rather, the vorticity at a point induces motion about it. This property makes Q and the motion

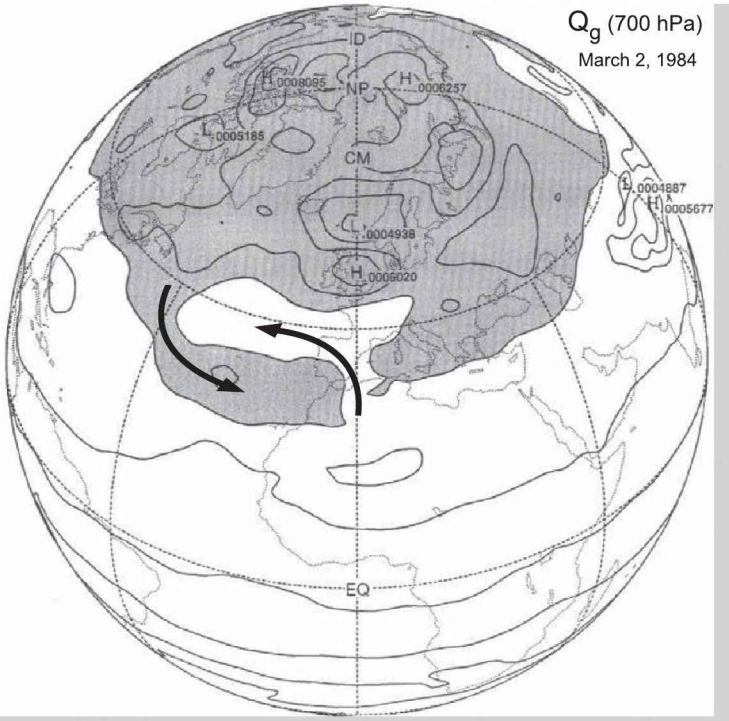

Figure 12.10 Distribution of quasi-geostrophic potential vorticity at 700 hPa on March 2, 1984, two days before the structure in Figs. 1.9a, 1.29. A cyclone off the coast of Africa has rearranged air, producing a dipole pattern in which high Q_g (shaded) has been folded south of low Q_g (cf. Fig. 16.6). A similar pattern appears over Europe, where Q_g has been folded by another cyclone.

field completely dependent on one another. According to the so-called *invertibility principle* (Hoskins et al., 1985), the distribution of Q at some instant uniquely determines the circulation. The conserved property Q may therefore be regarded as being self-advected.

In practice, friction and diabatic effects are slow enough away from the surface and outside convection for Q to be conserved over many advection times. Synoptic weather systems are marked by anomalies of potential vorticity (see Fig. 12.10). Forecasting such systems amounts to predicting the distribution of Q, which is controlled primarily by advection. Over time scales much longer than a day, nonconservative processes lead to production and destruction of Q (e.g., inside an individual air parcel). Turbulence, radiative transfer, and condensation eventually render the behavior of an air parcel diabatic. That, in turn, forces motion across isentropic surfaces. Such irreversibility leads to a vertical drift of air, motion that is ultimately manifest in the mean meridional circulation of the atmosphere (Sec. 3.6.1).

Unlike barotropic nondivergent motion (12.31), behavior described by (12.40) cannot be represented exclusively in terms of a streamfunction. Consequently,

the vorticity budget alone does not provide sufficient information to describe the motion. Divergence, although comparatively small, interacts with vorticity in (12.38). In large-scale numerical integrations, a closed prognostic system is formed by augmenting the vorticity budget with the budget of divergence, which follows in similar fashion (see, e.g., Haltiner and Williams, 1980).

12.5.3 Quasi-geostrophic motion

Under baroclinic and diabatic conditions, the governing equations are complex. An approximate prognostic system governing large-scale motion is therefore useful. Such a system can be derived via an expansion in Ro – as was used to introduce the diagnostic description of geostrophic motion. For the resulting system to remain prognostic, the expansion must retain terms higher order than those in (12.2). In particular, it must retain horizontal divergence, which forces changes of absolute vorticity through vertical stretching (12.38).

We consider motion in which meridional displacements of air are $O(Ro)$ and hence sufficiently narrow to ignore the Earth's curvature. Analogous to the f-plane development, spherical geometry is approximated in a Cartesian system tangent to the Earth at latitude ϕ_0 (Fig. 12.3). For consistency with other terms in the equations, the variation with latitude of the Coriolis force must now be retained to order Ro. Expanding f in a Taylor series in y (which reflects the meridional displacement of an air parcel) and truncating to first order yields the *β-plane approximation*

$$f = f_0 + \beta y \tag{12.41.1}$$

$$\beta = \left.\frac{df}{dy}\right|_{y=0}, \tag{12.41.2}$$

where f_0 and y are given by (12.3). The motion is also presumed to satisfy the so-called *Boussinesq approximation*: Variations of density are ignored, except where they accompany gravity in the buoyancy force. The Boussinesq approximation neglects changes in the density of an air parcel that are introduced by changes of its pressure. It retains only those density changes that are introduced thermally. Vertical displacements of air must then be shallow compared with H.

Following the development in Sec. 11.4, all variables are nondimensionalized by characteristic scale factors. Dependent variables are then expanded in a power series in Rossby number. The dimensionless horizontal velocity becomes

$$\boldsymbol{v}_h = \boldsymbol{v}_g + Ro\boldsymbol{v}_a + \ldots, \tag{12.42}$$

where $\boldsymbol{v}_g$ satisfies geostrophic balance with $f = f_0$ and the *ageostrophic velocity* $\boldsymbol{v}_a$ represents an $O(Ro)$ correction to it. Both are $O(1)$, as are all dependent variables in a formal scale analysis that consolidates the magnitudes of terms into dimensionless parameters like Ro (e.g., Charney, 1973). To streamline the development, we depart from the formal procedure by absorbing dimensionless parameters other than Ro into the dependent variables. Their magnitudes can then be inferred from the ensuing equations. This treatment enables the dimensionless equations to be expressed in forms nearly identical to their dimensional counterparts.

In log-pressure coordinates, the horizontal momentum equation, exclusive of friction, becomes

$$\begin{aligned} Ro\left\{\frac{\partial}{\partial t}+(\boldsymbol{v}_g+Ro\boldsymbol{v}_a+\ldots)\cdot\nabla_z\right\}(\boldsymbol{v}_g+Ro\boldsymbol{v}_a+\ldots)+Row\frac{\partial}{\partial z}(\boldsymbol{v}_g+Ro\boldsymbol{v}_a+\ldots)& \\ +(f_0+Ro\beta y)\boldsymbol{k}\times\ (\boldsymbol{v}_g+Ro\boldsymbol{v}_a+\ldots)& \\ =-\nabla_z(\Phi_g+Ro\Phi_a+\ldots),& \end{aligned} \tag{12.43}$$

where z denotes log-pressure height (11.65) and factors like β are understood to be dimensionless and $O(1)$. Because $\boldsymbol{v}_g$ satisfies (12.2), the Ro^0 balance drops out of (12.43). Under the Boussinesq approximation, w is smaller than $O(Ro)$, denoted $o(Ro)$. Thus vertical advection of momentum also drops out to $O(Ro)$. The momentum balance at $O(Ro)$ is then given by

$$\frac{d_g\boldsymbol{v}_g}{dt}+f_0\boldsymbol{k}\times\boldsymbol{v}_a+\beta y\boldsymbol{k}\times\boldsymbol{v}_g=-\nabla_z\Phi_a, \tag{12.44.1}$$

where

$$\frac{d_g}{dt}=\frac{\partial}{\partial t}+\boldsymbol{v}_g\cdot\nabla_z \tag{12.44.2}$$

is the time rate of change moving horizontally with the geostrophic velocity. According to (12.44), first-order departures from simple geostrophic equilibrium introduce a time rate of change or *tendency* into $\boldsymbol{v}_g$, behavior that is absent at $O(Ro^0)$.

The continuity equation (11.72.3) becomes

$$\begin{aligned} \frac{1}{\rho_0}\frac{\partial}{\partial z}(\rho_0 w)&=-\nabla_z\cdot(\boldsymbol{v}_g+Ro\boldsymbol{v}_a+\ldots) \\ &=-Ro\nabla_z\cdot\boldsymbol{v}_a. \end{aligned} \tag{12.45}$$

Thus, w follows directly from $\boldsymbol{v}_a$, through the associated divergence. The ageostrophic velocity introduces a *secondary circulation*. Unlike the $O(Ro^0)$ geostrophic motion, the secondary circulation involves vertical motion. Under adiabatic conditions, the thermodynamic equation (11.72.4) becomes

$$\left\{\frac{\partial}{\partial t}+(\boldsymbol{v}_g+Ro\boldsymbol{v}_a+\ldots)\cdot\nabla_z\right\}\frac{\partial}{\partial z}\left(\Phi_g+Ro\Phi_a+\ldots\right)+N^2w=0$$

or

$$\frac{d_g}{dt}\left(\frac{\partial\Phi_g}{\partial z}\right)+N^2w=0, \tag{12.46}$$

where N^2 is evaluated with the basic stratification T_0. The Boussinesq approximation requires N^2 to be large enough to render vertical displacements small. Therefore, the second term in (12.46) must be retained to leading order.

Equations (12.44), (12.45), and (12.46) describe *quasi-geostrophic motion* on a β-plane. Accurate to $O(Ro)$, they have dimensional counterparts that are nearly identical. Expressing the momentum budget as in (12.28) and applying $\boldsymbol{k}\cdot\nabla_z\times$ obtains the vorticity equation

$$\frac{d_g\zeta_g}{dt}+v\beta+f_0\nabla_z\cdot\boldsymbol{v}_a=0.$$

The budget of vorticity then becomes

$$\frac{d_g(\zeta_g + f)}{dt} = -f_0 \nabla_z \cdot \boldsymbol{v}_a, \tag{12.47.1}$$

where

$$\begin{aligned} \zeta_g &= \nabla_z^2 \psi \\ &= \frac{1}{f_0} \nabla_z^2 \Phi_g \end{aligned} \tag{12.47.2}$$

is the geostrophic vorticity. This is similar to the full vorticity equation in isentropic coordinates (12.38). However, the conditions of quasi-geostrophy make the relative vorticity ζ_g negligible compared with the planetary vorticity f_0 in the divergence term. With the continuity equation, (12.47) may be written

$$\frac{d_g(\zeta_g + f)}{dt} = f_0 \frac{1}{\rho_0} \frac{\partial}{\partial z} (\rho_0 w).^4$$

Then applying the operator $\frac{1}{\rho_0} \frac{\partial}{\partial z} (\rho_0)$ to the thermodynamic equation and eliminating w yields the *quasi-geostrophic potential vorticity equation*

$$\frac{d_g Q_g}{dt} = 0, \tag{12.48.1}$$

where

$$Q_g = \left\{ \nabla_z^2 \psi + f_0 + \beta y + \frac{1}{\rho_0} \frac{\partial}{\partial z} \left(\frac{f_0^2}{N^2} \rho_0 \frac{\partial \psi}{\partial z} \right) \right\} \tag{12.48.2}$$

is the *quasi-geostrophic potential vorticity*. Under the prevailing conditions, Q_g is a conserved property: It is invariant for individual air parcels. Because $\frac{d_g}{dt}$ involves only $\boldsymbol{v}_g$, (12.48) may be expressed in terms of the single dependent variable ψ

$$\left(\frac{\partial}{\partial t} - \frac{\partial \psi}{\partial y} \frac{\partial}{\partial x} + \frac{\partial \psi}{\partial x} \frac{\partial}{\partial y} \right) \left\{ \nabla_z^2 \psi + f_0 + \beta y + \frac{1}{\rho_0} \frac{\partial}{\partial z} \left(\frac{f_0^2}{N^2} \rho_0 \frac{\partial \psi}{\partial z} \right) \right\} = 0. \tag{12.49}$$

This is a generalization of the barotropic nondivergent vorticity equation (12.31) to weakly divergent motion.

Equation (12.49) constitutes a closed prognostic system for the streamfunction ψ. Like (12.31), it is quadratically nonlinear. With suitable initial and boundary conditions, it can be integrated for the structure and evolution of the motion. The conserved property Q_g is an analogue of isentropic potential vorticity (12.40.2). However, it is invariant following $\boldsymbol{v}_g$ rather than the actual horizontal motion.

Figure 12.10 shows the distribution of Q_g at 700 hPa 2 days prior to the analysis in Fig. 1.9. In the eastern Atlantic, cold high-Q_g air (shaded) is being drawn southeastward about a cyclone which matures into the one evident in Figs. 1.28 and 1.29. That cold air is being exchanged with warm low-Q_g air which is likewise being drawn about the cyclone, but in the opposite sense. These features mark a poleward transfer of warm air and an equatorward transfer of cold air. Together, they represent a poleward

[4] Under fully Boussinesq conditions, the stretching term simplifies to $f_0 \frac{\partial w}{\partial z}$ – the same as under incompressible conditions. With the density weighting retained, the approximation is referred to as *quasi-Boussinesq*. It accounts for vertical structure associated with the amplification of atmospheric waves (Chap. 14).

transfer of heat. The rearrangement of air introduces a dipole pattern, with high Q_g folded south of low Q_g. Similar structure appears over northern Europe, where the distribution of Q_g has been folded by a cyclone over the North Sea. Such systems are a ubiquitous feature of the tropospheric circulation. They continually develop along the jet stream, which coincides with the sharp temperature gradient that marks the polar front (Figs. 6.3, 6.4). The jet stream is thereby distorted, as warm air is swept poleward and cold air is swept equatorward (cf. Fig. 16.7). By exchanging high- and low-Q_g air, these disturbances to the jet stream transfer heat poleward. This dynamical heat transfer offsets radiative heating at low latitudes and radiative cooling at middle and high latitudes, maintaining thermal equilibrium locally (Sec. 1.5).

Observed structure of Q_g, like that in Fig 12.10, must be derived indirectly from temperature observations (12.48.2). Because that treatment requires repeated differentiation, the resulting structure tends to be noisy, contaminated by error. However, the basic signature emerges clearly in satellite imagery of water vapor, which, because it is conserved outside of cloud, registers large-scale air motion directly (cf. Figs. 16.6, 16.7).

The quasi-geostrophic equations describe motion in which the rotational component is dominant, only weakly coupled to the divergent component. As the equator is approached, f becomes small enough to invalidate those conditions. The divergent component of motion is then comparable to the rotational component. Tropical circulations must therefore be treated with the full primitive equations or with forms discriminated to the tropics, in which divergence and vorticity are both retained to leading order.

SUGGESTED REFERENCES

An Introduction to Dynamic Meteorology (2004) by Holton gives a complete treatment of gradient wind and an introduction to the concepts of vorticity and circulation.

Advanced treatments are presented in *Geophysical Fluid Dynamics* (1979) by Pedlosky and *Atmospheric and Oceanic Fluid Dynamics* (2006) by Vallis.

Hoskins et al. (1985) provides an overview of isentropic potential vorticity. Comparisons with quasi-geostrophic potential vorticity are given in *Atmosphere-Ocean Dynamics* (1982) by Gill.

PROBLEMS

1. The bullet train moves over straight and level track at 40° latitude. If the train's mass is 10^5 kg, how fast must it move to experience a transverse force equal to 0.1% of its weight?
2. Surface motion beneath a cyclone is described by the streamfunction and velocity potential

$$\psi(x, y) = \Psi\left[1 - e^{-\frac{(x^2+y^2)}{L^2}}\right]$$

$$\chi(x, y) = X e^{-\frac{(x^2+y^2)}{L^2}},$$

where Ψ and X are constants. Determine (a) the horizontal velocity, (b) the horizontal divergence, and (c) the vertical vorticity. (d) Sketch $\boldsymbol{v}_h(x, y)$ and discuss it in relation to $\psi(x, y)$ and $\chi(x, y)$. (e) Indicate the horizontal trajectory of an air parcel and discuss it in relation to 3-dimensional air motion.

3. The 500-hPa surface has height

$$z_{500} = \begin{cases} \overline{\overline{z}}_{500} - \overline{z}_{500}\left(\frac{y}{a}\right) - z'_{500}\left[1 + cos\left(\pi \frac{x^2+y^2}{L^2}\right)\right] & (x^2+y^2)^{\frac{1}{2}} \le L \\ \overline{\overline{z}}_{500} - \overline{z}_{500}\left(\frac{y}{a}\right) & (x^2+y^2)^{\frac{1}{2}} > L, \end{cases}$$

where the constants $\overline{\overline{z}}_{500}$, $\overline{z}_{500}$, and z'_{500} reflect global-mean, zonal-mean, and perturbation contributions to the height field; a is the radius of the Earth; and y is measured on a midlatitude f plane centered at latitude ϕ_0. (a) Provide an expression for the 500-hPa geostrophic flow $\boldsymbol{v}_{500}$. (b) Sketch $z_{500}(x, y)$ and $\boldsymbol{v}_{500}(x, y)$, presuming $z'_{500} \ll \overline{z}_{500}$. Discuss the contributions to $\boldsymbol{v}_{500}$, noting how the flow is influenced by the thermal perturbation. (c) Provide an expression for the absolute vorticity at 500 hPa and discuss its contributions.

4. A midlatitude cyclone centered at 45 N produces a radial height gradient at 500 hPa of 0.16 m km^{-1} at a characteristic radial distance of $R = a\Delta\theta$, with $\Delta\theta = 10°$. If the motion is sufficiently steady, calculate the corresponding (a) geostrophic wind and (b) gradient wind.

5. As in Prob. 12.4, but for a tropical cyclone centered at 10 N, which produces a radial height gradient at 850 hPa of 1.88 m km^{-1} at a characteristic radial distance corresponding to $\Delta\theta = 1°$.

6. A vertical sounding at 45 N reveals isothermal conditions with $T = 0°$C below 700 hPa, but vertical shear characterized by the following wind profile:

$$v = \begin{cases} 10 \text{ m s}^{-1} & \text{S} & 950 \text{ hPa} \\ 14.14 \text{ m s}^{-1} & \text{SW} & 850 \text{ hPa} \\ 10 \text{ m s}^{-1} & \text{S} & 750 \text{ hPa}, \end{cases}$$

where the wind blows from direction indicated. (a) Calculate the mean horizontal temperature gradient in the layers between 950 hPa and 850 hPa and between 850 hPa and 750 hPa. (b) Estimate the rate at which the preceding layers would warm/cool locally through temperature advection (e.g., were temperature approximately conserved). (c) Use the result of (b) to estimate the lapse rate created between those layers after one day, noting the physical implications.

7. Consider the core of a tornado that is isothermal and in rigid-body rotation with angular velocity Ω. Derive an expression for the radial profile of pressure inside the tornado's core in terms of the pressure p_0 at its center.

8. Isobaric height in the Venusian atmosphere varies locally as

$$\Phi(x, y) = \overline{\Phi}\left[1 + \epsilon \frac{x^2 + y^2}{L^2}\right].$$

(a) If the motion is steady and frictionless, provide an expression for the horizontal velocity. (b) Can a similar result be obtained if the flow is transient? Why?

9. A stratospheric sudden warming is accompanied by a reversal of westerlies that comprise the polar-night vortex (Fig. 1.10). Occurring in just a couple of days, this flow reversal follows from a rearrangement of air by planetary waves (see Fig. 14.26). Suppose that the initial motion at middle and high latitudes is approximated by rigid body rotation, with angular velocity 0.25Ω, and that the reversed motion at high latitude is likewise approximated by rigid body rotation, but with zonal easterlies at 75 N of 20 m s^{-1}. If, during the reversal, motion remains approximately nondivergent, estimate from where air that eventually prevails over the polar cap must have originated.

10. The zonal circulation is disrupted by a planetary wave that advects air northward from 10 N to 50 N. If wind at 10 N is easterly with speed of 5 m s^{-1} and relative vorticity of 1.2 10^{-5} s^{-1}, estimate the column-averaged vorticity at 50 N if (a) air motion is barotropic nondivergent, (b) air motion is confined between an isentropic surface near 1000 hPa and another near the tropopause, which slopes downward toward the pole from 100 hPa in the tropics to 300 hPa at 50 N.
11. (a) Determine the components of frictional geostrophic motion tangential and orthogonal to contours of height, in terms of the corresponding geostrophic velocity. (b) Construct an expression for the angle δ by which $\boldsymbol{v}_h$ deviates from height contours. Estimate δ for a Rayleigh-friction coefficient of $K = 4$ $days^{-1}$ at a latitude of (c) 45° and (d) 15°.
12. By applying the results of Prob. 12.11, (a) derive an expression for the divergence of frictional geostrophic motion on an f plane to show that, in the presence of Rayleigh friction, $\nabla \cdot \boldsymbol{v}_h$ is proportional to the $\nabla^2\Phi$. (b) From this expression, infer how vertical motion over a surface low depends on its latitude.
13. The Kelvin wave figures in tropical circulations. Representing a vertical overturning in the equatorial plane, it has the form of a traveling Walker circulation (Fig. 1.36). Horizontal motion in the Kelvin wave is zonal and described by

$$\boldsymbol{v}_h(x, y) = e^{-\left(\frac{y}{Y}\right)^2} e^{i(kx-\sigma t)}\boldsymbol{i},$$

where y is measured on an equatorial betaplane ($\phi_0 = 0$) and Y corresponds to 10° of latitude. (a) Sketch the velocity field over one wavelength in the x direction. (b) Calculate the vorticity and divergence of the wave, sketching each on the equatorial beta-plane. (c) Derive a system of equations that determines the streamfunction and velocity potential of the wave. Outline the solution of this system.
14. Consider steady, barotropic, nondivergent motion on a midlatitude beta plane. The motion is zonal and uniform with $\boldsymbol{v} = \overline{u}\boldsymbol{i}$ upstream of an extended NS ridge at $x = 0$, which deflects streamlines meridionally from their undisturbed latitudes. If the disturbed motion downstream deviates from the upstream motion by a small meridional perturbation v', (a) construct a differential equation governing the trajectory $y(x)$ of an air parcel initially at $y = 0$, (b) obtain the general solution downstream of the obstacle, (c) determine the trajectory if the parcel is deflected at $(0, 0)$ with a slope of $tan(\alpha)$, and (d) interpret the motion downstream of the obstacle in terms of a restoring force.
15. (a) Explain why solenoidal production of vorticity vanishes in isentropic coordinates (12.38). (Hint: How many thermodynamic degrees of freedom are present in general? along an isentropic surface?) (b) Apply this argument to the budget of vorticity in isobaric coordinates.
16. Consider a steady vortex with circular streamlines and azimuthal velocity v. (a) Determine the form of the velocity profile $v(r)$ that possesses no vorticity for $r > 0$. (b) Calculate the *circulation* $\Gamma(r) = \oint \boldsymbol{v}(r) \cdot d\boldsymbol{s} = \int_0^{2\pi} v(r) r d\phi$ about the vortex. (c) Use Stokes' theorem to interpret the distribution of vorticity.

CHAPTER

THIRTEEN

The planetary boundary layer

Previous development treats motion as a smoothly varying field property. However, atmospheric motion is always partially turbulent. Laboratory experiments provide a criterion for the onset of turbulence, in terms of the dimensionless *Reynolds number*

$$Re = \frac{LU}{\nu}, \tag{13.1}$$

where L and U are scales characterizing a flow and $\nu = \frac{\mu}{\rho}$ is the kinematic viscosity (Sec. 10.6). For Re greater than a critical value of about 5000, smooth laminar motion undergoes a transition to turbulent motion, which is inherently unsteady, 3-dimensional, and involves a spectrum of space and time scales. Even for a length scale as short as 1 m, the critical Reynolds number with $\nu = 10^{-5}$ m^2 s^{-1} is exceeded for velocities of only $U > 0.05$ m s^{-1}. Consequently, atmospheric motion inevitably contains some turbulence.[1]

Until now, turbulent transfers have been presumed small enough to treat an individual air parcel as a closed system. This approximation is valid away from the Earth's surface and outside convection. In the *free atmosphere*, the time scale for turbulent exchange is long, much longer than the 1-day time scale that characterizes advective changes of an air parcel. Budgets of momentum, internal energy, and constituents for an individual parcel may therefore be treated exclusive of turbulent exchanges with the parcel's environment – at least over time scales comparable to advection. This feature of the atmospheric circulation is reflected in the spectrum of kinetic energy (Fig. 13.1). In the free atmosphere, kinetic energy is concentrated at periods longer

[1] Stratification of mass leads to ν increasing exponentially with height. Therefore, a height is eventually reached where ν is sufficiently large to drive Re below the critical value and suppress turbulence. This transition occurs at the turbopause, see Fig. 1.4 (Prob. 13.3).

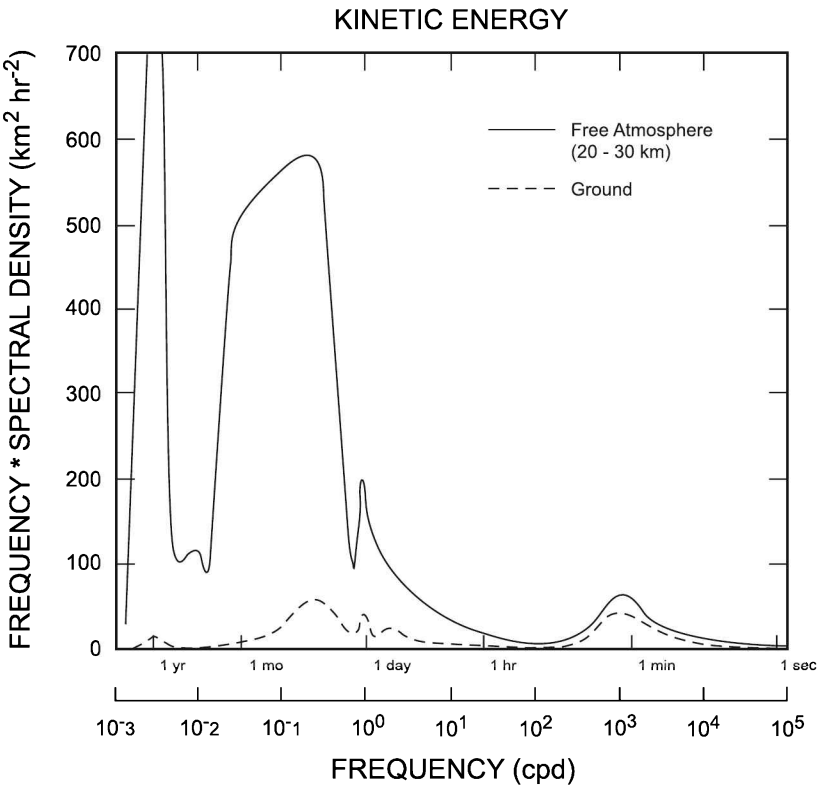

Figure 13.1 Power spectrum of atmospheric kinetic energy. Adapted from Vinnichenko (1970). Copyright (1970) Munksgaard International Publishers Ltd., Copenhagean, Denmark.

than a day, where it is associated with large-scale disturbances and seasonal variations. However, in a neighborhood of the surface, as much as half of the kinetic energy lies at periods of only minutes. Inside the *planetary boundary layer*, turbulent eddies are generated mechanically by strong shear as the flow adjusts sharply to satisfy the no-slip condition at the Earth's surface (see Fig. 13.3). Turbulence is also generated thermally through buoyancy, when the stratification is destabilized by heat transfer from the Earth's surface.

Inside the boundary layer, mixing between air parcels cannot be ignored. There, the time scale for turbulent exchange is comparable to that for advection. Turbulent exchanges of mass, heat, and momentum then make an air parcel an open system, rendering its behavior diabatic. Turbulent mixing transfers heat and moisture between the surface and the atmosphere. Because it destroys gradients inherent to large-scale motion, it also damps the circulation.

13.1 DESCRIPTION OF TURBULENCE

Turbulent fluctuations need not be hydrostatic. Therefore, the equations of motion are expressed most conveniently in physical coordinates. The limited vertical scale

of turbulent eddies makes compressibility nonessential. However, variations of density associated with temperature fluctuations play a key role in stratified turbulence because, through buoyancy, they couple the motion to gravity. These features are embodied in the Boussinesq approximation (Sec. 12.5). Equivalent to incompressibility, the Boussinesq approximation allows density to be treated as constant, except where accompanied by gravity in the buoyancy force.

Consider the motion-related stratification (Sec. 11.4), which is regarded as a small departure from static conditions. In terms of the static density $\rho_0(z)$, the specific buoyancy force experienced by an air parcel (11.35) is

$$f_b = -\frac{1}{\rho_0}\frac{\partial p}{\partial z} - \frac{\rho}{\rho_0}g. \tag{13.2}$$

The gas law and Poisson's relation for potential temperature, along with the neglect of compressibility, then imply

$$\begin{aligned}\frac{\rho}{\rho_0} &= -\frac{T}{T_0} + \frac{p}{p_0} \\ &\cong -\frac{\theta}{\theta_0}.\end{aligned} \tag{13.3}$$

Hence, the vertical momentum budget becomes

$$\frac{dw}{dt} - \frac{1}{\rho_0}\frac{\partial p}{\partial z} + g\frac{\theta}{\theta_0} - D_z. \tag{13.4}$$

Similarly, the thermodynamic equation becomes

$$\frac{d\theta}{dt} + w\frac{d\theta_0}{dz} = \frac{\theta_0}{c_p T_0}\dot{q}_{net}, \tag{13.5}$$

where $\theta_0(z)$ describes the basic stratification and θ the small departure from it. Under the Boussinesq approximation, the continuity equation reduces to a statement of 3-dimensional nondivergence. Then the equations governing turbulent motion become

$$\frac{du}{dt} - fv = -\frac{1}{\rho_0}\frac{\partial p}{\partial x} - D_x \tag{13.6.1}$$

$$\frac{dv}{dt} + fu = -\frac{1}{\rho_0}\frac{\partial p}{\partial y} - D_y \tag{13.6.2}$$

$$\frac{dw}{dt} = -\frac{1}{\rho_0}\frac{\partial p}{\partial z} + g\frac{\theta}{\theta_0} - D_z \tag{13.6.3}$$

$$\frac{\partial u}{\partial z} + \frac{\partial v}{\partial y} + \frac{\partial w}{\partial z} = 0 \tag{13.6.4}$$

$$\frac{d\theta}{dt} + w\frac{d\theta_0}{dz} = \frac{\theta_0}{c_p T_0}\dot{q}_{net}, \tag{13.6.5}$$

where

$$\begin{aligned}\frac{d}{dt} &= \frac{\partial}{\partial t} + \boldsymbol{v}\cdot\nabla \\ &= \frac{\partial}{\partial t} + u\frac{\partial}{\partial x} + v\frac{\partial}{\partial y} + w\frac{\partial}{\partial z}\end{aligned} \tag{13.6.6}$$

includes 3-dimensional advection. The frictional drag, $\boldsymbol{D} = -\frac{1}{\rho}\nabla\cdot\boldsymbol{\tau}$, follows from the deformation tensor $\boldsymbol{e}$ (10.23). Under the Boussinesq approximation, it reduces to

$$\boldsymbol{D} = -\nu\nabla^2\boldsymbol{v}. \tag{13.6.7}$$

Compared with the time scale of turbulent eddies, radiative heating in $\dot{q}_{net}$ is slow enough to be ignored. However, thermal diffusion (e.g., conduction) operates efficiently on small scales that are created through turbulent deformation (cf. Fig. 12.4). Diffusion of momentum and heat are both involved in dissipation of turbulence, which takes place on the smallest scales of motion. Sharp gradients produced when anomalies are strained down to small dimensions are acted upon efficiently by molecular diffusion.[2] When those gradients are destroyed, so too is the energy that has been transferred to small scales. The foregoing process reflects a cascade of energy from large scales of organized motion to small scales, where it is dissipated by molecular diffusion.

13.1.1 Reynolds decomposition

Of relevance to the large-scale circulation is the time-averaged motion and how it is influenced by turbulent fluctuations. To describe such interactions, each field variable is separated into a slowly-varying mean component, which is denoted by an overbar, and a fluctuating component, which is denoted by a prime, e.g.,

$$\boldsymbol{v} = \bar{\boldsymbol{v}} + \boldsymbol{v}', \tag{13.7.1}$$

with

$$\overline{\boldsymbol{v}'} = 0. \tag{13.7.2}$$

For this decomposition to be meaningful, time scales of the two components must be widely separated. Only then can averaging be performed over an interval long enough for a stable mean to be recovered from fluctuating properties yet short enough for mean properties to be regarded as steady.

The continuity equation (13.6.4) enables the material acceleration to be expressed in terms of the divergence of a momentum flux

$$\frac{du}{dt} = \frac{\partial u}{\partial t} + \nabla\cdot(\boldsymbol{v}u) \tag{13.8.1}$$

$$\frac{dv}{dt} = \frac{\partial v}{\partial t} + \nabla\cdot(\boldsymbol{v}v) \tag{13.8.2}$$

$$\frac{dw}{dt} = \frac{\partial w}{\partial t} + \nabla\cdot(\boldsymbol{v}w), \tag{13.8.3}$$

[2] The scale dependence of diffusion can be inferred from the viscous drag (13.6.7), which increases quadratically with the inverse scale of motion anomalies.

where terms on the far right describe the 3-dimensional momentum carried by the velocity $\boldsymbol{v}$. Likewise, the material rate of change of temperature in (13.6.7) can be expressed in terms of the divergence of a heat flux

$$\frac{d\theta}{dt} = \frac{\partial\theta}{\partial t} + \nabla\cdot(\boldsymbol{v}\theta). \tag{13.9}$$

Expanding as in (13.7) and averaging then obtains the equations governing the time-mean motion

$$\frac{\overline{d}\,\overline{u}}{dt} - f\overline{v} = -\frac{1}{\rho_0}\frac{\partial\overline{p}}{\partial x} - \left[\frac{\partial\overline{u'u'}}{\partial x} + \frac{\partial\overline{u'v'}}{\partial y} + \frac{\partial\overline{u'w'}}{\partial z}\right] \tag{13.10.1}$$

$$\frac{\overline{d}\,\overline{v}}{dt} + f\overline{u} = -\frac{1}{\rho_0}\frac{\partial\overline{p}}{\partial y} - \left[\frac{\partial\overline{u'v'}}{\partial x} + \frac{\partial\overline{v'v'}}{\partial y} + \frac{\partial\overline{v'w'}}{\partial z}\right] \tag{13.10.2}$$

$$\frac{\overline{d}\,\overline{w}}{dt} = -\frac{1}{\rho_0}\frac{\partial\overline{p}}{\partial z} + g\frac{\overline{\theta}}{\theta_0} - \left[\frac{\partial\overline{u'w'}}{\partial x} + \frac{\partial\overline{v'w'}}{\partial y} + \frac{\partial\overline{w'w'}}{\partial z}\right] \tag{13.10.3}$$

$$\frac{\partial\overline{u}}{\partial x} + \frac{\partial\overline{v}}{\partial y} + \frac{\partial\overline{w}}{\partial z} = 0. \tag{13.10.4}$$

$$\frac{\overline{d}\,\overline{\theta}}{dt} + \overline{w}\frac{d\theta_0}{dz} = -\left[\frac{\partial\overline{u'\theta'}}{\partial x} + \frac{\partial\overline{v'\theta'}}{\partial y} + \frac{\partial\overline{w'\theta'}}{\partial z}\right], \tag{13.10.5}$$

where

$$\frac{\overline{d}}{dt} = \frac{\partial}{\partial t} + \overline{\boldsymbol{v}}\cdot\nabla \tag{13.10.6}$$

is the time rate of change following the mean motion and diffusive transfers of momentum and heat on scales of the mean flow are slow enough to be ignored.

Terms in (13.10.1)-(13.10.3) involve time-averaged products of fluctuating velocities. They represent the convergence of an eddy momentum flux (e.g., of eddy momentum carried by the eddy velocity). Mean x momentum (13.10.1) is forced by the convergence of eddy x momentum flux and so forth. Then, according to the discussion in Sec. 10.6, fluxes of x momentum carried by the three components of fluctuating velocity

$$\tau_{xx} = -\rho_0\overline{u'u'} \tag{13.11.1}$$

$$\tau_{xy} = -\rho_0\overline{u'v'} \tag{13.11.2}$$

$$\tau_{xz} = -\rho_0\overline{u'w'} \tag{13.11.3}$$

represent stresses in the x direction that are exerted on the mean flow by turbulent motions. Referred to as *Reynolds stresses*, their convergence exerts a turbulent drag on the mean motion of an air parcel. Collectively, the Reynolds stresses define a turbulent stress tensor $\boldsymbol{\tau} = -\rho_0\overline{\boldsymbol{v}'\boldsymbol{v}'}$. $\boldsymbol{\tau}$ is a counterpart of the stress tensor in (10.22). Its convergence represents the absorption of eddy momentum by the mean flow, which, in turn, forces $\overline{\boldsymbol{v}}$ in (13.10.1) (13.10.3). A similar interpretation applies to the mean potential temperature. The latter is forced by the convergence of eddy heat flux in (13.10.5)

$$\frac{\boldsymbol{q}}{c_p} = \rho_0\overline{\boldsymbol{v}'\theta'}. \tag{13.12}$$

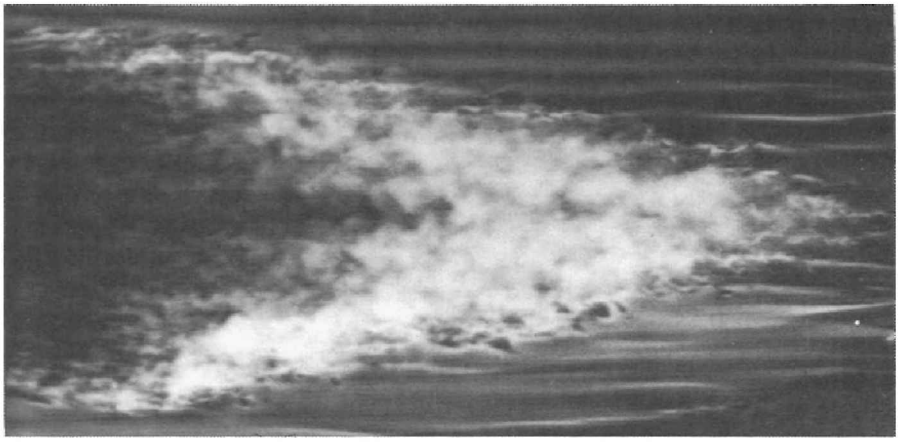

Figure 13.2 Turbulent spot introduced into a laminar flow (from right to left) at $Re = 4.0\ 10^5$. After Van Dyke (1982).

13.1.2 Turbulent diffusion

Reynolds decomposition provides a framework for describing how turbulent motions interact with the mean flow. However, it affords little insight into how the turbulent fluxes of momentum and heat that force mean motion can be determined. The description of mean motion (13.10) can be closed only by resorting to empirical or *ad hoc* prescriptions that relate eddy fluxes to the mean fields.

The closure scheme adopted most widely is inspired by molecular diffusion, which smoothes out gradients. Although more complex, turbulence has a similar effect on mean properties. Figure 13.2 shows the evolution of a turbulent spot that has been introduced into a uniform flow at large *Re*. Streaklines of smoke captured by the spot are dispersed across the turbulent region, which spreads laterally with distance downstream. Therefore, mean concentration inside the turbulent region decreases steadily, assuming progressively weaker gradient as smoke is diluted over an ever-expanding volume. Turbulent dispersion is responsible for mean concentrations of pollutants diminishing following the breakdown of the nocturnal inversion (Sec. 7.6.3). It is also responsible for the radial expansion of buoyant thermals (Sec. 9.3).

Turbulent dispersion acts on all conserved properties. It is analogous to molecular diffusion, at least qualitatively. In this spirit, the eddy momentum flux can be expressed in terms of the gradient of mean momentum (13.6.7)

$$\boldsymbol{\tau} = \rho_0 K_M \cdot \nabla \overline{\boldsymbol{v}}, \tag{13.13.1}$$

where the *eddy diffusivity* of momentum K_M is an analogue of the kinematic viscosity ν for molecular diffusion.[3] For the boundary layer, it suffices to consider mean motion that is horizontally homogeneous. Horizontal diffusion of momentum then vanishes and K_M pertains to the vertical flux alone. The vertical eddy flux of horizontal momentum

$$\overline{w'\boldsymbol{v}'} = -K_M \frac{\partial \overline{\boldsymbol{v}}}{\partial z} \tag{13.13.2}$$

[3] For anisotropic turbulence, wherein statistical properties vary with direction, K_M is a tensor. The components of K_M then refer to turbulent dispersion in the horizontal and vertical directions. Their application in 2-dimensional models is described in Andrews et al. (1987).

is then proportional to the vertical gradient of mean momentum. Likewise, the vertical heat flux becomes

$$\overline{w'\theta'} = -K_H \frac{\partial \overline{\theta}}{\partial z}, \tag{13.13.3}$$

where K_H is the eddy diffusivity of heat. It is proportional to the vertical gradient of mean θ.

Expressions (13.13) comprise the so-called *flux-gradient relationship*. Turbulent transfer in (13.10) then assumes the form of diffusion of mean properties (e.g., $K_M \nabla^2 \overline{\boldsymbol{v}}$). In principle, eddy diffusivities can be incorporated as above. In practice, however, K_M and K_H depend on fluctuating field properties, which are unknown. They must therefore be evaluated empirically, for example, in terms of the eddy fluxes $\overline{w'u'}$ and $\overline{w'\theta'}$. Inside the planetary boundary layer, measured eddy diffusivities of momentum range between 1 and 10^2 m^2 s^{-1}. These values of K_M are orders of magnitude greater than its counterpart for molecular diffusion ($\nu = 10^{-5}$ m^2 s^{-1}). For this reason, turbulent diffusion is the chief source of drag and mechanical heating experienced by the mean flow.

13.2 STRUCTURE OF THE BOUNDARY LAYER

13.2.1 The Ekman Layer

Consider motion inside a boundary layer in which mean properties are steady and horizontally homogeneous. In terms of eddy diffusivity, the horizontal momentum equations become

$$-f\overline{v} = -\frac{1}{\rho_0}\frac{\partial \overline{p}}{\partial x} + K\frac{\partial^2 \overline{u}}{\partial z^2} \tag{13.14.1}$$

$$f\overline{u} = -\frac{1}{\rho_0}\frac{\partial \overline{p}}{\partial y} + K\frac{\partial^2 \overline{v}}{\partial z^2}, \tag{13.14.2}$$

where $K = K_M$ is regarded as constant and the Boussinesq approximation has been invoked to ignore vertical advection of mean momentum. Eliminating the pressure gradient in favor of the geostrophic velocity, $\boldsymbol{v}_g = \frac{1}{\rho_0 f}\boldsymbol{k} \times \nabla p$, transforms (13.14) into

$$K\frac{\partial^2 \overline{u}}{\partial z^2} + f(\overline{v} - v_g) = 0 \tag{13.15.1}$$

$$K\frac{\partial^2 \overline{v}}{\partial z^2} - f(\overline{u} - u_g) = 0. \tag{13.15.2}$$

Multiplying (13.15.1) by $i = \sqrt{-1}$ and adding it to (13.15.2) obtains the single equation

$$K\frac{\partial^2 \chi}{\partial z^2} - if\chi = -if\chi_g \tag{13.16.1}$$

in terms of the consolidated variables

$$\chi = \overline{u} + i\overline{v} \tag{13.16.2}$$

$$\chi_g = u_g + iv_g. \tag{13.16.3}$$

If $\boldsymbol{v}_g$ does not vary through the boundary layer and is oriented parallel to the x axis, (13.16) has the general solution

$$\chi(z) = Ae^{(1+i)\gamma z} + Be^{-(1+i)\gamma z} + u_g \tag{13.17.1}$$

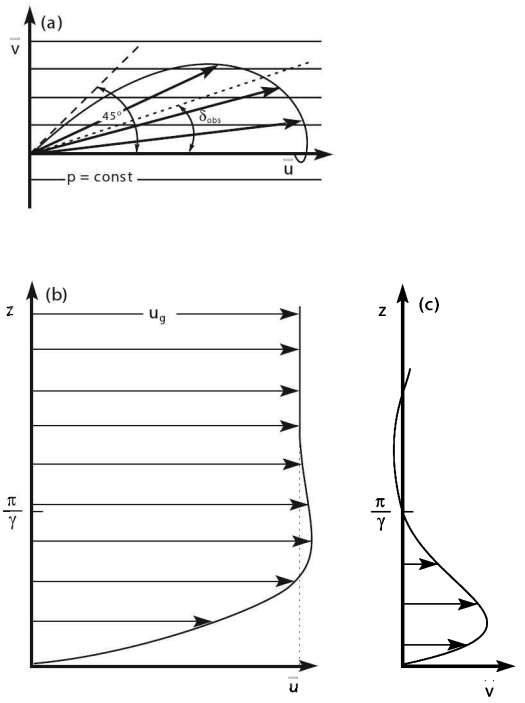

Figure 13.3 Mean horizontal motion inside an Ekman layer in which isobars are oriented parallel to the x axis. (a) Planform view of the Ekman spiral, with $\overline{\boldsymbol{v}} = (\overline{u}, \overline{v})$ shown at different levels. Vertical profiles of (b) $\overline{u}$ and (c) $\overline{v}$ through the boundary layer.

where

$$\gamma = \sqrt{\frac{f}{2K}}. \tag{13.17.2}$$

At the Earth's surface, the no-slip condition requires the horizontal velocity to vanish. Above the boundary layer, the motion must asymptotically approach the geostrophic velocity:

$$\begin{aligned} \overline{\boldsymbol{v}} &= 0 \qquad & z &= 0 \\ \overline{\boldsymbol{v}} &\sim u_g \boldsymbol{i} \qquad & z &\to \infty. \end{aligned} \tag{13.17.3}$$

Incorporating these boundary conditions and collecting real and imaginary parts then yield the component velocities

$$\overline{u}(z) = u_g \left(1 - e^{-\gamma z} cos\gamma z\right) \tag{13.18.1}$$

$$\overline{v}(z) = v_g e^{-\gamma z} sin\gamma z, \tag{13.18.2}$$

which define an *Ekman layer.*

The mean velocity in (13.18) describes an *Ekman spiral.* It is plotted in Fig. 13.3 as a function of height. Moving downward through the boundary layer witnesses a deflection of the mean velocity from its value in the free atmosphere, $\boldsymbol{v}_g = u_g \boldsymbol{i}$, across isobars: $\overline{v}$ is deflected to the left in the Northern Hemisphere, but to the right in the Southern Hemisphere – always toward low pressure (Sec. 12.3). At the ground, $\overline{\boldsymbol{v}}$ attains a limiting deflection of $\delta = 45°$.

The deflection from isobars measures the turbulent drag that is exerted on the mean flow. Such drag drives the motion out of geostrophic equilibrium. It increases with mean vertical shear. The effective depth of the Ekman layer is given by $z = \frac{\pi}{\gamma}$, where $\overline{v}$ reverses sign. Above this height, $\overline{\boldsymbol{v}}$ remains close to $\boldsymbol{v}_g$ (Fig. 13.3). Values of $K = 10\ \mathrm{m^2\ s^{-1}}$ and $f = 10^{-4}\ \mathrm{s^{-1}}$ give $\frac{\pi}{\gamma} \cong 1$ km. In practice, a pure Ekman spiral is seldom observed.[4] Nonetheless, it captures the salient structure of the planetary boundary layer. A deflection from surface isobars $\delta_{obs} \cong 25°$ is typical.

13.2.2 The surface layer

Within the lowest 15% of the boundary layer, the assumption that $K \cong$ const breaks down. Instead, K, which is determined by the characteristic velocity and length scales of turbulent eddies, varies with height linearly. Within the surface layer, the no-slip condition limits eddies to a characteristic length scale that is proportional to the distance z from the ground. It gives them a characteristic velocity scale

$$u_* = \left(-\overline{u'w'}\right)^{\frac{1}{2}}. \tag{13.19}$$

Known as the *friction velocity*, u_* reflects the turbulent shear stress near the ground. The flux-gradient relationship (13.13) then requires

$$u_*^2 = kzu_* \frac{\partial \overline{u}}{\partial z}, \tag{13.20}$$

where $\overline{\boldsymbol{v}} = \overline{u}\boldsymbol{i}$ near the surface has been presumed parallel to the x axis and $k = 0.4$ is the so-called *von Karman constant*. Integrating (13.20) gives the logarithmic vertical structure inside the surface layer

$$\left(\frac{\overline{u}}{u_*}\right) = \frac{1}{k} ln\left(\frac{z}{z_0}\right), \tag{13.21}$$

in which z_0 is a *roughness length* that characterizes the Earth's surface. The depth of the surface layer varies in relation to its roughness through z_0. For level vegetated terrain, z_0 has values less than 5 cm.

The structure (13.21) is a counterpart of the *viscous sublayer* that exists in turbulent flow over a flat plate (e.g., Schlicting, 1968). Inside it, fluxes of momentum and heat are independent of height. For neutral stability, the logarithmic behavior predicted by (13.21) is well-obeyed over a wide range of level terrain (Fig. 13.4). The same is true for stable stratification, within some distance of the surface.

13.3 INFLUENCE OF STRATIFICATION

Static stability modifies the character of the boundary layer by influencing the production and destruction of turbulence. Vertical shear of the mean flow leads to mechanical production of turbulent kinetic energy. Under neutral stability, that energy cascades equally into all three components of motion. The turbulence produced is isotropic.

[4] High Re characteristic of the atmosphere makes simple Ekman flow dynamically unstable.

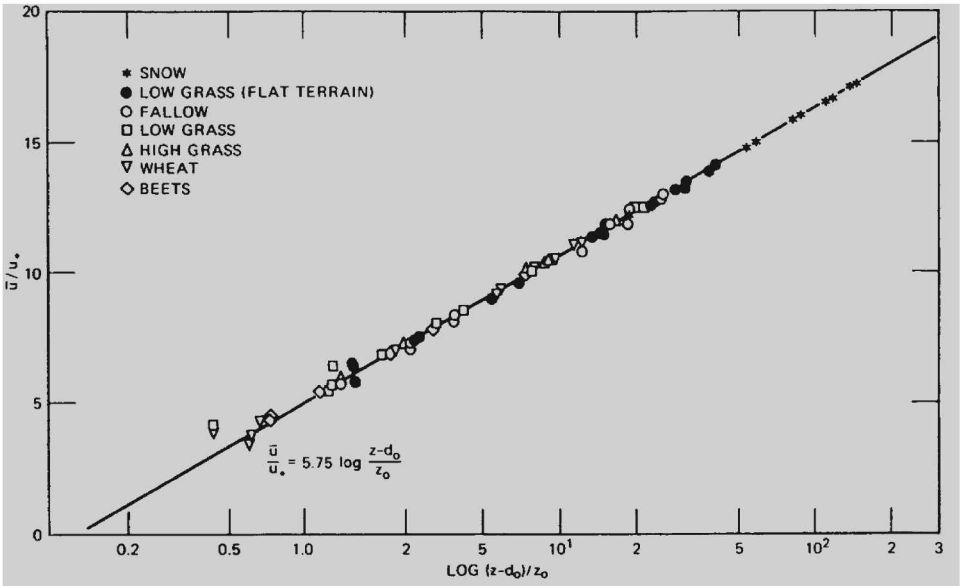

Figure 13.4 Observations of horizontal velocity versus height in terms of the friction velocity u_* and roughness length z_0 for different terrain characterized by the height d_0. After Paeschke (1937).

Turbulent kinetic energy is also produced through buoyancy. Unlike mechanical production, buoyancy can represent either a source or a sink of turbulent kinetic energy. Under unstable stratification, turbulent vertical velocities w' are reinforced by buoyancy. Under stable stratification, they are inhibited. In either event, buoyancy acts selectively on the vertical component of motion. Even though some of that energy cascades into the horizontal components, buoyancy makes turbulent motion anisotropic. In the presence of strong static stability, the vertical component may contain very little of the turbulent kinetic energy.

The degree of anisotropy is reflected in the dimensionless *flux Richardson number*

$$R_f = \frac{\frac{g}{\bar{\theta}}\overline{w'\theta'}}{\overline{w'u'}\frac{\partial \bar{u}}{\partial z}}. \tag{13.22}$$

It represents the ratio of thermal to mechanical production of turbulent kinetic energy. Unlike other dimensionless parameters, R_f is a function of position. Inside the surface layer, downward flux of positive x momentum exerts a positive drag on the ground. It makes the denominator of (13.22) negative. Under unstable stratification, the vertical heat flux must be positive to transfer heat from lower to upper levels and hence drive the stratification towards neutral stability (Sec. 7.5). These conditions lead to $R_f < 0$. Large negative values of R_f occur in the presence of weak shear. Turbulence is then driven chiefly by buoyancy, termed *free convection*. Alternatively, if the heat flux vanishes, $R_f = 0$. Turbulence is then driven exclusively by shear. Under stable stratification, the vertical heat flux must be negative (Prob. 13.11). It follows that $R_f > 0$. Buoyancy then opposes vertical eddy motion,

damping turbulent kinetic energy. Turbulence can be maintained under these conditions only if production of turbulent energy by shear exceeds its damping by buoyancy.

Analogous, but more readily evaluated, is the *gradient Richardson number*

$$Ri = \frac{\frac{g}{\overline{\theta}}\frac{\partial \overline{\theta}}{\partial z}}{\left(\frac{\partial \overline{u}}{\partial z}\right)^2} = \frac{N^2}{\left(\frac{\partial \overline{u}}{\partial z}\right)^2}. \tag{13.23.1}$$

With (13.13), the gradient Richardson number is related to the flux Richardson number as

$$R_f = \frac{K_H}{K_M} Ri. \tag{13.23.2}$$

If $K_m = K_H$, the two are equivalent. The gradient Richardson number reflects the dynamic stability of the mean flow. It therefore provides a criterion for the onset of turbulence. For $N^2 > 0$, Ri is positive. Buoyancy then stabilizes the motion by opposing vertical displacements. If the denominator in (13.13.1) is sufficiently small, so is the destabilizing influence of shear. Disturbances involving vertical motion are then damped out. Corresponding to Ri that is sufficiently large, these conditions describe sheared flow that is dynamically stable. Stability analysis reveals how large (e.g., Thorpe, 1969): For $Ri > \frac{1}{4}$, small disturbances are damped out by buoyancy. Sheared flow is then stable and turbulence is inhibited. Conversely, sheared flow becomes dynamically unstable if

$$Ri < \frac{1}{4}. \tag{13.24}$$

This criterion for dynamical instability is supported by laboratory experiments (Thorpe, 1971). It corresponds to shear production of turbulent kinetic energy that exceeds buoyancy damping by a factor of 4. Small disturbances then amplify into fully developed turbulence.[5] Sheared flow is also unstable for $Ri < 0$ (e.g., for $N^2 < 0$). Turbulence is then driven by both shear and buoyancy.

Stable stratification inhibits turbulence inside the boundary layer. But increasing shear near the Earth's surface eventually makes mechanical production of turbulent kinetic energy large enough to overcome damping by buoyancy. Consequently, a turbulent layer inevitably exists close to the ground. There, $\overline{u}$ varies with z logarithmically and fluxes of momentum and heat are independent of height (13.21). The depth of this layer is controlled by surface roughness and static stability. Strong stability limits the layer to a few tens of meters above the ground. Conversely, weak stability allows a deeper layer with smaller $\frac{\partial \overline{u}}{\partial z}$.

Static stability inside the boundary layer is controlled by heating and cooling of the surface layer. Under cloud-free conditions and over warm SST, surface heating

[5] Outside the boundary layer, the criterion for the onset of turbulence can be achieved locally (e.g., in association with fractus rotor cloud (Fig. 9.22) and severe turbulence found in the mountain wave; see Fig. 14.24).

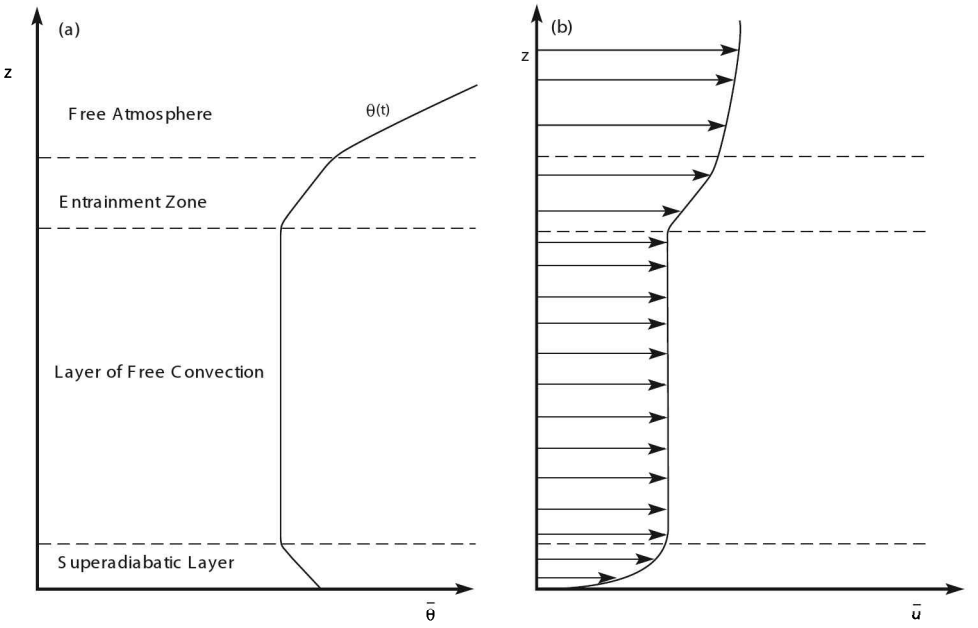

Figure 13.5 Schematic illustrating vertical profiles of mean potential temperature and horizontal motion inside a buoyantly-driven boundary layer. Air parcels emerging from the superadiabatic layer near the surface ascend through the layer of free convection, which extends to the stable layer aloft and in which $\overline{\theta}$ and $\overline{u}$ are homogenized. Continued heat supply at the surface enables the convective layer to advance upward by eroding the stable layer from below.

is strong. It favors buoyantly driven turbulence by destabilizing the stratification. These conditions lead to the formation of a superadiabatic layer immediately above the Earth's surface (Fig. 13.5a). Buoyant parcels emerge from the superadiabatic layer, entering a deeper layer of free convection. That layer is characterized by strong overturning and neutral stability ($\overline{\theta}$ = const). Vertical mixing of momentum makes the profile of mean horizontal motion likewise uniform (Fig. 13.5b).[6] The height of convective plumes is eventually limited by stable air overhead, which magnifies detrainment and mixing with the environment (Sec. 7.4). Nonetheless, continued heat supply at the surface enables the convective layer to expand upward, eroding the stable layer from below.

The foregoing process is responsible for the diurnal cycle of the boundary layer (Sec. 7.6.3). It is revealed by vertical soundings (Fig. 13.6). During early morning, θ increases upward in the lowest 300 m (Fig. 13.6a). Marking the nocturnal inversion, strong static stability has been neutralized only in a shallow layer near the surface. Specific humidity (Fig. 13.6b) decreases upward from the surface. By midday, surface

[6] The flux-gradient relationship (13.13.2) breaks down in the well-mixed layer. Turbulent drag can then be represented as Rayleigh friction (Sec. 12.3), the coefficient of which is determined by $\overline{v}$; see Holton (2004).

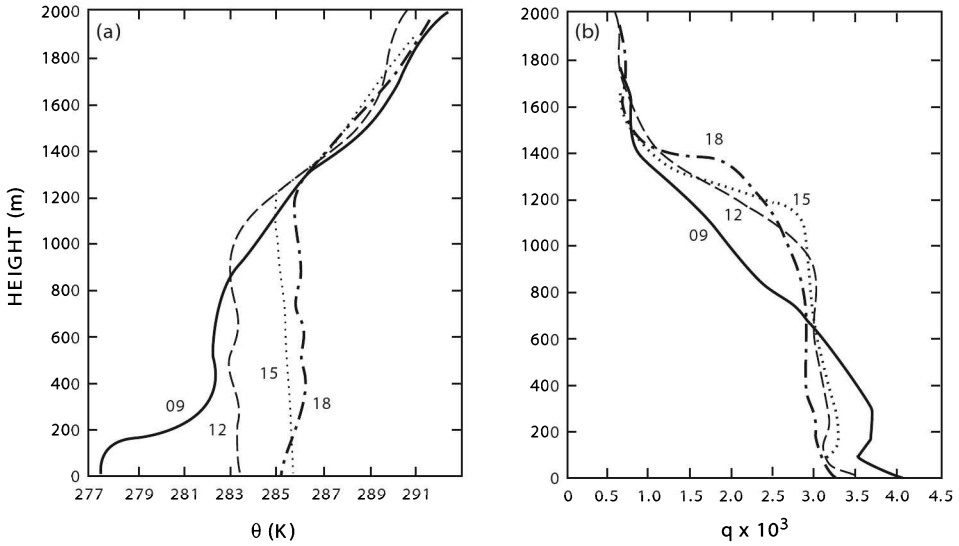

Figure 13.6 Observed profiles during the day of (a) potential temperature and (b) specific humidity. Adapted from Sun and Chang (1986).

convection has broken through the inversion and thoroughly mixed potential temperature and moisture across the lowest kilometer. Mean horizontal motion inside the layer of convective overturning (not shown) is likewise independent of height. Later during the day, the convective layer expands upward further, by a few hundred meters. By early evening, surface heating subsides, replaced by surface cooling. The nocturnal inversion then begins to be re-established.

13.4 EKMAN PUMPING

Turbulent drag inside the boundary layer drives the large-scale motion out of geostrophic equilibrium. By doing so, it introduces a divergent component of motion (Sec. 12.3). To satisfy continuity, divergence must be compensated by vertical motion. The latter imposes a secondary circulation on the $O(Ro^0)$ geostrophic flow in the free atmosphere. Frictional convergence inside the boundary layer leads to ascending motion above surface low pressure (Fig. 12.7). Frictional divergence leads to reversed motion above surface high pressure.

The secondary circulation imposed on the free atmosphere is forced by vertical motion at the top of the boundary layer. By continuity, the latter is related to the convergence of horizontal mass flux inside the Ekman layer. That, in turn, follows from the cross-isobaric component $\overline{v}$. Integrating vertically over the boundary layer obtains the column-integrated mass flux across isobars

$$\begin{aligned} M &= \rho_0(0)\int_0^\infty \overline{v}dz \\ &= \rho_0(0)\int_0^\infty u_g e^{-\gamma z} sin\gamma z dz, \end{aligned} \tag{13.25.1}$$

which reduces to

$$M = \frac{\rho_0(0)}{2\gamma} u_g. \tag{13.25.2}$$

Because $\overline{v}\boldsymbol{j}$ is perpendicular to $\boldsymbol{v}_g$, directed toward low pressure, the column-integrated mass flux across isobars may be expressed

$$\boldsymbol{M} = \frac{\rho_0(0)}{2\gamma} \boldsymbol{k} \times \boldsymbol{v}_g. \tag{13.26}$$

Integrating the continuity equation (13.10.4) in similar fashion obtains

$$\nabla_z \cdot \boldsymbol{M} + \rho_0(0) w_0 = 0, \tag{13.27}$$

where w_0 denotes the vertical velocity at the top of the boundary layer, or the *Ekman pumping*. Incorporating (13.26) then yields

$$w_0 = \frac{1}{2\gamma} \zeta_g(0), \tag{13.28.1}$$

where

$$\zeta_g(0) = \nabla_z^2 \psi(0) \tag{13.28.2}$$

is the geostrophic vorticity at the base of the free atmosphere. According to (13.28), Ekman pumping is directly proportional to the large-scale vorticity above the boundary layer. Positive vorticity (cyclonic motion) induces upward motion out of the boundary layer: Ekman pumping. It is compensated by frictional convergence inside the boundary layer (e.g., into surface low pressure). Negative vorticity (anticyclonic motion) induces subsidence into the boundary layer: *Ekman suction*. It is compensated by frictional divergence (e.g., out of surface high pressure). Values used previously to evaluate γ and $\zeta_g = 10^{-5}$ s^{-1}, typical of quasi-geostrophic motion, give w_0 of order 5 mm s^{-1}.

Frictional convergence and divergence inside the boundary layer, by redistributing mass, act to relieve imbalances of pressure. In doing so, they destroy pressure gradients that support large-scale motion. Divergent motion inside the boundary layer also has an indirect but more important influence. Upward motion out of the boundary layer must be compensated overhead by horizontal divergence in the free atmosphere (Fig. 13.7). According to the vorticity budget (12.36), such divergence weakens the absolute vorticity of air in the free atmosphere. To conserve angular momentum, a ring of air that expands radially must spin down. This loss of vorticity damps organized motion about a cyclone.

Under barotropic stratification, the horizontal velocity in the free atmosphere is independent of height (12.11). Integrating the continuity equation (13.10.4) from the top of the boundary layer to a height h where w has decreased to zero then yields

$$\begin{aligned} -w_0 &= h \nabla_z \cdot \boldsymbol{v} \\ &= h \nabla_z \cdot \boldsymbol{v}_a, \end{aligned} \tag{13.29}$$

where $\boldsymbol{v}_a$ is the ageostrophic velocity that comprises the secondary circulation. The vorticity equation for quasi-geostrophic motion (12.47) on an f plane reduces to

$$\frac{d_g \zeta_g}{dt} = -f_0 \nabla_z \cdot \boldsymbol{v}_a. \tag{13.30}$$

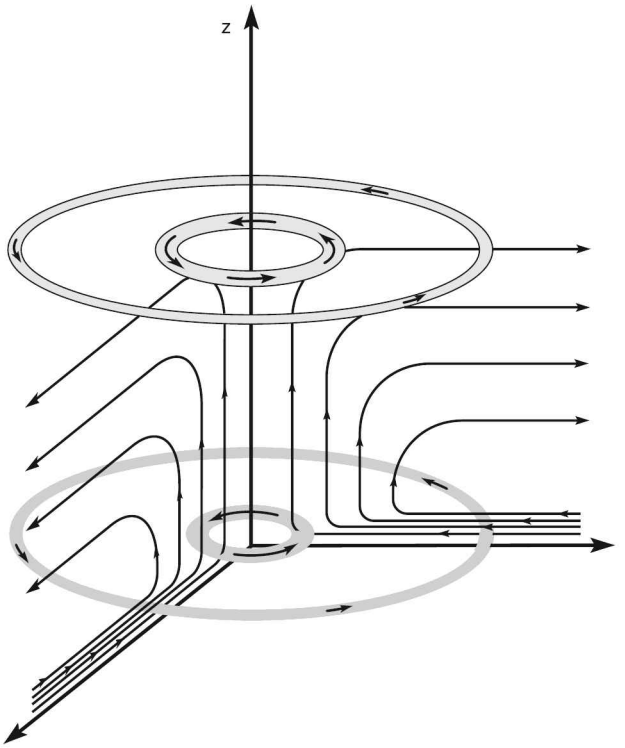

Figure 13.7 Schematic of the secondary circulation imposed on the $O(Ro^0)$ geostrophic motion above the boundary layer. Frictional convergence in the boundary layer beneath a cyclone is compensated by ascending motion and divergence in the free atmosphere. A ring of air diverging from the center of the cyclone must then spin down to conserve angular momentum, which decelerates organized motion above the boundary layer.

With (13.29) and (13.28), this becomes

$$\frac{d_g\zeta_g}{dt} = \frac{f_0}{2\gamma h}\zeta_g$$

or

$$\frac{1}{\zeta_g}\frac{d_g\zeta_g}{dt} = \left(\frac{f_0 K}{2h^2}\right)^{\frac{1}{2}}. \tag{13.31}$$

A vorticity anomaly, characteristic of a mid-latitude cyclone, thus decays exponentially as

$$\zeta_g = e^{-\frac{t}{\tau_E}}, \tag{13.32.1}$$

where

$$\tau_E = \left(\frac{f_0 K}{2h^2}\right)^{-\frac{1}{2}} \tag{13.32.2}$$

is an Ekman e-folding time. Hence, the secondary circulation imposed by Ekman pumping causes the primary circulation to spin down.[7] This process involves no actual dissipation. Rather, it reflects a redistribution of angular momentum, when absolute vorticity that is concentrated in a vorticity anomaly is diluted over a wider area. By Stokes theorem, the circulation along an expanding material contour $s(x, y)$

$$\begin{aligned} \Gamma &= \oint \boldsymbol{v}_g \cdot d\boldsymbol{s} \\ &= \int_A \zeta_g dA \end{aligned} \tag{13.33}$$

remains unchanged. With values representative of the troposphere, (13.32) gives an e-folding time for spin down of order days. This is an order of magnitude faster than frictional dissipation in the free atmosphere.

SUGGESTED REFERENCES

A First Course in Turbulence (1972) by Tennekes and Lumley presents an introduction to the subject at the graduate level. *Statistical Fluid Mechanics* (1973) by Monin and Yaglom is an advanced treatment that develops the Lagrangian description of turbulent dispersion.

A meteorological treatment at the graduate level is given in *An Introduction to Boundary Layer Meteorology* (1988) by Stull. Relevant observations may be found in *Structure of the Atmospheric Boundary Layer* (1989) by Sorbjan.

PROBLEMS

1. Evaluate the Reynolds number for the following flows: (a) Stokes flow about a spherical cloud droplet (Prob. 9.6) of radius 10 μm and fall speed of 3 mm s^{-1}, (b) cumulus convection of characteristic dimension 1 km and velocity 1 m s^{-1}, (c) a midlatitude cyclone of characteristic dimension 10^3 km and velocity 5 m s^{-1}.
2. Estimate how strong vertical shear must become before turbulence forms under stability representative of (a) mean conditions in the troposphere: $N^2 = 1.10^{-4}$ s^{-2} and (b) mean conditions in the stratosphere: $N^2 = 6.10^{-4}$ s^{-2}. (c) How would these values be affected if, locally, isentropic surfaces are steeply deflected from the horizontal?
3. Estimate the height of the turbopause based on characteristic length and velocity scales of 1 km and 10 m s^{-1}, respectively.
4. Frictional dissipation is an essential feature of turbulence because it cascades energy from large scales of organized motion to small scales, on which molecular diffusion operates efficiently. The specific energy dissipation rate for homogeneous isotropic turbulence is described by

$$\epsilon \cong \frac{U^3}{L},$$

where U and L are the characteristic velocity and length scales of the large-scale motion that drives the cascade. Hence the rate of energy dissipation, which is concentrated at small scales, is dictated by the motion at large scales, which is

[7] Should a disturbance's vertical structure make $\boldsymbol{v}_g(0) = 0$, Ekman pumping and divergence in the free atmosphere vanish. Ekman spin down is then eliminated.

nearly inviscid. Use this result to estimate the rate at which energy is dissipated inside a cumulonimbus cloud of characteristic dimension 10 km and velocity 10 m s^{-1}. Compare this value against the rate at which energy is generated by a large urban power plant (~1000 M W).

5. For the cumulonimbus cell in Prob. 13.4, estimate the precipitation rate necessary to sustain the motion.
6. A mid-latitude cyclone is associated with the disturbance height in the lower troposphere

$$z' = -Ze^{-\frac{x^2+y^2}{2L^2}},$$

where $Z = 200$ m, L = 1000 km, y is measured from 45°, and the boundary layer has an eddy diffusivity of 10 m^2 s^{-1}. Calculate the maximum vertical velocity atop the boundary layer.

7. Observations reveal a nearly logarithmic variation with height of mean wind below 100 m above prairie grass land that has a roughness length of 4 cm. If the mean wind is 5 m s^{-1} at the top of this layer, calculate the stress exerted on the ground.
8. Calculate the characteristic spin-down time due to Ekman pumping for a cyclone at 45°, vertical motion extending to the tropopause at 10 km, and an eddy diffusivity inside the boundary layer of 10 $m^2 s^{-2}$. Compare this spin-down time with the time scale of radiative damping.
9. Derive the flux form of the momentum equations (13.8).
10. Recover (13.20) governing mean motion inside the surface layer.
11. Demonstrate that the turbulent vertical heat flux must be positive (negative) under unstable (stable) stratification.
12. Show that divergence associated with the secondary circulation above the boundary layer does not alter the circulation $\Gamma = \oint \boldsymbol{v} \cdot d\boldsymbol{s}$ along a material contour.
13. Inside a *well-mixed boundary layer* of depth h, convection makes mean horizontal motion and potential temperature invariant with height (Fig. 13.5), rendering the flux-gradient relationship inapplicable. The vertical momentum flux then decreases linearly with height from a surface maximum described by

$$\overline{w'\boldsymbol{v}'}|_s = -c_d|\overline{\boldsymbol{v}}|\overline{\boldsymbol{v}},$$

where c_d is a dimensionless *drag coefficient*. (a) Construct a counterpart of the Ekman equations (13.15) governing mean motion inside the well-mixed layer to show that the effect of turbulence is then equivalent to Rayleigh friction (Sec. 12.3). (b) Determine $\overline{\boldsymbol{v}}$ if $\boldsymbol{v}_g = u_g\boldsymbol{i}$ above the well-mixed boundary layer. (c) Calculate the time scale of Rayleigh friction for $h = 1$ km, $c_d = 5\ 10^{-3}$, and a mean wind speed of 5 m s^{-1}.

14. The contrail formed from the exhaust of a commercial jet flying at 200 hPa contains liquid water. At a distance x from the jet, the contrail has a temperature $T(x)$ and a mixing ratio for total water $r_t(x)$. The contrail dissolves some distance x_d downstream of the jet through entrainment with ambient air, of temperature T_a and mixing ratio r_a. If, immediately aft of the jet, the exhaust plume has temperature $T(0) = T_0$ and total water mixing ratio $r_t(0) = r_0$, (a) formulate a differential equation governing $r_t(x)$, in terms of the entrainment length $L^{-1} = \frac{d(lnm)}{dx}$, which characterizes the rate at which the contrail expands through mixing with ambient air (Sec. 7.4.2), (b) derive expressions for $r_t(x)$ and $T(x)$, (c) derive an expression

for the saturation mixing ratio of the contrail $r_i(x)$, (d) determine the distance x_d at which the contrail dissolves for $L = 100$ m, $r_0 = 4$ g kg^{-1}, $r_a = 0.05$ g kg^{-1}, $T_0 = -20$ C, and $T_a = -50$ C, (e) as in (d), but under the warm moist conditions: $T_a = -30$ C, $r_a = 1.25$ g kg^{-1}, $T_0 = 0$ C, symbolic of conditions inside the warm sector of an advancing cyclone.

CHAPTER
FOURTEEN

Wave propagation

The governing equations support several forms of wave motion. Atmospheric waves are excited when air is disturbed from equilibrium (e.g., mechanically when air is displaced over elevated terrain or thermally when air is heated inside convection). By transferring momentum, wave motions convey the influence of one region to another. This mechanism of interaction enables tropical convection to influence the extratropical circulation. It also enables the troposphere to perturb the stratosphere, driving it out of radiative equilibrium (Fig. 8.27).

14.1 DESCRIPTION OF WAVE PROPAGATION

Wave motion is possible in the presence of a positive restoring force. By opposing disturbances from equilibrium, the latter supports local oscillations in field properties. Under stable stratification, buoyancy provides such a restoring force (Sec. 7.3). The compressibility of air provides another. The variation with latitude of the Coriolis force provides yet another restoring force. It will be seen to support large-scale atmospheric disturbances.

14.1.1 Surface water waves

The description of wave motion is illustrated with an example under nonrotating conditions, which will serve as a model of buoyancy oscillations in the atmosphere. Consider disturbances to a layer of incompressible fluid of uniform density ρ and depth H (Fig. 14.1). The layer is bounded below by a rigid surface. It is bounded above by a *free surface*, namely, one that adjusts position to relieve any stress. Motion

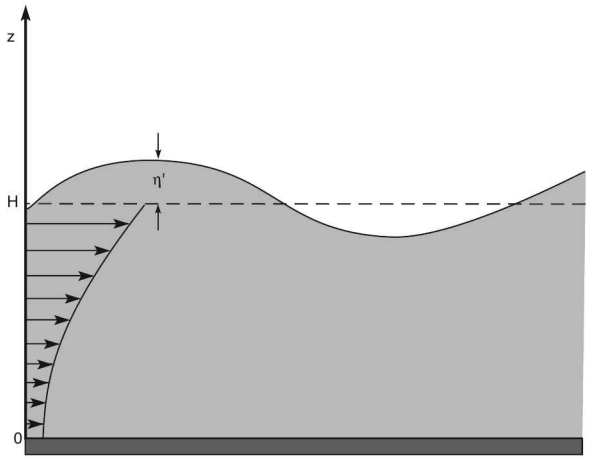

Figure 14.1 A layer of incompressible fluid of uniform density ρ and depth H. The layer is bounded below by a rigid surface and above by a free surface that has displacement η' from its mean elevation. The profile of horizontal motion for surface water waves is indicated.

inside this layer is governed by

$$\rho \frac{d\boldsymbol{v}}{dt} = -\nabla p - g\boldsymbol{k} \tag{14.1.1}$$

$$\nabla \cdot \boldsymbol{v} = 0, \tag{14.1.2}$$

with $\boldsymbol{v}$ and ∇ referring to 3-dimensional vector quantities.

We are interested in how the fluid layer responds to disturbances that are imposed through a deflection of its free surface. It is convenient to decompose the behavior into a zonal-mean basic state, which represents undisturbed conditions and is denoted by an overbar, and perturbations to it, which are denoted by a prime. For example,

$$\boldsymbol{v} = \overline{\boldsymbol{v}} + \boldsymbol{v}' \tag{14.2.1}$$

with

$$\overline{\boldsymbol{v}'} = 0. \tag{14.2.2}$$

This decomposition is analogous to the one applied in the treatment of turbulence (Chap. 13). For simplicity, the undisturbed zonal motion $\overline{\boldsymbol{v}} = \overline{u}\boldsymbol{i}$ is taken to be independent of x, analogous to motion in Fig. 1.8.

Incorporating (14.2) into equations (14.1) produces terms involving mean properties, perturbation properties, and products thereof. Perturbations are characterized by the wave amplitude ϵ. The latter symbolizes small departures from equilibrium, for instance, u', v', $p' = O(\epsilon)$. In the spirit of the asymptotic analysis for small Rossby number (Chap. 12), the resulting system can then be solved recursively to increasing order in ϵ. To zero order in ϵ (i.e., in the absence of waves), the governing equations reduce to a statement of hydrostatic equilibrium

$$\frac{\partial \overline{p}}{\partial z} = -\rho g, \tag{14.3}$$

which must be satisfied by the mean state. To first order in ϵ, with the basic state balance (14.3) eliminated, the governing equations reduce to

$$\frac{D\boldsymbol{v}'}{Dt} = -\nabla p' \tag{14.4.1}$$

$$\nabla \cdot \boldsymbol{v}' = 0, \tag{14.4.2}$$

where

$$\frac{D}{Dt} = \frac{\partial}{\partial t} + \overline{u}\frac{\partial}{\partial x} \tag{14.4.3}$$

defines the material derivative following the mean motion. Linear in perturbation quantities, equations (14.4) govern the wave field. They neglect products of perturbation quantities, specifically, the advective acceleration $\boldsymbol{v}' \cdot \nabla \boldsymbol{v}'$, which are $O(\epsilon^2)$.

The first-order equations ignore influences that the waves exert on the mean state. Such feedback is accounted for in the equations accurate to second order in ϵ. Upon eliminating the zero and first-order balances and averaging zonally, the second-order balance reduces to

$$\begin{aligned} \frac{\partial \overline{u}}{\partial t} &= -(\overline{\boldsymbol{v}' \cdot \nabla \boldsymbol{v}'}) \\ &= -\frac{\partial(\overline{v'u'})}{\partial y} - \frac{\partial(\overline{w'u'})}{\partial z}. \end{aligned} \tag{14.5}$$

Terms on the right-hand side of (14.5) are quadratic in perturbation velocity. They represent the convergence of wave momentum flux, $-\nabla \cdot \overline{\boldsymbol{v}'u'}$. This absorption of wave momentum exerts a drag on the mean flow. It forces zonal-mean motion – just as the convergence of turbulent momentum flux forces mean motion in (13.10). Corresponding changes in $\overline{u}$ then reflect a second-order correction to the zeroth-order steady motion.

The development is now restricted to the limit of small wave amplitude. Second-order terms in (14.5) are then small, so the basic state may be regarded as steady. Under these conditions, motion in the fluid layer is described by the equations accurate to first order in wave amplitude, which are said to have been *linearized*. If the basic state is in uniform motion, $\overline{u}$ is independent of position. Applying $\nabla\cdot$ to (14.4.1) and incorporating (14.4.2) consolidates the system into a single equation for the perturbation pressure

$$\nabla^2 p' = 0. \tag{14.6}$$

With fixed boundaries, Laplace's equation cannot describe wave propagation because it is diagnostic (Sec. 12.5). With boundaries that are time dependent, it can. Boundary conditions that govern the free surface introduce time dependence, making the complete system prognostic.

The free surface is an interface between fluids. It must satisfy two conditions. The *dynamic condition* requires the stress to vanish. As the surface is free, it adjusts to relieve any imbalance of forces. If the air pressure overhead is negligible, then the total pressure ($p = \overline{p} + p'$) must vanish. With hydrostatic equilibrium for the mean state (14.3), the total pressure on the free surface is

$$p = -\rho g \eta' + p' \qquad z = H + \eta', \tag{14.7.1}$$

where η' is the deflection of the free surface from its undisturbed elevation. Then the perturbation pressure at the top of the layer is given by

$$p' = \rho g \eta' \qquad z = H, \tag{14.7.2}$$

which, to the same degree of approximation in (14.6), is evaluated at the mean elevation of the free surface. The *kinematic condition* requires the free surface to be a material surface. Its vertical displacement must therefore satisfy

$$\frac{d\eta'}{dt} = w \qquad z = H + \eta'. \tag{14.8.1}$$

In the limit of small amplitude, this reduces to

$$\frac{D\eta'}{Dt} = w' \qquad z = H. \tag{14.8.2}$$

Combining the dynamic condition (14.7.2) and the kinematic condition (14.8.2) obtains

$$\frac{1}{\rho g}\frac{Dp'}{Dt} = w' \qquad z = H. \tag{14.9.1}$$

Incorporating (14.9.1) into the vertical momentum equation then gives the upper boundary condition

$$\frac{1}{g}\frac{D^2p'}{Dt^2} = -\frac{\partial p'}{\partial z} \qquad z = H. \tag{14.9.2}$$

Another boundary condition applies at the base of the layer, where vertical motion must vanish identically. There, the vertical momentum equation requires

$$\frac{\partial p'}{\partial z} = 0 \qquad z = 0. \tag{14.10}$$

14.1.2 Fourier synthesis

Consider a small disturbance to the free surface. The system is positively stratified because the density of the liquid is much greater than that of the overlying air, which is ignored. Buoyancy then provides a positive restoring force. It drives fluid back toward its undisturbed position, setting up oscillations. A compact initial disturbance therefore radiates away in the form of waves.

Wave activity radiating away from the initial disturbance may assume a complex form, for example, because the structure of the disturbance imposes that form initially or because individual components of the wave field propagate differently. Equations governing the wave field are linear in perturbation quantities. They also have coefficients that are independent of position and time.

These features enable the wave field to be constructed from a superposition of plane waves, each of the form $e^{i(kx+ly-\sigma t)}$. They are synthesized in the Fourier integral

$$\begin{aligned} p'(\mathbf{x}, t) &= \frac{1}{(2\pi)^3}\int\int\int_{-\infty}^{\infty} P_{kl}^{\sigma}(z) e^{i(kx+ly-\sigma t)}\, dk\, dl\, d\sigma \\ &= \frac{1}{(2\pi)^3}\int\int\int_{-\infty}^{\infty} P_{\mathbf{k}}^{\sigma}(z) e^{i(\mathbf{k}\cdot\mathbf{x}-\sigma t)}\, d\mathbf{k}\, d\sigma . \end{aligned} \tag{14.11.1}$$

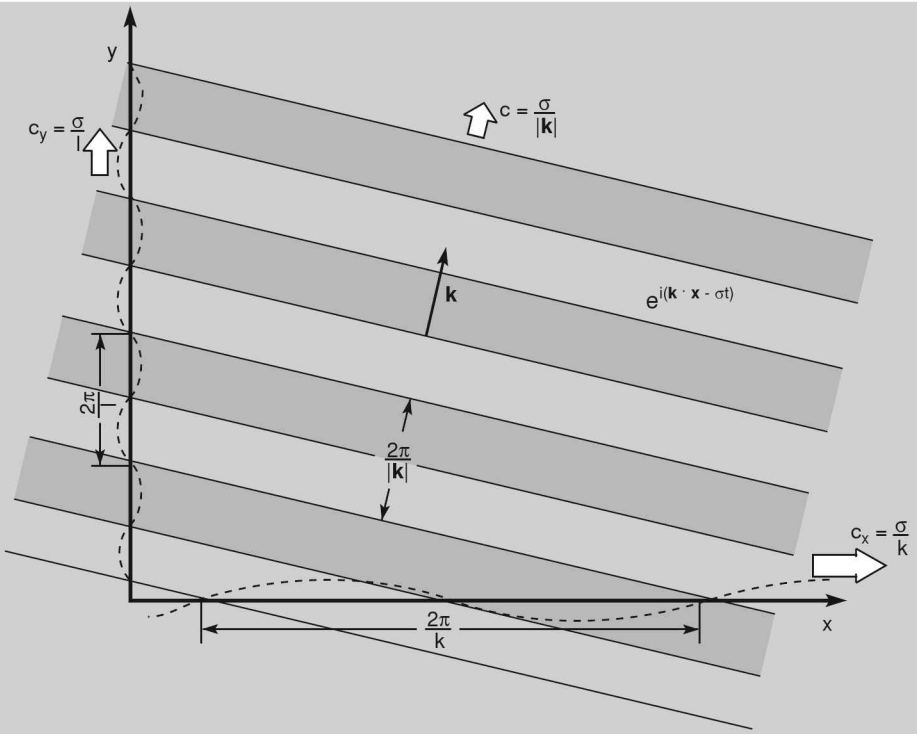

Figure 14.2 An individual plane wave component having wavenumber vector $\boldsymbol{k} = (k, l)$ and frequency σ. Lines of constant phase: $kx + ly - \sigma t =$ const, propagate parallel to $\boldsymbol{k}$ ($\sigma > 0$) or antiparallel to $\boldsymbol{k}$ ($\sigma < 0$), with *phase speed* $c = \frac{\sigma}{|\boldsymbol{k}|}$. Phase propagation in the x and y directions is described by the *trace speeds* $c_x = \frac{\sigma}{k}$ and $c_y = \frac{\sigma}{l}$. The latter equal or exceed c and are related to it through $\frac{1}{c_x^2} + \frac{1}{c_y^2} = \frac{1}{c^2}$, so they do not represent its components. As $\boldsymbol{k}$ becomes orthogonal to a direction, the trace speed in that direction becomes infinite.

Equation (14.11.1) represents an *inverse Fourier transform*. It describes p' at level z as a spectrum of monochromatic plane waves. Individual components of the spectrum have angular frequency σ and wavenumber vector $\boldsymbol{k} = (k, l)$. The complex amplitude $P_{kl}^{\sigma}(z)$ contains the magnitude and phase of wave component (k, l, σ). It must satisfy the governing equations, as well as boundary conditions. The corresponding wave component has lines of constant phase, $kx + ly - \sigma t =$ const (Fig. 14.2). The latter propagate in the direction of $\boldsymbol{k}$ with the *phase speed*

$$c = \frac{\sigma}{|\boldsymbol{k}|}, \tag{14.11.2}$$

where $|\boldsymbol{k}|^2 = k^2 + l^2$. Phase propagation in the x and y directions is described by the *trace speeds*

$$\begin{aligned} c_x &= \frac{\sigma}{k} \\ c_y &= \frac{\sigma}{l}. \end{aligned} \tag{14.11.3}$$

Note, $c_x^2 + c_y^2 \neq c^2$. According to Fig. 14.2, the trace speed in a given direction equals or exceeds the phase speed. As $\boldsymbol{k}$ becomes orthogonal to that direction, it approaches infinity.

By the Fourier integral theorem (e.g., Rektorys, 1969), the complex amplitudes in (14.11.1) follow as

$$P_{kl}^{\sigma}(z) = \int\int\int_{-\infty}^{\infty} p'(x, y, z, t) e^{-i(kx+ly-\sigma t)} dx dy dt. \tag{14.12.1}$$

Equation (14.12.1) is the *Fourier transform* of the variable p' at level z. It describes a spectrum of complex wave amplitude over the space-time scales k, l, and σ. Real p' requires the amplitude spectrum to satisfy the Hermitian property

$$P_{-k-l}^{-\sigma} = P_{kl}^{\sigma *}. \tag{14.12.2}$$

Equations (14.11.1) and (14.12.1) constitute a one-to-one mapping between $p'(\boldsymbol{x}, t)$ in physical space and $P_{kl}^{\sigma}(z)$ in Fourier space. The latter are therefore equivalent representations of the wave field. The *power spectrum*, $|P_{kl}^{\sigma}|^2$, then describes the distribution over wavenumber and frequency of variance $|p'|^2$. It characterizes the energy in the wave field. In general, a disturbance excites a continuum of space and time scales. Wave variance therefore involves an integral over wavenumber and frequency:

$$\int\int\int_{-\infty}^{\infty} |p'(\boldsymbol{x}, t)|^2 d\boldsymbol{x} dt = \frac{1}{(2\pi)^3} \int\int\int_{-\infty}^{\infty} |P_{\boldsymbol{k}}^{\sigma}|^2 d\boldsymbol{k} d\sigma. \tag{14.13}$$

The equivalence of wave variance in physical space and in Fourier space is known as *Parseval's theorem*.

Differentiating p' in physical space is equivalent to multiplying its transform P_{kl}^{σ} by the corresponding space and time scales:

$$\begin{aligned} \frac{\partial p'}{\partial x} &\leftrightarrow ikP_{kl}^{\sigma} \\ \frac{\partial p'}{\partial y} &\leftrightarrow ilP_{kl}^{\sigma} \\ \frac{\partial p'}{\partial t} &\leftrightarrow -i\sigma P_{kl}^{\sigma}. \end{aligned} \tag{14.14}$$

Then applying (14.12.1) transforms the material derivative into

$$\frac{Dp'}{Dt} \rightarrow -i\omega P_{kl}^{\sigma}, \tag{14.15.1}$$

where

$$\omega = \sigma - k\overline{u}. \tag{14.15.2}$$

ω is the *intrinsic frequency*, that relative to the medium, for the component with frequency σ and zonal wavenumber k. It is the frequency observed from a frame moving with the mean motion $\overline{u}$. The term $-k\overline{u}$ represents a Doppler shift of the intrinsic frequency by background motion. A component propagating opposite to $\overline{u}$ is Doppler shifted to higher intrinsic frequency: $\omega > \sigma$. One propagating in the same direction as $\overline{u}$ is Doppler shifted to lower intrinsic frequency: $\omega < \sigma$.

Considering solutions of the form $e^{i(kx+ly-\sigma t)}$ is equivalent to applying the Fourier transform (14.12.1). The governing equations in physical space, (14.6), (14.9.2), and (14.10), are then transformed into their counterparts in Fourier space:

$$\frac{\partial^2 P_{kl}^{\sigma}}{\partial z^2} - |\boldsymbol{k}|^2 P_{kl}^{\sigma} = 0 \tag{14.16.1}$$

$$\frac{\partial P_{kl}^{\sigma}}{\partial z} = 0 \qquad z = 0 \tag{14.16.2}$$

$$\frac{\partial P_{kl}^{\sigma}}{\partial z} - \frac{\omega^2}{g} P_{kl}^{\sigma} = 0 \qquad z = H. \tag{14.16.3}$$

Equations (14.16) govern the complex amplitude $P_{kl}^{\sigma}(z)$ of the plane wave component with wavenumber and frequency (k, l, σ). They depend on the intrinsic frequency ω, that relative to the mean flow $\overline{u}$. Differential dependence on x, y, and t has been reduced to algebraic dependence on the scales k, l, and σ for individual modes. The latter can be re-synthesized into $p'(\boldsymbol{x}, t)$ via the inverse Fourier transform (14.11.1).

The general solution of (14.16.1) satisfying the lower boundary condition (14.16.2) is of the form

$$P_{kl}^{\sigma}(z) = A cosh(|\boldsymbol{k}|z) \tag{14.17}$$

(Fig. 14.1). Substituting into the upper boundary condition (14.16.3) then yields the algebraic identity

$$\omega^2 = g|\boldsymbol{k}| tanh(|\boldsymbol{k}|H). \tag{14.18}$$

Equation (14.18) is called the *dispersion relation*. It must be satisfied by each component (k,l,σ) if the wave spectrum is to obey the governing equations. The dispersion relation expresses one of the space-time scales (e.g., frequency) in terms of the others. Therefore, the spatial scales of an individual wave component determine its frequency.

14.1.3 Limiting behavior

According to (14.18), different horizontal scales propagate relative to the mean flow at different intrinsic phase speeds

$$\begin{aligned} \hat{c} &= \frac{\omega}{|\boldsymbol{k}|} \\ &= \left[gH \frac{tanh(|\boldsymbol{k}|H)}{|\boldsymbol{k}|H} \right]^{\frac{1}{2}}. \end{aligned} \tag{14.19}$$

Phase speed is plotted as a function of $|\boldsymbol{k}|H$ in Fig. 14.3. It decreases with wavenumber monotonically. The longest waves ($|\boldsymbol{k}|H \to 0$) therefore travel fastest.

In the limit of long wavelength,

$$\hat{c} \sim \sqrt{gH} \qquad |\boldsymbol{k}|H \to 0. \tag{14.20}$$

The dispersion relation (14.20) describes *shallow water waves*. They have wavelengths $\lambda = \frac{2\pi}{|\boldsymbol{k}|}$ long compared with the depth H of the fluid. Phase speed is then independent of wavelength. Consequently, different components of a shallow water disturbance propagate in unison. For this reason, shallow water waves are *nondispersive*: A disturbance retains its initial shape. Shallow water waves are also fast. In an ocean 5 km deep, $\hat{c} > 200$ m s^{-1} – comparable to the speed of sound. This feature of shallow water

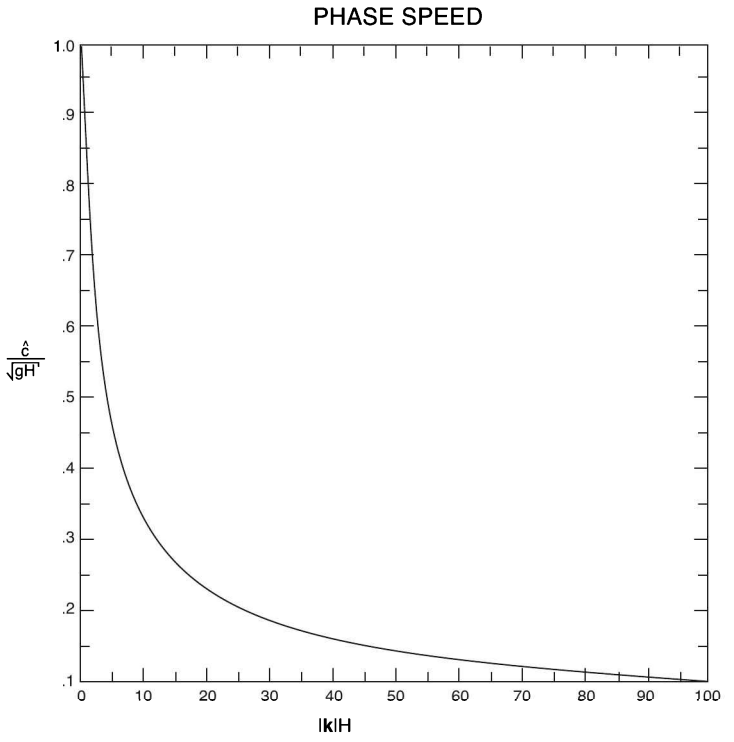

Figure 14.3 Intrinsic phase speed of surface water waves (equals phase speed in the absence of mean motion), as a function of horizontal wavenumber.

waves enables large-scale components of a tsunami to traverse an ocean basin in a matter of hours.[1]

In the longwave limit, amplitude (14.17) is independent of z (Fig. 14.4a). Then, by continuity (14.4.2) and the lower boundary condition, shallow water waves possess no vertical motion. Under these circumstances, the vertical momentum equation reduces to a statement of hydrostatic equilibrium. Hence, the longwave limit is equivalent to invoking hydrostatic balance. This feature of shallow water waves follows from the shallowness of vertical displacements in this limit, relative to horizontal displacements.

The opposite extreme is the limit of short wavelength. Then

$$\hat{c} \sim \sqrt{\frac{g}{|\boldsymbol{k}|}} \qquad |\boldsymbol{k}|H \to \infty. \tag{14.21}$$

The dispersion relation (14.21) describes *deep water waves*. They have wavelengths short compared with the depth of the fluid. In this limit, amplitude (14.17) decreases exponentially away from the free surface (Fig. 14.4b). It has the structure of an *edge wave*. Deep water waves do not sense the lower boundary because their energy there

[1] The tsunami excited by the magnitude-9 earthquake in Honshu Japan of March 11, 2011 reached California in just 10 hrs. http://www.youtube.com/user/NOAAPMEL?feature=mhum#p/c/3/PBZGH3yieLc (15/06/11)

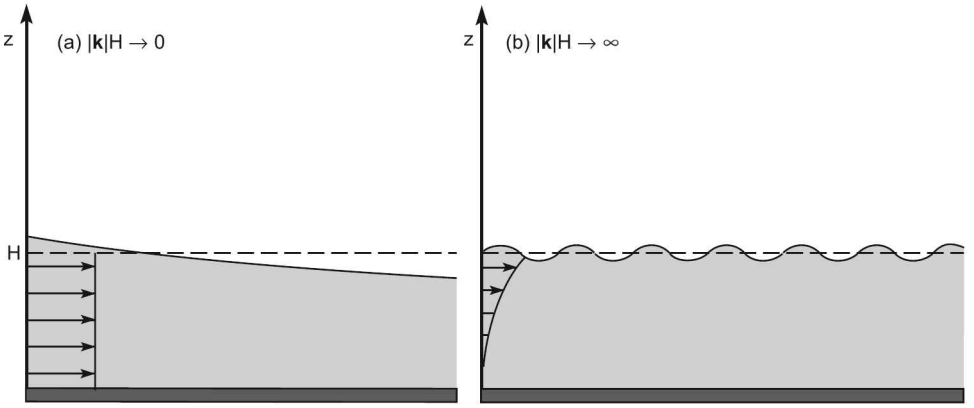

Figure 14.4 Surface water waves (a) in the longwave limit, where they assume the form of *shallow water waves*, with horizontal wavelengths long compared to the fluid depth and horizontal motion that is invariant with depth, and (b) in the shortwave limit, where they assume the form of *deep water waves*, with horizontal wavelengths short compared to the fluid depth and motion that decays exponentially away from the free surface as an edge wave.

is negligible. Unlike shallow water waves, they have phase speed that varies with wavelength. In a deep water disturbance, $\hat{c}$ increases with λ. Longer horizontal wavelengths in the disturbance are therefore faster than shorter wavelengths, which are left behind. For this reason, deep water waves are *dispersive*: A disturbance does not retain its initial shape. As it propagates away from its forcing, a deep water disturbance unravels into individual wave components.

14.1.4 Wave dispersion

Because a spectrum of waves is involved, interference among components can modify wave activity as it radiates away from the imposed disturbance. To illustrate such behavior, consider a *group* of plane waves defined by an incremental band of wavenumber that is centered at k, with l fixed (Fig. 14.5a). Wave activity in this band can be approximated by the rectangle shown. Variance is then shared equally by two discrete components with wavenumbers $k \pm dk$. Those components have frequencies $\sigma \pm d\sigma$, which are related to wavenumber through the dispersion relation (14.18). For unit amplitude, wave activity in the band is described by

$$\begin{aligned} \eta'_k(x,t) &= \frac{1}{2}\Big\{cos\big[(k-dk)x-(\sigma-d\sigma)t\big]+cos\big[(k+dk)x-(\sigma+d\sigma)t\big]\Big\} \\ &= cos(dk\cdot x - d\sigma\cdot t)\cdot cos(kx-\omega t), \end{aligned} \tag{14.22.1}$$

which follows from (14.11.1) with the amplitude spectrum approximated as above and with the Hermitian property (14.12.2). Wave activity in the band may then be expressed

$$\eta'_k(x,t) = cos\left[dk(x-\frac{\partial\sigma}{\partial k}t)\right]\cdot cos(kx-\sigma t). \tag{14.22.2}$$

As illustrated in Fig. 14.5b, (14.22) describes a disturbance with wavenumber k and trace speed $c_x = \frac{\sigma}{k}$ that is modulated by an envelope of wavenumber dk. The envelope

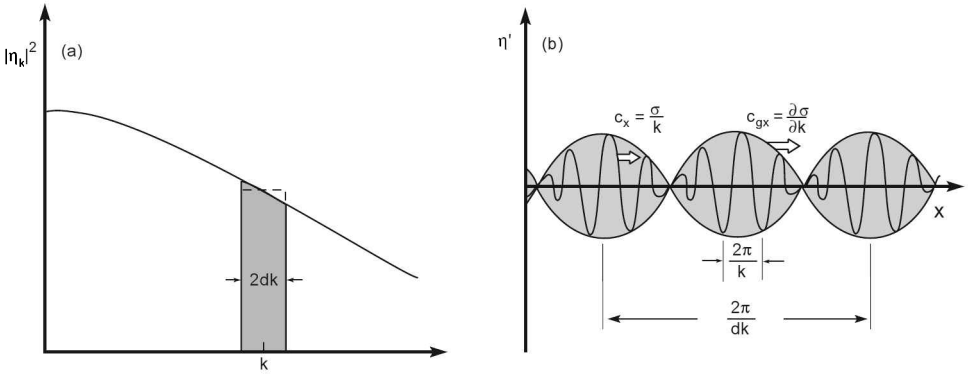

Figure 14.5 (a) Power spectrum of surface water waves as a function of zonal wavenumber. A *wave group* is defined by variance in the incremental band centered at k (shaded), which may be approximated by the rectangle shown. Wave activity is then carried by two discrete components at $k \pm dk$. (b) Wave activity in the band produces a disturbance of wavenumber k that is modulated by an envelope of wavenumber dk. Oscillations propagate with the trace speed $c_x = \frac{\sigma}{k}$. However, their envelope propagates with the *group speed* $c_{gx} = \frac{\partial\sigma}{\partial k}$.

propagates in the x direction with the *group speed*

$$\begin{aligned} c_{gx} &= \frac{\partial\sigma}{\partial k} \\ &= \frac{\partial\omega}{\partial k} + \overline{u}. \end{aligned} \tag{14.23.1}$$

Because it is concentrated inside the envelope, wave activity in the above band propagates, not with the phase speed, but with the group speed.

The two components in (14.22) approximate the spectrum inside a narrow band of wavenumber; they correspond to a discrete boxcar filter in k. Defining a group by a continuous Gaussian filter produces behavior analogous to that in Fig. 14.5b, but concentrated inside a Gaussian envelope. Of limited extent, it represents a packet of waves. Outside the envelope, oscillations vanish. Wave activity must therefore move with the envelope – regardless of the movement of individual crests and troughs inside it.

Similar reasoning applied to the wavenumber l, with k fixed, yields the group speed in the y direction:

$$\begin{aligned} c_{gy} &= \frac{\partial\sigma}{\partial l} \\ &= \frac{\partial\omega}{\partial l}. \end{aligned} \tag{14.23.2}$$

Wave activity thus propagates in the $x - y$ plane with the *group velocity*

$$\begin{aligned} \boldsymbol{c}_g &= \left(\frac{\partial\sigma}{\partial k}, \frac{\partial\sigma}{\partial l}\right) \\ &= \left(\frac{\partial\omega}{\partial k} + \overline{u}, \frac{\partial\omega}{\partial l}\right). \end{aligned} \tag{14.23.3}$$

A function of k and l, $\boldsymbol{c}_g$ describes the propagation of wave activity in individual bands of the spectrum (14.11.1). According to (14.23.3), background motion advects wave

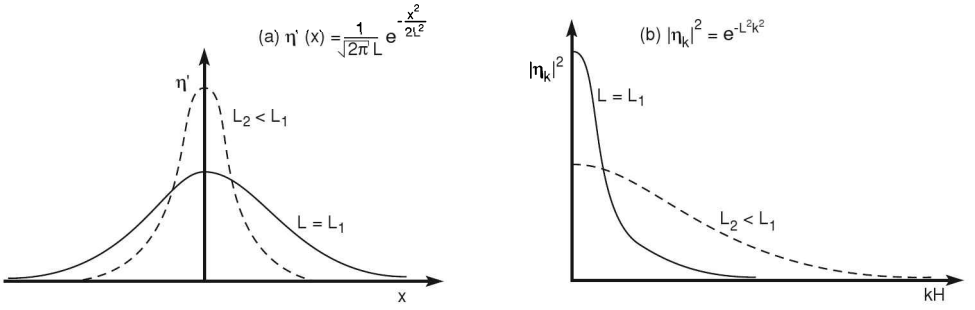

Figure 14.6 (a) A Gaussian disturbance imposed initially on the free surface. The length L characterizes the width of the disturbance. (b) The power spectrum of the disturbance, as a function of zonal wavenumber k. As L increases, variance becomes concentrated at small k in a *red* spectrum, which excites waves in the longwave limit. As L decreases, variance becomes distributed widely over k, approaching a *white* spectrum with most of the variance at large k, which excites waves in the shortwave limit.

activity with the basic flow. The intrinsic group velocity

$$\hat{\boldsymbol{c}}_g = \boldsymbol{c}_g - \overline{u}\boldsymbol{i} \tag{14.23.4}$$

gives the same information relative to the mean flow. According to (14.23.3), it is just the gradient of ω with respect to $\boldsymbol{k} = (k, l)$.

Let us return to the limiting forms of surface water waves described previously. They are considered in the absence of background motion, $\overline{u} = 0$. In the longwave limit, phase speed (14.20) is independent of $\boldsymbol{k}$. Because individual wave components all propagate with the same speed, a disturbance comprised of shallow water waves retains its initial shape. Such waves are nondispersive, because a disturbance that is initially compact remains so. The group speed of shallow water waves follows from (14.23) as

$$\begin{aligned} c_g &= \sqrt{gH} \\ &= c. \end{aligned} \tag{14.24}$$

Because all wavenumbers propagate with identical phase speed, a group of shallow water waves centered at wavenumber $\boldsymbol{k}$ propagates in the same direction and with the same speed.

An example is presented in Figs. 14.6 and 14.7. The free surface is initialized with a compact disturbance (Fig. 14.6a)

$$\eta'(x, y, 0) = \frac{1}{\sqrt{2\pi L}} e^{-\frac{x^2+y^2}{2L^2}}, \tag{14.25.1}$$

with characteristic horizontal scale L. Because it is not simple harmonic, that disturbance excites a continuum of waves. Transforming (14.25.1) via (14.12.1) with $t = 0$ gives its power spectrum (Fig. 14.6b)

$$|\eta_{kl}|^2 = e^{-L^2(k^2+l^2)}. \tag{14.25.2}$$

The excited wave field is then described by (14.11.1), with individual components subject to the dispersion relation (14.18). If the scale of the imposed disturbance is

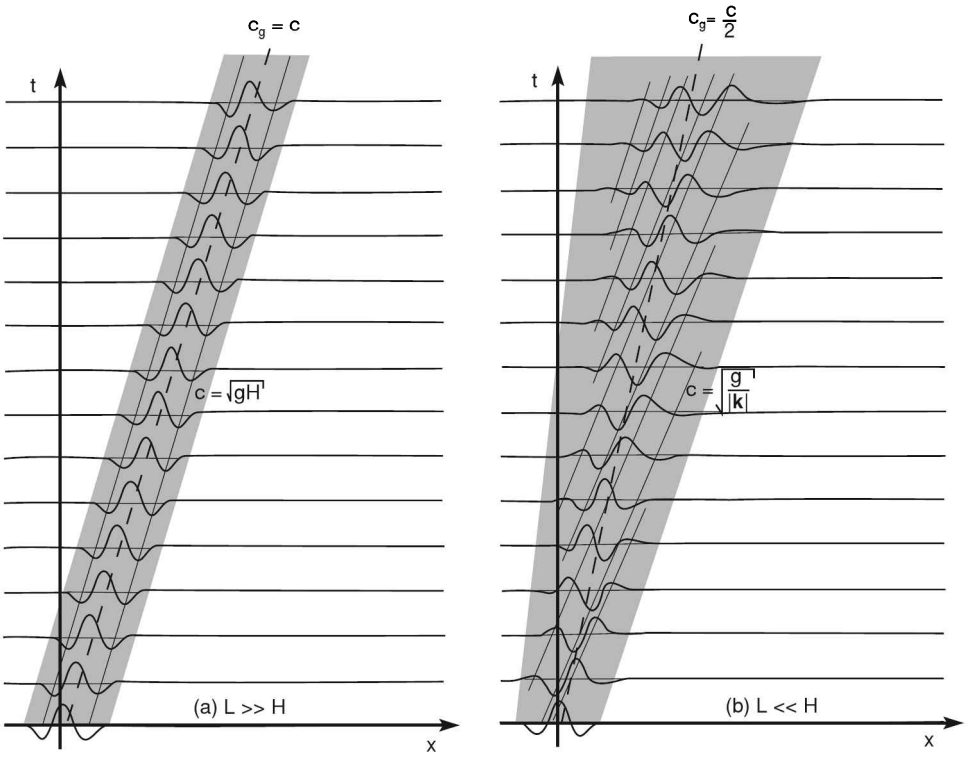

Figure 14.7 (a) Surface water waves produced by the initial disturbance in Fig. 14.6, with $L \gg H$. Shallow water waves radiate *nondispersively* away from the initial disturbance: Wave components with different k propagate at identical phase speed $c = \sqrt{gH}$ (solid). The envelope of wave activity then propagates at the same speed $c_g = c$ (dashed). Under these circumstances, the shape of the initial waveform is preserved, so wave activity (shaded) remains confined to the same range of x as initially. (b) As in (a) but for $L \ll H$ and a different x scale. Deep water waves radiate *dispersively* away from the initial disturbance: Wave components with different k propagate at different phase speeds $c = \sqrt{\frac{g}{|k|}}$ (solid), so the initial wave form unravels into a series of oscillations. Occupying a progressively wider range of x, the envelope of wave activity (shaded) propagates at half the median phase speed of individual components $c_g = \frac{c}{2}$ (dashed). Individual crests and troughs therefore overrun the envelope, disappearing at its leading edge, to be replaced by new ones at its trailing edge.

sufficiently long (e.g., $L = L_1 \gg H$), the power spectrum of η' (Fig. 14.6b) is very *red*: $|\eta_{kl}|^2$ decreases sharply with $(k^2 + l^2)$. Variance is then concentrated at small $|\boldsymbol{k}|H$, so the excited wave field is comprised chiefly of shallow water waves. Far from the initial disturbance, waves can be treated as planar. The disturbance (Fig. 14.7a) then translates outward jointly with its envelope at a uniform speed $c = c_g$, retaining its initial form. Therefore, wave activity (shaded) occupies the same range of x as initially, only displaced.

In the shortwave limit, the phase speed (14.21) depends on $|\boldsymbol{k}|$. Individual components (k, l) then propagate with different phase speeds. A disturbance comprised of deep water waves therefore cannot retain its initial shape. The difference in phase speed between components with small and large $|\boldsymbol{k}|$ causes a group to unravel with time. Such waves are said to be *dispersive* because a disturbance that is initially compact is eventually distributed over a wider domain. The group speed for deep water waves follows from (14.21) as

$$\begin{aligned} c_g &= \frac{1}{2}\sqrt{\frac{g}{|\boldsymbol{k}|}} \\ &= \frac{c}{2}. \end{aligned} \tag{14.26}$$

A group of deep water waves thus propagates at exactly half their median phase speed. In this limit, c and $\boldsymbol{c}_g$ both depend on $|\boldsymbol{k}|$.

The behavior predicted by (14.26) is readily observed with the toss of a stone into a pond. It is recovered from (14.25) if the horizontal scale of the disturbance in Fig. 14.6a is sufficiently short (e.g., $L = L_2 \ll H$). The power spectrum of η' is then nearly *white* (Fig. 14.6b): $|\eta_{kl}|^2$ decreases with $|\boldsymbol{k}|$ slowly. Most of the excited variance therefore lies at large $|\boldsymbol{k}|H$. The disturbance is then comprised chiefly of deep water waves. Under these circumstances, the initial disturbance unravels into a series of oscillations (Fig. 14.7b), which propagate at different speeds. Wave activity therefore occupies an increasingly wider range of x. Contrary to shallow water waves (Fig. 14.7a), the envelope of wave activity translates outward slower than individual crests and troughs, at only half their speed (14.26). Waves inside it therefore overrun the envelope. They disappear at its leading edge, replaced by new ones that appear at its trailing edge.

14.2 ACOUSTIC WAVES

The simplest wave motions supported by the governing equations are sound waves. Compressibility provides the restoring force for simple acoustic waves, which have time scales short enough to ignore rotation, heat transfer, friction, and buoyancy. Acoustic waves are longitudinal disturbances: Fluid displacements are parallel to the propagation vector $\boldsymbol{k}$. We may, therefore, consider motion in the x direction. Under these circumstances, air motion is governed by

$$\frac{du}{dt} = -\frac{1}{\rho}\frac{\partial p}{\partial x} \tag{14.27.1}$$

$$\frac{d\rho}{dt} + \rho\frac{\partial u}{\partial x} = 0 \tag{14.27.2}$$

$$p\rho^{-\gamma} \text{ conserved}, \tag{14.27.3}$$

where Poisson's relation (2.30) serves as a statement of the First Law under adiabatic conditions. Applying the logarithm to (14.27.3) followed by the material derivative obtains

$$\frac{1}{\gamma}\frac{dlnp}{dt} = \frac{1}{\rho}\frac{d\rho}{dt}.$$

Substituting into (14.27.2) yields

$$\frac{1}{\gamma}\frac{dlnp}{dt} + \frac{\partial u}{\partial x} = 0. \tag{14.28}$$

For a homogeneous basic state (e.g., one that is isothermal and in uniform motion), the first order perturbation equations are then

$$\begin{aligned} \frac{Du'}{Dt} &= -\frac{1}{\overline{\rho}}\frac{\partial p'}{\partial x} \\ \frac{Dp'}{Dt} &+ \gamma \overline{p}\frac{\partial u'}{\partial x} = 0. \end{aligned} \tag{14.29}$$

These may be consolidated into a single second order equation

$$\frac{D^2p'}{Dt^2} - \gamma R\overline{T}\frac{\partial^2 p'}{\partial x^2} = 0. \tag{14.30}$$

Equation (14.30) is a 1-dimensional wave equation for the perturbation pressure p'. From it, other field properties follow. The coefficients of (14.30) are independent of x and t. We may therefore consider solutions of the form $e^{i(kx-\sigma t)}$, tantamount to applying the Fourier transform (14.12.1). Substituting transforms (14.30) into the dispersion relation

$$\hat{c}^2 = \gamma R\overline{T}. \tag{14.31}$$

The right-hand side of (14.31) is the speed of sound. The intrinsic phase speed $\hat{c}$ is independent of k. Acoustic waves are thus nondispersive. Their group velocity equals their phase velocity.

14.3 BUOYANCY WAVES

More important to the atmosphere are disturbances that are supported by the positive restoring force of buoyancy. They exist under stable stratification. Known as *gravity waves*, these disturbances typically have time scales short enough to ignore rotation, heat transfer, and friction. Vertical motions induced by gravity waves need not be hydrostatic. The governing equations are therefore expressed most conveniently in physical coordinates. Gravity waves involve motion transverse to the propagation vector $\boldsymbol{k}$. Consequently, they must be described in two dimensions. In the $x - z$ plane, air motion is described by

$$\frac{du}{dt} = -\frac{1}{\rho}\frac{\partial p}{\partial x} \tag{14.32.1}$$

$$\frac{dw}{dt} = -\frac{1}{\rho}\frac{\partial p}{\partial z} - g \tag{14.32.2}$$

$$\frac{1}{\rho}\frac{d\rho}{dt} + \frac{\partial u}{\partial x} + \frac{\partial w}{\partial z} = 0 \tag{14.32.3}$$

$$\frac{dlnp}{dt} - \gamma\frac{dln\rho}{dt} = 0. \tag{14.32.4}$$

As they account for compressibility, (14.32) also describe acoustic waves, which, at low frequency, are modified by buoyancy.

For a basic state that is isothermal, in uniform motion, and in hydrostatic equilibrium, the perturbation equations become

$$\frac{Du'}{Dt} = -gH\frac{\partial \hat{p}'}{\partial x} \tag{14.33.1}$$

$$\frac{Dw'}{Dt} = -gH\frac{\partial \hat{p}'}{\partial z} + g\hat{p}' - g\hat{\rho}' \tag{14.33.2}$$

$$\frac{D\hat{\rho}'}{Dt} + \frac{\partial u'}{\partial x} + \frac{\partial w'}{\partial z} - \frac{w'}{H} = 0 \tag{14.33.3}$$

$$\frac{D}{Dt}\left(\hat{p}' - \gamma\hat{\rho}'\right) + \gamma\frac{N^2}{g}w' = 0, \tag{14.33.4}$$

where

$$\hat{p}' = \frac{p'}{\overline{p}} \qquad \hat{\rho}' = \frac{\rho'}{\overline{\rho}} \tag{14.33.5}$$

are scaled by the basic state stratification,

$$H = \frac{R\overline{T}}{g}, \tag{14.33.6}$$

and

$$\begin{aligned} \frac{N^2}{g} &= \frac{\partial ln\overline{\theta}}{\partial z} \\ &= \frac{\kappa}{H} \end{aligned} \tag{14.33.7}$$

corresponds to a buoyancy period of about 20 minutes.

Equations (14.33) constitute a closed system for the four unknowns: u', w', $\hat{p}'$, and $\hat{\rho}'$. Because the system has constant coefficients, solutions may be expressed in terms of plane waves (14.11.1). However, owing to the stratification of mass, a group of waves propagating vertically must adjust in amplitude to conserve energy. For quadratic quantities like $\overline{\rho}\overline{u'^2}$ (kinetic energy density) to remain constant following the group, u', w', $\hat{p}'$, and $\hat{\rho}'$ must amplify vertically like $\overline{\rho}^{-\frac{1}{2}} = e^{\frac{z}{2H}}$. Considering solutions of the form $e^{\frac{z}{2H}+i(kx+mz-\sigma t)}$, where m denotes vertical wavenumber, then transforms the differential system (14.33) into an algebraic one. Consolidating the algebraic equations yields the dispersion relation

$$m^2 = k^2\left(\frac{N^2}{\omega^2} - 1\right) + \frac{\omega^2 - \omega_a^2}{c_s^2}, \tag{14.34.1}$$

where

$$c_s^2 = \gamma R\overline{T} \tag{14.34.2}$$

is the speed of sound. The term

$$\omega_a = \frac{c_s}{2H} \tag{14.34.3}$$

is the *acoustic cutoff frequency* for vertical propagation. At frequencies $|\omega| < \omega_a$, acoustic waves do not propagate vertically.

Equation (14.34) describes *acoustic-gravity waves*, which involve buoyancy as well as compression. Their vertical propagation is controlled by the sign of m^2. For $m^2 > 0$, individual wave components oscillate in z. Vertically propagating, such waves are referred to as *internal waves* because their oscillatory structure occurs in the interior of a bounded domain.[2] Vertically propagating waves amplify upward like $e^{\frac{z}{2H}}$ (Fig. 14.8a). The upward amplification offsets the stratification of mass, making energy

[2] For freely propagating waves, which have form e^{imz}, this terminology is a misnomer. Internal modes, which have form $e^{imz} + e^{imz} = 2\cos mz$, are trapped vertically between boundaries, which lead to complete reflection.

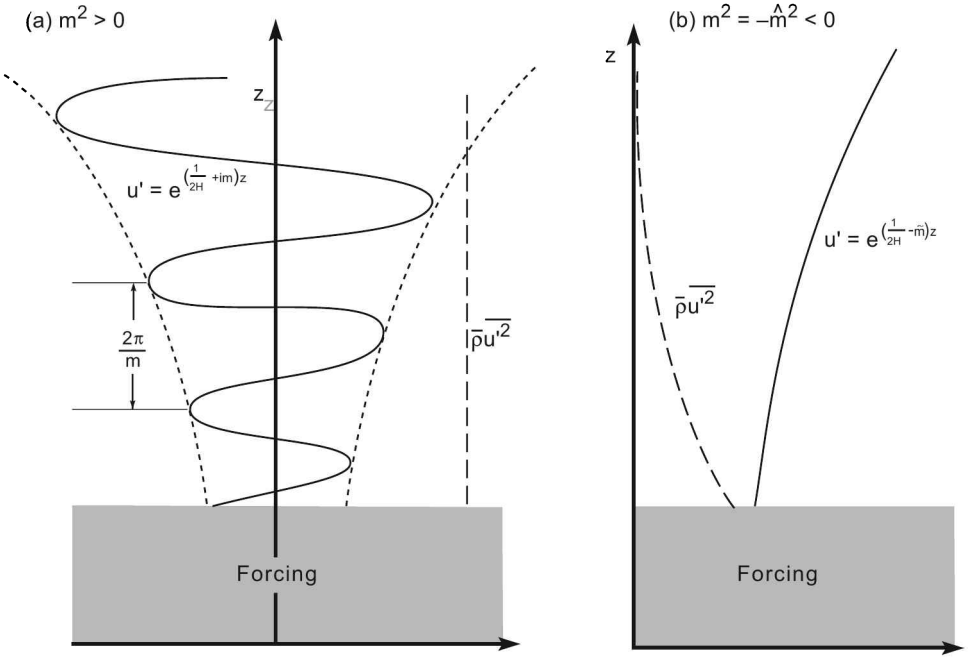

Figure 14.8 Vertical structure of (a) *internal waves* ($m^2 > 0$), which oscillate with z (solid) and amplify upward like $e^{\frac{z}{2H}}$ to make energy density (dashed) invariant with height, and (b) *external waves* ($m^2 < 0$), whose energy density (dashed) decays exponentially with height but whose amplitude (solid) can either amplify or decay depending on m.

density invariant with height. For $m^2 = -\hat{m}^2 < 0$, individual wave components vary exponentially in z (Fig. 14.8b). Oscillations then occur in-phase throughout the column. For the column energy to remain bounded, the energy density of these waves must decrease with height exponentially. Such waves are referred to as *evanescent* or *external* because they form along the exterior of a boundary. The edge-wave structure of surface water waves in the deep-water limit is an example (Fig. 14.4b). Even though their energy decreases upward, external waves in the range $\frac{1}{4H^2} < m^2 < 0$ amplify upward like $e^{(\frac{1}{2H} - \hat{m})z}$ due to stratification of mass.

The dispersion relation assumes two limiting forms associated with vertical propagation. They appear when m^2 is plotted as a function of k and ω (Fig. 14.9). For $\omega^2 \gg N^2$, (14.34) reduces to

$$k^2 + m^2 + \frac{1}{4H^2} \cong \frac{\omega^2}{c_s^2} \qquad \frac{\omega^2}{N^2} \to \infty. \tag{14.35.1}$$

This limiting behavior describes high-frequency acoustic waves that are modified by stratification. It is also recovered if $N \to 0$, which eliminates the restoring force of buoyancy. Acoustic waves propagate vertically for ω greater than values on the upper curve for $m^2 = 0$ in Fig. 14.9 (shaded). For $k^2 + m^2 \to \infty$, their intrinsic phase speeds approach the speed of sound. In the longwave limit ($k \to 0$), the minimum ω for vertical propagation equals the acoustic cutoff ω_a. In the shortwave limit ($k \to \infty$), the

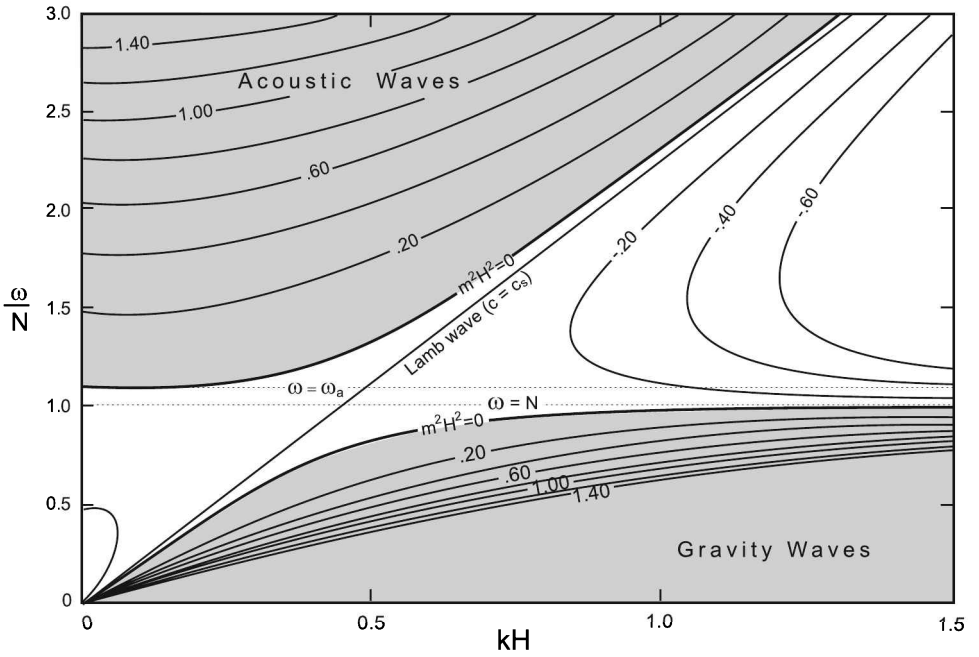

Figure 14.9 Vertical wavenumber squared contoured as a function of horizontal wavenumber and intrinsic frequency. Vertical propagation (shaded) occurs for acoustic waves at ω greater than the acoustic cutoff ω_a and for gravity waves at ω less than the buoyancy frequency N, where $\omega_a \cong 1.1N$ under isothermal conditions. The Lamb wave connects the limiting behavior of acoustic waves for $m^2 = 0$ and $k \to \infty$ to the limiting behavior of gravity waves for $m^2 = 0$ and $k \to 0$. It propagates horizontally at the speed of sound.

minimum ω for vertical propagation tends to infinity. The corresponding waves have horizontal phase speeds that approach the speed of sound.

For $\omega^2 \ll \omega_a^2$, (14.34) reduces to

$$k^2 + m^2 + \frac{1}{4H^2} \cong \frac{N^2}{\omega^2}k^2 \qquad \frac{\omega^2}{\omega_a^2} \to 0, \tag{14.35.2}$$

This limiting behavior describes low-frequency gravity waves that are modified by stratification of mass. It is also recovered if $c_s \to \infty$, which renders air motion incompressible. Gravity waves propagate vertically for ω less than values on the lower curve for $m^2 = 0$ in Fig. 14.9 (shaded). Unlike most vibrating systems, internal gravity waves have a high-frequency cutoff for vertical propagation: N. In the shortwave limit ($k \to \infty$), the maximum ω for vertical propagation approaches N. Horizontal phase speed then vanishes. The corresponding behavior describes column oscillations at the buoyancy frequency (7.11). In the longwave limit ($k \to 0$), the maximum ω for vertical propagation approaches zero. The corresponding waves propagate horizontally, with phase speeds that approach the speed of sound.

The regions of vertical propagation in Fig. 14.9 are well-separated. Between them, $m^2 < 0$ and waves are external (unshaded). Acoustic-gravity waves then propagate horizontally, with energy that decreases upward exponentially. They exert no net influence

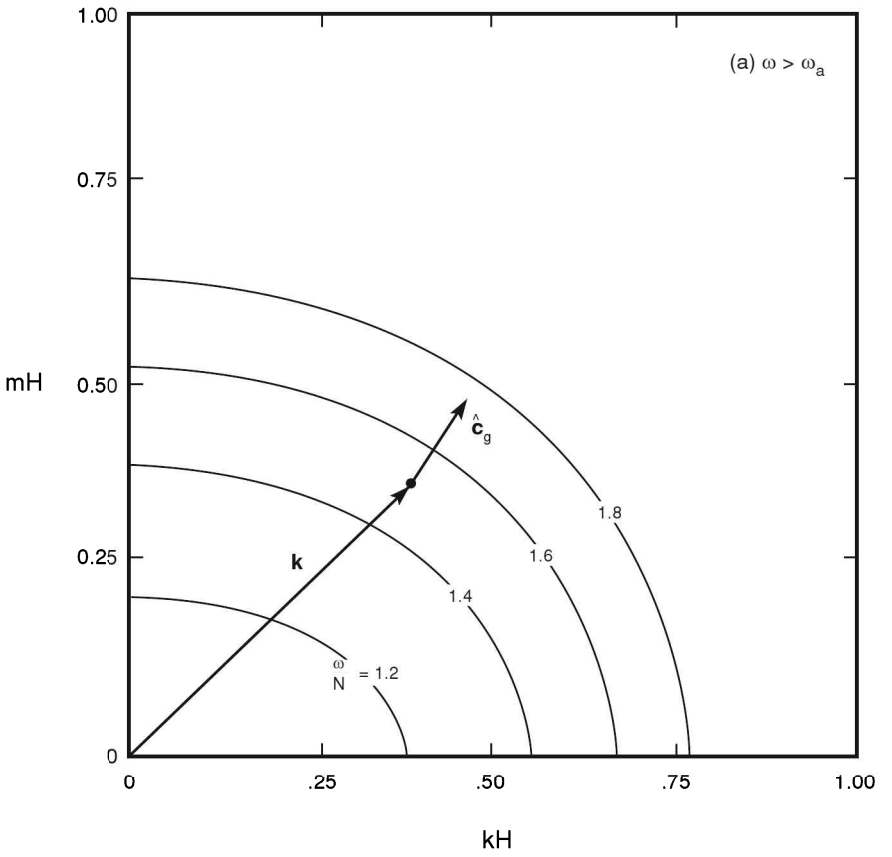

Figure 14.10 Intrinsic frequency of acoustic-gravity waves contoured as a function of wavenumber. Group velocity relative to the medium is directed orthogonal to contours of intrinsic frequency toward increasing ω. (a) Acoustic waves ($\omega > N$) have group velocity relative to the medium $\hat{\boldsymbol{c}}_g$ that is nearly parallel to phase propagation $\boldsymbol{k}$. (b) Gravity waves ($\omega < N$) have $\hat{\boldsymbol{c}}_g$ that is nearly orthogonal to $\boldsymbol{k}$, except close to $m = 0$, where both become horizontal.

in the vertical. Connecting the limiting behavior of internal acoustic waves for $k \to \infty$ and internal gravity waves for $k \to 0$ is the external *Lamb wave* (Lamb, 1910). It propagates horizontally at the speed of sound, for all k.

Dispersion characteristics of the acoustic and gravity branches of (14.34) are illustrated in Fig. 14.10, which plots ω as a function of $\boldsymbol{k} = (k, m)$. The intrinsic group velocity (14.23) is directed orthogonal to contours of intrinsic frequency toward increasing ω. On the other hand, phase propagates with the velocity $\hat{c}\frac{\boldsymbol{k}}{|\boldsymbol{k}|}$, parallel ($\omega > 0$) or anti-parallel ($\omega < 0$) to the wavenumber vector $\boldsymbol{k}$. For acoustic waves (Fig. 14.10a), contours of ω are elliptical. They are modified only slightly from their forms under unstratified conditions. The group velocity $\hat{\boldsymbol{c}}_g$ is then close to the phase velocity $c\frac{\boldsymbol{k}}{|\boldsymbol{k}|}$ for all $\boldsymbol{k}$. Hence, acoustic waves are only weakly dispersive.

For gravity waves (Fig. 14.10b), contours of ω are hyperbolic. The situation is then quite different. In the limit of short wavelength ($k^2 + m^2 \to \infty$), contours of ω become

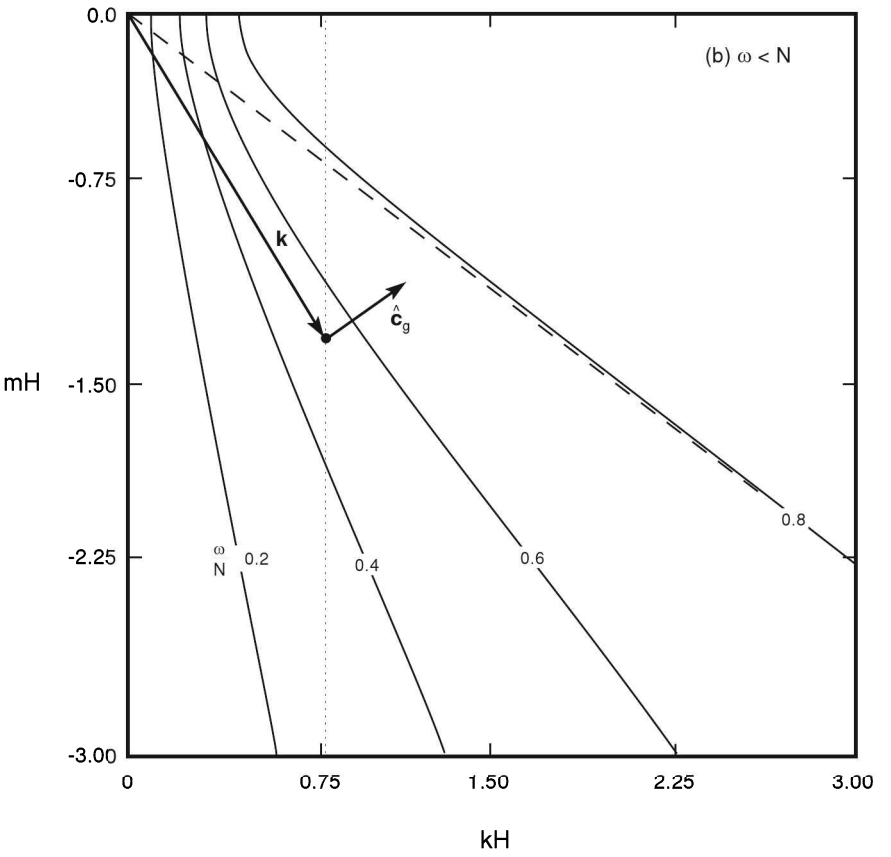

Figure 14.10 (*continued*)

straight lines that pass through the origin. The group velocity $\hat{\boldsymbol{c}}_g$ is then orthogonal to the phase velocity $\hat{c}\frac{\boldsymbol{k}}{|\boldsymbol{k}|}$. Such waves are thus highly dispersive. A wave group defined by the vector $\boldsymbol{k}$ in Fig. 14.10b has phase that propagates downward and to the right. However, its envelope propagates upward and to the right. A packet of gravity waves (Fig. 14.11) propagates parallel to lines of constant phase (e.g. along crests and troughs), not perpendicular to them, as is observed of more familiar acoustic waves.[3] Consequently, downward propagation of phase translates into upward propagation of wave activity. This peculiarity follows from the dispersive nature of gravity waves. It applies to all waves whose vertical restoring force is buoyancy. In the limit of long wavelength ($k^2 + m^2 \to 0$), contours of ω become parallel to the m axis. Group velocity is then horizontal.

At very low frequency, rotation cannot be ignored. The Coriolis force then modifies the dispersion relation. It also makes parcel trajectories 3-dimensional. Under these conditions, air motion (u, w) associated with buoyancy oscillations experiences a Coriolis force fu. The latter drives parcel trajectories out of the $x - z$ plane,

[3] Lighthill (1978) presents a laboratory demonstration.

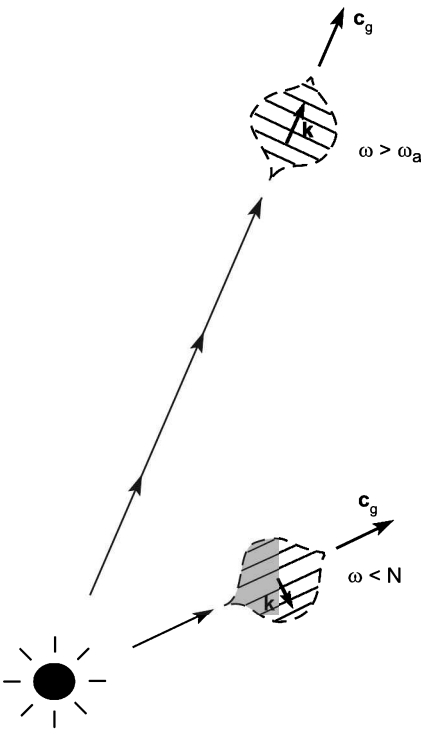

Figure 14.11 A packet of simple gravity waves ($\omega < N$) propagates along crests and troughs – just perpendicular to simple acoustic waves ($\omega > \omega_a$), which propagate orthogonal to crests and troughs.

introducing v. Disturbances in this range of frequency are referred to as *inertio-gravity waves*. They are treated in Gill (1982).

14.3.1 Shortwave limit

In the limit of short total wavelength ($k^2 + m^2 \to \infty$), the dispersion relation for gravity waves (14.35.2) reduces to

$$\begin{aligned} \frac{\omega^2}{N^2} &= \frac{k^2}{k^2 + m^2} \\ &= cos^2\alpha, \end{aligned} \tag{14.36}$$

where α is the angle that $\boldsymbol{k}$ makes with the horizontal (Fig. 14.12). Contours of ω are then straight lines – the limiting behavior in Fig. 14.10b, wherein $\hat{\boldsymbol{c}}_g$ becomes orthogonal to $\boldsymbol{k}$. Describing simple gravity waves, these disturbances have phase that propagates at progressively shallower angles as ω is increased. As ω approaches N, $\boldsymbol{k}$ becomes horizontal, with phase lines vertical.

The limiting behavior (14.36) applies to mountain waves (Fig. 9.22), which have horizontal wavelengths of about 10 km. Generated by forced ascent over elevated terrain, mountain waves are fixed with respect to the Earth. They have absolute frequencies $\sigma \cong 0$. Their intrinsic frequencies, however, do not vanish. Rather, they equal the Doppler shift $-k\overline{u}$. In westerly flow, contours of phase propagate westward relative to the medium. Recall that upward propagation of energy requires downward propagation of phase. Phase contours must therefore tilt westward with height above

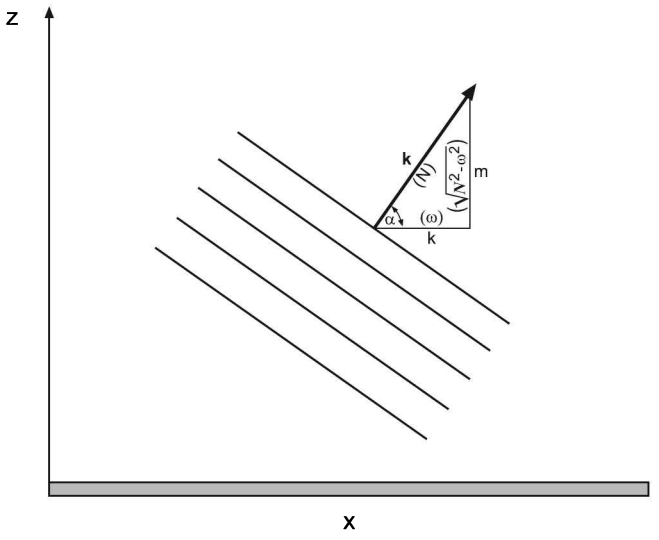

Figure 14.12 Schematic illustrating a simple gravity wave of wavenumber ***k*** that is inclined from the horizontal by an angle α.

their forcing. Such behavior is often observed in the leading edge of lenticular cloud (Fig. 9.22a).

Despite having zero phase velocity relative to the ground, orographically forced gravity waves have nonvanishing group velocity. Figure 14.13 displays the gravity wave pattern that is excited by steady westerly motion incident on a 2-dimensional ridge. Wave activity, manifest in oscillations of w', is transmitted upward and downstream. The dispersive nature of gravity waves leads to wave activity occupying a progressively wider range of x with increasing height above the source. Vertical motion induced by the oscillations can extend into the stratosphere (see Fig. 14.24). This feature of mountain waves has enabled sailplanes to reach altitudes as high as 50,000′ (17,000 m).

14.3.2 Propagation of gravity waves in an inhomogeneous medium

When the basic state is not isothermal and in uniform motion, wave propagation varies with position. Consider the propagation of gravity waves in a basic state that varies with height: $N^2 = N^2(z)$ and $\overline{u} = \overline{u}(z)$, and under the Boussinesq approximation (Sec. 12.5.3). The wave field is then governed by

$$\frac{Du'}{Dt} + w'\overline{u}_z = -gH\frac{\partial \hat{p}'}{\partial x} \tag{14.37.1}$$

$$\frac{Dw'}{Dt} = -gH\frac{\partial \hat{p}'}{\partial z} - g\hat{\rho}' \tag{14.37.2}$$

$$\frac{\partial u'}{\partial x} + \frac{\partial w'}{\partial z} = 0 \tag{14.37.3}$$

$$-\frac{D\hat{\rho}'}{Dt} + \frac{N^2}{g}w' = 0, \tag{14.37.4}$$

where (14.37.4) follows from (14.33.4) with the neglect of compressibility.

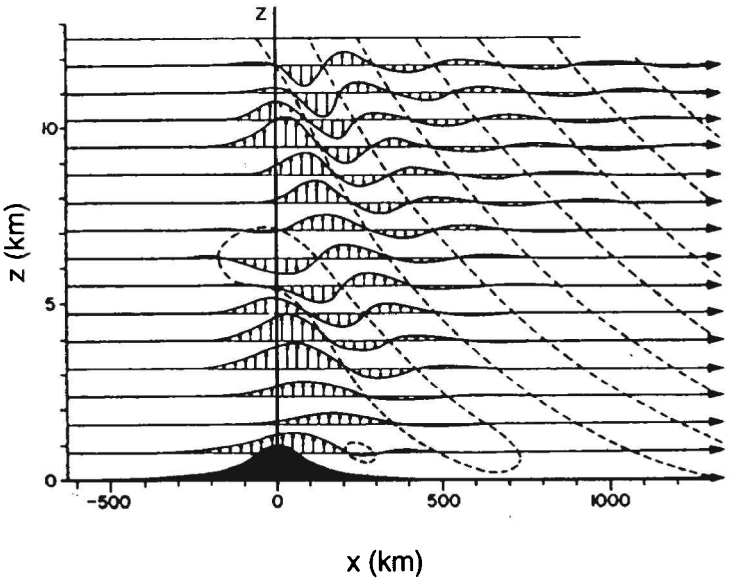

Figure 14.13 Streamlines and vertical motion accompanying a stationary gravity wave pattern that is excited by uniform flow over a two-dimensional ridge 100 km wide. After Queney (1948).

Applying the linearized material derivative to (14.37.2) gives

$$\frac{D^2w'}{Dt^2} + gH\frac{D}{Dt}\left(\frac{\partial \hat{p}'}{\partial z}\right) = -g\frac{D\hat{\rho}'}{Dt}.$$

With (14.37.4), this becomes

$$\left[\frac{D^2}{Dt^2} + N^2\right] w' + gH\frac{D}{Dt}\left(\frac{\partial \hat{p}'}{\partial z}\right) = 0. \tag{14.38}$$

As coefficients are still independent of x and t, we consider solutions of the form $e^{i(kx-\sigma t)}$. Combining (14.37.1) with (14.37.3) obtains

$$gH\frac{\partial P_k^\sigma}{\partial z} = \frac{i}{k}\left\{(c_x - \overline{u})\frac{\partial^2 W_k^\sigma}{\partial z^2} + \overline{u}_{zz}W_k^\sigma\right\}, \tag{14.39}$$

where $P_k^\sigma(z)$ denotes the complex amplitude of $\hat{p}'$ (14.12.1). Then incorporating (14.39) into (14.38) yields

$$\frac{\partial^2 W_k^\sigma}{\partial z^2} + m^2(z)W_k^\sigma = 0, \tag{14.40.1}$$

in which

$$m^2(z) = \frac{N^2}{(c_x - \overline{u})^2} - k^2 + \frac{\overline{u}_{zz}}{c_x - \overline{u}} \tag{14.40.2}$$

serves as a 1-dimensional *index of refraction.*

Known as the *Taylor-Goldstein equation,* (14.40) describes the vertical propagation of wave activity in terms of local refractive properties of the medium. For $m^2 > 0$, $W_k^\sigma(z)$ is oscillatory in z. Wave activity then propagates vertically with a

local wavelength $\frac{2\pi}{m(z)}$. Unlike propagation under homogeneous conditions (14.33), variations of m^2 can lead to reflection of wave activity. This effect couples upward and downward propagation. Oscillations governed by (14.40) do not amplify vertically, owing to the Boussinesq approximation that neglects compressibility. For $m^2 < 0$, vertical structure is evanescent. Vertical propagation is then prohibited. Wave activity incident on a region of $m^2 < 0$ must therefore be reflected.

The restoring force for buoyancy oscillations is controlled by static stability. In (14.40.2), increasing N^2 increases m^2, which supports vertical propagation. The greater N^2, the shorter is the vertical wavelength and the more vertical propagation is favored. On the other hand, increasing k^2 reduces m^2. Short horizontal wavelengths (large k) are therefore less able to propagate vertically than long horizontal wavelengths (small k). Vertical propagation is also influenced by the mean flow, chiefly through the intrinsic trace speed $c_x - \overline{u}$. For small flow curvature ($\overline{u}_{zz} \cong 0$), the first two terms on the right-hand side of (14.40.2) dominate. Increasing $|c_x - \overline{u}|$ corresponds to faster propagation relative to the mean flow or, for stationary waves, to stronger wind. It reduces m^2, inhibiting vertical propagation. The elongated vertical wavelength also makes wave activity increasingly vulnerable to reflection – because refractive properties do not vary gradually relative to the phase of oscillations. If m^2 is reduced to zero, the vertical wavelength becomes infinite (see Fig. 14.14b). Continued vertical propagation is then prohibited. Wave activity must therefore be fully reflected. The height where this occurs is called the *turning level*. Above the turning level, wave structure is external ($m^2 < 0$).

Decreasing $|c_x - \overline{u}|$ has the reverse effect. It favors vertical propagation by increasing m^2. The vertical wavelength is then shortened. This averts reflection by making variations in refractive properties comparatively gradual. Should $|c_x - \overline{u}|$ decrease to zero, (14.40) becomes singular. The index of refraction then becomes unbounded and the vertical wavelength collapses to zero (see Fig. 14.15b). The height where this occurs is called the *critical level*. Contrary to a turning level, which leads to reflection, the condition $m^2 \to \infty$ at the critical level leads to absorption of wave activity.

14.3.3 The WKB approximation

Analytical solutions to (14.40) can be obtained only for idealized profiles of $N^2(z)$ and $\overline{u}(z)$. However, an approximate class of solutions is valid when the basic state varies slowly compared with the phase of oscillations. It affords insight into how wave activity propagates – even under more general circumstances. The approximate solutions

$$W^{\pm}(z) = \frac{W_0^{\pm}}{\sqrt{m(z)}} e^{\pm i \int m(z) dz} \tag{14.41}$$

satisfy the related equation

$$\frac{\partial^2 W^{\pm}}{\partial z^2} + m^2(z) W^{\pm} = -R(z) m^2(z) W^{\pm}, \tag{14.42.1}$$

where

$$R(z) = \frac{1}{2m^3} \frac{\partial^2 m}{\partial z^2} - \frac{3}{4m^4} \left(\frac{\partial m}{\partial z} \right)^2. \tag{14.42.2}$$

The factor $R(z)$ accounts for the interdependence of W^+ and W^- and, hence, for wave reflection.

In the limit of $R \to 0$ everywhere, (14.42) reduces to the general form of (14.40). Reflection then vanishes and the upward- and downward-propagating waves may be treated independently. In the absence of dissipation, wave activity then propagates conservatively along *rays* that are smoothly refracted through the medium. The solution (14.41) defines the so-called *slowly varying* or *WKB approximation*.[4] Its validity (e.g., $R \ll 1$) rests on refractive properties changing on a scale long compared to the vertical wavelength. In practice, (14.41) often provides a qualitatively correct description of wave propagation, even when it cannot be justified formally. Should R become $O(1)$ somewhere, reflection ensues. It introduces the other of the components in (14.41). Clearly, $m^2 = 0$ violates the above condition. At the turning level, the local vertical wavelength is infinite, introducing strong reflection. There, the WKB approximation breaks down. Nevertheless, the wave field can be matched analytically across the turning level (see, e.g., Morse and Feschbach, 1953).

14.3.4 Method of geometric optics

Under conditions of the WKB approximation, wave activity can be traced from its source along rays that are defined by the local group velocity $\boldsymbol{c}_g$. If

$$\overline{u}_{zz} \ll \frac{N^2}{|c_x - \overline{u}|}, \tag{14.43}$$

(14.40.2) has the same form as the dispersion relation for simple gravity waves in the limit of short wavelength (14.36). Components of $\boldsymbol{c}_g$ then follow from (14.23) as

$$\begin{aligned} c_{gx} &= \frac{m^2\omega}{k(k^2+m^2)} + \overline{u} \\ c_{gz} &= -\frac{m\omega}{(k^2+m^2)}, \end{aligned} \tag{14.44}$$

with $m = m(z)$, $\overline{u} = \overline{u}(z)$. A ray is everywhere tangent to $\boldsymbol{c}_g$, with local slope in the $x - z$ plane

$$\frac{dz}{dx} = \frac{c_{gz}}{c_{gx}}. \tag{14.45}$$

Specifying its initial coordinates then determines the ray associated with an individual component (k, m) of the wave spectrum.

Turning Level

Orographically forced gravity waves involve a spectrum of horizontal wavenumbers k, all with zero frequency. Figure 14.14 presents rays of two components with $\sigma = 0$, under the conditions of (14.43), for $N^2 = \text{const}$, and $\overline{u}(z)$ representative of the wintertime troposphere and stratosphere (Fig. 14.14a). Each ray emanates from

[4] The letters stand for Wentzel (1926), Kramer (1926), and Brillouin (1926), who rediscovered the procedure in different problems, after being introduced originally by Liouville (1837) and Green (1838).

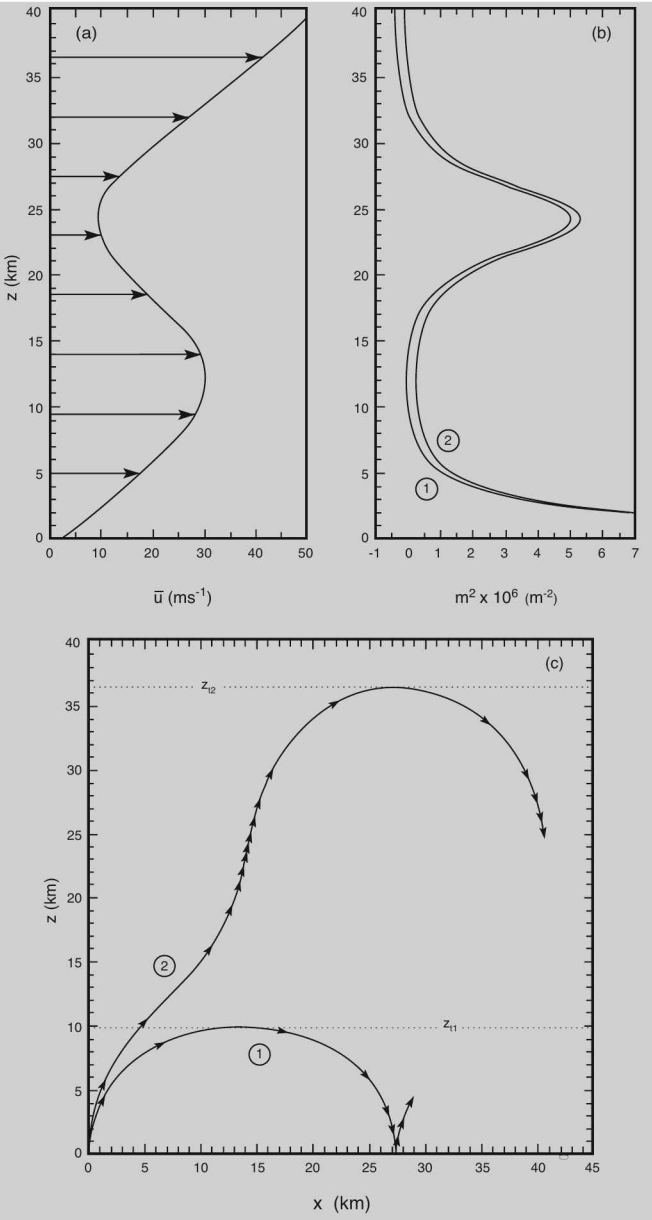

Figure 14.14 (a) Zonal motion representative of the extratropical troposphere and stratosphere during winter. (b) Vertical refractive index squared following from mean motion in (a) and uniform static stability. (c) Rays for two stationary wave components with a source at $(x, z) = (0, 0)$. Arrow heads mark uniform increments of time moving along the ray at the group velocity c_g. Component 1, which has short horizontal wavelength, encounters a *turning level* in the troposphere, where it is reflected downward. Component 2, which has longer horizontal wavelength, propagates into the stratosphere before encountering a turning level.

a point source located at the origin of the $x-z$ plane. Component 1 has short horizontal wavelength (large k). Westerly shear then drives ω^2 to N^2 and m^2 to zero near the tropopause (Fig. 14.14b). The ray for that component (Fig. 14.14c) is reflected at its turning level z_{t1}. Above z_{t1}, wave amplitude decays with height exponentially.

Because $m = 0$ at the turning level,

$$\begin{aligned} c_{gx} &= \overline{u} \\ c_{gz} &= 0 \end{aligned} \qquad z = z_{t1}. \tag{14.46}$$

Thus, relative to the medium, wave activity at $z = z_{t1}$ is motionless. Consider the time for wave activity to reach the turning level from some neighboring level below. The time for wave activity to propagate from a level z_0 to a level z is given by

$$\Delta t = \int_{z_0}^{z} \frac{dz'}{c_{gz}}. \tag{14.47}$$

Near the turning level,

$$c_{gz} \sim -\frac{\omega m}{k^2} \qquad z \to z_{t1}. \tag{14.48.1}$$

Because $\omega = -k\overline{u} < 0$ for $z < z_{t1}$ and $\overline{u}_z > 0$,

$$\omega \sim -N - k\overline{u}_z(z - z_{t1}) \qquad z \to z_{t1}. \tag{14.48.2}$$

Substituting into the dispersion relation (14.36) obtains

$$m \sim k\left[2\frac{k}{N}\overline{u}_z(z_{t1} - z)\right]^{\frac{1}{2}} \qquad z \to z_{t1}. \tag{14.48.3}$$

Then, near the turning level, the vertical group speed behaves as

$$c_{gz} \sim \left[2\frac{N}{k}\overline{u}_z(z_{t1} - z)\right]^{\frac{1}{2}} \qquad z \to z_{t1}. \tag{14.49}$$

Incorporating (14.49) into (14.47) gives for the approach time

$$\begin{aligned} \Delta t &= \left[\frac{2k}{N\overline{u}_z}(z_{t1} - z)\right]^{\frac{1}{2}}\Bigg|_{z}^{z_0} \\ &< \infty \qquad z \to z_{t1}. \end{aligned} \tag{14.50}$$

The time for wave activity to reach the turning level is finite, even though c_{gz} vanishes there. So is the time for it to rebound and propagate away. It follows that wave activity can rebound from the turning level having suffered only finite dissipation. This is the premise for interpreting behavior near z_{t1} as reflection.

Wave activity trapped between its turning level and the surface is ducted horizontally inside the troposphere. Such trapping can produce oscillations far downstream of a wave source. It is revealed by extensive wave patterns in satellite cloud imagery (Fig. 1.11). In contrast, wave activity that propagates freely in the vertical (Fig. 14.13) produces only a few oscillations downstream. Cloud bands are therefore confined near the wave source (Fig. 9.22).

Component 2 of the wave spectrum has long horizontal wavelength (small k). Consequently, it does not encounter a turning level until wave activity has

propagated well into the stratospheric jet (Fig. 14.14b). Although m^2 is reduced in strong westerlies of the tropospheric jet, it remains positive. This allows component 2 to propagate to higher levels. The region of small m^2 in the upper troposphere coincides with small vertical group speed. Propagation is then refracted into a shallower angle (Fig. 14.14c), only to be refracted more steeply again when wave activity emerges into weak westerlies of the lower stratosphere. At greater height, westerlies intensify again, with a commensurate decrease of m. Eventually, $\overline{u}$ in the stratospheric jet becomes strong enough to drive m^2 to zero. This occurs at the turning level z_{t2}, below which component 2 is vertically trapped.

Critical level

Consider now conditions representative of summer. Figure 14.15 shows the same features for component 2, but for easterly flow in the stratosphere. Having $c_x = 0$, component 2 is Doppler shifted to zero where $\overline{u}$ vanishes: the zero-wind line. There, the mean velocity matches the zonal trace speed: $\overline{u} = c_x = 0$. This condition occurs not far above the tropopause (Fig. 14.15a). At the critical level z_{c2}, $m^2 \to \infty$ and the vertical wavelength shrinks to zero (Fig. 14.15b).

Because $\omega = 0$ at the critical level,

$$\begin{matrix} c_{gx} = \overline{u} = 0 \\ c_{gz} = 0 \end{matrix} \qquad z = z_{c2}. \tag{14.51}$$

Wave activity is again motionless relative to the medium. Consider the time for it to reach the critical level from some neighboring level z_0 below. For z near the critical level,

$$c_{gz} \sim -\frac{\omega}{m} \qquad z \to z_{c2}. \tag{14.52}$$

Because $\omega = -k\overline{u} < 0$ for $z < z_{c2}$ and $\overline{u}_z < 0$,

$$\omega \sim -k\overline{u}_z(z - z_{c2}) \qquad z \to z_{c2}. \tag{14.53.1}$$

Substituting into the dispersion relation gives

$$m \sim \frac{N}{\overline{u}_z(z - z_{c2})} \qquad z \to z_{c2}. \tag{14.53.2}$$

Then, near the critical level, the vertical group speed behaves as

$$c_{gz} \sim \frac{k}{N}\overline{u}_z^2(z - z_{c2})^2 \qquad z \to z_{c2}. \tag{14.54}$$

Incorporating (14.54) into (14.47) obtains for the approach time

$$\begin{aligned} \Delta t &= \frac{N}{k\overline{u}_z^2}(z - z_{c2})^{-1}\Big|_z^{z_0} \\ &\to \infty \qquad z \to z_{c2}. \end{aligned} \tag{14.55}$$

Unlike behavior at a turning level, the time for wave activity to reach the critical level is infinite. The critical level is, therefore, never actually encountered. Instead, wave activity becomes frozen relative to the medium, remaining in that state for infinite duration. Dissipation can then absorb it. The ray for component 2 (Fig. 14.15c) is refracted into the critical level, where it stalls and terminates.

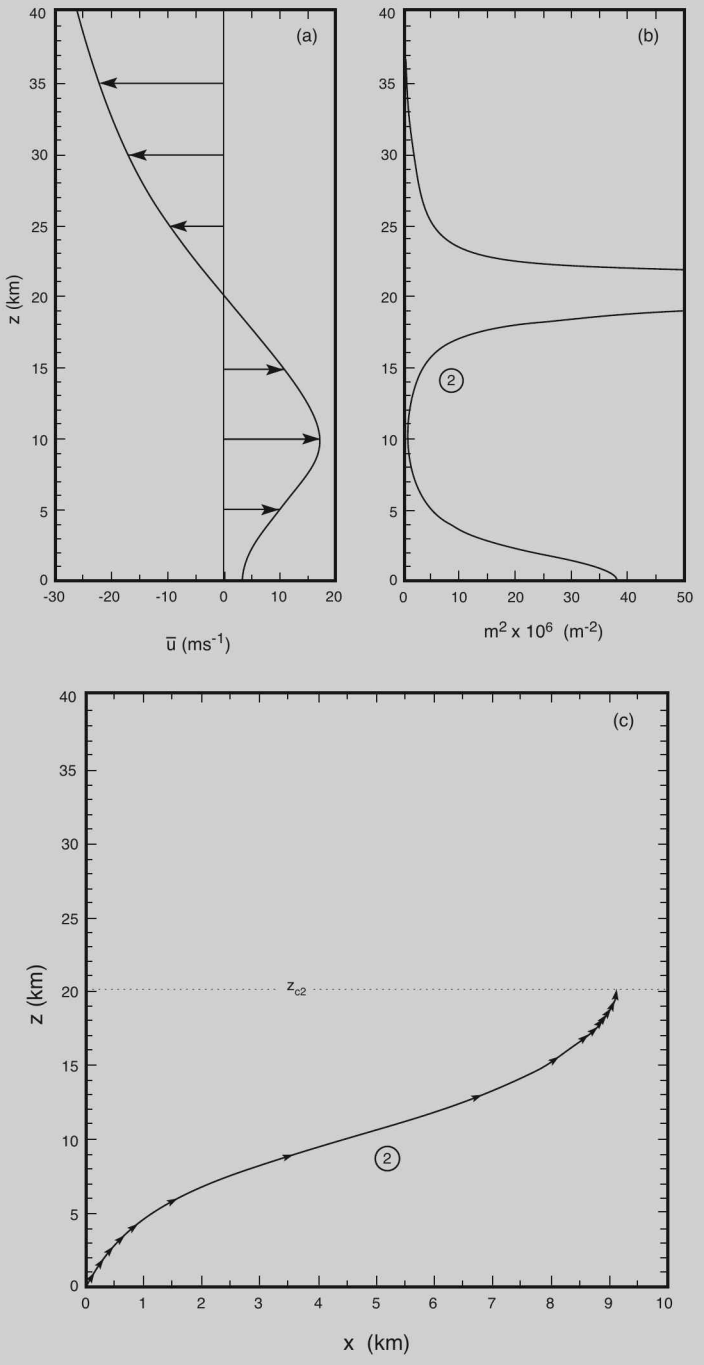

Figure 14.15 As in Fig. 14.14, except for conditions representative of summer and for component 2, the wave is Doppler-shifted to zero intrinsic phase speed: $c_x - \overline{u} = 0$, at the critical level, where $m^2 \to \infty$, group propagation stalls, and the ray terminates.

14.4 THE LAMB WAVE

Consider oscillations in an unbounded atmosphere and in the absence of forcing. These conditions define an unforced or eigenvalue problem. The latter determines the free modes or *normal modes* of the system. Their frequencies, at which waves can exist without forcing, are called *eignenfrequencies*. Should forcing be present at the one of the eigenfrequencies, the corresponding normal mode is greatly amplified relative to other wave components.

For oscillations that are hydrostatic, the perturbation equations (14.33) reduce to

$$\frac{Du'}{Dt} = -gH\frac{\partial \hat{p}'}{\partial x} \tag{14.56.1}$$

$$\left(H\frac{\partial}{\partial z} - 1\right)\hat{p}' + \hat{\rho}' = 0 \tag{14.56.2}$$

$$\frac{D\hat{\rho}'}{Dt} + \frac{\partial u'}{\partial x} + \left(\frac{\partial}{\partial z} - \frac{1}{H}\right)w' = 0 \tag{14.56.3}$$

$$\frac{D}{Dt}(\hat{p}' - \gamma\hat{\rho}') + \gamma\frac{\kappa}{H}w' = 0. \tag{14.56.4}$$

Considering solutions of the form $e^{i(kx-\sigma t)}$ transforms (14.56) into

$$-i\omega U_k^\sigma = -ikgHP_k^\sigma \tag{14.57.1}$$

$$\left(H\frac{\partial}{\partial z} - 1\right)P_k^\sigma + \rho_k^\sigma = 0 \tag{14.57.2}$$

$$-i\omega\rho_k^\sigma + ikU_k^\sigma + \left(\frac{\partial}{\partial z} - \frac{1}{H}\right)W_k^\sigma = 0 \tag{14.57.3}$$

$$-i\omega(P_k^\sigma - \gamma\rho_k^\sigma) + \gamma\frac{\kappa}{H}W_k^\sigma = 0. \tag{14.57.4}$$

Using (14.57.2) to eliminate density in (14.57.4) gives the vertical velocity

$$W_k^\sigma = \frac{i\omega H}{\kappa}\left[H\frac{\partial}{\partial z} - \kappa\right]P_k^\sigma. \tag{14.58}$$

Then, incorporating (14.58), (14.57.1), and (14.57.3) yields a 2nd-order differential equation for the perturbation amplitude $P_k^\sigma(z)$

$$\frac{\partial^2 P_k^\sigma}{\partial z^2} - \frac{1}{H}\frac{\partial P_k^\sigma}{\partial z} + \frac{\kappa g}{H}\frac{k^2}{\omega^2}P_k^\sigma = 0. \tag{14.59}$$

Solutions to (14.59) must satisfy boundary conditions. At the surface, w' must vanish. The upper boundary condition depends on whether the solution is vertically propagating or evanescent. If the solution is evanescent, it must have bounded column energy. If it is vertically propagating, far above the source, the solution must transmit wave activity upward - away from the region of excitation. These conditions define the so-called *finite-energy condition* and *radiation condition*, respectively. They apply at $z \to \infty$. Collectively, $P_k^\sigma(z)$ must then satisfy

$$\frac{\partial^2 P_k^\sigma}{\partial z^2} - \frac{1}{H}\frac{\partial P_k^\sigma}{\partial z} + \frac{\kappa g}{H}\frac{k^2}{\omega^2}P_k^\sigma = 0 \tag{14.60.1}$$

$$H\left[\frac{\partial}{\partial z} - \kappa\right]P_k^\sigma = 0 \qquad z = 0 \tag{14.60.2}$$

$$\text{finite energy/radiation} \qquad z \to \infty. \tag{14.60.3}$$

Equations (14.60) define a homogeneous boundary value problem for the vertical structure $P_k^\sigma(z)$, namely, one that has no forcing in the interior or on the boundaries. Nontrivial solutions exist only at particular frequencies.

Seeking solutions of the form $e^{(\frac{1}{2H}+im)z}$ transforms (14.60.1) into the dispersion relation

$$m^2 + \frac{1}{4H^2} = \frac{N^2}{\omega^2}k^2. \tag{14.61}$$

Equation (14.61) may be recognized as (14.35.2) in the conditional limit $k \to 0$. Horizontal wavelength is then long enough for vertical displacements to be hydrostatic. If $m^2 > 0$, solutions are vertically propagating. By (14.44), upward energy propagation (14.60.3) requires $m\omega < 0$, which corresponds to downward phase propagation. For $\omega > 0$, this requires $m < 0$. It is readily verified that these solutions do not satisfy the homogeneous lower boundary condition (14.60.2). Nor do their counterparts for $\omega < 0$. If $m^2 = -\hat{m}^2 < 0$, the solutions of (14.60.1) are external. The upper boundary condition, which requires bounded column energy, is satisfied by solutions of the form $e^{(\frac{1}{2H}-\hat{m})z}$. One of these also satisfies the lower boundary condition, namely, $\hat{m} = \frac{\kappa-\frac{1}{2}}{H}$. Representing a normal mode of the unbounded atmosphere, it has the vertical eigenstructure

$$P_k^\sigma(z) = e^{\kappa\frac{z}{H}}. \tag{14.62.1}$$

This vertical structure defines the *Lamb mode*. It makes w' vanish – not just at the surface, but everywhere (14.58). Buoyancy oscillations then vanish identically. The restoring force for Lamb waves is provided entirely by compressibility. For this external structure, (14.61) reduces to

$$\begin{aligned} \hat{c}^2 &= \gamma gH \\ &= c_s^2. \end{aligned} \tag{14.62.2}$$

Lamb waves propagate horizontally at the speed of sound. They bridge the acoustic and gravity manifolds in Fig. 14.9. Lamb waves are the normal modes of an unbounded, compressible, stratified atmosphere. Even though their energy decreases upward as an edge wave, Lamb waves amplify vertically. This feature makes them important in the upper atmosphere.

Because they are normal modes of the atmosphere, Lamb waves are excited preferentially by forcing that is indiscriminate over frequency. For example, an impulsive disturbance, such as a volcanic eruption, excites many wavenumbers and frequencies. The response spectrum to such forcing is unbounded at those wavenumbers and frequencies that satisfy (14.62.2). Removed from the source, it is therefore dominated by Lamb waves. Meteorological records include several impulsive disturbances to the atmosphere that were observed far from the source. Notable was the eruption of Krakatoa in 1883 (Chap. 9). Disturbances in surface pressure emanating from the eruption completed several circuits around the Earth before dissipating. Taylor (1929) used barometric records of the event to infer the vertical structure of atmospheric normal modes. By comparing arrival times at several stations, he showed that the compression wave emanating from Krakatoa propagated at the speed of sound. Then, with the aid of a system like (14.60), Taylor deduced the Lamb structure for atmospheric normal modes. A similar analysis was performed by Whipple (1930) for the impact of the great Siberian meteor in 1908. The Lamb vertical structure applies to atmospheric

normal modes at all frequencies. It applies even at very low frequency, where another form of wave motion is supported by the Earth's rotation (Dikii, 1968).

14.5 ROSSBY WAVES

At frequencies below 2Ω, another class of wave motion exists, one that is possible only in a rotating medium. It is named for C.G. Rossby, who established its connection to weather phenomena (Rossby et al., 1939). These waves are also referred to as *rotational waves* and, on the gravest dimensions, *planetary waves*. The restoring force for Rossby waves is provided by the variation with latitude of the Coriolis force. It links them to the Earth's rotation.

14.5.1 Barotropic nondivergent Rossby waves

The simplest model of Rossby waves relies on the solenoidal character of large-scale motion (Sec. 12.1). Under nondivergent conditions, atmospheric motion is governed by conservation of absolute vorticity (12.30). On a beta plane, the latter is expressed by

$$\frac{d\zeta}{dt} + \beta v = 0.$$

Linearizing about a basic state that is barotropically stratified and in uniform motion yields the perturbation vorticity equation

$$\frac{D\zeta'}{Dt} + \beta v' = 0. \tag{14.63}$$

As the motion is nondivergent, it can be represented in terms of a streamfunction

$$\boldsymbol{v}'_h = \boldsymbol{k} \times \nabla \psi'. \tag{14.64}$$

Then the perturbation vorticity equation becomes

$$\frac{D}{Dt}\nabla^2 \psi' + \beta \frac{\partial \psi'}{\partial x} = 0. \tag{14.65}$$

Equation (14.65) is just the linearized form of the barotropic nondivergent vorticity equation (12.31), in which the absolute vorticity of an air parcel is conserved. Known as the *Rossby wave equation*, it reflects a balance between changes in the relative vorticity of an air parcel and changes in its planetary vorticity due to meridional displacement. The interaction of those influences is illustrated by an eastward-moving parcel that is deflected equatorward (Fig. 14.16). The parcel then experiences reduced planetary vorticity ($\delta f < 0$). To conserve absolute vorticity, it must spin up cyclonically ($\delta\zeta > 0$). Northward motion is therefore induced ahead of the parcel. It deflects the parcel's trajectory poleward – back toward its undisturbed latitude ϕ_0. Upon overshooting ϕ_0, the parcel spins up anticyclonically. Southward motion ahead of the parcel then deflects its trajectory equatorward – again back toward its undisturbed latitude. The variation with latitude of f thus exerts a torque on displaced air. It is analogous to the positive restoring force of buoyancy under stable stratification. This reaction enables air to cycle back and forth about its undisturbed latitude.

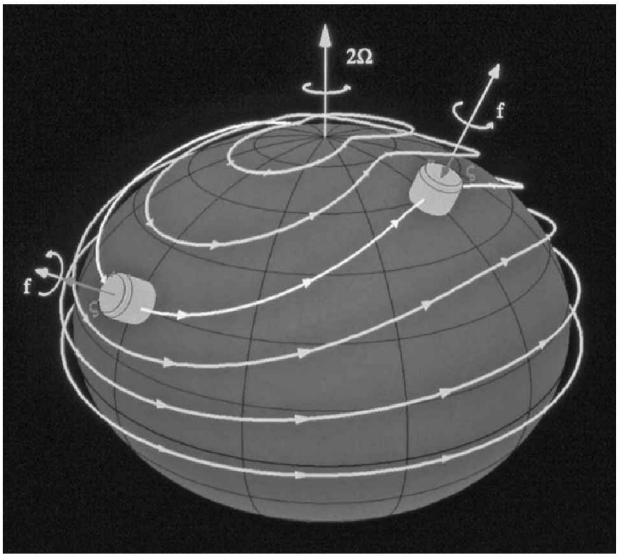

Figure 14.16 Schematic illustrating the reaction of an air parcel to meridional displacement. Displaced equatorward, an eastward-moving parcel spins up cyclonically to conserve absolute vorticity. Northward motion induced ahead of it then deflects the parcel's trajectory poleward, back toward its undisturbed latitude. The reverse process occurs when the parcel overshoots and is displaced poleward of its undisturbed latitude. See color plate section: Plate 10.

The coefficients of (14.65) are constant. Solutions may therefore be considered of the form $e^{i(kx+ly-\sigma t)}$. Substitution leads to the dispersion relation for Rossby waves

$$c_x - \overline{u} = -\frac{\beta}{k^2 + l^2}. \tag{14.66}$$

Relative to the mean motion, Rossby waves propagate only westward.[5]

The intrinsic trace speed: $c_x - \overline{u} = \frac{\omega}{k}$, is proportional to the local gradient of planetary vorticity, β (12.41). It is inversely proportional to the horizontal wavenumber squared. The latter dependence makes Rossby waves dispersive. The gravest dimensions propagate westward fastest. Consequently, small scales have slow phase speeds. In westerly flow, they are swept eastward. Such behavior is typical of synoptic disturbances to the jet stream (Fig. 1.9). On the other hand, stationary Rossby waves, which are forced orographically, have $c_x = 0$. The dispersion relation can be satisfied only if $\overline{u} > 0$. Thus, stationary Rossby waves propagate away from forcing only if the mean flow is westerly.

The intrinsic frequency $|\omega|$ of Rossby waves is proportional to β. It has a high-frequency cutoff: 2Ω. This limiting frequency is analogous to the high-frequency cutoff N for the vertical propagation of gravity waves (Sec. 14.3).

The solenoidal character of Rossby waves distinguishes them from gravity waves, which, in contrast, are nearly irrotational. Because Rossby waves are almost nondivergent, the Helmholtz theorem (12.4) implies that, to leading order, horizontal motion

[5] The direction of Rossby wave propagation can be deduced from the vorticity pattern in Fig. 14.16 and its influence on the material contour shown. Southward motion behind the cyclonic anomaly displaces that segment of the material contour equatorward, shifting the wave trough westward. Northward motion ahead of it has the same effect on the wave crest.

is characterized by the vorticity field. To the same degree of approximation, vertical motion can be ignored. Conversely, gravity waves are determined chiefly by vertical motion, which interacts with buoyancy. To leading order, they are characterized by the divergence field. Although the essential properties of Rossby waves follow from the rotational component of motion, divergence nevertheless enters by forcing absolute vorticity (12.36).

14.5.2 Rossby wave propagation in three dimensions

To describe 3-dimensional wave propagation, divergence must be accounted for. Within the framework of quasi-geostrophy, air motion is governed by conservation of quasi-geostrophic potential vorticity. Linearizing (12.49) about an isothermal basic state in uniform motion recovers the perturbation potential vorticity equation for wave motion on a beta plane

$$\frac{D}{Dt}\left[\nabla^2\psi' + \left(\frac{f_0^2}{N^2}\right)\frac{1}{\overline{\rho}}\frac{\partial}{\partial z}\left(\overline{\rho}\frac{\partial\psi'}{\partial z}\right)\right] + \beta\frac{\partial\psi'}{\partial x} = 0, \tag{14.67}$$

where z refers to log-pressure height and $\psi' = \frac{1}{f_0}\Phi'$ is the geostrophic streamfunction.

The coefficients are again constant. We therefore consider solutions of the form $e^{\frac{z}{2H}+i(kx+ly+mz-\sigma t)}$. Substitution into (14.67) recovers the dispersion relation for *quasi-geostrophic Rossby waves*

$$c_x - \overline{u} = -\frac{\beta}{k^2 + l^2 + \left(\frac{f_0^2}{N^2}\right)\left(m^2 + \frac{1}{4H^2}\right)}. \tag{14.68}$$

The denominator represents the effective total wavenumber squared. Equation (14.68) then has form analogous to (14.66), but modified by the stratification of mass. In the limit of strong stability ($\frac{N^2}{f_0^2} \to \infty$), (14.68) reduces to the dispersion relation for barotropic nondivergent Rossby waves. Much the same holds in the limit of long vertical wavelength ($m \to 0$).

Because their intrinsic phase speeds depend on wavenumber, Rossby waves are dispersive. Expressing (14.68) as

$$\omega = -\frac{\beta k}{k^2 + l^2 + \left(\frac{f_0^2}{N^2}\right)\left(m^2 + \frac{1}{4H^2}\right)} \tag{14.69}$$

leads to the components of group velocity

$$c_{gx} - \overline{u} = \beta\frac{k^2 - l^2 - \left(\frac{f_0^2}{N^2}\right)\left(m^2 + \frac{1}{4H^2}\right)}{\left[k^2 + l^2 + \left(\frac{f_0^2}{N^2}\right)\left(m^2 + \frac{1}{4H^2}\right)\right]^2} = \frac{\omega}{k}\left(1 + \frac{2\omega k}{\beta}\right) \tag{14.70.1}$$

$$c_{gy} = \frac{2\beta kl}{\left[k^2 + l^2 + \left(\frac{f_0^2}{N^2}\right)\left(m^2 + \frac{1}{4H^2}\right)\right]^2} = \frac{2l\omega^2}{\beta k} \tag{14.70.2}$$

$$c_{gz} = \frac{2\beta mk\left(\frac{f_0^2}{N^2}\right)}{\left[k^2 + l^2 + \left(\frac{f_0^2}{N^2}\right)\left(m^2 + \frac{1}{4H^2}\right)\right]^2} = \left(\frac{f_0^2}{N^2}\right)\frac{2m\omega^2}{\beta k}. \tag{14.70.3}$$

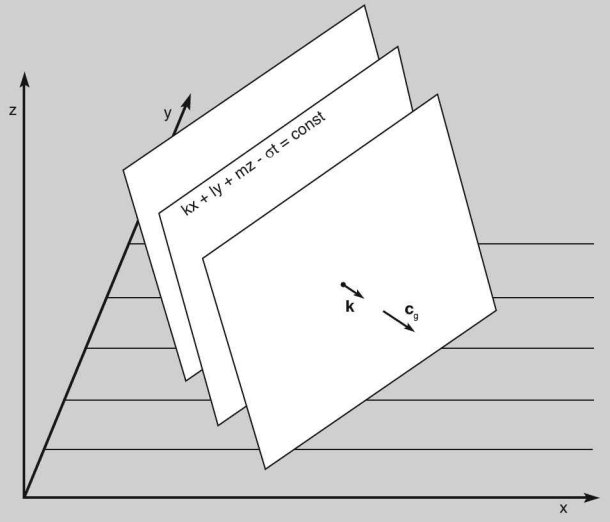

Figure 14.17 A stationary Rossby wave with group velocity that is upward and equatorward tilts westward in the same directions. Phase propagation relative to the medium is anti-parallel to ***k***.

Wave activity propagates in the positive y direction if $kl > 0$. It propagates in the positive z direction if $km > 0$. Because $\omega < 0$, the exponential form adopted for ψ' then implies phase propagation in the opposite directions. Thus, equatorward phase propagation corresponds to energy propagation that is poleward. Downward phase propagation corresponds to energy propagation that is upward. For stationary waves in the presence of westerly flow, these conditions translate into phase surfaces that tilt westward in the direction of energy propagation. Under the foregoing circumstances, phase surfaces tilt westward in the upward and equatorward directions (Fig. 14.17).

Unlike c_{gy} and c_{gz}, the sign of $c_{gx} - \overline{u}$ depends on the magnitude of k. For $k < \frac{\beta}{2|\omega|}$ (long zonal wavelength), group propagation relative to the medium is westward. However, for $k > \frac{\beta}{2|\omega|}$ (short zonal wavelength), intrinsic group propagation is eastward. Separating westward and eastward group propagation is the locus of wavenumbers for which $c_{gx} - \overline{u}$ vanishes

$$k^2 = l^2 + \left(\frac{f_0^2}{N^2}\right)\left(m^2 + \frac{1}{4H^2}\right). \tag{14.71}$$

These features of Rossby wave propagation can be inferred from the dispersion characteristics $\omega(k, l, m) = \text{const}$ (Fig. 14.18). Expressing (14.69) as

$$\left(k - \frac{\beta}{2|\omega|}\right)^2 + l^2 + \left(\frac{f_0^2}{N^2}\right) m^2 = \left(\frac{\beta}{2\omega}\right)^2 - \left(\frac{1}{2H}\right)^2 \tag{14.72}$$

shows that surfaces of constant ω are nested ellipsoids centered on the points $(k, l, m) = (\frac{\beta}{2|\omega|}, 0, 0)$. The intrinsic group velocity (14.23) is directed orthogonal to those surfaces, toward increasing ω. Thus, $\hat{\boldsymbol{c}}_g$ is upward for $m > 0$. It is equatorward

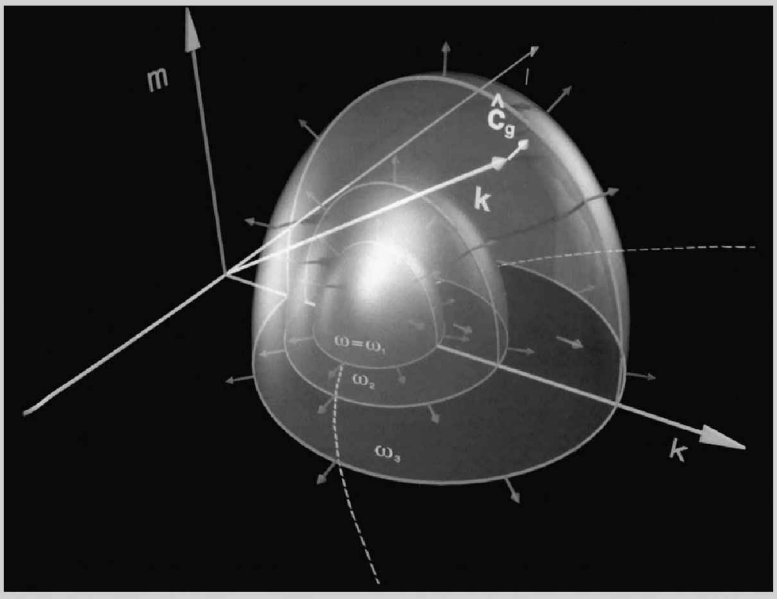

Figure 14.18 Intrinsic frequency for Rossby waves illustrated as a function of 3-dimensional wavenumber $\boldsymbol{k} = (k, l, m)$, with $\omega_3 > \omega_2 > \omega_1$. Group velocity relative to the medium is directed orthogonal to surfaces of intrinsic frequency toward increasing ω. For given l, zonal wavenumbers k greater than a critical value (dashed) have eastward $\hat{\boldsymbol{c}}_g$, whereas smaller k have westward $\hat{\boldsymbol{c}}_g$.

for $l < 0$. Each corresponds to phase propagation in the opposite direction. For k smaller than values defined by (14.71), indicated in Fig. 14.18 by the dashed curve, $\hat{\boldsymbol{c}}_g$ is westward. Larger k propagate eastward.

The dispersion relation may be rearranged for the vertical wavenumber

$$m^2 = \left(\frac{N^2}{f_0^2}\right)\left[\frac{\beta}{\overline{u} - c_x} - |\boldsymbol{k}_h|^2\right] - \frac{1}{4H^2}. \tag{14.73}$$

The gradient of planetary vorticity β provides the restoring force for horizontal displacements. It increases m^2 - analogous to the role played by N^2 for gravity waves (14.40). According to (14.73), Rossby waves propagate vertically only for a restricted range of zonal trace speed, specifically, for westward phase propagation relative to the mean flow ($c_x - \overline{u} < 0$). As for gravity waves, short horizontal wavelengths ($|\boldsymbol{k}_h|$ large) are less able to propagate upward than large horizontal wavelengths ($|\boldsymbol{k}_h|$ small).

For stationary waves ($c_x = 0$), (14.73) admits $m^2 > 0$ only for mean flow in the range

$$0 < \overline{u} < \frac{\beta}{|\boldsymbol{k}_h|^2 + \frac{f_0^2}{4N^2H^2}}. \tag{14.74}$$

If the mean flow is easterly, Rossby waves are external. The same holds if the mean flow is westerly and exceeds a cutoff speed given by the right-hand side of (14.74). The influence of Rossby waves is then exponentially small far above their forcing. Notice that the cutoff wind speed decreases with increasing $|\boldsymbol{k}_h|^2$. Therefore, even when zonal

wind is westerly, only the gravest horizontal wavelengths ($|\boldsymbol{k}_h|$ small) propagate vertically. Those wavelengths correspond to planetary waves (Fig. 1.10). Shorter wavelengths, characteristic of synoptic weather systems, have energy that is trapped near the surface.

These features of Rossby wave propagation were advanced by Charney and Drazin (1961) to explain observations from the International Geophysical Year (IGY), the first comprehensive campaign to observe the atmosphere. Collected during 1958, observations from the IGY revealed that the synoptic-scale disturbances which dominate the tropospheric circulation are conspicuously absent in the stratosphere (cf. Figs. 1.9, 1.10). In the summer stratosphere, eddies of all scales are absent. The time-mean circulation is then nearly circumpolar. The tropospheric circulation involves a spectrum of horizontal wavelengths. According to the preceding analysis, only planetary scale components of the wave spectrum can propagate into strong westerlies of the winter stratosphere (Fig. 1.8). Shorter components encounter turning levels not far above the tropopause (Fig. 14.14), below which they are trapped. During summer, stratospheric easterlies prevent all horizontal scales from propagating vertically. Rossby waves then encounter critical levels (Fig. 14.15), where $c_x = \overline{u}$ and wave activity is absorbed.

In the troposphere, kinetic energy is concentrated in synoptic-scale disturbances. Charney and Drazin argued that these features of Rossby wave propagation prevent kinetic energy from propagating to high levels. Were vertical propagation possible for energy-bearing eddies in the troposphere, the $e^{\frac{z}{2H}}$ amplification introduced by stratification would produce enormous temperatures at high altitude. The atmosphere would then possess a corona, similar to the sun. That, in turn, would result in the loss of nitrogen, oxygen, and, hence, of atmospheric mass (Figs. 1.5, 1.6).

Easterly flow in the tropical troposphere has a similar effect. It blocks horizontal wave propagation between the Northern and Southern Hemispheres. Large orographic features, such as the Alps and Himalayas, excite amplified planetary waves in the Northern Hemisphere. Owing to easterlies in the tropics, those planetary waves exert little influence on the circulation of the Southern Hemisphere, where orographic forcing of planetary waves is comparatively weak. These inter-hemispheric differences yield a broken storm track in the Northern Hemisphere, where amplified wave motions reinforce and weaken the storm track. However, they leave the storm track of the Southern Hemisphere comparatively undisturbed and hence zonally uniform (see Fig. 15.10).

14.5.3 Planetary wave propagation in sheared mean flow

Westerly mean flow during winter enables planetary-scale Rossby waves to radiate into the stratosphere. Due to stratification of mass, those waves amplify vertically. Where planetary wave activity propagates and is absorbed can be understood from a ray tracing analysis.

Consider zonal-mean flow that varies with latitude and height $\overline{u} = \overline{u}(y, z)$. Linearizing the quasi-geostrophic potential vorticity equation (12.49), with $-\frac{\partial \overline{\psi}}{\partial y} = \overline{u}$, yields the perturbation potential vorticity equation

$$\frac{D}{Dt}\left[\nabla^2\psi' + \frac{1}{\overline{\rho}}\frac{\partial}{\partial z}\left(\frac{f_0^2}{N^2}\overline{\rho}\frac{\partial \psi'}{\partial z}\right)\right] + \beta_e \frac{\partial \psi'}{\partial x} = 0, \tag{14.75.1}$$

where

$$\begin{aligned}\beta_e &= \beta - \overline{u}_{yy} - \frac{1}{\overline{\rho}}\frac{\partial}{\partial z}\left(\frac{f_0^2}{N^2}\overline{\rho}\frac{\partial \overline{u}}{\partial z}\right) \\ &= \frac{\partial \overline{Q}}{\partial y},\end{aligned} \tag{14.75.2}$$

referred to as *beta effective*, represents the meridional gradient of zonal-mean vorticity. According to (14.75), positive curvature of $\overline{u}$ reduces β_e. It therefore weakens the restoring force introduced by meridional displacements of air. Conversely, negative curvature of $\overline{u}$ increases β_e. This dependence on mean shear is analogous to that of gravity wave propagation (14.40).

Considering solutions of the form $e^{\frac{z}{2H}+i(kx-\sigma t)}$ transforms (14.75) into a Helmholtz equation

$$\frac{\partial^2 \Psi_k^\sigma}{\partial y^2} + \frac{\partial}{\partial z}\left(\frac{f_0^2}{N^2}\frac{\partial \Psi_k^\sigma}{\partial z}\right) + \nu^2(y,z)\Psi_k^\sigma = 0, \tag{14.76.1}$$

where

$$\nu^2(y,z) = \frac{\beta_e}{\overline{u} - c_x} - k^2 - \frac{f_0^2}{4N^2H^2} \tag{14.76.2}$$

represents a 2-dimensional index of refraction that describes propagation in the $y-z$ plane. In regions where $\nu^2(y,z) > 0$, solutions oscillate. In regions where $\nu^2(y,z) \leq 0$, they are evanescent. Therefore, propagation is excluded from regions where β_e is sufficiently small or where $\overline{u}$ is sufficiently strong. Should $\overline{u}(y,z) \to c_x$, ν^2 is unbounded. Equation (14.76) is then singular. The critical region defined by this condition differs from that of gravity waves, for which ν^2 is unbounded to either side of the critical line (cf. Fig. 14.15b). For Rossby waves, $\nu^2 \to +\infty$ on one side of the critical line, but $-\infty$ on the opposite side. Wave structure therefore oscillates rapidly on one side of the critical line but is sharply evanescent on the other.

Analytical solutions to (14.76) exist only under idealized circumstances. However, within the framework of the WKB approximation, wave propagation can be described in terms of monochromatic behavior along rays. The dispersion relation then assumes the same form as (14.69), but with β_e in place of β. Under these circumstances, propagation in the $y-z$ plane is controlled by

$$l^2 + \left(\frac{f_0^2}{N^2}\right)m^2 = \frac{\beta_e}{\overline{u} - c_x} - k^2 - \frac{f_0^2}{4N^2H^2}, \tag{14.77}$$

which is analogous to (14.40.2) for gravity waves. Figure 14.19 shows, for two stationary wave components, rays that are introduced into mean zonal flow that is representative of the wintertime troposphere and stratosphere. For component 1, planetary wave activity radiates upward and poleward into strengthening westerlies of the polar-night jet. It eventually encounters a turning line, where $l^2 + m^2$ vanishes and wave activity is reflected.

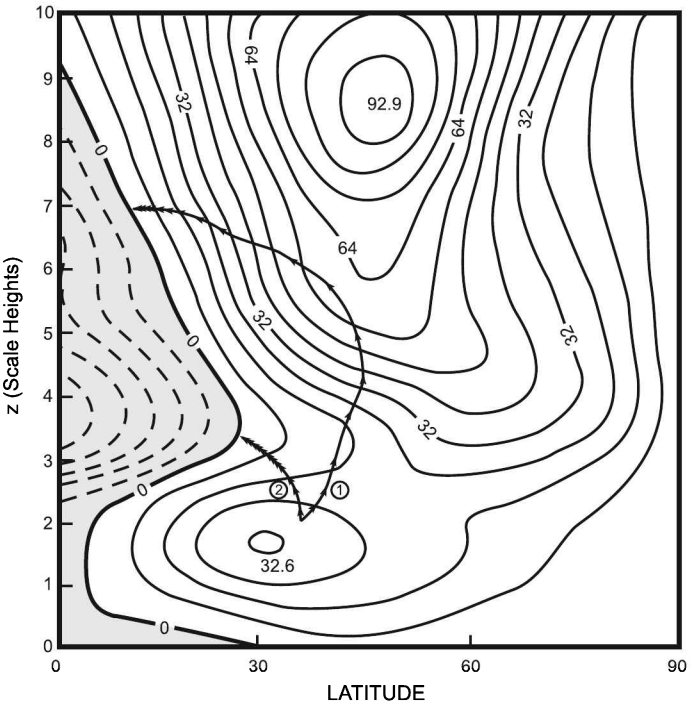

Figure 14.19 Rays of two stationary planetary wave components introduced into the lower stratosphere in zonal-mean winds (contoured in m s^{-1}) representative of northern winter on a mid-latitude beta plane. The ray for component 1, which initially propagates upward and poleward, encounters a turning line in strong westerlies of the polar-night jet, where wave activity is refracted equatorward. As the ray approaches easterlies, it next encounters a critical line ($\overline{u} = 0$), where c_g vanishes. Propagation then stalls, leaving wave activity to be absorbed, so the ray terminates. The ray for component 2 is initially directed upward and equatorward, so wave activity encounters the critical line and is absorbed even sooner. Thus wave activity introduced between tropical easterlies and strong polar westerlies can propagate vertically only a limited distance before being absorbed. Arrow heads mark uniform increments of time moving along a ray at the group velocity c_g.

Wave activity is then refracted equatorward, toward easterlies. The ray eventually encounters a critical line, where ω and the group velocity vanish. There, the ray stalls and terminates. Analysis similar to that in Sec. 14.3.4 for gravity waves shows that, ahead of the critical line, planetary wave activity is frozen in the medium. It is therefore absorbed. For component 2, planetary wave activity radiates initially upward and equatorward, toward easterlies. It encounters a critical line even sooner, so it too is absorbed. Dickinson (1968) used the foregoing analysis to explain the observed amplitudes of planetary waves. They are weaker than predicted by Charney and Drazin's (1961) 1-dimensional analysis, in which the longest horizontal wavelengths amplify vertically with little attenuation. The preceding analysis shows that planetary wave activity can propagate upward only a limited distance before it is refracted or reflected into easterlies, where it encounters a critical line and suffers strong absorption.

Horizontal wave propagation can be diagnosed in similar fashion. Figure 14.20a plots the anomalous planetary wave pattern observed in the troposphere during disturbed northern winters of El Nino. A series of positive and negative height anomalies marks a planetary wavetrain. Symbolic of wave activity along a ray, it radiates poleward from anomalous heating in the equatorial Pacific (stipled), where convection is amplified during El Nino. Along the wavetrain, β_e decreases poleward. At sufficiently high latitude, ν^2 has decreased to zero, representing a turning latitude. There, wave activity is reflected equatorward, influencing North America. According to (14.76), turning latitudes are encountered sooner by large k than small k. Hence, the gravest scales, those of planetary dimension, propagate poleward farthest. The resulting wavetrain is called a *teleconnection pattern*. It describes the influence of one region (e.g., the equatorial Pacific) on other regions.

The prominent ridge over western Canada and trough over the eastern United States characterize the so-called Pacific North America (PNA) pattern. The PNA pattern is observed in northern winters during El Nino, when convection and latent heating are amplified in the equatorial central Pacific. The anomalies in Fig. 14.20a disturb the extratropical planetary wave field, manifest in undulations of the jet stream (dashed). They upset the storm track and hence the development and propagation of synoptic weather systems.

Similar behavior is recovered in calculations in which anomalous convective heating is imposed in the equatorial central Pacific (Fig. 14.20b). As in observed structure, planetary wave activity propagates chiefly into the winter hemisphere. Propagation into the summer hemisphere is comparatively weak, blocked by easterlies in the summer subtropics that pose a critical line to planetary waves of low frequency. Such calculations capture the salient features of observed structure. However, there is considerable variance among them, as there is in observed structure; see Nigam (2003) for a review. These discrepancies reflect the involvement of many wavenumbers and frequencies, which are excited by unsteady convection. Those wave components disperse along different rays; Hoskins and Karoly (1981) present a ray-tracing analysis of stationary components. They also make the radiated response transient and sensitive to the distribution of zonal-mean wind (Jin and Hoskins, 1995; Branstator, 2002). The transient response is especially sensitive to tropical easterlies. The latter discriminate the wave response to westward components that propagate faster than easterlies neighboring the wave source (Garcia and Salby, 1987).

14.5.4 Transmission of planetary wave activity

Owing to the rotational nature of Rossby waves, the property propagated by them is related closely to vorticity. Under conservative conditions, the perturbation vorticity equation (14.75) may be written

$$\frac{DQ'}{Dt} + \frac{\partial \overline{Q}}{\partial y} v' = 0, \tag{14.78.1}$$

where

$$Q' = \nabla^2 \psi' + \left(\frac{f_0^2}{N^2} \right) \frac{1}{\overline{\rho}} \frac{\partial}{\partial z} \left(\overline{\rho} \frac{\partial \psi'}{\partial z} \right). \tag{14.78.2}$$

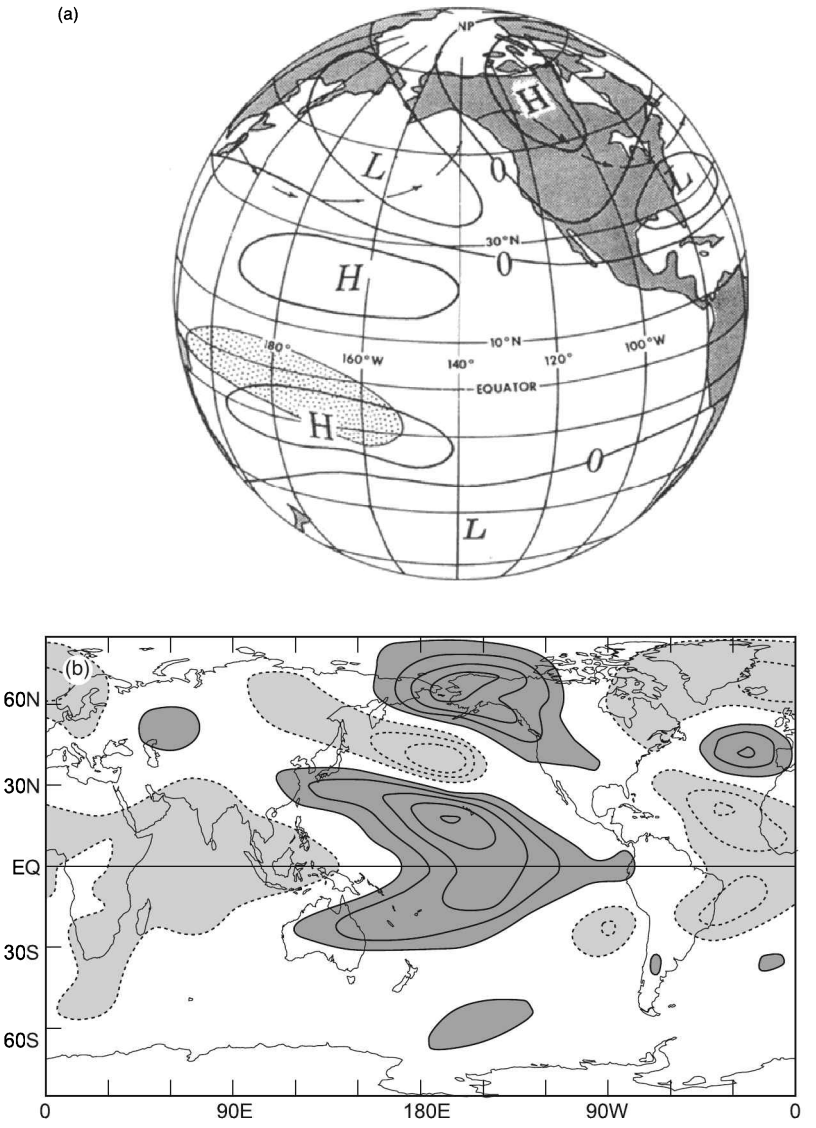

Figure 14.20 (a) Anomalous planetary wave field for northern winters during El Nino, when anomalous convection (stippled) is positioned in the tropical central Pacific. The anomalous ridge over western Canada and trough over the eastern United States characterize the so-called *Pacific North America (PNA) pattern* that upsets the normal track of the jet stream (wavy trajectory) and cyclone activity during El Nino winters. After Horel and Wallace (1981). (b) Anomalous height in the upper troposphere introduced by anomalous latent heating in the equatorial central Pacific. After de Weaver and Nigam (2004).

Multiplying by Q' and averaging zonally gives

$$\frac{\partial}{\partial t}\left(\frac{\overline{Q'^2}}{2}\right)+\frac{\partial \overline{Q}}{\partial y}\overline{v'Q'}=0. \tag{14.79.1}$$

Incorporating (14.78.2) and (12.2.2) and integrating by parts, with field variables cyclic in x, then yields

$$\frac{\partial}{\partial t}\left(\frac{\overline{\rho}}{\frac{\partial \overline{Q}}{\partial y}}\frac{\overline{Q'^2}}{2}\right)-\frac{\partial}{\partial y}\left(\overline{\frac{\partial \psi'}{\partial x}\frac{\partial \psi'}{\partial y}}\right)+\left(\frac{f_0^2}{N^2}\right)\frac{1}{\overline{\rho}}\frac{\partial}{\partial z}\left(\overline{\rho}\,\overline{\frac{\partial \psi'}{\partial x}\frac{\partial \psi'}{\partial z}}\right)=0. \tag{14.79.2}$$

With the hydrostatic relation (11.67), (14.79.2) may be cast into the canonical form

$$\frac{\partial A}{\partial t}+\nabla\cdot\boldsymbol{F}=0, \tag{14.80.1}$$

where

$$A=\frac{\overline{\rho}}{\frac{\partial \overline{Q}}{\partial y}}\left(\frac{\overline{Q'^2}}{2}\right) \tag{14.80.2}$$

and

$$F_y=-\overline{\rho}\cdot\overline{u'v'} \tag{14.80.2}$$

$$F_z=\frac{f_0 R}{N^2 H}\overline{\rho}\cdot\overline{v'T'}. \tag{14.80.3}$$

Equation (14.80.1) has the form of a conservation relation. A represents the density of wave activity associated with Rossby waves. Proportional to the *potential enstrophy* $\frac{\overline{Q'^2}}{2}$, A is an analogue of wave action for gravity waves (Lighthill, 1978). The vector field $\boldsymbol{F}$ is the *Eliassen-Palm* (*EP*) *flux*. It represents the flux of wave activity. EP flux is therefore related to group velocity as

$$\boldsymbol{F}=\boldsymbol{c}_g A. \tag{14.81}$$

$\boldsymbol{F}$ is everywhere tangential to rays. Under conservative conditions, the property A is propagated along rays without loss. The divergence of EP flux is, from (14.79.1) and (14.80.1), seen to equal the northward flux of potential vorticity

$$\nabla\cdot\boldsymbol{F}=\overline{v'Q'}. \tag{14.82}$$

As Q is a conserved property, its northward flux describes meridional transport in general, namely, of all conserved properties. $\nabla\cdot\boldsymbol{F}$ is thus a direct measure of meridional transport by Rossby waves.

According to (14.80), $\boldsymbol{F}$ also represents the flux of westward momentum, the property transmitted by Rossby waves. $\nabla\cdot\boldsymbol{F}$ therefore equals the convergence of momentum flux. Describing wave absoption, it will be seen in Chap. 18 to represent the effective wave forcing of zonal-mean momentum. The basic state (e.g., $\overline{u}$ and $\overline{T}$) is, in general, influenced by wave activity through the convergence of wave momentum flux and of wave heat flux, as illustrated by (14.5). Equations (14.80) show that, for Rossby waves, those fluxes do not operate independently. The upward flux of westward momentum, F_z is determined by the northward flux of heat $\overline{v'T'}$. Together with (14.82), equations (14.80) show further that, if the wave field is conservative

and steady,

$$\nabla \cdot \boldsymbol{F} = \overline{v'Q'} = 0. \tag{14.83}$$

The convergence of EP flux then vanishes, as does the northward flux of potential vorticity. The waves then exert no net influence on the mean state. Under these conditions, meridional transport likewise vanishes. Rossby waves therefore influence the mean state and induce meridional transport only through nonvanishing $\nabla \cdot \boldsymbol{F}$. Associated with absorption or emission of wave activity, $\nabla \cdot \boldsymbol{F}$ is introduced by dissipation and transience.

14.6 WAVE ABSORPTION

In the absence of dissipation, wave activity is conserved following a wavepacket (e.g., moving along a ray with the velocity $\boldsymbol{c}_g$).[6] When dissipation is present, this is no longer true. Wave activity is then absorbed from individual wavepackets. Deposited in the mean flow, it forces $\overline{u}$ through the convergence of momentum flux (14.5). To illustrate how absorption alters the wave field, we consider the propagation of planetary waves in the presence of radiative damping.

Planetary waves have vertical wavelengths much longer than a scale height. Radiative transfer then reduces to LW cooling to space (Sec. 8.6). For small departures from the equilibrium temperature, such radiative transfer is approximated by Newtonian cooling (8.79). The linearized form of the thermodynamic equation (12.46) then becomes

$$\frac{D}{Dt}\left(\frac{\partial \Phi'}{\partial z}\right) + N^2 w' = -\alpha\left(\frac{\partial \Phi'}{\partial z}\right), \tag{14.84.1}$$

where the Newtonian cooling rate α describes the damping of temperature perturbations (units of inverse time). Rearranging terms casts (14.84.1) into the form

$$\left(\frac{D}{Dt} + \alpha\right)\frac{\partial \psi'}{\partial z} + \frac{N^2}{f_0} w' = 0. \tag{14.84.2}$$

Equation (14.84.2) can be used to eliminate w' in the linearized vorticity equation (12.47),

$$\left[\frac{d(\zeta + f)}{dt}\right]' = f_0 \frac{1}{\overline{\rho}} \frac{\partial}{\partial z}\left(\overline{\rho} w'\right), \tag{14.85}$$

where the left-hand side accounts for shear in the mean flow $\overline{u} = \overline{u}(y, z)$. The perturbation vorticity equation then becomes

$$\frac{D}{Dt}\left[\nabla^2 \psi' + \frac{1}{\overline{\rho}} \frac{\partial}{\partial z}\left(\frac{f_0^2}{N^2} \overline{\rho} \frac{\partial \psi'}{\partial z}\right)\right] + \alpha \frac{1}{\overline{\rho}} \frac{\partial}{\partial z}\left(\frac{f_0^2}{N^2} \overline{\rho} \frac{\partial \psi'}{\partial z}\right) + \beta_e \frac{\partial \psi'}{\partial x} = 0. \tag{14.86}$$

Equation (14.86) is a generalization of (14.75) that accounts for thermal dissipation.

Within the framework of the WKB approximation, solutions are considered of the form $e^{\frac{z}{2H} + i(kx + ly + mz - \sigma t)}$. This transforms (14.86) into the dispersion relation

$$\left[1 + i\left(\frac{\alpha}{\omega}\right)\right] m^2 = m_0^2, \tag{14.87.1}$$

[6] Amplitude, however, varies along a ray (14.41); see Lighthill (1978).

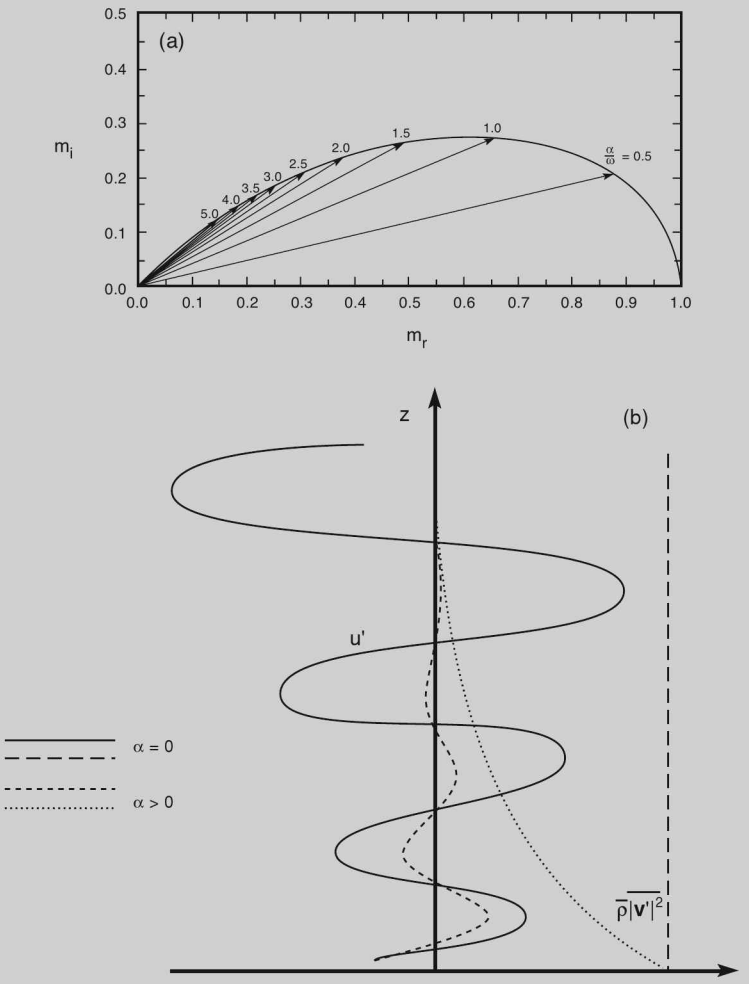

Figure 14.21 (a) Polar representation of complex vertical wavenumber for Rossby waves in the presence of Newtonian cooling with coefficient α. (b) Vertical structure and kinetic energy density of an individual wave component for $\alpha = 0$ (solid/dashed) and $\alpha > 0$ (short dashed/dotted).

where

$$m_0^2 = \left(\frac{N^2}{f_0^2}\right)\left[\frac{\beta_e}{\overline{u} - c_x} - |\boldsymbol{k}_h|^2\right] - \frac{1}{4H^2} \tag{14.87.2}$$

satisfies the dispersion relation in the absence of damping (14.77). Solving for the vertical wavenumber gives

$$m = m_r + im_i = \frac{e^{i\frac{\phi}{2}}}{\left[1 + \left(\frac{\alpha^2}{\omega^2}\right)\right]^{\frac{1}{2}}} m_0, \tag{14.88.1}$$

where (because $\omega < 0$)

$$\phi = tan^{-1}\left(\frac{\alpha}{|\omega|}\right). \tag{14.88.2}$$

Figure 14.21a plots m in the complex plane, as a function of cooling rate and intrinsic frequency. An individual wave component has vertical structure

$$e^{\left(\frac{1}{2H}+im\right)z} = e^{\left(\frac{1}{2H}-m_i\right)z} \cdot e^{im_r z}.$$

Because $m_0 > 0$ for downward phase propagation, (14.88) implies $m_i > 0$. Hence, thermal damping introduces an imaginary component to m that makes wave energy decay upward. It offsets the vertical amplification of wave activity that is introduced by stratification of mass (Fig. 14.21b). According to (14.88), m_i follows from the ratio of time scales for wave oscillation and damping. Under weakly damped conditions, it increases with increasing $\left(\frac{\alpha}{\omega}\right) m_0$. Wave amplitude then grows with height, but slower than under adiabatic conditions. Kinetic energy density (e.g., $\overline{\rho}|\boldsymbol{v}_h'|^2$) therefore decreases upward, as progressively more wave activity is absorbed. For $\left(\frac{\alpha}{\omega}\right) m_0$ sufficiently large, even wave amplitude decreases with height. Components with small intrinsic frequency or short vertical wavelength (large m_0) therefore decay vertically above their forcing.

In practice, thermal dissipation is introduced whenever the circulation is driven out of radiative equilibrium. Wave motions do this naturally by displacing air from one radiative environment to another. In the stratosphere, the polar-night vortex is displaced out of radiative equilibrium by planetary waves. They drive air across latitude circles (cf. Fig. 1.10). Longwave cooling to space then acts on individual air parcels in proportion to their departure from local radiative equilibrium. It destroys anomalous temperature and, with it, the accompanying motion. Air that is displaced into polar darkness, where the radiative-equilibrium temperature is very cold, finds itself anomalously warm. It therefore cools through LW emission to space (Fig. 8.27). In the summer stratosphere, the vortex remains relatively undisturbed – because planetary wave propagation from below is blocked (Sec. 14.5). The summertime circulation therefore remains close to radiative equilibrium.

Newtonian cooling is proportional to temperature and hence to the vertical derivative of ψ'. Short vertical wavelengths are therefore damped faster than long vertical wavelengths. For vertical wavelengths comparable to H, the cool-to-space approximation breaks down. As shown in Fig. 8.29, LW exchange between neighboring layers then makes α itself strongly scale dependent. The cooling rate is much faster for short vertical wavelengths than for long vertical wavelengths.

Absorption can change along a ray because α varies spatially. According to Fig. 8.29, the time scale for thermal damping decreases from several weeks in the troposphere to only a couple of days in the upper stratosphere. Of greater significance is vertical shear, which can sharply reduce ω. If the intrinsic frequency is Doppler-shifted to zero, $\left(\frac{\alpha}{\omega}\right) m_0 \to \infty$. This is precisely what occurs near a critical line. There, oscillations become stationary relative to the medium, allowing wave activity to be fully absorbed.

14.7 NONLINEAR CONSIDERATIONS

Under inviscid adiabatic conditions, the equations governing wave propagation become singular at a critical line, where the mean velocity matches the trace speed:

$\overline{u} = c_x$. For stationary waves, this condition is achieved at the zero wind line ($\overline{u} = 0$). Dissipation removes the singularity by absorbing wave activity as the local wavelength shrinks and $\boldsymbol{c}_g$ approaches zero. Strong gradients of the wave field near its critical line then magnify thermal damping. They also magnify diffusion. By smoothing out gradients, both act to destroy organized wave motion.

These conclusions follow from considerations of the first-order equations, in which only simple forms of dissipation are represented. More generally, however, singular behavior near a critical line invalidates those equations. In the limit of small dissipation, wave stress exerted on the mean flow (14.5) becomes concentrated at the critical line and unbounded (Dickinson, 1970). Even with plausible dissipation, the convergence of momentum flux there implies large accelerations of $\overline{u}$ locally. Consequently, $\overline{u}$ cannot remain steady. Such behavior represents nonlinear interaction between wave activity and the mean flow. The same circumstances magnify nonlinear interaction between components of the wave spectrum.

Recall that the governing equations may be linearized so long as second-order terms such as $\boldsymbol{v}' \cdot \nabla \boldsymbol{v}'$ are much smaller than those first order in wave amplitude. For an individual wave component, the material derivative is

$$\begin{aligned} \frac{d}{dt} &= \frac{D}{Dt} + \boldsymbol{v}' \cdot \nabla \\ &= -i\omega + i\boldsymbol{v}' \cdot \boldsymbol{k} \\ &= -ik\left[(c_x - \overline{u}) - \boldsymbol{v}' \cdot \frac{\boldsymbol{k}}{k} \right]. \end{aligned} \tag{14.89}$$

Ignoring second order behavior is therefore tantamount to requiring the intrinsic trace speed $|c_x - \overline{u}|$ to be large compared with the eddy velocity $|\boldsymbol{v}'|$ that is induced by the wave. Near a critical line, this requirement breaks down because $|c_x - \overline{u}| \to 0$. Instead of experiencing a small oscillation during the passage of wave activity, an individual parcel then undergoes finite displacement. The latter can lead to a permanent rearrangement of air.[7]

Attention was first drawn to this issue by Kelvin (1880). He noted the peculiar behavior in Fig. 14.22a at the critical level of a gravity wave, under incompressible conditions and neutral stratification. For $N^2 = 0$, (14.40) implies a total streamfunction relative to the medium which is symmetric about $z = z_c$ and which contains closed streamlines within a neighborhood of the critical level.[8] Known as *Kelvin's cat's eye pattern*, this distribution of ψ describes a series of vortices. They overturn air inside the critical region, which is eventually wound up (Fig. 14.22d). Gradients that support organized wave motion are then sheared down to small scales, where diffusion destroys them efficiently (Fig. 12.4). The evolution culminates in the absorption of wave activity that is incident on the critical level.

In the limit of weak dissipation, another scenario is possible. It operates even under stable stratification, as supports gravity wave propagation. Mixing, implied by the motion in Fig. 14.22, will homogenize the distribution of potential temperature, driving $\frac{\partial \theta}{\partial z}$ and N^2 to zero (Sec. 7.6). Under the same conditions, vorticity u_z is also

[7] Dissipation keeps displacements bounded by introducing an imaginary component to $c_x - \overline{u}$.
[8] Rossby waves behave similarly, but with β_e in place of $-\overline{u}_{zz}$.

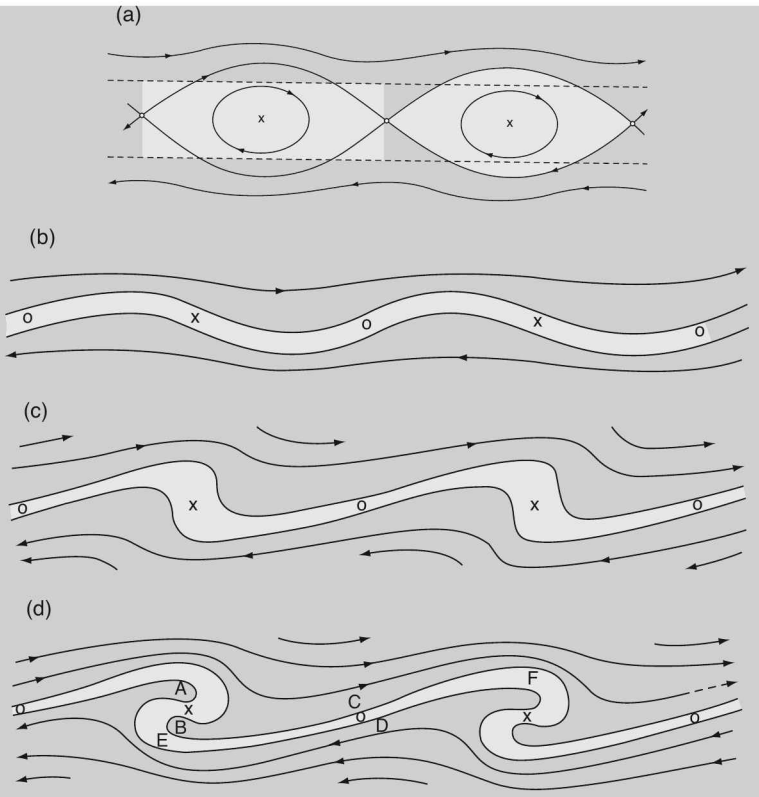

Figure 14.22 (a) Streamfunction at the critical level of a simple gravity wave under neutral stratification, which assumes the form of *Kelvin's cat's eye pattern*. (b) Evolution of a material contour initialized at the critical level. Adapted from Scorer (1978).

conserved. $\overline{u}_{zz}$ will thus likewise be driven to zero. Mixing thus culminates in the refractive index m^2 vanishing in some neighborhood of $z = z_c$ (14.40.2). Wave activity incident on the critical level is then not absorbed, but reflected.

Rossby waves produce such behavior through horizontal advection. Figure 14.23 shows planetary wave activity incident on a critical line at low latitude. Under weakly dissipative conditions (Fig. 14.23a), nonlinear advection near the critical line overturns material contours. The latter coincide with contours of potential vorticity Q, which is approximately conserved under these conditions. Air inside the critical region is rolled up in a series of vortices. They destroy organized wave motion on large scales by shearing it down to small scales, where diffusion is effective. Efficient horizontal mixing homogenizes Q near the critical line. It thus drives the refractive index there to zero (14.76). Wave activity is subsequently reflected from the critical line. This limiting behavior is implied by the weak phase tilt with latitude (dashed). The time required to establish this limiting behavior is relevant. If it is longer than the time scale for seasonal transience of $\overline{u}$ (e.g., in the stratosphere, where $\overline{u}$ reverses between winter and summer), reflection may never be achieved (Geisler and Dickinson, 1974).

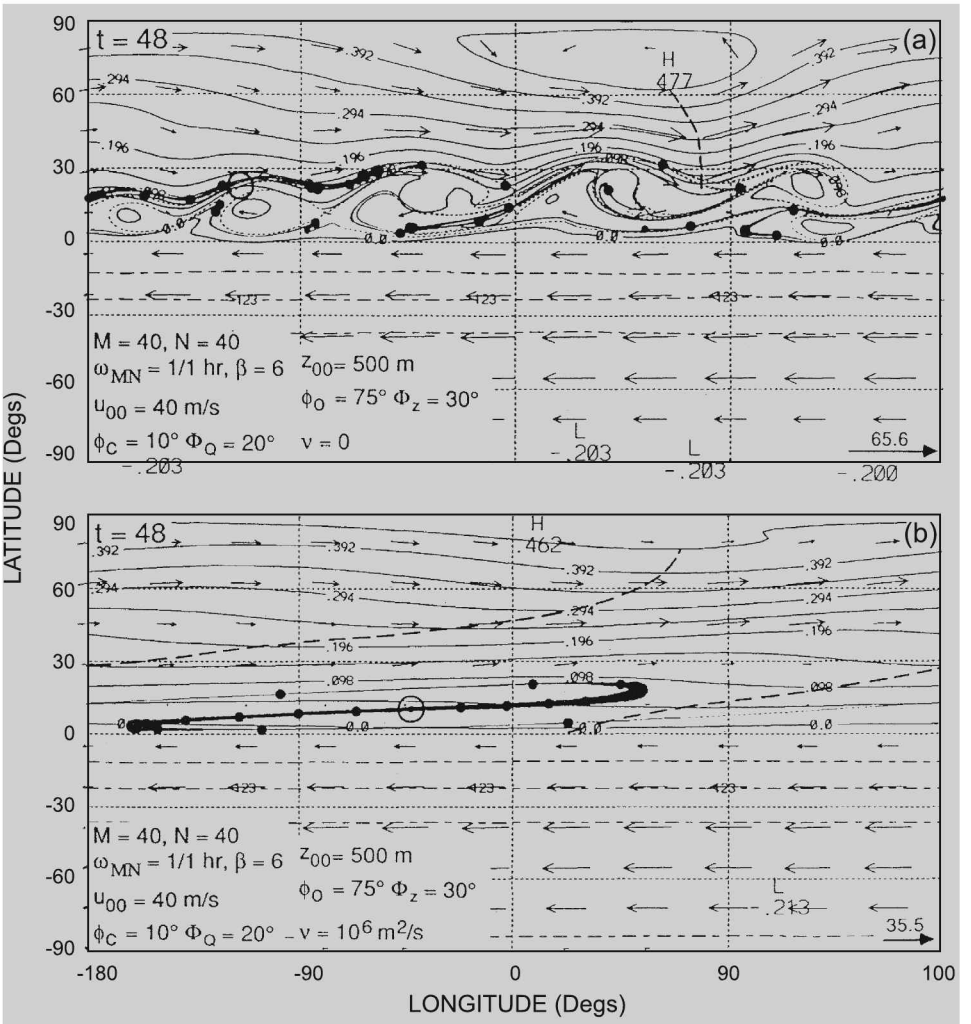

Figure 14.23 Nonlinear evolution of a planetary wave critical layer under barotropic conditions and with zonal wavenumber 1 incident on it, illustrated in terms of potential vorticity (contoured) and the position and thickness of a material contour (bold/broken curve and dots) that was initialized at the critical latitude. (a) In the presence of weak dissipation, potential vorticity is rolled into a series of vortices that mix air inside the critical layer, driving $\beta_e = \frac{\partial \overline{Q}}{\partial y}$ to zero. Wave activity is then reflected from the critical region, as manifested by the absence of phase tilt (dashed). (b) In the presence of strong dissipation, diffusion prevents the formation of sharp gradients that support vortex roll up, so $\frac{\partial \overline{Q}}{\partial y} > 0$ is maintained. The incident planetary wave then continues to propagate equatorward and be absorbed, as is manifested by its systematic meridional tilt. After Salby et al. (1990).

Under strongly dissipative conditions (Fig. 14.23b), the wave field evolves very differently. Diffusion then prevents the formation of sharp gradients that promote vortex roll-up. Wave activity therefore continues to propagate equatorward and be absorbed at the critical line. This limiting behavior is evident from the steep westward tilt of phase with decreasing latitude. It contrasts sharply with the limiting structure under weakly dissipative conditions (Fig. 14.23a), which exhibits little phase tilt.

Nonlinearity is also introduced by large wave amplitude. It likewise makes $|\boldsymbol{v}'| = O(|c_x - \overline{u}|)$. Figure 14.24 displays an amplified mountain wave over the Colorado Rockies, which was observed during an intense wind storm. Air moves along isentropic surfaces (solid), undergoing large vertical displacements. In the lee of the continental divide, it descends almost 5 km. The steep slope of isentropic surfaces reduces $\frac{\partial\theta}{\partial z}$ and static stability locally. In addition, the large amplitude exaggerates vertical shear. Both effects destabilize the organized motion, through the gradient Richardson number and mechanisms discussed in Sec. 13.3. Richardson numbers less than $\frac{1}{4}$ then produce intense turbulence. The latter damps the wave by cascading energy to small scales, where it is dissipated efficiently. Advected downstream, turbulence can be violent. It is visible only in the isolated rotor cloud at 600 hPa (Fig. 9.22). During the event shown, a Boeing 707 was on approach to Denver airport. It experienced impulsive accelerations in excess of 3 g's. Similar conditions were encountered during the 1950s in the Sierra Wave Project. The jet stream was then observed by instrumented sailplanes. The following excerpt from a chronicle of the project (Lincoln, 1972) describes an episode familiar to aviators:

> Editor's Note: On the day described, Larry Edgar was flying a Pratt-Read, one of the strongest sailplanes ever built, and he had the ultimate experience of flying turbulence in the rotor. This story has probably saved the lives of a number of aviators who have learned the indicated lesson and treat rotor clouds with respect.
>
> "Lloyd Licher and I examined the wreckage and compared notes with others. The nose pulled off just at the seats, by what seemed to be a tension failure of the steel tubing. Considering Larry's weight and the instrumentation, this should have required just in excess of 16 g's.... The wreckage showed the left wing to have broken at altitude. It broke downward near the root. The tail boom was broken cleanly from the fuselage pod, at altitude, and appears to have come off upward. The various control cables going from nose to tail were pulled apart completely – in a bunch. The force needed to do this should be far over 10,000 pounds."
>
> Joachim P. Kuettner

(The pilot survived.)

Large amplitude results naturally from vertical propagation. Upon reaching sufficient height, a gravity wave will have achieved a perturbation potential temperature θ' that is large enough to cancel the mean vertical gradient of potential temperature $\frac{\partial\overline{\theta}}{\partial z}$, which underpins vertical stability. At that level, the vertical gradient of total potential temperature is driven to zero

$$\frac{\partial\theta}{\partial z} = \frac{\partial\overline{\theta}}{\partial z} + \frac{\partial\theta'}{\partial z} = 0. \tag{14.90}$$

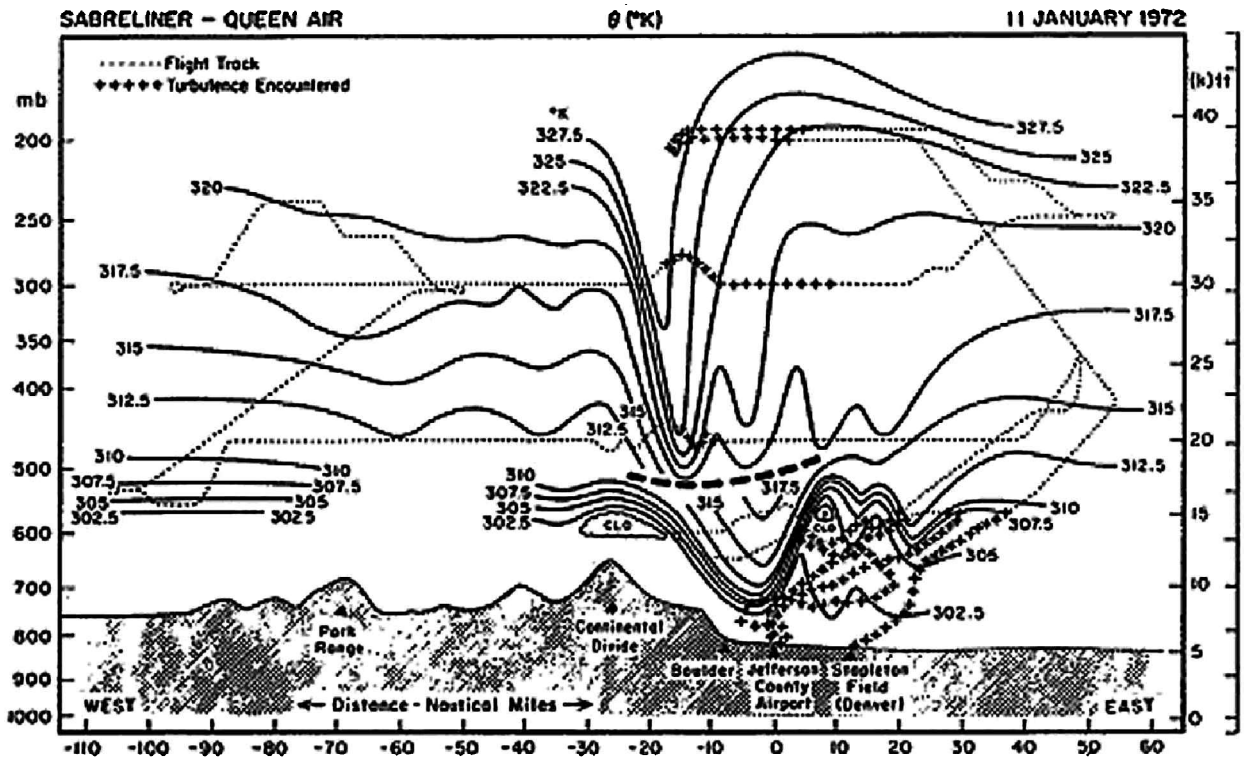

Figure 14.24 Cross section of isentropic surfaces in the mountain wave during a major wind storm over the Colorado Rockies. Severe turbulence (+) is found at elevations of the mountain cap cloud and below, as well as near the tropopause. It is visible, however, only in the isolated rotor cloud near 600 hPa. After Lilly (1978).

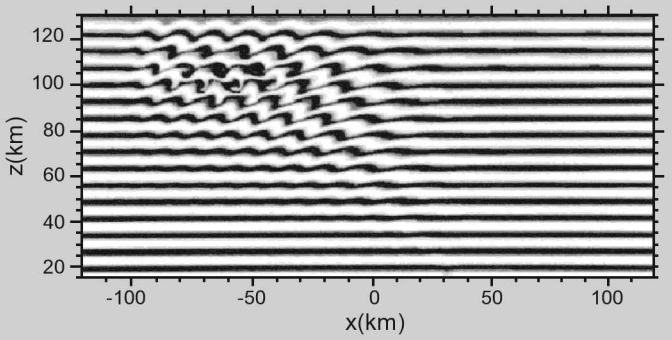

Figure 14.25 Potential temperature distribution in the presence of gravity waves that are excited in the troposphere by a moving bump analogous to a squall line. Positioned near $x = 30$ km, the disturbance is 10 km wide and migrates eastward. Gravity waves amplify with height sufficiently to break in the mesosphere, where they overturn θ surfaces. Note: Wave activity propagates eastward relative to the medium, so phase lines tilt eastward with height. Courtesy of R. Garcia.

Isentropic surfaces are then vertical. Such structure corresponds to neutral stability. The gravity wave then *breaks*, overturning the stratification. Such behavior is analogous to the breaking of a surface water wave that is incident on a shoreline. Air of low θ is folded over air of higher θ. Figure 14.25 displays such behavior for a gravity wave that has propagated to the mesosphere. By overturning isentropic surfaces locally, stable stratification is transformed into unstable stratification. In addition to being statically unstable, this structure violates the Ri criterion for dynamic stability. The ensuing stratification culminates in vigorous mixing. Wave momentum is then deposited at the breaking height, where wave activity is absorbed.

Planetary waves introduce similar behavior by rearranging air horizontally. Figure 14.26 shows the rearrangement of air by planetary waves under amplified conditions typical of the wintertime stratosphere. Anticyclonic motion has displaced the cyclonic polar-night vortex out of zonal symmetry. Mid-latitude air is then advected into the polar cap. To conserve potential vorticity, that air spins up anticyclonically. It establishes a reversed circulation about the pole, with circumpolar easterlies. Such behavior may be regarded as an expansion of the critical region in Fig. 14.23a, where $|\boldsymbol{v}'| = O(|c_x - \overline{u}|)$. Both are characterized by closed streamlines that lead to a complex rearrangement of air.

Behavior such as that in Fig. 14.26 occurs sporadically in the stratosphere during northern winter (cf. Fig. 18.13). Planetary waves forced by large orography in the Northern Hemisphere often amplify sufficiently to form closed streamlines at middle and high latitudes. Termed *sudden stratospheric warmings*, such episodes are marked by an abrupt reversal of the zonal-mean flow. Through thermal wind balance, the latter is attended by abrupt warming at high latitude – as much as 50°K in just a couple of days. Air over the winter pole, which lies in perpetual darkness, then becomes warmer than air in the sunlit tropics, which experiences ozone heating. Figure 1.10a illustrates the 10-hPa circulation during a stratospheric warming. In concert with Fig. 14.26, it shows that this dramatic change in zonal-mean properties actually follows from a complex rearrangement of air.

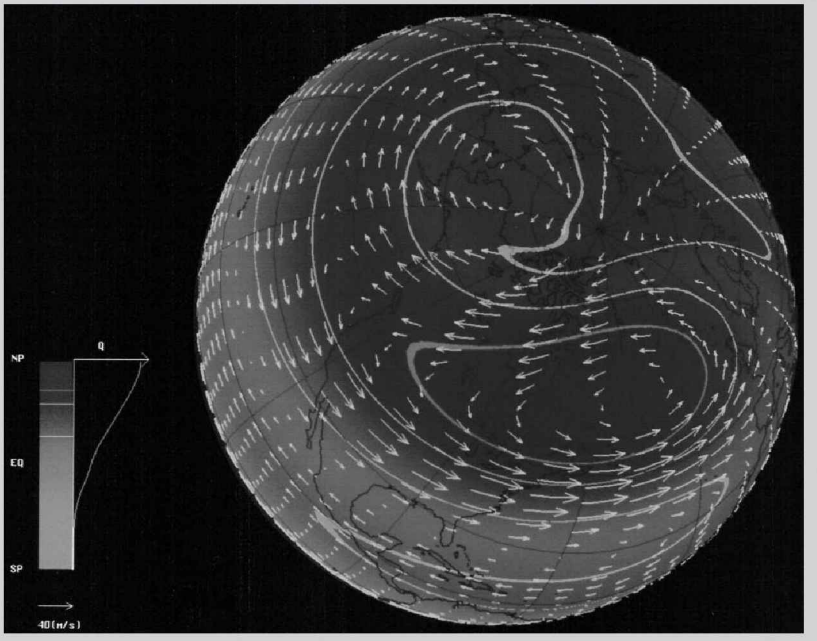

Figure 14.26 Distribution of potential vorticity Q and horizontal motion in a 2-dimensional calculation representative of the stratospheric circulation at 10 hPa under disturbed conditions. Color and velocity scales shown at left. High-Q polar air (blue), which marks the polar-night vortex, has been displaced well off the pole and distorted by an amplified planetary wave. Replacing it is low-Q air from equatorward (red), which has been advected into the polar cap. It spins up anticyclonically, forming a reversed circulation with easterly circumpolar flow at high latitude. These features are characteristic of a *stratospheric sudden warming* (cf. Fig. 18.13). See color plate section: Plate 11.

In the Southern Hemisphere, orographic features at the Earth's surface are comparatively small. Planetary waves are therefore weaker. For this reason, sudden stratospheric warmings and the disturbed conditions that accompany them are rare in the Southern Hemisphere. Less disturbed, the Antarctic polar-night vortex therefore remains closer to radiative equilibrium, much colder than its counterpart over the Arctic.

SUGGESTED REFERENCES

Atmosphere-Ocean Dynamics (1982) by Gill develops gravity waves at the graduate level. Advanced treatments are presented in *Atmospheric Waves* (1975) by Gossard and Hooke and *Waves in Fluids* (1978) by Lighthill.

An Introduction to Dynamic Meteorology (2004) by Holton develops Rossby waves. An advanced treatment, along with implications for transport, is presented in *Middle Atmosphere Dynamics* (1987) by Andrews et al.

PROBLEMS

1. Derive the zonal-mean momentum budget (14.5).
2. Lenticular cloud (Chap. 9) forms preferentially during winter. Explain its seasonality in relation to conditions that favor gravity waves.
3. Derive the group velocity (14.44) for simple gravity waves.
4. Demonstrate that, in mean westerlies, phase lines of a stationary gravity wave forced at the surface (e.g., the undulation of isentropic surfaces) must slope westward with height.
5. The Manti-La Sal mountains in southern Utah comprise an isolated range that has a characteristic width of 10 km and is oriented NS. If winds blow from the SW, the range's NS extent is much longer than 10 km, and static stability is characterized by $N^2 = 2.0\ 10^{-4}\ \mathrm{s}^{-2}$, (a) at what polar angle will lenticular cloud be found from the center of the range? (b) What will be the orientation of individual cloud bands relative to the range?
6. A gravity wave of zonal wavenumber $k = 0.5\ \mathrm{km}^{-1}$ propagates vertically through mean westerlies of uniform positive shear

$$\overline{u} = \overline{u}_0 + \Lambda z,$$

with $\overline{u}_0 = 10\ \mathrm{m\ s}^{-1}$, $\Lambda = 0.1\ \mathrm{m\ s}^{-1}\mathrm{km}^{-1}$, and constant static stability $N^2 = 2.0\ 10^{-4}\ \mathrm{s}^{-2}$. In the framework of the Boussinesq and WKB approximations, sketch the profiles of intrinsic frequency and vertical wavenumber if the gravity wave (a) is stationary, (b) propagates westward at $10\ \mathrm{m\ s}^{-1}$, and (c) propagates eastward at $10\ \mathrm{m\ s}^{-1}$.
7. A stationary gravity wave of the form

$$w'(x, z) = W(z)e^{ikx}$$

is excited by flow over elevated terrain. The horizontal and vertical scales are short enough for wave propagation to be controlled by local conditions. If the upstream flow $\overline{u}$ is independent of height but the stratification varies as

$$N^2(z) = N_0^2\left(1 - \frac{z^2}{H^2}\right),$$

(a) characterize the propagation according to levels where wave activity is vertically propagating and external, (b) sketch the vertical wave structure, and (c) determine the range of $\overline{u}$ for which wave activity is trapped at the surface.
8. Barometric registrations following the eruption of Krakatoa revealed an oscillatory disturbance in surface pressure having an amplitude of 1 hPa. If the period of the oscillation was 1 hour, estimate the amplitude of (a) the pressure perturbation at 80 km, (b) the wind perturbation at 80 km.
9. In terms of the vorticity budget (12.36), discuss how volume heating excites planetary waves.
10. Stationary planetary wave activity is generated by westerly flow over elevated terrain. Show that such wave activity will be found downstream of its topographic forcing.
11. Show that the flux of zonal momentum transmitted vertically by simple gravity waves, $\rho_0\overline{u'w'}$, is positive (negative) if their group velocity is upward and they propagate eastward (westward).

12. On approach to JFK airport in New York, winds are gusting nearly along the shoreline. Yet, white caps are observed to approach the shore virtually head on. Construct a simple model based on shallow water waves propagating in the $x-y$ plane, with depth decreasing linearly to zero at the shoreline, which coincides with $y=0$. For a wavepacket characterized initially by $\boldsymbol{k}=(k_0, l_0)$, (a) determine $\boldsymbol{k}(y)$, (b) sketch phase lines corresponding to successive positions of the wavepacket for $l_0>0$, (c) plot rays that are initially oriented 60° and 30° from the shoreline.
13. Obtain the dispersion relation (14.34) for acoustic-gravity waves. (Hint: What condition must be satisfied for a homogeneous system of linear equations to have nontrivial solution?)
14. Show that wave activity for simple gravity waves propagates vertically one vertical wavelength for each horizontal wavelength that it propagates horizontally.
15. A gravity wave of wavenumber $\boldsymbol{k}=(k, m)$ propagates into a region where potential temperature varies with height as

$$\frac{\theta}{\theta_0}=-\frac{(z-z_0)^2}{H^2},$$

with $H=$ const. (a) Describe propagation in the $x-z$ plane, sketching the corresponding ray. (b) Sketch the vertical structure of the wave. (c) Describe the behavior under fully nonlinear conditions.
16. *Inertio-gravity waves* are buoyancy waves with horizontal scales long enough to be influenced by rotation. Within the framework of the Boussinesq approximation, (a) provide a set of equations governing such motion on an f plane. (b) Show that these waves satisfy the dispersion relationship

$$\frac{m^2}{k^2}=\frac{N^2-\omega^2}{\omega^2-f^2},$$

which is a generalization of (14.36) and illustrates that inertio-gravity waves propagate vertically only for $|\omega|>|f|$. Atmospheric tides, which are generated by diurnal variations of heating, are inertio-gravity waves. Estimate the range of latitude for vertical propagation of (c) the diurnal tide: $\sigma=1.0$ cpd, and (d) the semidiurnal tide $\sigma=2.0$ cpd.
17. Show that the Lamb mode is the only nontrivial solution to the homogeneous boundary value problem (14.60).
18. Steady, barotropic, and nondivergent flow over an isolated mountain excites Rossby waves. The effect of the mountain may be treated as a vorticity source

$$Q(x, y)=\frac{Q_0}{2\pi L^2}e^{-\frac{x^2+y^2}{2L^2}}.$$

(a) Provide a rationale for treating surface forcing in this manner. (b) Provide an equation governing the motion. (c) Express the streamfunction in terms of a Fourier integral to recover the wave field, subject to the condition of radiation away from the source region. (d) Plot the wave field.
19. Consider quasi-geostrophic motion in spherical geometry. (a) Provide an equation governing the propagation of planetary waves in latitude and height. For a stationary wave that is invariant with height ($\frac{\partial \psi'}{\partial z}=0$) and propagates horizontally

through uniform westerlies of 20 m s^{-1}, estimate the polar turning latitude for (b) zonal wavenumber 1, (c) zonal wavenumber 4.

20. In light of Prob. 14.19, describe the wave propagation that could be established with a source at mid-latitudes if potential vorticity is homogenized at low latitudes by horizontal mixing (Sec. 14.7).

CHAPTER
FIFTEEN

The general circulation

Thermal equilibrium requires that, for the Earth-Atmosphere system as a whole, net radiative heating must vanish. Although it applies globally, this requirement need not hold locally. In fact, net radiation (Fig. 1.34c during DJF) shows that low latitudes experience radiative heating: They receive more energy through absorption of SW than they lose through emission to space of LW. Conversely, middle and high latitudes experience radiative cooling, especially in the winter hemisphere: They lose more energy through emission to space of LW than they receive through absorption of SW. To preserve thermal equilibrium, these local imbalances in the radiative energy budget must be compensated by a poleward transfer of heat. Accomplished mechanically, the latter transfers energy from tropical regions, where it offsets the surplus of radiative energy, to extratropical regions, where it offsets the deficit of radiative energy. The poleward transfer of heat is accomplished by the general circulation of the Earth-atmosphere system, 60% of it by the circulation of the atmosphere (see Fig. 17.10).

The simplest mechanism to transfer heat poleward is a steady, zonally symmetric circulation between the equator and poles. Such motion is driven by atmospheric heating in the tropics and cooling in the extratropics. Atmospheric heating is concentrated at low latitude, where it derives from latent heat release inside centers of convection (Fig. 9.41b). Together with radiative cooling at higher latitude, it forces vertical motion across isentropic surfaces (Secs. 2.5, 3.6). The latter must be compensated by horizontal motion. The resultant overturning in the meridional plane transfers heat between regions of heating and cooling. Maintaining thermal equilibrium locally, it represents a *thermally direct circulation*. The Hadley circulation is of this form (Fig. 1.35). However, the observed Hadley circulation extends poleward to only about $\pm 30°$. It cannot achieve the global heat transfer required to maintain thermal equilibrium. The observed circulation is more complex, especially on individual days (Fig. 1.9).

How meridional heat transfer is actually accomplished in the atmosphere is influenced profoundly by the Earth's rotation. Net radiation is almost uniform in longitude. It therefore tends to establish thermal structure that is zonally symmetric, with temperature decreasing poleward. According to the hypsometric relation (6.12), isobaric height would then assume similar form, likewise decreasing poleward. Under these circumstances, contours of isobaric height would remain parallel to latitude circles. Geostrophic equilibrium would then require air motion to likewise be zonally symmetric: nearly zonal, with only a weak meridional component to transfer heat poleward. Such motion represents a skewed equator-to-pole circulation, with velocity deflected into the zonal direction. Air motion would then be nearly perpendicular to the thermally direct overturning hypothesized above. This peculiarity of the implied circulation is a manifestation of the geostrophic paradox (Sec 12.1). The zonally symmetric circulation would also be nearly perpendicular to the temperature gradient. It would therefore transfer little heat poleward.

With no offset to radiative heating and cooling, the meridional temperature gradient must steepen. It would continue to steepen until temperature in the tropics became sufficiently warm (increasing LW emission) and temperature in the extratropics became sufficiently cold (decreasing LW emission) to reduce net radiation in each region – just enough to be offset by the weak poleward heat transfer of the zonally symmetric circulation. This form of thermal equilibrium, however, would produce a meridional temperature gradient that is much steeper than observed (Fig. 10.1).

By thermal wind balance (12.11), the steep meridional temperature gradient must be accompanied by steep vertical shear and hence by a strong zonal jet overhead. The strength of the implied jet can be inferred from conservation of angular momentum. An air parcel drifting poleward in the zonally symmetric circulation conserves its angular momentum, $(u + \Omega a cos\phi) a cos\phi$ (11.29). If initially motionless at the equator, the parcel must then assume zonal velocity at latitude ϕ of

$$u = \Omega a \frac{sin^2\phi}{cos\phi}.$$

Upon reaching a latitude of 45°, poleward-moving air must therefore attain wind speed in excess of 300 m s^{-1} – namely, of order Mach 1.

The observed circulation never even approaches such speed (Fig. 1.8). Long before it is attained, the circulation develops zonally asymmetric structure – large-scale disturbances, which completely alter the extratropical circulation. Those asymmetric motions transfer heat poleward far more efficiently than can a zonally symmetric circulation in the presence of rotation. Inherently unsteady, extratropical disturbances are fueled by reservoirs of atmospheric energy and exchanges amongst them, which shape the general circulation.

15.1 FORMS OF ATMOSPHERIC ENERGY

From the time it is absorbed until it is eventually rejected to space, energy undergoes a complex series of transformations between three basic reservoirs:

1. Thermal energy, which is represented in the temperature and humidity of air.
2. Gravitational potential energy, which is represented in the horizontal distribution of atmospheric mass.
3. Kinetic energy, which is represented in air motion.

Transformations from thermal and potential energy to kinetic energy are responsible for setting the atmosphere into motion. They maintain the circulation against frictional dissipation.

15.1.1 Moist static energy

The thermal energy of moist air has two contributions: Sensible heat content reflects the molecular energy of dry air, which is the dominant component of moist air. Latent heat content reflects the energy that can be imparted to the dry air component when the vapor component condenses. These contributions are collected in the specific enthalpy (Sec. 5.3)

$$h = c_p T + l_v r + h_0. \tag{15.1}$$

$c_p T$ measures the sensible heat content of a moist parcel, whereas $l_v r$ measures its latent heat content.

The First Law (2.15) implies that the specific enthalpy of an individual air parcel changes according to

$$\frac{dh}{dt} - \alpha \frac{dp}{dt} = \dot{q}_{net}, \tag{15.2.1}$$

where $\dot{q}_{net}$ is the net rate heat is absorbed by the parcel. Incorporating hydrostatic equilibrium allows (15.2.1) to be expressed

$$\frac{dh}{dt} + g\frac{dz}{dt} = \dot{q}_{net}$$

or with (15.1)

$$\begin{aligned} \frac{d}{dt}(c_p T + l_v r + \Phi) &= \dot{q}_{net} \\ &= \dot{q}_{rad} + \dot{q}_{mech}, \end{aligned} \tag{15.2.2}$$

where $\dot{q}_{rad}$ and $\dot{q}_{mech}$ denote radiative and mechanical components of heat transfer. The quantity $(c_p T + l_v r + \Phi)$ defines the *moist static energy* of the air parcel. It includes thermal as well as potential energy. A parcel's moist static energy changes only through heat transfer with its environment. It is unaffected by vaporization and condensation, which involve only internal exchanges of sensible and latent heat contents.[1]

Mechanical heat transfer is dominated by turbulent mixing. It leads to exchanges of sensible heat (temperature) and latent heat (humidity)

$$\dot{q}_{mech} = \dot{q}_{sen} + \dot{q}_{lat}. \tag{15.3}$$

These components of turbulent heat transfer can be represented in terms of mean gradients of temperature and humidity and corresponding eddy diffusivities (13.13).

Equation (15.2.2) describes an air parcel's moist static energy in terms of advection and the distributions of sources and sinks. A parcel will acquire moist static energy at low latitude through absorption of radiative, sensible, and latent heats from the Earth's surface. Upon reaching middle and high latitudes, the parcel will lose moist static energy through radiative cooling to space. Completing a meridional circuit (symbolized

[1] This differs from the development in Sec. 10.7, which focuses on the dry air component. The latter must account for transfer of latent heat from the vapor component.

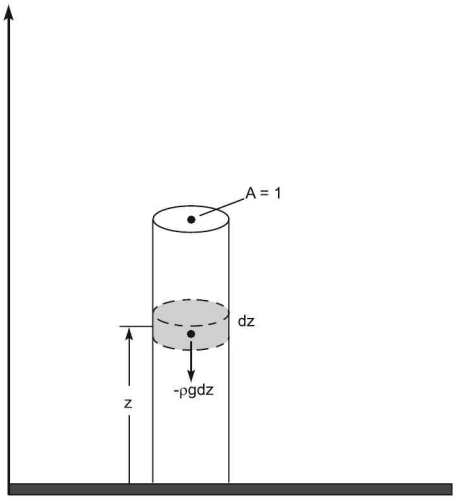

Figure 15.1 Incremental volume of unit cross-sectional area and height z inside an atmospheric column.

in Fig. 6.7) then results in a net poleward transfer of moist static energy. The latter compensates TOA radiative heating at low latitude and radiative cooling at middle and high latitudes. Integrating (15.2) over the entire atmosphere and averaging over time obtains the mean change of moist static energy. Under thermal equilibrium, it must vanish. Net heat transfer to the atmosphere must therefore likewise vanish

$$\overline{\dot{q}_{rad}} + \overline{\dot{q}_{sen}} + \overline{\dot{q}_{lat}} = 0, \tag{15.4}$$

where overbar denotes global and time mean. Net radiative cooling of the atmosphere (Fig. 8.24) must then be balanced by transfers of sensible and latent heat from the Earth's surface (Fig. 1.32).

Inside the boundary layer, turbulent diffusion of heat and absorption of LW radiation from the Earth's surface increase an air parcel's sensible heat content. Absorption of water vapor from the surface of ocean increases its latent heat content. Both increase the moist static energy of the parcel. Outside the boundary layer and convection, turbulent diffusion is small enough to be ignored. Radiative cooling then becomes the primary diabatic process. It gradually depletes the parcel's store of moist static energy, which is subsequently replenished when it returns to regions of positive heat transfer.

15.1.2 Total potential energy

Thermal energy is reflected in the internal energy of dry air. Heat transfer from the Earth's surface increases an atmospheric column's temperature and hence its internal energy. The hypsometric relationship (6.12) then implies vertical expansion of the column. Because it elevates the column's center of mass, a process that increases the column's internal energy must also increase its potential energy.

Consider a dry atmosphere in hydrostatic equilibrium and in which air motion occurs on a time scale short enough to be regarded as adiabatic. An incremental volume of unit cross-sectional area (Fig. 15.1) has internal energy

$$d\mathcal{U} = \rho c_v T dz. \tag{15.5.1}$$

Integrating upward from the surface gives the column internal energy

$$\mathcal{U} = c_v \int_0^\infty \rho T dz. \tag{15.5.2}$$

The potential energy of the incremental volume is

$$\begin{aligned} d\mathcal{P} &= \rho g z dz \\ &= -z dp. \end{aligned} \tag{15.6.1}$$

Then the column potential energy up to a height z is given by

$$\mathcal{P}(z) = \int_{p(z)}^{p_s} z' dp', \tag{15.6.2}$$

where $z' = z'(p')$ and the integral is evaluated in the direction of increasing pressure. Integrating by parts transforms this into

$$\begin{aligned} \mathcal{P}(z) &= z' p' \Big|_{p(z)}^{p_s} + \int_0^z p dz' \\ &= -z p(z) + R \int_0^z \rho T dz', \end{aligned}$$

which, for $z \to \infty$, reduces to

$$\mathcal{P} = R \int_0^\infty \rho T dz. \tag{15.7}$$

A similar expression holds for the column internal energy (15.5.2). Thus,

$$\begin{aligned} \frac{\mathcal{P}}{\mathcal{U}} &= \frac{R}{c_v} \\ &= \gamma - 1. \end{aligned} \tag{15.8}$$

Equation (15.8) asserts that the internal and potential energies of an atmospheric column preserve a constant ratio. This interdependence is a consequence of hydrostatic equilibrium. It follows that energy can then be drawn from those reservoirs only in a fixed proportion. Adding the internal and potential energies of the column obtains

$$\begin{aligned} \mathcal{P} + \mathcal{U} &= \int_0^\infty \rho c_p T dz \\ &= \frac{c_p}{g} \int_0^{p_s} T dp \\ &= \mathcal{H}, \end{aligned} \tag{15.9}$$

which is just the column enthalpy. It defines the *total potential energy* (Margules, 1903).

Consider the atmosphere as a whole and, for the sake of illustration, in the absence of heat transfer at its boundaries. Because p vanishes at the top of the atmosphere and w vanishes at its bottom, no work is performed on this system as well. Then the First Law for the entire atmosphere, inclusive of kinetic energy $\mathcal{K}$, asserts that the change of total energy vanishes

$$\Delta(\mathcal{H} + \mathcal{K}) = 0. \tag{15.10.1}$$

Therefore

$$\begin{aligned} \Delta\mathcal{K} &= -\Delta\mathcal{H} \\ &= -\Delta(\mathcal{P}+\mathcal{U}), \end{aligned} \tag{15.10.2}$$

where column properties are understood to be integrated globally. Under adiabatic conditions, the atmosphere's kinetic energy is drawn from its reservoir of total potential energy.

15.1.3 Available potential energy

Of the atmosphere's total potential energy, only a small fraction is actually available for conversion to kinetic energy. Consider an atmosphere that is initially motionless and barotropically stratified (Sec. 12.2). Isobaric surfaces then coincide with isentropic surfaces, as illustrated in Fig. 12.5a. Under adiabatic conditions, air parcels must move along θ surfaces. Consequently, no pressure gradient exists in the directions of possible motion. A barotropically stratified atmosphere thus possesses no means of generating motion internally. It follows that none of its potential energy is available for conversion to kinetic energy.

Suppose the above atmosphere is now heated at low latitude and cooled at middle and high latitudes, with net global heating of zero. By the First Law, the atmosphere's total energy is unchanged. If the atmosphere remains motionless, so is its total potential energy (15.10.1). Locally, however, total potential energy clearly does change. Increased temperature increases total potential energy at low latitude. Reduced temperature decreases total potential energy at middle and high latitudes. By the hypsometric relationship, the vertical spacing of isobaric surfaces is then expanded at low latitude but compressed at middle and high latitudes. Isobaric surfaces are thus tilted "clockwise" into the positions assumed in Fig. 12.5b. Under positive static stability, just the reverse occurs for isentropic surfaces. Heating increases potential temperature at low latitude. Because θ increases upward, it brings down greater values of θ from above. Conversely, cooling reduces θ at middle and high latitudes. It brings up smaller values of θ from below. Isentropic surfaces are thus tilted "counterclockwise." In this fashion, the nonuniform distribution of heating and cooling drives isobaric surfaces out of coincidence with isentropic surfaces. It thus drives thermal structure into baroclinic stratification.

Under such stratification, the atmosphere possesses a pressure gradient along isentropic surfaces (Fig. 15.2). An air parcel can then accelerate through the pressure-gradient force. Potential energy is thus available for conversion to kinetic energy. Even though no potential energy has been added to the atmosphere as a whole, that energy reservoir has been tapped by introducing a horizontal gradient of buoyancy. Analogous reasoning applies to uniformly heating the atmosphere. The latter clearly increases the atmosphere's store of total potential energy. However, it introduces none that is available for conversion to kinetic energy.

From hydrostatic equilibrium, the variation of pressure along a θ surface reflects a nonuniform distribution of mass above that surface. The situation is analogous to two immiscible fluids of different densities that have been juxtaposed horizontally (Fig. 15.3). Hydrostatic equilibrium implies a horizontal pressure-gradient force, directed from the heavier fluid to the lighter one. Motion will then develop internally to alleviate the mechanical imbalance. The nonrotating system in Fig. 15.3 accomplishes this by

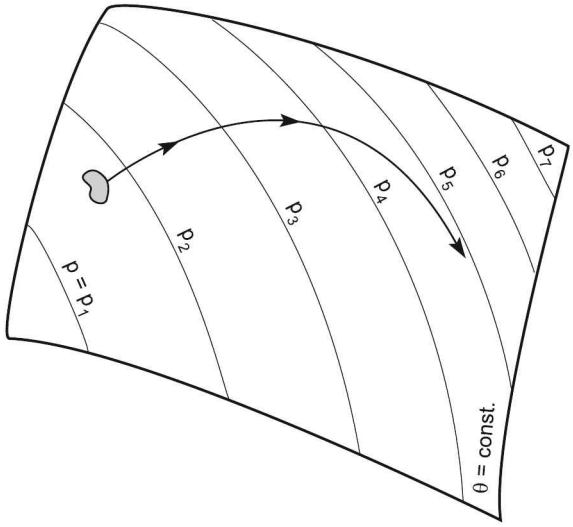

Figure 15.2 Variation of pressure along an isentropic surface under baroclinic stratification. The pressure variation vanishes under barotropic stratification.

rearranging mass so that heavier fluid undercuts and eventually comes to rest beneath lighter fluid. The system's final state is then hydrostatically stable. By lowering the center of gravity of the system, this process releases potential energy, which is converted into kinetic energy. The latter is eventually dissipated by viscosity, increasing the system's internal energy.

In the atmosphere, horizontal rearrangement of mass is inhibited by rotation. The Coriolis force deflects air motion parallel to isobars (into and out of the page in Fig. 15.3). Nevertheless, the pressure gradient along θ surfaces enables air motion to develop. Though more complex, it neutralizes the mechanical imbalance. The Coriolis force makes those motions highly rotational, a feature that favors horizontal mixing (Fig. 12.4). Such behavior is illustrated by interleaving swirls of tropical and polar air

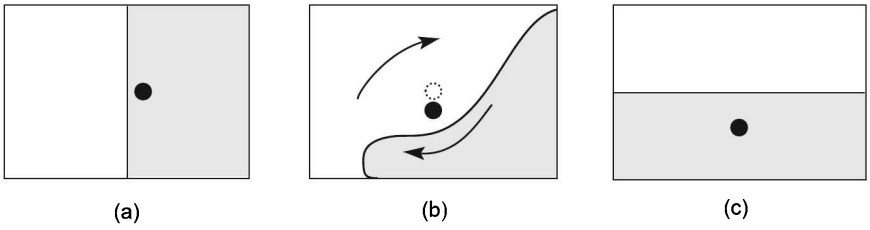

Figure 15.3 Schematic illustrating the rearrangement of mass in a system of two immiscible fluids of different densities that are initially juxtaposed horizontally. In the absence of rotation, heavier fluid (shaded) undercuts and comes to rest beneath lighter fluid. This process renders the system hydrostatically stable, while lowering its center of mass (solid circle). Rotation modifies this adjustment by deflecting upper motion out of the page (e.g., westerly) and lower motion into the page (e.g., easterly). Adapted from Wallace and Hobbs (1977).

in the cyclone off the coast of Africa in Fig. 1.18 (cf. Fig. 1.29). By mixing air horizontally, synoptic weather systems homogenize the horizontal distribution of mass over isentropic surfaces. This rearrangement of air drives isobaric surfaces back into coincidence with isentropic surfaces, restoring thermal structure to barotropic stratification. Such motion also results in a net poleward transfer of heat and moisture. Air drawn poleward from low latitude has greater moist static energy than replacement air that is drawn equatorward from middle and high latitudes. By making the horizontal mass distribution uniform, air motions lower the overall center of gravity of the atmosphere. Potential energy is therefore converted into kinetic energy. The latter, in turn, is dissipated by viscosity, converted into internal energy, and eventually rejected to space as heat.

Air motion responsible for this redistribution of mass is fueled by a conversion of potential energy to kinetic energy. It develops through *baroclinic instability*, wherein the source of energy is related to baroclinicity of the stratification. Temperature then varies along isobaric surfaces. By thermal wind balance, the energy source of baroclinic disturbances is also related to vertical shear.

Adiabatic adjustment

The potential energy available for conversion to kinetic energy is reflected in the departure from barotropic stratification. Consider an adiabatic redistribution of mass from a given baroclinic state. Because air must move along θ surfaces, horizontal mixing will eventually render the distributions of mass and pressure uniform over those surfaces. It therefore restores thermal structure to barotropic stratification. In that limiting state, the atmosphere possesses no more potential energy available for conversion, so $\mathcal{H} = \mathcal{H}_{min}$.

The *available potential energy A* (Lorenz, 1955) is defined as the difference between the total potential energy for the state under consideration and the minimum that would result through an adiabatic rearrangement of mass

$$\mathcal{A} = \mathcal{H} - \mathcal{H}_{min}. \tag{15.11}$$

Available potential energy has the following properties:

1. $\mathcal{A} + \mathcal{K}$ is preserved under adiabatic rearrangement. Hence $\Delta\mathcal{K} = -\Delta\mathcal{A}$.
2. $\mathcal{A}$ is positive for baroclinic stratification and zero for barotropic stratification.
3. $\mathcal{A}$ is uniquely determined by the distribution of mass.

To derive an expression for $\mathcal{A}$, consider an isentropic surface of area S. The average pressure on this surface

$$\overline{p} = \frac{1}{S}\int_S p\,dS \tag{15.12}$$

is conserved under adiabatic rearrangement (Prob. 15.8). The atmosphere as a whole has total potential energy

$$\begin{aligned}\mathcal{H} &= \int_S dS \int_0^\infty \rho c_p T\,dz \\ &= \frac{c_p}{g}\int_S dS \int_0^{p_s} T\,dp.\end{aligned} \tag{15.13}$$

In terms of potential temperature, this becomes

$$\begin{aligned}\mathcal{H} &= \frac{c_p}{g p_0^\kappa}\int_S dS\int_0^{p_s}\theta\, p^\kappa\, dp \\ &= \frac{1}{p_0^\kappa(1+\kappa)\Gamma_d}\int_S dS\int_0^{p_s}\theta\, dp^{1+\kappa},\end{aligned} \tag{15.14}$$

where $\Gamma_d = \frac{g}{c_p}$ is the dry adiabatic lapse rate. Because the atmosphere is vertically stable, θ increases with height monotonically. It may therefore be interchanged with p for the vertical coordinate. Integrating (15.14) by parts obtains

$$\mathcal{H} = \frac{S}{p_0^\kappa(1+\kappa)\Gamma_d}\left[\overline{\theta\, p^{1+\kappa}}\Big|_0^{p_s} + \int_{\theta_s}^{\infty}\overline{p^{\kappa+1}}\,d\theta\right], \tag{15.15}$$

with θ_s denoting the potential temperature at the surface. The limit $p = 0$ in the first term in brackets vanishes. Defining $p = p_s$ for $\theta < \theta_s$ enables (15.15) to be expressed as

$$\mathcal{H} = \frac{S}{p_0^\kappa(1+\kappa)\Gamma_d}\int_0^{\infty}\overline{p^{\kappa+1}}\,d\theta. \tag{15.16}$$

When the stratification has been rendered barotropic, $\mathcal{H} = \mathcal{H}_{min}$ and p has become uniform over isentropic surfaces. Because p then equals $\overline{p}$,

$$\mathcal{H}_{min} = \frac{S}{p_0^\kappa(1+\kappa)\Gamma_d}\int_0^{\infty}\overline{p}^{\kappa+1}\,d\theta. \tag{15.17}$$

Hence, the state under consideration has available potential energy

$$\mathcal{A} = \frac{S}{p_0^\kappa(1+\kappa)\Gamma_d}\int_0^{\infty}\left[\overline{p^{\kappa+1}} - \overline{p}^{\kappa+1}\right]d\theta. \tag{15.18}$$

For small departures p' and T' from their areal averages, (15.18) is approximated by

$$\mathcal{A} = \frac{RS}{2gp_0^\kappa}\int_0^{\infty}\overline{p}^{1+\kappa}\left(\frac{\overline{p'^2}}{\overline{p}^2}\right)d\theta \tag{15.19.1}$$

and

$$\mathcal{A} = \frac{gS}{2}\int_0^{p_s}\frac{1}{\overline{N}^2}\left(\frac{\overline{T'^2}}{\overline{T}^2}\right)dp, \tag{15.19.2}$$

demonstration of which is left as an exercise. The variance of pressure on an isentropic surface reflects the degree of baroclinicity. So does the variance of temperature on an isobaric surface. According to (15.19), each is a direct measure of available potential energy. Under typical conditions, as little as 0.1% of the atmosphere's total potential energy is available for conversion to kinetic energy (Prob. 15.4).

15.2 HEAT TRANSFER IN A ZONALLY SYMMETRIC CIRCULATION

Available potential energy is released by meridional air motion, which transfers heat poleward. Such motion is influenced importantly by the Coriolis force. To explore

how rotation influences poleward heat transfer, we consider a simple model of the meridional circulation within the framework of the Boussinesq approximation (Sec. 12.5.3). A spherical atmosphere of finite vertical extent H is bounded below by a rigid surface and above by a free surface. The lower boundary is maintained at a zonally symmetric temperature $T_0(\phi)$, with T_0 decreasing poleward. The upper boundary is maintained at $T_0(\phi) + \Delta T$, with ΔT = const. If $\Delta T < 0$, this corresponds to heat being supplied at the atmosphere's lower boundary and rejected at its upper boundary.[2]

Following Charney (1973), we consider zonally symmetric motion $\overline{\boldsymbol{v}} = (\overline{u}, \overline{v}, \overline{w})$ in the presence of turbulent diffusion. Scaling variables as in Sec. 11.4 casts the governing equations into nondimensional form. The prevailing balances can then be identified in terms of the dimensionless Rossby number and *Ekman number*:

$$Ro = \frac{U}{2\Omega a} \qquad E = \frac{K}{2\Omega H^2}, \tag{15.20}$$

where $K = K_M = K_H$ is a constant eddy diffusivity (Sec. 13.1).

The limit of fast rotation and small friction makes $E \leq O(Ro) \ll 1$. To streamline the development, we follow the convention adopted in Sec. 12.5. Other than Ro and E, dimensionless factors are absorbed into the dependent variables. This enables the nondimensional equations to be expressed in a form nearly identical to their dimensional counterparts. Prevailing balances can then be identified in dimensional form because, at a specified order of Ro and E, those dimensionless parameters drop out. Proceeding as we did earlier casts the governing equations in log-pressure coordinates into

$$Ro\left\{\frac{\overline{v}}{a}\frac{\partial \overline{u}}{\partial \phi} + \overline{w}\frac{\partial \overline{u}}{\partial z}\right\} - f\overline{v} = EK\frac{\partial^2 \overline{u}}{\partial z^2} \tag{15.21.1}$$

$$Ro\left\{\frac{\overline{v}}{a}\frac{\partial \overline{v}}{\partial \phi} + \overline{w}\frac{\partial \overline{v}}{\partial z}\right\} + f\overline{u} = -\frac{1}{a}\frac{\partial \overline{\Phi}}{\partial \phi} + EK\frac{\partial^2 \overline{v}}{\partial z^2} \tag{15.21.2}$$

$$\frac{\partial \overline{\Phi}}{\partial z} = \frac{R\overline{T}}{H} \tag{15.21.3}$$

$$\frac{1}{a\cos\phi}\frac{\partial}{\partial \phi}(\cos\phi\,\overline{v}) + \frac{\partial \overline{w}}{\partial z} = 0 \tag{15.21.4}$$

$$Ro\left\{\frac{\overline{v}}{a}\frac{\partial \overline{T}}{\partial \phi} + \overline{w}\frac{\partial \overline{T}}{\partial z}\right\} = EK\frac{\partial^2 \overline{T}}{\partial z^2}, \tag{15.21.5}$$

where factors like a, $f = \sin\phi$, and K are understood to be dimensionless and $O(1)$. At the rigid lower boundary, no-slip and the imposed temperature require

$$\begin{aligned} &\overline{u} = \overline{v} = \overline{w} = 0 \\ &\overline{T} = T_0(\phi) \end{aligned} \qquad z = 0. \tag{15.21.6}$$

At the free surface, the stresses $\tau_{xz} = K\frac{\partial \overline{u}}{\partial z}$ and $\tau_{yz} = K\frac{\partial \overline{v}}{\partial z}$ must vanish. Further, for motion that is nearly geostrophic, vertical deflections of the free surface are small. The kinematic condition (Sec. 14.1) can then be replaced by the requirement of no

[2] It is through imposed temperature contrast that laboratory simulations are driven thermally. They will be seen in the next section to provide a mechanical analogue of this theoretical model.

vertical motion. With those approximations, the upper boundary conditions become

$$\frac{\partial \overline{u}}{\partial z} = \frac{\partial \overline{v}}{\partial z} = 0 \qquad \overline{w} = 0 \qquad z = H. \tag{15.21.7}$$
$$\overline{T} = T_0(\phi) + \Delta T$$

The dominant balances in (15.21) are geostrophic and hydrostatic equilibrium. Advective acceleration and friction introduce a small ageostrophic component into the momentum balance. As in Chap. 12, we consider an asymptotic series solution, one that is now valid in the limit $E \to 0$. Expanding dependent variables in power series of $E^{\frac{1}{2}}$, for example,

$$\overline{\boldsymbol{v}} = \overline{\boldsymbol{v}}^{(0)} + E^{\frac{1}{2}}\overline{\boldsymbol{v}}^{(1)} \ldots, \tag{15.22}$$

enables the motion to be determined recursively to successively higher accuracy.[3]

To $O(E^0)$, the governing equations reduce to

$$f\overline{v}^{(0)} = 0 \tag{15.23.1}$$

$$f\overline{u}^{(0)} = -\frac{1}{a}\frac{\partial \overline{\Phi}^{(0)}}{\partial \phi} \tag{15.23.2}$$

$$\frac{\partial \overline{\Phi}^{(0)}}{\partial z} = \frac{R}{H}\overline{T}^{(0)} \tag{15.23.3}$$

$$\frac{1}{a\cos\phi}\frac{\partial}{\partial \phi}\left(\cos\phi\,\overline{v}^{(0)}\right) + \frac{\partial \overline{w}^{(0)}}{\partial z} = 0, \tag{15.23.4}$$

which are identical to their dimensional counterparts. Equations (15.23) imply that, to lowest order, the motion is zonal and in geostrophic balance. Cross-differentiating (15.23.2) and (15.23.3) obtains the thermal wind relation

$$\frac{\partial \overline{u}^{(0)}}{\partial z} = -\frac{R}{aHf}\frac{\partial \overline{T}^{(0)}}{\partial \phi}. \tag{15.24}$$

With (15.23.1) and the boundary conditions, (15.23.4) gives

$$\overline{w}^{(0)} \equiv 0. \tag{15.25}$$

Then the thermodynamic equation (15.21.5) implies

$$\frac{\partial^2 \overline{T}^{(0)}}{\partial z^2} = 0. \tag{15.26.1}$$

According to (15.26.1) the vertical heat flux is nondivergent. The circulation is therefore in diffusive equilibrium. Heat absorbed at the atmosphere's lower boundary is transferred without loss to its upper boundary, where it is rejected. The solution of (15.26.1) satisfying the boundary conditions of imposed temperature is

$$\overline{T}^{(0)}(\phi, z) = T_0(\phi) + \Delta T\left(\frac{z}{H}\right). \tag{15.26.2}$$

[3] Powers of $E^{\frac{1}{2}}$ are the appropriate form for the expansion because K enters the equations with second-order derivatives.

Then (15.24) implies that the E^0 motion intensifies with height linearly

$$\overline{u}^{(0)}(z) = -\frac{R}{aHf}\frac{\partial T_0}{\partial \phi} z. \tag{15.27}$$

The $O(E^{\frac{1}{2}})$ equations have the same form as (15.23). Proceeding along similar lines leads to

$$\overline{v}^{(1)} \equiv 0 \tag{15.28.1}$$

$$\overline{w}^{(1)} \equiv 0. \tag{15.28.2}$$

$$\overline{T}^{(1)} \equiv 0. \tag{15.28.3}$$

Thermal wind balance (15.24) then implies that the $O(E^{\frac{1}{2}})$ zonal flow is independent of height

$$\overline{u}^{(1)} \neq \overline{u}^{(1)}(z). \tag{15.29}$$

The solution accurate to $O(E^{\frac{1}{2}})$ has constant vertical shear. It therefore violates the upper boundary conditions of no stress on the free surface. This deficiency follows from the neglect of viscous terms, which reduces the order of the governing equations. Instead, the full solution must possess a boundary layer, wherein the motion adjusts sharply to meet boundary conditions. Viscous terms are then nonnegligible in a shallow neighborhood of the upper and lower boundaries. There, friction drives the motion out of geostrophic balance, which is inherent to the preceding equations.

To obtain an $O(E^{\frac{1}{2}})$ solution that is uniformly valid, we introduce a stretching transformation that accounts for sharp changes near the upper and lower surfaces. Boundary conditions can be satisfied by augmenting the first-order geostrophic motion with an ageostrophic correction

$$\overline{\boldsymbol{v}}^{(1)} = \overline{u}_g^{(1)}\boldsymbol{i} + \overline{\boldsymbol{v}}_a^{(1)}, \tag{15.30}$$

where $\overline{u}_g^{(1)}$ is the inviscid motion described by (15.29). The ageostrophic velocity $\overline{\boldsymbol{v}}_a^{(1)}$ imposes a secondary circulation onto the geostrophic flow. It is analogous to Ekman pumping (Sec. 13.4). The secondary circulation transports heat poleward by driving the motion across isotherms.

Inside the upper boundary layer, the stretching transformation

$$H - z = E^{\frac{1}{2}}\zeta \tag{15.31}$$

magnifies sharp changes. It makes viscous terms comparable to others in the momentum balance there, preserving the order of the governing equations. Then the $O(E^{\frac{1}{2}})$ momentum equations reduce to the Ekman balance

$$-f\overline{v}_a^{(1)} = K\frac{\partial^2 \overline{u}_a^{(1)}}{\partial \zeta^2} \tag{15.32.1}$$

$$f\overline{u}_a^{(1)} = K\frac{\partial^2 \overline{v}_a^{(1)}}{\partial \zeta^2}, \tag{15.32.2}$$

with the geostrophic contribution automatically satisfied by $\overline{u}_g^{(1)}$. Requiring the total solution accurate to $O(E^{\frac{1}{2}})$ to satisfy (15.21.7) provides boundary conditions at the

free surface

$$\frac{\partial \overline{u}^{(0)}}{\partial z} - \frac{\partial \overline{u}_a^{(1)}}{\partial \zeta} = 0 \qquad \frac{\partial \overline{v}_a^{(1)}}{\partial \zeta} = 0 \qquad \zeta = 0. \tag{15.32.3}$$

For the solution to reduce to the inviscid behavior outside the boundary layer, the ageostrophic corrections must also satisfy

$$\overline{u}_a^{(1)} \sim 0 \qquad \overline{v}_a^{(1)} \sim 0 \qquad \zeta \to \infty. \tag{15.32.4}$$

The boundary value problem (15.32) has solution

$$\overline{u}_a^{(1)}(\zeta) = \frac{1}{2\gamma} \frac{\partial \overline{u}^{(0)}}{\partial z} e^{-\gamma\zeta} \left(sin\gamma\zeta - cos\gamma\zeta\right) \tag{15.33.1}$$

$$\overline{v}_a^{(1)}(\zeta) = \frac{1}{2\gamma} \frac{\partial \overline{u}^{(0)}}{\partial z} e^{-\gamma\zeta} \left(sin\gamma\zeta + cos\gamma\zeta\right), \tag{15.33.2}$$

where

$$\gamma = \sqrt{\frac{f}{2K}} \tag{15.33.3}$$

is the same parameter that defines the Ekman spiral in Sec. 13.2.1 (Figs. 15.4a,b).

Because $\overline{v}$ is concentrated inside the boundary layer, meridional transfer of mass is proportional to

$$\begin{aligned} \int_{\substack{H-\zeta \\ \zeta\to\infty}}^{H} E^{\frac{1}{2}} \overline{v}^{(1)} dz &= E \int_0^\infty \overline{v}_a^{(1)} d\zeta \\ &= -E \frac{KR}{aHf^2} \frac{\partial T_0}{\partial \phi}. \end{aligned} \tag{15.34}$$

As $\frac{\partial T_0}{\partial \phi} < 0$, mass transfer along the upper surface is poleward and $O(E)$ (Fig. 15.4c). Integrating the continuity equation (15.21.4) gives the vertical motion just beneath the boundary layer

$$\begin{aligned} \overline{w}(H) &= \int_{\substack{H-\zeta \\ \zeta\to\infty}}^{H} \frac{1}{acos\phi} \frac{\partial}{\partial \phi} \left(cos\phi v\right) dz \\ &= E \int_0^\infty \frac{1}{acos\phi} \frac{\partial}{\partial \phi} \left(cos\phi \overline{v}_a^{(1)}\right) d\zeta. \end{aligned}$$

It too is $O(E)$. Thus, vertical motion beneath the upper boundary layer is

$$\overline{w}^{(2)}(H) = -\frac{KR}{Ha^2 cos\phi} \frac{\partial}{\partial \phi} \left(\frac{cos\phi}{f^2} \frac{\partial T_0}{\partial \phi} \right). \tag{15.35}$$

At this order, $O(E)$, the zonal momentum equation in the interior reduces to

$$\begin{aligned} -f\overline{v}^{(2)} &= K \frac{\partial^2 \overline{u}^{(0)}}{\partial z^2} \\ &= 0. \end{aligned} \tag{15.36}$$

Continuity then implies

$$\frac{\partial \overline{w}^{(2)}}{\partial z} = 0.$$

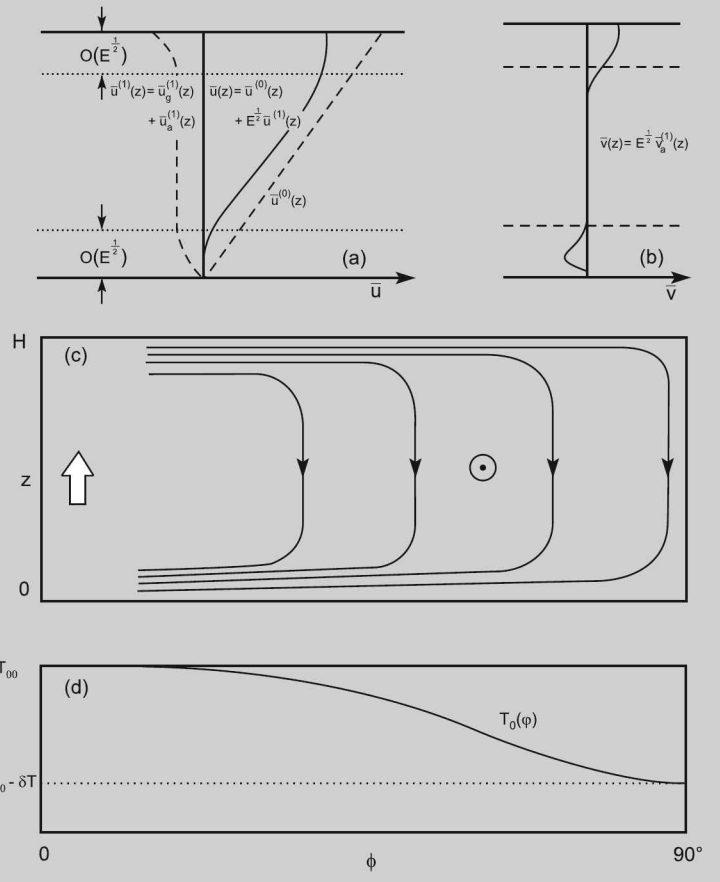

Figure 15.4 Zonally symmetric circulation in a Boussinesq spherical atmosphere of depth H that is driven thermally by imposing different temperatures along its rigid lower boundary and upper free surface. Motion is valid in the limit of fast rotation and small friction, which makes the *Ekman number* E small. The solution accurate to $O(E^{\frac{1}{2}})$: $\overline{\boldsymbol{v}} = \overline{\boldsymbol{v}}^{(0)} + E^{\frac{1}{2}}\overline{\boldsymbol{v}}^{(1)}$, is characterized by a strong zonal jet, with meridional motion confined to shallow boundary layers along the bottom and top. (a) Zonal motion. (b) Meridional motion. (c) Streamfield in a meridional cross section. (d) Meridional profile of imposed temperature. Adapted from Charney (1973) with permission of Kluwer Academic Publishers.

Hence, in the interior, poleward motion vanishes, whereas $\overline{w}^{(2)}$ is independent of height, equal to $\overline{w}^{(2)}(H)$. Air expelled from the upper boundary layer drives a gentle $O(E)$ subsidence in the interior. Subsiding air must be absorbed in another boundary layer at the bottom surface.

The lower boundary is a rigid surface. Consequently, motion there has the form of a conventional Ekman layer. Inside the lower boundary layer, the stretching transformation

$$z = E^{\frac{1}{2}}\xi \tag{15.37}$$

magnifies sharp changes. It makes viscous terms comparable to others in the momentum balance there, preserving the order of the governing equations. Then, at $O(E^{\frac{1}{2}})$, the momentum equations reduce to the Ekman balance

$$-f\overline{v}_a^{(1)} = K\frac{\partial^2\overline{u}_a^{(1)}}{\partial\xi^2} \tag{15.38.1}$$

$$f\overline{u}_a^{(1)} = K\frac{\partial^2\overline{v}_a^{(1)}}{\partial\xi^2}, \tag{15.38.2}$$

with the geostrophic contribution again automatically satisfied by $\overline{u}_g^{(1)}$. Requiring the total solution accurate to $O(E^{\frac{1}{2}})$ to satisfy (15.21.6) and reduce to the inviscid behavior outside the boundary layer yields the boundary conditions

$$\overline{u}_g^{(1)} + \overline{u}_a^{(1)} = 0 \qquad \overline{v}_a^{(1)} = 0 \qquad \xi = 0 \tag{15.38.3}$$

$$\overline{u}_a^{(1)} \sim 0 \qquad \overline{v}_a^{(1)} \sim 0 \qquad \xi \to \infty. \tag{15.38.4}$$

The boundary value problem (15.38) has solution

$$\overline{u}_a^{(1)}(\xi) = -\overline{u}_g^{(1)} e^{-\gamma\xi} cos\gamma\xi \tag{15.39.1}$$

$$\overline{v}_a^{(1)}(\xi) = \overline{u}_g^{(1)} e^{-\gamma\xi} sin\gamma\xi, \tag{15.39.2}$$

which is analogous to the Ekman structure in Fig. 13.3 (Fig. 15.4a,b).

Because $\overline{v}$ vanishes in the interior, poleward mass transfer inside the upper boundary layer must be exactly compensated by equatorward mass transfer inside the lower boundary layer. This requires $\overline{v}_a^{(1)}$ to satisfy the condition

$$\begin{aligned} E\int_0^\infty \overline{v}_a^{(1)} d\xi &= -E\int_0^\infty \overline{v}_a^{(1)} d\zeta \\ &= E\frac{KR}{aHf^2}\frac{\partial T_0}{\partial\phi}. \end{aligned} \tag{15.40.1}$$

Similarly, thermal wind (15.24) implies

$$\overline{u}_g^{(1)} = \frac{R}{aH\gamma f}\frac{\partial T_0}{\partial\phi} \tag{15.40.2}$$

for the $O(E^{\frac{1}{2}})$ geostrophic motion. Equations (15.40) complete the solution to this order.

Figure 15.4 illustrates the motion for the profile $T_0(\phi) = T_{00} - \delta T sin^4\phi$ (Fig. 15.4d). This temperature structure is symbolic of the distribution of radiative heating (Fig. 1.34c). At low latitude, it is sufficiently flat for the solution to remain valid up to the equator. The motion characterizes a zonally symmetric Hadley cell, one that extends from the equator to the pole. Air heated near the equator rises, entering the Ekman layer at the upper boundary. It then spirals poleward in a strong westerly jet, which maximizes at $z = H$. At extratropical latitudes, air is expelled from the upper Ekman layer, sinking through the interior. It eventually enters the Ekman layer at the lower boundary, wherein it returns equatorward. In the interior, forces are in geostrophic balance. Horizontal motion there is zonal and parallel to isotherms. Meridional heat flux therefore vanishes. Poleward heat transfer is thus confined to the shallow Ekman layers at the upper and lower boundaries.

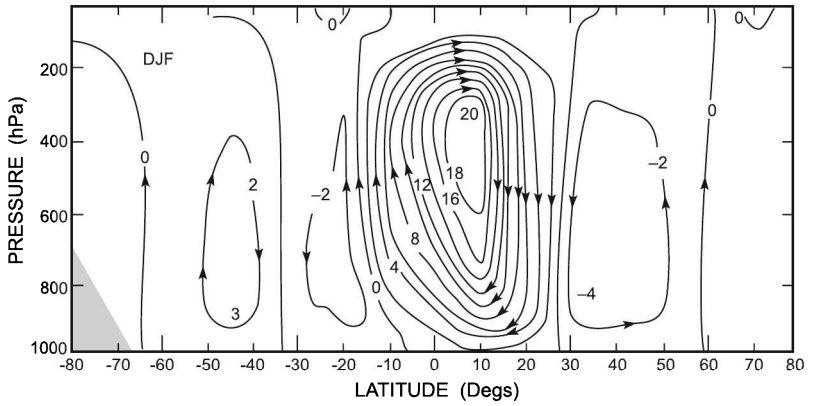

Figure 15.5 Zonal-mean meridional streamfunction observed during December–February. Meridional overturning equatorward of 30° comprises the Hadley circulation, which is strongest in the winter hemisphere. Poleward of downwelling is meridional overturning of opposite sense, Ferrell cells that prevail at mid-latitude. Adapted from Peixoto and Oort (1992).

The Ekman layers have thickness that is $O(E^{\frac{1}{2}})$. Meridional motion, $\overline{v}$, inside the Ekman layers is likewise $O(E^{\frac{1}{2}})$. Net poleward heat flux is thus $O(E)$. As Ω increases, $E \to 0$. So then does poleward heat transfer by the zonally symmetric circulation, which becomes increasingly inhibited or choked by rotation.

Plotted in Fig. 15.5, in zonal-mean motion, is the observed meridional circulation of the atmosphere. It qualitatively resembles the idealized Hadley cell – but only in the tropics. Rising motion appears near the equator in the summer hemisphere. It coincides with the ITCZ and organized latent heat release (Fig. 9.41). That rising motion is compensated in the subtropics of each hemisphere by sinking motion, chiefly in the winter hemisphere. Strong meridional motion appears near the tropopause and the Earth's surface, but only equatorward of 30°. Like subsidence, that ageostrophic motion is found chiefly in the winter hemisphere. It is there that the meridional temperature gradient and vertical wind shear are steepest (15.40); cf. Figs. 6.3, 6.4.

The limited extent of the Hadley cell can be understood from conservation of angular momentum, as discussed at the beginning of this chapter. Air moving poleward in the upper troposphere is deflected by the Coriolis force. To conserve angular momentum, it accelerates into strong westerlies (see Fig. 15.11a). The westerly acceleration, however, is observed only out to the poleward flank of the Hadley cell. The latter coincides with the subtropical jet, where westerlies maximize (cf. Fig. 1.8). At higher latitude, the thermally direct Hadley cell is replaced by a thermally indirect *Ferrell cell* (cf. Fig. 1.35). There, air sinks at low latitude and rises at high latitude.[4] In contrast to the Hadley cell, which is driven thermally by heating at low latitude, the Ferrell cell is driven mechanically by zonally asymmetric disturbances. They develop in strong

[4] This thermally indirect motion is actually an artifact of the Eulerian mean along latitude circles. In other representations, it disappears (see, e.g., Holton, 2004). For this reason, the Ferrell cell is not the principal mechanism of meridional heat transfer at extratropical latitudes.

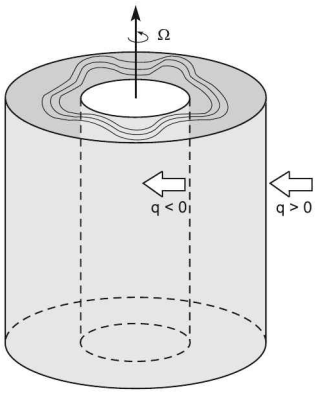

Figure 15.6 Schematic of a rotating cylindrical annulus that is driven thermally by imposing high temperature along its outer wall and low temperature along its inner wall.

westerlies that flank the Hadley cell. Associated with synoptic weather systems, those transient disturbances dominate the extratropical circulation, driving it out of zonal symmetry (Fig. 1.9).

15.3 HEAT TRANSFER IN A LABORATORY ANALOGUE

Insight into why the observed meridional circulation differs from the zonally symmetric model comes from laboratory simulations. A rotating cylindrical annulus (Fig. 15.6) is driven thermally by imposing high temperature along its outer wall, which represents the equator, and low temperature along its inner wall, which represents the pole. Figure 15.7 shows motion at the upper surface that is observed in the rotating frame, as a function of increasing rotation rate Ω. At slow rotation, the motion is zonally symmetric. It has the form of a thermally-direct Hadley cell, but with motion deflected into the zonal direction. Fluid along the upper surface gradually spirals inward, converging at the inner wall, where it sinks. As Ω increases, fluid moving inward experiences an intensified Coriolis force. Motion is therefore deflected increasingly into the zonal direction, parallel to isotherms. It forms a strong zonally symmetric jet in the interior, where forces are in geostrophic balance. Radial heat transfer then becomes confined to shallow Ekman layers that form along the upper and lower boundaries. With increasing Ω, that heat transfer decreases like E.

Beyond a critical rotation rate, zonally asymmetric disturbances appear. They develop from a steep temperature gradient that forms in the interior when radial heat transfer is choked. The zonally symmetric stratification is then strongly baroclinic. It therefore possesses available potential energy. By thermal wind balance (12.11), the radial temperature gradient is accompanied by strong vertical shear. Together, these features render the zonally-symmetric circulation *baroclinically unstable* (Chap. 16). Small disturbances to the flow then amplify by converting available potential energy of the zonal-mean state to eddy kinetic energy. Baroclinic disturbances accomplish this by transferring heat radially in *sloping convection*. Warm inward-moving fluid overrides heavier fluid and ascends. Simultaneously, cool outward-moving fluid undercuts lighter fluid and descends (cf. Fig. 15.3). The result is net heat transfer inward.

Behavior similar to that in Fig. 15.7 occurs at constant Ω if the imposed temperature contrast exceeds a critical value. It too renders the zonally symmetric circulation baroclinically unstable. Asymmetric heat transfer by baroclinic disturbances occupies much of the interior. Consequently, it is far more efficient than the $O(E)$ heat transfer

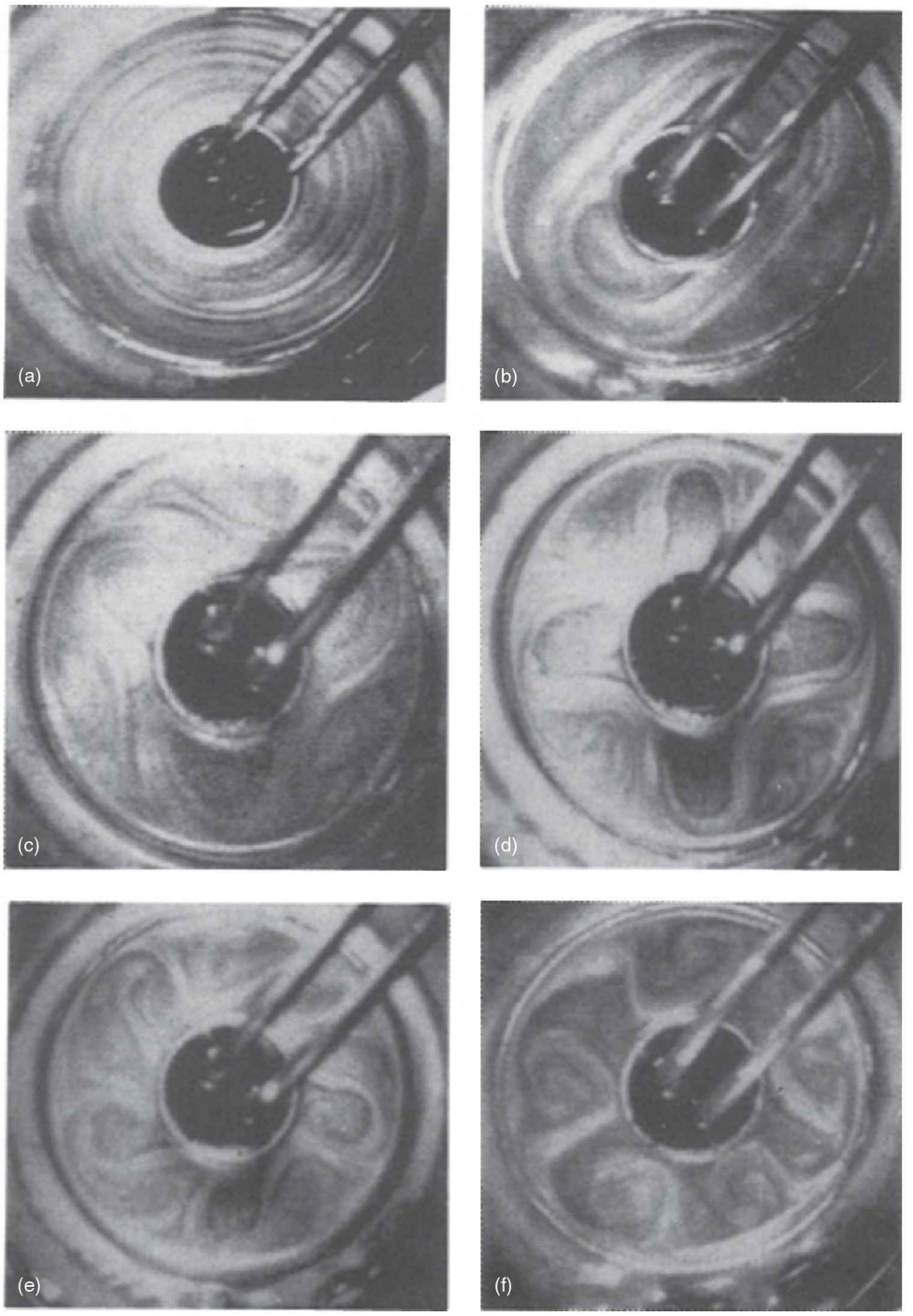

Figure 15.7 Surface flow pattern in the rotating cylindrical annulus for fixed temperature contrast and as a function of increasing rotation rate. Adapted from Hide (1966).

of the zonally symmetric circulation. Owing to rotation, the latter is confined inside shallow Ekman layers along the upper and lower surfaces. Sloping convection, although more complex, achieves the same result as the zonally symmetric circulation: it lowers the overall center of gravity, releasing available potential energy.

The dominant baroclinic disturbance has zonal wavelength that decreases with increasing rotation rate (Fig. 15.7b–e). At slow Ω, the circulation contains only wavenumbers 0 and 1; it is almost zonally symmetric. At intermediate Ω, wavenumbers 2 and 3 appear. Faster rotation leads to wavenumbers 5 and greater. In certain ranges of Ω, the annulus circulation resembles observed structure in the troposphere. The pentagonal structure in Fig. 15.7e is similar to patterns that are observed in the Southern Hemisphere (Fig. 2.10). There, the storm track is continuous, almost zonally symmetric (cf. Fig. 15.10b). Synoptic weather systems inside it often appear uniformly spaced in longitude, assuming baroclinic modal structure of the cylindrical annulus. At sufficiently fast rotation, the dominant wavelength in the annulus becomes small enough to make the disturbance itself unstable.[5] Undulations then wrap up, forming closed vortices. Attaining finite amplitude, those eddies transfer heat efficiently by mixing fluid across the annulus. This process acts to homogenize the horizontal distribution of temperature. It thus acts to restore barotropic stratification, eliminating strong vertical shear while exhausting available potential energy.

In the troposphere, the nonuniform distribution of radiative heating and cooling (Figs. 1.34c; 9.41b) continually drives thermal structure into baroclinic stratification. It therefore continually generates available potential energy, which fuels baroclinic disturbances. Baroclinicity is strongest at mid-latitudes, between the tropics, which experience radiative heating, and polar latitudes, which experience radiative cooling. Associated with steep meridional temperature gradient and steep vertical shear (Figs. 6.3, 6.4), strong baroclinicity coincides with the subtropical jet (Fig. 1.8). Synoptic disturbances along the poleward flank of the jet amplify through baroclinic instability. By transferring heat poleward in sloping convection, they limit the meridional temperature gradient, vertical shear, and hence the strength of the jet. In the stratosphere, the horizontal distribution of radiative heating and cooling is comparatively uniform. Baroclinicity therefore remains weak. Supported by strong static stability (15.19.2), this feature of the stratosphere limits available potential energy.

By transferring heat poleward, baroclinic disturbances and the Hadley circulation make the general circulation of the troposphere behave as a heat engine (Fig. 6.7). Air is heated at high temperature while near the equator and surface. After being displaced upward and poleward, it is cooled at low temperature. The Second Law then implies that, over a thermodynamic cycle (e.g., during a circuit between the tropics and extratropics), an individual air parcel performs net work. Kinetic energy produced in this fashion maintains the circulation against frictional dissipation. In the troposphere, about half of the dissipation of organized kinetic energy takes place inside the planetary boundary layer, where turbulent mixing is strong (Sec. 13.1.2). Kinetic energy is then cascaded efficiently to small scales, where it is absorbed by molecular

[5] Vertical shear of the disturbance reinforces that of the zonal-mean flow. This makes shear strong enough locally to render motion there baroclinically unstable. A parallel exists in the Northern Hemisphere. Planetary waves reinforce zonal-mean shear in the North Pacific and North Atlantic. Intensified shear there forms localized storm tracks, where conditions are favorable for the amplification of baroclinic weather systems (Sec. 15.4.2).

diffusion. The remainder takes place in the free atmosphere, through turbulence that is generated by dynamical instability and convection and, indirectly, through radiative damping of temperature anomalies (Secs. 14.7, 8.6).

15.4 QUASI-PERMANENT FEATURES

The observed circulation varies with horizontal position and time. In the troposphere, much of the variability is concentrated in synoptic weather systems, which dominate the extratropical circulation (Fig. 1.9). Averaging over a season removes those disturbances. The seasonal-mean circulation is smoother. Nonetheless, it too varies with horizontal position and time of year. The respective features characterize local climate and how it varies from one region to another and between seasons. Those variations are forced by the annual drift of solar insolation (Fig. 1.33). The latter modifies the TOA energy budget and hence local values of net radiation (Fig. 1.34c). Local conditions are also influenced by topography of the Earth's surface: elevated terrain and its interaction with the circulation. In addition, they are influenced by temperature of the Earth's surface, which dictates local heat transfer to the atmosphere.

15.4.1 Thermal properties of the Earth's surface

Surface temperature is shaped by optical and thermal properties, which determine the fate of energy that is supplied to or removed from the Earth's surface through radiation. The most important are the contrasting thermal properties of continent and ocean:

Ocean

- Water has a large specific heat capacity (Appendix B). A specified absorption of heat therefore results in a comparatively small increase of temperature (2.16). A specified removal of heat results in a comparatively small decrease of temperature.
- Because it is a fluid system, ocean is mobile. Heat that is supplied to or removed from the surface introduces anomalous energy which can therefore be redistributed downward efficiently through convection. Anomalous energy is thereby diluted over a deep volume.
- Radiative heating is offset by evaporative cooling, which transfers latent heat to the atmosphere.

These features combine to moderate the seasonal variation of ocean temperature. During summer, ocean becomes only modestly warmer than its annual-mean temperature. During winter, it becomes only modestly cooler.

Continent

- The specific heat capacity of land is comparatively small, less than 20% of that of water. The same absorption or removal of heat therefore results in a comparatively-large increase or decrease of temperature.
- Because it is solid, land is immobile. Heat that is supplied to or removed from the surface introduces anomalous energy which can therefore be redistributed downward

only through conduction. The latter is orders of magnitude slower than convection. Anomalous energy therefore remains concentrated in a shallow layer beneath the surface.

- Without evaporative cooling, radiative heating is offset only by sensible heat transfer to the atmosphere, which is comparatively small (Fig. 1.32).

These features combine to produce a large seasonal variation of continental temperature. During summer, continent becomes sharply warmer than its annual-mean temperature. During winter, it becomes sharply colder than its annual mean temperature – especially in the Northern Hemisphere, where landmasses extend into polar regions. How much warmer and colder it becomes is governed by the annual swing of solar insolation, which increases with latitude (Fig. 1.33).

These differences in the annual variation of temperature introduce large differences of temperature between continent and ocean during an individual season. During summer, continent becomes warmer than neighboring ocean. Overlying air then experiences anomalous heating. This makes it anomalously warm, while forcing upward motion across isentropic surfaces. By the hypsometric relation (6.12), the vertical spacing of isobaric surfaces in the lower troposphere is expanded. Isobaric surfaces near the ground are therefore displaced downward. This introduces low pressure over continent. Frictional convergence into low surface pressure reinforces upward motion (Sec. 12.3). During the same season, ocean is anomalously cool. It exerts the opposite influence. Overlying air then experiences anomalous cooling. This makes it anomalously cold, while forcing downward motion across isentropic surfaces. By the hypsometric relation, the vertical spacing of isobaric surfaces in the lower troposphere is pinched. Isobaric surfaces near the ocean surface are therefore displaced upward. This introduces high pressure over ocean. Frictional divergence from high surface pressure reinforces downward motion.

During winter, the horizontal pattern is reversed. Continent then becomes anomalously cold, favoring high surface pressure and downward motion. Conversely, ocean becomes anomalously warm, favoring low surface pressure and upward motion.

Plotted in Fig. 15.8 is the annual variation of surface temperature, displayed in the difference between the solstices: January–July. The annual variation is dominated by large changes at high latitudes of the Northern Hemisphere, where landmasses are prevalent. In the Siberian Arctic, wintertime temperature is as much as 60 K colder than summertime temperature. It is almost that much colder than the neighboring Pacific, where wintertime temperature is depressed comparatively little below its annual mean. Wintertime temperature is also sharply depressed in the Canadian Arctic. Like Siberia, it is therefore sharply colder than neighboring ocean. At lower latitudes, the annual variation of temperature becomes weak. This latitudinal dependence mirrors that in the annual swing of insolation (Fig. 1.33). Although weaker, distinct maxima appear in desert regions: the Sahara and Kalahari in Africa, the Atacama in South America, and central Australia. Situated in the subtropics, those regions experience strong warming during summer, when they remain relatively cloudless. In the Southern Hemisphere, the annual variation of temperature is conspicuously smaller than in the Northern Hemisphere. This distinction reflects the distribution of continent and ocean. Except for Antarctica, landmasses in the Southern Hemisphere are confined to lower latitude. Unlike Asia and North America, they are surrounded by ocean, which moderates temperature extremes.

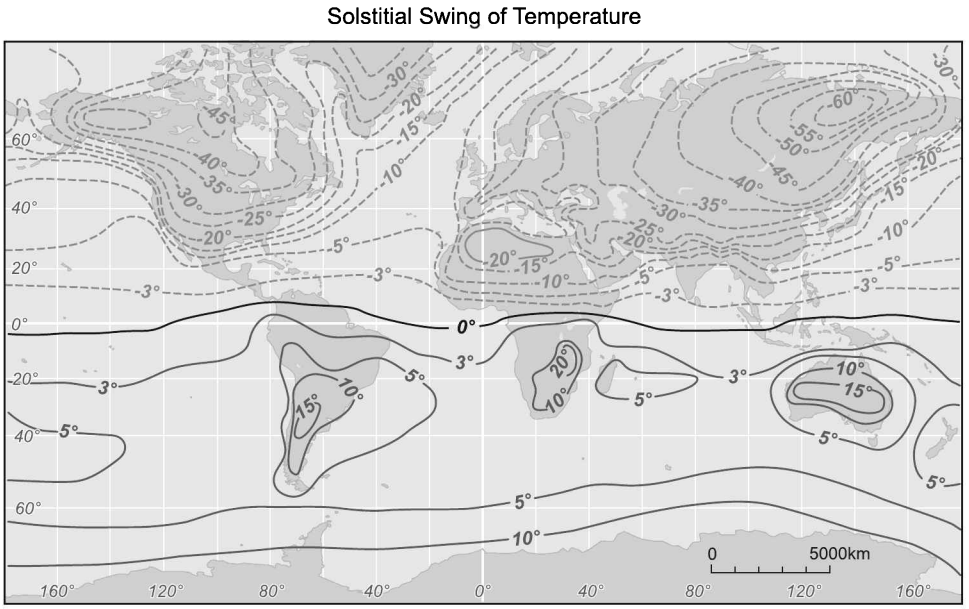

Figure 15.8 Annual swing of surface temperature: January–July. See color plate section: Plate 12.

15.4.2 Surface pressure and wind systems

Large anomalies of surface temperature introduce localized atmospheric heating and cooling, especially during the solstices. Augmenting them are anomalies of surface terrain, orographic features that displace the air stream vertically. Both force planetary waves. The latter are manifested at the surface by zonal asymmetries in the circulation.

Plotted in Fig. 15.9a is the distribution of SLP and surface motion during January. The Northern Hemisphere is punctuated by strong anomalies. They reflect anomalous surface temperature. Dominating Asia is the *Siberian High*. It coincides with anomalously cold Arctic surface, which cools overlying air. Over North America is the *Canadian High*, likewise coincident with cold Arctic surface. About both features is anticyclonic motion. It is accompanied by frictional divergence. The latter must be compensated aloft by subsidence. Contrasting with those continental regions is neighboring ocean. Comparatively warm, it is dominated by low-pressure anomalies: the *Icelandic Low* over the North Atlantic and the *Aleutian Low* over the North Pacific. Cyclonic motion about centers of low pressure is accompanied by frictional convergence. Over the subtropics are secondary centers of high pressure: the *Bermuda-Azores High* and the *Hawaiian High*. Those features are weaker than anomalies at higher latitude. They comprise the *subtropical high*, which forms beneath descending motion of the Hadley circulation. Divergent motion from those high-pressure centers, augmented by that from continental high pressure, fuels the north-easterly *trade winds* that prevail at low latitudes of the Northern Hemisphere. The trades converge into low pressure along the equator, which coincides with the ITCZ and nearly windless conditions (the *doldrums*). Positioned just south of the equator, the ITCZ lies beneath ascending motion of the Hadley circulation. Accompanying it is deep convection, with heavy

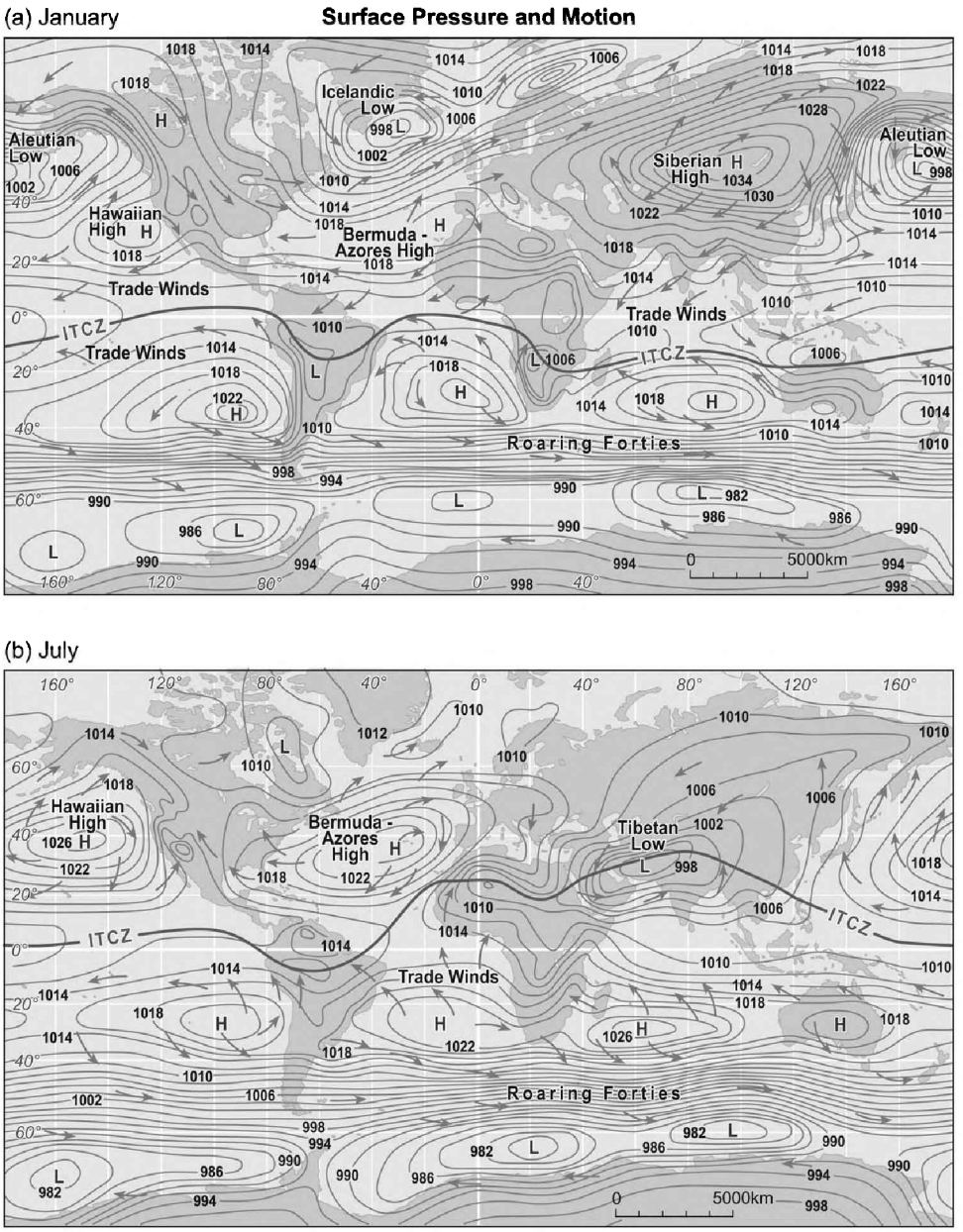

Figure 15.9 Climatological-mean SLP and surface motion for (a) January and (b) July. See color plate section: Plate 13.

precipitation (Figs. 1.30b; 9.41). Centers of low pressure form in the tropical Southern Hemisphere (in summer) over heated continent: equatorial Africa, South America, and northern Australia. In coastal regions, such as northern Australia, such structure defines the *monsoon low*; see Fig. 15.11c. These centers of convection contribute substantially to ascending motion of the Hadley circulation. Farther south are

intensified centers of high pressure. Situated in the summer hemisphere, they form over comparatively cool ocean. Like counterpart features in the winter hemisphere, those centers comprise the subtropical high. Frictional divergence from them fuels the southeasterly trade winds in the Southern Hemisphere. Mirroring northeasterly trade winds opposite the equator, they converge into the ITCZ.

Plotted in Fig. 15.9b is the pattern for July. The distribution of highs and lows is now reversed. In the Northern Hemisphere (in summer), lows form over heated continent. Conversely, highs form over comparatively cool ocean. Asia is dominated by the *Tibetan Low*. Accompanied by frictional convergence, it is associated with the Asian monsoon. Counterparts are visible over heated regions of Africa and North America, albeit weaker. Over comparatively cool ocean are the *Bermuda-Azores High* and the *Hawaiian High*. They are sharply amplified, now prevailing across the North Atlantic and North Pacific. As during January, frictional divergence from those high-pressure centers fuels the north-easterly trade winds in the Northern Hemisphere, which converge into the ITCZ. During July, the ITCZ is displaced well north of the equator, as far as the Tibetan Low and the Asian monsoon. In the Southern Hemisphere (in winter), the subtropical high is almost zonally uniform. Because the Earth's surface in the Southern Hemisphere is chiefly maritime, it develops only weak temperature contrast (Fig. 15.8). This leads to centers of high pressure in the subtropics forming over ocean as well as continent. Frictional divergence from those centers fuels southeasterly trade winds of the Southern Hemisphere. After crossing the equator, they eventually converge into the ITCZ. Also exhibiting strong zonal symmetry is low pressure at polar latitude. Situated over the Southern Ocean, it circumscribes the much colder Antarctic.

Notice that, at mid-latitudes of the Southern Hemisphere, isobars remain zonal throughout the year. They are accompanied by circumpolar westerlies, the *Roaring Forties*. By contrast, at mid-latitudes of the Northern Hemisphere, the zonal circulation is disrupted by strong localized anomalies – especially during winter, when they extend to high latitude. Much stronger than counterpart features in the Southern Hemisphere, those anomalies represent planetary waves. They are amplified in the Northern Hemisphere by strong anomalies of surface heating and cooling and major orographic features.[6] These distinctions introduce hemispheric asymmetry into the general circulation.

Amplified planetary waves in the Northern Hemisphere yield a broken storm track. Plotted in Fig. 15.10, as a function of horizontal position, is the mean pressure of cyclonic depressions. It measures the average intensity of synoptic weather systems. During northern winter (Fig. 15.10a), synoptic weather systems in the Northern Hemisphere are concentrated over the North Atlantic and North Pacific. Those envelopes of cyclonic activity coincide with strong westerlies, steep meridional temperature gradient, and steep vertical shear (Figs. 1.9b, 6,3, 6.4). They represent the North Atlantic and North Pacific storm tracks. Closely related are the Icelandic Low and Aleutian Low, which reinforce westerlies to their south. Contrasting structure appears in the Southern Hemisphere (in summer). There, synoptic weather systems are distributed over longitude almost uniformly. That envelope of cyclonic activity represents the continuous storm track of the Southern Hemisphere, which circumscribes the Antarctic.

[6] During winter, these circulation anomalies tilt westward with height, signifying upward propagation of planetary wave activity (Sec. 14.5.2). In the stratosphere, the Aleutian Low is therefore replaced by the Aleutian High (Fig. 1.10b).

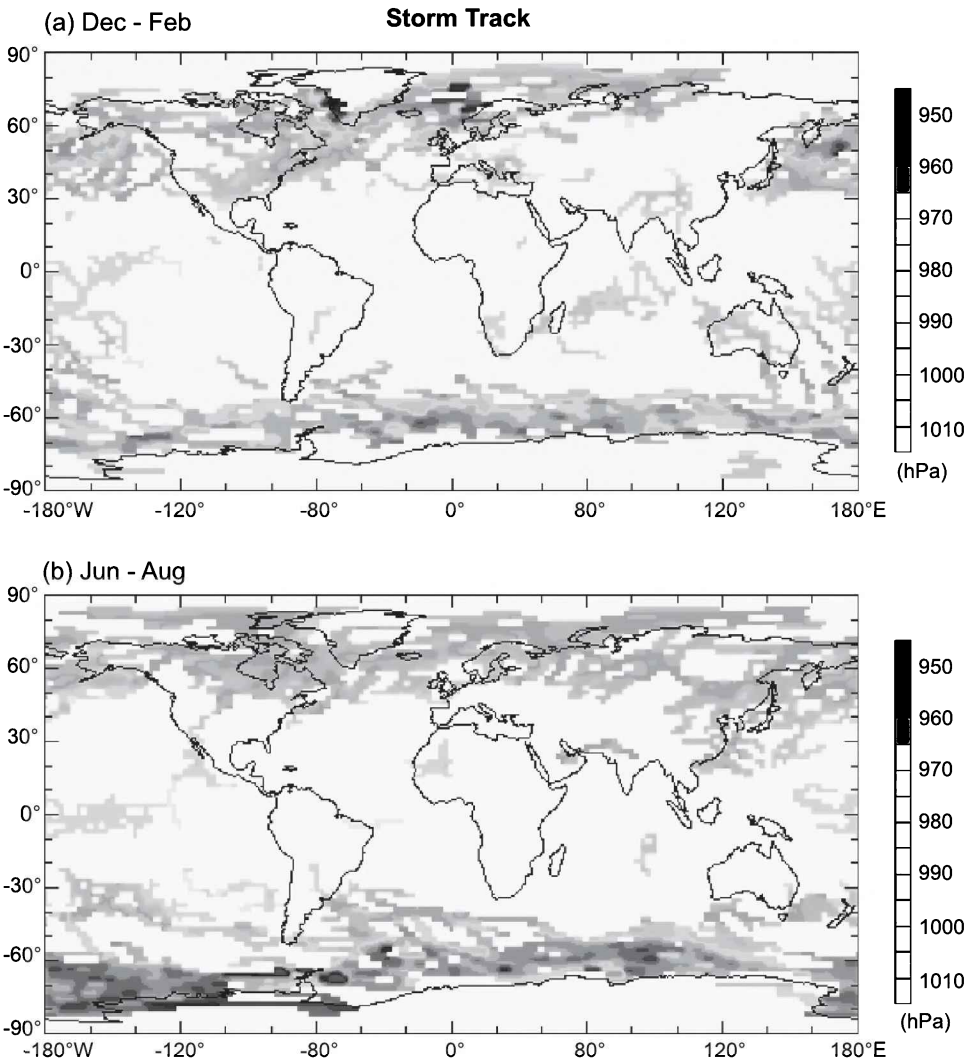

Figure 15.10 Mean intensity of cyclonic disturbances, measured by their depression of SLP, during (a) December–February 1984 and (b) June–August 1984. *Source*: http://data.giss.nasa.gov (10.07.10). See color plate section: Plate 14.

Much the same picture prevails during southern winter (Fig. 15.10b). Synoptic weather systems in the Southern Hemisphere thus develop at all longitudes. On individual days, they can assume a coherent global pattern, resembling baroclinic modal structure of the cylindrical annulus (Fig. 2.10).

15.4.3 Tropical circulations

At low latitude, the Coriolis force is weak. This feature of the momentum balance allows the tropical circulation to involve a greater contribution from the divergent

component of motion and to be thermally direct (Sec. 12.1). In the tropics, the temperature distribution is relatively flat (Fig. 6.3). Implied is little available potential energy to drive large-scale motion. The primary source of energy for the tropical circulation is, instead, latent heat release inside organized convection. The latter, in turn, follows from evaporative cooling of the ocean.

Precipitation inside the ITCZ exceeds evaporation from the underlying surface (Fig. 9.41). Moisture must therefore be imported from surrounding areas. Much of it converges in the easterly and equatorward trade winds that prevail at low latitude. The trades comprise the lower branch of the zonal-mean Hadley cell in Fig. 15.5. They develop when equatorward-moving air is deflected westward by the Coriolis force. Air subsiding in the subtropics from the upper branch of the Hadley cell dries the troposphere. It also stabilizes the troposphere through mechanisms discussed in Sec. 7.4.4. By inhibiting convection, subsidence in the descending branch of the Hadley cell maintains desert conditions. It is no accident that all major deserts on Earth are found in the subtropics.

Although the zonal-mean overturning in Fig. 15.5 is intuitively appealing, the actual Hadley circulation is not zonally uniform. It varies with longitude according to surface temperature and humidity, which determine upward fluxes of sensible and latent heat. The local intensity of the Hadley circulation is reflected in upper-tropospheric divergence. Plotted in Fig. 15.11a is the streamfield at 200 hPa. Divergent motion is visible along much of the equator. However, it is concentrated in three major centers: equatorial Africa, equatorial South America, and, by far the largest, the equatorial Indian Ocean and western Pacific. The latter coincides with warm ocean surface, where SST exceeds 26°C (Fig. 5.1). Inside centers of convection, deep heating elevates isobaric surfaces in the upper troposphere (6.12). This favors anomalous high pressure above anomalous low pressure. Beneath each center of divergence at 200 hPa is convergent motion at 850 hPa (Fig. 15.11b). To conserve potential vorticity (12.36), that air motion spins up cyclonically (e.g., in the monsoon low over northern Australia). After being convected to the upper troposphere, it then diverges from the convective center, spinning up anticyclonically (Fig. 15.11a).[7] As air streams poleward at 200 hPa, it is deflected by the Coriolis force, forming strong westerlies that prevail at midlatitudes. Intensified jets appear to the east of Asia and North America, where isotachs exceed 45 m/s (shaded). Associated with steep vertical shear, they coincide with the North Atlantic and North Pacific storm tracks (cf. Fig. 15.10a).

In addition to the Hadley circulation, the tropics involve two other classes of circulation. They too are thermally direct, as well as zonally asymmetric. Monsoon circulations develop during summer over subtropical landmasses, such as India and northern Australia, which become warmer than neighboring ocean. Presented in Fig. 15.11c is instantaneous SLP and IR imagery under conditions characteristic of the Australian monsoon. Over the Northern Territory is the monsoon low. Much of that region is covered by cold high cloud. It marks divergent motion in the upper troposphere. Representing cirrus anvil from deep cumulonimbus, cold cloud spirals outward anticyclonically. It reflects diverging air that spins up anticyclonically to conserve potential vorticity. Convection in the monsoon circulation is fueled by moisture convergence at low levels. The latter is reinforced near the surface by frictional convergence into the

[7] Notice the reversal of curvature over South America where streamlines cross the equator.

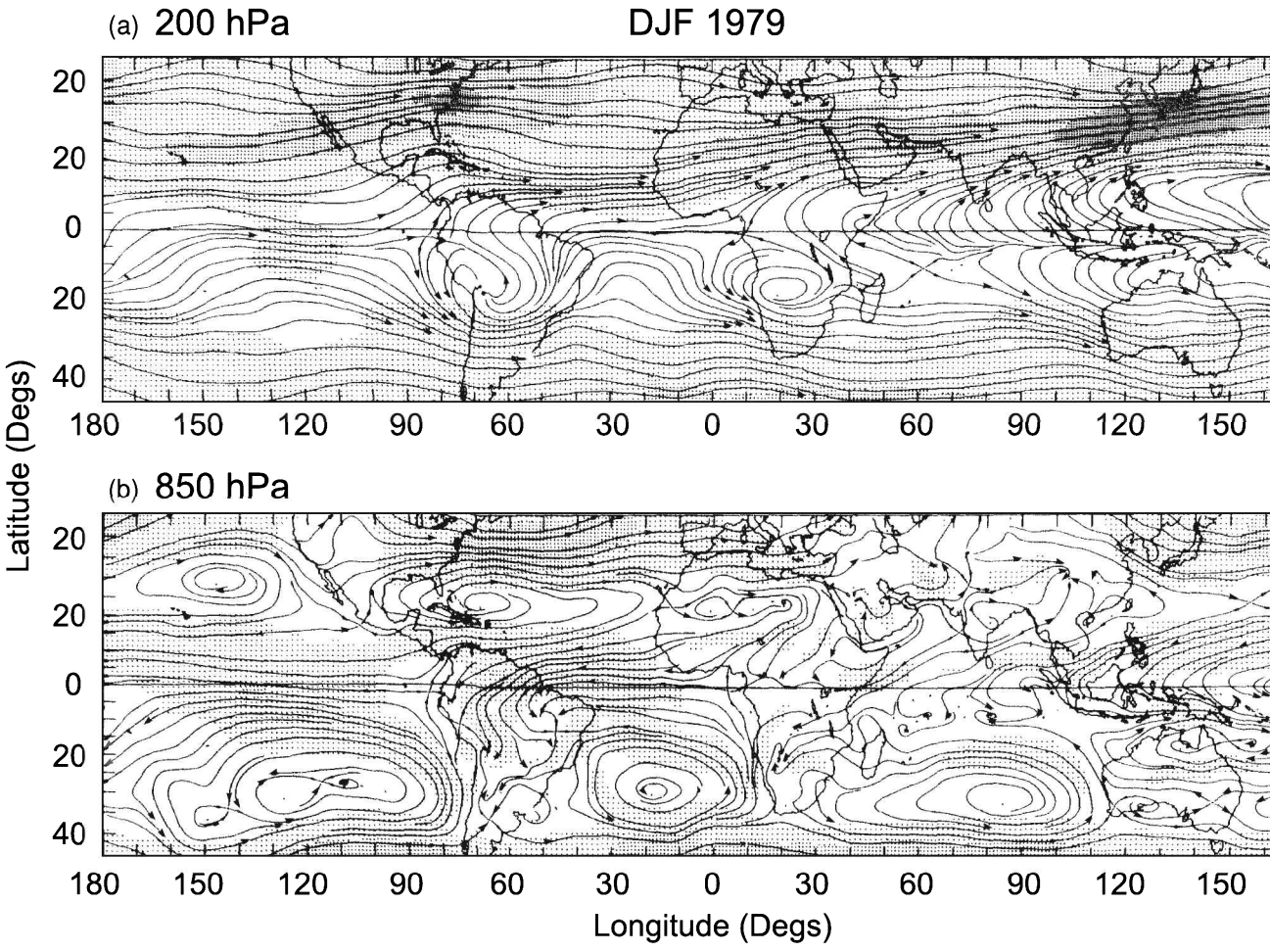

Figure 15.11 (*continued*)

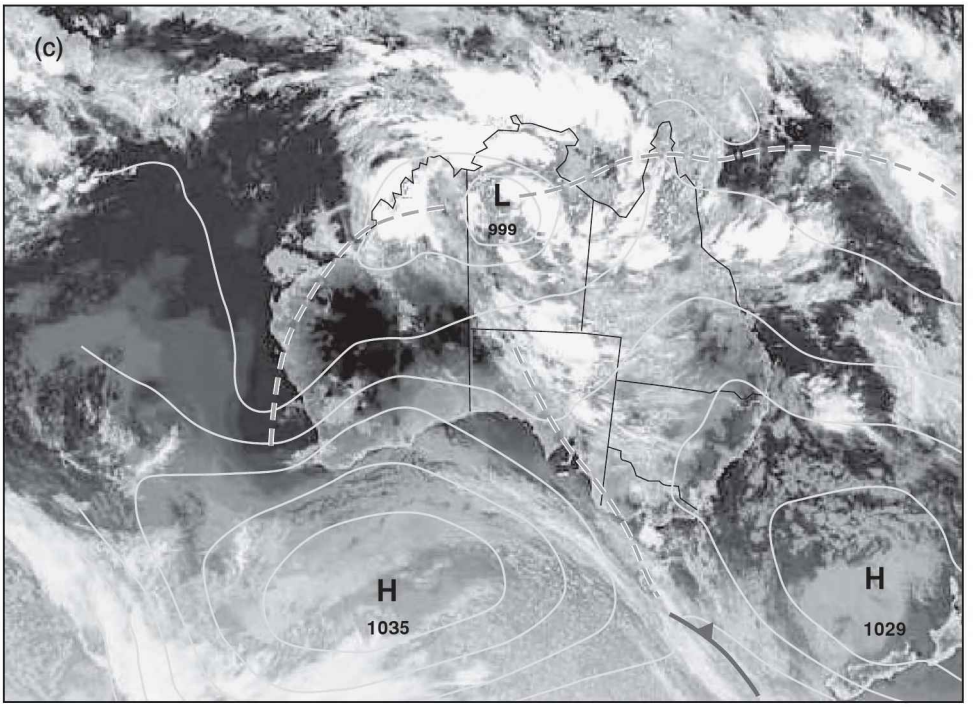

Figure 15.11 Streamlines and wind speed (stippled) during December 1978–February 1979 at (a) 200 hPa and (b) 850 hPa. *Trade winds* are manifested at 850 hPa by southwestward flow across the tropical western Pacific, Atlantic, and Indian oceans. Outflow at 200 hPa over tropical Africa, South America, and Indonesia assumes anticyclonic curvature as it diverges away from those convective centers. Note the reversal of curvature to conserve potential vorticity as streamlines cross the equator. Strong jets at 200 hPa east of North America and Asia mark the *North Atlantic* and *North Pacific storm tracks* (cf. Fig. 9.41), where the mean temperature gradient is steep and cyclone development is favored. Stipling of isotachs at $|\boldsymbol{v}_h| = 15$–30 m s^{-1}, 30–45 m s^{-1}, > 45 m s^{-1}. Adapted from Lau (1984). (c) Instantaneous SLP and IR imagery under conditions typical of the Australian monsoon. Deep convection is organized by the monsoon low, as well as trough axes that emanate from it. Cirrus blow off at upper levels spirals outward anticyclonically. See color plate section: Plate 15.

monsoon low. The convergence of water vapor increases θ_e near the surface, rendering the lower troposphere potentially unstable (Fig. 7.12). Through mechanisms described in Sec 7.4.3, frictional convergence also leads to reduced vertical stability. These changes provide conditions favorable to deep convection, enabling air to reach the Level of Free Convection (LFC). From there, it accelerates upward through positive buoyancy, until reaching the Level of Neutral Buoyancy (LNB), which is typically between 250 and 150 hPa (Sec. 7.7).

The summer monsoon is an onshore circulation. It is analogous to a seabreeze circulation, which is likewise generated through a horizontal gradient of heating. Both may be understood from solenoidal production of horizontal vorticity, which occurs

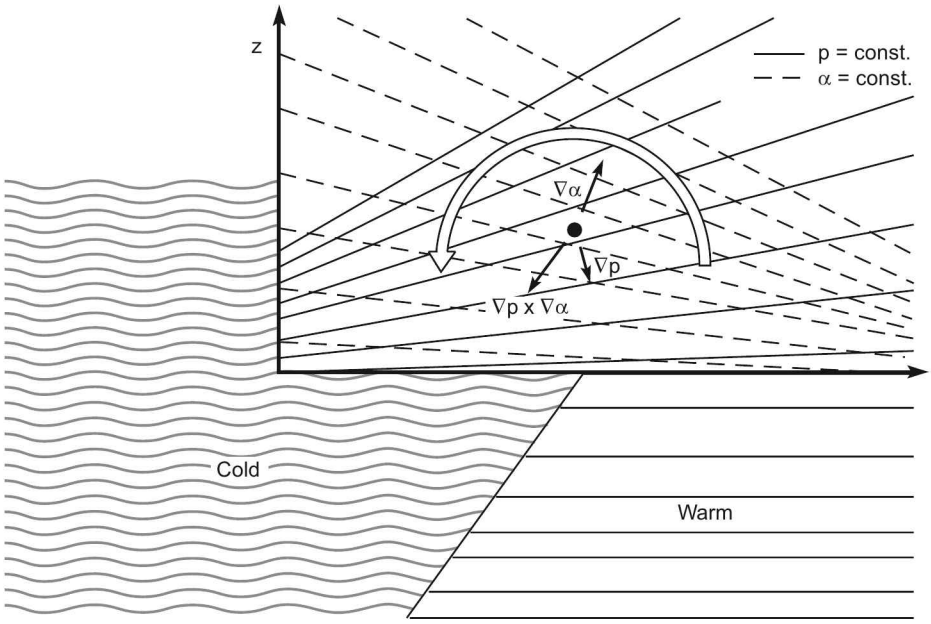

Figure 15.12 Schematic of a thermally-direct monsoon circulation that is established through solenoidal production of horizontal vorticity under baroclinic stratification. Heating over continent expands the vertical spacing of isobaric surfaces (solid), whereas it draws down isochoric surfaces (dashed) of larger α from aloft. The reverse occurs from cooling over ocean. The nonuniform distribution of heating drives isochoric surfaces out of coincidence with isobaric surfaces, producing baroclinic stratification.

under baroclinic stratification (Fig. 15.12). Nonuniform heating between continent and ocean introduces a horizontal variation of temperature. It drives isochoric surfaces (α = const) out of coincidence with isobaric surfaces. The budget of horizontal vorticity then includes a solenoidal production term, proportional to $\nabla p \times \nabla \alpha$. That source of horizontal vorticity is analogous to solenoidal production that appears in the budget of vertical vorticity (12.36). Derived from baroclinic stratification, it spins up horizontal vorticity as an onshore circulation, with upwelling over the region of heating and downwelling over the region of cooling.

The other class of circulation important in the tropics is the Walker cell, depicted in Fig. 1.36. The Walker cell is a zonally asymmetric overturning in the equatorial plane. It is characterized by upwelling over regions of heating and downwelling to the east and west. The Pacific Walker cell is forced by latent heating over the western Pacific, where ocean is anomalously warm. Low surface pressure in the equatorial western Pacific supports deep convection, in the same way it supports the monsoon circulation. Strong surface easterlies along the equator fuel convection with moisture that has been absorbed by air during its traversal of the western Pacific. There, SST in excess of 28°C provides an abundant source of water vapor (Fig. 5.1).

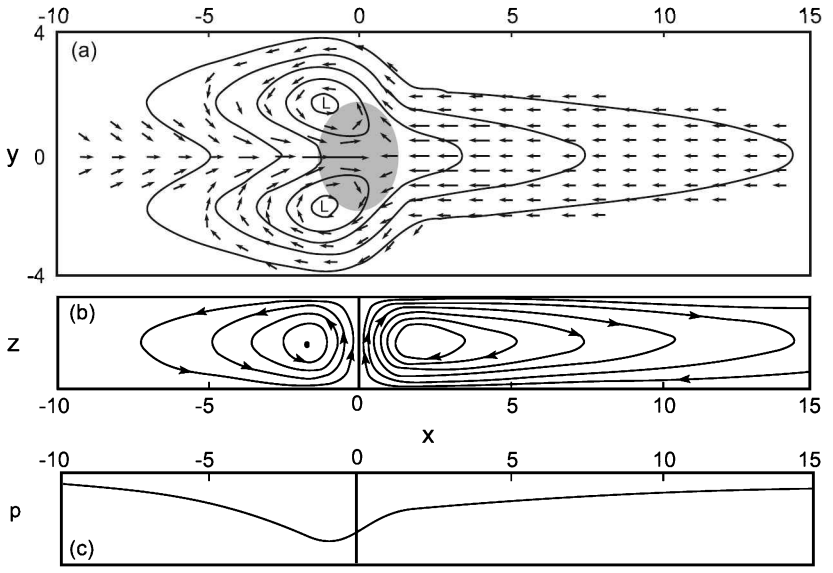

Figure 15.13 Zonally asymmetric circulation produced by a deep heating anomaly over the equator (shaded). (a) Planform view of surface motion. (b) Streamfield in a vertical cross section over the equator. (c) Surface pressure distribution. Adapted from Gill (1980).

Latent heating that drives zonal overturning in the Walker cell simultaneously drives meridional overturning. Associated with the Hadley circulation, it too is zonally asymmetric. Figure 15.13 plots the circulation produced by a localized and steady heating anomaly over the equator (shaded). At the surface, equatorial easterlies converge into the region of heating (Fig. 15.13a). Resembling the Pacific Walker cell, they are mirrored in the upper troposphere by equatorial westerlies (Fig. 15.13b). Surface low pressure forms just to the west of the heating anomaly (Fig. 15.13c). Ascending motion in the region of heating is flanked in the subtropics of each hemisphere by cyclonic gyres. Those features reinforce inflow along the equator to the west of the heating. They represent a Rossby wave mode that is trapped about the equator (see, e.g., Gill, 1982). Analogous structure is evident in the 200-hPa streamfield over the western Pacific, where deep convection is concentrated (Fig. 15.11a). Likewise for zonal flow to the east that comprises the Pacific Walker cell.

15.5 FLUCTUATIONS OF THE CIRCULATION

Beyond its annual variation, the general circulation also changes between years, as well as during individual seasons. Those changes comprise climate variability. They dominate the variation of regional properties (Fig. 1.38). Yet, because they are spatially incoherent, interannual changes need not contribute to the variation of global-mean properties. It is for this reason that the annual record of regional climate is generally incoherent with that of global-mean climate. Some components of climate

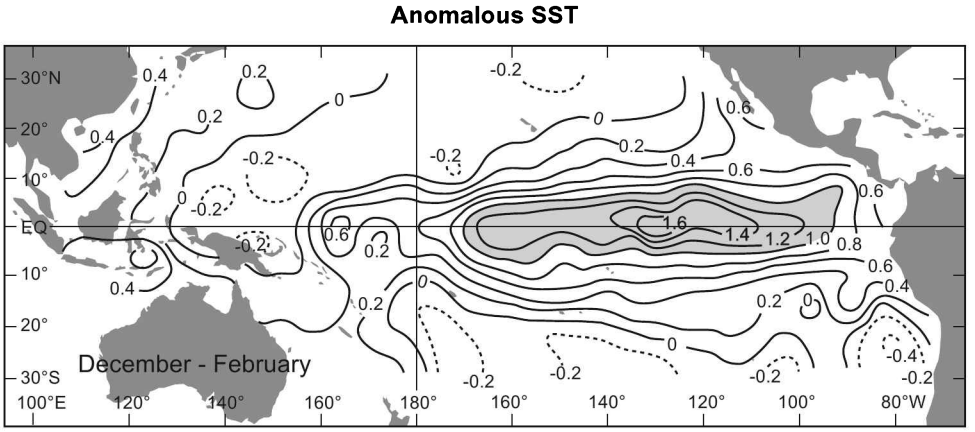

Figure 15.14 Anomalous SST (°K) during El Nino. After Rasmusson and Carpenter (1982).

variability, though mostly random, operate on a recurring basis and do possess spatial coherence.

15.5.1 Interannual changes

El Nino

The Pacific Walker cell fluctuates on interannual time scales. The respective changes characterize El Nino Southern Oscillation (*ENSO*). *El Nino* is a perturbation to the tropical circulation that occurs with a frequency of 3–5 years. It involves anomalously warm SST in the eastern and central Pacific (Fig. 15.14).[8] The equatorial Pacific is especially sensitive to temperature perturbations because, there, SST exceeds 26°C. Owing to exponential dependence in the Claussius-Clapeyron equation (4.39), small changes of SST produce large changes in evaporation and latent heat transfer to the atmosphere (Fig. 9.41). When the temperature anomaly in Fig. 15.14 is introduced, the warmest SST and convection, normally found in the western Pacific (Fig. 9.40a), shift eastward into the central Pacific.

El Nino involves a seesaw in surface pressure between the western and eastern Pacific: a longitudinal dipole. Known as the *Southern Oscillation*, this dipole shifts low pressure from the western Pacific and Indian ocean to the central and eastern Pacific. It is evidenced by the anti-correlation of pressure fluctuations in those regions (Fig. 15.15). During El Nino, SLP is anomalously low over the central and eastern Pacific, whereas it is anomalously high over the Indian ocean and western Pacific. The opposite phase of the Southern Oscillation is *La Nina* ("the girl"). SLP is then anomalously low over the Indian ocean and western Pacific, whereas it is anomalously high over the central and eastern Pacific.

ENSO upsets the pattern of tropical convection. Through anomalous latent heating, it perturbs the tropical circulation. In the Walker cell, upwelling is displaced from the

[8] The name El Nino ("the boy") refers to warm water off the coast of Peru that develops around Christmas.

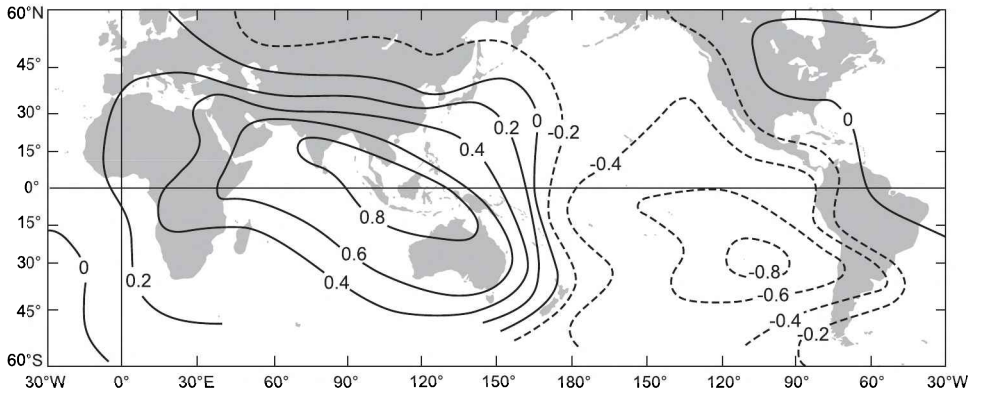

Figure 15.15 Correlation of monthly mean surface pressure in the Pacific with that at Jakarta. Oppositely phased variations in the eastern and western Pacific characterize the *Southern Oscillation*. Adapted from Berlage (1957).

equatorial western Pacific eastward into the central Pacific, along with downwelling to its east and west (Fig. 15.16); cf. Fig. 1.36. Subsidence is then positioned over the maritime continent and northern Australia. There, it inhibits monsoon activity during El Nino years. Those conditions favor drought and recurrent bush fire (McBride and Nichols, 1983); see Cover, discussion in Sec. 9.5.1, and color plate section.

ENSO is also felt at extratropical latitudes. Anomalous latent heating excites anomalous planetary wave activity that radiates poleward. Figure 14.20a plots anomalous

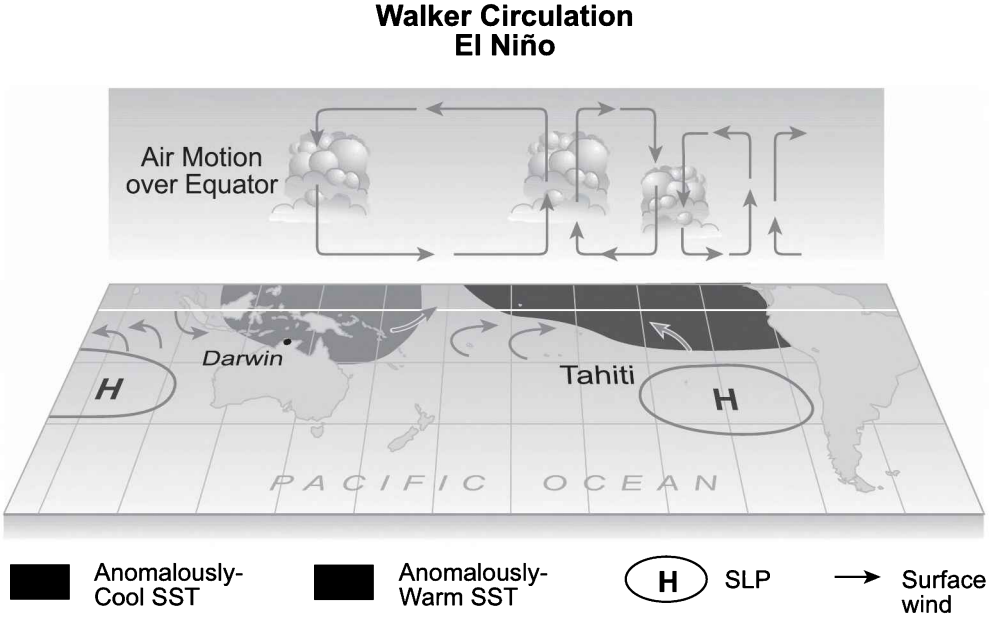

Figure 15.16 Disturbed Walker circulation during El Nino. Adapted from http://www.bom.gov.au (11.07.10). See color plate section: Plate 16.

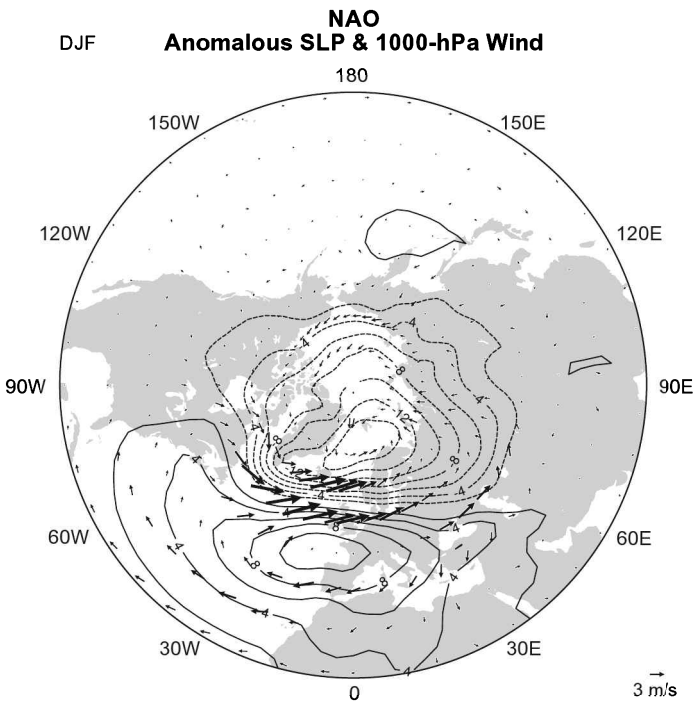

Figure 15.17 Anomalous SLP and 1000-hPa motion (scaled by 0.5) associated with the positive phase of the North Atlantic Oscillation (NAO). After Hurrel et al. (2003).

upper-tropospheric height for northern winters during El Nino, when convection is positioned in the central Pacific. A planetary wavetrain radiates poleward from anomalous convection. It is eventually refracted equatorward along a great circle route. Known as the *Pacific North American (PNA) pattern*, this perturbation to the height field modifies the extratropical circulation. It introduces a prominent ridge over western Canada, flanked to its east by a trough. The jet stream (wavy trajectory in Fig. 14.20a) is then deflected meridionally: northward over the western United States and Canada and southward over the eastern United States. The jet stream divides tropical and polar air (Fig. 6.3). Those deflections therefore introduce anomalously warm temperature over the western United States and Canada, but anomalously-cold temperature over the eastern United States. By perturbing the storm tracks, they also modify the development and movement of synoptic weather systems.

North Atlantic oscillation

Regional climate over Europe and Asia is moderated by maritime air, which is conveyed from the Atlantic by westerlies. This process is influenced importantly by the Icelandic Low and its equatorward complement, the Bermuda-Azores High (Fig. 15.9). The gradient between those features intensifies westerlies. Intensified with them is the advection of maritime air that moderates conditions over Europe and Asia.

The Icelandic Low and Bermuda-Azores High fluctuate between years, coherently but out of phase. These fluctuations form a meridional dipole in SLP. Known as the *North Atlantic Oscillation* (*NAO*), the dipole is plotted in Fig. 15.17. It is measured by the difference of SLP between the aforementioned sites. In its positive phase, the NAO reinforces the Icelandic Low and, simultaneously, the Bermuda-Azores High. Intensified westerlies between those features intensify the advection of maritime air, moderating conditions over northern Europe during winter and summer. In its negative phase, the NAO suppresses the Icelandic Low and the Bermuda-Azores High. This weakens westerlies across northern Europe, along with the advection of maritime air. In its place is colder air that advances southward from the North Sea and Arctic. The storm track is then displaced southward, toward southern Europe and the Mediterranean. So too are rain-bearing weather systems. Under these conditions, northern Europe and Asia experience winters that are anomalously cold and summers that are anomalously warm and dry.

The NAO is associated with much of the interannual variability over Europe and the northern Atlantic. It also influences the eastern seaboard of North America. There, anomalous southeasterlies advect maritime air. They also inhibit the outbreak and southward advance of cold air from the Canadian Arctic. Both changes moderate wintertime conditions.

Plotted in Fig. 15.18 is the anomalous wintertime temperature associated with positive phase of the NAO. Temperature is anomalously warm over northern Europe and Asia. The warm anomaly coincides with the region that experiences anomalous advection of warmer maritime air from the Atlantic (Fig. 15.17). Temperature is also anomalously warm over eastern North America. That warm anomaly bears a similar relationship to anomalous advection. Temperature is anomalously cold over north Africa and Labrador. Those regions experience anomalous advection of colder continental and Arctic air.

As for El Nino, zonal structure in the NAO involves changes of the planetary wave field. In its negative phase, the NAO weakens the Icelandic Low. Those conditions favor blocking highs over the North Atlantic, which impede the eastward migration of synoptic weather systems (Lejenas and Okland, 1983; Stein, 2008). They are associated with a modulation of planetary waves (Lejenas and Madden, 1992; Shabbar et al., 2001). The NAO also has implications for the tropical circulation. Divergent motion from the Bermuda-Azores High fuels southeasterly trade winds. The NAO should therefore interact with the Hadley circulation, which is coupled to the trades. Implied likewise is an influence on tropical cyclones. Some evidence suggests that tropical depressions track preferentially into the Gulf of Mexico during one phase of the NAO, but toward the eastern seaboard of the United States during the opposite phase. Although influences of the NAO on regional climate over Europe are well established, the mechanisms behind this fluctuation of the circulation remain poorly understood.

Arctic oscillation

Although defined from anomalies in the surface pattern, the NAO involves fluctuations with vertical structure. That structure links the NAO to a more general phenomenon, one that is closely related to planetary waves.

Fluctuations of SLP can be represented as a superposition of horizontally coherent structures that occur preferentially in the observational record. The structures

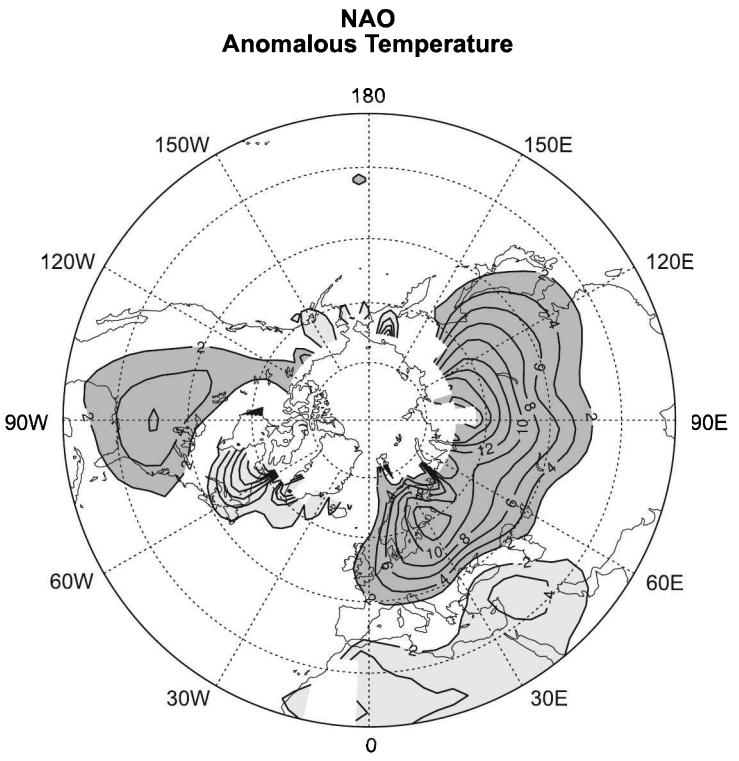

Figure 15.18 Anomalous wintertime surface temperature (scaled by 0.1 K) associated with the positive phase of the NAO. After Hurrel et al. (2003).

are called *Empirical Orthogonal Functions* (*EOF*s); Monahan et al. (2009) present an overview. Also known as *Principal Component Analysis*, the EOF description of fluctuations determines horizontal variations that operate coherently.[9] EOFs are ordered according to the fraction of overall variance that they represent. The first EOF represents the greatest variance, the second the next greatest, and so forth. Dynamical fluctuations are inherently red, with variance concentrated in the lowest wavenumbers (Sec. 14.1.4). For this reason, the leading EOFs, beyond representing the greatest variance, also represent the lowest wavenumbers and the largest spatial scales.

The *Arctic Oscillation* (*AO*) is defined as the leading EOF of SLP or its counterpart, 1000-hPa height. Plotted in Fig. 15.19b is anomalous structure associated with positive phase of the AO. It involves anomalous low pressure (height) over the Arctic, where the AO is almost zonally symmetric (wavenumber 0). Flanking it at subpolar latitudes are two centers of anomalous high pressure (wavenumbers 0 and 2): one over the North Atlantic, neighboring the Bermuda-Azores High, and another over the North Pacific, neighboring the Hawaiian High. Together with anomalous low pressure over the Arctic, which neighbors the Icelandic and Aleutian Lows, those features modulate

[9] By construction, EOFs are orthogonal: the product of two different EOFs vanishes when averaged over the Earth. Consequently, different EOFs are structurally independent. Nonetheless, different EOFs can represent the same phenomenon, which makes them physically interdependent.

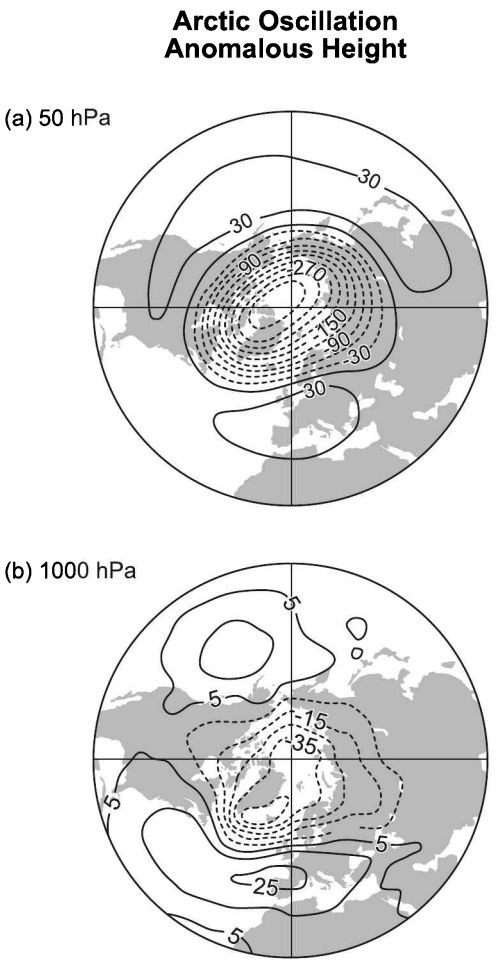

Figure 15.19 Anomalous height associated with the positive phase of the Arctic Oscillation (AO) at (a) 50 hPa and (b) 1000 hPa. Adapted from Baldwin and Dunkerton (1999).

westerlies in the storm tracks over the north Atlantic and north Pacific. Accordingly, they exert influences analogous to those exerted on Europe by the NAO.

Vertical structure associated with the AO is illustrated by coherent fluctuations at higher levels. The pattern of anomalous height at 50 hPa is plotted in Fig. 15.19a. Zonally symmetric fluctuations over the Arctic are vertically coherent. They appear at all levels, nearly in phase across the troposphere and stratosphere. Those fluctuations amplify upward during winter. They have the horizontal structure of the polar-night vortex, which prevails in the wintertime stratosphere (cf. Fig. 1.10b). The polar-night vortex thus interacts with the tropospheric circulation. It is manifest in the AO as low as the Earth's surface (Fig. 15.19b). Owing to its deep vertical structure and zonal symmetry at polar latitudes, the AO is also referred to as the *Northern Annular Mode* (*NAM*).

In the zonal mean, the AO represents a meridional dipole, with anomalous height of one sign over the pole and of opposite sign at subpolar latitudes. Reflected in the high-latitude anomaly is the polar-night vortex. It develops through cold temperature that prevails over the Arctic during winter (Fig. 1.8). Plotted in Fig. 15.20 is anomalous

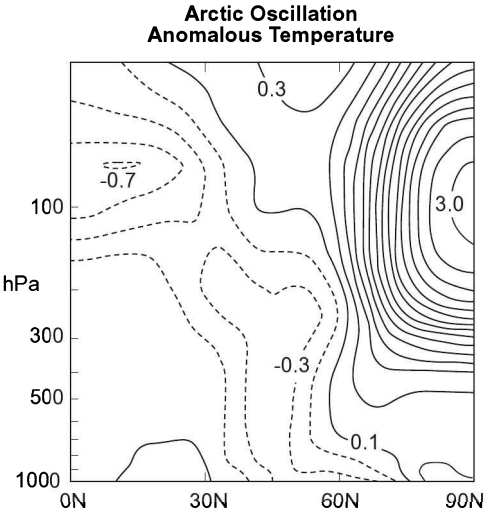

Figure 15.20 Anomalous zonal-mean temperature associated with the *negative phase* of the AO (1 std deviation). Corresponds to Jan–Mar temperature over the Arctic that is anomalously warm. Adapted from Thompson and Wallace (2000).

zonal-mean temperature associated with negative phase of the AO (opposite to the phase in Fig. 15.19). Temperature is anomalously warm in the Arctic stratosphere. Through the hypsometric relation (6.12), that temperature anomaly corresponds to the height anomaly over the Arctic in Fig. 15.19 (but of reversed sign). The Arctic vortex is then anomalously warm and weak. In the opposite phase (positive AO, displayed in Fig. 15.19), the polar-night vortex is anomalously cold and strong.

The warm anomaly in Fig. 15.20 is a signature of anomalous downwelling and adiabatic warming. It penetrates well into the Arctic troposphere, as low as 500 hPa. Flanking it in the tropics is a cold anomaly. A signature of anomalous upwelling and adiabatic cooling, it maximizes just above the tropical tropopause. That temperature anomaly, in fact, has a form very similar to that of the cold tropical tropopause (Fig. 1.7). It represents an upward expansion of positive lapse rate from the troposphere, with commensurate cooling of the tropical tropopause (Sec. 18.8).

The changes over the tropics vary coherently but out of phase with the signature of anomalous downwelling over the Arctic. They imply the involvement of the Hadley circulation. Through upwelling and associated deep convection, the Hadley circulation controls the tropical tropopause (Secs. 7.7, 9.3.4). Varying in similar fashion is anomalous divergence near the tropical tropopause (Thuburn and Craig, 2000; Salby and Callaghan, 2005). Likewise for anomalous surface motion in the subtropics, which comprises the trade winds (Thompson and Wallace, 2000). Their involvement is consistent with the origin of the trades, outflow from the Bermuda-Azores High and the Hawaiian High, which are modulated by the AO (Fig. 15.9).

In the AO, fluctuations in the troposphere and stratosphere are coupled. On short time scales, amplifications of the AO appear first in the stratosphere and then descend. Plotted in Fig. 15.21 is a height-time section of the AO during an individual winter. Several amplifications appear in the upper stratosphere, descending over the course of a couple of weeks. The one in late winter, when the polar-night vortex is weak, descends into the troposphere. There, it modulates quasi-permanent features like the Icelandic Low and the Bermuda-Azores High. Such modulation perturbs the storm tracks over the north Atlantic and north Pacific, thereby influencing the development of synoptic weather systems.

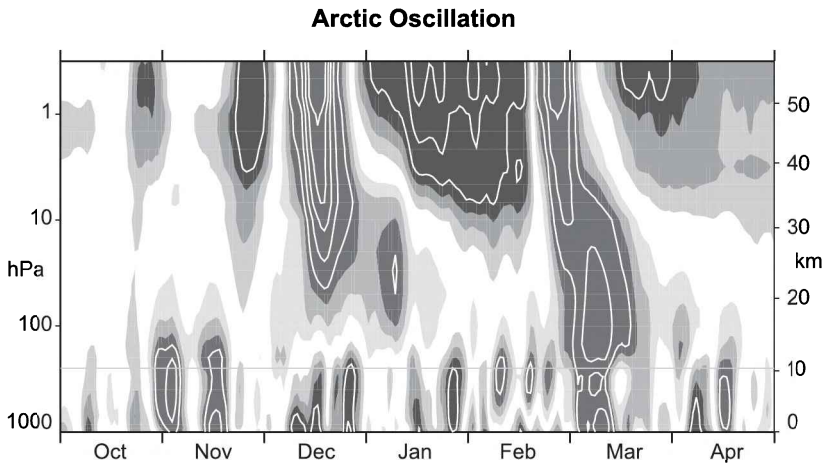

Figure 15.21 Time-height section of dimensionless AO index during 1998–1999. AO index represents the intensity of the leading EOF of geopotential height. After Baldwin and Dunkerton (2001). See color plate section: Plate 17.

The AO has varied systematically over consecutive years. Between the 1970s and 1990s, wintertime values intensified, reflecting an intensification of the polar-night vortex. The systematic change involves a trend in the Icelandic Low and Bermuda-Azores High. The accompanying trend in advection of warm maritime air (Fig. 15.17) accounts for about half of the observed warming over Eurasia (Hurrell, 1996; Thompson et al., 2000). Eventually, however, the systematic change collapsed, the AO then returning toward earlier values. The reversal echoes previous episodes in the observational record, when the AO varied systematically over even longer periods, before swinging in the opposite direction (IPCC, 2007).

The AO shares major structure with the NAO. Whether the two describe distinct phenomena is a matter of debate. Much of the uncertainty revolves about whether the anomalies over the north Atlantic and north Pacific operate coherently (Deser, 2000; Ambaum et al., 2001). The interdependence of those features hinges on the time scale of fluctuations, for example, manifest in daily versus interannual anomalies. Relevant as well is the discrimination to a single EOF. The AO is defined arbitrarily as the leading EOF of SLP. By ignoring neighboring EOFs, this definition can exaggerate spatial coherence.

It will be seen in Chap. 18 that the salient structure of the AO emerges as well from anomalous planetary wave activity that is transmitted upward to the stratosphere. The latter forces anomalous downwelling over the Arctic, which modulates the polar-night vortex. In the troposphere, anomalous planetary wave activity is associated with the fluctuation of quasi-permanent features, such as the Icelandic and Aleutian Lows. It is therefore accompanied by a perturbation of the storm tracks over the north Atlantic and north Pacific. Fluctuations of the planetary wave pattern are thus central to the AO. The mechanisms responsible for those fluctuations, like those behind the NAO, remain poorly understood.

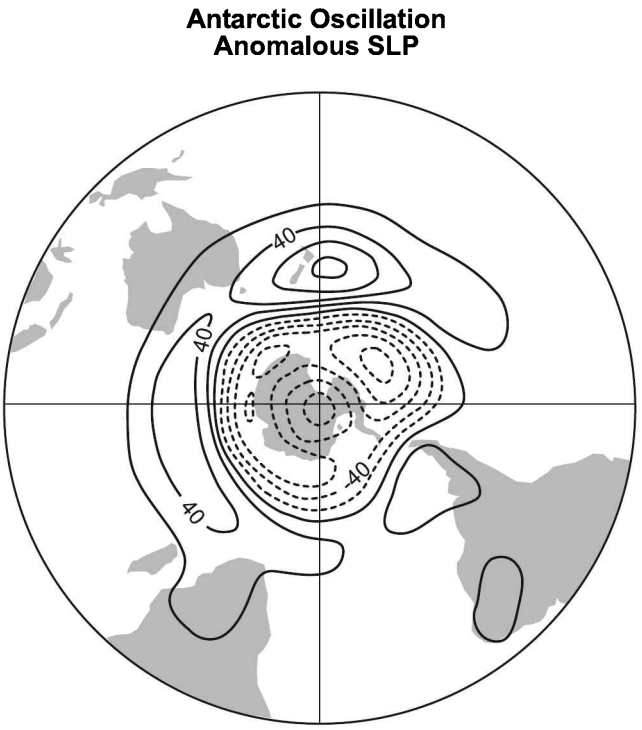

Figure 15.22 Anomalous SLP associated with of the Antarctic Oscillation (AAO) in its positive phase (arbitrary scaling). After Gong and Wang (1999).

Antarctic Oscillation

As it is a matter of definition, the AO has a counterpart over the Southern Hemisphere. The leading EOF of SLP (1000-hPa height) there defines the *Antarctic Oscillation* (*AAO*). Plotted in Fig. 15.22 is anomalous structure associated with positive phase of the AAO. Like the AO, the AAO involves anomalous low pressure over the pole, flanked at subpolar latitudes by anomalous high pressure.[10] The AAO, however, is almost zonally symmetric at all latitudes. At subpolar latitudes, anomalous high pressure has crescent structure, zonally continuous except for a break between 0E and 90W. As for the AO, it shares zonal structure with the storm track (Fig. 15.10). Fluctuations of the AAO therefore perturb strong westerlies that comprise the jet stream. Associated with a displacement of the storm track, they have been related to fluctuations of rainfall over Australia (Hendon et al., 2007).

Zonally symmetric fluctuations over the Antarctic are vertically coherent. Like the AO, they operate in phase across the troposphere and stratosphere, amplifying upward during winter. That structure has the form of the Antarctic polar-night vortex. Owing to its deep vertical structure and zonal symmetry at polar latitudes, the AAO is also referred to as the *Southern Annular Mode* (*SAM*).

[10] Owing to its high elevation, surface pressure over Antarctica is closer to 700 hPa.

The AAO has also varied systematically over consecutive years. It intensified between the 1970s and 1990s (Marshall, 2003). That trend in the AAO is concentrated in summer and autumn. Accompanying it is cooling over the Antarctic, with possible influence on Antarctic ice (IPCC, 2007). Mechanisms suggested for the trend include ozone depletion, which, through the ozone hole, favors an intensified polar-night vortex. However, the ozone hole has distinct seasonality that limits it to late winter and spring (Chap. 18). By summer, when the AAO trend appears, the ozone hole has dissolved. More significantly, the AAO trend that prevailed during closing decades of the twentieth century eventually reversed. Thereafter, the AAO returned toward earlier values. The reversal echoes previous episodes in the observational record, when a trend of the AAO persisted in one direction, before eventually swinging in the opposite direction (Jones and Widmann, 2004).

The global circulation also changes through interaction with other variations, some of which are inherent to the ocean, the stratosphere, and solar activity (Secs. 17.6, 18.8).

15.5.2 Intraseasonal variations

On time scales shorter than seasonal, variability of the circulation is dominated by synoptic weather systems, which prevail at mid-latitudes. In the tropics, another large-scale fluctuation operates. It leads to a global perturbation of convection and thermally direct circulations.

Madden-Julian Oscillation

Zonal wind over the equator fluctuates, conspicuously with periods of 1–2 months. Propagating eastward, this disturbance is named the *Madden-Julian Oscillation* (*MJO*), after its discoverers (Madden and Julian, 1971). Figure 15.23a plots, as a function of period and wavenumber, the space–time spectrum of 850-hPa zonal wind over the equator. Fluctuations of zonal wind are concentrated at wavenumber 1 and eastward periods of 40–80 days. These fluctuations account for much of the intraseasonal variance in equatorial u_{850}. Plotted in Fig. 15.23b is the same information, but for OLR, which measures anomalous cloud cover and deep convection over the equator (Fig. 1.30). The space–time spectrum of convection is comparatively broad, with variance appearing in a red distribution over zonal wavenumber and eastward frequency (Sec. 14.1.4). Yet, like the spectrum of u_{850}, fluctuations of convection are concentrated at wavenumbers 1–2 and eastward periods of 40–80 days. The concentration of u_{850} and OLR variance at the same space and time scales indicates an interaction between the tropical circulation and the convective pattern.

Figure 15.24 illustrates anomalous motion and SLP at successive phases of the disturbance. Initially, the disturbance involves anomalous upwelling and low SLP over the Indian Ocean. Accompanying those perturbations is anomalous convection and latent heating. Thermally direct motion to the west and east has the form of a transient Walker circulation. Zonal structure is of planetary scale, principally wavenumber 1. These features amplify and migrate eastward into the Pacific. As they move into colder water of the eastern Pacific (Fig. 5.1), the convective anomaly collapses. Anomalous motion, however, continues eastward, eventually completing a circuit around the Earth.

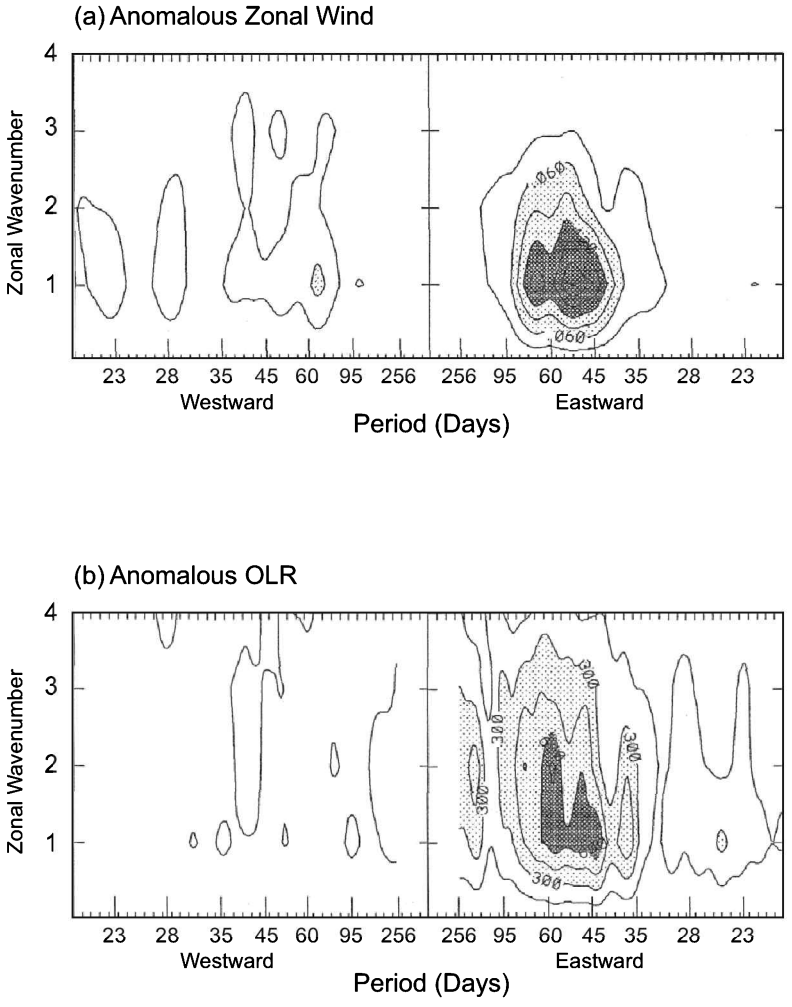

Figure 15.23 Space-time spectrum, as function of zonal wavenumber and period, of (a) anomalous equatorial zonal wind at 850 hPa and (b) anomalous OLR. After Salby and Hendon (1994).

Straddling anomalous zonal motion along the equator are gyres in the subtropics of each hemisphere (Madden, 1986; Hendon and Salby, 1994). They give the MJO horizontal structure which is similar to that produced by a localized heat source (Fig. 15.13), but which propagates eastward. In fact, moisture convergence by the MJO introduces anomalous convection and latent heating (Maloney and Hartmann, 1998). The latter operate sympathetically with the anomalous circulation: Anomalous motion leads to anomalous moisture convergence, which fuels anomalous latent heating, which in turn reinforces anomalous motion. Such feedback enables the MJO to sustain itself against frictional dissipation and amplify.

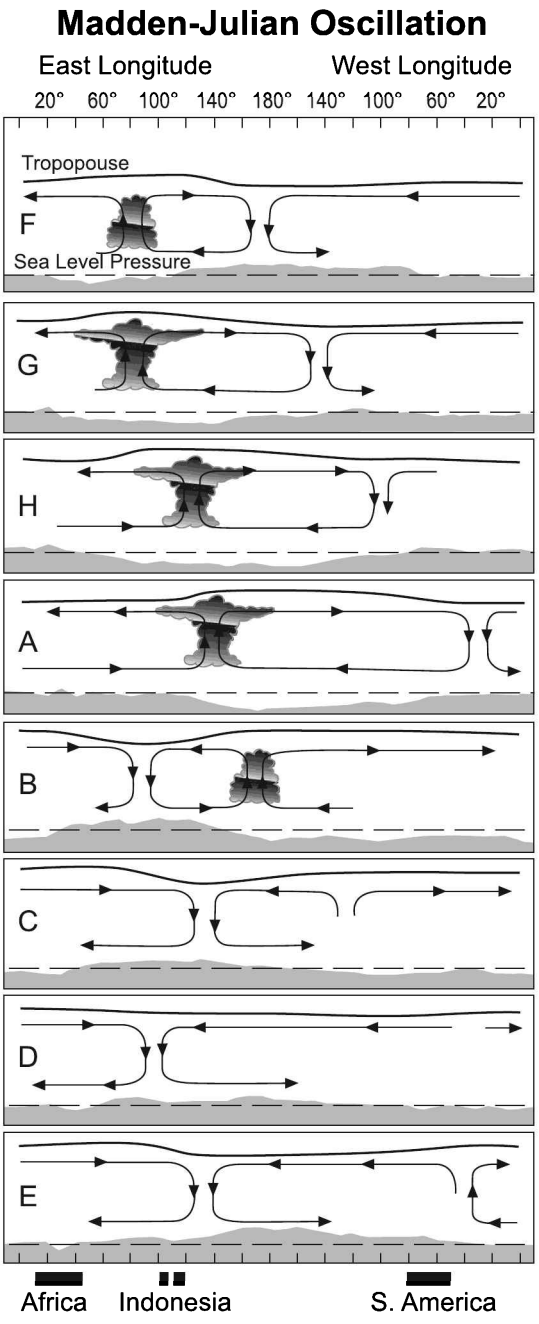

Figure 15.24 Schematic of anomalous equatorial motion, SLP (shaded), and convection during the life cycle of the Madden-Julian Oscillation (MJO). After Madden and Julian (1972).

The positioning of moisture convergence is key to this process. It determines the phase of anomalous convection relative to anomalous temperature. If they are in phase, anomalous heating reinforces anomalously-warm temperature, amplifying the disturbance. If they are out of phase, anomalous heating suppresses anomalously-cold temperature, damping the disturbance. The distribution of divergent motion is therefore central (Sec 12.1.1). Moisture convergence is magnified near the equator. There, f is small enough for geostrophic balance to give way to frictional balance. Moisture then converges into anomalous low pressure along the equator. Flanked overhead by anomalous high pressure, the latter coincides with anomalously warm temperature (6.12). Frictional convergence into low surface pressure thus humidifies the lower troposphere at sites where temperature is anomalously warm. This feature enables the MJO to amplify through positive feedback with convection (ibid; Wang and Rui, 1990; Salby et al., 1994).

The MJO is also accompanied by coherent fluctuations of ocean temperature. Anomalous SST is of order 0.5 K in the equatorial Indian and Pacific oceans, sites where anomalous convection amplifies (Zhang, 1996; Shinoda and Hendon, 1998). Anomalous SST develops through (1) a modulation of evaporative cooling, which accompanies anomalous latent heat flux to the atmosphere, and (2) a modulation of SW heating, which is suppressed by cloud cover (Waliser, 1996; Maloney and Kiehl, 2002). These changes induce anomalously warm SST ahead of anomalous convection. It can reinforce moisture flux convergence and the organization of convection, providing additional feedback from the ocean (Wang and Xie, 1998). Like other elements of climate variability, these features form some of the challenges to large-scale simulation by GCMs.

SUGGESTED REFERENCES

An Introduction to Dynamic Meteorology (2004) by Holton treats the zonal-mean circulation and its relationship to baroclinic eddies.

Global Physical Climatology (1994) by Hartmann discusses eddy transports of heat and momentum, along with their roles in the general circulation.

Observations relevant to the general circulation are presented in *Physics of Climate* (1992) by Peixoto and Oort.

Tropical circulations are developed in *Atmosphere-Ocean Dynamics* (1982) by Gill.

An overview of GCMs is presented in *The Development of Atmospheric General Circulation Models* (2010), edited by Donner, Schubert, and Somerville.

PROBLEMS

1. Relate the change of moist static energy $h_{tot} = c_p T + l_v r + \Phi$ of an air parcel to the change of its equivalent potential temperature θ_e.
2. Consider an air parcel that moves equatorward at sea level, ascends adiabatically in the tropics, returns poleward at a constant altitude of 15 km, and then descends in the extratropics – as symbolized by the idealized thermodynamic circuit in Fig. 6.7. If heat transfer is restricted to upper and lower legs of the circuit and if, along the lower leg, the parcel's initial temperature and mixing ratio in the extratropics are 250°K and 1 g kg^{-1}, whereas it assumes a temperature and mixing

ratio in the tropics of 300°K and 20 g kg^{-1}, calculate the radiative heat transfer that occurs along the upper leg of the circuit.

3. Consider the following thermal structure, representative of zonal-mean stratification in the troposphere:

$$T(\phi, p) = \overline{T}(p) - T'(\phi, p),$$

where

$$\overline{T}(p) = \overline{T}_0 - \Gamma \bar{H} ln\left(\frac{p_0}{p}\right) + \frac{\Delta T}{4}\left(\frac{p}{p_0}\right),$$

$$T'(\phi, p) = \Delta T |sin\phi|^3 \left(\frac{p}{p_0}\right) - \frac{\Delta T}{4}\left(\frac{p}{p_0}\right),$$

and overbar denotes global average. For $\overline{T}_0 = 268°K$, $\Gamma = 4°K\ km^{-1}$, $\bar{H} = 8$ km, $\Delta T = 70°K$, $\phi_0 = 45°$, and $p_0 = 1000$ hPa, (a) plot the thermal structure and zonal wind as functions of latitude and $\frac{z}{H} = ln(\frac{p_0}{p})$, (b) calculate the available potential energy $\mathcal{A}$ of the atmosphere, and (c) plot the vertical concentration of available potential energy $\frac{\partial \mathcal{A}}{\partial z}$ as a function of $\frac{z}{H}$.

4. For the atmosphere in Prob. 15.3, determine the fraction of total potential energy that is available for conversion to kinetic energy.
5. For the atmosphere in Prob. 15.3, determine a characteristic eddy velocity if thermal structure is driven adiabatically into barotropic stratification and if the kinetic energy produced is concentrated between ±30° and ±60° latitude.
6. (a) Use observed distributions of precipitation rate (Fig. 9.41) and total precipitable water vapor (Fig. 1.19) to calculate a characteristic time scale for the column abundance of water vapor in the tropics. (b) Discuss this time scale in relation to the efficiency of dehydration inside individual convective cells, their fractional coverage, and the efficiency with which water vapor is produced at the Earth's surface.
7. Atmospheric heating in Fig. 9.41b is concentrated about the equator. It is distinctly narrower than net radiative heating of the Earth-atmosphere system as a whole, represented in the TOA energy budget (Fig. 1.34c). Explain why and how.
8. Show that the pressure averaged over an isentropic surface $\overline{p}$ is preserved under an adiabatic rearrangement of mass.
9. Derive expressions (15.19) for available potential energy.
10. Zonal-mean flow in the troposphere is easterly at low latitude but westerly at middle and high latitudes (Fig. 1.8). Surface drag must therefore represent a sink of easterly momentum at low latitudes, which is equivalent to a source of westerly momentum. Conversely, it must represent a sink of westerly momentum at middle and high latitudes. On average, the atmosphere's angular momentum remains constant. Mechanical equilibrium therefore requires that the source of westerly momentum at low latitude and the sink of westerly momentum at middle and high latitudes be compensated by a poleward transfer of westerly momentum. This requirement is analogous to the poleward transfer of heat required by thermal equilibrium. (a) Demonstrate that transport of angular momentum by the zonal-mean Hadley circulation produces a momentum flux $\bar{u}\bar{v}$ of the correct sense to accomplish this transfer of westerly momentum. (b) Not all of the momentum transfer required to maintain mechanical equilibrium is accomplished by the

zonal-mean Hadley circulation. The remainder occurs through large-scale eddy transport. In terms of horizontal phase structure and group velocity, describe the meridional propagation of Rossby waves needed to accomplish the remaining momentum transfer between tropical and extratropical regions.

11. The length of day can vary through exchanges of momentum between the atmosphere and solid Earth. (a) Estimate the fluctuation of air velocity over the equator corresponding to observed fluctuations in the length of day of order 10^{-3} s, if the Earth has a mean density of order $5\ 10^3$ kg m^{-3} and if the atmosphere compensates through uniform changes of angular velocity. (b) More generally, where would velocity fluctuations most effectively introduce changes in the length of day?
12. The height of convective towers is dictated by the moist static energy of surface air, in concert with the profile of environmental temperature, which determine CAPE (Sec. 7.4.1). Moist static energy, in turn, is determined by fluxes of sensible and latent heat from the surface (15.2). A surge of extratropical air enters the tropics, producing the temperature profile

$$T(z) = \begin{cases} T_0 - \Gamma z & z < z_T \\ \\ T_T & z \geq z_T, \end{cases}$$

where $T_0 = 290°$K, $\Gamma = 7.5°$K km^{-1}, $z_T = 12$ km, and $T_T = 200°$K. (a) If, through contact with an isolated landmass, surface air attains a temperature of 300°K and a mixing ratio of 23 g kg^{-1}, calculate the respective CAPE. (b) As in (a) but if the air is dry. (c) Estimate the height to which convection would develop under the conditions of (a) and (b).

CHAPTER
SIXTEEN

Dynamic stability

Disturbances in the rotating cylindrical annulus are a laboratory analogue of synoptic weather systems, which prevail outside the tropics. Each develops through instability of the zonal-mean circulation. Instability was considered earlier in relation to the vertical stratification of mass (Chap. 7). If distributions of temperature and humidity violate the conditions for static stability, then small displacements lead to parcels accelerating away from their undisturbed positions. Unlike the response under stable stratification, this reaction leads to finite displacements of air. Fully developed convection then rearranges air, driving the stratification toward neutral stability.

Two classes of instability are possible. *Parcel instability* follows from reinforcement of air displacements by a negative restoring force, as occurs in the development of convection. *Wave instability* occurs in the presence of a positive restoring force, but one that amplifies parcel oscillations inside wave motions. Unstable waves amplify by extracting energy from the mean circulation, for example, from available potential energy that accompanies baroclinic stratification and vertical shear (Chap. 15). Strong zonal wind that follows from the nonuniform distribution of atmospheric heating, in concert with geostrophic balance, makes this class of instability the one most relevant to the large-scale circulation. Like parcel instability, it develops to neutralize instability in the mean flow. This objective is achieved through the rearrangement of air.

16.1 INERTIAL INSTABILITY

The simplest form of large-scale instability relates to the inertial oscillations described in Sec. 12.4. Consider disturbances to a geostrophically-balanced zonal flow $\overline{u}$ on an f plane. If the disturbances introduce no pressure perturbation, the total motion is

governed by the horizontal momentum balance

$$\frac{du}{dt} - fv = 0 \tag{16.1.1}$$

$$\frac{dv}{dt} + f(u - \overline{u}) = 0, \tag{16.1.2}$$

where geostrophic equilibrium has been used to eliminate pressure in favor of $\overline{u}$.

Because a parcel's motion satisfies

$$v = \frac{dy}{dt}, \tag{16.2}$$

(16.1.1) implies

$$\frac{du}{dt} = f\frac{dy}{dt}. \tag{16.3}$$

Integrating from the parcel's initial position y_0 to its displaced position $y_0 + y'$ gives

$$u(y_0 + y') - \overline{u}(y_0) = fy'.$$

To first order in parcel displacement, this may be expressed

$$u(y_0) + \frac{\partial \overline{u}}{\partial y}y' - \overline{u}(y_0) = fy'$$

or

$$(u - \overline{u})\big|_{y_0} - \left(f - \frac{\partial \overline{u}}{\partial y}\right)y' = 0.$$

Then incorporating (16.1.2) yields

$$\frac{d^2y'}{dt^2} + f\left(f - \frac{\partial \overline{u}}{\partial y}\right)y' = 0. \tag{16.4}$$

If the mean flow is without shear, (16.4) reduces to a description of the inertial oscillations considered previously. In the presence of shear, displacements either oscillate, decay exponentially, or amplify without bound. The system possesses unstable solutions if the absolute vorticity of the mean flow

$$f + \overline{\zeta} = f - \frac{\partial \overline{u}}{\partial y} \tag{16.5}$$

has sign opposite to the planetary vorticity f. Displacements then amplify exponentially. The zonal flow is said to be *inertially unstable*. These circumstances make the specific restoring force $f(f + \overline{\zeta})y'$ negative. The ensuing instability is therefore a form of parcel instability. Because $f + \overline{\zeta}$ is dominated by planetary vorticity, it usually has the same sign as f. The criterion for inertial instability is thus tantamount to the absolute vorticity reversing sign somewhere.

Inertial instability does not play a major role in the atmosphere. Extratropical motions tend to remain inertially stable, even locally in the presence of synoptic and planetary wave disturbances. However, the criterion for inertial instability is violated more easily near the equator, where f is small. There, even modest shear can lead to a reversal of absolute vorticity. Evidence of inertial instability exists in the tropical stratosphere. Horizontal shear that flanks strong zonal jets in the winter and summer stratosphere (Fig. 1.8) can violate the criterion for inertial stability.

16.2 SHEAR INSTABILITY

More relevant to the large-scale circulation is instability that derives directly from shear. Shear instability is a form of wave instability. It therefore requires a more involved analysis. Like the treatment of wave motions, the description of shear instability requires the solution of partial differential equations that govern perturbation or eddy properties. Closed form solutions can be found only for idealized profiles of zonal-mean flow $\overline{u}(y, z)$. However, an illuminating criterion for instability, due originally to Rayleigh, can be developed under fairly general circumstances.

16.2.1 Necessary conditions for instability

Consider quasi-geostrophic motion on a beta plane in an atmosphere that extends upward indefinitely and is bounded below and laterally at $y = \pm L$ by rigid walls. Disturbances to the zonal-mean flow $\overline{u}(y, z)$ are governed by first-order conservation of potential vorticity (14.75)

$$\frac{DQ'}{Dt} + v'\beta_e = 0, \tag{16.6.1}$$

where $\frac{D}{Dt} = \frac{\partial}{\partial t} + \overline{u}\frac{\partial}{\partial x}$,

$$Q' = \nabla^2\psi' + \frac{1}{\rho_0}\frac{\partial}{\partial z}\left(\frac{f_0^2}{N^2}\rho_0\frac{\partial\psi'}{\partial z}\right) \tag{16.6.2}$$

$$\begin{aligned}\beta_e &= \beta - \frac{\partial^2\overline{u}}{\partial y^2} - \frac{1}{\rho_0}\frac{\partial}{\partial z}\left(\frac{f_0^2}{N^2}\rho_0\frac{\partial\overline{u}}{\partial z}\right)\\ &= \frac{\partial\overline{Q}}{\partial y},\end{aligned} \tag{16.6.3}$$

and z denotes log-pressure height. Requiring vertical motion to vanish at the Earth's surface (which is treated as an isobaric surface) gives, via the thermodynamic equation and thermal wind balance, the lower boundary condition

$$\frac{D}{Dt}\left(\frac{\partial\psi'}{\partial z}\right) - \frac{\partial\overline{u}}{\partial z}\frac{\partial\psi'}{\partial x} = 0 \qquad z = 0. \tag{16.6.4}$$

Physically meaningful solutions must also have bounded column energy. The latter provides the upper boundary condition

$$\text{finite energy condition} \quad z \to \infty. \tag{16.6.5}$$

At the lateral walls, v' must vanish, so $\psi' = \text{const}$. It suffices to prescribe

$$\psi' = 0 \qquad y = \pm L. \tag{16.6.6}$$

Equations (16.6) define a second-order boundary value problem for the eddy streamfunction $\psi'(\boldsymbol{x}, t)$ – one that is homogeneous. Involving no imposed forcing, (16.6) describes a system that is self-governing or autonomous. Nontrivial solutions (i.e., other than $\psi' \equiv 0$) exist only for certain *eigenfrequencies* that enable boundary conditions to be satisfied. Those eigenfrequencies are determined by solving the

homogeneous boundary value problem for a given zonal flow $\overline{u}(y, z)$. They are, in general, complex.

Consider solutions of the form

$$\psi' = \Psi(y, z)e^{ik(x-ct)}, \tag{16.7}$$

where Ψ and $c = c_r + ic_i$ can assume complex values. Substituting (16.7) transforms (16.6) into

$$(\overline{u} - c)\left[\frac{\partial^2\Psi}{\partial y^2} + \frac{1}{\rho_0}\frac{\partial}{\partial z}\left(\frac{f_0^2}{N^2}\rho_0\frac{\partial\Psi}{\partial z}\right) - k^2\Psi\right] + \beta_e\Psi = 0. \tag{16.8.1}$$

The lower boundary condition (16.6.4) becomes

$$(\overline{u} - c)\frac{\partial\Psi}{\partial z} - \frac{\partial\overline{u}}{\partial z}\Psi = 0 \qquad z = 0. \tag{16.8.2}$$

For c real, (16.8) is singular at a critical line where $\overline{u} = c$. The singularity disappears if $c_i \neq 0$. Behavior (16.7) then involves an exponential modulation in time. If the flow is stable, wave activity incident on the critical line is absorbed when dissipation is included (Sec. 14.3). The wave field then decays exponentially. If the flow is unstable, wave activity can be produced at the critical line. The wave field then amplifies exponentially.

Multiplying the conjugate of (16.8) by Ψ and (16.8) by the conjugate of Ψ and then subtracting yields

$$\left[\Psi\frac{\partial^2\Psi^*}{\partial y^2} - \Psi^*\frac{\partial^2\Psi}{\partial y^2}\right] + \left[\Psi\frac{1}{\rho_0}\frac{\partial}{\partial z}\left(\frac{f_0^2}{N^2}\rho_0\frac{\partial\Psi^*}{\partial z}\right) - \Psi^*\frac{1}{\rho_0}\frac{\partial}{\partial z}\left(\frac{f_0^2}{N^2}\rho_0\frac{\partial\Psi}{\partial z}\right)\right] - 2ic_i\frac{|\Psi|^2}{|\overline{u} - c|^2}\beta_e = 0 \tag{16.9.1}$$

and

$$\Psi\frac{\partial\Psi^*}{\partial z} - \Psi^*\frac{\partial\Psi}{\partial z} + 2ic_i\frac{|\Psi|^2}{|\overline{u} - c|^2}\frac{\partial\overline{u}}{\partial z} = 0 \qquad z = 0. \tag{16.9.2}$$

The chain rule enables terms in the first set of brackets in (16.9.1) to be expressed

$$\Psi\frac{\partial^2\Psi^*}{\partial y^2} - \Psi^*\frac{\partial^2\Psi}{\partial y^2} = \frac{\partial}{\partial y}\left[\Psi\frac{\partial\Psi^*}{\partial y} - \Psi^*\frac{\partial\Psi}{\partial y}\right].$$

Terms in the second set of brackets may be expressed similarly. Then (16.9.1) can be written

$$\frac{\partial}{\partial y}\left[\Psi\frac{\partial\Psi^*}{\partial y} - \Psi^*\frac{\partial\Psi}{\partial y}\right] + \frac{1}{\rho_0}\frac{\partial}{\partial z}\left[\frac{f_0^2}{N^2}\rho_0\left(\Psi\frac{\partial\Psi^*}{\partial z} - \Psi^*\frac{\partial\Psi}{\partial z}\right)\right] - 2ic_i\frac{|\Psi|^2}{|\overline{u} - c|^2}\beta_e = 0. \tag{16.10}$$

Integrating over the domain unravels the exterior derivatives in (16.10), leaving

$$\int_0^\infty\left[\Psi\frac{\partial\Psi^*}{\partial y} - \Psi^*\frac{\partial\Psi}{\partial y}\right]_{y=-L}^{y=L}\rho_0 dz + \int_{-L}^{L}\left[\frac{f_0^2}{N^2}\rho_0\left(\Psi\frac{\partial\Psi^*}{\partial z} - \Psi^*\frac{\partial\Psi}{\partial z}\right)\right]_{z=0}^{z=\infty}dy - 2ic_i\int_{-L}^{L}\int_0^\infty\frac{|\Psi|^2}{|\overline{u} - c|^2}\beta_e dy\rho_0 dz = 0. \tag{16.11}$$

By (16.6.6), the first integral vanishes. The finite energy condition makes the upper limit inside the second integral also vanish. Then incorporating (16.9.2) for the

lower limit yields the identity

$$c_i \left\{ \int_0^\infty \int_{-L}^{L} \beta_e \frac{\rho_0 |\Psi|^2}{|\overline{u} - c|^2} dy dz - \int_{-L}^{L} \left[\frac{f_0^2}{N^2} \frac{\rho_0 |\Psi|^2}{|\overline{u} - c|^2} \frac{\partial \overline{u}}{\partial z} \right]_{z=0} dy \right\} = 0. \tag{16.12}$$

Equation (16.12) must be satisfied for $\Psi(y, z)$ to be a solution of (16.6). Advanced by Charney and Stern (1962), it provides "necessary conditions" for instability of the zonal-mean flow $\overline{u}(y, z)$. If c is complex, (16.7) describes a disturbance whose amplitude varies in time exponentially

$$e^{ik(x-ct)} = e^{kc_i t} \cdot e^{ik(x-c_r t)},$$

with the growth/decay rate kc_i. Without loss of generality, k may be taken to be positive. The existence of unstable solutions then requires $c_i > 0$. Unstable solutions are thus possible only if the quantity in braces vanishes. If it does not, (16.12) requires that $c_i = 0$. Solutions to (16.6) are then stable.

16.2.2 Barotropic and baroclinic instability

Requiring (16.12) to be satisfied with $c_i > 0$ provides two alternative criteria for instability:

1. If $\frac{\partial \overline{u}}{\partial z}$ vanishes at the lower boundary, by thermal wind balance, so does the temperature gradient. Then $\beta_e = \frac{\partial \overline{Q}}{\partial y}$ must reverse sign somewhere in the interior. β_e is normally positive, dominated by the gradient of planetary vorticity β. A region of negative potential vorticity gradient, $\frac{\partial \overline{Q}}{\partial y} < 0$, is therefore identified as one where the mean flow is unstable.
2. If $\beta_e > 0$ throughout the interior, $\frac{\partial \overline{u}}{\partial z}$ must be positive somewhere on the lower boundary. By thermal wind balance, this implies the existence of an equatorward temperature gradient at the surface.

Other combinations are also possible, but these necessary conditions are the ones most relevant to the atmosphere. Neither represents a "sufficient condition" for instability. Satisfying criterion (1) or (2) does not ensure the existence of unstable solutions.

Criterion (1) defines the necessary condition for *free-field instability*, namely, instability for which boundaries do not play an essential role. From (16.6.3), the mean gradient of potential vorticity can reverse sign through strong meridional curvature of the mean flow or through strong (density-weighted) vertical curvature of the mean flow. It is customary to distinguish these contributions to $\frac{\partial \overline{Q}}{\partial y}$. If the necessary condition for instability is met through horizontal shear, amplifying disturbances are referred to as *barotropic instability*. If it is met through vertical shear (which is proportional to the horizontal temperature gradient and the departure from barotropic stratification), amplifying disturbances are referred to as *baroclinic instability*. Realistic conditions often lead to criterion (1) being satisfied by both contributions. Amplifying disturbances are then combined barotropic-baroclinic instability.

In the absence of rotation, criterion (1) reduces to Rayleigh's (1880) necessary condition for instability of 1-dimensional shear flow (Prob. 16.3). Criterion (1) is then equivalent to requiring the mean flow profile to possess an inflection point. Because β is everywhere positive, rotation is stabilizing. It provides a positive restoring force that inhibits instability and supports stable wave propagation.

Recall that, if $c_i = 0$, (16.8) is singular at a critical line, where $\overline{u} = c_r$. Exponential amplification removes the singularity by making $c_i > 0$. When boundaries do not play an essential role, amplifying solutions usually possess a critical line inside the unstable region, where $\frac{\partial \overline{Q}}{\partial y} < 0$ (e.g., Dickinson, 1973). Rather than serving as a localized sink of wave activity, as it does under stable conditions ($\frac{\partial \overline{Q}}{\partial y} > 0$), the critical line then serves as a localized source of wave activity (Sec. 14.5.4). Under these conditions, wave activity flux (14.81) diverges from the critical line, where it is produced by a conversion from the mean flow. Alternatively, wave activity incident on the critical line is "overreflected": More radiates away than is incident on the unstable region.

Criterion (2) describes instability that is produced through the direct involvement of the lower boundary. This criterion applies to baroclinic instability because it requires a temperature gradient at the surface and hence baroclinic stratification. Because air must move parallel to it, the boundary can then drive motion across mean isotherms. Through $\boldsymbol{v}' \cdot \nabla \overline{T}$, such motion transfers heat meridionally (e.g., in sloping convection). If it transfers heat poleward, eddy motion weakens the zonal-mean gradient of temperature, which is directed equatorward. Eddy heat transfer then weakens baroclinicity, driving mean thermal structure toward barotropic stratification. It thus releases available potential energy, which is converted to eddy kinetic energy (Sec. 15.1). Such behavior is intrinsic to the development of extratropical cyclones that typify synoptic weather systems. Those systems amplify through baroclinic instability, which releases available potential energy. The latter is continually re-generated by the nonuniform distribution of atmospheric heating and cooling (Figs. 1.34c, 9.41b).

16.3 THE EADY MODEL

The simplest description of baroclinic instability is due to Eady (1949). Consider disturbances to a mean flow that is invariant in y, bounded above and below by rigid walls at $z = 0$ and H on an f plane, and within the Boussinesq approximation (Sec. 12.5). A uniform meridional temperature gradient is imposed. By thermal wind balance, it corresponds to constant vertical shear (Fig. 16.1)

$$\overline{u} = \Lambda z \qquad \Lambda = \text{const.} \tag{16.13}$$

Under these circumstances, $\frac{\partial \overline{Q}}{\partial y}$ vanishes in the interior. Instability can therefore follow solely from the temperature gradient along the boundaries.

Disturbances to this system are governed by the eddy potential vorticity equation in log-pressure coordinates

$$\frac{D}{Dt}\left[\nabla^2 \psi' + \frac{f_0^2}{N^2}\frac{\partial^2 \psi'}{\partial z^2}\right] = 0. \tag{16.14.1}$$

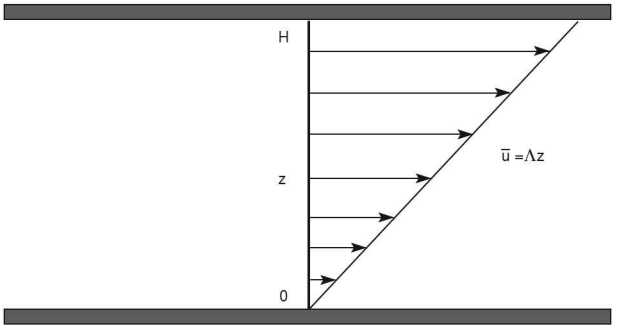

Figure 16.1 Geometry and mean zonal flow in the Eady problem of baroclinic instability.

With the thermodynamic equation, the boundary conditions become

$$\frac{D}{Dt}\left(\frac{\partial \psi'}{\partial z}\right) - \frac{\partial \bar{u}}{\partial z}\frac{\partial \psi'}{\partial x} = 0 \qquad z = 0, H. \tag{16.14.2}$$

Considering solutions of the form

$$\psi' = \Psi(z) cos(ly) e^{ik(x-ct)} \tag{16.15}$$

reduces (16.14) to the 1-dimensional boundary value problem

$$\frac{d^2\Psi}{dz^2} - \alpha^2 \Psi = 0 \tag{16.16.1}$$

$$(\bar{u} - c)\frac{d\Psi}{dz} - \Lambda \Psi = 0 \qquad z = 0, H, \tag{16.16.2}$$

where

$$\alpha = \frac{N}{f_0}|\boldsymbol{k}_h|, \tag{16.16.3}$$

with $|\boldsymbol{k}_h|^2 = k^2 + l^2$, is a stability-weighted horizontal wavenumber.[1] Solutions of (16.16.1) are of the form

$$\Psi = A cosh(\alpha z) + B sinh(\alpha z). \tag{16.17}$$

Substituting (16.17) into the boundary conditions (16.16.2) leads to a homogeneous system of two algebraic equations for the coefficients A and B. Nontrivial solutions exist only if the determinant of that system vanishes. Incorporating that condition yields the dispersion relation for Eady modes

$$\left(c - \frac{\Lambda H}{2}\right)^2 = \Lambda^2 H^2 \left[\frac{1}{4} - \frac{coth(\alpha H)}{\alpha H} + \frac{1}{(\alpha H)^2}\right]. \tag{16.18}$$

If the right-hand side of (16.18) is positive, c is real. The system is then stable. If the right-hand side is negative, unstable solutions exist. Because $c - \frac{\Lambda H}{2}$ must then

[1] Considering structure of the form $cos(ly) = \frac{1}{2}\left(e^{ily} + e^{-ily}\right)$ implicitly presumes that disturbances are trapped meridionally (e.g., by rigid walls at $y = \pm\frac{\pi}{2l}$).

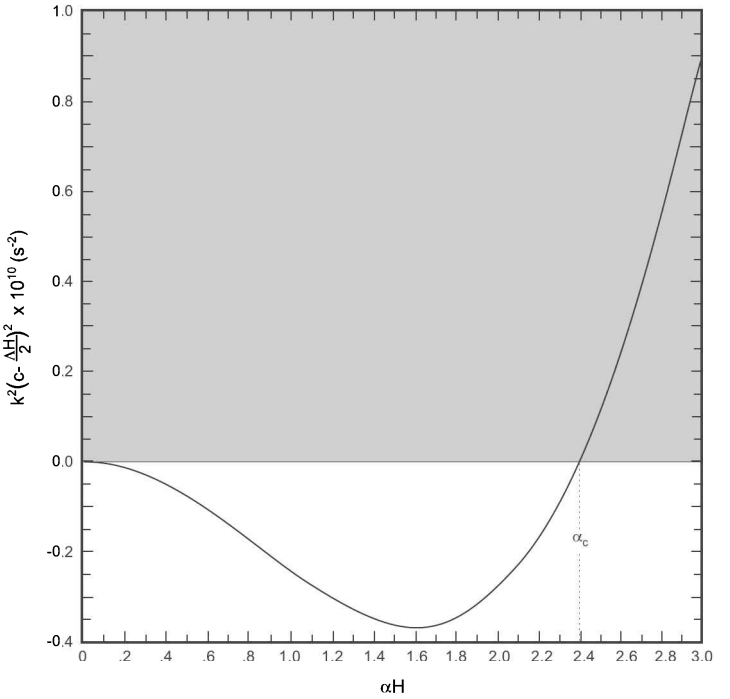

Figure 16.2 Frequency squared of Eady modes as a function of scaled horizontal wavenumber. Instability occurs for wavenumbers smaller than the cutoff α_c.

be imaginary,

$$c_r = \frac{\Lambda H}{2}. \tag{16.19}$$

Thus amplifying disturbances have phase speeds equal to the mean flow at the middle of the layer. They are advected eastward by $\overline{u}$ with its speed at the *steering level*: $z = \frac{H}{2}$. Although influenced by rotation, baroclinic disturbances are not Rossby waves in a strict sense. As the Eady model demonstrates, they can exist even on an f plane. Baroclinic disturbances can therefore exist in the absence of β, which provides the restoring force for Rossby waves.

The quantity $k^2\left(c - \frac{\Lambda H}{2}\right)^2$ reflects the square of the complex frequency. It is plotted as a function of horizontal wavenumber, αH, in Fig. 16.2. For α greater than a critical value, $\alpha_c \cong 2.4$, $k^2\left(c - \frac{\Lambda H}{2}\right)^2 > 0$ and solutions do not amplify. The system thus possesses a "short-wave cutoff" for instability. Amplifying solutions exist only for smaller α (larger horizontal scales). Wavenumbers $\alpha < \alpha_c$ are unstable: $k^2\left(c - \frac{\Lambda H}{2}\right)^2 < 0$. A maximum growth rate kc_i is achieved at $\alpha H \cong 1.6$ for $l = 0$. This value of αH also maximizes the growth rate for waves of nonzero aspect ratio $\frac{l}{k}$, which have smaller kc_i. For square waves ($k = l$) and values typical of the troposphere, $\alpha H \cong 1.6$. It predicts a wavenumber of order 5, typical of extratropical cyclones (see Fig. 2.10).

The maximum growth rate is proportional to the vertical shear Λ. By thermal wind balance, (12.11), it is therefore proportional to the meridional temperature gradient.

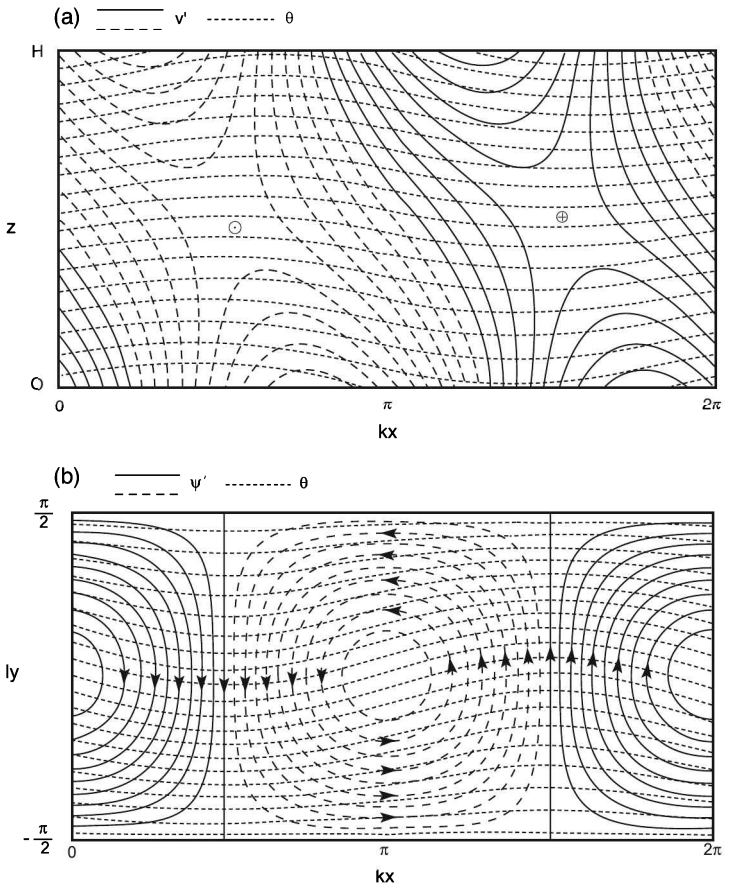

Figure 16.3 Structure of the fastest-growing square Eady mode ($k = l$). (a) Vertical section in the zonal plane at $y = 0$ of eddy meridional velocity v' (solid/dashed) and isentropic surfaces $\theta = \text{const}$ (dotted). Potential temperature increases upward. $\odot$ marks equatorward motion ($v' < 0$) and $\oplus$ marks poleward motion ($v' > 0$). (b) Horizontal section at $z = \frac{H}{2}$ of eddy streamlines (solid/dashed) and isentropes (dotted). Potential temperature increases equatorward.

Representative values give an e-folding time for amplification of a couple of days. The latter is broadly consistent with the observed development of extratropical cyclones.

Insight into how instability is achieved follows from the structure of the most unstable disturbance. The lower boundary condition (16.16.2) implies the following relationship between the coefficients in (16.17)

$$\frac{B}{A} = -\frac{\Lambda}{\alpha c}. \tag{16.20}$$

It yields the eddy thermal structure and motion in Fig. 16.3 for $k = l$. Plotted in Fig. 16.3a, on a vertical section passing zonally through the center of

the disturbance ($y = 0$), is the eddy meridional velocity v' (solid/dashed). Superimposed is the distribution of isentropes: $\theta = \overline{\theta} + \theta'$ (dotted). The fastest-growing Eady mode is characterized by a westward tilt with height. It places streamfunction anomalies about 90° out of phase between the lower and upper boundaries, as is evident from $v' = ik\psi'$.

Eddy motion maximizes at $z = 0$ and H. It assumes the form of two edge waves that are sandwiched between the upper and lower boundaries. Owing to the temperature gradient along them, those boundaries drive air across mean isotherms. They also trap instability, enabling the disturbance to amplify. Each edge wave decays vertically with the Rossby height scale $H_R = \alpha^{-1}$. In the limit $|\boldsymbol{k}_h| \to \infty$, $\alpha \gg \alpha_c$. H_R is then short enough for the two edge waves to be isolated from one another. Neither has vertical phase tilt. Hydrostatic balance (11.72.2) therefore implies a temperature anomaly that is in phase with the streamfunction anomaly (Prob. 16.4). The eddy velocity $v' = ik\psi'$ is therefore 90° out of phase with θ'. The two are said to be *in quadrature*. The eddy heat flux averaged over a wavelength $\overline{v'\theta'}$ then vanishes. Under these circumstances, eddy motion leaves the baroclinic stratification of the mean state unchanged. No available potential energy is released. It is for this reason that short wavelengths in the Eady model are stable.

For $\alpha < \alpha_c$, H_R is tall enough for the two edge waves to influence one another. Phase shifted, they produce the westward tilt apparent in Fig. 16.3a. The temperature anomaly is then no longer in phase with the streamfunction anomaly. Isentropes (dotted) actually tilt slightly eastward with height, making θ' positively correlated with v': Cold air ($\theta' < 0$) moves equatorward ($v' < 0$): out of the page. Warm air ($\theta' > 0$) moves poleward ($v' > 0$): into the page.[2] Both motions contribute positively to $\overline{v'\theta'}$. Consequently, they achieve poleward eddy heat flux. The latter releases available potential energy, which is converted into eddy kinetic energy. The mode's amplification is thus directly related to its westward tilt with height.

Plotted in Fig. 16.3b, for a horizontal section at $z = \frac{H}{2}$, is the eddy streamfunction (solid/dashed), along with the distribution of isentropes (dotted). At the center is a cyclonic anomaly, which moves eastward. Ahead of it, warm air (high θ) is displaced poleward. Behind it, cold air (low θ) is displaced equatorward. As the motion is adiabatic, air moves along isentropic surfaces. Plotted in Fig. 16.4, for a meridional section at $kx = \frac{3\pi}{2}$, is the eddy motion. Superimposed is the distribution of zonal-mean isentropes: $\overline{\theta}$ (dotted). Zonal-mean isentropes slope upward toward the pole (cf. Fig. 12.5). Eddy motion has similar slope. Consequently, poleward-moving air ahead of the cyclonic anomaly in Fig. 16.3b ascends. Equatorward-moving air behind the anomaly descends. Characteristic of sloping convection, this motion has the same form that it would were air to move along zonal-mean isentropic surfaces. However, eddy motion in Fig. 16.4 has only half the slope of those surfaces (Prob. 16.13). Eddy motion is therefore directed across zonal-mean isentropic surfaces. Its impact is manifest in the horizontal distribution of θ (Fig. 16.3b): Warm air is displaced poleward, whereas cold air is displaced equatorward. Both displacements represent a poleward transfer of heat. The latter releases available potential energy, enabling the disturbance

[2] At the steering level, $z = \frac{H}{2}$, v' and θ' are perfectly in phase.

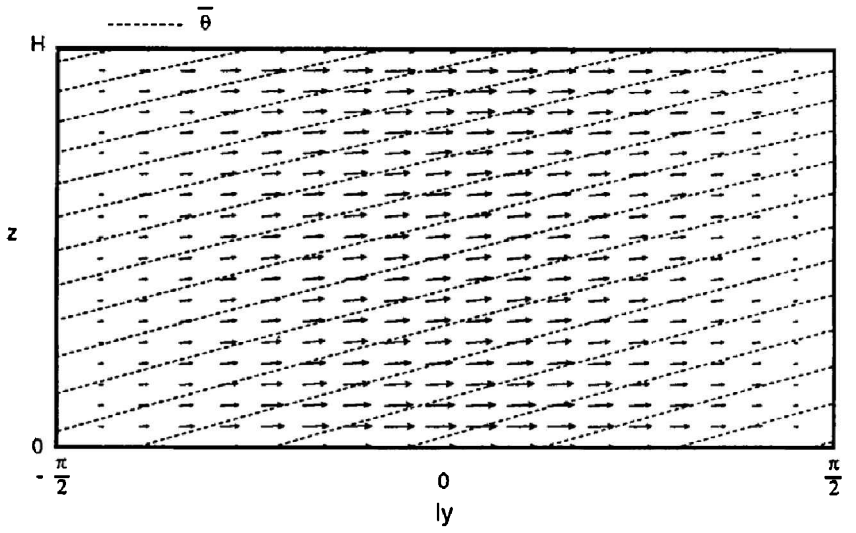

Figure 16.4 Vertical section in the meridional plane at $kx = \frac{3\pi}{2}$ of zonal-mean isentropic surfaces (dotted) and motion for the fastest-growing square Eady mode. Potential temperature increases upward and equatorward (cf. Fig. 12.5).

to amplify. Simultaneously, poleward heat transfer weakens the meridional gradient of zonal-mean temperature, which is directed equatorward. Through thermal wind balance, it must also weaken the strong zonal jet that accompanies that temperature gradient. These influences of the amplifying disturbance are equivalent to driving zonal-mean thermal structure toward barotropic stratification. By eliminating baroclinicity, they deplete available potential energy, which is converted into eddy kinetic energy.

Extratropical cyclones have qualitatively similar structure during their development. Figure 16.5 shows distributions of 700-hPa height and temperature for an amplifying cyclone situated off the coast of Africa on March 2, 1984. This disturbance is the precursor to the cyclone apparent in Figs. 1.18 and 1.29 two days later. During amplification, the system tilts westward. This transfers heat poleward and releases available potential energy – analogous to an unstable Eady mode with $\alpha < \alpha_c$. Eddy heat flux tends to maximize near 700 hPa, which typifies the steering level of observed cyclones. This is lower than the steering level predicted by the Eady model. However, an unbounded model treated by Charney (1947) reproduces the observed steering level while retaining the essential features captured by Eady's solution.

Isotherms in Fig. 16.5 (dashed) exhibit the characteristic signature of sloping convection: Analogous to behavior in the Eady model, a tongue of warm (high-θ) air is drawn poleward ahead of the closed low. Simultaneously, a tongue of cold (low-θ) air is drawn equatorward behind it (cf. Figs. 16.3b; 12.10). Those bodies of air have disparate histories, which are reflected in contemporaneous IR and water vapor imagery (Figs. 16.6a,b). A tongue of high cloud cover and humidity extends northwestward from the African coast. It marks the *warm sector* ahead of the cyclone (delineated by the warm and cold fronts in Fig. 16.5). A complementary tongue of cloud-free air and low humidity is simultaneously being drawn equatorward behind the cyclone. Sharp

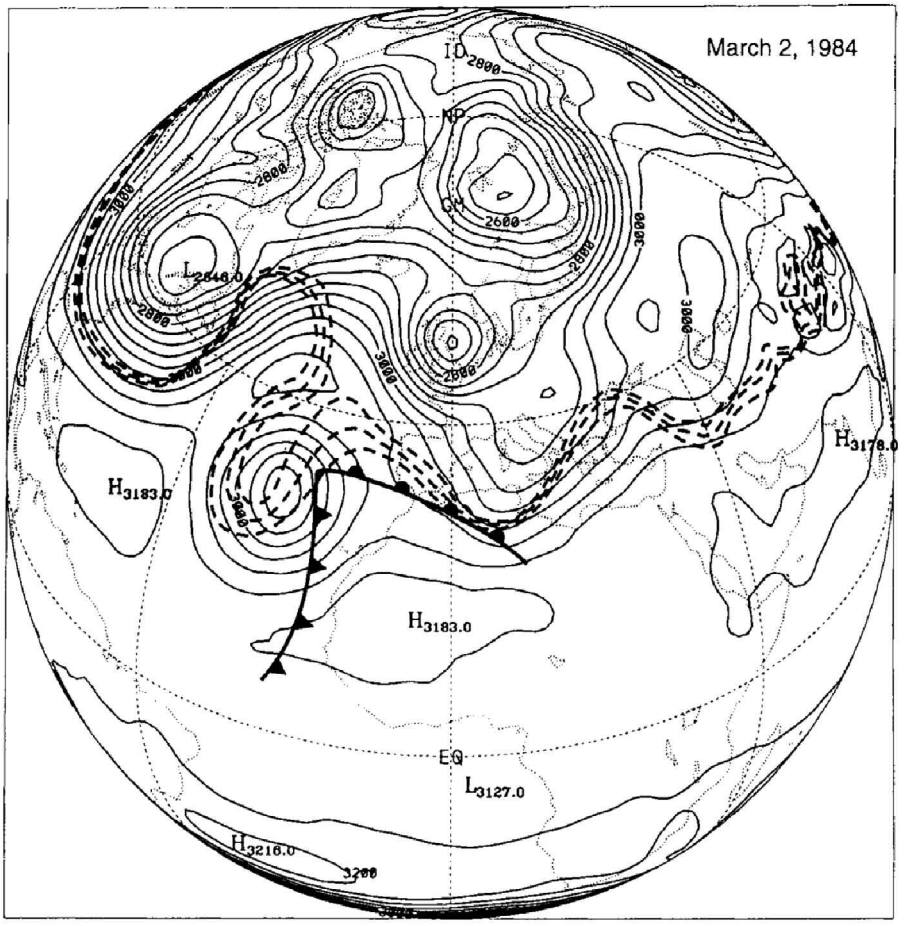

Figure 16.5 700-hPa height (solid) and selected isotherms (dashed) on March 2, 1984. A surface frontal analysis is superposed. Cold (warm) front marked by pointed (rounded) barbs. In the eastern Atlantic, isotherms have been deflected poleward ahead of the amplifying cyclone and equatorward behind it (cf. Figs 16.3b; 12.10).

gradients separating those bodies of air represent warm and cold fronts at the surface. Humid air comprising the warm sector can be traced, in water vapor imagery (Figs. 16.6d, 1.29), back to its source: the Amazon basin. There, tropical convection humidifies the troposphere (Sec. 9.3.4). Air advancing behind the cold front undercuts the warm sector in sloping convection. Humid air is then lifted, producing the extensive cloud shield in Fig. 16.6a.

16.4 NONLINEAR CONSIDERATIONS

While capturing the essential features of cyclone development, Eady's solution provides only a hint of their behavior at maturity. Conversion of available potential energy into eddy kinetic energy enables a baroclinic disturbance to intensify and eventually attain finite amplitude. Finite horizontal displacements then invalidate the

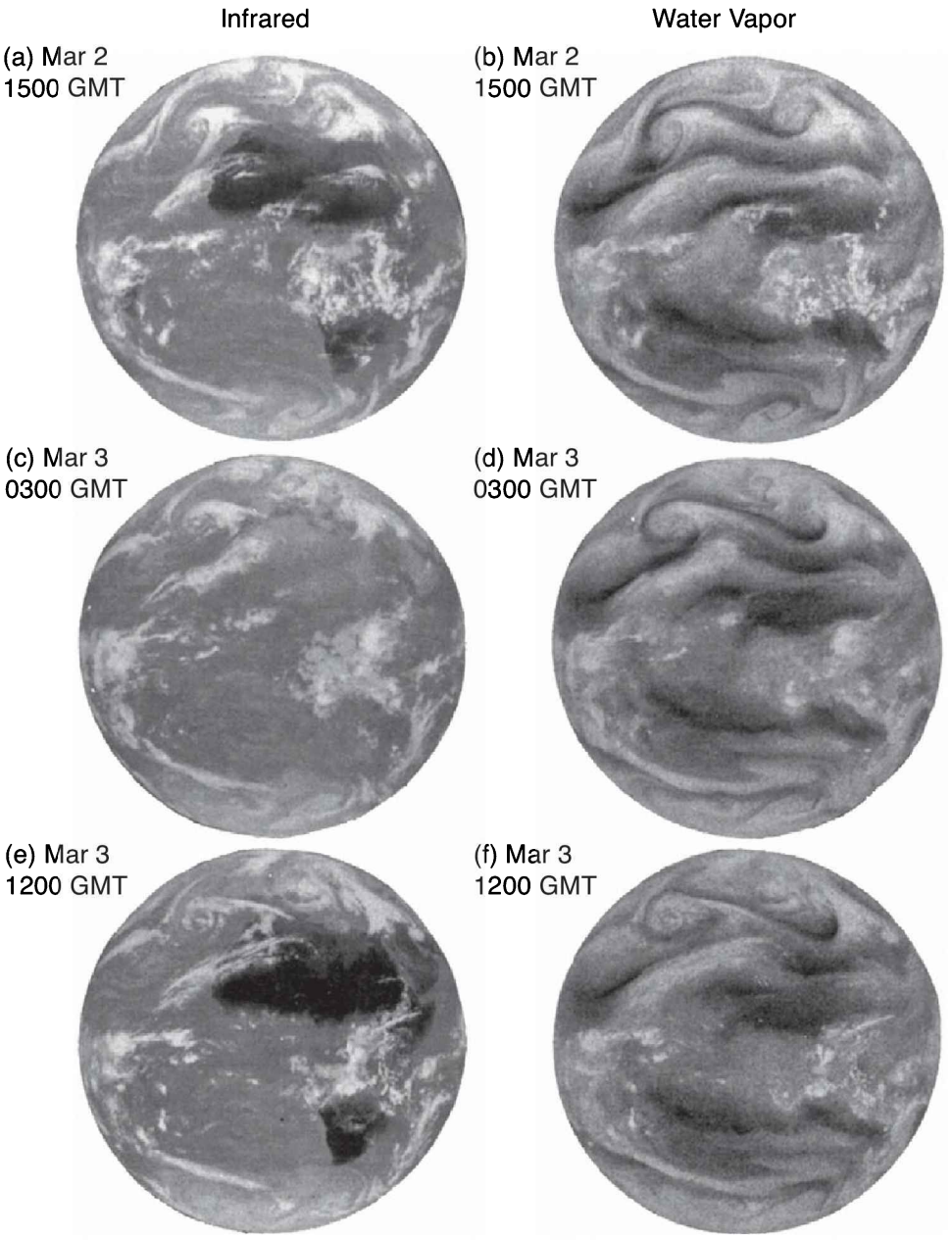

Figure 16.6 Infrared and water vapor imagery from Meteosat between March 2 and March 4, 1984, which reveals the evolution of an extratropical cyclone off the northwest coast of Africa. In the water vapor imagery, humid air is represented light and dry air dark. The warm sector ahead of the cyclone is marked by a tongue of high cloud and moisture that slopes northwestward on March 2. That air mass subsequently overturns near the juncture of cold and warm fronts that delineate it, forming an occlusion in which cold and warm air are entrained and mixed horizontally (cf. Fig. 9.21).

linear description on which Eady's model is based. The latter predicts exponential amplification to continue indefinitely. The situation is analogous to convective displacements under statically unstable conditions (Sec. 7.3). At finite amplitude, second-order effects enter. They modify the zonal-mean state, eventually limiting the amplification of a baroclinic disturbance.

As a baroclinic disturbance amplifies, horizontal displacements become increasingly exaggerated (Fig. 16.3b). Warm tropical air is eventually folded north of cold polar air. Such behavior is evident in the distribution of potential vorticity on March 2, 1984 (Fig. 12.10). Deformations experienced by those air masses steepen potential temperature gradients that separate warm and cold air (e.g., Fig. 12.4). The accompanying fronts are thus intensified. Continued advection leads to tongues of warm and cold air eventually encircling the low. The warm sector has then wound up at the junction of the warm and cold fronts, as is revealed by water vapor in Fig. 16.6 (see also cloud cover in Fig. 9.21). Upon reaching this stage, the cyclone in Fig. 16.5 is said to have *occluded*. Warm and cold fronts overlap in the center of the disturbance. There, the warm air mass has been swept over the cold air mass.[3] Characteristic of sloping convection, this structure marks the mature stage of the cyclone's life cycle. The surface low is then positioned beneath the upper-level low. This eliminates the disturbance's westward tilt, its poleward heat flux, and hence the release of available potential energy. The disturbance is then analogous to a stable Eady mode, with $\alpha > \alpha_c$. Cold and warm air drawn into the occlusion are subsequently wound together and mixed horizontally. By homogenizing temperature, this process drives thermal structure toward barotropic stratification. It thereby exhausts the supply of available potential energy.

Figure 16.6 shows sequences of IR and water vapor imagery while the disturbance in Fig. 16.5 matures. At 1500 UT on March 2 (Fig. 16.6a,b), the cold front is approaching the warm front near their junction. The warm sector is clearly defined, assuming the form of an inverted V. Twelve hours later, the 700 hPa low has deepened (not shown). The warm sector in IR and water vapor imagery (Fig. 16.6c,d) has then been sheared to the northwest. There, cold dry air is being entrained with warm humid air inside the occlusion that has formed. This process culminates in cold and warm air at the occlusion winding up into a spiral. It resembles behavior in the cylindrical annulus at fast rotation (Fig. 15.7f). By 1200 UT on March 3 (Figs. 16.6e,f), air inside the occlusion has wound up into a tight vortex, separating from the remaining warm sector to its south and east. Interleaving bands of cold and warm air are apparent in both cloud cover and humidity. They symbolize efficient horizontal mixing. One day later (Figs. 1.18, 1.28), that mass of air has become nearly homogeneous. The 700 hPa low has then weakened. Similarly, high cloud that developed earlier through sloping convection is dissipating. Only a broad spiral of equatorward-moving air remains. It is being drawn cyclonically around the now-diffuse anomaly of potential vorticity, wherein cold and warm air have been mixed.

Since θ (more generally, θ_e) is conserved for individual air parcels, horizontal mixing weakens the meridional gradient of temperature, rendering potential temperature nearly uniform. By thermal wind balance, it simultaneously weakens the strong zonal jet that accompanies baroclinic stratification (cf Figs. 6.3 and 6.4). The impact on the

[3] The occlusion actually forms as the surface low (not shown) separates from the junction of warm and cold fronts and deepens farther back into the cold air mass.

jet is illustrated in Fig. 16.7, which displays conditions that accompany an amplifying baroclinic system that has reached maturity. SLP is marked by a closed low over southern Australia (Fig. 16.7a). Extending equatorward from the low is a cold front, which divides warm/humid tropical air at the surface from cold/dry extratropical air.

The air masses are clearly distinguished in the contemporaneous water vapor image (Fig. 16.7b). Humid tropical air (light) has been drawn poleward, forming a warm sector with characteristic V shape. It wraps up inside the closed low, where the system has occluded. West of the warm sector is dry extratropical air (dark) that is being entrained with humid tropical air inside the occlusion. The deformation of warm and cold air masses exerts a similar influence on the horizontal temperature gradient. Through thermal wind balance, the distorted structure is conveyed into the horizontal distribution of vertical shear and, hence, into the horizontal structure of the jet stream. Superimposed in Fig. 16.7a are 300-hPa isotachs stronger than 20 m/s (shaded). The jet has been overturned, mirroring the interface between air masses.

Subsequent evolution homogenizes the meridional temperature gradient that existed initially, with a commensurate weakening of the jet. The amplifying system thus drives thermal structure toward barotropic stratification. Baroclinic instability that was present initially has then been neutralized. No more potential energy is available for conversion to eddy kinetic energy. The available potential energy has been exhausted. This process is a counterpart of vertical mixing by convection, which neutralizes static instability (Sec. 7.3). In each, unstable disturbances modify the mean state. Such interaction contrasts with wave propagation under stable conditions. Parcel displacements are then bounded. Outside regions of dissipation, where wave activity is absorbed (Sec. 14.5.4), they leave the mean state largely unaffected.

The preceding treatment applies formally to a zonally symmetric mean state. In practice, the results also lend insight into localized regions of instability. Amplified planetary waves in the Northern Hemisphere reinforce zonal-mean vertical shear, producing a broken storm track. The latter is marked by localized jets east of Asia and North America (cf. Figs. 15.11a). The North Atlantic and North Pacific storm tracks are strongly baroclinic. They are preferred sites of cyclone development (Fig. 15.10). Calculations in a zonally asymmetric basic state reveal that planetary waves concentrate unstable amplification in such zones (Simmons et al., 1983; Frederiksen, 2006). Through locally intensified shear, they make the fastest growth rate under zonally symmetric conditions even faster, while removing the shortwave cutoff for instability. The fastest-growing modes, which are shaped by the prescribed planetary wave pattern, then share features with teleconnection patterns (Sec. 14.5.3).

In the Southern Hemisphere, planetary waves are weaker. They leave the mean state close to zonal symmetry, producing a continuous storm track. This enables cyclones in the Southern Hemisphere to assume a distribution in longitude that is more uniform than is observed in the Northern Hemisphere. Occasionally, they assume the form of baroclinic modes in a rotating annulus, wherein the mean state is zonally symmetric (cf. Figs. 2.10, 15.7e).

The criteria for instability also have implications to planetary waves that have attained large amplitude. The situation is analogous to the breaking of gravity waves. The latter overturn isentropic surfaces (Fig. 14.25), folding high θ beneath

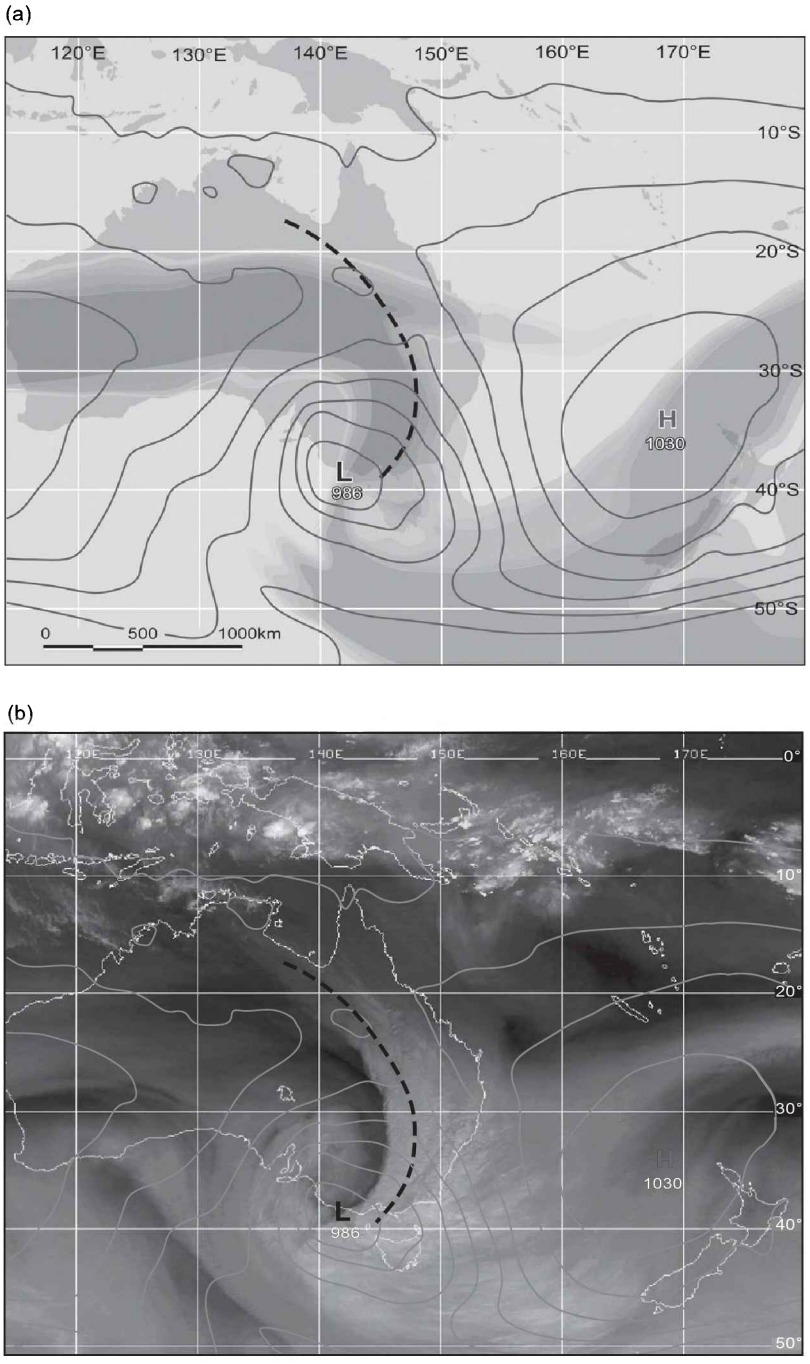

Figure 16.7 Conditions accompanying an amplifying baroclinic system that has reached maturity. (a) Distribution of SLP (contoured) and 300-hPa isotachs stronger than 20 m/s, which delineate the jet stream (shaded). (b) Contemporaneous water vapor image from MTSAT, representing humid air (light) and dry air (dark). See color plate section: Plate 18.

low θ. This makes $\frac{\partial\theta}{\partial z} < 0$ locally, rendering the region statically unstable. Convective mixing that ensues absorbs organized wave motion. Simultaneously, it drives $\frac{\partial\theta}{\partial z}$ to zero, neutralizing the instability. Planetary waves of sufficient amplitude exert an analogous influence on horizontal structure. They overturn the distribution of the conserved property Q (Fig. 14.26). High-potential vorticity is then folded south of low-potential vorticity. This makes $\frac{\partial Q}{\partial y} < 0$ locally, rendering the horizontal motion dynamically unstable (Sec. 16.2). At that point, the planetary wave field breaks. Small-scale eddies develop in the region of instability (Fig 14.23). They mix Q horizontally. This process absorbs organized wave motion. Simultaneously, it drives $\frac{\partial Q}{\partial y}$ to zero, neutralizing the instability.

SUGGESTED REFERENCES

An Introduction to Dynamic Meteorology (2004) by Holton provides a thorough treatment of baroclinic disturbances.

Atmosphere-Ocean Dynamics (1982) by Gill compares the Charney and Eady models of baroclinic instability.

A synoptic description of extratropical cyclones is presented in *Atmospheric Science: An Introductory Survey* (2006) by Wallace and Hobbs.

PROBLEMS

1. In the atmosphere of a newly discovered planet, the circulation is described by the barotropic zonal flow

$$\overline{u}(y) = -U\cos(2\phi),$$

where $U = 0.55\Omega a$. (a) Characterize the inertial stability of this flow as a function of latitude. (b) Describe the zonal-mean circulation toward which inertial instability will drive the flow.

2. Consider westerly flow that corresponds to an angular velocity $A(z) = \frac{\overline{u}}{a\cos\phi}$ that varies only with height. (a) Within the framework of quasi-geostrophic motion and the Boussinesq approximation, what sign of curvature must the velocity profile $A(z)$ have for shear instability to develop? (b) At what latitudes is shear instability favored most if $A(z) = \epsilon(z) \cdot 2\Omega$, with $\epsilon \ll 1$?
3. Show that, in the absence of rotation, criterion (1) in Sec. 16.2.2 recovers Rayleigh's condition for instability: A barotropic flow must possess an inflection point in its interior. (b) Discuss the influence rotation has on shear instability.
4. Demonstrate that the limiting structure of Eady modes for $H \to \infty$ has v' in quadrature with θ'.
5. Derive an expression for the shortwave cutoff α_c for instability in the Eady problem.
6. Show that the maximum growth rate of Eady modes is achieved for $l = 0$. (b) Express the growth rate of the fastest-growing square Eady mode ($k = l$) in terms of that of the fastest growing Eady mode ($l = 0$).

7. Calculate the e-folding times of square Eady modes ($k = l$) for an f plane at 45°, $N^2 = 10^{-4}$ s^{-2}, vertical shear of 3 m s^{-1} km^{-1}, a rigid lid at 10 km, and for zonal wavenumbers 1–8.
8. Use the Eady problem to explain (a) why mid-latitude cyclones develop and track along the jet stream, (b) how baroclinic instability would be altered if the jet were displaced equatorward.
9. Precipitation inside cyclones often assumes a banded structure. Discuss this feature in relation to the evolution in Fig. 16.6, the distribution of potential vorticity Q_g, and Ekman pumping (Sec. 13.4).

10. Unlike extratropical cyclones, tropical cyclones are driven by latent heat release. Suppose a typhoon drifts poleward from the ITCZ; see color plate section: Plate 0. (a) Describe its evolution as it migrates over colder SST. (b) What structure of mid-latitude westerlies will enable it to sustain itself?
11. Show that, for Eady modes, the eddy heat flux $\overline{v'\theta'}$ is positive and independent of height.
12. Derive a necessary condition for instability of a quasi-geostrophic zonal flow that is bounded vertically at $z = 0$ and H by rigid walls.
13. Show that, for the fastest-growing Eady mode, the maximum slope of motion in the meridional plane is only about half the slope of mean isentropic surfaces.
14. Within the framework of an initial value problem, describe the structure and evolution predicted by the Eady model if the flow in Prob. 15.7 is initialized with random structure having a broad wavenumber spectrum (a) under inviscid adiabatic conditions, (b) in the presence of linear dissipation[4] with a time scale equal to the shortest e-folding time of zonal wavenumber 2 under inviscid adiabatic conditions, (c) in the presence of linear dissipation with a time scale equal to the shortest e-folding time of zonal wavenumber 4 under inviscid adiabatic conditions.
15. A wave packet approaches its critical line with phase speed c_r equal to the real part of c in (16.8.1). Describe the wave packet's evolution in the presence of weak dissipation if, under inviscid adiabatic conditions, (a) c in (16.8.1) is real, (b) c in (16.8.1) is complex.

[4] Rayleigh friction and Newtonian cooling of the same time scale.

CHAPTER

SEVENTEEN

Influence of the ocean

Regional climate is strongly influenced by thermal properties of the Earth's surface, in particular, by neighboring ocean that moderates extreme conditions (Chap. 15). An analogous influence is exerted on global-mean climate. Owing to its large heat capacity and capacity to hold substances in solution, the ocean serves as a reservoir of energy and carbon. It thereby provides thermal inertia to the climate system, figuring importantly in exchanges with the atmosphere of heat and carbon dioxide.

The Earth has only one ocean. It is compartmentalized in major basins, like the Atlantic and Pacific. Those bodies of water are interconnected by currents, circulation systems that exchange mass between ocean basins. Ocean circulations are driven by atmospheric wind stress, which transfers momentum to the ocean. They are also driven by transfers of heat and moisture, which, through density, influence the buoyancy of seawater.

17.1 COMPOSITION AND STRUCTURE

Seawater is a solution of pure water and a variety of salts, mostly sodium chloride, which accounts for more than 80% of its ionic composition. *Salinity S* is the relative concentration of dissolved material, measured in grams per kilogram or parts per thousand (‰). Each is approximately equal to Practical Salinity Units (PSU). Displayed in Fig. 17.1 is surface salinity. It varies between 30 and 40 g/kg. However, values are clustered about 35 g/kg. High salinity is found in the subtropical Atlantic and the Mediterranean Sea. There, as over the subtropical Pacific, salinity is increased by evaporation.

Figure 17.2 compares, in zonal-mean values, salinity (dashed) against net evaporation (solid). The latter equals the evaporation rate minus the precipitation rate. Maxima

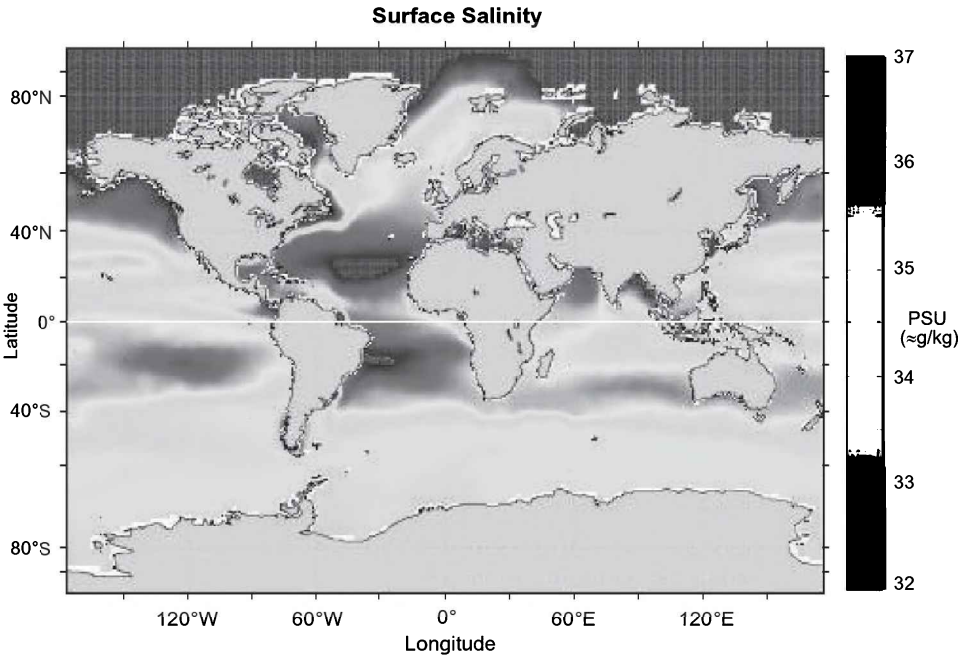

Figure 17.1 Annual-mean surface salinity, in Practical Salinity Units (PSU), approximately equal to g/kg. *Source:* Antonov et al. (2006). See color plate section: Plate 19.

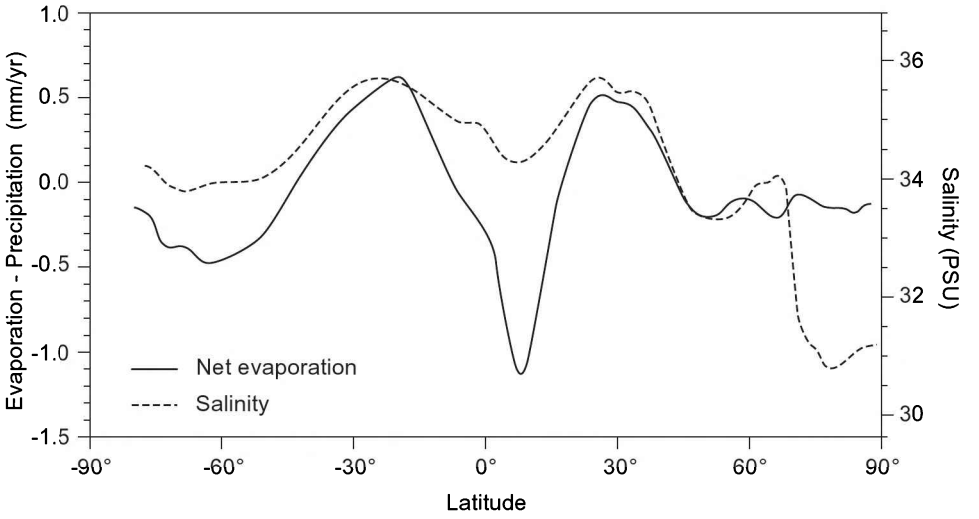

Figure 17.2 Zonal-mean surface salinity (solid) compared against net evaporation, equal to evaporation–precipitation (dashed). Adapted from Stewart (2008).

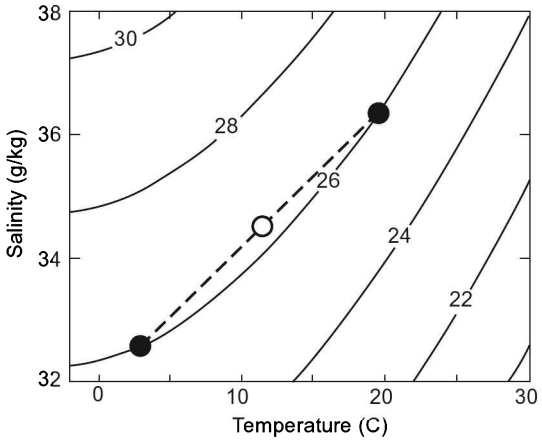

Figure 17.3 Density anomaly σ (kg/m^3), at sea level, as a function of salinity and temperature (solid). Superimposed are different mixing ratios of two bodies of water that have different values of salinity and temperature (solid circles) but identical $\sigma = 26$ g/kg (dashed). Mixing in equal proportion results in intermediate values (open circle).

of salinity appear in the subtropics. They coincide with positive maxima of net evaporation, which act to increase salinity. Those maxima reflect cloud-free conditions beneath the descending branch of the Hadley circulation, conditions that inhibit precipitation and maximize SW heating. Just the reverse appears near the equator, where salinity achieves a minimum. There, net evaporation attains a sharp negative minimum. It reflects net precipitation, which acts to reduce salinity. Concentrated inside the ITCZ, heavy precipitation lies beneath the ascending branch of the Hadley circulation (Fig. 9.41). The sharp minimum of S will be seen to follow also from upwelling of fresher water, which prevails in a neighborhood of the equator (Sec. 17.4.1).

The distribution of sea surface temperature (SST) is displayed in Fig. 5.1. It maximizes near the equator, exceeding 28°C in the Indian Ocean and western Pacific. Temperature decreases poleward, approaching 0°C in ice-laden regions at high latitude.

As seawater is a mixture, its state is determined by two thermodynamic properties plus salinity (Sec. 5.3). Density then has the form $\rho = \rho(T, p, S)$, analogous to $\theta = \theta(p, T, r)$ for moist air. Changes of density are small departures from the mean density of seawater (1027 kg/m^3). Discriminating to them is the *density anomaly*

$$\sigma(T, p, S) = \rho(T, p, S) - 1000\,\mathrm{kg/m^3}.$$

In the upper ocean, pressure remains small enough for seawater to be treated as incompressible. The density anomaly then depends only on temperature and salinity

$$\sigma = \sigma(T, S).$$

The forgoing represents the equation of state for seawater. Nonlinear, it is determined empirically. Figure 17.3 plots the dependence of density on T and S (at SLP). Density increases with decreasing temperature and increasing salinity. Isopleths of density (isochores or, in oceanographic vernacular, *isopycnals*) are concave in the same sense: toward decreasing temperature and increasing salinity. This nonlinear dependence

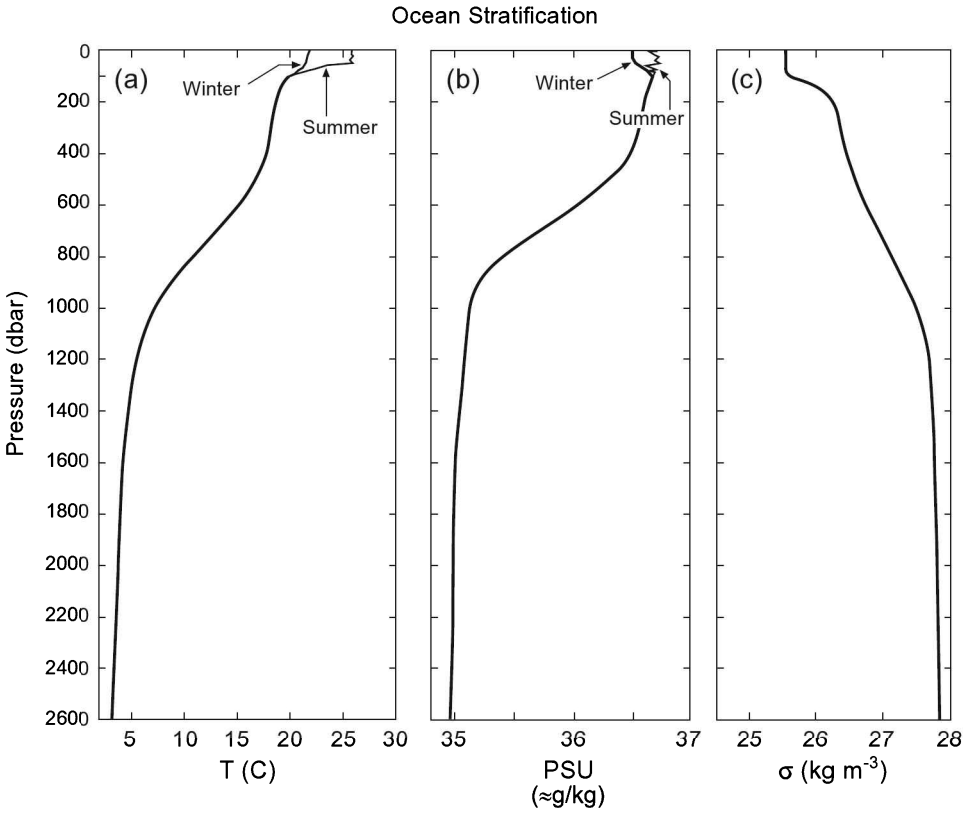

Figure 17.4 Profiles of (a) temperature and (b) salinity in Atlantic, near Bermuda, under summertime and wintertime conditions. (c) Corresponding mean profile of density anomaly. (1 dbar = 0.1 bar translates into approximately 1 m of depth.) *Sources:* Phillips and Joyce (2007), Java Ocean Atlas, http://www.epic.noaa.gov/epic (21.03.10).

has an important consequence for the buoyancy of seawater. Two water parcels of identical density but different salinity, upon being mixed, then achieve greater density. As indicated in Fig. 17.3, both parcels must initially lie on the same isopleth of σ. Because T and S are conserved, their ratio must be as well. The mixture must therefore lie on a line of constant $\frac{T}{S}$, intermediate to the two initial states. This positions the mixture at higher values of σ. Known as *cabbeling*, this process forms dense water in regions where surface currents converge. Such water, in turn, sinks to greater depth.

17.1.1 Stratification

As in the atmosphere, ocean properties are shaped by the vertical distribution of mass. Near the surface is a layer of 10–100 m in which vertical overturning prevails. Known as the *mixed layer*, it is the oceanic counterpart of the troposphere. Inside the mixed layer, temperature and salinity are invariant with depth (Fig. 17.4). So too then is density. Its uniform vertical distribution corresponds to neutral stability, which is achieved by efficient overturning.

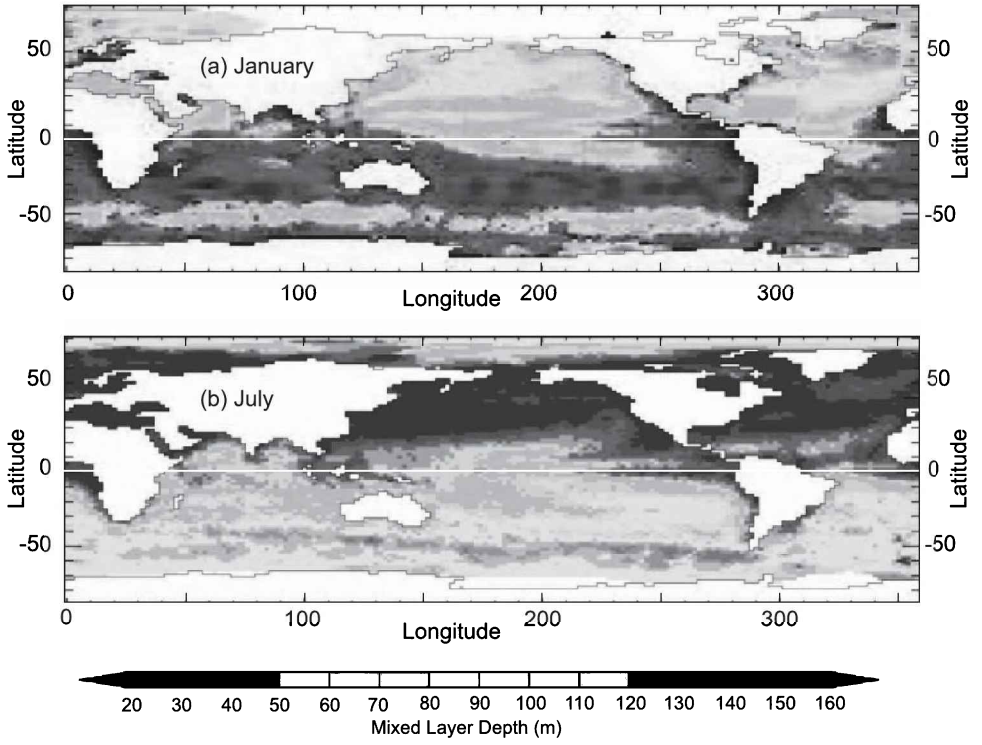

Figure 17.5 Depth of the mixed layer, as function of geographical position, during (a) January and (b) July. *Source:* http:/www./locean-ipsl.upmc.fr. See color plate section: Plate 20.

The mixed layer is maintained by two processes: Surface cooling destabilizes underlying ocean, driving thermal overturning (Fig. 7.11). Surface wind and accompanying wave motion drive mechanical overturning. Both influences are amplified during winter. As is evident from Fig. 17.4, the mixed layer is then deepest. During summer, surface cooling is replaced by surface heating. It stabilizes underlying ocean, while surface wind is weak. The mixed layer is then shallowest.

The depth of the mixed layer is plotted in Fig. 17.5. During January (Fig. 17.5a), the mixed layer is expanded in the north Atlantic and north Pacific. Driven by cooling and surface wind in the storm tracks, its depth there exceeds 100 m. At low latitudes, and in the summer hemisphere, it is shallower, with depth of 30–50 m. During July (Fig. 17.5b), the mixed layer is expanded adjacent to Antarctica, in the storm track of the Southern Hemisphere. Its depth then is again shallowest in the summer hemisphere, where values decrease to 20 m.

Beneath the mixed layer is the *thermocline*, in which temperature decreases and density increases downward (Fig. 17.4).[1] The downward increase of density makes the thermocline strongly stable. Together with continuity, which requires $\frac{d\rho}{dt} = 0$, this feature constrains water to move along isopycnal surfaces. Quasi-horizontal in the

[1] Salinity also influences the downward increase of density, which is known more generally as the *pycnocline*. However, in the open ocean, the variation of temperature dominates (cf. Fig. 17.4a,c). The pycnocline is then equivalent to the thermocline.

open ocean, isopycnal surfaces are the counterpart of isentropic surfaces in the atmosphere (for which $\frac{d\theta}{dt} = 0$). From the base of the mixed layer, where temperature is of order 20°C, the thermocline extends downward to a depth of about 1000 m, where temperature is 2–4°C.

Beneath the thermocline is the *deep ocean*. There, temperature and salinity vary with depth only gradually (Fig. 17.6). Characterized by temperatures of ~4°C, this layer represents 80% of the ocean's overall mass. Water in the deep ocean is largely sequestered from the surface. It therefore experiences limited interaction with the atmosphere. Such interaction is concentrated in those regions near the surface where *deep water* is produced and destroyed.

The submerged ocean layers vary with latitude. As illustrated in Fig. 17.6a, they are deepest in the tropics and shallowest at high latitude. Because SST decreases poleward (Fig. 5.1), the submerged layers eventually intersect the surface at high latitude, forming outcroppings. There, deep water and surface water interact.

17.1.2 Motion

Observations of the ocean circulation are mostly limited to a neighborhood of the surface. Plotted in Fig. 17.7 is the mean surface circulation. Large-scale motion is dominated by anticyclonic gyres that prevail in the subtropics of each hemisphere. Near the equator, they form strong easterly motion: the *North* and *South Equatorial Currents*. Compensating them at high northern latitudes is strong westerly motion: the *North Pacific* and *North Atlantic Currents*. These EW currents are bridged by coastal currents in the NS direction: In the Pacific, the *California Current* flows equatorward along North America, whereas the *Kuroshio Current* flows poleward along Asia. By transferring warm water poleward and cold water equatorward, they lead to poleward transport of heat. Similar motion prevails in other basins. In the Atlantic, the *Gulf Stream* flows poleward along North America. It eventually forms the *North Atlantic Current*, which moderates the temperature of air that is carried across Europe by westerlies. The same influence maintains most of the north Atlantic ice-free. The *Canary Current* flows equatorward along Europe and Africa. Mirroring the preceding features are coastal currents in the Southern Hemisphere: In the Pacific, the *Humboldt Current* flows equatorward along South America, whereas the *East Australian Current* flows poleward along Australia. In the Atlantic, the *Benguela Current* flows equatorward along Africa, whereas the *Brazil Current* flows poleward along South America.

The large-scale gyres in Fig. 17.7 have velocities of order 0.5 m/s. They are intensified along the western boundaries of ocean basins, where coastal currents transfer warm water poleward. There, motion is concentrated in jets, which are stronger and narrower than other legs comprising the gyres. The basin-scale circulations will be seen in Sec. 17.4 to be driven by wind stress that is exerted on the ocean surface.

Close to the equator, the easterly motion that prevails at low latitude reverses. The *Equatorial Counter Current* is westerly. Evident around the Earth, it will be seen to follow from certain features of equatorial dynamics. Crossing the equatorial Atlantic is northward motion. It transports water from the Southern Hemisphere to the Northern Hemisphere. That inter-hemispheric transport must be compensated by subsurface transport in the opposite direction.

At high latitudes are the Arctic Ocean and the Southern Ocean. The Arctic Ocean has limited interaction with surface water in other basins. Such interaction is concentrated

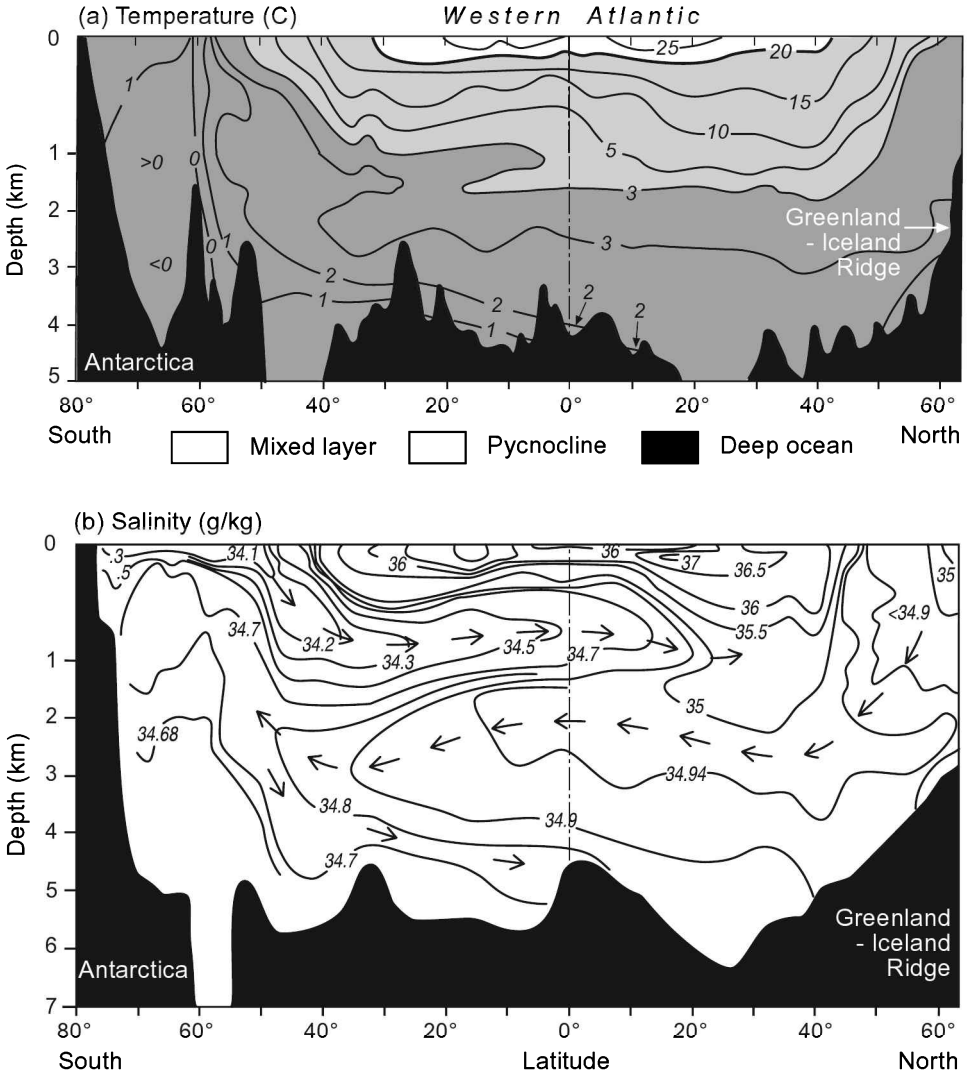

Figure 17.6 Latitude-depth cross section in western Atlantic of (a) temperature (°C) and (b) salinity (g/kg). *Sources:* Dietrich et al. (1980), Lynn and Reid (1968).

in the *Norwegian Current*, which pumps warm water from lower latitudes into the Arctic basin. Compensating that inflow is outflow of cold water along the coasts of Labrador and Greenland. At high southern latitudes is the *Antarctic Circumpolar Current*. Unbroken by continents, it is composed of a continuous westerly drift. The Antarctic Circumpolar Current coincides with SST of 4°C and colder. It therefore represents the motion of deep water, which is exposed at high latitude (Fig. 17.6a).

Observations of subsurface motion are hampered by limited coverage, as well as slow velocity that is characteristic of the deep ocean. Of order 1 mm/s, such motion is difficult to measure. At this speed, water that enters the deep ocean at one end

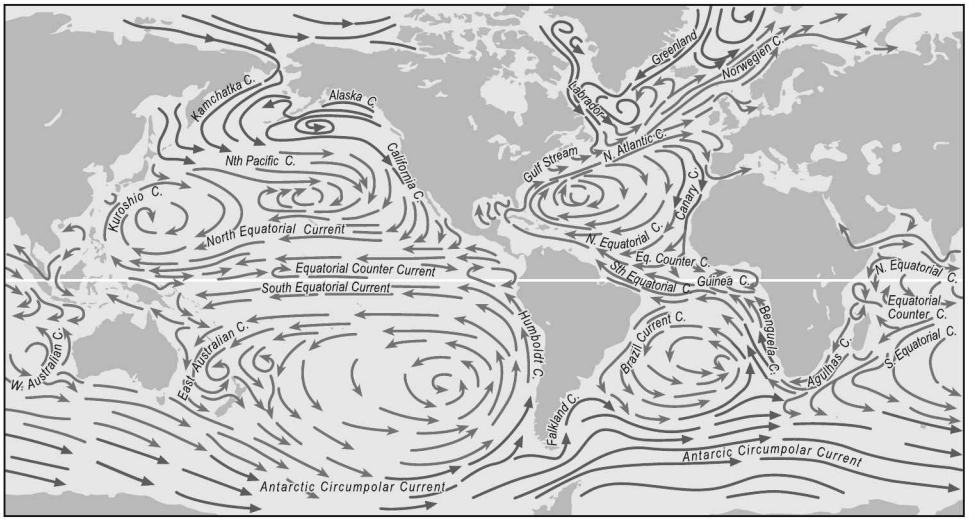

Figure 17.7 Surface circulation during January, illustrating water that is comparatively warm (red) and cold (blue). *Source:* US Navy Oceanographic Office. See color plate section: Plate 21.

of its circulation remains there for many centuries, before eventually emerging at the other end.

The deep ocean circulation is driven by buoyancy. Because density is determined by both temperature and salinity, the resulting motion is called the *thermohaline circulation* (also the *abyssal circulation* and *meridional overturning circulation*). The thermohaline circulation controls properties of the deep ocean and, therefore, most of the ocean's store of heat and carbon. Despite this pivotal role, observational limitations leave the thermohaline circulation poorly documented. Illustrated in Fig. 17.8, it must be inferred from the structure of conserved properties such as salinity, which serves as a tracer of motion (Fig. 17.6b).

At high latitude, seawater experiences strong cooling during winter, which renders it negatively buoyant. Further, some of it freezes, removing fresh water. Analogous to evaporation, this process enriches salinity, reinforcing negative buoyancy. Anomalously cold and salty, the resultant water has properties of deep water. It sinks along isopycnal surfaces, which become quasi-horizontal in the open ocean (Fig. 17.6a). The thermohaline circulation is thus initiated at sites where deep water is produced.

In the far north Atlantic, near Greenland, seawater experiences strong cooling by continental air from the Canadian Arctic (Fig. 15.9). Supported by freezing and enrichment of salinity, cooling produces *North Atlantic Deep Water* (indicated blue in Fig. 17.8). Anomalously dense, that water sinks through convection and then moves southward along isopycnal surfaces. It is marked in Fig. 17.6b by the tongue of salty water that extends southward near 3000 m. Upon reaching Antarctica, it overrides even denser *Antarctic Bottom Water*, which is produced through similar processes in the shallow Weddell Sea. Deep water then drifts eastward around Antarctica, eventually bifurcating: Part drifts northward into the Indian Ocean. The rest continues into the Pacific, where it drifts northward. Through mechanisms that remain obscure, both components of deep water become less dense, eventually finding their way to shallower

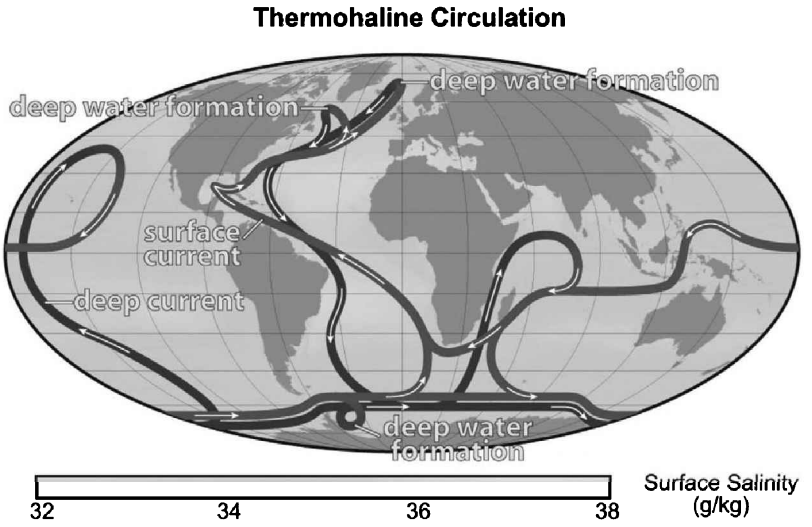

Figure 17.8 Schematic of the thermohaline circulation, along with surface salinity (shaded). Deep water (blue) forms in the far North Atlantic, near Greenland, and in the Weddell Sea, near Antarctica. After meandering through the global ocean, it eventually percolates upward, forming surface water (red). The time for the entire circuit to be completed is 1000–2000 years. *Source:* http://earthobservatory.nasa.gov. See color plate section: Plate 22.

depths (red).[2] There, the two streams from the deep ocean are thought to reunite in the Indian Ocean. After drifting into the surface circulation of the South Atlantic, the resultant water is carried north, first by the Benguela and Atlantic Equatorial Currents, then across the equator, and finally into the Gulf Stream, which returns it to the North Atlantic. The time for water to complete this circuit is longer than 1000 years.

Motion that comprises the thermohaline circulation is initiated by negative buoyancy. However, the circuit also involves vertical mixing. On long time scales, weak vertical mixing gradually diffuses deep water upward, enabling it to percolate through the stable thermocline and complete the circuit. Negative buoyancy is produced at high latitudes, especially in the far North Atlantic. There, cooling and freezing of seawater force downwelling. These diabatic processes must be attended by transfers to the atmosphere of sensible and latent heat. On long time scales, those transfers represent additional heating of air that is carried across Europe by westerlies. A weakening of the thermohaline circulation would therefore favor colder conditions over Europe. Such weakening has been hypothesized in relation to the Little Ice Age (Sec. 1.6.2). However, without a more concrete understanding of the deep ocean circulation, severely limited by available observations, that remains a speculation.

17.2 ROLE IN THE HEAT BUDGET

Because it covers 70% of the Earth, the ocean absorbs much of the overall SW energy that arrives at the Earth's surface. But even per m^2, ocean is particularly efficient as an

[2] On long time scales that characterize the thermohaline circulation, weak vertical mixing enables deep water to gradually percolate upward.

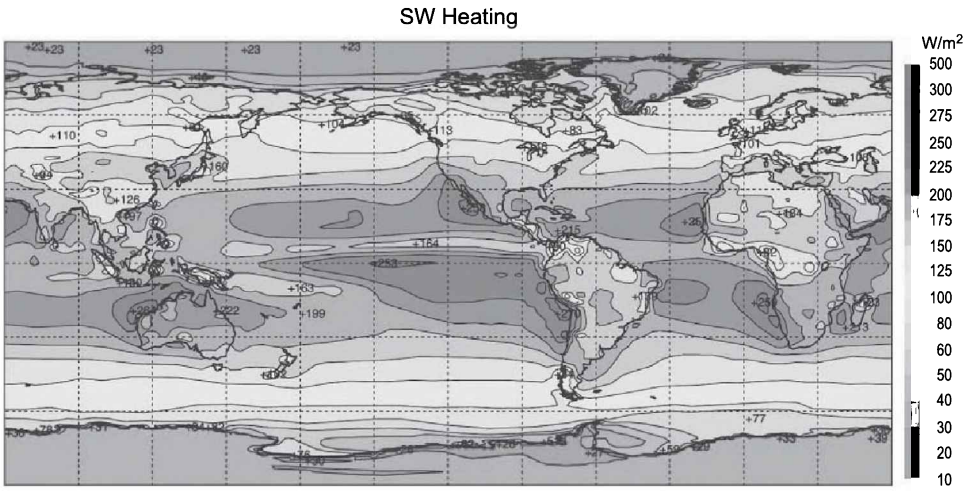

Figure 17.9 Annual-mean absorption of SW radiation at the Earth's surface. SW heating maximizes in the subtropics, especially in the eastern oceans, which are comparatively free of cloud and have large albedo. Derived from ERA-40 reanalysis. *Source:* Kallberg et al. (2005). See color plate section: Plate 23.

absorber. The darkest scenes in visible imagery are cloud-free ocean (Fig. 1.29). They lead to time-mean albedo of less than 20% (Fig. 1.34a).[3]

Plotted in Fig. 17.9 is the distribution of SW absorption at the Earth's surface. SW heating is concentrated in the subtropics. There, cloud cover is inhibited by downwelling of the Hadley circulation (Sec. 15.4.3). SW absorption is greatest over ocean, owing to its low albedo. It maximizes in the eastern oceans, where cloud-free conditions are maintained by cold SST and downwelling of the Walker circulation (Figs. 5.1, 1.36). In concert with small solar zenith angle and the low albedo of ocean, such conditions lead to column-integrated heating of the ocean in excess of 250 W/m^2.

The SW energy absorbed by the ocean is eventually transferred to the atmosphere, mostly through latent heat (Fig. 1.32). Plotted in Fig. 9.41b is the distribution of column-integrated heating of the atmosphere. Positive values mirror the pattern of precipitation (Fig. 9.41a). Latent heating thus provides a major source of energy for the atmosphere, energy transmitted from the ocean through evaporative cooling. Precipitation is concentrated inside the ITCZ, where atmospheric heating exceeds 400 W/m^2. Secondary maxima appear in the storm tracks over the north Atlantic and north Pacific. Elsewhere, values are negative. Atmospheric cooling is greatest in the subtropical eastern oceans. There, extensive coverage by low (comparatively warm) marine stratocumulus yields magnified albedo with strong LW emission, permitting efficient LW cooling to space.

During summer, the ocean acquires energy through enhanced absorption of SW, which then dominates emission of LW. The excess energy, which warms the ocean, is transferred downward. On seasonal time scales, it is redistributed across the mixed layer. During winter, the reverse operates. The ocean then loses energy through

[3] For overhead sun, instantaneous albedo is even smaller, approaching zero.

reduced absorption of SW, which leaves LW emission unbalanced. The energy lost is then drawn from the mixed layer, which, on seasonal time scales, transfers energy upward. The mixed layer thus serves as the principal repository of anomalous energy that is transferred to/from the ocean – at least on seasonal time scales. A similar process operates for continent. However, in continent, heat is transferred vertically only through conduction (Sec. 15.4). The affected depth is therefore shallow, limited to of order 1 m. These contrasting properties sharply differentiate the storage of heat in ocean and continent.

Columns of water and land have comparable density, each of order 10^3 kg/m^3. However, they differ in specific heat and, notably, in the depth that is affected by the annual variation of radiative heating and cooling. The ratio of ocean heat content to land heat content (per square meters^2) then involves the product of three ratios: (1) the ratio of specific heats, (2) the ratio of anomalous temperatures, and (3) the ratio of affected depths. The specific heat of water is four times that of most substances comprising land. The seasonal swing of ocean temperature, on the other hand, is less than one fourth that of land (Fig. 15.8). However, the depth over which it is distributed is two orders of magnitude greater. Additionally, coverage of the Earth's surface by ocean is twice that by land. Consequently, on seasonal time scales, the heat storage of ocean is two orders of magnitude greater than that of continent (Prob 17.4). It is concentrated in the mixed layer.

Most of the heat absorbed by the mixed layer during the annual cycle is transferred to the atmosphere. On time scales longer than seasonal, however, heat is exchanged with the deep ocean through convection and vertical diffusion. The latter is the same process that, in the gradual thermohaline circulation, eventually transfers deep water to the surface. Heat that is transferred into the deep ocean is sequestered for centuries, transported thereafter only by the slow drift of the thermohaline circulation. To the degree that it influences SST, such heat transfer imposes a long time scale on atmospheric climate. A stable average, one truly representative of climatological mean conditions, would then require averaging over centuries, if not millennia (Sec 1.6).

Absorption by the ocean of SW (Fig. 17.9) accounts for much of the positive net radiation that prevails at low latitudes in the TOA energy budget (Fig. 1.34c). What is not transferred to the atmosphere (Fig. 9.41b) must be transported poleward by the ocean to maintain thermal equilibrium.

Plotted in Fig. 17.10 is the northward transport of heat by the atmosphere and ocean, in petawatts (10^{15} W). Total poleward transport (solid) maximizes at latitudes near 30°, where it exceeds 5 PW. Most of that heat transport is accomplished by the atmosphere (dashed). Coincident with steep meridional temperature gradient and strong baroclinicity (Fig. 6.3), it is performed by baroclinic disturbances. Heat transport by the ocean is inferred as a residual between the total, which is required by the TOA distribution of net radiation (Fig. 1.34c), and heat transport by the atmosphere, which is better observed. Heat transport by the ocean (dotted) is generally smaller. However, it rivals that by the atmosphere equatorward of 20°, where the two are comparable. There, it reflects equatorial portions of the wind-driven gyres, which exchange warm tropical water with cooler extratropical water (Fig. 17.7). The thermohaline circulation, although poorly documented, may be equally important. Despite being comparatively weak, that handicap of the thermohaline circulation is offset by its vastly greater depth. In tandem, these features of the deep ocean can produce poleward heat transport as large as the surface circulation.

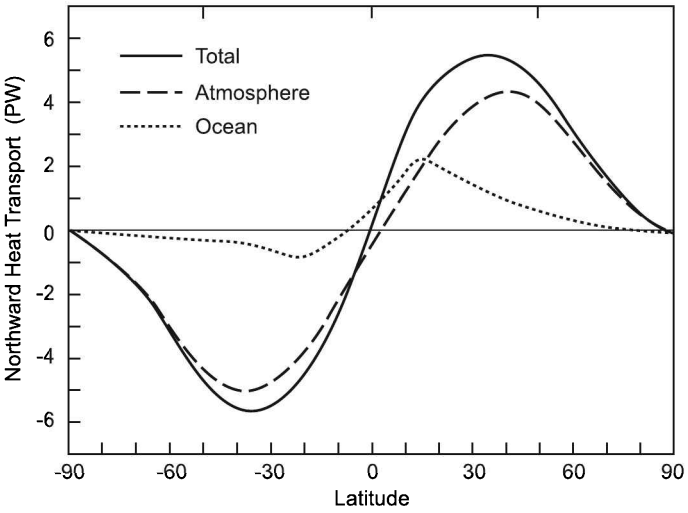

Figure 17.10 Northward transport of heat: total (solid), contribution from the atmosphere (dashed), and contribution from the ocean (dotted). Contribution from the ocean inferred as a residual between the total and atmospheric contributions. *Source:* Wunsch (2005).

17.3 ROLE IN THE CARBON CYCLE

Carbon dioxide dissolves readily in seawater. Its saturation mixing ratio increases with decreasing temperature. More CO_2 can therefore be absorbed into solution with cold water than with warm water. Alternatively, saturated water that is heated leads to outgassing of CO_2. Consequently, absorption of CO_2 is favored at polar latitudes, where it is carried into the deep ocean by the thermohaline circulation. Conversely, emission of CO_2 is favored at tropical latitudes, where deep water, rich in CO_2, percolates upward through weak vertical mixing (Fig. 17.8).

When it is absorbed, CO_2 combines with H_2O to produce carbonic acid

$$CO_2 + H_2O \rightleftharpoons H_2CO_3. \tag{17.1.1}$$

The formation of H_2CO_3 lowers the *pH* of seawater, which, owing to the presence of salt, is slightly alkaline: *pH* values of 7.5–8.5. Carbonic acid dissociates, producing bicarbonate ions

$$H_2CO_3 \rightleftharpoons H^+ + HCO_3^-. \tag{17.1.2}$$

They in turn dissociate, producing carbonate ions

$$H^+ + HCO_3^- \rightleftharpoons 2H^+ + CO_3^-. \tag{17.1.3}$$

The carbonate ion combines with other species to form organic matter that comprises marine organisms, for example, calcium carbonate.

Photosynthesis by phytoplankton has a similar effect by converting CO_2 into oxygen and carbohydrate. Phytoplankton account for as much as 50% of the emission of oxygen and absorption of CO_2. There is some evidence of a decline in phytoplankton during the the latter half of the twentieth century, by as much as 40% (Boyce et al.,

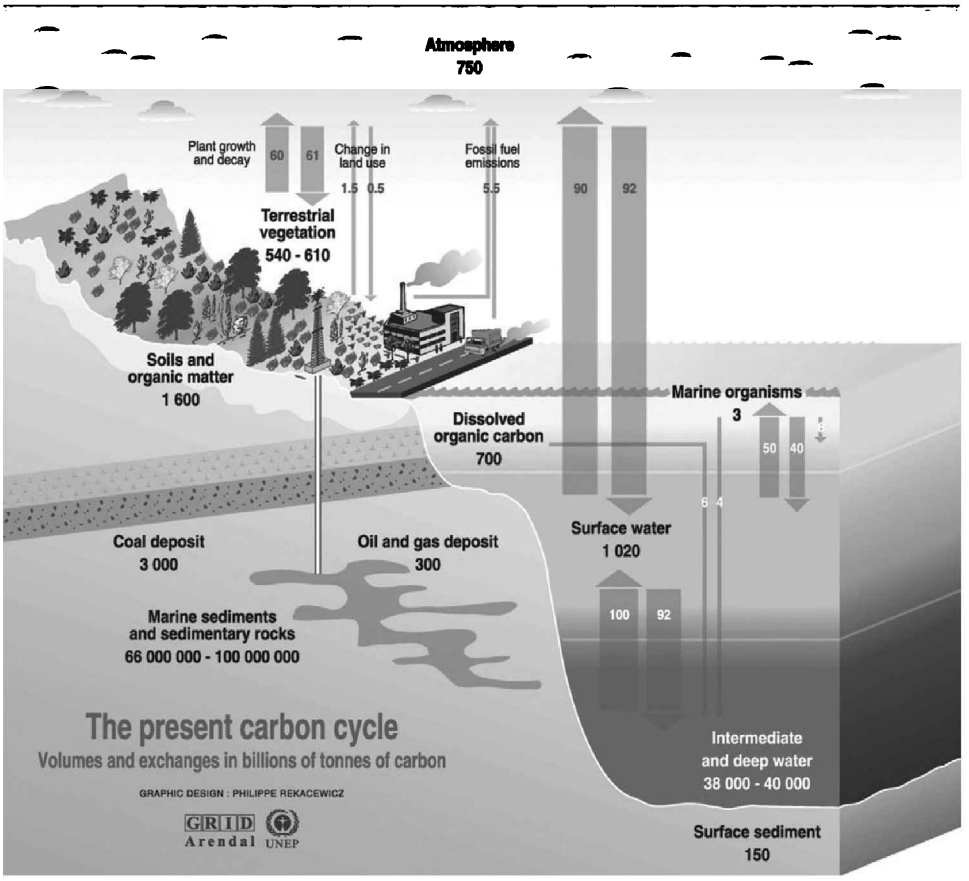

Figure 17.11 Estimated global carbon cycle, illustrating stores of carbon, in GtC, and transfers in GtC/yr, where 1 GtC = 10^9 tons of carbon. *Source:* http://maps.grida.no/go/graphic/the-carbon-cycle, design by Philippe Rekacewicz, UNEP/GRID-Arendal (11.07.10). See color plate section: Plate 24.

2010). Associated with increasing SST, such a decline would represent a significant decrease of CO_2 absorption. That would be equivalent to an anomalous source of CO_2 (cf. Sec. 8.7.1).

When marine organisms die, organic matter precipitates to the ocean floor, where it forms reduced carbon. A small fraction becomes sequestered in sediments, removing carbon from the ocean. However, most is reabsorbed into the ocean by living organisms.[4]

The storage of CO_2 is illustrated in Fig. 17.11. Except for deep sedimentary rock, which is sequestered, most of the carbon is stored in the ocean. It accounts for some 40,000 gigatons (10^{12} kg) of carbon (GtC), in the form of dissolved CO_2 and organic matter. Most resides in the deep ocean, where cold water supports the greatest observed

[4] The sequestration of organic matter in ocean sediments prevents its subsequent oxidation through decomposition. Otherwise, the latter process would systematically absorb oxygen from the climate system, depleting the atmosphere of O_2.

concentrations. There, dissolved CO_2 is controlled by the thermohaline circulation. Land and the adjoining biosphere account for only about 2000 GtC. The atmosphere contains less than 1000 GtC, concentrated in CO_2. Hence, the store of carbon in the ocean is two orders of magnitude greater than the store in the atmosphere.

Equally significant are transfers of carbon into and out of the ocean. Of order 100 GtC/yr, they exceed those into and out of land. Together, emission from ocean and land sources (~150 GtC/yr) is two orders of magnitude greater than CO_2 emission from combustion of fossil fuel. These natural sources are offset by natural sinks, of comparable strength. However, because they are so much stronger, even a minor imbalance between natural sources and sinks can overshadow the anthropogenic component of CO_2 emission (cf Secs 1.6.2, 8.7.1).

The values in Fig. 17.11 can be used to estimate the effective turnover time of atmospheric CO_2. At an absorption rate of 100 GtC/yr, the ocean will absorb the atmospheric store of CO_2 of 1000 GtC in about a decade. That absorption of CO_2, which is concentrated in cold SST at polar latitudes, is nearly offset by emission of CO_2 from warm SST at tropical latitudes. Warming of SST (by any mechanism) will increase the outgassing of CO_2 while reducing its absorption. Owing to the magnitude of transfers with the ocean, even a minor increase of SST can lead to increased emission of CO_2 that rivals other sources (Sec. 8.7.1). Further, if the increase of SST involves heat transfer with the deep ocean, the time for equilibrium to be reestablished would be centuries (Sec. 17.1.2).

17.4 THE WIND-DRIVEN CIRCULATION

The depth of the mixed layer maximizes in the storm tracks, where surface wind is strong (Fig. 17.5). This feature points to the importance of momentum transfer from the atmosphere, which is transmitted through wind stress on the ocean surface. By stirring the mixed layer, wind stress drives the surface circulation of the ocean.

17.4.1 The Ekman layer

A parallel of surface motion was treated earlier in the idealized zonally symmetric circulation (Sec. 15.2). There, the free surface is analogous to the ocean surface. Beneath the free surface is a shallow Ekman layer. Inside it, frictional-geostrophic balance enables the motion to adjust sharply to meet the boundary condition of zero stress. The ocean surface, on the other hand, experiences nonzero wind stress,

$$\boldsymbol{\tau}_0 = \tau_{0xz}\boldsymbol{i} + \tau_{0yz}\boldsymbol{j},$$

following from the drag exerted on it by surface wind. The wind stress is tantamount to a downward flux of horizontal momentum (Sec. 10.6). That flux must be continuous across the atmosphere-ocean interface.

Inside the Ekman layer, motion that is steady, in the presence of turbulent diffusion, but with the neglect of advective acceleration, is governed by the momentum balance

$$f\boldsymbol{k} \times \boldsymbol{v} = -\nabla\Phi + \frac{1}{\rho}\frac{\partial \boldsymbol{\tau}}{\partial z}, \tag{17.2.1}$$

where the geopotential Φ of isobaric surfaces follows from hydrostatic balance (14.7),

$$\boldsymbol{\tau} = \rho K \frac{\partial \boldsymbol{v}}{\partial z} \tag{17.2.2}$$

is the turbulent shear stress at level z, and K is the eddy diffusivity. Continuity requires

$$\nabla \cdot \boldsymbol{v} + \frac{\partial w}{\partial z} = 0. \tag{17.3}$$

Expressing motion in terms of a geostrophic component $\boldsymbol{v}_g$ plus an ageostrophic (Ekman) component $\boldsymbol{v}_E$, which varies sharply with depth, reduces the momentum balance inside the Ekman layer to

$$\begin{aligned} f\boldsymbol{k} \times \boldsymbol{v}_E &= \frac{1}{\rho}\frac{\partial \boldsymbol{\tau}}{\partial z} \\ &= K\frac{\partial^2 \boldsymbol{v}_E}{\partial z^2}, \end{aligned} \tag{17.4.1}$$

where z is understood to be a stretched vertical coordinate that renders frictional terms comparable to others in the momentum balance (Sec. 15.2). At the ocean surface, frictional stress must equal the imposed wind stress. At the bottom of the Ekman layer, it must vanish, requiring ageostrophic motion to disappear. Boundary conditions are thus

$$\begin{aligned} \rho K\frac{\partial \boldsymbol{v}_E}{\partial z} &= \boldsymbol{\tau}_0 \qquad & z = 0 \\ \boldsymbol{v}_E &\sim 0 \qquad & z \to -\infty \end{aligned} \tag{17.4.2}$$

If surface wind is northward,

$$\boldsymbol{\tau}_0 = \tau_0 \boldsymbol{j},$$

then (17.4) has solution

$$\begin{aligned} u_E &= v_0 e^{\gamma z} cos\left(\gamma z + \frac{\pi}{4}\right) \\ v_E &= v_0 e^{\gamma z} sin\left(\gamma z + \frac{\pi}{4}\right), \end{aligned} \tag{17.5.1}$$

where, analogous to (13.17.2),

$$\gamma = \sqrt{\frac{f}{2K}} \qquad v_0 = \frac{\tau_0}{\rho\sqrt{fK}}. \tag{17.5.2}$$

The ageostrophic motion has the form presented in Fig. 17.12; it is analogous to structure in Fig. 13.3. At the ocean surface, where

$$u_E = v_E = \frac{v_0}{\sqrt{2}},$$

Ekman current is deflected 45° to the right of wind in the Northern Hemisphere. This feature is in agreement with reports of mariners that sea ice drifts to the right of wind. With increasing depth, Ekman current veers increasingly to the right and weakens, until the total current $\boldsymbol{v} = \boldsymbol{v}_g + \boldsymbol{v}_E$ eventually becomes geostrophic. The depth of the Ekman layer is approximated by that depth where $\boldsymbol{v}_E$ first reverses:

$$d_E = \frac{\pi}{\gamma}. \tag{17.6}$$

It increases with eddy diffusivity, which, in turn, increases with wind stress. It decreases with latitude.

Motion at an individual level depends on the frictional formulation and, hence, on K. However, column-integrated transport within the Ekman layer does not. The

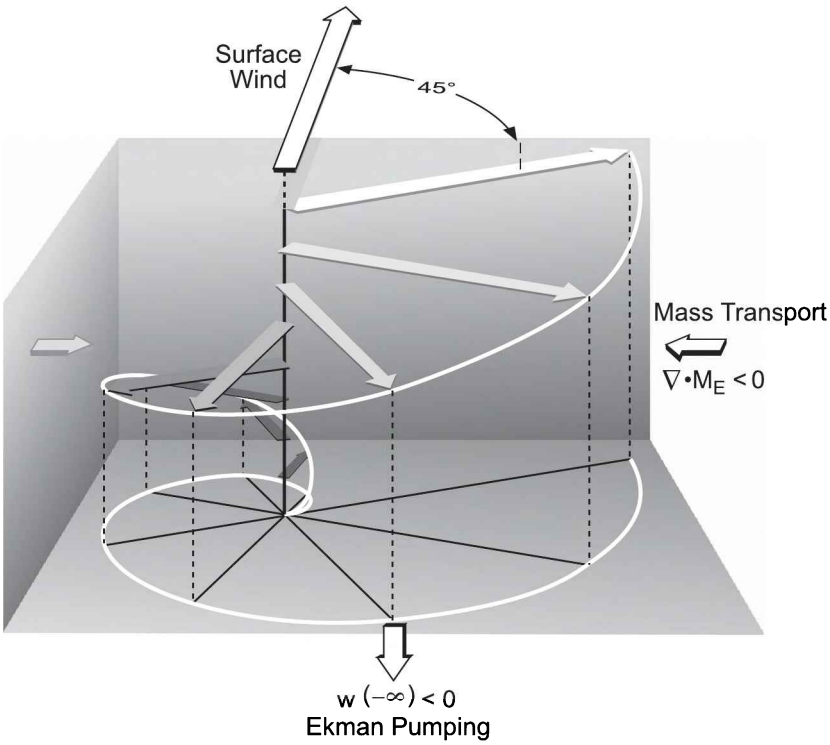

Figure 17.12 Ageostrophic current inside the Ekman layer. Mass transport $\boldsymbol{M}_E$ is orthogonal to surface wind, to the right in the Northern Hemisphere. Its convergence produces Ekman pumping from the frictional layer. Copyright American Meteorological Society, with permission.

ageostrophic *mass transport* is

$$\boldsymbol{M}_E = \int_{-\infty}^{0} \rho \boldsymbol{v}_E dz.$$

Integrating the momentum balance vertically, together with boundary conditions (17.4.2), reduces (17.4.1) to

$$f\boldsymbol{k} \times \boldsymbol{M}_E = \boldsymbol{\tau}_0.$$

Operating across by $\boldsymbol{k}\times$ then obtains

$$\boldsymbol{M}_E = -\frac{1}{f}\boldsymbol{k} \times \boldsymbol{\tau}_0. \tag{17.7}$$

Ekman transport is determined entirely by the wind stress. More notably, it is directed just perpendicular to $\boldsymbol{\tau}_0$ – to the right in the Northern Hemisphere. This peculiarity of the surface current is another manifestation of the geostrophic paradox (Chap. 10).

Integrating the continuity equation in similar fashion reduces (17.3) to

$$\nabla \cdot \boldsymbol{M}_E + \rho [w(0) - w(-\infty)] = 0.$$

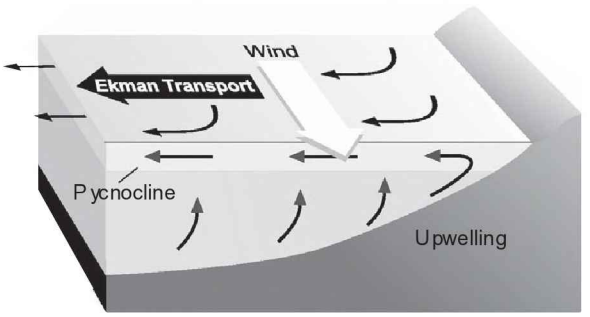

Figure 17.13 Coastal upwelling induced by along-shore wind through Ekman transport. Copyright American Meteorological Society, with permission.

At the ocean surface, steady vertical motion must vanish. With (D.7), vertical motion at the base of the frictional layer then follows as

$$\begin{aligned} w(-\infty) &= \nabla \cdot \boldsymbol{M}_E \\ &= \frac{1}{\rho} \boldsymbol{k} \cdot \nabla \times \left(\frac{\boldsymbol{\tau}_0}{f} \right). \end{aligned} \tag{17.8}$$

Representing Ekman pumping (Sec. 13.4), $w(-\infty)$ is proportional to the curl of the wind stress. The latter represents a torque that is exerted on the ocean surface. It creates relative vorticity, providing a parallel of Ekman pumping in the atmosphere (13.28). Wind stress that is anticyclonic produces Ekman pumping: $w(-\infty) < 0$. Mass is expelled from the Ekman layer at its base. Wind stress that is cyclonic produces Ekman suction: $w(-\infty) > 0$. Mass is absorbed by the Ekman layer at its base. As in the free atmosphere, vertical motion at the base of the Ekman layer imposes a secondary circulation on the geostrophic circulation of the deep ocean.

Together, Ekman transport and pumping have important implications for surface conditions. Along the eastern boundary of ocean basins (at the west coast of continents), surface wind has an equatorward component, induced by subtropical high pressure over ocean (Fig. 15.9). Both features are intensified during summer. Their influence on the ocean is exemplified by currents along the coast of California (Fig. 17.13). Northerly wind along the California coast drives Ekman transport in the ocean that is directed to the right and therefore offshore. The latter forces surface divergence along the coastal shelf. It must be compensated by upwelling of cold water from the deep ocean. Upwelling elevates the thermocline (Fig. 17.14), producing anomalously cold SST along the coast (Fig. 17.15).

Cold SST exerts a major influence on regional climate along the west coast of continent. By cooling the atmosphere from below, it stabilizes the troposphere, inhibiting deep convection (Fig. 7.11). Instead, cold SST favors surface fog, which forms when humidified air is cooled to saturation. Such conditions prevail over San Francisco during summer, when fog is swept inland by the onshore component of wind. They encourage semi-arid climate along the west coast of continent. There, regular rainfall is limited to winter, when coastal upwelling is weak and synoptic weather systems are active. Deep water, beyond being cold, is also nutrient rich.[5] For this reason, upwelling

[5] From the decomposition of dead organisms that have settled to the ocean floor.

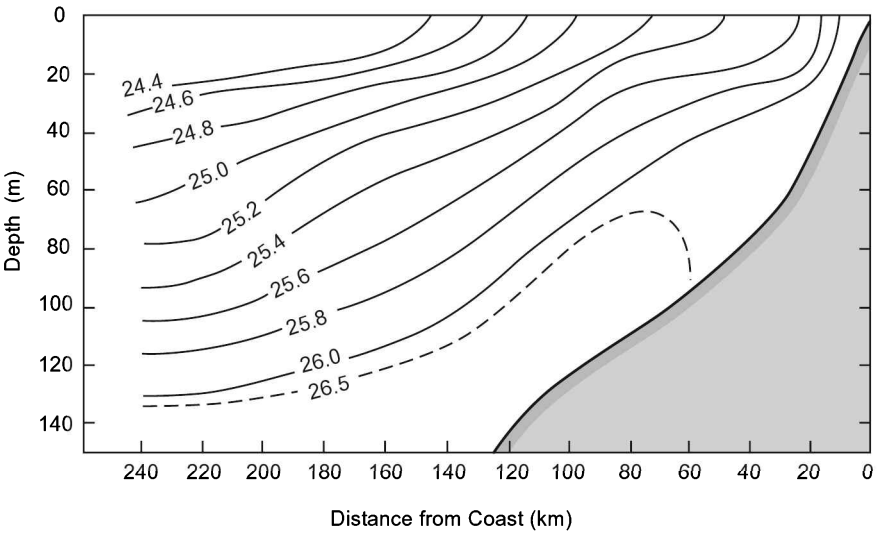

Figure 17.14 Cross section of density anomaly, orthogonal to Peruvian coast during May. *Source:* Strub et al. (1998).

simultaneously supports marine productivity. The west coasts of continents are sites of major fisheries. The catch off the coast of Peru alone accounts for a fifth of the global harvest.

Near the equator, subtropical highs in the atmosphere drive easterlies: the NE and SE trade winds (Fig. 15.9). As illustrated in Fig. 17.16a, Ekman transport is then northward in the Northern Hemisphere and southward in the Southern Hemisphere (17.7). This makes the equator a region of surface divergence. It too must be compensated by upwelling (Fig. 17.16b). Such vertical motion favors cold SST and low salinity along the equator, as is evident in Fig. 17.1. These features are amplified at the eastern boundaries of ocean basins, where equatorial upwelling is reinforced by coastal upwelling. Cold SST inhibits atmospheric convection. For this reason, the ITCZ tends to form to either side of the equator, but not directly over it (cf. Figs. 1.30b; 9.41).

When it deflects isopycnal surfaces, upwelling along the equator also introduces a deflection of isobaric surfaces. Vertical motion must satisfy

$$\begin{aligned} w &= \frac{dz}{dt} \\ &= \frac{1}{g}\frac{d\Phi}{dt}. \end{aligned} \tag{17.9.1}$$

For steady motion, (17.9.1) reduces to

$$\begin{aligned} w &= \frac{1}{g}\boldsymbol{v}\cdot\nabla\Phi \\ &\cong \frac{1}{g}\boldsymbol{v}_g\cdot\nabla\Phi. \end{aligned} \tag{17.9.2}$$

Upwelling associated with Ekman transport therefore implies anomalously high Φ in a neighborhood of the equator. Geostrophic balance (12.2) then forms current with low Φ to its left (right) in the Northern (Southern) Hemisphere. The result is westerly

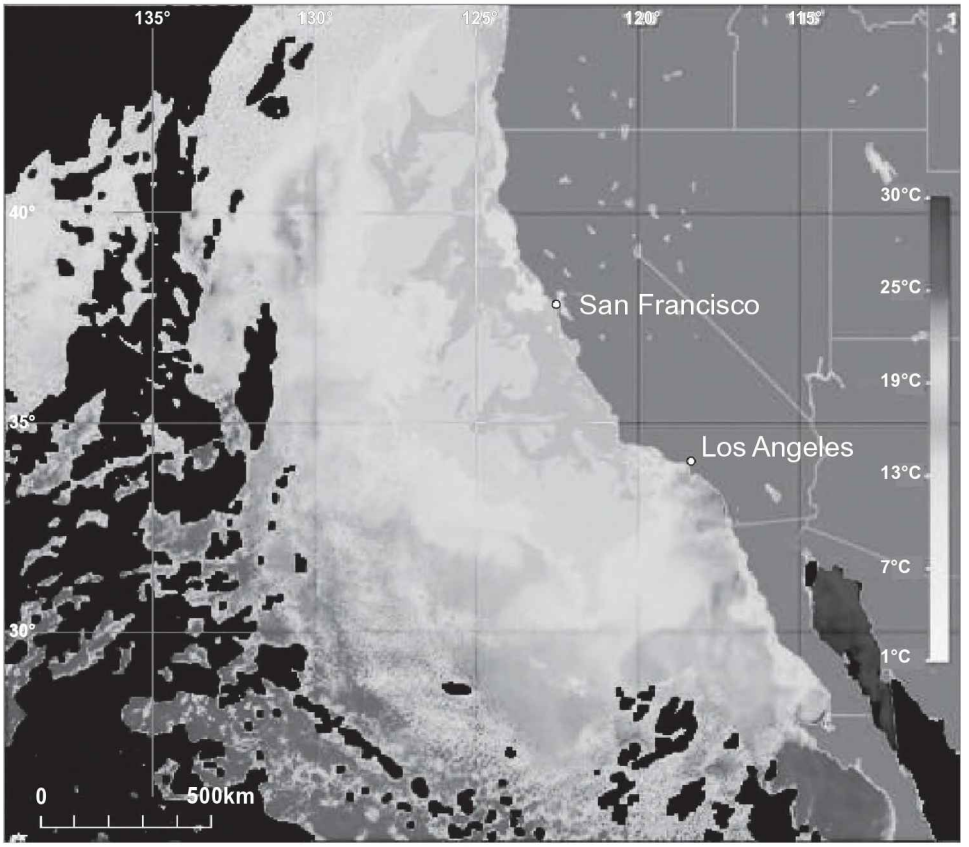

Figure 17.15 Surface temperature off the California coast. Temperature decreases shoreward, attaining values 10–15°C colder than in the open ocean. Black shading represents sites that are overcast, where data is unavailable. *Source:* http://oceanmotion.org. See color plate section: Plate 25.

current along the equator – just opposite to the easterly wind stress exerted by the trades. Reflecting the equatorial countercurrent (Fig. 17.7), it emerges naturally from the essential momentum balance governing the upper ocean.

17.4.2 Sverdrup balance

The upper ocean circulation is driven by the torque of wind stress, which forces vorticity. As in the treatment of geostrophic motion (12.47), applying $\boldsymbol{k} \cdot \nabla \times$ reduces (17.2.1) to the vorticity balance

$$\beta v + f \nabla \cdot \boldsymbol{v} = \frac{1}{\rho} \frac{\partial}{\partial z} \boldsymbol{k} \cdot \nabla \times \boldsymbol{\tau}. \tag{17.10}$$

With continuity (17.3), this becomes

$$\beta v - f \frac{\partial w}{\partial z} = \frac{1}{\rho} \frac{\partial}{\partial z} \boldsymbol{k} \cdot \nabla \times \boldsymbol{\tau}. \tag{17.11}$$

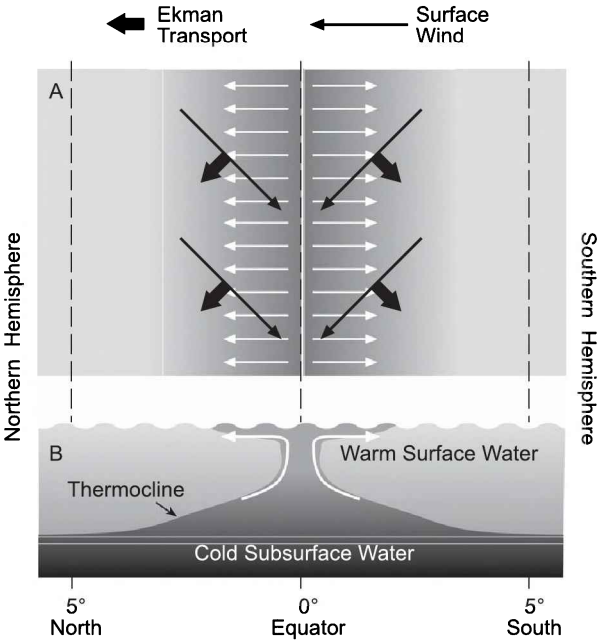

Figure 17.16 Schematic of equatorial upwelling introduced through Ekman transport. (a) Surface current (white arrows). Superimposed are surface trade winds (black arrows) and and Ekman transport (heavy black arrows). (b) Vertical section across equator, illustrating upwelling of cold subsurface water. Copyright American Meteorological Society, with permission.

Integrating vertically, introducing the column-integrated mass transport,

$$\boldsymbol{M} = \int_{-\infty}^{0} \rho \boldsymbol{v} dz,$$

and requiring boundary conditions (17.4.2) and vertical motion to vanish at $z = 0$ and $z = -\infty$, then yields

$$\beta M_y = \boldsymbol{k} \cdot \nabla \times \boldsymbol{\tau}_0 \tag{17.12.1}$$

$$\nabla \cdot \boldsymbol{M} = 0. \tag{17.12.2}$$

Poleward transport of mass is determined entirely by the curl of the wind stress. Known as *Sverdrup balance*, (17.12.1) asserts that column motion can cross contours of planetary vorticity (e.g., basic-state potential vorticity) only through the creation of relative vorticity by the curl of the wind stress. Like (17.7), the column-integrated transport is independent of the frictional formulation.

Sverdrup balance describes how motion in the ocean interior is forced by surface wind through the Ekman layer. Ekman pumping leads to a downward displacement of isopycnals immediately beneath the surface layer. Vortex tubes in the ocean interior are therefore compressed, compensated by horizontal divergence. Conservation of potential vorticity then requires an anticyclonic adjustment of absolute vorticity (Fig. 12.9).

Such motion forces an equatorward drift (toward weaker planetary vorticity) and the anticyclonic gyres that prevail in the subtropics (Fig. 17.7).

In tandem with continuity (17.12.2), Sverdrup balance determines the horizontal distribution of ocean current from the distribution of wind stress. Equations (17.12), however, are only first order in $\boldsymbol{M}$. Consequently, they enable only one boundary condition to be satisfied. Despite this limitation, Sverdrup balance provides great insight into the ocean circulation.

Requiring motion to be tangential to the coastline at the eastern boundary of ocean basins yields the distribution of mass transport in Fig. 17.17. Displayed is the streamfunction of equivalent volume transport, presented in units of Sverdrups (1 Sv = 10^6 $m^3/s \Leftrightarrow$ Mt/s). For its simplicity, Sverdrup balance captures the major features of the upper ocean circulation: Anticyclonic gyres prevail in the subtropics of each major basin. Represented likewise is an equatorial countercurrent, which was the original interest of Sverdrup (1947).

17.5 THE BUOYANCY-DRIVEN CIRCULATION

Descriptions of the thermohaline circulation, also known as the *abyssal circulation*, are mostly heuristic. Their qualitative nature reflects the dearth of quantitative documentation of motion in the deep ocean.

A simple model is due to Stommel and Arons (1960). It considers the deep ocean as a single homogeneous layer of depth H that extends from the ocean floor to the base of the thermocline. The layer is forced convectively at high latitude. There, injection of dense water from overhead (e.g., deep water formed through cooling at the ocean surface) serves as a concentrated mass source. Compensating it across the layer's upper surface is upwelling, which is weak but (except at sites of convection) horizontally uniform. Removing mass from the layer at the same rate, it serves as a distributed mass sink. Mass lost through upwelling eventually returns to the surface through vertical diffusion, which ventilates the thermocline with water from the deep ocean. Linking the mass source and mass sink is a western boundary current, which carries dense water equatorward to satisfy continuity (Fig. 17.18).

In the absence of turbulence, the vorticity balance (17.11) reduces to

$$\beta v = f \frac{\partial w}{\partial z}. \tag{17.13}$$

Advection of vorticity is then balanced by vertical stretching (Sec. 12.5). Vertical motion vanishes at the bottom of the layer, which is presumed flat. By construction, it is upward and horizontally uniform at the top of the layer. Integrating (17.13) vertically across the layer obtains

$$v = \frac{f}{\beta} \frac{w_0}{H}, \tag{17.14}$$

where w_0 is the vertical velocity at the top of the layer (i.e., at the base of the thermocline). Because $w_0 > 0$ throughout, meridional motion inside the layer must be everywhere poleward.

The implied circulation is illustrated in Fig. 17.18 for a sectoral basin symbolic of the North Atlantic. At the apex of the sector is a point source that represents the injection of North Atlantic deep water. Once introduced, dense water flows southward

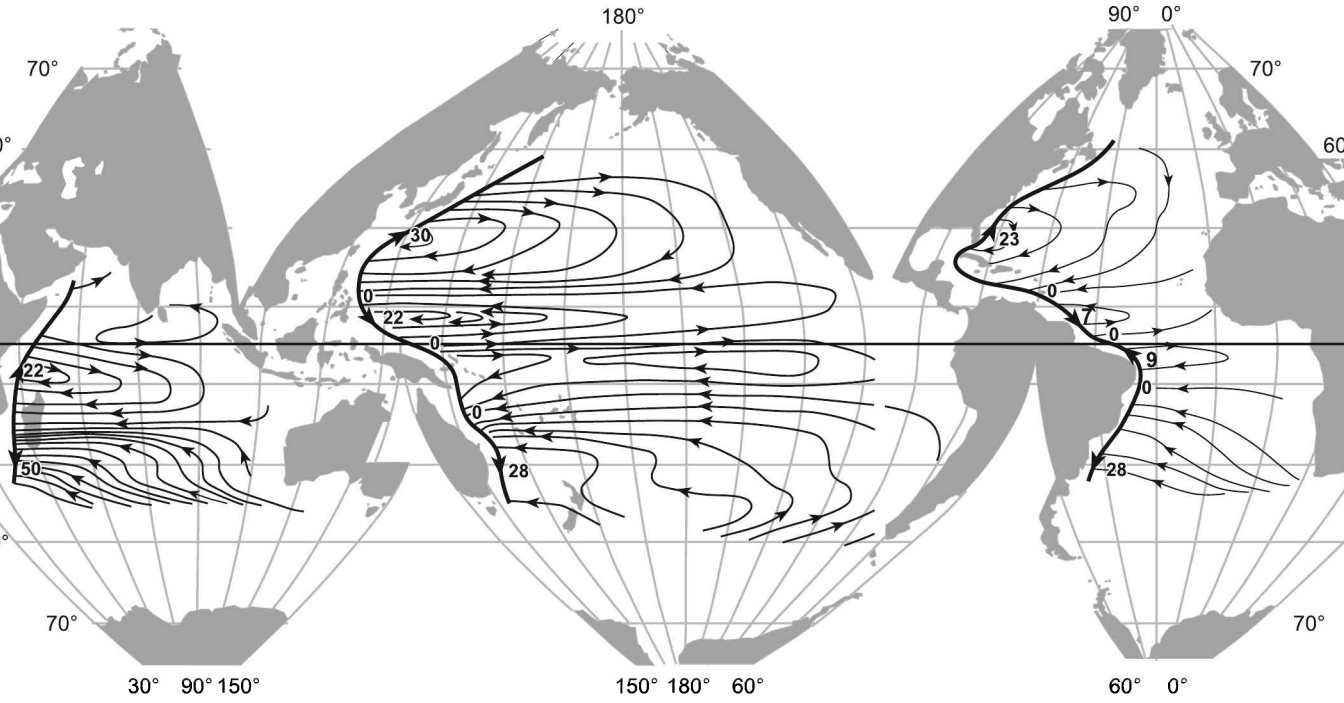

Figure 17.17 Column-integrated volume transport, forced by annual-mean wind stress, that results under Sverdrup balance with motion required to be tangential to the eastern boundaries of ocean basins. Transport streamfunction contoured at increments of 5 Sv (1 Sv = 10^6 m^3/s). Superimposed are the western-boundary currents required for continuity (heavy arrows). Adapted from Welander (1959).

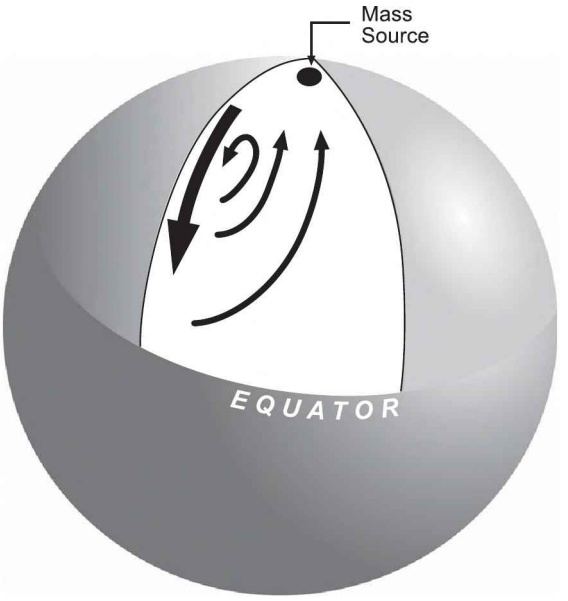

Figure 17.18 Sectoral basin in Stommel and Arons (1961) model of the deep-ocean circulation. Superimposed is the point source of deep water, which forces the circulation, and the western-boundary current required by continuity.

along the western boundary of the basin. Compensating it in the interior is northward motion (17.14), which converges to form upwelling. Southward transport by the western-boundary current exceeds northward transport in the interior. Some of the northward stream must therefore peel off, rejoining southward motion at the western boundary in regions of recirculation.

The strength of the thermohaline circulation is determined by the horizontal gradient of surface buoyancy (e.g., by the formation of deep water in source regions). However, it is also determined by turbulent diffusion, which enables water from the deep ocean to percolate through the stable thermocline and, hence, return to the surface and complete the circuit. Tracer analyses such as that in Fig. 17.6b imply that deep water formation is concentrated in the Atlantic: in the North Atlantic near Greenland and in the South Atlantic at the Weddell Sea. Serving as mass sources for the deep ocean, those regions of dense water formation drive the gradual overturning that comprises the thermohaline circulation (Fig. 17.8). By contrast, the Pacific is virtually devoid of surface sources. It is supplied instead by deep water from the Atlantic, via the Southern Ocean.

Before returning to the surface, deep water must traverse the Indian and Pacific Oceans through a convoluted circuit. The overturning time depends on the path followed back to the surface. The time for water to reach the surface via the Indian Ocean is centuries. The time for it to return to the North Atlantic via the Pacific, which is devoid of major sources of deep water, is of order 2000 years.

17.6 INTERANNUAL CHANGES

As in the atmosphere, the circulation in the ocean varies. The wind-driven circulation evolves naturally with the annual cycle of surface pressure, wherein trade winds and the ITCZ migrate from one side of the equator to the other (Fig. 15.9). It also varies between years.

ENSO

El Nino Southern Oscillation involves a swing between extreme states of the circulation in the equatorial Pacific (Sec. 15.5.1). It is characterized by the *Southern Oscillation Index* (*SOI*), which describes fluctuations of SLP in the eastern and western Pacific that are coherent but out of phase (Fig. 15.15). SOI is defined traditionally as SLP at Tahiti minus SLP at Darwin, Australia. Although alternative definitions exist, all measure the phase of the dipole oscillation across the equatorial Pacific. Negative SOI signifies SLP that is anomalously low in the eastern Pacific and anomalously high in the western Pacific. Easterly trade winds across the equatorial Pacific are then weak. Representing *El Nino* conditions, SOI < 0 corresponds to SST that is anomalously warm in the central and eastern Pacific and anomalously cold in the western Pacific. Positive SOI signifies SLP that is anomalously low in the western Pacific and anomalously high in the eastern Pacific. Easterly trade winds across the equatorial Pacific are then intensified. Representing *La Nina* conditions, SOI > 0 corresponds to SST that is anomalously cold in the central and eastern Pacific and anomalously warm in the western Pacific.

Figure 17.19 plots the record of normalized SOI, along with a measure of background variability that is unrelated to the southern oscillation. Contrary to its name, the southern oscillation is aperiodic. The greatest negative swing of SOI occurred during the 1982–1983 El Nino (Fig. 17.19a). SST in the eastern Pacific then warmed above its climatological mean by 7 K. That warm event, however, was not the strongest. During the 1997–1998 El Nino, SST in the eastern Pacific warmed by 8 K. Precipitation then was centered over the dateline (Fig. 17.20b). It was shifted well east of its climatological-mean position (Fig. 9.41a), leaving the western Pacific anomalously dry. Occurring simultaneously was conspicuous warming of global-mean temperature (Fig. 1.39). It reflects increased atmospheric heating, principally in the tropics. Through increased θ_e at the Earth's surface, increased heating is achieved through deeper convection and intensified cumulus heating of the troposphere (Sec. 7.7). Warm events (SOI < 0) also appear in SOI around 1987, 1993, 2005, and 2010. The protracted event around 2005 supported widespread forest fires in Indonesia. Dense haze produced by those fires led to health restrictions and public closures. Apparent in visible imagery (Cover; Plate 0), such haze is being drawn into one of two tropical cyclones that developed in the equatorial Pacific. Also punctuating the record of SOI are cold events (SOI > 0). La Nina conditions occurred around 1989, 1999, and 2007. During the 1998–1999 La Nina, precipitation was concentrated in the western Pacific (Fig. 17.20a). Its distribution then was not dissimilar to the climatological-mean pattern (Fig. 9.41a).

The warm and cold events must be considered in light of background variability, which is independent of ENSO. Such variability is reflected in the average of SLP at Tahiti and Darwin (Fig. 17.19b). Representing fluctuations across the Pacific that are coherent but in phase, the latter exceed 1–2 std deviations. Consequently, only strong events in SOI stand out clearly above random variability, which characterizes climate noise.

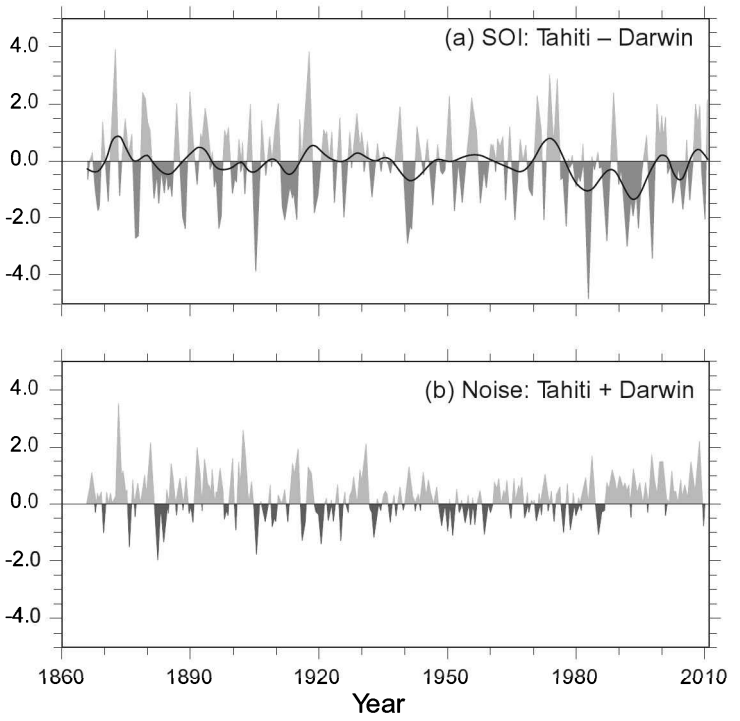

Figure 17.19 (a) Southern Oscillation Index (SOI), defined as SLP at Tahiti minus SLP at Darwin (shaded), along with the smoothed record (solid). Large deviations of SOI, which occur sporadically, represent fluctuations of SLP that are out of phase between those stations, characeristic of ENSO. (b) Fluctuations of SLP that are independent of SOI, defined by SLP at Tahiti plus SLP at Darwin. They represent fluctuations unrelated to ENSO. *Source:* http://www.cp.ncep.gov (14.07.10).

El Nino represents a perturbation to the annual cycle of SST. As depicted in Fig. 17.21, initial signs appear during the preceding northern summer, when anomalously warm SST appears off the coast of Peru. By autumn, the anomaly intensifies and expands westward, forming a tongue of warm SST that extends into the central Pacific. Reflecting the collapse of upwelling, the appearance of warm SST is attended by the disappearance of nutrient-rich water. The latter is followed by a rapid decline of fish populations off the coast of Peru. By winter, the warm anomaly has moved into the central Pacific. There, it forces anomalous convection and atmospheric heating (Fig. 17.20b). The influence of those anomalies is transmitted poleward through anomalous planetary waves (Fig. 14.20). During spring and the following summer, the warm SST anomaly decays, eventually replaced off the coast of Peru by a cold SST anomaly and the gradual return to climatological-mean conditions.

This perturbation to the annual cycle of SST depends intrinsically on the trade winds, whose EW structure comprises the Walker circulation. Under normal conditions, the mixed layer is warm and deep in the western Pacific, where the thermocline is depressed well beneath the surface (Fig. 17.22a). Conversely, the mixed layer is cold and shallow in the eastern Pacific. There, the thermocline is not far beneath the

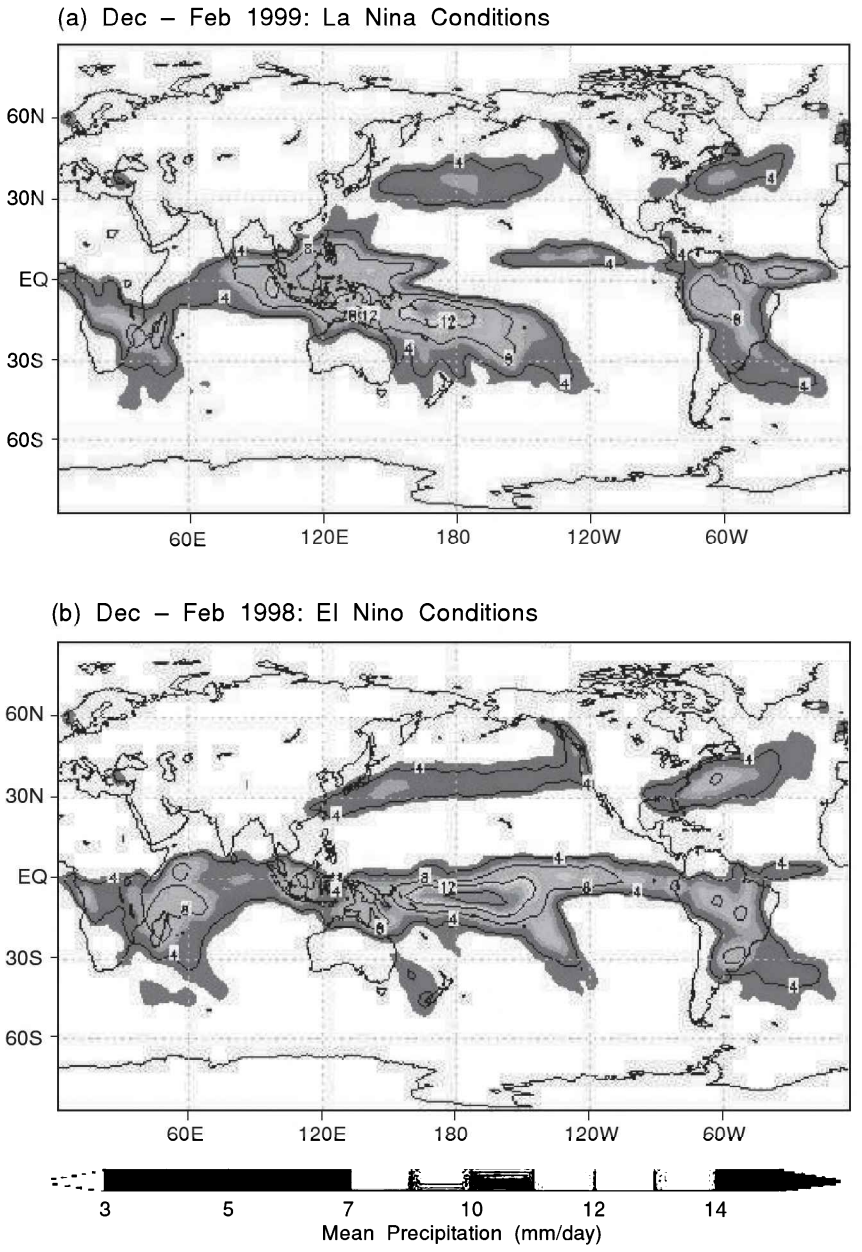

Figure 17.20 Global distribution of precipitation (a) during Dec–Feb 1999, under La Nina conditions, when rainfall was concentrated in the western Pacific, and (b) during Dec–Feb 1998, under El Nino conditions, when rainfall was displaced eastward into the central Pacific. Also evident during northern winter are the storm tracks over the North Atlantic and North Pacific, where precipitation is organized by amplifying synoptic weather systems. *Source:* http://www.esrl.noaa.gov (15.07.10). See color plate section: Plate 26.

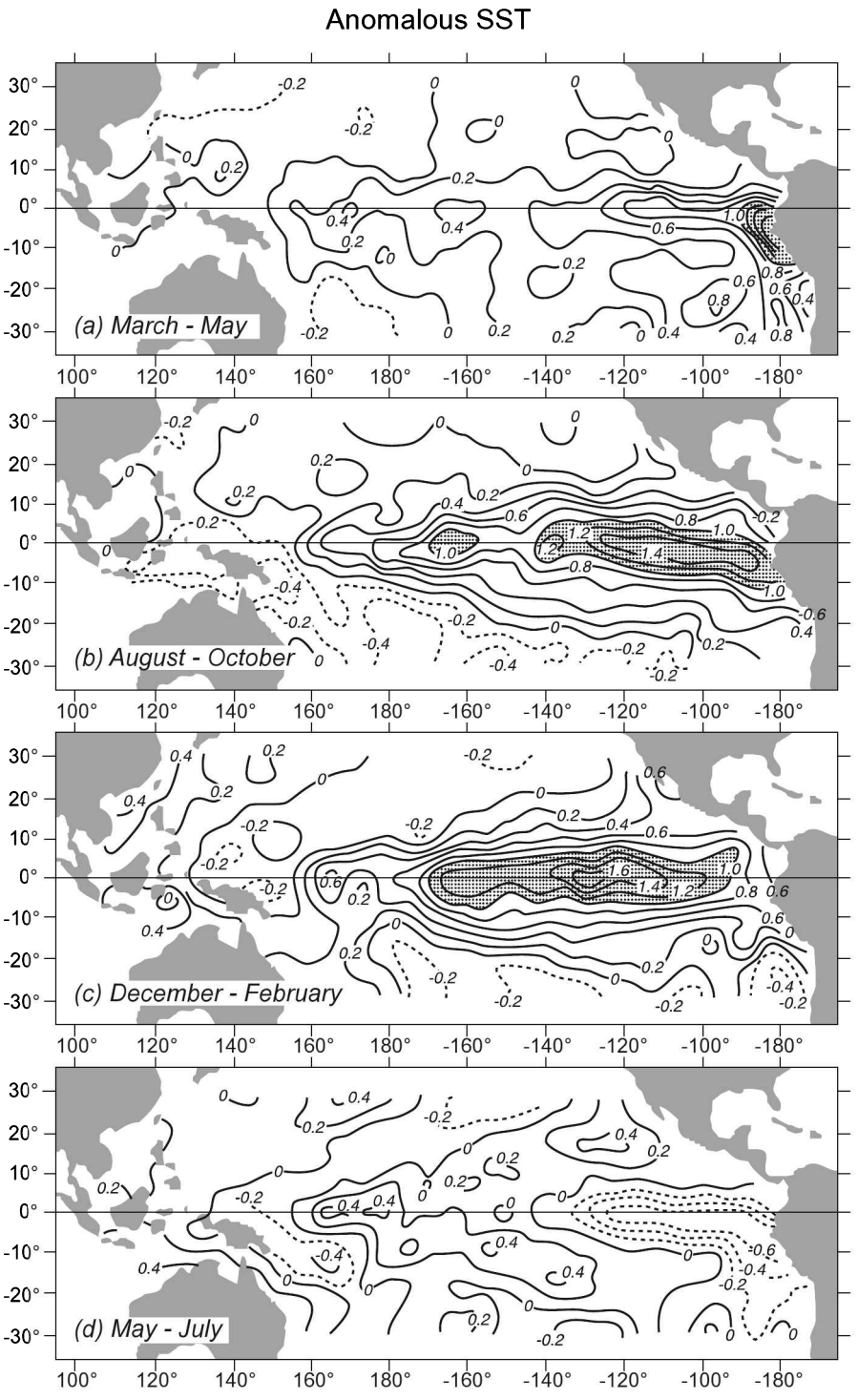

Figure 17.21 Seasonal evolution of anomalous SST during El Nino (°C). After Stewart (2008), adapted from Rasmusson and Carpenter (1982).

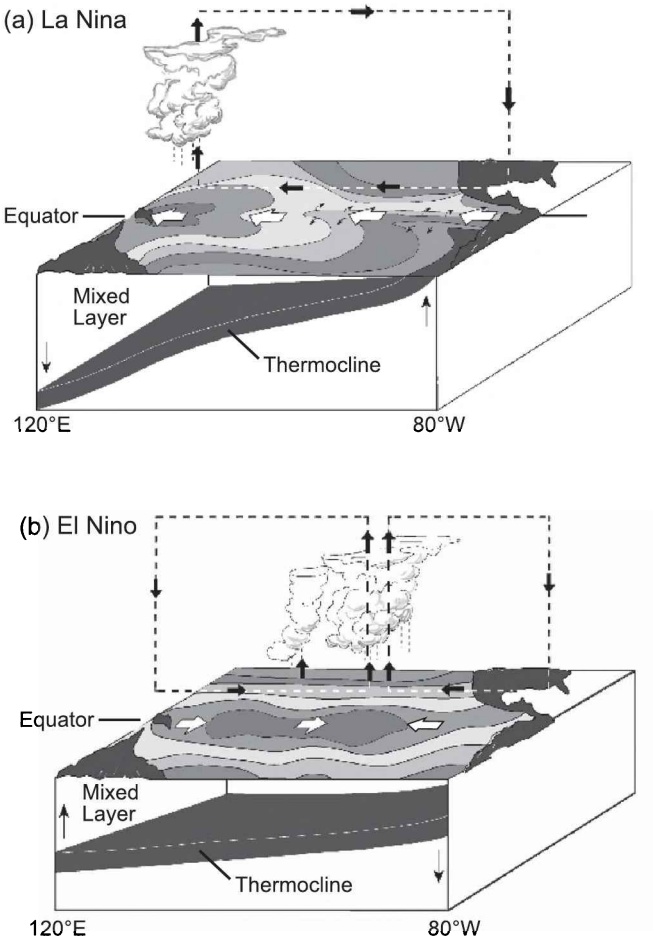

Figure 17.22 Ocean thermal structure, surface wind, SST (contoured, with red warmest), and Walker circulation under (a) La Nina conditions and (b) El Nino conditions. *Source:* http://www.pmel.noaa.gov. See color plate section: Plate 27.

surface, emerging in upwelling at the coast of South America. Characteristic of La Nina, these conditions are maintained by strong easterlies that prevail across the equatorial Pacific. The latter, through Ekman transport, induce equatorial upwelling that elevates the thermocline and produces cold SST across the eastern Pacific (Fig. 17.16). Warm SST and convection are then concentrated in the western Pacific. Warm water that has been dragged westward by the trades accumulates there, after being heated during its traversal of the equatorial Pacific. It forms a dome of high sea level in the western Pacific. About 0.5 m higher than sea level in the eastern Pacific, that elevation is maintained by easterly drag.

The onset of El Nino coincides with a weakening of the trades. This weakens upwelling that maintains cold SST in the eastern Pacific. It also weakens easterly stress

that maintains the dome of warm water in the western Pacific.[6] Weakened easterlies and upwelling enable the mixed layer in the eastern Pacific to expand downward, lowering the thermocline there (Fig. 17.22b). Simultaneously, SST warms, flattening the EW gradient of temperature. This flattens the gradient of atmospheric heating, and hence the EW pressure gradient. The result is to further weaken easterly trade winds. The dome of warm water and the deep mixed layer in the western Pacific then surge eastward, behind an eastward-propagating wave front that traverses the equatorial Pacific in 2–3 months.[7] Upon arrival of the wave front, sea level, SST, and mixed layer depth all increase in the eastern Pacific. Accompanying those changes are low SLP and weak easterlies. Left behind the wave front in the western Pacific are westerlies. Along with easterlies in the eastern Pacific, they converge in the central Pacific, fueling upwelling and deep convection.

Together, these features represent a perturbed Walker circulation, with upwelling in the central Pacific and downwelling to the east and west (cf. Figs. 15.16; 1.36). As deep convection also comprises the upwelling branch of the Hadley circulation, the latter is likewise perturbed. The dynamical response to ENSO thus involves anomalous EW motion and anomalous NS motion, as results from a localized heating anomaly (Fig. 15.13). Especially sensitive to such changes are subtropical latitudes of the western Pacific (e.g., SE Asia and Australia). There, the regional Hadley circulation controls which sites experience upwelling and copious rainfall versus downwelling and cloud-free conditions (Fig. 15.11).

Figures 17.21 and 14.20a portray average conditions during warm events. In practice, however, ENSO varies considerably from one event to another. The 1982–1983 El Nino was accompanied by severe drought over eastern Australia. Yet the 1997–1998 El Nino, which was even stronger, was accompanied by normal rainfall. The El Nino of 2010 was accompanied by flooding. How such anomalous regional conditions develop clearly involves more than anomalous SLP and SST. The wide variance from these simple proxies underscores the role of dynamical changes that transmit those influences to individual regions. Those mechanisms remain poorly understood.

Pacific Decadal Oscillation

Another fluctuation of climate surrounds anomalous SST in the North Pacific. The *Pacific Decadal Oscillation* (*PDO*) is defined as the leading EOF of North Pacific SST (Sec. 15.5.1). Despite its name, it too is aperiodic. The PDO is displayed in Fig. 17.23 for opposite phases, along with accompanying anomalies of SLP and surface wind. In its positive phase, the PDO is characterized by SST that is anomalously cold in the northwestern Pacific and anomalously warm in the equatorial eastern Pacific (Fig. 17.23a). Accompanying anomalously cold SST in the North Pacific is anomalously low SLP and intensified westerlies in the North Pacific storm track. In its negative phase, the PDO is characterized by anomalies of opposite sign and weakened westerlies in the storm track (Fig. 17.23b). Like the AO, the change of circulation between opposite phases of the PDO influences the advection of maritime air, which moderates

[6] During sporadic episodes of the Madden-Julian oscillation (Sec. 15.5.2), the trades may even reverse. Equatorial westerlies then result in downwelling, compensated by the convergence of warm surface water. They also exert westerly drag on warm water to the west.

[7] Known as an *equatorial Kelvin wave*, it is a special form of deep water waves (Sec. 14.1).

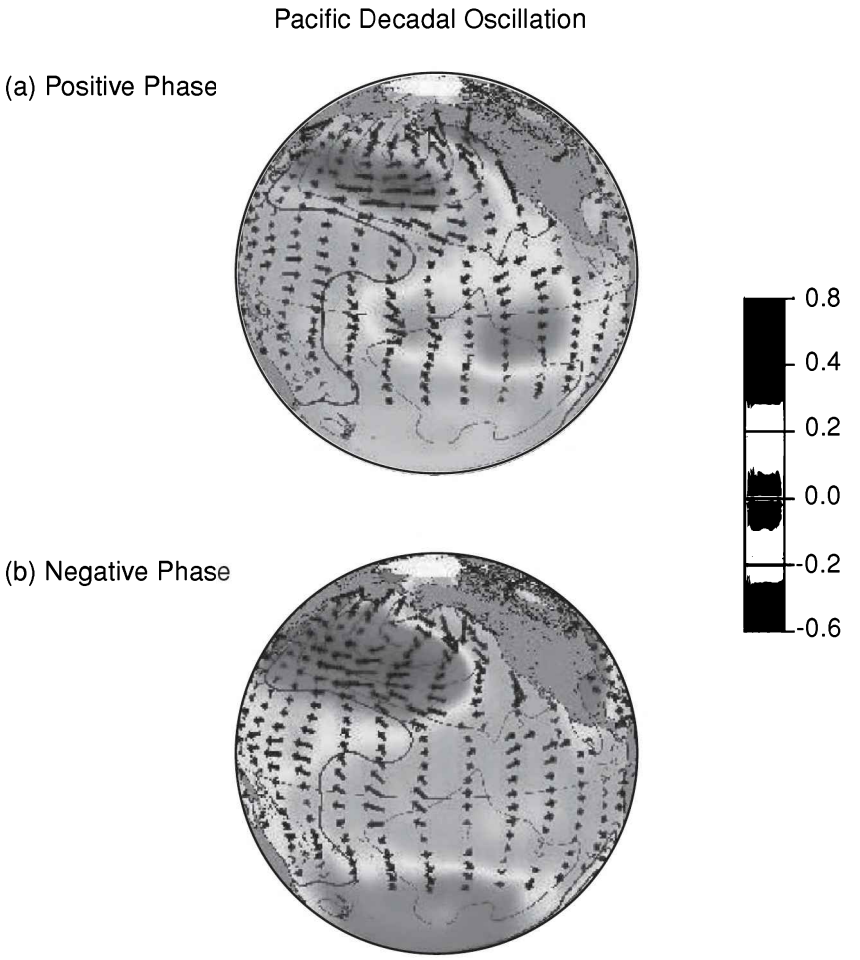

Figure 17.23 Anomalous SST (shaded), SLP (contoured), and surface wind associated with the Pacific Decadal Oscillation (PDO) during its (a) positive phase, when SST in the equatorial eastern Pacific is anomalously warm, and (b) negative phase, when SST in the equatorial eastern Pacific is anomalously cool. *Source:* http://jisao.washington.edu. See color plate section: Plate 28.

temperature extremes over neighboring continent (Sec. 15.5.1). Anomalous SST appears at high latitude, where isopycnals of the deep ocean intersect the surface. The PDO can therefore interact directly with the thermohaline circulation.

Cold temperature of the North Pacific, in concert with the exponential dependence on temperature of the Classius-Clapeyron relation (4.39), limits the PDO's interaction with the atmosphere through latent heat transfer. Perhaps relevant is the PDO's structure, which shares features with the extratropical response of El Nino (Fig. 14.20). Some fluctuations, in fact, operate coherently with those of SST in the tropics (Deser et al., 2004). There is also evidence of coherent changes in the Southern Hemisphere (Mantua and Hare, 2002).

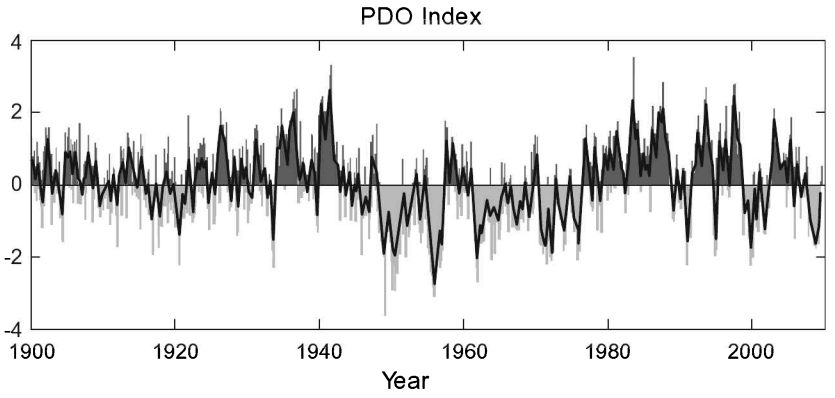

Figure 17.24 PDO index. The index fluctuates randomly, remaining of the same sign for several consecutive years, occasionally for longer than a decade. *Source:* http://jisao.washington.edu.

What distinguishes the PDO from ENSO is its time scale. Plotted in Fig. 17.24 is the PDO index, which reflects the sign and strength of the anomaly pattern. Although it fluctuates on time scales of years, the PDO remains of one sign for decades at a time. During the 1950s, 1960s, and 1970s, it was consistently negative. The PDO subsequently reversed phase. From the late 1970s until the close of the twentieth century, it was consistently positive. Since then, the PDO has again been mostly negative. A parallel exists in global-mean temperature (cf. Fig. 1.41). It varied consistently over similar periods, notably after the close of the 20th century. However, in view of the long correlation time of the PDO, the records are too short to establish a meaningful relationship. The mechanism behind this variation of SST, as well as how its influence is transmitted to other regions, remain poorly understood.

Other fluctuations

Other oceanic variations have been cited – more than a handful. A couple are worthy of mention. In the Atlantic is a counterpart of the PDO. The *Atlantic Multidecadal Oscillation* (*AMO*) is manifest in anomalous SST over much of the North Atlantic. Aperiodic, it varies on time scales of half a century or longer. The resolution of this feature in available records is therefore limited. Because it involves SST at high latitude, the AMO can also interact with the thermohaline circulation. There is some evidence that it influences Atlantic hurricanes, as well as drought in the United States.

The Indian Ocean exhibits an EW seesaw in SST, analogous to ENSO. Plotted in Fig. 17.25, the *Indian Ocean Dipole* (*IOD*) involves variations of SST in the eastern Indian Ocean, off the coast of Sumatra, and in the western Indian Ocean, off the coast of Africa, that are coherent but out of phase. The IOD emerges in the second EOF of SST, accounting for ~10% of the variance. Emerging in the leading EOF is ENSO, which accounts for ~30% of the variance.[8] Each perturbs the annual cycle of SST.

[8] ENSO (EOF 1) leads to anomalous SST that is in phase across the Indian Ocean. The IOD (EOF 2), which is out of phase across the Indian Ocean, thus has the structure of the first harmonic of ENSO.

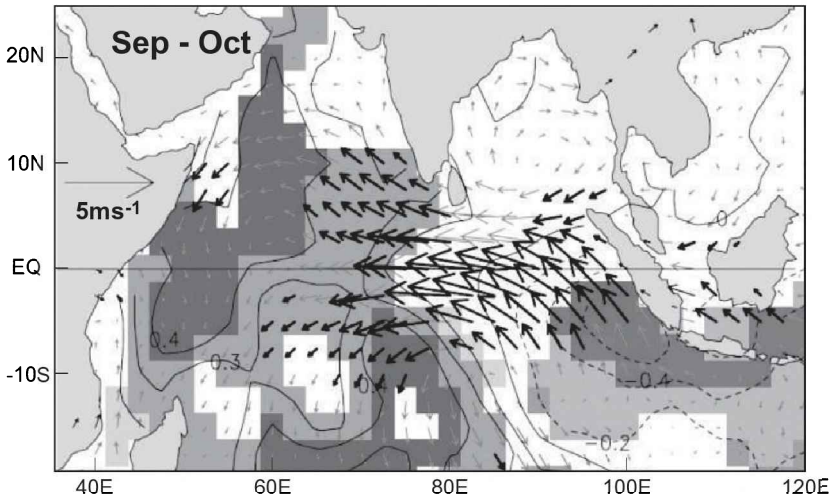

Figure 17.25 Anomalous SST (contoured), regions of >90% significance shaded, with red significant and warm and blue significant and cold, and surface wind associated with Indian Ocean dipole (IOD). After Saji et al. (1999). Reprinted by permission of Macmillan Publishers Ltd: *Nature* (Saji et al., 1999), Copyright (1999). See color plate section: Plate 29.

The IOD is aperiodic, fluctuating on a time scale of years. Anomalous surface wind that accompanies this variation of SST leads to an intensification and weakening of trade winds across the the equatorial Indian Ocean. The IOD has been associated with episodes of drought in Australia and excessive rainfall in Africa. However, like other fluctuations of SST, it represents only a fraction of the overall variance. This property limits the interpretation of individual episodes. The mechanism behind the IOD, as well as how its influence is conveyed to individual regions, suffer from considerations similar to those surrounding the AMO. They remain poorly understood.

SUGGESTED REFERENCES

The dynamics of ocean circulation are developed in *Atmosphere-Ocean Dynamics* (1982) by Gill and in *Introduction to Physical Oceanography* (2008) by Stewart.

Advanced treatments may be found in *Geophysical Fluid Dynamics* (1979) by Pedlosky and in *Atmospheric and Oceanic Fluid Dynamics* (2006) by Vallis.

Chemical considerations are discussed in *World's Oceans* (2003) by Sverdrup et al.

PROBLEMS

1. Suppose that warm salty water in the Gulf Stream, with temperature and salinity of 15°C and 36 g/kg, encounters water in the North Atlantic with temperature and salinity of 4°C and 33 g/kg. If the bodies of water mix in equal proportion, determine the (a) initial density anomaly of water in the Gulf stream, (b) initial density anomaly of water in the North Atlantic, (c) final density anomaly of the mixture; compare it to the average of the two initial density anomalies. What is the consequence of such mixing?

2. Surface salinity exceeds 36 g/kg in the subtropics of the south Pacific (Fig. 17.1). (a) If the mixed layer has a depth of 20 m, (a) what depth of water must be evaporated to increase its salinity from 35 g/kg, characteristic of the surroundings, to 36 g/km? (b) If achieved over a season, what is the attendant transfer of latent heat to the atmosphere in W/m^2? (c) If ocean temperature remains approximately constant, from where is that heat supplied? (d) Where is the latent heat that is transferred to the atmosphere eventually released? (e) Compare the area in (d) to that in (a); what is the implication?
3. Suppose that, in the North Atlantic, ambient temperature and salinity are 4°C and 33 g/kg, respectively. (a) Use the limiting behavior Fig. 17.4 to determine how much salinity would have to increase, with temperature fixed, to produce deep water. (b) If the mixed layer has a depth of 50 m, what depth of water must freeze to achieve that state? (c) If the freezing takes place over a season, how much heat transfer with the atmosphere must occur in W/m^2?
4. Demonstrate that, on seasonal time scales, heat storage of the ocean is two orders of magnitude greater than that of continent.
5. Suppose that heat transfer from the deep ocean leads to a gradual increase of SST in the tropics. Discuss the reestablishment of equilibrium between CO_2 in the ocean and atmosphere (cf. Fig. 1.43).
6. Show that the Ekman velocity satisfies the frictional momentum balance (17.4.1).
7. Consider a rectangular ocean basin of dimensions $L_x = a$ and $L_y = L_x/2$ that is narrow enough to be treated on an f plane at latitude 30°. Suppose that surface wind is geostrophic and controlled by a closed subtropical high, which is characterized by the 1000-hPa geopotential

$$\Phi_0(x, y) = 400 \cdot \cos\left(\frac{x}{X}\right)\cos\left(\frac{y}{Y}\right),$$

where $-\frac{L_x}{2} < x < \frac{L_x}{2}$, $-\frac{L_y}{2} < y < \frac{L_y}{2}$, and $X = L_x/\pi$, $Y = L_y/\pi$. If, in the spirit of Rayleigh friction, the surface stress can be described as

$$\boldsymbol{\tau}_0 = \rho\alpha\boldsymbol{v}_0$$

with $\alpha = 10^{-5}$ m/s, calculate and plot (a) the surface wind field, (b) the horizontal distribution of Ekman transport, (c) the horizontal distribution of Ekman pumping.
8. (a) For the conditions in Prob. 17.7, describe the horizontal distribution of SST implied by the motion. (b) As in (a), but if, opposite the equator, are a mirror-image ocean basin and surface wind.
9. With reference to the First Law (Sec. 10.7) and net radiation (Sec. 1.4.2), explain why northward transport of heat must assume the form in Fig. 17.10.
10. (a) For the conditions in Prob. 17.7, but on a β plane, calculate and plot the horizontal distribution of column-integrated mass transport under Sverdrup balance. (b) Compare the resulting transport against the Ekman transport in Prob. 17.7. (c) What additional feature is necessary to satisfy continuity?

CHAPTER
EIGHTEEN

Interaction with the stratosphere

Above the tropopause, the horizontal gradient of heating is generally weak enough to leave thermal structure close to barotropic stratification. For this reason, baroclinic instability generated through conversion of available potential energy does not play an essential role. Further, strong westerlies in the winter stratosphere and easterlies in the summer stratosphere trap baroclinic disturbances in the troposphere. Their presence in the stratosphere is therefore limited to a neighborhood of the tropopause. These features leave the circulation in the stratosphere less disturbed than in the troposphere (Fig. 1.10). Exceptions are planetary waves. Unlike baroclinic disturbances, they propagate through strong westerlies of the polar-night jet (Sec. 14.5.2). Vertical amplification enables planetary waves to disturb the polar vortex. During major amplifications, they completely disrupt the circumpolar flow. Air then moves freely between tropical and polar regions, experiencing sharply different radiative environments. Global-scale disturbances such as the one in Fig. 1.10a play a key role in establishing mean distributions of radiatively active constituents.

With convection inhibited by strong static stability, the energy budget of the stratosphere is dominated by radiative transfer. It therefore remains closer to radiative equilibrium than the troposphere (Fig. 8.24). The radiative energy budget is controlled by SW heating due to ozone absorption, principally in the Hartley and Huggins bands (Sec. 8.3.1), and LW cooling due to CO_2 emission to space at 15 μm. Ozone, in concert with CO_2, thus shapes the thermal structure of the middle atmosphere. Through hydrostatic and geostrophic equilibrium, the latter controls the circulation. For this reason, ozone underpins much of the observed behavior of the middle atmosphere.

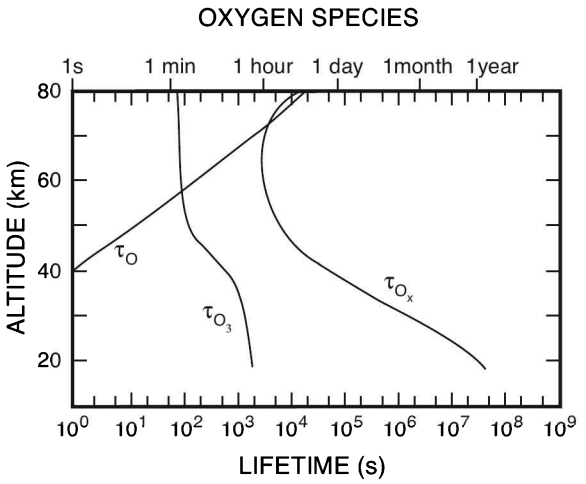

Figure 18.1 Photochemical lifetimes of oxygen species. *Source:* Brasseur and Solomon (1986).

18.1 OZONE PHOTOCHEMISTRY

The simplest treatment of ozone photochemistry is due to Chapman (1930). It considers a pure oxygen atmosphere. Composition is then governed by the following reactions

$$O_2 + h\nu \rightarrow O + O \qquad (J_2) \qquad (18.1.1)$$

$$O + O_2 + M \rightarrow O_3 + M \qquad (k_2) \qquad (18.1.2)$$

$$O + O_3 \rightarrow 2O_2 \qquad (k_3) \qquad (18.1.3)$$

$$O_3 + h\nu \rightarrow O_2 + O \qquad (J_3), \qquad (18.1.4)$$

where rate coefficients, indicated parenthetically to the right, characterize the speeds of individual reactions.[1] Reactions (18.1.1) and (18.1.4) describe photodissociation or *photolysis* of O_2 by UV radiation in the Herzberg continuum near 242 nm and of O_3 in the Hartley and Huggins bands near 310 nm. Reaction (18.1.4) operates at all wavelengths shorter than 1 μm. Reactions (18.1.2) and (18.1.3) describe recombination of O_2 and O_3 with O. The molecule M represents a third body needed to conserve momentum and energy in the recombination of O and O_2 (e.g., air molecules, which are abundant). Atomic oxygen that is produced by photolysis of ozone in (18.1.4) recombines immediately with molecular oxygen in (18.1.2) to re-form ozone. Hence those reactions constitute a closed cycle, one that leaves O and O_3 unchanged yet absorbs UV radiation efficiently.

18.1.1 The chemical family

The rate coefficients determine the photochemical lifetimes of these species, which are presented in Fig. 18.1 as functions of altitude (Prob. 18.1). Lifetimes of the odd oxygen

[1] Dimensions of $\left(\frac{\text{molecules}}{\text{volume}}\right)^{-2}$ time^{-1} for k_2, $\left(\frac{\text{molecules}}{\text{volume}}\right)^{-1}$ time^{-1} for k_3, and time^{-1} for J_2 and J_3.

species O and O_3 are short by comparison with that of O_2, which is present in fixed proportion. Moreover, the lifetimes of O and O_3 differ by several orders of magnitude. This feature complicates their treatment in numerical calculations. For this reason, it is convenient to introduce the *odd oxygen family*

$$O_x = O + O_3. \tag{18.2}$$

Individual members of the family have lifetimes much shorter than that of O_x. They can therefore be treated as being in photochemical equilibrium with one another. Reactions (18.1) then describe comparatively slow changes in O_x that are attended by immediate adjustments of O and O_3 within the family to maintain photochemical equilibrium. Such changes are introduced whenever an air parcel is displaced from one radiative environment to another.

The relative abundance or *partitioning* of family members is determined by reactions (18.1.2) and (18.1.4), which operate much faster than the others. Those reactions preserve odd oxygen. Consequently, they represent a simple redistribution between O and O_3. The rate of destruction of O_3 in (18.1.4) is expressed by

$$\left.\frac{d[O_3]}{dt}\right|_{destruction} = -J_3[O_3], \tag{18.3.1}$$

where [ ] denotes the number density $\left(\frac{\text{molecules}}{\text{volume}}\right)$ and $\frac{d}{dt}$ represents the Lagrangian derivative. (The chemical budget should formally be expressed in terms of mixing ratio to account for expansion and compression of an air parcel (Sec. 1.2). For the moment, however, motion is ignored.) The rate of production of O_3 in (18.1.2) is given by

$$\left.\frac{d[O_3]}{dt}\right|_{production} = k_2[O_2][O][M]. \tag{18.3.2}$$

Adding yields the net rate of production of O_3 in (18.1.2) and (18.1.4)

$$\left.\frac{d[O_3]}{dt}\right|_{net} = k_2[O_2][O][M] - J_3[O_3]. \tag{18.3.3}$$

Photochemical equilibrium within the family requires the left-hand side to vanish. Therefore,

$$J_3[O_3] = k_2[O_2][O][M] \tag{18.4}$$

governs the partitioning of its member species. Below 60 km, O_3 is the dominant member of O_x. Consequently, ozone tracks the behavior of odd oxygen. The lifetime of O_x in the lower stratosphere (Fig. 18.1) is several weeks. It is an order of magnitude longer than the time scale of advection ($\sim$ 1 day). However, its lifetime decreases with height rapidly, shortening to less than 1 day above about 30 km.

18.1.2 Photochemical equilibrium

The remaining reactions (18.1.1) and (18.1.3) govern production and destruction of O_x. These reactions operate on time scales much longer than reactions for the individual member species. For photochemical equilibrium of the family as well, the net rate of production of $[O_x]$ must also vanish. The rate at which O_x molecules are produced in

(18.1.1) is expressed by

$$\left.\frac{d[O_x]}{dt}\right|_{production} = 2J_2[O_2]. \tag{18.5.1}$$

The rate at which they are destroyed in (18.1.3) is given by

$$\left.\frac{d[O_x]}{dt}\right|_{destruction} = -2k_3[O][O_3]. \tag{18.5.2}$$

Adding yields the net rate of production of $[O_x]$

$$\left.\frac{d[O_x]}{dt}\right|_{net} = 2J_2[O_2] - 2k_3[O][O_3]. \tag{18.5.3}$$

Photochemical equilibrium of O_x requires

$$J_2[O_2] = k_3[O][O_3]. \tag{18.6}$$

Eliminating [O] from (18.4) and (18.6) then obtains the equilibrium ozone number density

$$[O_3] = [O_2]\left(\frac{k_2 J_2}{k_3 J_3}[M]\right)^{\frac{1}{2}}, \tag{18.7}$$

which follows in terms of the number densities of molecular oxygen and air.

The profile of $[O_3]$ predicted by (18.7) is plotted in Fig. 18.2. For its simplicity, Chapman chemistry (solid) is remarkably successful. It reproduces the essential vertical structure of observed ozone, which is superposed for tropical (dashed) and extratropical latitudes (dotted). From TOA, ozone number density increases downward due to increasing $[O_2]$ and photolysis in (18.1.1). A maximum in $[O_3]$ is achieved near 30 km. At lower levels, UV flux and J_2 decrease sharply due to attenuation by photolysis.

Despite this general agreement, the behavior predicted by (18.7) deviates importantly from the observed distribution of ozone. Ozone number density is overpredicted at tropical latitudes, where much of ozone is concentrated (Fig. 1.20). For this reason, (18.7) gives total ozone that is too large, $\Sigma_{O_3} \cong 1000$ DU (Fig. 1.21). At extratropical latitudes, $[O_3]$ is underpredicted in the lower stratosphere and overpredicted in the upper stratosphere. Note the observed profile of $[O_3]$ is displaced downward from that in the tropics. Maximum concentration at extratropical latitudes is found below 20 km (cf. Fig. 1.20). At those latitudes, as much as 30% of total ozone lies in the troposphere. Tropospheric ozone increases during winter and spring (London, 1985; Logan, 1999). It also manifests an upward trend, long-term evolution that is not understood (WMO, 2006). When the horizontal distribution of total ozone is considered (Figs. 1.21, 1.22), the discrepancy with observed behavior is even more serious. Observed Σ_{O_3} at 60° is almost twice as great as in the tropics. By contrast, (18.7) predicts total ozone to minimize at high latitude – because there UV flux and hence J_2 are small. The latter vanish inside polar night, where observed values of Σ_{O_3} are, in fact, greatest.

These discrepancies are attributable to two key ingredients that are not accounted for by (18.7). First, ozone chemistry involves species other than oxygen. Catalytic cycles involving free radicals of hydrogen, nitrogen, and chlorine deplete odd oxygen. They make ozone dependent on a wide array of chemical species. The second factor not accounted for is motion. Below 30 km, where the ozone column is concentrated, the photochemical lifetime is long enough for O_3 to be transported by the circulation.

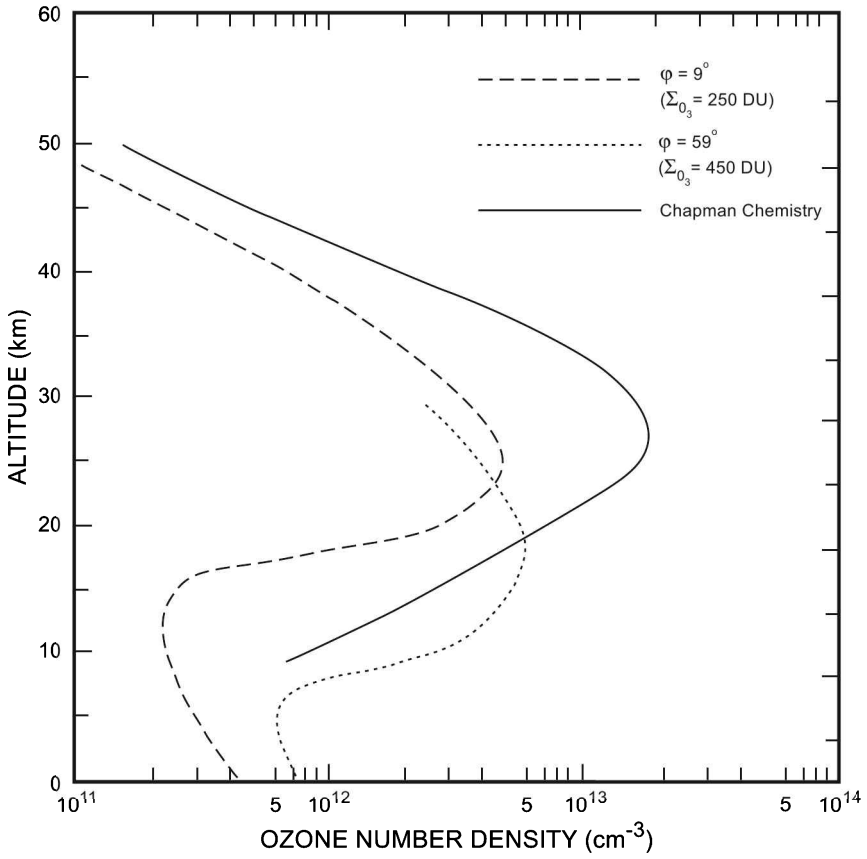

Figure 18.2 Vertical profile of ozone number density under photochemical equilibrium, as calculated from Chapman chemistry (solid), and observed at tropical (dashed) and extratropical (dotted) latitudes. Chapman chemistry was calculated with rate coefficients from Brasseur and Solomon (1986) and Nicolet (1980). It yields realistic vertical structure, but a column abundance of $\Sigma_{O_3} \cong$ 1000 DU. Observed data are from Hering and Borden (1965) and Krueger (1973).

It therefore passes between widely differing photochemical environments. Even at higher altitude, other species that participate in the complex photochemistry of ozone are influenced importantly by transport.

18.2 INVOLVEMENT OF OTHER SPECIES

Photodissociation by UV radiation produces a number of free radicals, derived from less reactive reservoir species of tropospheric origin. Photochemically active, the free radicals can then go on to destroy ozone in catalytic cycles that leave the free radical unchanged.

18.2.1 Nitrous oxide

The free radical nitric oxide NO represents an important link to human activities. Nitric oxide is a byproduct of inefficient combustion (e.g., in aircraft exhaust). In the stratosphere, the principal source of NO is dissociation of nitrous oxide N_2O through reaction with atomic oxygen

$$N_2O + O \rightarrow 2NO. \tag{18.8}$$

Nitrous oxide is produced in the troposphere by natural as well as anthropogenic sources (Chap. 1). Away from the surface, N_2O is long-lived, having a photochemical lifetime of order 100 years (Fig. 18.3). Further, nitrous oxide is not water soluble. It is therefore immune to normal scavenging mechanisms associated with precipitation (Sec. 9.5.2). These properties allow N_2O to become well-mixed in the troposphere. They also make it useful as a tracer of air motion in the stratosphere.

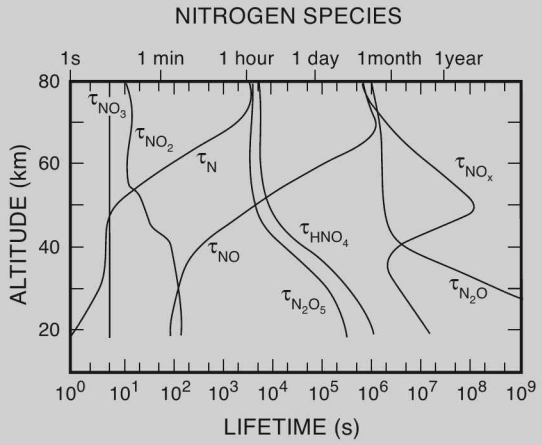

Figure 18.3 Photochemical lifetimes of nitrogen species. *Source:* Brasseur and Solomon (1986).

After entering the stratosphere, N_2O is photodissociated according to the reaction

$$N_2O + h\nu \rightarrow N_2 + O. \tag{18.9}$$

Reaction (18.9) is the primary destruction mechanism for nitrous oxide. It is responsible for the upward decrease of its mixing ratio r_{N_2O} near the tropopause (Fig. 1.23). The mixing ratio of N_2O is largest near the tropical tropopause (Fig. 18.4). In view of its long lifetime, this structure reveals how air enters the stratosphere. A plume of high values reflects upwelling in the tropical stratosphere, where N_2O-rich air is carried across the tropical tropopause from its tropospheric reservoir below.

The free radical NO forms via (18.8). Once produced, it can efficiently destroy ozone through the catalytic cycle

$$NO + O_3 \rightarrow NO_2 + O_2 \tag{18.10.1}$$

$$NO_2 + O \rightarrow NO + O_2. \tag{18.10.2}$$

Adding yields the net effect

$$O_3 + O \rightarrow 2O_2 \quad \text{(Net)}. \tag{18.10.3}$$

This closed cycle leaves $NO + NO_2$ unchanged. One molecule of nitric oxide can therefore destroy many molecules of ozone.

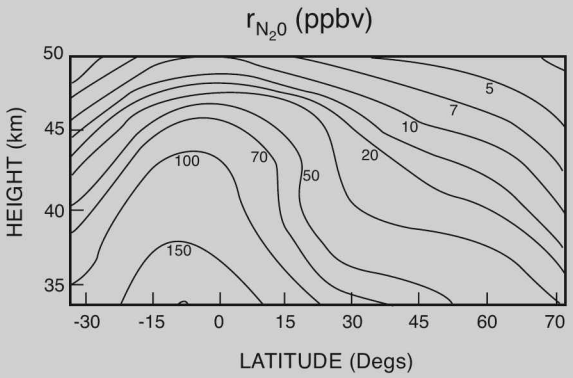

Figure 18.4 Zonal-mean mixing ratio of nitrous oxide N_2O on January 9, 1992, as observed by the ISAMS instrument on board the Upper Atmosphere Research Satellite (UARS). Adapted from Ruth et al. (1994).

Reactions with other nitrogen compounds make NO dependent on a number of species. Because reactions among those species are fast, it is convenient to introduce the *odd nitrogen family*

$$NO_x = N + NO + NO_2 + NO_3 + 2N_2O_5 + HNO_4, \tag{18.11}$$

the members of which may be treated in photochemical equilibrium with one another. Despite the short lifetimes of some its members, the lifetime of NO_x is much longer than the time scale for advection (Fig. 18.3). The abundance of NO then follows from $[NO_x]$ and from partitioning within the family. On a longer time scale, NO_x reacts with other families like O_x.

18.2.2 Chlorofluorocarbons

Free radicals of chlorine represent another important link to human activities. Atomic chlorine is produced naturally in the stratosphere through photodissociation of methyl chloride CH_3Cl, which is a product of ocean processes. Oxidation of CH_3Cl by reactive species likewise produces Cl. Atomic chlorine is also produced by photodissociation of CFCs, the sole source of which is industrial. Like N_2O, CFC-11 ($CFCl_3$) and CFC-12 (CF_2Cl_2) are long-lived – at least in the troposphere (Fig. 18.5). CFCs have photochemical lifetimes of several years. They are also water insoluble, which circumvents normal scavenging mechanisms. These properties allow CFCs to become homogenized in the troposphere (Fig. 1.23).

In the stratosphere, this picture breaks down. There, CFC-11 and CFC-12 decrease upward through photodissociation. This process releases free chlorine

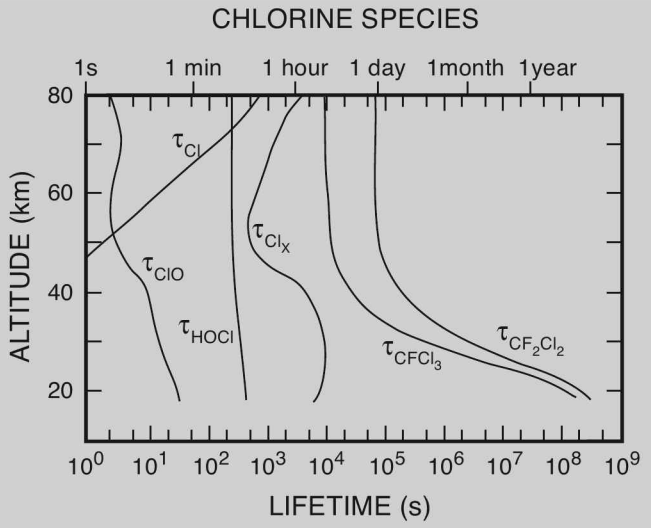

Figure 18.5 Photochemical lifetimes of chlorine species, including CFC-11 ($CFCl_3$) and CFC-12 (CF_2Cl_2). *Source:* Brasseur and Solomon (1986).

in the reactions

$$CFCl_3 + h\nu \rightarrow CFCl_2 + Cl \tag{18.12.1}$$

$$CF_2Cl_2 + h\nu \rightarrow CF_2Cl + Cl \tag{18.12.2}$$

that operate at wavelengths shorter than 225 nm. Once produced, free Cl reacts with ozone in the catalytic cycle involving chlorine monoxide ClO

$$Cl + O_3 \rightarrow ClO + O_2 \tag{18.13.1}$$

$$ClO + O \rightarrow Cl + O_2. \tag{18.13.2}$$

Adding yields the net effect

$$O_3 + O \rightarrow 2O_2 \quad \text{(Net)}. \tag{18.13.3}$$

This closed cycle leaves Cl + ClO unchanged. One atom of chlorine can therefore destroy many atoms of ozone.

Like free radicals of nitrogen, atomic chlorine can react with other species on widely varying time scales. It is therefore convenient to introduce the *odd chlorine family*

$$Cl_x = Cl + ClO + HOCl. \tag{18.14}$$

The abundance of Cl then follows via the partitioning of member species. Unlike O_x in the lower stratosphere and NO_x, Cl_x is short-lived relative to air motion (Fig. 18.5). Therefore, it is not passively advected by the circulation. Nevertheless, Cl_x is much longer-lived than its members, streamlining the numerical treatment of chlorine species. Odd chlorine can interact with odd nitrogen through the reaction

$$ClO + NO \rightarrow Cl + NO_2. \tag{18.15}$$

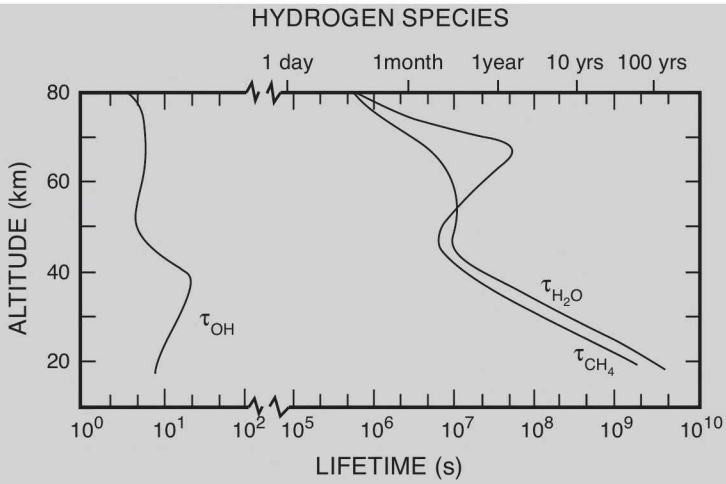

Figure 18.6 Photochemical lifetimes of hydrogen species. *Source:* Brasseur and Solomon (1986).

Reaction (18.15) regenerates free Cl, coupling the families NO_x and Cl_x. Other interactions among O_x, NO_x, and Cl_x bear importantly on ozone depletion in the polar stratosphere (Sec. 18.7).

18.2.3 Methane

Methane enters considerations of ozone because it interacts with NO_x and O_x. In addition to being radiatively active, CH_4 represents an important link between chemical constituents in the stratosphere and water vapor. For both, the troposphere serves as a reservoir. Like N_2O, methane has a photochemical lifetime of many years below 40 km (Fig. 18.6). It too is water insoluble. These properties allow CH_4 to become well-mixed in the troposphere (Fig. 1.23). They also make it useful as a tracer of air motion in the stratosphere. Figure 18.7 presents the zonal-mean

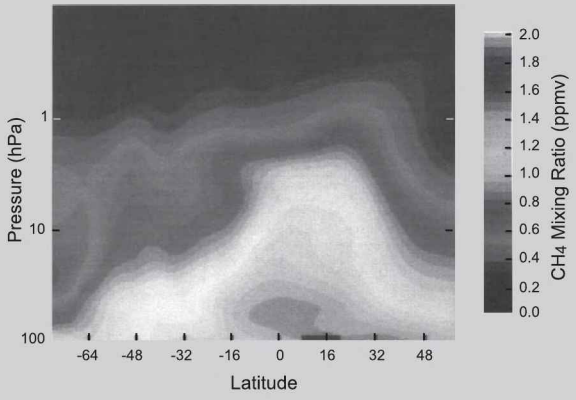

Figure 18.7 Zonal-mean mixing ratio of methane CH_4, as observed by the HALOE instrument on board UARS. Adapted from Bithell et al. (1994).

distribution of r_{CH_4} in the middle atmosphere. Mirroring structure in the N_2O distribution is a plume of high mixing ratio above the tropical tropopause. It reflects upwelling in the equatorial stratosphere.

Decreasing mixing ratio in the stratosphere follows from chemical destruction of CH_4. Methane is oxidized by the hydroxyl radical in the reaction

$$CH_4 + OH \rightarrow CH_3 + H_2O. \tag{18.16.1}$$

It is also destroyed by atomic oxygen and chlorine in the reactions

$$CH_4 + O \rightarrow CH_3 + OH \tag{18.16.2}$$

$$CH_4 + Cl \rightarrow CH_3 + HCl. \tag{18.16.3}$$

The latter represents an important sink of reactive Cl_x. The free radical CH_3 produced in reactions (18.16) immediately combines with molecular oxygen to form CH_3O_2. Two reactions involving NO_x

$$CH_3O_2 + NO \rightarrow CH_3O + NO_2 \tag{18.17.1}$$

$$NO_2 + h\nu \rightarrow NO + O \tag{18.17.2}$$

then form a closed cycle. They have the net effect

$$CH_3O_2 + h\nu \rightarrow CH_3O + O \quad \text{(Net)}. \tag{18.17.3}$$

Methane oxidation thus leads to production of O_x. As the partitioning of O_x fixes the abundance of O_3, reactions (18.18) provide a potentially important source of ozone in the lower stratosphere.

The free radical OH initiates the above process. It is produced by dissociation of water vapor

$$H_2O + O \rightarrow 2OH. \tag{18.18}$$

Above the tropopause, the lifetime of H_2O is many years (Fig. 18.6). Consequently, it too behaves as a tracer at these heights. Water vapor mixing ratio decreases sharply in the troposphere, attaining a minimum at the *hygropause* (Fig. 18.8). Found a couple of kms above the tropopause, the hygropause is characterized by mixing ratio of 1–2 ppmv. Notice that driest air is found at the altitude of highest cloud, cumulus overshoots that make data in Fig 18.8 unavailable (cf Fig 9.26). The steep decrease with height in the troposphere reflects convection, which dehydrates air by limiting r_{H_2O} to saturation values. Above the hygropause, r_{H_2O} increases due to oxidation of methane, as r_{CH_4} decreases. How much of the observed increase of water vapor actually follows from reactions (18.16) remains unclear.

18.3 MOTION

Photochemical considerations predict that ozone column abundance will maximize at low latitude, where UV radiation and photolysis maximize. The observed distribution, however, maximizes at high latitude (Fig. 1.21). Approaching 500 DU during late winter and spring, total ozone there increases from its fall minimum of about 270 DU by nearly 100%. This shortcoming of Chapman chemistry is unchanged by the addition

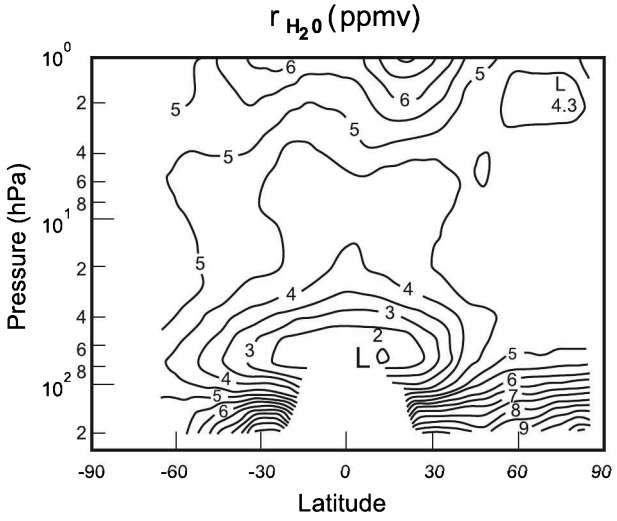

Figure 18.8 Zonal-mean mixing ratio of water vapor observed by Nimbus-7 LIMS. Masking beneath 60 hPa denotes sites in the tropics that are obscured by cloud, where data are unavailable. Adapted from Remsberg et al. (1984).

of other chemical species. The high-latitude maximum of Σ_{O_3} can be understood only through dynamical considerations.

18.3.1 The Brewer-Dobson circulation

In the winter stratosphere, ozone heating establishes an equatorward temperature gradient over a deep layer (Fig. 1.7). By thermal wind balance (12.11), this forces strong circumpolar westerlies. Stratospheric westerlies intensify upward along the *polar-night terminator*, where SW absorption vanishes. They form the polar-night jet (Fig. 1.8), which circumscribes the polar-night vortex (Fig. 1.10b). In the summer stratosphere there is a poleward gradient of heating, which follows from the distribution of daily insolation (Fig. 1.33). It produces a deep temperature gradient of the opposite sense, forcing strong circumpolar easterlies.

In each season, air motion is nearly zonal. Under radiative equilibrium, it is zonally symmetric, experiencing no net heating. By the First Law, individual air parcels then do not cross isentropic surfaces. This implies no net vertical motion and, by continuity, no meridional motion.

The situation is analogous to the zonally symmetric circulation in Sec. 15.2. Away from boundaries, where frictional drag is negligible, the motion is geostrophic and zonal. It accomplishes no transport. Meridional transport is confined to shallow Ekman layers along the upper and lower boundaries. There, frictional drag drives the motion out of geostrophic balance. It introduces an ageostrophic secondary circulation that transfers air across latitude circles. In the stratosphere, planetary waves play a similar role. When absorbed (Sec. 14.6), they exert a drag on the mean flow. It forces the motion out of geostrophic balance. An ageostrophic secondary circulation is then imposed onto the strong zonal motion. It forces air across latitude circles and therefore out of radiative equilibrium.

The nature of this secondary circulation is revealed by the structure of long-lived tracers (Figs. 18.4, 18.7). Distributions of N_2O and CH_4 imply upwelling in the tropics, where tropospheric air enters the stratosphere. Continuity then requires downwelling at middle and high latitudes. Connected by poleward motion, these regions of vertical motion comprise an equator-to-pole circulation (see Fig. 18.11). Although weak compared with zonal motion, this ageostrophic secondary circulation explains the large column abundance of ozone that is observed at high latitude. Ozone-rich air is drawn poleward from the chemical source region in the tropics, increasing r_{O_3} and total ozone at high latitude. When it descends, that air undergoes compression. This increases the absolute concentration ρ_{O_3} at high latitude (Fig. 1.20). Through adiabatic warming, it also increases temperature. Air descending over the pole warms by ~10 K for each kilometer that it sinks. During winter, it sinks several tens of kilometers. Adiabatic warming thus provides a major offset to LW cooling, which prevails inside polar darkness.

This gradual overturning in the meridional plane was first inferred by Dobson (1930) and Brewer (1949) to explain balloon observations of trace species. Known as the *Brewer-Dobson circulation*, it figures centrally in chemical considerations by shaping the distributions of many species. The Brewer-Dobson circulation also influences lower levels. Downwelling over the pole transfers stratospheric air into the troposphere (see Fig. 18.11). It must be compensated over the equator by upwelling that returns air to the stratosphere at the same rate. The Brewer-Dobson circulation thus couples the troposphere to the stratosphere.

18.3.2 Wave driving of mean meridional motion

Although characterized by a zonally symmetric overturning in the meridional plane, the Brewer-Dobson circulation actually develops through zonally asymmetric processes. A clue to its origin lies in the radiative-equilibrium state of the middle atmosphere (Fig. 18.9). During solstice, the sharp gradient of heating across the polar-night terminator produces radiative-equilibrium temperature T_{RE} colder than 150°K (Fig. 18.9a). This is much colder than observed temperature (Fig. 1.7). More uniform, observed temperature in the Northern Hemisphere remains above 200°K. With thermal wind balance (12.11), the deep layer of sharp temperature gradient implies radiative-equilibrium wind that intensifies upward – to more than 300 m s^{-1} (Fig. 18.9b). Analogous to temperature, this is much stronger than observed wind (Fig. 1.8).

The observed polar-night vortex is warmer than radiative equilibrium. It must therefore experience net radiative cooling (Sec. 8.5). Observed temperature and ozone imply a cooling rate inside polar darkness greater than 8°K day^{-1} (Fig. 8.27). By the First Law (2.36), that cooling must reduce the potential temperature of air inside the vortex. In concert with positive stability ($\frac{\partial \theta}{\partial z} > 0$), it implies downwelling across isentropic surfaces. Calculations in which this diabatic cooling is prescribed (Murgatroyd and Singleton, 1961) qualitatively reproduce the meridional circulation that was inferred from tracer behavior by Brewer and Dobson.

In the Southern Hemisphere, polar temperature is colder – as cold as 180°K. The Antarctic polar-night vortex, which is less disturbed by planetary waves, is thus colder and stronger than its counterpart over the Arctic. Closer to radiative equilibrium, it should therefore experience weaker radiative cooling. That, in turn, implies weaker downwelling at extratropical latitudes. Analogous considerations apply to the

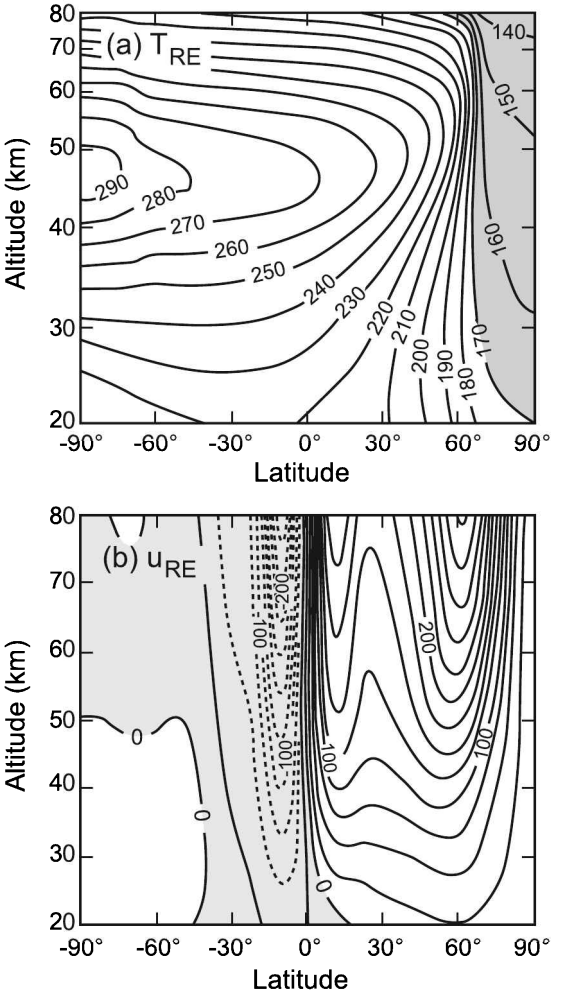

Figure 18.9 Radiative-equilibrium (a) temperature and (b) zonal wind in the middle atmosphere during solstice, as calculated in a radiative–convective–photochemical model. Thermal structure adapted from Fels (1985). Zonal wind calculated from thermal wind balance and from climatological motion at 20 km in Fig. 1.8.

summertime circulation (Fig. 8.27), in which strong easterlies block planetary wave propagation from the troposphere (Sec. 14.5).[2]

Understanding these inter-hemispheric differences requires an understanding of how the circulation is maintained out of radiative equilibrium. Observed motion during winter is rarely in a quiescent state of zonal symmetry. This is especially true in the Northern Hemisphere. There, the circumpolar flow is routinely disturbed by

[2] The absence of eddy motion during summer enabled the cloud of volcanic debris in Fig. 9.6 to remain confined meridionally. Once westerlies developed after equinox, planetary waves were able to propagate upward from the troposphere, disturbing the zonal flow. The volcanic cloud was then quickly dispersed across the hemisphere.

amplified planetary waves that propagate upward from the troposphere. Planetary waves in the Northern Hemisphere are stronger than those in the Southern Hemisphere, because of large orographic forcing and land-sea contrast (Sec. 15.4). Able to penetrate into strong westerlies of the winter stratosphere, they drive the circulation out of zonal symmetry and away from radiative equilibrium. As illustrated by Fig. 1.10a, air then flows meridionally between sharply different radiative environments: from the sunlit tropics, where it experiences net SW heating, into polar darkness, where it experiences only LW cooling. Such air motion operates on a time scale short compared with radiative adjustment. The heat transfer experienced by individual air parcels is therefore irreversible (Figs. 3.5, 3.6).

Figure 18.10a presents, from a numerical integration, the horizontal trajectory of an air parcel inside the polar-night vortex. Superposed are instantaneous distributions of motion and potential vorticity Q (Sec. 12.5). The parcel shown orbits about the disturbed vortex, which is sporadically displaced from zonal symmetry and distorted by planetary waves. In its thermodynamic state space (Fig. 18.10b), the parcel therefore cycles between sharply different radiative-equilibrium temperatures (solid). The short time scale of advection prevents the parcel from adjusting to local radiative equilibrium. Instead, it trails behind the ambient value of T_{RE} by a finite temperature difference. The parcel is therefore out of thermodynamic equilibrium. By the Second Law, the heat transfer it experiences is irreversible. This introduces a hysteresis into the parcel's thermodynamic state, one that accumulates with each circuit about the vortex. Net cooling during successive circuits then causes the parcel to drift across isentropic surfaces to lower θ (cf. Fig. 3.6). (Notice that the descent rate $\frac{d\theta}{dt}$ increases with the parcel's departure from local radiative equilibrium.) Superimposed is the parcel's evolution in the absence of mechanical forcing by planetary waves (dotted). The parcel then adjusts to radiative equilibrium, bringing vertical motion to a halt.

Downwelling is accompanied by the rejection of heat. The latter derives ultimately from work that is performed on the circulation by planetary waves when they experience dissipation. Analogous to paddle work, the latter makes the circulation of the stratosphere behave as a radiative refrigerator (Sec. 2.2.2). The work performed by planetary waves follows from drag that is exerted on the mean flow when wave momentum is absorbed. Measured by the convergence of wave activity flux (e.g., of EP flux in Sec. 14.5.4), planetary wave drag drives the motion out of geostrophic balance. Ageostrophic motion that is introduced then produces meridional transport. Involving a poleward drift of air (Fig. 18.10a), such transport is analogous to that produced by frictional drag in the zonally symmetric circulation of Sec. 15.2. Compensating it over the pole is downwelling. Accompanied by adiabatic warming, downwelling maintains the polar-night vortex warmer and weaker than it would be under radiative equilibrium – as much as 50 K warmer. The strength of downwelling follows in proportion to the absorption of wave activity. Amplified planetary waves of the Northern Hemisphere therefore drive the Arctic vortex farther from radiative equilibrium than the Antarctic vortex, for which planetary wave absorption is comparatively weak.[3]

[3] The Antarctic vortex is also reinforced by anomalous LW cooling, through exchange with the Antarctic plateau. Much colder than surrounding ocean. the Antarctic surface induces a strong meridional gradient of cooling in the stratosphere, one that is transmitted upward through the 9.6-μm band of ozone (Francis and Salby, 2001). Independent of planetary wave forcing, this radiative forcing of the Antarctic vortex accounts for about half of the observed difference with the Arctic vortex.

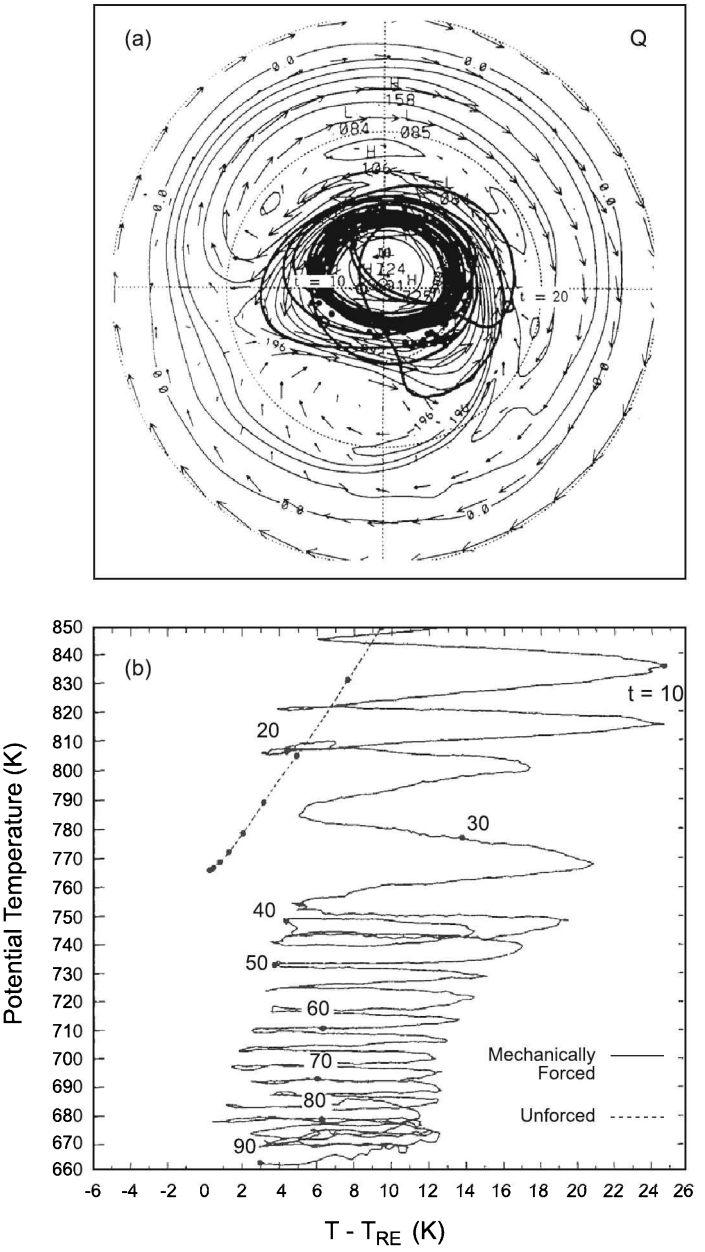

Figure 18.10 (a) Distributions of potential vorticity Q and horizontal motion in a 2-dimensional calculation representative of the polar-night vortex (cf. Fig. 14.26). Greenwich meridian is positioned at 0600 and International Dateline at 1200 on the clock dial. Bold line shows the trajectory of one of an ensemble of air parcels (solid circles) initialized inside the vortex. The folding of contours along the edge of the vortex and regions where the Q distribution has been homogenized by secondary eddies symbolize horizontal mixing. (b) Evolution of the parcel whose trajectory is shown in (a) in its thermodynamic state space (solid), represented in terms of the parcel's departure from local radiative equilibrium. Irreversible heat transfer introduces a hysteresis into the parcel's state with each circuit about the displaced vortex, which produces a steady drift of air to lower θ. In the same calculation, but without planetary waves to maintain the circulation out of radiative equilibrium (dotted), the parcel adjusts to radiative equilibrium, which halts subsequent cooling and descent inside the vortex. After Fusco and Salby (1994), copyright by the American Geophysical Union.

Planetary waves suffer absorption through thermal dissipation. Represented by cooling in Fig. 18.10, thermal dissipation damps perturbation temperature (Sec. 8.6). Planetary waves also suffer absorption through mechanical dissipation, notably, through quasi-horizontal mixing. By destroying large-scale gradients, it damps perturbation motion. As it operates on time scales short compared with radiative adjustment, mixing conserves θ, homogenizing all conserved properties along isentropic surfaces. Isentropic mixing is evidenced in Fig. 18.10a by the conserved property Q. Contours of potential vorticity have folded at the edge of the vortex (near 0 E; 0600 on the clock dial), where an anticyclonic eddy prevails and the distribution of Q has been homogenized. Those features neighbor the critical line of stationary planetary waves (cf. Fig. 14.23). There, large eddy displacements overturn the distribution of Q, folding contours of potential vorticity. By reversing the gradient of Q, this renders the local motion dynamically unstable (Sec. 16.2). Air is then wound up in secondary eddies. They cascade large-scale tracer structure to small scale, where it is absorbed by diffusion. Like thermal dissipation, mechanical dissipation of planetary waves acts to maintain the polar-night vortex warmer and weaker than it would be under radiative equilibrium.

18.3.3 Transformed Eulerian description

Although 3-dimensional, it is convenient to describe motion 2-dimensionally in terms of the zonal-mean circulation $\overline{\boldsymbol{v}} = (\overline{u}, \overline{v}, \overline{w})$. This representation is especially attractive in light of the numerous chemical species that must be described in the photochemistry of ozone. In this framework, zonal-mean distributions of motion and chemical species interact, with one another and with the wave field.

In log-pressure coordinates, motion is governed by

$$\frac{d\boldsymbol{v}}{dt} + w\frac{\partial \boldsymbol{v}}{\partial z} + f\boldsymbol{k} \times \boldsymbol{v} = -\nabla\Phi \tag{18.19.1}$$

$$\nabla \cdot \boldsymbol{v} + \frac{1}{\rho_0}\frac{\partial}{\partial z}(\rho_0 w) = 0 \tag{18.19.2}$$

$$\frac{dT}{dt} + \frac{N^2 H}{R} w = \frac{\dot{q}}{c_p}, \tag{18.19.3}$$

where $\rho_0 = \rho_0(z)$, $\boldsymbol{v} = \boldsymbol{v}_h$,

$$\frac{d}{dt} = \frac{\partial}{\partial t} + \boldsymbol{v} \cdot \nabla, \tag{18.19.4}$$

and T is related to Φ through hydrostatic equilibrium (11.72):

$$\frac{\partial \Phi}{\partial z} = \frac{RT}{H}. \tag{18.19.5}$$

In the budget of zonal momentum (18.19.1), it is convenient to express the Lagrangian acceleration in flux form. Multiplying by ρ_0 and incorporating (D.5) obtains

$$\rho_0 \frac{du}{dt} + \rho_0 w \frac{\partial u}{\partial z} = \rho_0 \frac{\partial u}{\partial t} + \nabla \cdot (\rho_0 \boldsymbol{v} u) + \frac{\partial}{\partial z}(\rho_0 w u) - u\left\{\nabla \cdot (\rho_0 \boldsymbol{v}) + \frac{\partial}{\partial z}(\rho_0 w)\right\}.$$

With continuity (18.19.2), this reduces to

$$\rho_0 \frac{du}{dt} + \rho_0 w \frac{\partial u}{\partial z} = \rho_0 \frac{\partial u}{\partial t} + \nabla \cdot (\rho_0 \boldsymbol{v} u) + \frac{\partial}{\partial z}(\rho_0 w u). \tag{18.20}$$

Expanding in terms of zonal-mean and perturbation quantities, as in Sec. 14.5.4, applying the zonal average $\overline{(\ )}$, and then incorporating the zonal-mean continuity equation

$$\nabla \cdot \overline{\boldsymbol{v}} + \frac{1}{\rho_0} \frac{\partial}{\partial z}(\rho_0 \overline{w}) = 0$$

obtains

$$\rho_0 \overline{\frac{du}{dt}} + \rho_0 \overline{w \frac{\partial u}{\partial z}} = \frac{\overline{d}}{dt}(\rho_0 \overline{u}) + \frac{\partial}{\partial y}(\rho_0 \overline{u'v'}) + \frac{\partial}{\partial z}(\rho_0 \overline{u'w'}), \tag{18.21.1}$$

where

$$\frac{\overline{d}}{dt} = \frac{\partial}{\partial t} + \overline{v} \frac{\partial}{\partial y} + \overline{w} \frac{\partial}{\partial z}. \tag{18.21.2}$$

For quasi-geostrophic motion on a beta plane (Sec. 12.5.3),

$$\overline{w} = 0 \tag{18.22.1}$$

and

$$\begin{aligned} \overline{v} &= \overline{\frac{\partial \psi}{\partial x}} \\ &= 0, \end{aligned} \tag{18.22.2}$$

as motion is cyclic in x. The zonal-mean Lagrangian acceleration then reduces to

$$\rho_0 \overline{\frac{du}{dt}} + \rho_0 \overline{w \frac{\partial u}{\partial z}} = \rho_0 \frac{\partial \overline{u}}{\partial t} + \frac{\partial}{\partial y}(\rho_0 \overline{u'v'}). \tag{18.23}$$

Applying the zonal average to (18.19) and incorporating (18.23) yield equations that govern the zonal-mean circulation:

$$\frac{\partial \overline{u}}{\partial t} - f\overline{v} = -\frac{\partial}{\partial y}(\overline{u'v'}) \tag{18.24.1}$$

$$f\overline{u} = -\frac{\partial \overline{\Phi}}{\partial y} \tag{18.24.2}$$

$$\frac{\partial \overline{v}}{\partial y} + \frac{1}{\rho_0} \frac{\partial}{\partial z}(\rho_0 \overline{w}) = 0 \tag{18.24.3}$$

$$\frac{d\overline{T}}{dt} + \frac{N^2 H}{R} \overline{w} = -\frac{\partial}{\partial y}\left(\overline{v'T'}\right) + \frac{\overline{q}}{c_p}. \tag{18.24.4}$$

The zonal-mean circulation is forced by the convergence of eddy momentum flux, which forces zonal-mean wind, and the convergence of eddy heat flux, which forces zonal-mean temperature. For planetary waves, those forcings cannot modify zonal wind and temperature independently. Their impacts are coupled through

geostrophic equilibrium (18.24.2) and hydrostatic equilibrium (18.19.5), which require the thermal wind balance

$$\frac{\partial \overline{u}}{\partial z} = \frac{R}{fH}\frac{\partial \overline{T}}{\partial y}. \tag{18.25}$$

A perturbation to the system (e.g., through convergence of wave momentum flux) must induce an ageostrophic circulation $(\overline{v}, \overline{w})$ that simultaneously modifies wind and temperature structure to restore thermal wind balance. The nature of the induced circulation is revealed by steady adiabatic conditions. The convergence of momentum flux in (18.24.1) must then be balanced by the Coriolis acceleration, which requires mean meridional motion $\overline{v}$. The convergence of eddy heat flux in (18.24.4) must be balanced by adiabatic cooling, which requires mean vertical motion $\overline{w}$. The two components of mean motion are coupled through continuity (18.24.3). These balances between eddy and zonal-mean terms are approximately satisfied even under unsteady conditions. Consequently, the induced mean circulation achieves a near cancellation with the eddy flux convergences of heat and momentum. The net circulation induced, the part that actually produces a tendency in (18.24), therefore follows as a small residual between those terms.

The *residual mean circulation* is defined as

$$\overline{v}^* = \overline{v} - \frac{R}{N^2 H}\frac{1}{\rho_0}\frac{\partial}{\partial z}\left(\rho_0 \overline{v'T'}\right) \tag{18.26.1}$$

$$\overline{w}^* = \overline{w} + \frac{R}{N^2 H}\frac{\partial}{\partial z}\left(\overline{v'T'}\right). \tag{18.26.2}$$

It represents that part of the induced meridional circulation that is not canceled by the convergence of eddy heat flux. Incorporating (18.26) reduces (18.24) to

$$\frac{\partial \overline{u}}{\partial t} - f\overline{v}^* = \frac{1}{\rho_0}\nabla \cdot \boldsymbol{F} \tag{18.27.1}$$

$$\frac{\partial \overline{v}^*}{\partial y} + \frac{1}{\rho_0}\frac{\partial}{\partial z}\left(\rho_0 \overline{w}^*\right) = 0 \tag{18.27.2}$$

$$\frac{d\overline{T}}{dt} + \frac{N^2 H}{R}\overline{w}^* = \frac{\overline{q}}{c_p}, \tag{18.27.3}$$

where

$$F_y = -\rho_0 \overline{u'v'} \tag{18.27.4}$$

$$F_z = \frac{fR}{N^2 H}\rho_0 \cdot \overline{v'T'}. \tag{18.27.5}$$

The vector $\boldsymbol{F}$ is recognized as the EP flux that was defined in Sec. 14.5.4. In this framework, eddy flux of heat enters only through the zonal momentum equation, where it translates into an upward flux of momentum.

The system (18.27) comprises the *Transformed Eulerian Mean* equations (Andrews and McIntyre, 1976). Unlike the system that governs the conventional Eulerian mean (18.24), it is forced exclusively in the momentum equation by the divergence of EP

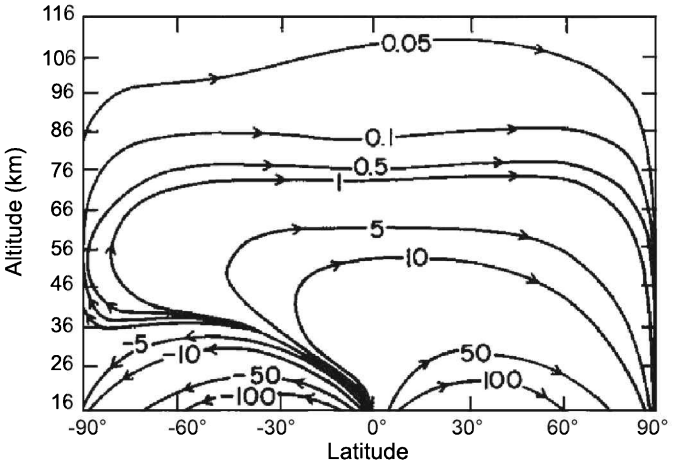

Figure 18.11 Streamlines of the residual mean circulation. Adapted from Garcia and Solomon (1983), copyright by the American Geophysical Union.

flux. As developed in Chap. 14, $\nabla \cdot \boldsymbol{F}$ describes the convergence of wave activity flux and (westward) momentum flux. It represents a westward drag that is exerted on the zonal-mean flow when planetary wave activity is absorbed.

These equations, supported by discussion in Sec. 14.5.4, show that residual mean motion is generated only if $\nabla \cdot \boldsymbol{F}$ is nonzero. This occurs if the waves are transient or if they experience dissipation, which results in the absorption of wave activity. As illustrated by (14.83) for potential vorticity, mean meridional transport of conserved properties then follows directly from $\nabla \cdot \boldsymbol{F}$.

Similar analysis applies to chemical species. If r is the mixing ratio of a long-lived species, then its zonal mean is governed by the continuity equation

$$\frac{\partial \overline{r}}{\partial t} + \overline{v}^* \frac{\partial \overline{r}}{\partial y} + \overline{w}^* \frac{\partial \overline{r}}{\partial z} = 0. \tag{18.28}$$

In concert with (18.27), planetary waves are seen to influence the distribution of $\overline{r}$ only if $\nabla \cdot \boldsymbol{F}$ is nonzero.[4]

Plotted in Fig. 18.11 is the residual mean circulation, calculated under conditions of northern winter. In the lower stratosphere are two equator-to-pole cells. They transport ozone-rich air from the photochemical source region in the tropics to extratropical regions. Meridional transport, accompanied by downwelling, explains the large total ozone observed at high latitude (Figs. 1.21; 18.2). Strong when planetary waves are amplified, that transport also explains the pronounced seasonality of total ozone. Maximum values of Σ_{O_3} appear during late winter and spring, just after the period of amplified planetary wave activity. Contemporaneous with downwelling, this is also when ozone increases in the troposphere (London, 1985).

In the mesosphere, the residual mean circulation is transformed into a pole-to-pole cell. At those heights, air passes from the radiatively-heated summer

[4] If the species undergoes chemical production and destruction, a chemical source term appears on the right-hand side of (18.28). It involves zonal-mean production and destruction, as well as interaction between eddy motion and chemistry (Andrews et al, 1987).

hemisphere to the radiatively-cooled winter hemisphere. Despite the distribution of net heating (Fig. 8.27), the summer mesosphere is actually colder than the winter hemisphere (Fig. 1.7). Like the winter stratosphere, the mesosphere is driven out of radiative equilibrium by mechanical disturbances that propagate up from below. Planetary waves play a role at these altitudes. However, gravity waves play an even greater role in disturbing the mesosphere. Their influence is reflected in the departure from radiative equilibrium. Unlike the stratosphere, which is disturbed chiefly in the winter hemisphere, both hemispheres of the mesosphere are disturbed from radiative equilibrium. This feature is consistent with the bi-directional propagation of gravity waves. Westward-propagating gravity waves can propagate through westerlies of the winter stratosphere without encountering a critical level (Sec. 14.3.4). Eastward-propagating gravity waves can do the same through easterlies of the summer stratosphere – unlike planetary waves. Upon reaching mesospheric heights, gravity waves excited in the troposphere have amplified sufficiently to break (Fig. 14.25). Momentum absorbed from the waves then exerts a drag on the zonal-mean flow. To maintain thermal wind balance, that drag induces a meridional circulation, which in turn drives thermal structure out of radiative equilibrium.

18.4 SUDDEN STRATOSPHERIC WARMINGS

During northern winter, the circulation often becomes highly disturbed. Accompanying an amplification of planetary waves, the disturbed motion is characterized by an abrupt deceleration of zonal-mean westerlies, even by their reversal into zonal-mean easterlies. Simultaneously, temperature over the polar cap increases sharply – by as much as 50 K. The winter pole, in darkness, then becomes warmer than the sunlit tropics. This dramatic sequence of events takes place in just a couple of days. It comprises a *sudden stratospheric warming.*

A stratospheric warming is underway on the day shown in Fig. 1.10a. Zonal-mean wind on the same day (Fig. 18.12b) has reversed across much of the winter stratosphere, from 30 hPa upward. Zonal-mean temperature (Fig. 18.12a) is anomalously warm from 70 hPa upward. Polar temperature is some 40 K warmer than climatological-mean temperature (Fig. 1.7). It is warmer even than temperature over the equator. The meridional temperature gradient is therefore reversed. These dramatic changes in the zonal-mean circulation result from an amplification of planetary waves. Enhanced absorption of wave activity ($\nabla \cdot \boldsymbol{F}$) intensifies the drag exerted on the mean flow, along with the residual mean circulation driven by it (18.27).

Although defined in term of zonal-mean properties, the stratospheric warming is a phenomenon that is inherently zonally asymmetric. Figure 1.10a reveals that zonal-mean deceleration on this day actually follows from a displacement of the cyclonic low out of the polar cap. It has been replaced by an anticyclonic high, which has invaded the polar cap from mid-latitudes. The zonally-asymmetric flow that results corresponds to an amplification of planetary wavenumber 1. It rapidly exchanges air between tropical and extratropical latitudes. Rather than operating on the long time scale of the residual mean circulation, this exchange operates on the time scale of only a day. Figure 18.13 shows contemporaneous distributions of motion and potential vorticity near 10 hPa. The cyclonic vortex has been displaced well off the pole and has suffered a complex distortion. High-latitude air (blue) is being drawn equatorward around the anticyclone that has invaded the polar cap. Notice that large eddy displacements have

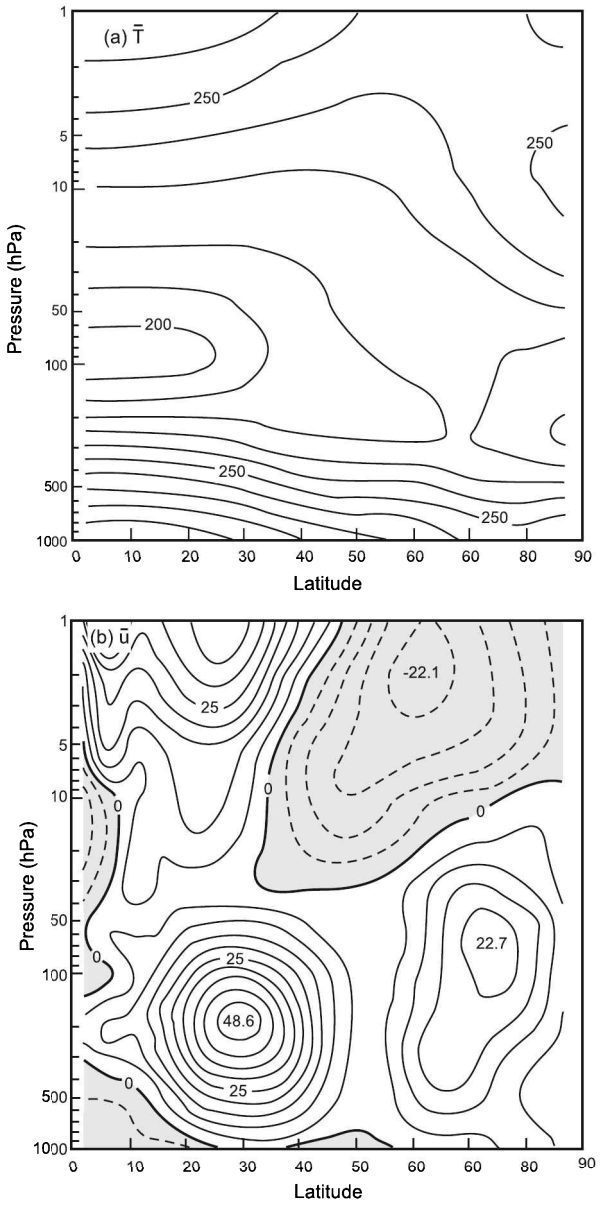

Figure 18.12 Zonal-mean temperature (a) and zonal wind (b) on March 4, 1984, during a stratospheric sudden warming (cf. Fig. 1.10a).

overturned the potential vorticity distribution near (135W,45N), reversing $\frac{\partial Q}{\partial y}$. Motion there is dynamically unstable (Sec. 16.2). The planetary wave field then breaks, forming secondary eddies that appear downstream (McIntyre and Palmer, 1983).

Secondary eddies in the region of instability lead to an irreversible rearrangement of air. Mid-latitude air (red) drawn poleward spins up anticyclonically to conserve potential vorticity. It thus forms easterly flow over the polar cap that prevails

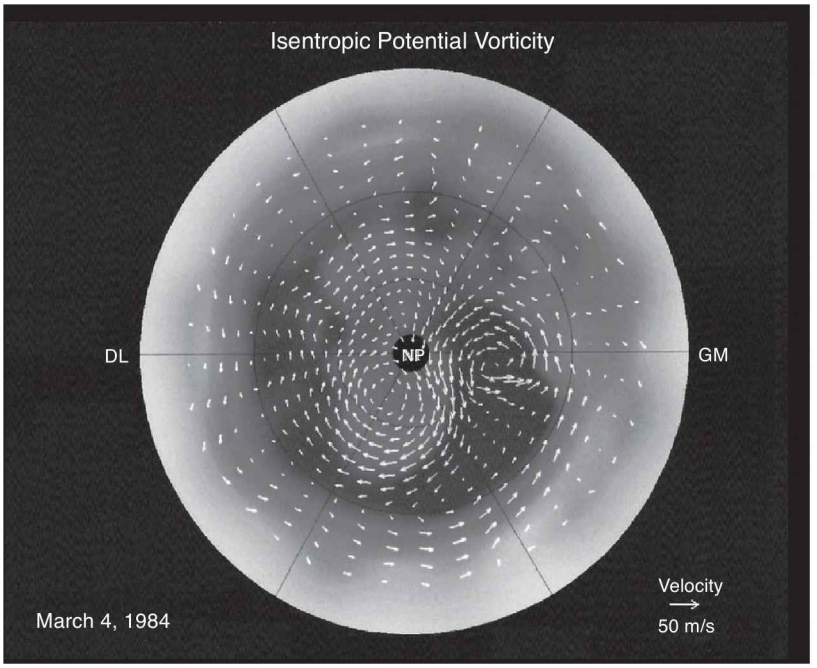

Figure 18.13 Distributions of potential vorticity Q and horizontal motion on the 850°K isentropic surface (near 10 hPa) for March 4, 1984. High-Q polar air (blue), which marks the polar-night vortex, has been displaced off the pole and distorted by a large amplitude planetary wave, with secondary eddies appearing along its tail. Low-Q air from equatorward (red) that is advected into the polar cap spins up anticyclonically, forming a reversed circulation with easterly circumpolar flow at high latitude (cf. 14.26). See color plate section: Plate 30.

in the zonal mean (Fig. 18.12). At the same time, polar air drawn equatorward degenerates into small anomalies of cyclonic vorticity; they are only suggested in the analyzed distribution of Q.[5] The foregoing behavior resembles an expanded critical layer, one that engulfs the winter stratosphere when the wave field amplifies and overturns the Q distribution (cf. Figs. 14.23; 14.26).

Motion during a stratospheric warming leads to a major rearrangement of air and chemical species. Ozone then flows freely from its chemical source region at low latitude to middle and high latitudes. Air advected poleward moves approximately along isentropic surfaces. In the lower stratosphere, where the ozone column is concentrated, isentropic surfaces slope downward toward the pole. Poleward-moving air then descends, undergoing compression. Through secondary eddies, it simultaneously experiences irreversible mixing. On a longer time scale, air displaced to high latitude also experiences radiative cooling, which produces downwelling across isentropic surfaces. These mechanisms are the same ones involved in residual mean motion. By

[5] The Q distribution must be derived from meteorological analyses, which, because they are based largely on temperature observations, have limited ability to resolve such features.

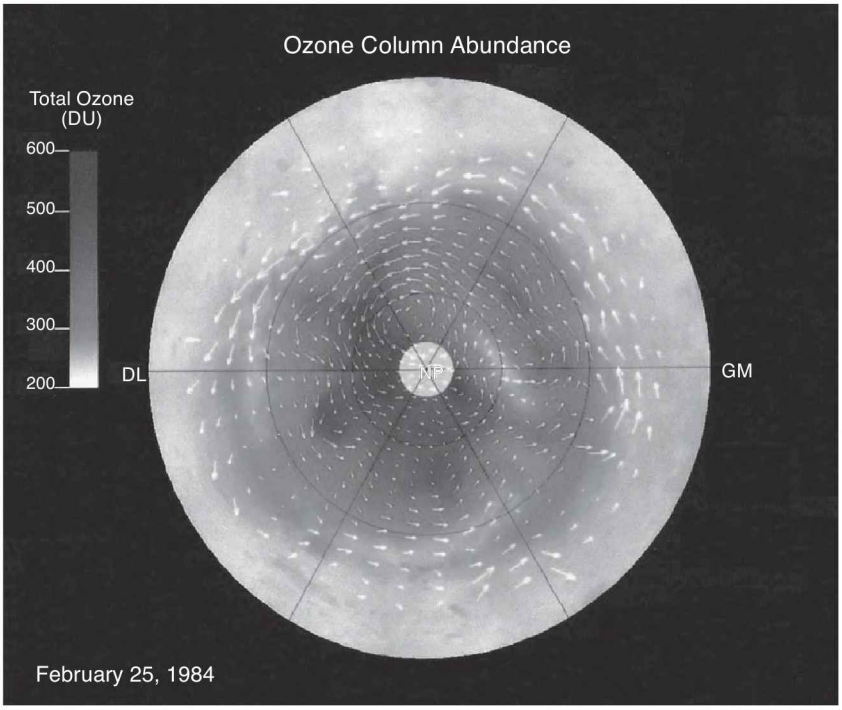

Figure 18.14 Total ozone Σ_{O_3} and horizontal motion on the 400°K isentropic surface in the Northern Hemisphere on February 25, 1984, during a stratospheric warming when zonal flow was disturbed down to 70 hPa. A tongue of enhanced Σ_{O_3} coincides with cross-polar flow between longitudes of 150 E and 30 W, where air descends along isentropic surfaces and undergoes compression. Air displaced equatorward in the Eastern Hemisphere ascends isentropically and undergoes expansion, introducing anomalously low Σ_{O_3}. See color plate section: Plate 31.

amplifying meridional displacements, a stratospheric warming therefore accelerates the residual mean circulation.

Stratospheric warmings are accompanied by a sharp increase of total ozone at high latitude. Plotted in Fig. 18.14 are distributions of Σ_{O_3} and 400 K isentropic motion on February 25, 1984, when zonal-mean motion was reversed down to 70 hPa. A tongue of enhanced total ozone ($\Sigma_{O_3} > 500$ DU) coincides with cross-polar flow. There, ozone-rich air from lower latitude descends along isentropic surfaces. It undergoes compression, increasing ρ_{O_3} and Σ_{O_3} (at the expense of ozone in the surroundings). In the Eastern Hemisphere, air is displaced equatorward. It experiences the reverse effect, leading to reduced Σ_{O_3}.

Stratospheric warmings occur primarily in the Northern Hemisphere, where planetary waves are strong. However, behavior like that described above closes the winter season of both hemispheres. Spring witnesses a weakening of the equatorward temperature gradient that supports strong zonal motion. Circumpolar westerlies then collapse in the *final warming*, replaced during summer by circumpolar easterlies.

18.5 THE QUASI-BIENNIAL OSCILLATION

The circulation in the tropics is also chiefly zonal. However, it is modified importantly by interannual variations. Figure 18.15 presents zonal wind averaged over equatorial stations, as a function of time and height. Prevalent at heights of 15–30 km is a cyclic variation of 24–36 months. Known as the *quasi-biennial oscillation* (QBO), this variation descends with time in an alternating series of easterlies and westerlies. They attain speeds of 20–30 m s^{-1}. At higher levels, the QBO gives way to the *semi-annual oscillation*, the second harmonic of the seasonal cycle. The QBO is symmetric about the equator, concentrated at latitudes of less than 15°.

Although nearly periodic, the QBO is not a harmonic of the seasonal cycle. It therefore cannot be explained merely as seasonality that is imparted to the equatorial stratosphere from other regions. Latent heating in the troposphere contains no preferred period on time scales of the QBO. Likewise, diabatic heating in the equatorial stratosphere is unable to explain the oscillation (Wallace, 1967). This leaves momentum transfer. During the westerly phase of the QBO, air over the equator moves faster than the Earth. Its specific angular momentum therefore exceeds that available from other latitudes. This feature rules out horizontal advection, which conserves angular momentum (11.29).

The QBO is thought to be driven mechanically by upward-propagating waves that transmit momentum from the troposphere. The particular waves involved remain under discussion. However, there is no debate over their origin. Unsteady latent heating inside tropical convection excites a spectrum of wave activity. Much of it propagates upward into the middle atmosphere. Upon being absorbed, that wave activity transfers momentum to the zonal-mean flow, which is thereby accelerated toward the phase speeds of individual waves.

As illustrated in Fig. 18.16, eastward- and westward-propagating waves have transmission and absorption characteristics that differ between easterly and westerly layers of the QBO. These characteristics are determined by the intrinsic frequencies of the waves, which in turn depend on zonal-mean wind (Sec. 14.6). The differences enable wave absorption to establish a westerly critical line. There, mean wind matches the phase speed of westerly waves, which are therefore absorbed. Flanking it overhead is an easterly critical line, where mean wind matches the phase speed of easterly waves that are likewise absorbed. Transfers of westerly and easterly momentum at those sites of wave absorption cause both critical lines to descend, as is observed in Fig. 18.15 (Lindzen and Holton, 1968; Holton and Lindzen, 1972).

The tropical QBO has an extratropical counterpart. During years when equatorial wind is easterly, the polar-night vortex is warmer, weaker, and more disturbed than during years when equatorial wind is westerly (Labitzke, 1982; Holton and Tan, 1980). Similar interannual variability is manifest by total ozone. A signature of the QBO appears in Σ_{O_3} at mid-latitudes, forced by the residual mean circulation of the QBO (Hasebe, 1983; Lait et al., 1989; Tung and Yang, 1994). The Antarctic ozone hole also varies with equatorial wind (Garcia and Solomon, 1987), although more so with planetary wave forcing of the residual mean circulation (Sec. 18.8).

The extratropical QBO results from a displacement of the critical line for planetary waves (e.g., the zero-wind line), to which the polar-night vortex is sensitive. The easterly phase of the QBO displaces the critical line into the winter hemisphere (green in Plates 32 and 34). In a neighborhood of the critical line, large eddy displacements

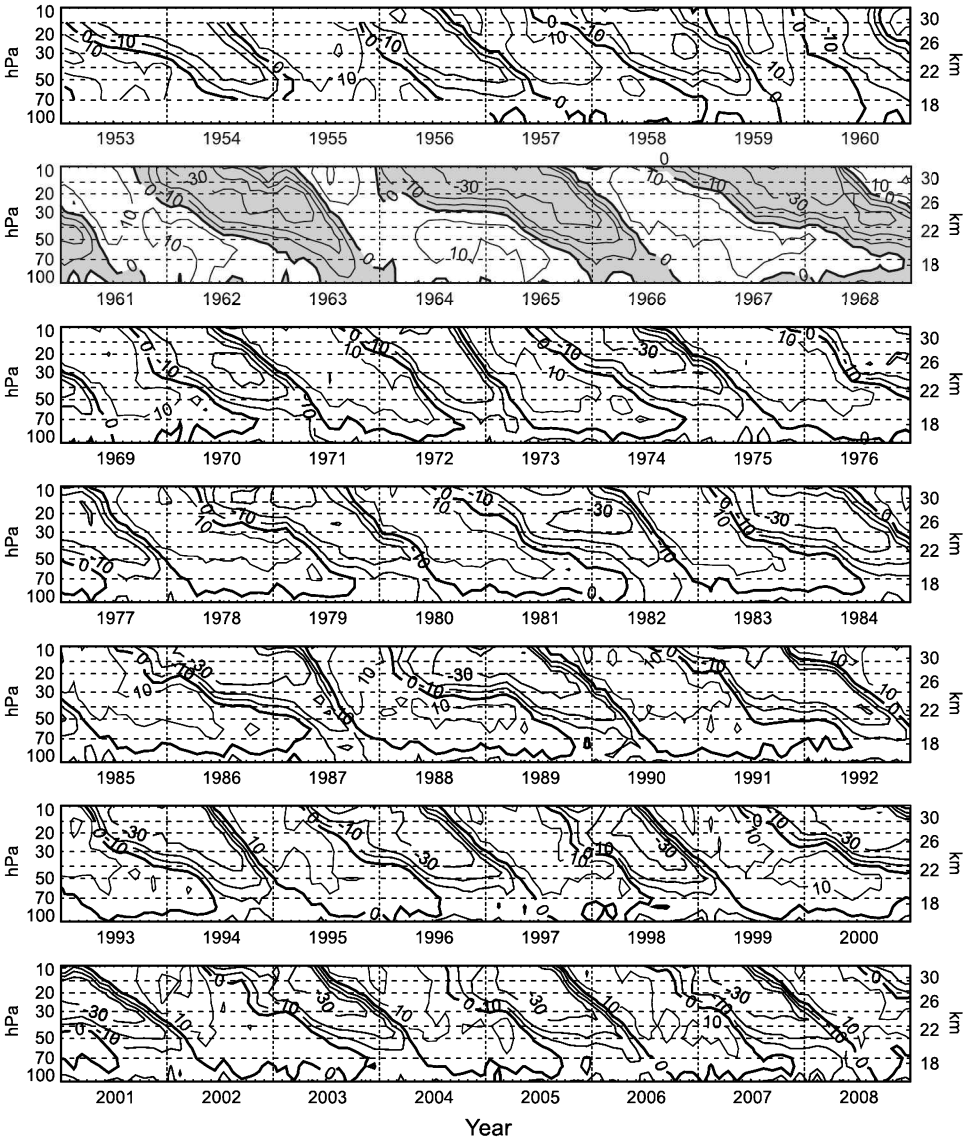

Figure 18.15 Monthly mean zonal wind (m s^{-1}) averaged over equatorial rawinsonde stations. Updated from Naujokat (1986). *Source:* http://www.geo.fu-berlin.de/en/met/ (10.07.10).

disturb the polar-night vortex, intensifying mean downwelling and adiabatic warming over the pole (Fig. 18.17a). Conversely, the westerly phase of the QBO removes the critical line into the summer hemisphere. This leaves the polar-night vortex comparatively undisturbed (Fig. 18.17b).

Because it occupies the lower stratosphere, the QBO influences the tropical tropopause, along with neighboring properties. Anomalous temperature can, by modifying stability, alter tropopause height and temperature. The latter, in turn, influence

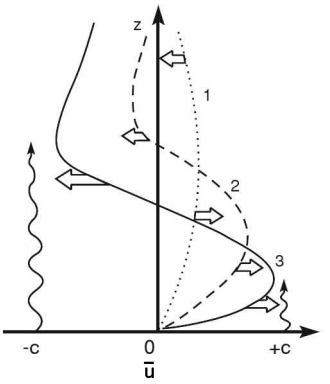

Figure 18.16 Schematic illustrating the differential transmission and absorption characteristics of vertically propagating eastward- and westward-traveling waves with phase speed c. Absorption of momentum from the eastward-traveling wave accelerates the zonal-mean flow toward the phase speed of that wave. Westerlies then form a critical level, where eastward-traveling wave activity is fully absorbed. The westward-traveling wave propagates through those westerlies without encountering a critical level, but it experiences absorption at higher levels in easterly shear. Absorption of its momentum accelerates the zonal-mean flow there toward the phase speed of the westward-traveling wave, producing a critical level where that wave is fully absorbed. Continued absorption of eastward and westward momentum at the critical levels of the two waves then causes the layers of easterlies and westerlies to descend. Adapted from Plumb (1982).

the height of overshooting cumulus (Collimore et al., 2003). Similarly, anomalous zonal wind can modify the steering level of tropical storms. The QBO's influence has been reported in relation to hurricanes (Shapiro, 1989).

18.6 DIRECT INTERACTION WITH THE TROPOSPHERE

The stratosphere is driven by the troposphere, indirectly by upward-propagating waves that transmit momentum. Vertical motion in the residual mean circulation also enables the stratosphere to interact directly with the troposphere. Chemical tracers like N_2O and CH_4 imply that tropospheric air enters the stratosphere across the tropical tropopause. By continuity, air must be returned to the troposphere at middle and high latitudes. The transfer of stratospheric air into the extratropical troposphere is explicit in the residual mean circulation (Fig. 18.11). Estimates of mass transfer suggest a residence time in the middle atmosphere of about 3 years (Holton, 1990). Exchanges of air between the troposphere and stratosphere are complex and poorly documented. However, tracer observations like those in Figs. 18.4 and 18.7 point to the involvement of tropical convection and mid-latitude weather systems.

Water vapor mixing ratio reaches a minimum at the hygropause, reflecting moisture in tropospheric air being limited to saturation values (Fig. 18.8). In the tropics, the hygropause is found as high as 18 km – a couple of kilometers above the mean elevation

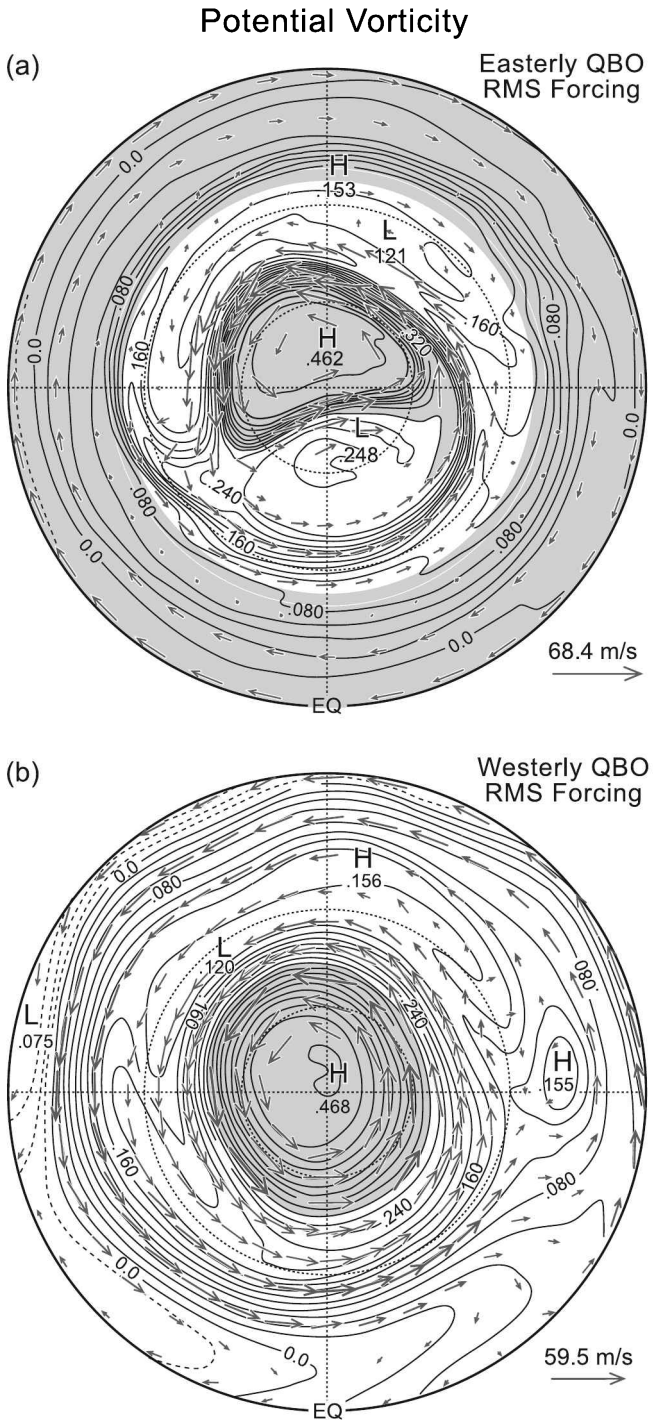

Figure 18.17 Distributions of potential vorticity and motion in a 2-dimensional calculation representative of the polar-night vortex (a) during the QBO easterlies (red), when the zero-wind line (green), which is the critical line for stationary planetary waves, invades the winter subtropics, and (b) during the QBO westerlies, when the critical line for stationary planetary waves recedes into the summer subtropics. Adapted from O'Sullivan and Salby (1990). See color plate section: Plate 32.

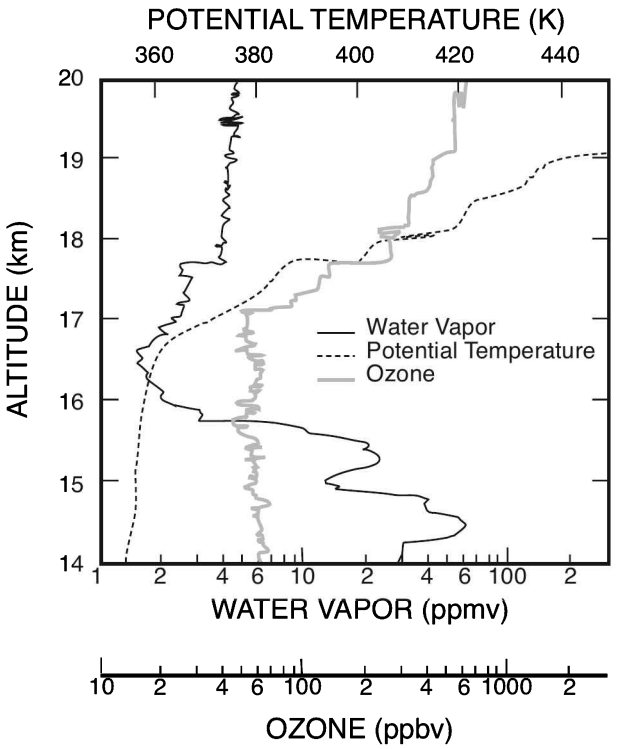

Figure 18.18 Vertical profiles of water vapor and ozone mixing ratio and potential temperature over Darwin Australia on January 13, 1987. *Source:* Kelly et al. (1993).

of the tropopause. Figure 18.18 plots the profile of water vapor mixing ratio over Darwin Australia, along with the mixing ratio of ozone and potential temperature. Well-mixed air below 18 km is marked by nearly uniform r_{O_3} and slowly increasing θ, the latter reflecting neutral stability under saturated conditions. Having been processed by deep convection, that air is characterized by r_{H_2O} that decreases exponentially to a broad minimum between 16 and 18 km. The minimum in water vapor mixing ratio extends about a kilometer above the local tropopause. Achieving values smaller than 2 ppmv, it is significantly drier than saturation values corresponding to the mean temperature of the tropical tropopause. These features indicate that tropospheric air enters the stratosphere in the tropics through overshooting cumulus, with temperatures of 190 K and colder. As discussed in Secs. 7.7 and 9.3, overshooting cumulus lead to mixing of tropospheric and stratospheric air. This process maintains the tropopause against radiative drive, which acts to extend the stratosphere downward. By mixing θ_e, it temporarily elevates the tropopause, extending neutral stability and positive lapse rate upward (Fig. 7.8).

Vertical mixing that occurs when cumulus updrafts invade stable air overhead can lead to upwelling across the tropical tropopause. A cumulus updraft that overshoots its Level of Neutral Buoyancy eventually collapses into cirrostratus anvil

(Fig. 7.7), cloud that is most extensive near the LNB (Fig. 9.25). There, tropospheric and stratospheric air are mixed.[6] Mixing of low-θ air from the overshooting updraft into high-θ air in its surroundings reduces the potential temperature of the environment. According to (2.36), this process serves as a mechanical heat sink for the environment at levels above the LNB. There, cumulus detrainment drives environmental air to temperatures colder than radiative equilibrium. By decreasing θ, it forces downwelling at sites of overshooting cumulus. Apparent in Fig. 9.26a, environmental downwelling extends some distance above the LNB (Gage et al., 1991; Salby et al., 2004a). After leaving those sites, environmental air that has been cooled through cumulus detrainment experiences radiative heating, which acts to restore it to radiative equilibrium. By increasing θ, radiative heating then produces upwelling across isentropic surfaces in the tropical stratosphere. Tropical upwelling must operate in unison with downwelling at extratropical latitudes. Forced by the absorption of planetary wave activity (Sec. 18.3), downwelling pumps stratospheric air into the extratropical troposphere. The latter must be compensated in the tropics by air being returned to the stratosphere at the same rate.

For this process to explain the observed distribution of water vapor, air introduced into the tropical stratosphere must be relatively free of water in condensed phase. Otherwise, that condensate would sublimate, increasing r_{H_2O} over the very lean values observed (Holton, 1984). Cumulonimbus anvil, in which tropospheric and stratospheric air have been mixed, is supplied with condensate by detrainment from cumulus updrafts. However, anvil is destabilized by radiative transfer: LW heating at its base and LW cooling at its top drive vertical overturning (Sec. 9.4). By encouraging particle growth, vertical motion enables condensate to precipitate out (Danielsen, 1982). In fact, airborne observations reveal a sink of total water at levels of cumulonimbus anvil (Kelly et al., 1993). This feature is consistent with the negative anomaly of mixing ratio found above the LNB, where anvil is most extensive (Fig. 9.26b). Appearing just above a layer of nearly saturated environmental conditions, it reflects efficient removal of ice particles that have grown large enough to precipitate to lower levels. This process acts to dehydrate air that has been mixed with stratospheric air and detrained into cumulonimbus anvil.

Stratospheric air enters the troposphere at high latitude. Vertical mixing is believed to be involved in this transfer as well, but on the larger scale of synoptic weather systems. The importance of those systems is underscored by the concentration of ozone column abundance between 10 and 20 km, where synoptic weather systems still influence motion (Figs. 1.20; 18.2). The daily distribution of total ozone (Fig. 1.22a) is, in fact, punctuated by anomalies of high Σ_{O_3}. Comparison with contemporaneous horizontal motion in Fig. 1.9a reveals that those anomalies are positively correlated with mid-latitude cyclones. The pressure on the 375 K isentropic surface (contoured in Fig. 1.22; Plate 1) indicates that, over mid-latitude cyclones, θ surfaces in the lower stratosphere are deflected downward to greater pressure. Ozone-rich air moving along isentropic surfaces must therefore experience compression. This magnifies Σ_{O_3} locally – by as much as 100% (Salby and Callaghan, 1993). Analogous behavior occurs on planetary dimensions during a stratospheric warming, when air is advected poleward along isentropic surfaces (Fig. 18.14; Plate 31).

[6] An updraft advances only with the entrainment of environmental air (Fig. 9.16), which, for an overshooting cumulus, is stratospheric.

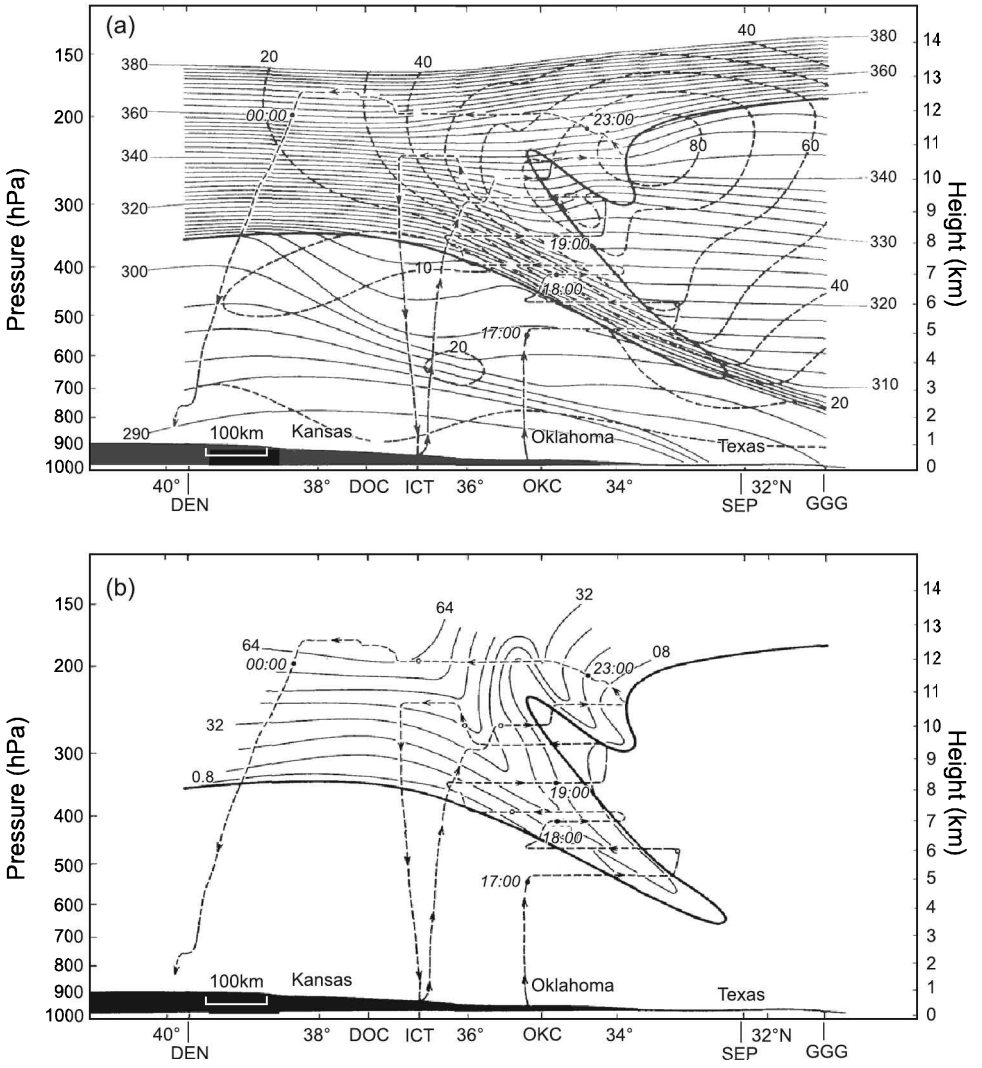

Figure 18.19 Vertical cross section through a tropopause fold. (a) Distributions of θ (solid) and wind speed (dashed). The jet is flanked by a baroclinic frontal zone in which isentropic surfaces descend into the troposphere from stratospheric levels. (b) Distribution of ozone mixing ratio. Tracer values advected isentropically decrease along the tropospheric intrusion, reflecting small-scale mixing and dilution of stratospheric ozone. Vertical arrows mark the flight path of airborne measurements from which the analyzed fields were inferred. After Shapiro (1982).

In meteorological analyses, isentropic surfaces undergo vertical deflections of a couple of kilometers. Airborne measurements, however, record stratospheric species as low as 700 hPa. Stratospheric air enters the troposphere inside *tropopause folds*, where isopleths of long-lived species are overturned (see Fig. 18.19). There, stratospheric air is drawn downward along the frontal zone that intensifies during the

development of a baroclinic system. The impact of such transport is manifest in zonal-mean ozone mixing ratio (Fig. 1.20). $\overline{r}_{O_3}$ is deflected downward at high latitude. Such structure enhances ozone number density along the poleward flank of the subtropical jet – where baroclinic systems develop (Chap. 15).

Figure 18.19 plots a cross section of a tropopause fold. Isentropic surfaces (Fig. 18.19a) reflect stratospheric air in strong vertical stability (large $\frac{\partial \theta}{\partial z}$). They have been drawn downward, concentrated in a tilting frontal zone that divides cold and warm air. Strongly baroclinic, that region develops from deformation during the amplification of a baroclinic disturbance (Hoskins, 1982). Mirroring this structure is the distribution of ozone mixing ratio (Fig. 18.19b). Long lived at these altitudes (Fig. 18.1), r_{O_3} marks stratospheric air that has been drawn into the frontal zone. Anomalous mixing ratio is diluted by small-scale mixing, which reduces r_{O_3} along the intrusion. Once it enters the troposphere, O_3 is quickly transferred by convection to the Earth's surface, where it is destroyed through oxidation processes.

18.7 HETEROGENEOUS CHEMICAL REACTIONS

The chemical reactions considered in Secs. 18.1 and 18.2 involve species only in gas phase. During the 1970s and 1980s, these and other elements of gas-phase photochemistry were the focus of intensive investigation. Although an impact of anthropogenic species was suggested, it was not expected to emerge clearly before the twenty-first century. Even then, it was expected to reduce the column abundance of ozone by only about 5%. The timing and magnitude of anticipated changes were set by two considerations: (1) Reactive species had to increase to relatively high concentrations before catalytic destruction of ozone via (18.10) and (18.13) became sufficiently fast. (2) Those reactions were favored at higher altitudes, where only a small fraction of the ozone column resides.

For these reasons, the discovery of the Antarctic ozone hole in 1985 caught much of the scientific community by surprise. Moreover, the order-of-magnitude greater depletions observed were found at polar latitudes (Fig. 1.22b), where ozone was thought to be photochemically inert – because UV fluxes there are small. The key ingredient not considered previously was the presence of solid phase, which is normally excluded from the stratosphere by very low mixing ratios of water vapor.

Polar stratospheric cloud (Sec. 9.3) was already recognized to form over the Antarctic because of its very cold temperature. However, it was regarded largely as a curiosity. PSC appears far more frequently in the Antarctic stratosphere than in the warmer Arctic stratosphere (Fig. 18.20). During late Austral winter, when temperature is coldest, fractional coverage over the Antarctic exceeds 50%, chiefly by very tenuous cloud in the PSC I category. It is now widely accepted that PSC provides the surfaces on which certain reactions proceed much faster than they can in gas phase alone. Moreover, the presence of PSC shifts catalytic destruction of ozone from the upper stratosphere, where only a small fraction of the ozone column resides, to the lower stratosphere, where Σ_{O_3} is concentrated.

Figure 18.21 shows profiles of ozone concentration over Antarctica during Austral winter (solid) and shortly after equinox (dashed), when the sun rises above the horizon. A marked reduction of ozone has occurred between 10 and 20 km. Those are the levels where the ozone column is normally concentrated. Decreases in Σ_{O_3} of 50% are

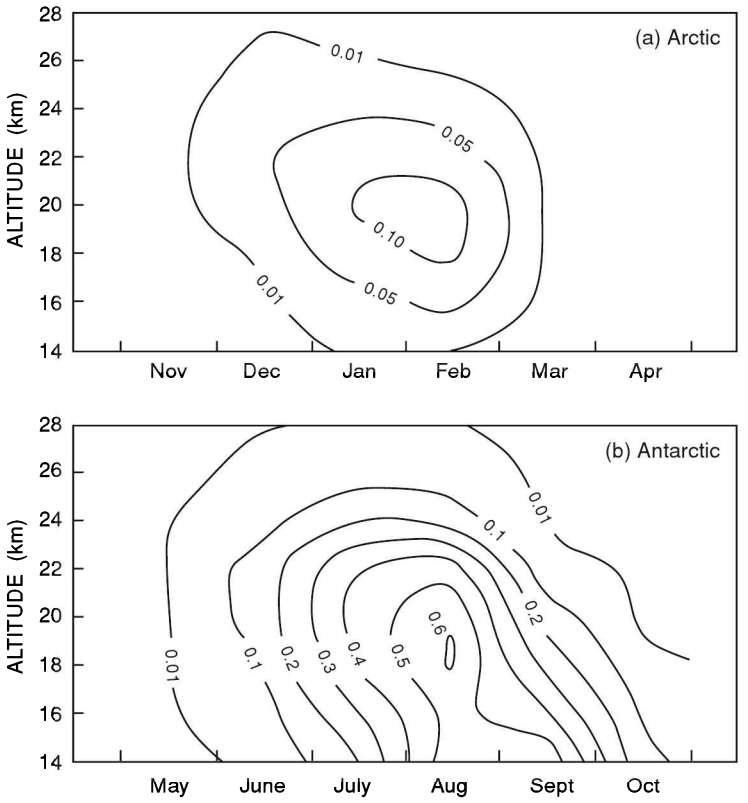

Figure 18.20 Relative frequency of polar stratospheric cloud sightings in satellite observations from SAM II, as a function of height and month, over (a) the Arctic and (b) the Antarctic. After WMO (1991).

observed at this time of year, with column abundances as low as 100 DU having been recorded. Superposed in Fig. 18.21 is the profile of ClO (stippled), which is produced by destruction of ozone (18.13). Consistent with the observed ozone depletion, r_{ClO} maximizes between 10 and 25 km. Those are the same levels where PSC is sighted (Fig. 18.20). A correspondence between reduced O_3 and increased ClO is also apparent across the edge of the polar-night vortex, which delineates the ozone hole (Fig. 18.22). Ozone decreases sharply where chlorine monoxide increases sharply. Both transitions are found where temperature becomes colder than 196 K, the threshold temperature for the formation of type I PSC.

The reactions now recognized to be primarily responsible for the ozone loss in Figs. 1.22b, 18.21, and 18.22 involve two stages: First, inactive chlorine species such as HCl and $ClONO_2$ are converted to reactive forms of Cl_x through heterogeneous reactions like

$$HCl(s) + ClONO_2(g) \rightarrow Cl_2(g) + HNO_3(s) \qquad (18.29.1)$$

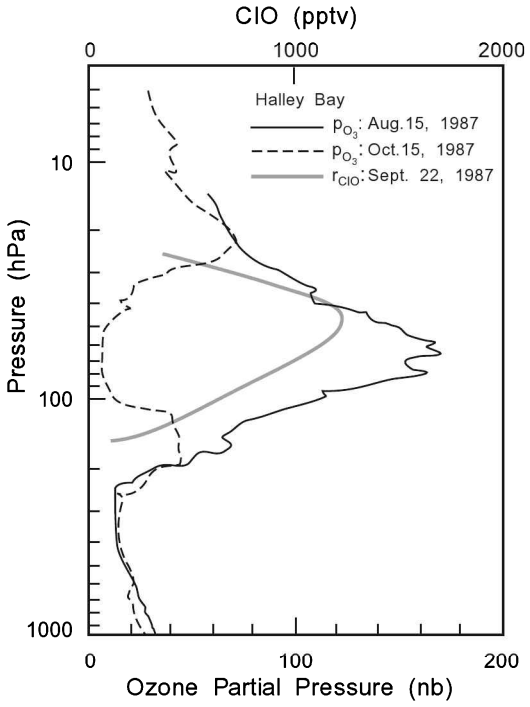

Figure 18.21 Profiles of ozone partial pressure over Antarctica during Austral winter (solid) and shortly after spring equinox (dashed). Profile of chlorine monoxide mixing ratio (stippled) after equinox is superposed. *Sources:* WMO (1988), Solomon (1990).

and

$$H_2O(s) + ClONO_2(g) \rightarrow HNO_3(s) + HOCl(g) \qquad (18.29.2)$$

that involve solid (s) as well as gas (g) phases. These reactions proceed rapidly on ice, but slowly in gas phase alone. Once produced, Cl_2 and HOCl are readily photolyzed by sunlight, releasing free chlorine

$$Cl_2 + h\nu \rightarrow 2Cl \qquad (18.29.3)$$

$$HOCl + h\nu \rightarrow OH + Cl, \qquad (18.29.4)$$

which is a reactive form of Cl_x. Then the sequence of reactions

$$Cl + O_3 \rightarrow ClO + O_2 \qquad (18.30.1)$$

$$2ClO + M \rightarrow Cl_2O_2 + M \qquad (18.30.2)$$

$$Cl_2O_2 + h\nu \rightarrow Cl + ClO_2 \qquad (18.30.3)$$

$$ClO_2 + M \rightarrow Cl + O_2 + M \qquad (18.30.4)$$

destroys ozone catalytically. It has the net effect

$$2O_3 + h\nu \rightarrow 3O_2 \text{ (Net)}. \qquad (18.30.5)$$

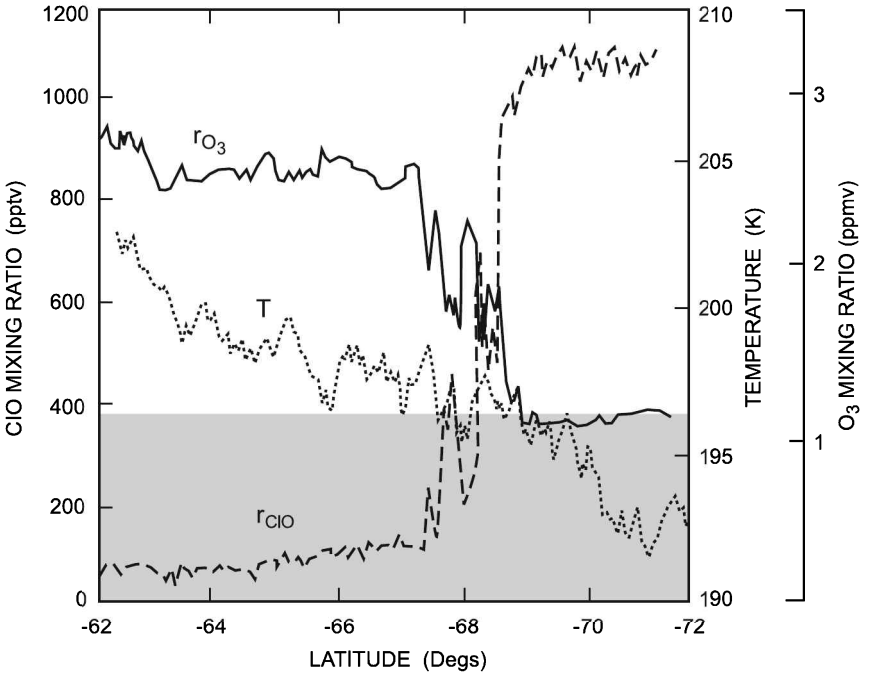

Figure 18.22 Ozone, chlorine monoxide, and temperature along a flight path into the Antarctic polar-night vortex. Temperatures colder than about 196°K (shaded) coincide with the formation of type I PSC. Source of O_3 and ClO profiles: Anderson et al. (1989).

A similar influence on ozone is exerted by bromine. Although less abundant, reactive bromine is some 50 times more effective at destroying ozone than reactive chlorine (WMO, 2006). With established reaction rates, observed mixing ratios of $r_{ClO} \cong 1$ ppbv are adequate to explain the observed ozone depletion rate of about 2% per day. The observed concentration of ClO is two orders of magnitude greater than that predicted by gas-phase photochemistry alone. However, it is consistent with calculations that include heterogeneous reactions like (18.30).[7]

The catalytic sequence (18.30) is initiated by free chlorine, which originates largely from photolysis of CFCs (18.12). Produced exclusively by industry, CFCs have led to steadily-increasing levels of atmospheric chlorine (Fig. 18.23). Above a natural background level of about 0.6 ppbv associated with ocean processes (Sec. 18.2.2), atmospheric chlorine has increased five fold since the 1950s – shortly after the introduction of CFCs in industrial applications. Tending in the opposite sense is the signature of ozone depletion over Antarctica. It accelerates after 1980, presumably when chlorine levels exceeded a threshold for reactions (18.30) to become an important sink of O_3 (Solomon, 1990).

[7] Those calculations rest on the photolysis rate of Cl_2O_2 (18.30.3), which has come into question (Pope et al., 2007; Schiermeier, 2007).

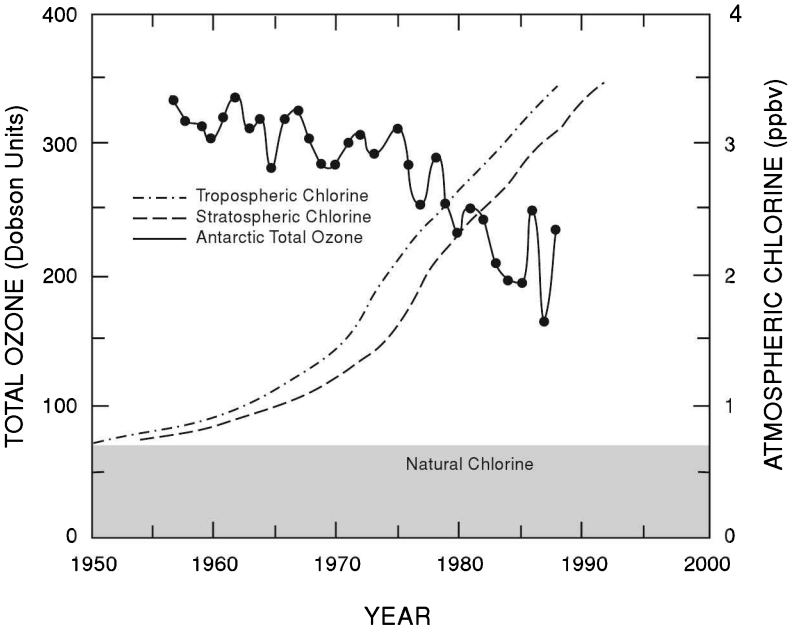

Figure 18.23 Time series of atmospheric total chlorine and total ozone over Halley Bay, Antarctica. Adapted from Solomon (1990).

While converting inert forms of chlorine into reactive Cl_x, heterogeneous reactions (18.29) have the opposite effect on reactive nitrogen. They convert NO_x into relatively inactive nitric acid. This bears importantly on ozone depletion because NO_x regulates the abundance of reactive chlorine. The principal means by which Cl_x is converted back to inactive forms is via reaction with nitrogen dioxide

$$ClO + NO_2 + M \rightarrow ClONO_2 + M. \qquad (18.31)$$

The abundance of NO_2 thus controls the duration over which reactive chlorine is available to destroy ozone in (18.30). Because PSC is composed of hydrated forms of nitric acid (Sec. 9.3), its formation removes NO_x from the gas phase. Should PSC particles become large enough to undergo sedimentation, NO_x is removed altogether. The stratosphere is then denitrified, leaving reactive chlorine available much longer to destroy ozone.

Figure 18.24 compares the seasonal cycle of Σ_{O_3} over Antarctica based on the historical record against that based on years after the appearance of the ozone hole (cf. Fig. 1.21). The two evolutions diverge near Austral spring. Solar radiation then triggers reactions (18.29.3) and (18.29.4) that release reactive chlorine, setting the stage for catalytic destruction of ozone in (18.30). Minimum column abundance is observed in October. By December, increasing values restore Σ_{O_3} toward historical levels, when ozone-rich air is imported from low latitudes during the final warming. But, even then, total ozone remains ~5% below historical levels, due to the dilution of

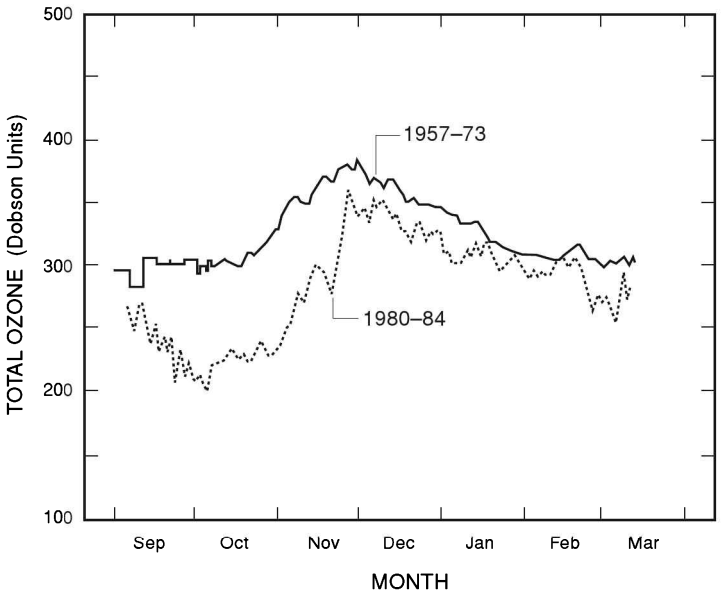

Figure 18.24 Seasonal cycle of total ozone over Halley Bay, Antarctica, based on the historical record since 1957 and on years since the appearance of the Antarctic ozone hole. After Solomon (1990).

subpolar air with ozone-depleted air from inside the polar-night vortex. As illustrated by Fig. 18.25, the breakdown of the vortex during Austral spring involves a complex rearrangement of air. Meridional displacements then allow ozone-depleted air (white), previously confined inside the vortex, to escape from the polar cap. Anomalies created in this fashion can survive for weeks before they are eventually destroyed by small-scale mixing and diffusion (e.g., Hess and Holton, 1985). Even after they dissolve into the wider air mass, the associated ozone deficit dilutes summertime ozone across much of the Southern Hemisphere (cf. Fig. 18.24).

Airborne observations have established that the same reactions which operate over the Antarctic operate over the Arctic. However, owing to the warmer temperature of the Arctic polar-night vortex, PSC is relatively infrequent. Moreover, free chlorine that is produced in isolated PSC via (18.29) is quickly acted on by dynamical effects. By elevating temperature, those effects reverse the process through other chemical reactions (e.g., Garcia, 1994). This limits the amount of reactive chlorine present when the sun rises over the Arctic, which in turn limits catalytic destruction of ozone via (18.30). Similar considerations apply to mid-latitudes, where ozone depletions of 5–10% have been reported (WMO, 1991). Temperature there is too warm to support cloud formation. Those depletions, however, may involve heterogeneous reactions that are supported by background aerosol in the Junge layer (Sec. 9.1.3).

The limiting factor in ozone depletion appears to be temperature, which controls the formation of PSC (Sec. 9.3). Indeed, the deepest reductions of Antarctic Σ_{O_3} are observed during the coldest winters. This dependence mirrors the spatial correspondence between temperature and perturbed photochemistry (Fig. 18.22). Consequently,

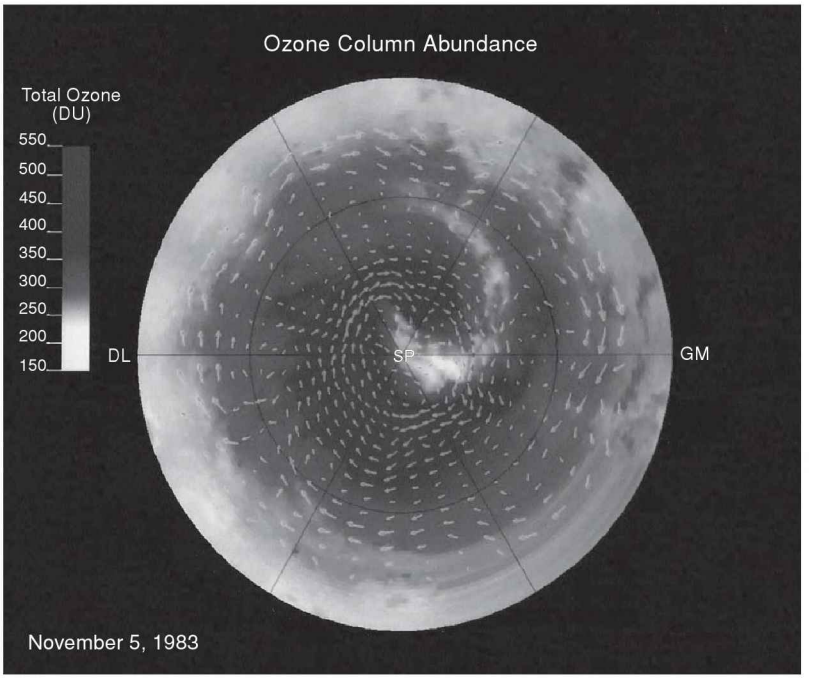

Figure 18.25 Distributions of total ozone and horizontal motion on the 325°K isentropic surface over the Southern Hemisphere on November 5, 1983, during the final warming. Ozone-depleted air (white), which had previously been confined inside the polar-night vortex, escapes in a tongue of anomalously-lean values that spirals anticyclonically into mid-latitudes to conserve potential vorticity. See color plate section: Plate 33.

dynamical disturbances that control temperature inside the vortex (Sec. 18.3) exert a major influence on ozone depletion at high latitude.

18.8 INTERANNUAL CHANGES

The stratosphere contains an internal mechanism for varying between years. In the QBO, the equatorial circulation swings between easterlies and westerlies. As noted in Sec. 18.5, those changes are also manifest in the polar-night vortex, which, through planetary waves, is sensitive to equatorial wind. Changes of $\nabla \cdot \boldsymbol{F}$ introduced by the QBO modify the residual mean circulation. It in turn modifies polar temperature and the strength of the polar-night vortex. The modulated influence of planetary waves (Fig. 18.17) makes stratospheric warmings more frequent during the easterly phase of the QBO than during its westerly phase (Naito and Hirota, 1997; Gray et al., 2004).

The QBO's influence on the vortex favors wintertime polar temperature that is anomalously warm during its easterly phase but anomalously cold during its westerly phase. Such dependence is manifest in polar temperature during many years – but not all of them. Plotted in Fig. 18.26 is anomalous wintertime temperature in the Arctic stratosphere, separated into years when wind in the equatorial stratosphere

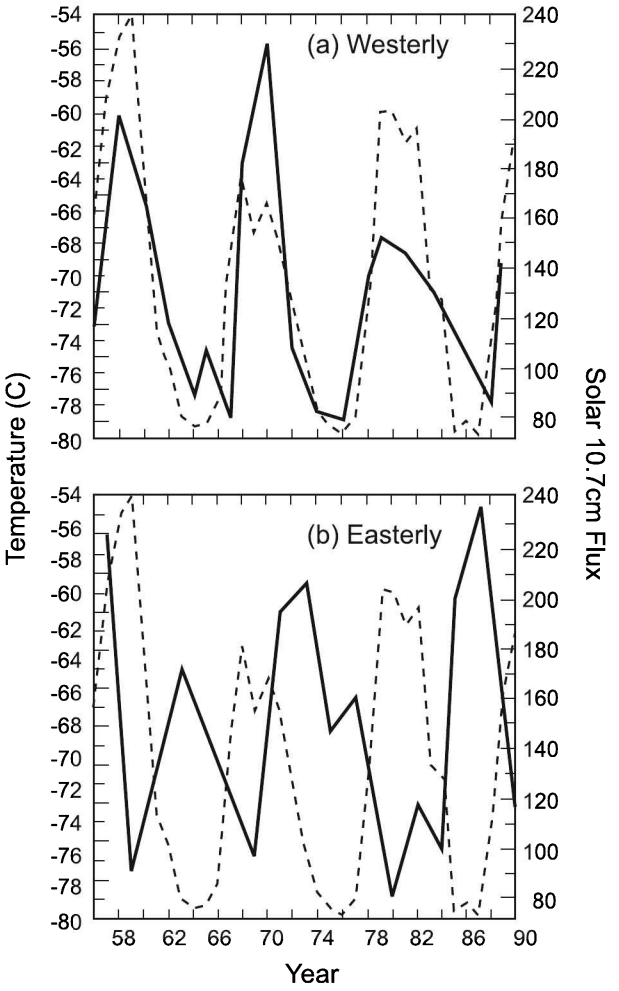

Figure 18.26 Anomalous 30-hPa temperature over the North Pole during Jan–Feb (solid) for years when the QBO in equatorial wind at 50 hPa is (a) westerly and (b) easterly. Superimposed is the 10.7-cm solar flux (dashed). After Labitzke and van Loon (1988). Reprinted from *J Atmos Terr Phys*, **50**, Labitzke K and H van Loon, Association between the 11-yr solar cycle, the QBO, and the atmosphere, 197–206, Copyright (1988), with permission from Elsevier.

is westerly and years when it is easterly (solid). During the westerly phase of the QBO (Fig. 18.26a), wintertime polar temperature evolves systematically, cycling on the time scale of a decade. Superimposed is 10.7-cm solar irradiance, a measure of net solar flux (dashed). It too evolves systematically – through the 11-year cycle of solar activity (Sec. 8.1.1). Polar temperature evolves coherently, in phase with solar flux. Much the same appears during the easterly phase of the QBO, (Fig. 18.26b). Polar temperature then also evolves systematically, coherently but out of phase with solar flux.

The change in overall flux during the solar cycle is small, of order 0.1% (Willson et al., 1986). This limits its direct impact at the Earths' surface, where most wavelengths in the SW spectrum are absorbed. In the stratosphere, however, the impact of the solar cycle can be substantially greater. The stratosphere is forced radiatively by ozone heating (Fig. 8.24). This feature makes it intrinsically sensitive to UV at wavelengths shorter than 200 nm. At those wavelengths, the 11-year variation of SW flux is of order 10%.

Variations of polar temperature in Fig. 18.26 imply the following relationship: For winters near solar min, polar temperature is anomalously warm during the easterly phase of the QBO, but anomalously cold during its westerly phase. This is the dependence implied by the QBO's influence on the extratropical circulation (Fig. 18.17). However, for winters near solar max, polar temperature obeys almost the reverse relationship: In those winters, polar temperature tends to be anomalously cold during the easterly phase of the QBO, but anomalously warm during its westerly phase.

The mechanism behind this decadal variation is poorly understood. One suggestion is a decadal modulation of planetary wave absorption, induced by differences of the polar-night jet between solar min and solar max (Kodera and Kuroda, 2002). Another involves the QBO directly. The QBO's period drifts between 24 and 36 months. That variation, however, is not altogether random. Presented in Fig. 18.27a, as a function year, is the anomalous frequency of the QBO, the deviation from its climatological mean. The QBO's frequency drifts, on the time scale of a decade. It increases near solar max, when its period approaches 24 months. It decreases near solar min, when its period approaches 36 months. The QBO induces its own residual mean circulation, with vertical motion of one sign over the equator flanked in the subtropics of each hemisphere by vertical motion of opposite sign (see, e.g., Andrews et al., 1987). Through adiabatic warming and cooling, that vertical motion introduces anomalous temperature. Plotted in Fig. 18.27b is the running power spectrum of temperature in the subtropical stratosphere. Variance associated with the QBO is concentrated about a period near 30 months. However, it drifts systematically on the time scale of a decade, cycling between shorter and longer period.[8]

The drift in frequency introduces a systematic drift of the QBO's phase with respect to winter months, when the extratropical circulation is sensitive to equatorial wind. Plotted in Fig. 18.28a, for years during the easterly phase of the QBO, is the correlation between February temperature and solar flux. The correlation is significant in the subtropical lower stratosphere and upper troposphere (shaded). Its implication is illustrated in Fig. 18.28b, which plots the respective time series at 100 hPa. February temperature near the tropopause evolves systematically, coherently and in phase with solar flux.

Thermal wind balance requires a corresponding drift in zonal wind – in the subtropical anomaly that is induced directly by the QBO. Neighboring the critical line of planetary waves, anomalous zonal wind there would introduce a modulation of $\nabla \cdot \boldsymbol{F}$. The latter would then force anomalous residual motion and polar temperature. Behavior analogous to that shaded in Fig. 18.28a, although weaker, is also evident at tropospheric levels (see Labitzke, 2005; Crooks and Gray, 2005; Salby and Callaghan, 2006).

[8] The signature of the QBO becomes obscure after 1980. That loss is contemporaneous with the introduction in meteorological analyses of satellite data, which have vertical resolution inadequate to resolve the QBO (Huesmann and Hitchman, 2003).

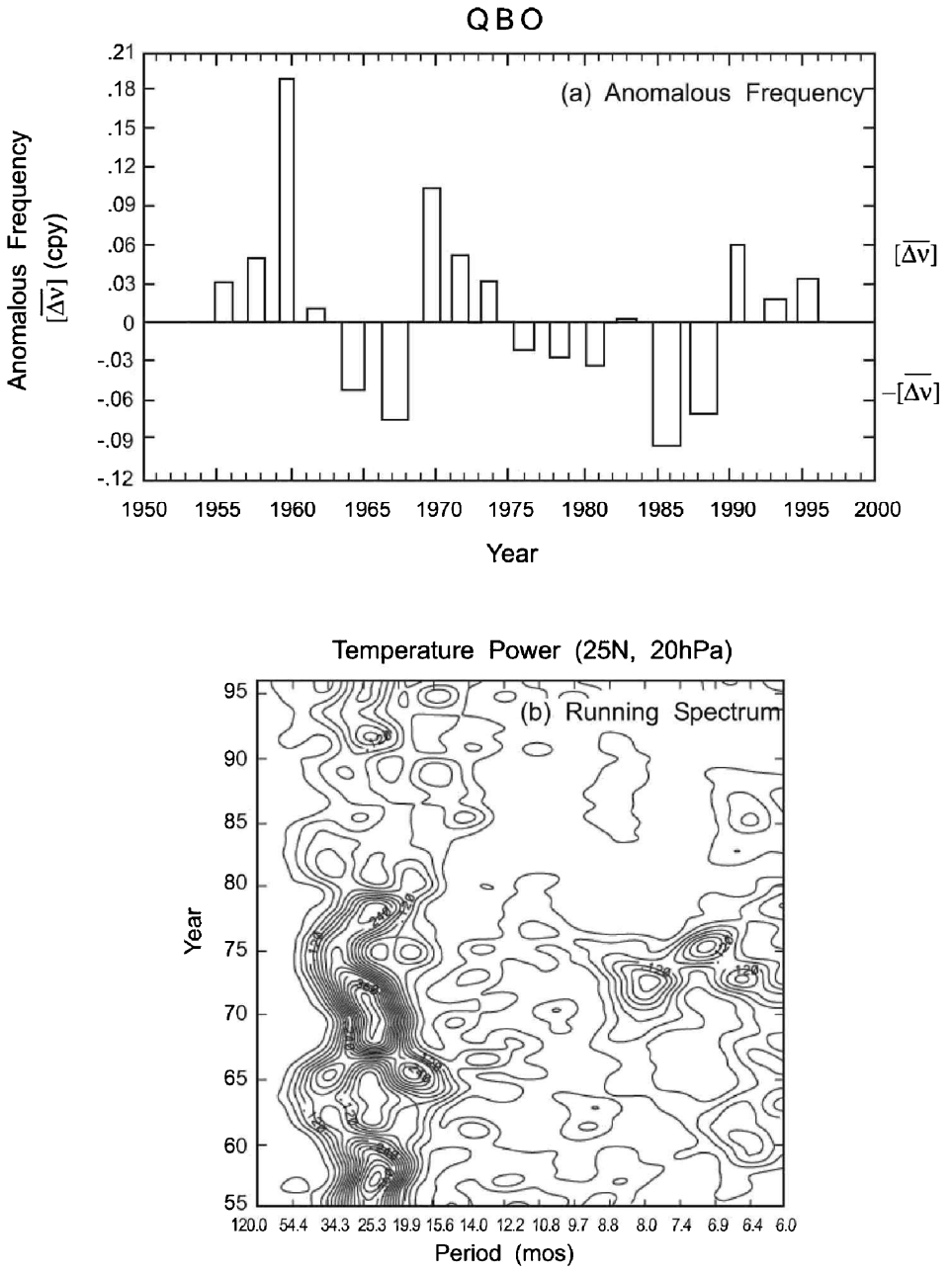

Figure 18.27 (a) Anomalous frequency of the QBO (deviation from its climatological mean: 0.41 $yr^{-1} = (29.2\ mos)^{-1}$), during westerly intervals of the QBO. Indicated at right is rms drift of frequency that varies coherently with the 11-year solar cycle. (b) Running power spectrum of temperature at 25N and 20 hPa, as function of year. After Salby and Callaghan (2000; 2006).

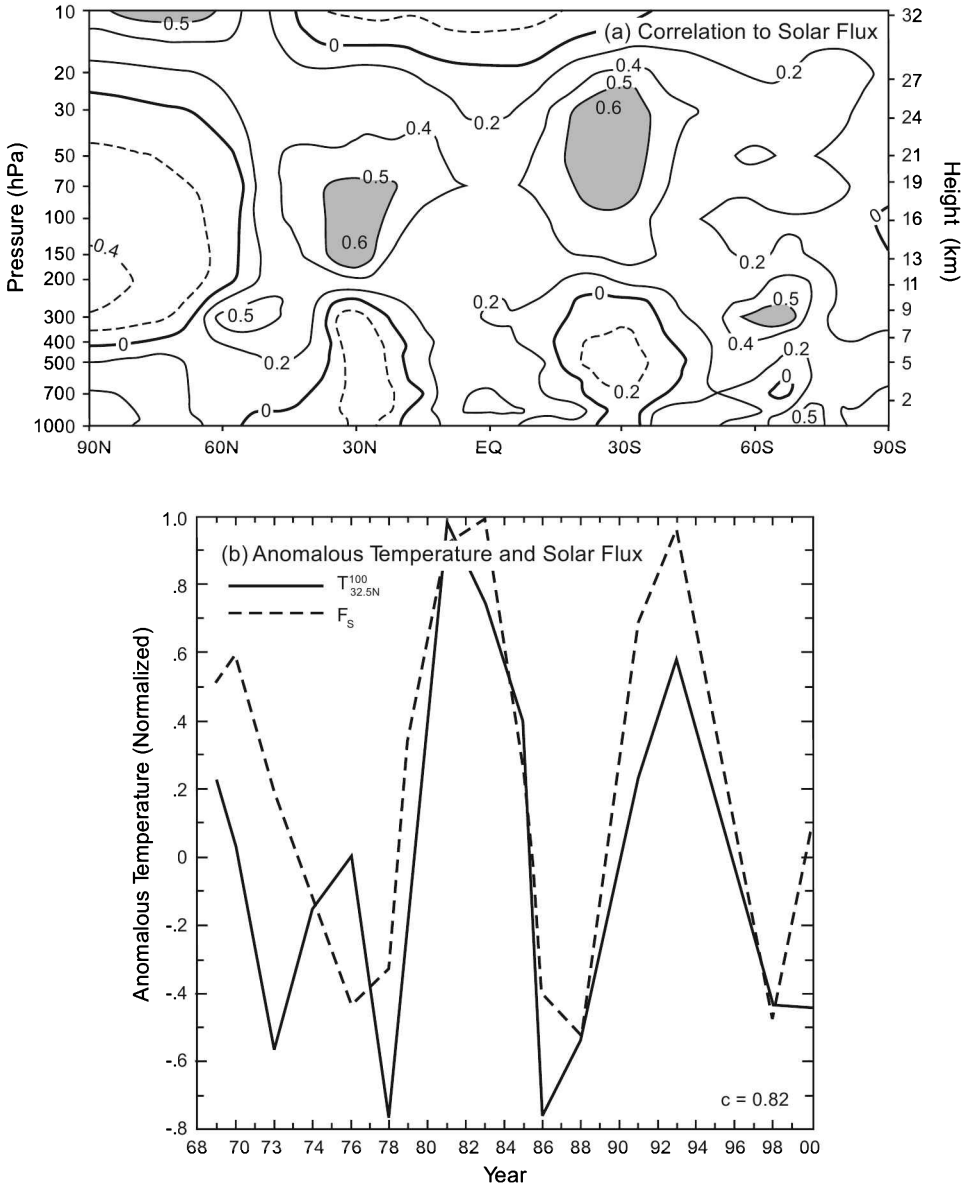

Figure 18.28 For years during the easterly phase of QBO, (a) correlation between February temperature and 10.7-cm solar flux (with regions of statistical significance shaded) and (b) as function of year, anomalous February temperature at 32N and 100 hPa (solid) and 10.7-cm solar flux (dashed). Correlation between the annual records is 0.82. After Labitzke (2005) and Salby and Callaghan (2006). Reprinted from *J Atmos Solar Terr Phys*, 67, K Labitzke, On the solar cycle – QBO relationship: A summary, 45–54, Copyright (2005), with permission from Elsevier.

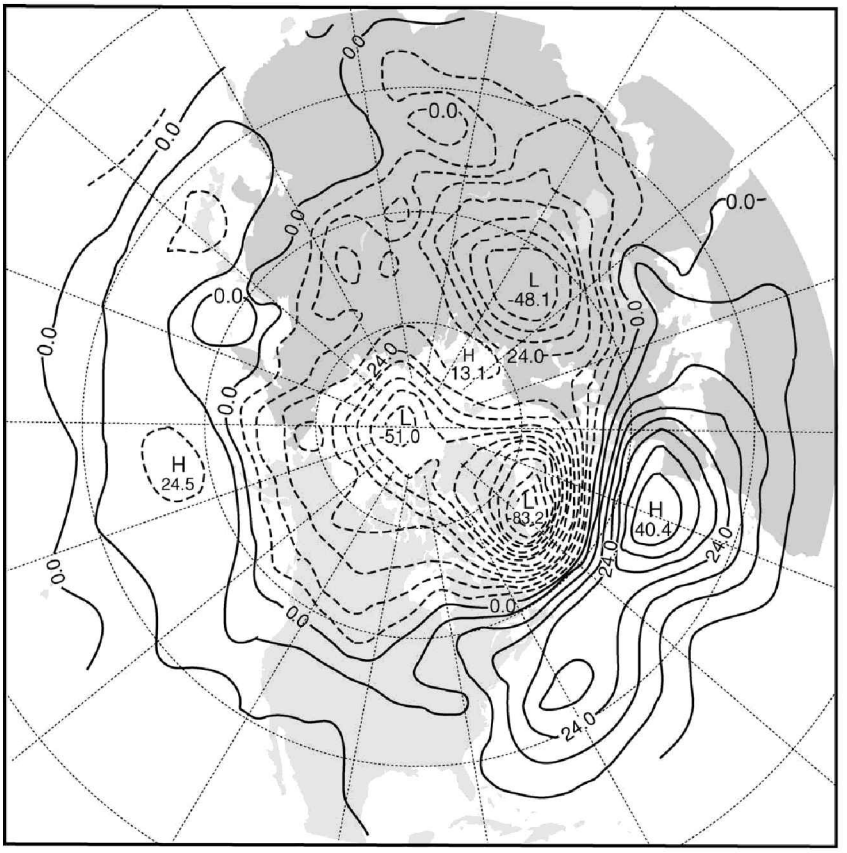

Figure 18.29 Anomalous 1000-hPa height (proxy for SLP) that varies coherently with the equatorial QBO. Compare with Figs. 15.17, 15.19b. After Holton and Tan (1980).

The QBO's influence on the extratropical circulation is conveyed poleward through a modulation of residual mean motion. As the residual circulation couples the stratosphere and troposphere, a change in $(\overline{v}^*, \overline{w}^*)$ must also exert an influence in the troposphere. Displayed in Fig. 18.29 is anomalous SLP that varies coherently with the equatorial QBO. It is marked by anomalously-low SLP over the Icelandic Low and anomalously-high SLP over the Bermuda-Azores High. These are the salient features of the NAO (Fig. 15.17). Closely related is the AO (Fig. 15.19). Indeed, power spectra associated with the AO evidence a peak at periods of the QBO (Coughlin and Tung, 2001).

The AO's relationship to the residual mean circulation is manifest in its structure. Annular at high latitude, AO structure extends upward like the polar-night vortex. The relationship is also manifest in signatures of vertical motion. Plotted in Fig. 18.30 is anomalous wintertime temperature that varies between years coherently with stratospheric temperature over the North Pole (open circle). Positive anomalous temperature over the winter pole is a signature of adiabatic warming and anomalous downwelling. From stratospheric levels, it extends downward coherently into the Arctic troposphere – as low as 500 hPa. Accompanying it at subpolar latitudes is negative

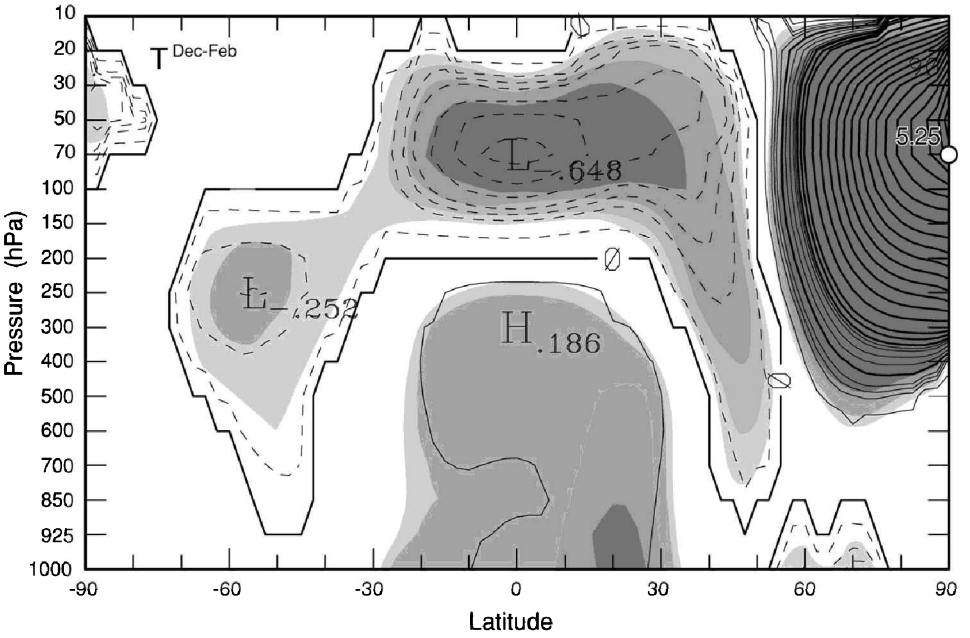

Figure 18.30 Anomalous wintertime tendency of temperature (Mar–Dec) that varies coherently with anomalous temperature at 70 hPa over the North Pole (open circle), which is a measure of anomalous downwelling. Values correspond to an rms intensification of downwelling in the Arctic stratosphere. Regions significant at the 90% and 95% levels are shaded. Compare with structure of the AO in Fig. 15.20. After Salby and Callaghan (2005).

anomalous temperature, a signature of adiabatic cooling and anomalous upwelling. Visible in the troposphere of both hemispheres, it joins a stronger signature of anomalous upwelling in the tropical stratosphere. The AO exhibits much the same structure (Fig. 15.20).

Inside the tropical troposphere, the signature of adiabatic cooling in Fig. 18.30 is interrupted by positive anomalous temperature. Although comparatively weak, it too is coherent with anomalous downwelling in the polar stratosphere. The warm anomaly appears equatorward of 30° and below 200 hPa – the LNB of cumulus updrafts (Sec. 7.7). At those levels, updrafts are positively buoyant. Cumulus detrainment there acts to heat the environment. Anomalous temperature becomes negative above 200 hPa. The cold anomaly maximizes just above the tropical tropopause. At those levels, updrafts are negatively buoyant. Cumulus detrainment there acts to cool the environment. Tropical anomalies at both levels operate coherently with anomalous downwelling over the winter pole. They imply an intensification of upwelling at upper levels of the Hadley circulation, one that accompanies an intensification of downwelling over the winter pole (Thuburn and Craig, 2000; Salby and Callaghan, 2005).

A similar relationship is implied for the tropical tropopause. The cold anomaly above the LNB acts to extend positive lapse rate upward. Its coherence with polar temperature implies a tropical tropopause that is anomalously cold and high when anomalous downwelling over the winter pole is anomalously strong. This relationship

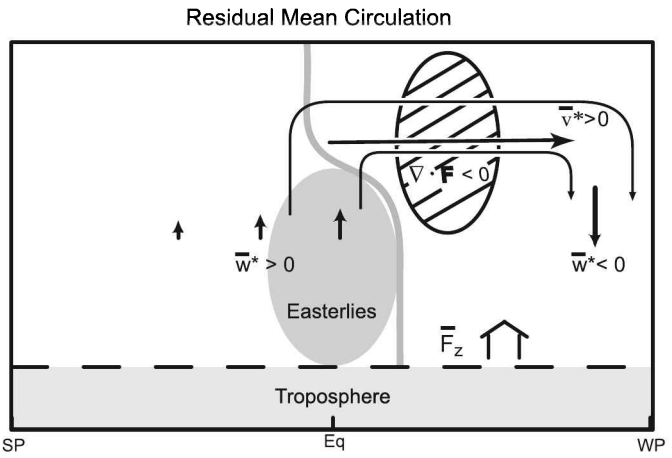

Figure 18.31 Schematic representation of the residual mean circulation $(\overline{v}^*, \overline{w}^*)$. Driven by absorption of EP flux $(\nabla \cdot \boldsymbol{F})$ that is transmitted upward by planetary waves (18.27). The latter is measured by the upward EP flux at 100 hPa, integrated over latitude $\overline{F}_z$ (18.32). During QBO easterlies (red), the zero-wind line (green), which is the critical line for stationary planetary waves, invades the winter hemisphere (cf. Fig. 18.17a). See color plate section: Plate 34.

is consistent with the seasonality of the tropical tropopause. The latter is highest during northern winter, when planetary waves are amplified (Yulaeva et al., 1994).

Some insight into these changes follows from the mechanisms behind anomalous vertical motion, illustrated in Fig. 18.31. Those mechanisms are embodied in the transformed Eulerean mean equations. Under time-mean conditions, planetary wave drag is balanced by the Coriolis acceleration (18.27.1). At levels of wave absorption $(\nabla \cdot \boldsymbol{F} < 0)$, wave drag induces a poleward drift

$$\begin{aligned} \overline{v}^* &= -\frac{1}{\rho_0 f} \nabla \cdot \boldsymbol{F} \\ &> 0. \end{aligned} \tag{18.32.1}$$

Averaging over the middle atmosphere, where EP flux is fully absorbed, and applying the divergence theorem recovers the poleward drift of mass in terms of the upward EP flux at 100 hPa integrated over latitude, $\overline{F}_z$. If $\nabla \cdot \boldsymbol{F}$ is sufficiently narrow in latitude to be treated on an f plane, then the poleward drift of mass reduces to

$$\langle \rho_0 \overline{v}^* \rangle = \frac{1}{f} \overline{F}_z, \tag{18.32.2}$$

where $\langle\ \rangle$ denotes the integral over the region of wave absorption. The poleward drift of mass is proportional to the net transmission of momentum from the troposphere by planetary waves.

Integrating the continuity equation (18.27.2) vertically and incorporating (18.32.1) yields an expression for mean vertical motion:

$$\overline{w}^* = -\frac{1}{\rho_0} \frac{\partial}{\partial y} \left[\frac{1}{f} \int_z^\infty \nabla \cdot \boldsymbol{F} \, dz' \right]. \tag{18.32.3}$$

Vertical motion at height z is determined by the collective wave absorption overhead. The region of wave absorption is characterized by $\nabla \cdot \boldsymbol{F} < 0$. Along its equatorward flank, $\nabla \cdot \boldsymbol{F}$ decreases northward, so $\overline{w}^* > 0$. That region experiences upwelling and adiabatic cooling. Along the poleward flank of wave absorption, $\nabla \cdot \boldsymbol{F}$ increases northward, so $\overline{w}^* < 0$. That region experiences downwelling and adiabatic warming. Indicated in Fig. 18.31, these vertical motions imply the anomalous temperature structure evident in Fig. 18.30.

Anomalous temperature in Fig. 18.30 represents changes of thermal structure that are spatially coherent. Nearly identical structure characterizes anomalous temperature that varies coherently with $\overline{F}_z$ and the QBO (Salby and Callaghan, 2002). By modulating $\nabla \cdot \boldsymbol{F}$, the latter force an anomalous residual circulation (18.32.2). Through adiabatic warming and cooling, it induces anomalous temperature. Most of the temperature anomaly follows from $\overline{F}_z$, which modulates the magnitude of $\nabla \cdot \boldsymbol{F}$ (18.32.3).

Anomalous residual motion also influences the distribution of total ozone. By modulating poleward transport of ozone-rich air, anomalous $\overline{v}^*$ introduces anomalous total ozone at extratropical latitude. Plotted in Fig. 18.32, as a function of year, is the anomalous wintertime increase of NH total ozone (solid). It reflects the springtime maximum of total ozone; cf. Fig. 1.21. Superimposed is the component of ozone that varies coherently with anomalous $\overline{F}_z$ and the QBO, adjusted for sporadic enhancements of volcanic aerosol (dashed). Anomalous NH ozone closely tracks anomalous forcing of the residual circulation. Achieving a correlation to observed changes of 0.95, anomalous dynamical forcing accounts for nearly all of the interannual variance of NH ozone. Most of the ozone anomaly derives from changes of $\overline{F}_z$.

Similar considerations apply to polar ozone. However, those changes are complicated by the dependence on temperature of heterogeneous chemical destruction. The formation of PSC, which activates chlorine, is intrinsically sensitive to temperature (Sec. 9.3.1). Polar temperature, in turn, is determined by downwelling and, hence, by the residual mean circulation. Because the residual circulation also transports ozone to high latitude, the dynamics and chemistry of polar ozone are intertwined. This is especially true in the Northern Hemisphere, where amplified planetary waves sharply disturb the vortex (Fig. 1.10a).

In the Arctic stratosphere, wintertime temperature varies between years by as much as 10 K. The polar-night vortex thus varies from conditions representative of the Arctic, disturbed and warm, to those representative of the Antarctic, undisturbed and cold. The latter conditions support the formation of PSC and, hence, heterogeneous chemical destruction of ozone (18.29). Indeed, during cold winters, Arctic ozone is anomalously low (Muller et al., 2003; Tilmes et al., 2003; Rex et al., 2004). Reduced ozone then is consistent with accelerated chemical depletion. However, cold winters are also distinguished by diminished transport into the Arctic. With the latter, reduced ozone is likewise consistent. Unraveling contributions from anomalous transport and chemical destruction is complicated by their inter-dependence, through temperature.

A clue to the individual roles of transport and chemical destruction comes from the 3-dimensional structure of ozone. Compared in Fig. 18.33 is the distribution of r_{O_3} during March following warm winters against that following cold winters (solid). March r_{O_3} corresponds to the spring maximum of total ozone (Fig. 1.21). It is the culmination of increases during the winter season, when the vortex is disturbed and the residual circulation is active (Fig. 1.21). Superimposed in Fig. 18.33 are isentropic

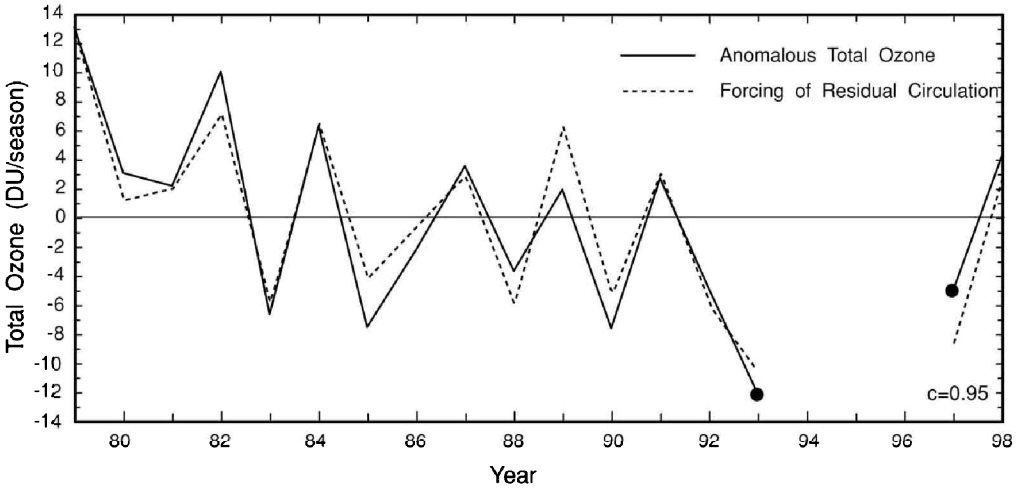

Figure 18.32 Anomalous wintertime tendency of NH total ozone, which dictates springtime ozone (solid). Superimposed is the component that varies coherently with anomalous forcing of the residual circulation, represented in $\overline{F}_z$ and the QBO, adjusted for sporadic enhancements of volcanic aerosol (dashed). Correlation between the wintertime records is 0.95. *Source:* Fusco and Salby (1999), Salby and Callaghan (2004b).

surfaces in the lower stratosphere (dashed), where total ozone is concentrated (cf. Fig. 18.2). Following cold winters (Fig. 18.33b), mixing ratio surfaces have been deflected downward across isentropic surfaces at extratropical latitudes of the winter hemisphere. That structure is a signature of downwelling by the residual mean circulation. It causes r_{O_3} to increase poleward along isentropic surfaces. Total ozone then also increases poleward – but only up to the edge of the vortex, where ozone accumulates. Poleward of 60N, r_{O_3} decreases along isentropic surfaces. Total ozone therefore decreases into the Arctic. During warm winters (Fig. 18.33a), r_{O_3} has similar structure – but not at high latitude. Poleward of 60N, mixing ratio surfaces have been laid flat. They have been driven into coincidence with isentropic surfaces. Total ozone then increases into the Arctic. It attains values some 60 DU greater than during cold winters, when ozone-rich air does not invade the Arctic.

The difference in total ozone follows from the structure of ozone mixing ratio surfaces. They are driven into coincidence with isentropic surfaces during warm winters but not during cold winters. Only one process achieves that structure. Isentropic mixing by planetary waves homogenizes long-lived species along θ surfaces. It offsets the deflection of mixing ratio surfaces across θ surfaces by the residual mean circulation (Holton, 1986). By exchanging air at low and high latitudes, isentropic mixing transfers ozone-rich air into the Arctic (Figs. 14.26; 18.13; 18.14). In concert with intensified downwelling, it increases Arctic ozone during warm winters over that during cold winters. In observed structure, these forms of transport account for some two thirds of the 60-DU anomaly that distinguishes Arctic ozone between warm and cold winters (Salby and Callaghan, 2007).

A similar conclusion follows from numerical simulations. Plotted in Fig. 18.34 is anomalous total ozone between simulations that were performed under conditions of

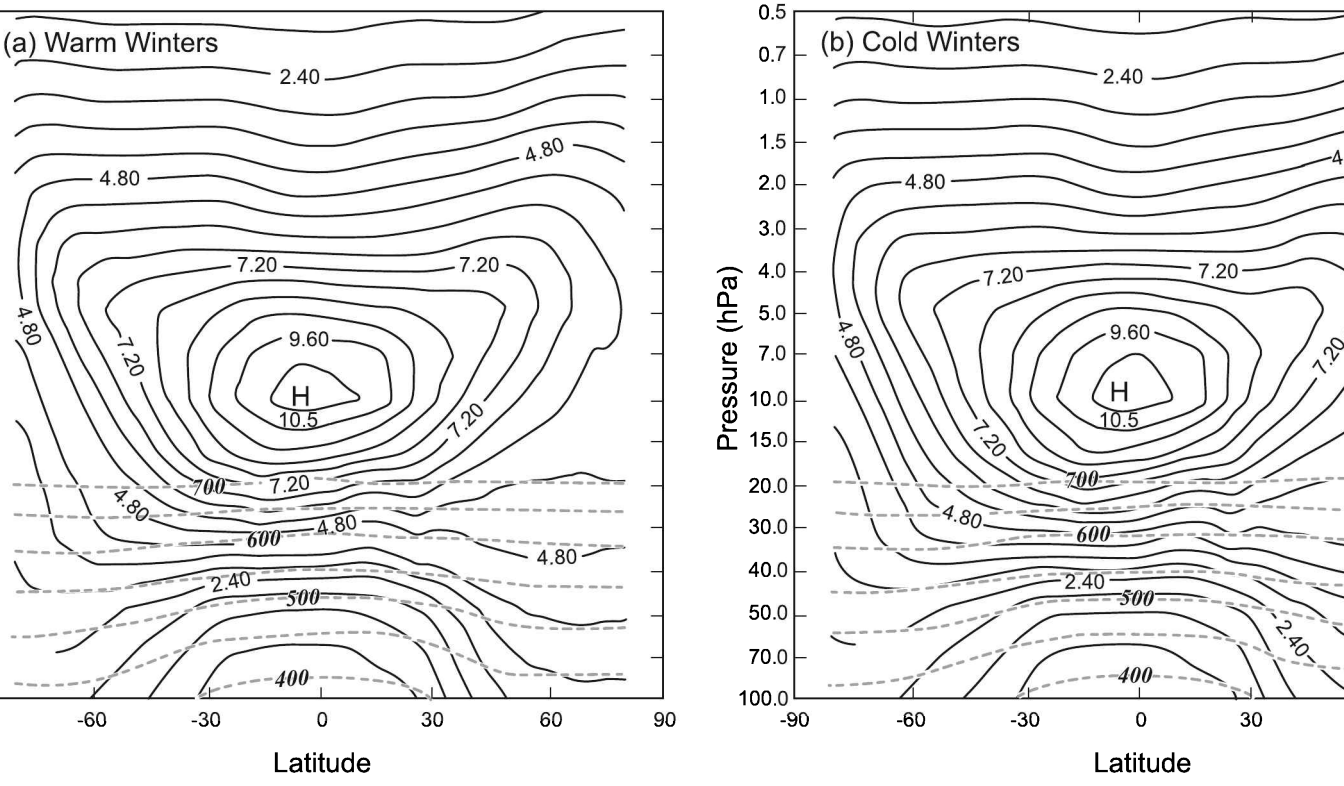

gure 18.33 Zonal-mean ozone mixing ratio during spring following (a) warm winters and (b) cold winters (solid). Superimposed is aneous structure of isentropic surfaces (dashed). The difference corresponds to anomalous Arctic ozone between warm and cold U. After Salby and Callaghan (2007).

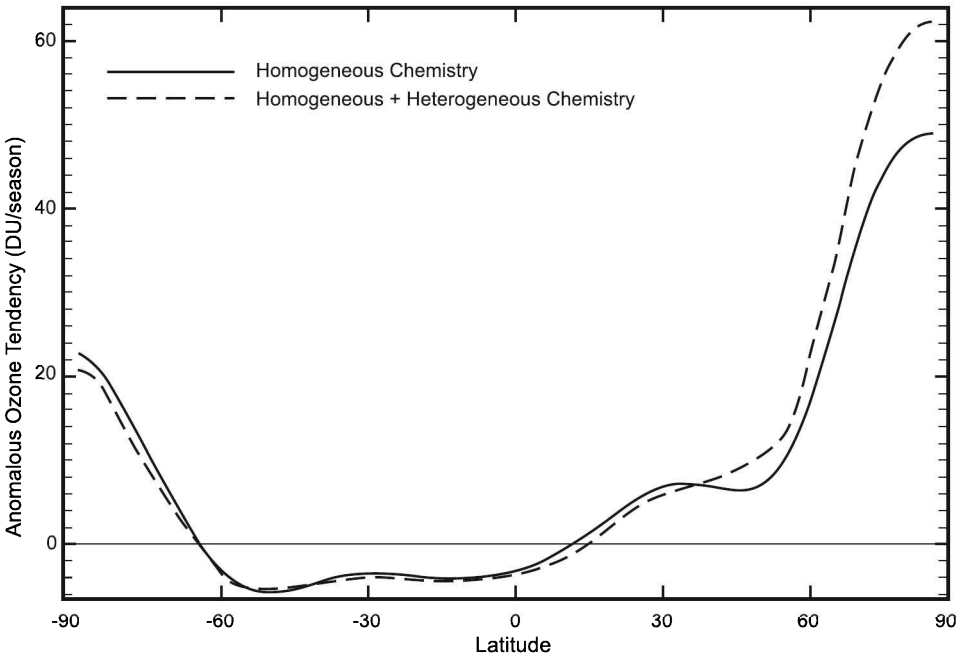

Figure 18.34 Simulation of anomalous springtime ozone between dynamical conditions representative of warm and cold winters. Simulated in the presence of homogeneous chemistry (solid) and inclusive of heterogeneous processes (dashed). Simulations performed in a 3-dimensional model based on the dynamical treatment of Callaghan et al. (1999) and the chemical treatment of Mozart-3 (Horowitz et al., 2003). Adapted from Salby (2011).

cold winters and warm winters. In one simulation, the polar-night vortex is strongly perturbed by amplified planetary waves, which are imposed from observed tropospheric structure during warm winters. In the other simulation, it is weakly perturbed by weak planetary waves, which are imposed from observed tropospheric structure during cold winters. Plotted in solid is anomalous total ozone (strongly perturbed – weakly perturbed) in the presence of only homogeneous (gas-phase) chemistry. Negative values appear in the tropics, where anomalous upwelling introduces ozone-lean air from the troposphere. From there, anomalous ozone increases poleward, exceeding 48 DU over the Arctic. Superimposed is the anomaly inclusive of full heterogeneous chemistry (dashed). Equatorward of 50N, it is nearly identical to the ozone anomaly that forms under homogeneous chemistry. At higher latitude, however, it diverges. Exceeding 60 DU over the Arctic, the computed anomaly is broadly consistent with the observed anomaly between warm and cold winters. Most of the contribution from heterogeneous chemistry enters through the simulation under weakly-perturbed conditions. Arctic temperature then decreases to 187 K. This magnifies PSC, accelerating chlorine activation and ozone depletion. The contribution from heterogeneous chemistry (ozone depletion) accounts for about 30% of the overall anomaly between warm and cold winters. The rest follows from changes of transport.

Over the Antarctic, similar considerations apply. However, weaker planetary waves of the Southern Hemisphere leave the Antarctic vortex cold enough to form

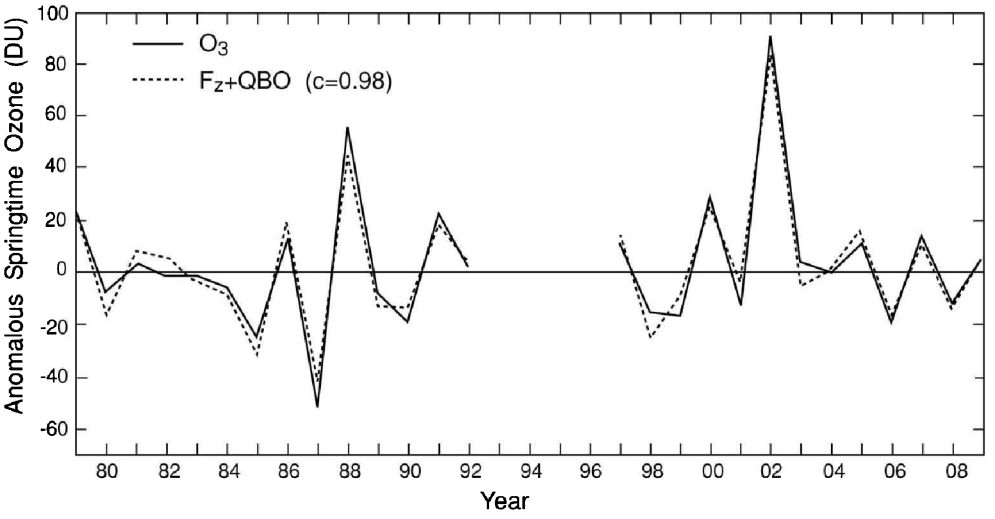

Figure 18.35 Interannual anomaly of springtime ozone (Sep–Nov) over the Antarctic (solid). Superimposed is the component that varies coherently with anomalous forcing of the residual circulation (dashed). Follows application of highpass filter that discriminates to periods shorter than a decade. Correlation between the records of springtime ozone is 0.98. After Salby et al., (2011).

PSC during all winters. How much forms depends on how cold temperature becomes. Plotted in Fig. 18.35 is the interannual anomaly of springtime ozone over the Antarctic (solid). Reflecting changes of the Antarctic ozone hole (Fig. 1.22b), it varies between neighboring years by 50–100 DU. This is almost as large as the mean depletion of ozone that defines the ozone hole. Superimposed is the component of ozone that varies coherently with anomalous $\overline{F}_z$ and the QBO (dashed). Changes of the ozone hole closely track anomalous forcing of the residual circulation. Achieving a correlation of 0.98, anomalous dynamical forcing accounts for nearly all of the interannual variance of the ozone hole. Most of the ozone anomaly derives from changes of $\overline{F}_z$, which modulate downwelling over the Antarctic (Huck et al., 2005; Salby et al., 2011). Through adiabatic warming, those changes shorten and prolong the period of coldest temperature which supports PSC. The latter, in turn, modulates the net activation of chlorine and hence springtime depletion of ozone (18.29).

The anomaly in Fig. 18.35 represents changes of springtime ozone between neighboring years. Introduced by anomalous forcing of the residual circulation, those changes describe the *climate variability* of Antarctic ozone (Sec. 1.6). Removing them leaves the component of anomalous ozone that is unrelated to dynamically-induced changes. Plotted in Fig. 18.36 is the record of springtime ozone that is independent of $\overline{F}_z$ and the QBO (solid). Representing the *secular variation* of Antarctic ozone, the part coherent over a decade and longer (Sec. 1.6), it declines over the 1980s and early 1990s, until that portion of the satellite record ends. By the late 1990s, when the satellite record resumes, the secular variation of Antarctic ozone manifests a gradual but systematic rebound. The upward trend is visible for almost as long as was the downward trend during earlier years. Reflecting ozone recovery, it follows

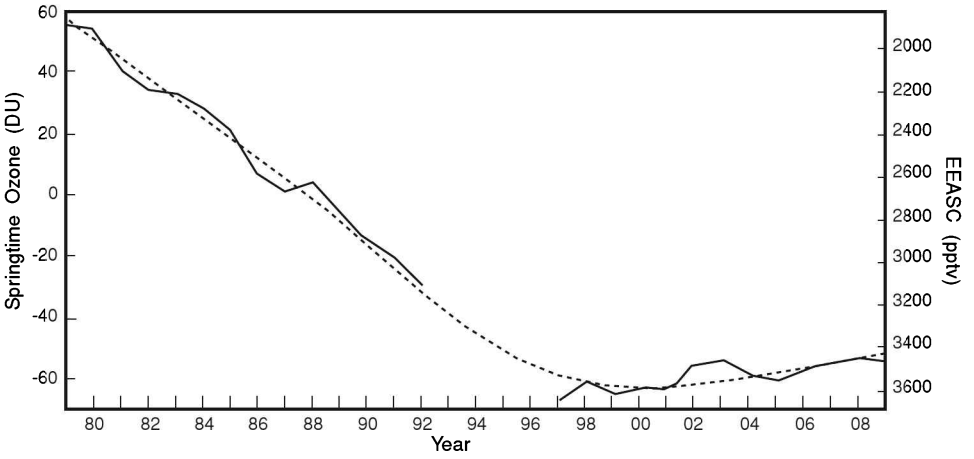

Figure 18.36 Component of springtime ozone over the Antarctic that is independent of dynamically-induced changes (solid). The upward trend after 1996 is significant at the 99.5% level. Superimposed is Equivalent Effective Stratospheric Chlorine for the Antarctic (with inverted scale), corresponding to a mean age of air of 5 years and a bromine scale factor of 60 (dashed). After Salby et al. (2011).

the elimination of CFC production by the Montreal Protocol, which has led to a gradual reduction of chlorine reservoir species (18.29). Superimposed in Fig. 18.36 (with inverted scale) is the record of Equivalent Effective Stratospheric Chlorine (EESC), inclusive of bromine (dashed). From its peak in the late 1990s, EESC has declined gradually, by ~15%. Tracking it is the secular variation of Antarctic ozone. In the full record of ozone, the systematic variation is obscured by dynamically-induced changes. Those changes, which represent climate variability, dominate the current evolution of Antarctic ozone. Owing to the gradual decline of chlorine, which is characteristic of secular changes of climate, this will remain the case for some time (WMO, 2006).

SUGGESTED REFERENCES

Interaction between planetary waves and the mean meridional circulation is developed in *An Introduction to Dynamic Meteorology* (2004) by Holton. An advanced treatment is presented in *Middle Atmosphere Dynamics* (1987) by Andrews et al.

Holton et al. (1995) presents an overview of stratosphere-troposphere exchange.

Atmospheric Physics (2000) by Andrews includes an overview of stratospheric chemistry and transport. A detailed treatment of gas phase photochemistry is presented in *Aeronomy of the Middle Atmosphere* (1986) by Brasseur and Solomon. Heterogeneous processes are reviewed in WMO (2006).

PROBLEMS

1. Photochemical lifetime is defined from reactions that destroy a species X as $\tau_X^{-1} = -\frac{1}{X}\frac{dX}{dt}$. Within the framework of Chapman chemistry, derive expressions for the photochemical lifetimes of O_3 and O_x. If below 50 km $[O_x] \cong [O_3]$, and if

the rate coefficients in cgs units are $k_2 = 6.0\ 10^{-34}\left(\frac{300}{T}\right)[M]$, $k_3 = 8.0\ 10^{-12}e^{-\frac{2060}{T}}$, where T is in Kelvin, and $[M]$ is the number density of air, $J_2 = 4.35\ 10^{-15}$, $7.44\ 10^{-11}$, $1.01\ 10^{-9}$, and $J_3 = 4.47\ 10^{-4}$, $7.80\ 10^{-4}$, $6.96\ 10^{-3}$ at 100 hPa, 10 hPa, and 1 hPa, respectively, evaluate τ_{O_3} and τ_{O_x} at (a) 100 hPa, (b) 10 hPa, (c) 1 hPa.

2. Ozone is useful as a tracer in the lower stratosphere, yet O_3 has a photochemical lifetime there of only hours (e.g., Fig. 18.1). Resolve this discrepancy.
3. Use observed temperature (Fig. 1.7), radiative-equilibrium temperature (Fig. 18.9), and the coefficient of Newtonian cooling (Fig. 8.29) to estimate the radiative cooling rate (°K day^{-1}) inside the polar-night vortex at (a) 100 hPa, (b) 10 hPa, (c) 1 hPa.
4. According to the Brewer-Dobson circulation (Fig. 18.11), air enters the stratosphere from the tropical troposphere. Estimate the water vapor mixing ratio, in ppmv, for the tropical lower stratosphere if tropospheric air entering the stratosphere (a) evolves through a thermodynamic state corresponding to the mean temperature and height of the tropical tropopause (Fig. 1.7), (b) is actually introduced through isolated convective overshoots that have a mean height and temperature of 16.5 km and 185°K, (c) as in (b), but if, after entering the stratosphere, tropospheric air inside convective overshoots mixes with subtropical stratospheric air that has a mixing ratio of 5 ppmv.
5. Depleted ozone at high latitude introduces anomalous radiative transfer. Discuss how, by influencing the polar-night vortex, such changes can represent a positive feedback.

6. The residual mean circulation (Fig. 18.11) gives no indication of equatorward transport in the lower stratosphere. (a) How might subtropical air in Prob. 18.4c be supplied to the equator? (b) Why does such transport not appear in the residual mean circulation?
7. Methane oxidation is thought to be responsible for about 25% of stratospheric water vapor. Given the reactions

$$CH_4 + OH \rightarrow H_2O + CH_3 \quad (k_a)$$
$$H_2O + O \rightarrow 2OH \quad (k_b),$$

with the rate coefficients in cgs units: $k_a = 2.4\ 10^{-12}e^{-\frac{1710}{T}}$ and $k_b = 2.2\ 10^{-10}$, calculate the photochemical-equilibrium mixing ratio of water vapor produced by methane oxidation at 20 km, where $r_{CH_4} \cong 1.3$ ppmv, $r_{OH} \cong 1.5\ 10^{-13}$, and $r_O \cong 4.9\ 10^{-19}$. Compare this value with observed mixing ratios at this altitude.
8. Photochemical lifetime is treated in Prob. 18.1, for the family O_x. Consider now Chapman chemistry, but augmented by the catalytic cycle (18.13) involving Cl_x. Determine the photochemical lifetime of O_x at 100 hPa for (a) rate coefficients for (18.13.1) and (18.13.2) in cgs units of $k_a = 8.5\ 10^{-12}$ and $k_b = 3.7\ 10^{-11}$, respectively, and a ClO mixing ratio of 100 pptv, which are representative of gas-phase chemistry under unperturbed conditions, and (b) rate coefficients of $k_a = 8.5\ 10^{-10}$ and $k_b = 3.7\ 10^{-9}$, respectively, and a ClO mixing ratio of 1000 pptv, which are representative of heterogeneous chemistry involving (18.30) under chemically perturbed conditions. (c) Compare the photochemical lifetimes of O_x in (a) and (b) with those under pure oxygen chemistry calculated in Prob. 18.1.

Appendix A: Conversion to SI units

Physical Quantity	Unit	SI (MKS) Equivalent
Length	ft	0.305 m
	μm	10^{-6} m
	nm	10^{-9} m
Time	day	$8.64\ 10^{4}$ s
Mass	lb	0.454 kg
Temperature	F	$273 + (F\text{-}32)/1.8$ K
Volume	liter	10^{-3} m^3
Velocity	mph	0.447 m s^{-1}
	Knots	0.515 m s^{-1}
	km hr^{-1}	0.278 m s^{-1}
	fps	0.305 m s^{-1}
Force	kg m s^{-2}	1 N
	lb	0.138 N
	dyne	10^{-5} N
Pressure	N m^{-2}	1 Pa
	bar	10^{5} Pa
	mb	10^{2} Pa
Energy	kg m^2 s^{-2}	1 J
	Nm	1 J
	erg	10^{-7} J
	cal	4.187 J
Power	kg m^{-2} s^{-3}	1 W
	J s^{-1}	1 W
	Langley day^{-1}	$4.84\ 10^{-1}$ W m^{-2}
Specific Heat	cal gm^{-1}	$4.184\ 10^{3}$ J kg^{-1}
Energy Flux	cal cm^{-2} min^{-1}	$6.97\ 10^{2}$ W m^{-2}

Appendix B: Thermodynamic properties of air and water

Dry Air	
Mean Molecular Weight	$M_d = 28.96$ g mol^{-1}
Specific Gas Constant	$R = 287.05$ J kg^{-1} K^{-1}
Density	$\rho = 1.293$ kg m^{-3} (at STP*)
Number Density (Loschmidt No.)	$n = 2.687\ 10^{25}$ m^{-3} (at STP)
Isobaric Specific Heat Capacity	$c_p = 1.005\ 10^3$ J kg^{-1} K^{-1} (at 273 K)
Isochoric Specific Heat Capacity	$c_v = 7.19\ 10^2$ J kg^{-1} K^{-1} (at 273 K)
Ratio of Specific Heats	$\gamma = \frac{c_p}{c_v} = 1.4$
	$\kappa = \frac{\gamma - 1}{\gamma} = \frac{R}{c_p} = 0.286$
Coefficient of Viscosity	$\mu = 1.73\ 10^{-5}$ kg m^{-1} s^{-1} (at STP)
Kinematic Viscosity	$\nu = 1.34\ 10^{-5}$ m^2 s^{-1} (at STP)
Coefficient of Thermal Conductivity	$k = 2.40\ 10^{-2}$ W m^{-1} K^{-1} (at STP)
Sound Speed	$c_s = 331$ m s^{-1} (at 273 K)
Water	
Mean Molecular Weight	$M_v = 18.015$ g mol^{-1}
	$\epsilon = \frac{M_v}{M_d} = 0.622$
Specific Gas Constant	$R = 461.51$ J kg^{-1} K^{-1}
Density (Liquid Water)	$\rho = 10^3$ kg m^{-3} (at STP)
Density (Ice)	$\rho = 9.17\ 10^2$ kg m^{-3} (at STP)
Isobaric Specific Heat Capacity (Vapor)	$c_p = 1.85\ 10^3$ J kg^{-1} K^{-1} (at 273 K)
Isochoric Specific Heat Capacity (Vapor)	$c_v = 1.39\ 10^3$ J kg^{-1} K^{-1} (at 273 K)
Ratio of Specific Heats (Vapor)	$\gamma = \frac{c_p}{c_v} = 1.33$
Specific Heat Capacity (Liquid Water)	$c = 4.218\ 10^3$ J kg^{-1} K^{-1} (at 273 K)
Specific Heat Capacity (Ice)	$c = 2.106\ 10^3$ J kg^{-1} K^{-1} (at 273 K)
Specific Latent Heat of Fusion	$l_f = 3.34\ 10^5$ J kg^{-1}
Specific Latent Heat of Vaporization	$l_v = 2.50\ 10^6$ J kg^{-1}
Specific Latent Heat of Sublimation	$l_s = l_f + l_v$
Specific Surface Tension	$\sigma = 0.076$ s^{-2} (at 273 K)

* Standard Temperature and Pressure (STP) = 1013 mb and 273 K.

Appendix C: Physical constants

Avogadro's Number	$N_A = 6.022\ 10^{26}\ \text{mol}^{-1}$
Universal Gas Constant	$R^* = 8.314\ \text{J mol}^{-1}\ \text{K}^{-1}$
Boltzmann Constant	$k = 1.381\ 10^{-23}\ \text{J K}^{-1}$
Planck Constant	$h = 6.6261\ 10^{-34}\ \text{J s}^{-1}$
Stefan-Boltzmann Constant	$\sigma = 5.67\ 10^{-8}\ \text{W m}^{-2}\ \text{K}^{-4}$
Speed of Light	$c = 2.998\ 10^{8}\ \text{m s}^{-1}$
Solar Constant	$F_s = 1.372\ 10^{3}\ \text{W m}^{-2}$
Radius of the Earth	$a = 6.371\ 10^{3}\ \text{km}$
Standard Gravity	$g_0 = 9.806\ \text{m s}^{-2}$
Earth's Angular Velocity	$\Omega = 7.292\ 10^{-5}\ \text{s}^{-1}$

Appendix D: Vector identities

$$\boldsymbol{A} \times (\boldsymbol{B} \times \boldsymbol{C}) = (\boldsymbol{A} \cdot \boldsymbol{C})\boldsymbol{B} - (\boldsymbol{A} \cdot \boldsymbol{B})\boldsymbol{C} \tag{D.1}$$

$$\boldsymbol{A} \cdot (\boldsymbol{B} \times \boldsymbol{C}) = (\boldsymbol{A} \times \boldsymbol{B}) \cdot \boldsymbol{C} = \boldsymbol{B} \cdot (\boldsymbol{C} \times \boldsymbol{A}) \tag{D.2}$$

$$(\boldsymbol{A} \times \boldsymbol{B}) \cdot (\boldsymbol{C} \times \boldsymbol{D}) = (\boldsymbol{A} \cdot \boldsymbol{C})(\boldsymbol{B} \cdot \boldsymbol{D}) - (\boldsymbol{A} \cdot \boldsymbol{D})(\boldsymbol{B} \cdot \boldsymbol{C}) \tag{D.3}$$

$$\nabla(fg) = f\nabla g + g\nabla f \tag{D.4}$$

$$\nabla \cdot (f\boldsymbol{A}) = \nabla f \cdot \boldsymbol{A} + f\nabla \cdot \boldsymbol{A} \tag{D.5}$$

$$\nabla \times (f\boldsymbol{A}) = \nabla f \times \boldsymbol{A} + f\nabla \times \boldsymbol{A} \tag{D.6}$$

$$\nabla \cdot (\boldsymbol{A} \times \boldsymbol{B}) = \boldsymbol{B} \cdot (\nabla \times \boldsymbol{A}) - \boldsymbol{A} \cdot (\nabla \times \boldsymbol{B}) \tag{D.7}$$

$$\nabla \cdot \nabla \times \boldsymbol{A} = 0 \tag{D.8}$$

$$\nabla \times \nabla f = 0 \tag{D.9}$$

$$\nabla \cdot \nabla f = \nabla^2 f \tag{D.10}$$

$$\nabla \times \nabla \times f = \nabla(\nabla \cdot f) - \nabla^2 f \tag{D.11}$$

$$\nabla(\boldsymbol{A} \cdot \boldsymbol{B}) = \boldsymbol{A} \cdot \nabla\boldsymbol{B} + \boldsymbol{B} \cdot \nabla\boldsymbol{A} + \boldsymbol{A} \times \nabla\boldsymbol{B} + \boldsymbol{B} \times \nabla \times \boldsymbol{A} \tag{D.12}$$

$$\nabla(\boldsymbol{A} \times \boldsymbol{B}) = \boldsymbol{B} \cdot \nabla\boldsymbol{A} - \boldsymbol{A} \cdot \nabla\boldsymbol{B} + \boldsymbol{A}(\nabla \cdot \boldsymbol{B}) - \boldsymbol{B}(\nabla \cdot \boldsymbol{A}) \tag{D.13}$$

$$\boldsymbol{A} \cdot \nabla\boldsymbol{A} = \frac{1}{2}\nabla(\boldsymbol{A} \cdot \boldsymbol{A}) - \boldsymbol{A} \times (\nabla \times \boldsymbol{A}) \tag{D.14}$$

Appendix E: Curvilinear coordinates

Spherical Coordinates (λ, ϕ, r)

$$\nabla\psi = \frac{1}{r\cos\phi}\frac{\partial\psi}{\partial\lambda}\boldsymbol{e}_{\lambda} + \frac{1}{r}\frac{\partial\psi}{\partial\phi}\boldsymbol{e}_{\varphi} + \frac{\partial\psi}{\partial r}\boldsymbol{e}_{r} \tag{E.1}$$

$$\nabla\cdot\boldsymbol{A} = \frac{1}{r\cos\phi}\frac{\partial A_{\lambda}}{\partial\lambda} + \frac{1}{r\cos\phi}\frac{\partial}{\partial\phi}(\cos\phi A_{\phi}) + \frac{1}{r^2}\frac{\partial}{\partial r}(r^2 A_r) \tag{E.2}$$

$$\begin{aligned}\nabla\times\boldsymbol{A} = \frac{1}{(r^2\cos\phi)}\Bigg\{ & r\cos\phi\left[\frac{\partial A_r}{\partial\phi} - \frac{\partial(rA_{\phi})}{\partial r}\right]\boldsymbol{e}_{\lambda} \\ & + r\left[\frac{\partial}{\partial r}(r\cos\phi A_{\lambda}) - \frac{\partial A_r}{\partial\lambda}\right]\boldsymbol{e}_{\varphi} + \left[\frac{\partial(rA_{\phi})}{\partial\lambda} - \frac{\partial}{\partial\varphi}(r\cos\phi A_{\lambda})\right]\boldsymbol{e}_{r}\Bigg\}\end{aligned} \tag{E.3}$$

$$\nabla^2\psi = \frac{1}{r^2\cos^2\phi}\frac{\partial^2\psi}{\partial\lambda^2} + \frac{1}{r^2\cos\phi}\frac{\partial}{\partial\phi}\left(\cos\phi\frac{\partial\psi}{\partial\phi}\right) + \frac{1}{r^2}\frac{\partial}{\partial r}\left(r^2\frac{\partial\psi}{\partial r}\right) \tag{E.4}$$

$$\begin{aligned}\nabla^2\boldsymbol{A} = & \left[\nabla^2 A_{\lambda} - \frac{A_{\lambda}}{r^2\cos^2\varphi} + \frac{2}{r^2\cos\varphi}\frac{\partial A_r}{\partial\lambda} + \frac{2}{r^2}\frac{\sin\varphi}{\cos^2\varphi}\frac{\partial A_{\varphi}}{\partial\lambda}\right]\boldsymbol{e}_{\lambda} \\ & + \left[\nabla^2 A_{\varphi} - \frac{A_{\varphi}}{r^2\cos^2\varphi} + \frac{2}{r^2}\frac{\partial A_r}{\partial\varphi} - \frac{2}{r^2}\frac{\sin\varphi}{\cos^2\varphi}\frac{\partial A_{\lambda}}{\partial\lambda}\right]\boldsymbol{e}_{\varphi} \\ & \left[\nabla^2 A_r - \frac{2}{r^2}A_r - \frac{2}{r^2\cos\varphi}\frac{\partial}{\partial\varphi}(\sin\varphi A_{\varphi}) - \frac{2}{r^2\cos\varphi}\frac{\partial A_{\lambda}}{\partial\lambda}\right]\boldsymbol{e}_{r}\end{aligned} \tag{E.5}$$

Cylindrical Coordinates (r, ϕ, z)

$$\nabla\psi = \frac{\partial\psi}{\partial r}\boldsymbol{e}_r + \frac{1}{r}\frac{\partial\psi}{\partial\phi}\boldsymbol{e}_{\varphi} + \frac{\partial\psi}{\partial z}\boldsymbol{e}_z \tag{E.6}$$

$$\nabla\cdot\boldsymbol{A} = \frac{1}{r}\frac{\partial}{\partial r}(rA_r) + \frac{1}{r}\frac{\partial A_{\phi}}{\partial\phi} + \frac{\partial A_z}{\partial z} \tag{E.7}$$

$$\nabla \times \boldsymbol{A} = \left(\frac{1}{r}\frac{\partial A_z}{\partial \phi} - \frac{\partial A_\phi}{\partial z}\right)\boldsymbol{e}_r + \left(\frac{\partial A_r}{\partial z} - \frac{\partial A_z}{\partial r}\right)\boldsymbol{e}_\varphi + \left(\frac{1}{r}\frac{\partial (rA_\phi)}{\partial r} - \frac{1}{r}\frac{\partial A_r}{\partial \phi}\right)\boldsymbol{e}_z \quad (E.8)$$

$$\nabla^2 \psi = \frac{1}{r}\frac{\partial}{\partial r}\left(r\frac{\partial \psi}{\partial r}\right) + \frac{1}{r^2}\frac{\partial^2 \psi}{\partial \phi^2} + \frac{\partial^2 \psi}{\partial z^2} \quad (E.9)$$

$$\nabla^2 \boldsymbol{A} = \left[\nabla^2 A_r - \frac{A_r}{r^2} - \frac{2}{r^2}\frac{\partial A_\phi}{\partial \phi}\right]\boldsymbol{e}_r + \left[\nabla^2 A_\phi - \frac{A_\phi}{r^2} + \frac{2}{r^2}\frac{\partial A_r}{\partial \phi}\right]\boldsymbol{e}_\varphi + \nabla^2 A_z \boldsymbol{e}_z \quad (E.10)$$

Appendix F: Pseudo-adiabatic chart

Adiabats (blue-solid), which are characterized by constant values of potential temperature θ; pseudo-adiabats (red-dashed), which are characterized by constant values of equivalent potential temperature θ_e; and isopleths of saturation mixing ratio with respect to water r_w (green), all as functions of temperature and pressure with the ordinate proportional to $\left(\frac{p_0}{p}\right)^{\kappa}$. See color plate section: Plate 35.

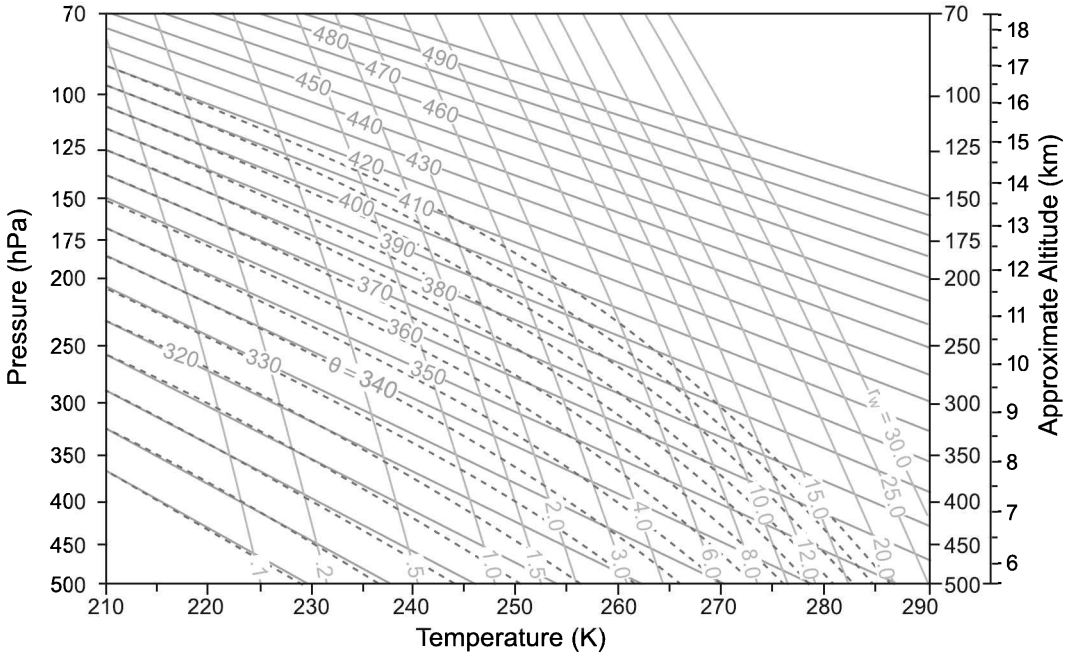
Pressure (hPa)
Temperature (K)
Approximate Altitude (km)
70
100
125
150
175
200
250
300
350
400
450
500
210
220
230
240
250
260
270
280
290
480
470
490
460
450
440
430
420
410
400
390
380
370
360
350
θ = 340
330
320
r_w = 30.0
25.0
20.0
15.0
12.0
10.0
8.0
6.0
4.0
3.0
2.0
1.5
1.0
.5
.2
.1
18
17
16
15
14
13
12
11
10
9
8
7
6

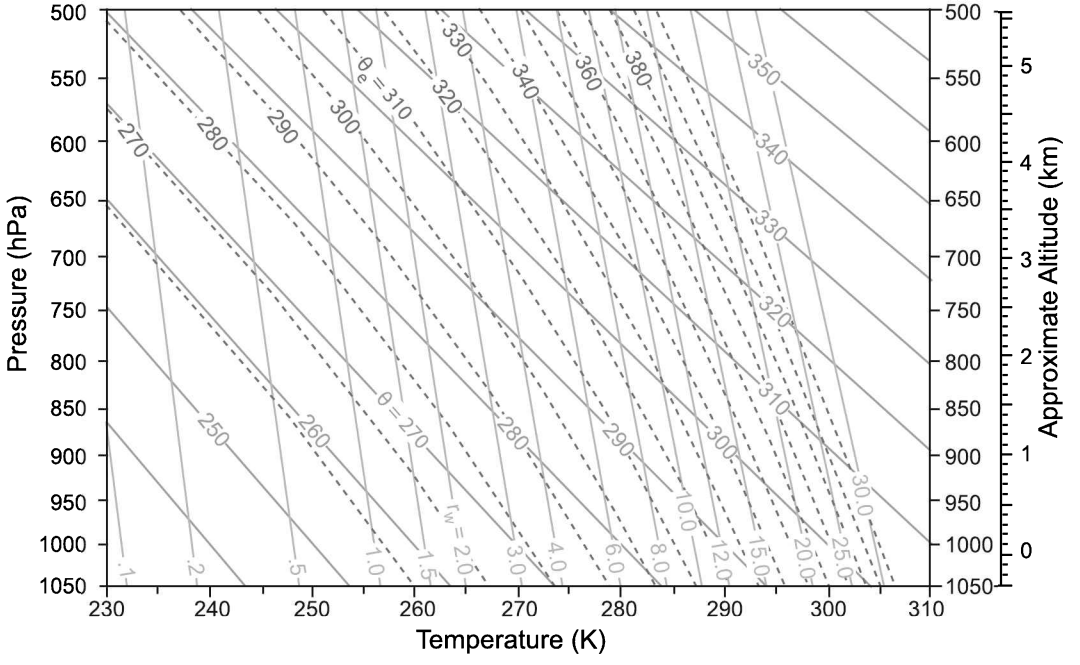
Pressure (hPa)
Temperature (K)
Approximate Altitude (km)
500
550
600
650
700
750
800
850
900
950
1000
1050
230
240
250
260
270
280
290
300
310
330
320
θe = 310
340
360
380
350
340
330
320
310
300
290
280
270
θ = 270
260
250
r_w = 2.0
30.0
25.0
20.0
15.0
12.0
10.0
8.0
6.0
4.0
3.0
2.0
1.5
1.0
.5
.2
.1
5
4
3
2
1
0

Appendix G: Acronyms

AAO	Antarctic Oscillation
AO	Arctic Oscillation
CAPE	Convective Available Potential Energy
CFC	Chlorofluorocarbon
DU	Dobson Units
EESC	Equivalent Effective Stratospheric Chlorine
ENSO	El Nino Southern Oscillation
EOF	Empirical Orthogonal Function
EP Flux	Eliassen-Palm Flux
ERBE	Earth Radiation Budget Experiment
GCM	Global Climate Model
GMT	Global Mean Temperature
HFC	Hydrofluorocarbon
IPCC	Intergovernmental Panel on Climate Change
IR	Infrared
ITCZ	Inter-Tropical Convergence Zone
LW	LongWave
LCL	Lifting Condensation Level
LFC	Level of Free Convection
LNB	Level of Neutral Buoyancy
MSU	Microwave Sounding Unit
MJO	Madden-Julian Oscillation
NAO	North Atlantic Oscillation
OLR	Outgoing Longwave Radiation
PDO	Pacific Decadal Oscillation
PL	Penetration Level
PNA	Pacific North America (pattern)
PSC	Polar Stratospheric Cloud

QBO	Quasi-Biennial Oscillation
RH	Relative Humidity
SLP	Sea Level Pressure
SST	Sea Surface Temperature
SOI	Southern Oscillation Index
SW	ShortWave
TOA	Top Of Atmosphere
UT	Universal Time (Local time at Greenwich England)
UV	Ultraviolet
WKB	Slowly Varying (short-wavelength) approximation, due to Wentzel, Kramers, and Brillouin
WMO	World Meteorological Organization

Answers to Selected Problems

CHAPTER 1

2. $\frac{V_i}{V_d} = \frac{r_i}{\epsilon_i}$.
3. $\frac{V_i}{V_d} = \frac{n_i}{n_d}$.
6. (a) $N_{H_2O} = 0.0231$, (b) $\overline{M} = 28.71$ g mol^{-1}, (c) $\overline{R} = 289.58$ J kg^{-1} K^{-1}, (d) $\rho_{H_2O} = 0.0173$ kg m^{-3}, (e) $r_{H_2O} = 0.0147$, (f) $\frac{V_i}{V_d} = 0.0236$.
8. $\Sigma_{H_2O} = \frac{1000}{\rho_w} \int_0^\infty r_{H_2O} \rho_d dz$ (mm).
9. (a) 47 mm, (b) 9.7 mm.
12. $\Delta T_e = 4.4$ K.
13. (a) 0.
15. $T(z) = \frac{gh^2}{2Rz}\left[1 + \left(\frac{z}{h}\right)^2\right]$.
16. 236 K.

CHAPTER 2

1. (a) 5 km, (b) 0.9 km.
2. (a) $\theta_{950} = 30$ C.
3. (a) 3.06 10^3 J, (b) 3.10 10^3 J, (c) 4.06 10^4 J.
6. 15.85.

CHAPTER 3

1. (a) 298 K, (b) -6.3 J K^{-1}, (c) 7.05 J K^{-1}, (d) 0.75 J K^{-1}.
2. (a) -20.7 J K^{-1}, (b) 21.5 J K^{-1}.
3. 0.90.
4. (a) 0.967.
5. (a) 277 K, (b) 285 K.
7. 199 J K^{-1} kg^{-1}.
9. (a) 1.3 10^2 J K^{-1} mol^{-1}, (b) 5.2 10^4 J mol^{-1}.

CHAPTER 4

2. (a) 95 C, (b) 86 C, (c) 71 C.
3. (a) 599 K.
4. (a) 188 K, (b) in the wintertime Antarctic stratosphere.

CHAPTER 5

1. (a) 33 C, (b) 10.2 g kg^{-1}, (c) 26%.
5. (a) 75%, (b) 25 C, (c) 325 K, (d) 770 hPa, (e) 400 K, (f) 22.5 g kg^{-1}, (g) 450 hPa.
6. 53%.
7. (a) 53%, (b) 100%.
8. (a) 20.1 C, (b) 32.6 C.
10. (e) 328 K.
11. 9 C.
12. (a) 920 hPa, (b) 610 hPa.
13. 9%.
14. (a) 5.4%, (b) 0.51 kg, (c) 7.22 10^6 J.
16. (a) 13.6 km.
17. 3.4 km.
22. (a) $T(z,t;x) = T_\infty(z - h(x-ct)) - \Gamma_d h(x-ct)$, (b) $r(z,t;x) = r_\infty(z - h(x-ct))$.
26. (d) 1.3 km.

CHAPTER 6

4. (a) $z = \frac{R}{g}\left\{(\overline{\overline{T}} + \overline{T}cos\phi)\xi - T'\left(\frac{\xi_T}{\pi}\right)e^{-\frac{\lambda^2+(\phi-\phi_0)^2}{L^2}}sin\left(\frac{\pi\xi}{\xi_T}\right)\right\}$ $(\xi < \xi_T)$; $\frac{R}{g}\left\{(\overline{\overline{T}} + \overline{T}cos\phi)\xi\right\}$ $(\xi \geq \xi_T)$.
5. 23 K.
6. (a) $z = \frac{R\overline{T}}{g}(\xi - \xi_s)\left\{1 - \frac{\xi_s\left[1-e^{\alpha(\xi_s-\xi)}\right]}{(\xi_s-\xi)}\right\}$.
8. (a) 158 m.
10. $w = -R\oint T d\ln p = -RA$.
11. $w = c_p(T_2 - T_1)\left[1 - \left(\frac{p_{34}}{p_{12}}\right)\right] > 0$.

CHAPTER 7

2. (a) unstable: $z < z_c$, stable: $z > z_c$; $z_c = h_1 ln\left(\frac{h_1}{h_2}\right)$, (b) $N^2 = g\frac{\frac{1}{h_1}e^{-\frac{z}{h_1}} - \frac{1}{h_2}}{e^{-\frac{z}{h_1}} - \frac{z}{h_2}}$.
4. 1.24 10^{-4} kg s^{-2}, (b) 5.41 10^{-4} 10^{-4} kg s^{-2}.
5. (a) $\frac{w_0}{N}$.
6. (a) $\theta = T_0\frac{a}{a+z}e^{\frac{\Gamma_d}{T_0}\left(z+\frac{z^2}{2a}\right)}$, (b) unstable: $z < z_c$, stable: $z > z_c$; $z_c = \sqrt{\frac{aT_0}{\Gamma_d}} - a$.
8. (a) $T_{trigger} = T_0 + \frac{3\Gamma_d}{2}$, (b) $\Delta t \cong 5$ hrs.
11. (a) 27 km.
12. 15 km.
15. (a) stable: $z < a$, unstable: $z > a$; (b) $\Delta z = 2a$ (exclusive of instability).
16. $\frac{d\theta_e}{dz} > 0$ (stable), $\frac{d\theta_e}{dz} = 0$ (neutral), $\frac{d\theta_e}{dz} < 0$ (unstable).
19. 57 m s^{-1}.
20. (a) $TI(z) = 4z - 20$, (b) 5 km, (c) $w_{max} = 58$ m s^{-1} at 5 km, $z_{max} = 9.5$ km.
21. (a) $K' > 0$ for $z < 9.8$ km, (b) $K' > 0$ for $z < 5.7$ km, (c) $K' > 0$ for $z < 5.3$ km.

23. $\theta_e' = 244$ K at 13 km.
24. (a) potentially unstable (stable) for $z < 1.6$ km ($z > 1.6$ km), (b) potentially unstable (stable) for $z < 4.8$ km ($z > 4.8$ km).

CHAPTER 8

1. (a) 254 K, (b) 290 K, (c) 270 K, (d) 240 K.
2. −32.4 K.
3. (a) 4.6 K.
4. (a) $u_\lambda(z) = \rho_0 rH e^{-\left(\frac{\lambda-\lambda_0}{\alpha}\right)^2 - \frac{z}{H}}$.
7. (a) 227 K.
8. (a) 95%, (b) 3.4.
9. (a) 393 K, (b) 393$\frac{1}{4}$ K.
10. (a) $T_{RE} = \left(\frac{a_{SW}}{a_{LW}}\frac{F_s}{\sigma}\right)^{\frac{1}{4}}$, (b) 278 K.
11. $T(t) = \left[0.12\sigma t + \frac{1}{T_0^3}\right]^{-\frac{1}{3}}$.
12. $\frac{2-a_{LW}^{atm}+a_{LW}^{atm}a_{LW}^{hood}}{2-a_{LW}^{atm}} a_{SW}^{hood} F_s cos\theta_s = a_{LW}^{hood}\sigma T_{hood}^4$; (a) 298 K, (b) 392 K.
13. (a) 324 K, (b) 212 K.
14. −97 K.
17. (a) 16 days, (b) 0.
18. (a) 4.6 K, (b) 17.6 K.
21. (a) $\left[a_{SW} + (1 - a_{SW})\, a_{LW}\right] F_0 \sum_{n=0}^{\infty}\left(\frac{a_{LW}}{2}\right)^n$, (b) 252 K.
22. (a) 291 K, (b) 252 K, (c) 294 K.
23. (a) 5.0 hPa, (b) 6.4 hPa.
24. (a) $F_s = F_0\frac{2}{2-a}$ $(N = 1)$, $F_0\frac{2+a}{2-a}$ $(N = 2), \ldots F_0\frac{2+(N-1)a}{2-a} = F_0\left[\frac{2}{2-a} + (N-1)\frac{a}{2-a}\right](N)$.

CHAPTER 9

1. (a) $\frac{dS}{d(loga)} = 4\pi a^2\frac{dn}{d(loga)}$, (b) $\frac{dM}{d(loga)} = \frac{4}{3}\pi a^3\rho\frac{dn}{d(loga)}$.
3. $\Delta G = \frac{16\pi\sigma^3}{3\left[n_w KT ln\left(\frac{e}{e_w}\right)\right]^2}$
4. (a) 0.60 μm, (b) 0.19 μm.
5. (a) ∼100 m.
6. (a) $w_t = \frac{2}{9}\frac{\rho_w g a^2}{\mu}$, (b) 87 μm, (c) 88 μm.
8. (a) 0.76 yrs, (b) 76 yrs.
11. (a) 0.013, (b) 0.051, (c) 0.301.
13. (a) 3.1 mm day^{-1}.
15. (a) 150 m, (b) 1500 m.
20. $cos\Theta = cos\theta\, cos\theta' + sin\theta\, sin\theta'_2 cos(\phi - \phi')$.
21. (b) $\beta_s(\pi) = \frac{64\pi^5}{\lambda^4}\frac{n}{\eta^2}a^6\left(\frac{m^2-1}{m^2+2}\right)^2$.
23. (a) $a_e = 5.7$ μm, (b) $\Sigma_l = 785$, (c) $\tau_c = 208$.
24. $\tau_c = 410$.
25. (a) (9.40), but with $C = \frac{E_-\alpha_- e^{-\gamma\tau_c^*} - E_+\alpha_+ e^{-\frac{\beta}{\mu_s}\tau_c^*} - (1-a)\alpha_+ E_-\left(e^{-\gamma\tau_c^*} - e^{-\frac{\beta}{\mu_s}\tau_c^*}\right)}{\alpha_+^2 e^{\gamma\tau_c^*} - \alpha_-^2 e^{-\gamma\tau_c^*} + (1-a)\alpha_+\alpha_-\left(e^{-\gamma\tau_c^*} - e^{\gamma\tau_c^*}\right)}$

$D = \frac{E_+\alpha_- e^{-\frac{\beta}{\mu_s}\tau_c^*} - E_-\alpha_+ e^{\gamma\tau_c^*} + (1-a)\alpha_- E_-\left(e^{\gamma\tau_c^*} - e^{-\frac{\beta}{\mu_s}\tau_c^*}\right)}{\alpha_+^2 e^{\gamma\tau_c^*} - \alpha_-^2 e^{-\gamma\tau_c^*} + (1-a)\alpha_+\alpha_-\left(e^{-\gamma\tau_c^*} - e^{\gamma\tau_c^*}\right)}$.

27. $C_{SW} = -131$ Wm^{-2}, $C_{LW} = 125$ Wm^{-2}, $C = -6$ Wm^{-2}. (b) 3.1 mm day^{-1}.

28. Strong forward scattering implies that the reduction of direct transmission is offset by an enhancement of diffuse transmission.
30. (a) $\Sigma_l = 240$ g m^{-2}, (b) $\rho_l = 0.24$ g m^{-3}.

CHAPTER 10

2. (c) For a given time interval, the deformation experienced by a material volume decreases as its dimension decreases. Letting the volume's dimension go to zero averts deformation indefinitely.
3. (a) $\frac{d\rho}{dt} = \nabla \cdot \boldsymbol{v} = 0$, (b) $\frac{d\theta}{dt} = 0$.
4. $\boldsymbol{v}$ orthogonal to $\nabla\psi$.
6. (a) 6.9°, (b) 69.3°, (c) 693°, (d) 0.019, 0.19, 1.9.

CHAPTER 11

3. (b) $w = -\frac{1}{\rho g}\omega$, (c) -19 mm/s.
6. (a) $u_g = -\frac{1}{fa}\frac{\partial\Phi}{\partial\phi}$; $v_g = \frac{1}{facos\phi}\frac{\partial\Phi}{\partial\lambda}$, (b) $u_g = -\frac{1}{fa}\frac{\partial\Psi}{\partial\phi}$; $v_g = \frac{1}{facos\phi}\frac{\partial\Psi}{\partial\lambda}$.
7. $-\frac{\partial \boldsymbol{v}_g}{dt} ln p = \frac{R}{f}\boldsymbol{k} \times \nabla_p T$.
12. $\frac{d}{dt}[(u + \Omega r cos\phi) r cos\phi] = -r cos\phi\left[\frac{1}{\rho r cos\phi}\frac{\partial p}{\partial\lambda} + D_\lambda\right]$.
15. $\frac{\partial \boldsymbol{v}_h}{dt} + f\boldsymbol{k} \times \boldsymbol{v}_h = -\nabla_\pi \Phi - \boldsymbol{D}_h$; $\frac{\partial\Phi}{\partial\pi} = -\theta$; $\frac{\partial}{\partial\pi}(\pi^{\frac{1}{\kappa}-1}\dot{\pi}) + \pi^{\frac{1}{\kappa}-1}\nabla_\pi \cdot \boldsymbol{v}_h = 0$;
$\frac{d\theta}{dt} = \frac{\dot{q}}{\pi}$; $\frac{d}{dt} = \frac{\partial}{\partial t} + \boldsymbol{v}_h \cdot \nabla_\pi + \dot{\pi}\frac{\partial}{\partial\pi}$.
16. (a) $w = \zeta h\{1 - e^{-\frac{z^*}{h}}\}$, (b) Convergence inside boundary layer must be compensated by divergence aloft.

CHAPTER 12

1. 105 m s^{-1}.
2. (a) $\boldsymbol{v} = \frac{2}{L^2}e^{-\frac{x^2+y^2}{L^2}}\{-(\Psi y + Xx)\boldsymbol{i} + (\Psi x - Xy)\boldsymbol{j}\}$, (b) $\nabla \cdot \boldsymbol{v} = \frac{4}{L^2}Xe^{-\frac{x^2+y^2}{L^2}}\left[\frac{x^2+y^2}{L^2} - 1\right]$,
(c) $\boldsymbol{k} \cdot (\nabla \times \boldsymbol{v}) = -\frac{4}{L^2}\Psi e^{-\frac{x^2+y^2}{L^2}}\left[\frac{x^2+y^2}{L^2} - 1\right]$.
3. (a) $\boldsymbol{v}_{500} = \frac{g}{f}\left\{\left[\frac{\overline{z}_{500}}{a} - \frac{2\pi y}{L^2}z'_{500}sin\left(\pi\frac{x^2+y^2}{L^2}\right)\right]\boldsymbol{i} + \left[\frac{2\pi x}{L^2}z'_{500}sin\left(\pi\frac{x^2+y^2}{L^2}\right)\right]\boldsymbol{j}\right\}$,
(c) $(\zeta + f) = \frac{g}{f}\frac{4\pi}{L^2}z'_{500}\left\{sin\left(\pi\frac{x^2+y^2}{L^2}\right) + \pi\frac{(x^2+y^2)}{L^2}cos\left(\pi\frac{x^2+y^2}{L^2}\right)\right\} + f_0$.
4. (a) 16 m s^{-1}, (b) 14.3 m s^{-1}.
5. (a) 768 m s^{-1}, (b) 45 m s^{-1}.
6. (a) 950–850: $\frac{\partial\overline{T}}{\partial x} = 0$, $\frac{\partial\overline{T}}{\partial y} = -.032$ K km^{-1}; 850–750: $\frac{\partial\overline{T}}{\partial x} = 0$, $\frac{\partial\overline{T}}{\partial y} = +.028$ K km^{-1},
(b) 950–850: 32 K day^{-1}; 850–750: -28 K day^{-1}, (c) 63 K km^{-1}.
7. $p = p_0 e^{\frac{\Omega^2 r^2}{2RT}}$.
8. (a) $\boldsymbol{v} = \pm\left(\frac{r}{L}\right)\sqrt{2\epsilon\overline{\Phi}}\boldsymbol{e}_\phi$.
9. 33°.
10. (a) $\zeta = -7.5\ 10^{-5}$ s^{-1}, (b) $\zeta = -8.3\ 10^{-5}$ s^{-1}.
11. (a) $v_\parallel = \frac{f^2 v_g}{K^2+f^2}$, $v_\perp = -\frac{fKv_g}{K^2+f^2}$ (b) $\delta = tan^{-1}\left(\frac{K}{f}\right)$, (c) 24.2°, (d) 60.7°.
12. $\nabla \cdot \boldsymbol{v}_h = -\frac{K}{K^2+f^2}\nabla^2\Phi$.
13. (b) $\zeta = \frac{2\gamma}{Y^2}e^{-\left(\frac{y}{Y}\right)^2}e^{i(kx-\sigma t)}$; $\nabla \cdot \boldsymbol{v}_h = ike^{-\left(\frac{y}{Y}\right)^2}e^{i(kx-\sigma t)}$;
(c) $\nabla^2\chi = ike^{-\left(\frac{y}{Y}\right)^2}e^{i(kx-\sigma t)}$; $\psi = \frac{i}{k}\frac{\partial\chi}{\partial y}$.
14. (a) $\frac{\partial^2 y}{\partial x^2} + \frac{\beta}{u}y = 0$, (b) $y(x) = Ae^{i\sqrt{\frac{\beta}{u}}x} + Be^{-i\sqrt{\frac{\beta}{u}}x}$.

15. (b) Solenoidal production is absent in isobaric coordinates as well, but tilting remains.

CHAPTER 13

1. (a) .003, (b) 10^8, (c) 5 10^{11}.
2. (a) 20 m s^{-1} km^{-1}, (b) 50 m s^{-1} km^{-1}.
3. 87 km for H = 7.3 km.
4. 10^5 MW (!).
6. 8.9 mm s^{-1}
7. 0.08 N m^{-2}.
8. 4.5 days.
13. (a) $K\overline{u} - f\overline{v} = 0$; $K\overline{v} + f(\overline{u} - u_g) = 0$; $K = \frac{c_d|\overline{\boldsymbol{v}}|}{h}$, (b) $\overline{\boldsymbol{v}} = \frac{u_g}{1+\frac{K^2}{f^2}}(\boldsymbol{i} + \frac{K}{f}\boldsymbol{j})$,
(c) 0.46 days.
14. (a) $\frac{\partial r_t}{\partial x} = -\frac{1}{L}(r_t - r_a)a$, (b) $r_t(x) = (r_0 - r_a)e^{-\frac{x}{L}} + r_a$; $T(x) = (T_0 - T_a)e^{-\frac{x}{L}} + T_a$,
(c) $r_i(x) = \frac{\epsilon}{p}10^{10.55 - \frac{2667}{T_0 e^{-\frac{x}{L}} + T_a}}$.
(d) Dissolution occurs at $(r_0 - r_a)e^{-\frac{x_d}{L}} + r_a = \frac{\epsilon}{p}10^{10.55 - \frac{2667}{(T_0 - T_a)e^{-\frac{x}{L}} + T_a}}$, which can be solved graphically for x_d.

CHAPTER 14

8. (a) 0.0004 hPa, (b) 5.1 m s^{-1}.
12. (a) $\boldsymbol{k} = \left(k_0^2, \frac{\sigma^2}{gH(y)} - k_0^2\right)$.
18. (a) Through divergence, the mountain acts as a vorticity source,
(b) $\frac{D}{Dt}\nabla^2\psi' + \beta\frac{\partial\psi'}{\partial x} = \frac{Q_0}{2\pi L^2}e^{-\frac{x^2+y^2}{2L^2}}$,
(c) $\psi(x, y) = \frac{1}{2\pi}\int_{-\infty}^{\infty} dk \int_{-\infty}^{\infty} dl \Psi_{kl} e^{i(kx+ly)}$;
$\Psi_{kl} = \frac{i}{k}\left(\frac{Q_0}{2\pi}\right)\frac{e^{-\frac{(k^2+l^2)L^2}{2}}}{\overline{u}(k^2+l^2)-\beta}$; $xc_{gx} + yc_{gy} > 0$, with $\boldsymbol{c}_g = \frac{2\overline{u}^2 k}{\beta}\boldsymbol{k}$.
19. (a) $\frac{1}{a^2 COS\phi}\frac{\partial}{\partial\phi}\left(cos\phi\frac{\partial\psi'}{\partial\phi}\right) + \frac{1}{\rho}\frac{\partial}{\partial z}\left(\frac{f^2}{N^2}\overline{\rho}\frac{\partial\psi'}{\partial z}\right) + \nu^2\psi' = 0$,
with
$\nu^2 = \frac{\beta_e}{\overline{u}-c} - k^2$
$\beta_e = \beta - \frac{1}{a^2 COS\phi}\frac{\partial}{\partial\phi}\left(cos\phi\frac{\partial\overline{u}}{\partial\phi}\right) - \frac{1}{\rho}\frac{\partial}{\partial z}\left(\frac{f^2}{N^2}\overline{\rho}\frac{\partial\overline{u}}{\partial z}\right)$,
(b) 74°, (c) 45°.

CHAPTER 15

1. $dh_{tot} = c_p T d ln\theta_e$.
2. −9.8 10^4 J kg^{-1}.
3. (b) 2.6 10^{21} J.
4. 0.0013.
5. 40.5 m s^{-1}.
6. (a) 6 days.
10. (b) Phase lines tilt SW - NE in the Northern Hemisphere, so that wave activity propagates equatorward with $c_{gy} < 0$.
11. (a) 2.9 m s^{-1}.
12. (a) 9.2 10^3 J kg^{-1}, (b) 7.8 10^2 J kg^{-1}, (c) 13.3 km; 4.4 km.

CHAPTER 16

1. (a) unstable (stable) equatorward (poleward) of 25°.
2. (a) positive, (b) $\phi = cos^{-1}\left(\sqrt{\frac{\epsilon(z)}{1-\frac{f^2}{N^2}a^2\frac{\partial^2\epsilon}{\partial z^2}}}\right)$.
5. $\frac{\alpha_c H}{2} = coth\left(\frac{\alpha_c H}{2}\right)$.
7. 6.1 days, 3.2 days, 2.25 days, 1.86 days, 1.71 days, 1.77 days, 2.22 days, ∞.

CHAPTER 17

1. (a) 26.7 kg/m^3, (b) 26.25 kg/m^3, (c) 26.6 kg/m^3.
2. (a) -0.560 m, (b) 155 W/m^3.
3. (a) $S_f \cong 35.2$ g/kg, (b) -3.125 m, (c) 114.5 W/m^3.
7. (a) $\boldsymbol{v}_0(x,y) = -\frac{200}{fY}\left\{\sin\left(\frac{x}{X}-\frac{y}{Y}\right)-\sin\left(\frac{x}{X}+\frac{y}{Y}\right)\right\}\boldsymbol{i} - \frac{200}{fX}\left\{\sin\left(\frac{x}{X}-\frac{y}{Y}\right)+\sin\left(\frac{x}{X}+\frac{y}{Y}\right)\right\}\boldsymbol{j}$
   (b) $\boldsymbol{M}_E = -200\cdot\frac{\rho\alpha}{f^2X}\left\{\sin\left(\frac{x}{X}-\frac{y}{Y}\right)+\sin\left(\frac{x}{X}+\frac{y}{Y}\right)\right\}\boldsymbol{i}$
   $+200\cdot\frac{\rho\alpha}{f^2Y}\left\{\sin\left(\frac{x}{X}-\frac{y}{Y}\right)-\sin\left(\frac{x}{X}+\frac{y}{Y}\right)\right\}\boldsymbol{j}$ (c) $w(-\infty) = \frac{\alpha}{\rho f}\nabla^2\psi = -\frac{\alpha}{\rho f}\left(\frac{1}{X^2}+\frac{1}{Y^2}\right)\psi$
10. (a) $M_y = -200\cdot\frac{\rho\alpha}{\beta f}\left(\frac{1}{X^2}+\frac{1}{Y^2}\right)\left\{\cos\left(\frac{x}{X}-\frac{y}{Y}\right)+\cos\left(\frac{x}{X}+\frac{y}{Y}\right)\right\}$
    $M_x = 200\cdot\frac{\rho\alpha}{\beta f}\frac{X}{Y}\left(\frac{1}{X^2}+\frac{1}{Y^2}\right)\left\{-\cos\left(\frac{x}{X}-\frac{y}{Y}\right)+\cos\left(\frac{x}{X}+\frac{y}{Y}\right)+2\sin\left(\frac{y}{Y}\right)\right\}$.

CHAPTER 18

1. $\tau_{O_3} = \frac{1}{J_3+k_3[O]}$; $\tau_{O_x} = \frac{1}{2k_3[O]}$, (a) $\tau_{O_3} = 37$ mins; $\tau_{O_x} = 32$ yrs,
   (b) $\tau_{O_3} = 21$ mins; $\tau_{O_x} = 15$ days, (c) $\tau_{O_3} = 2.4$ mins; $\tau_{O_x} = 3.8$ hrs.
4. (a) 16.4 ppmv, (b) 1.6 ppmv, (c) 3.3 ppmv.
7. 1.26 ppmv.
8. (a) $\tau_{O_x} = \frac{1}{2k_3[O]+2k_a[Cl]}$; $[O] = \frac{J_2[O_2]}{k_3[O_3]+k_b[ClO]}$, (a) 8 yrs, (b) 3.1 days.

References

Abramowitz and Stegun, 1972: *Handbook of Mathematical Functions.* Dover, New York, 1046 pp.

Ackerman, T, 1988: Aerosols in climate modeling. In *Aerosol and Climate*, P Hobbs and P McCormick eds., A. Deepak Publishing, Hampton, VA, pp. 335–348.

Adhikari and Kumon, 2001: MWP, JAPAN (wiki)

Ambaum, M, Hoskins, B, and D Stephenson, 2001: Arctic oscillation or North Atlantic oscillation? *J Climate*, **14**, 3495–3507.

Anderson, J, WH Bruce and MH Proffitt, 1989: Ozone destruction by chlorine radicals within the Antarctic vortex: The spatial and temporal evolution of $ClO - O_3$ anticorrelation based on *in situ* ER-2 data. *J Geophys Res*, **94**, 11, 465–11,479.

Andrews, D and M McIntyre, 1976: Planetary waves in horizontal and vertical shear: The generalized Eliassen-Palm relation and the mean zonal acceleration. *J Atmos Sci*, **33**, 2031–2048.

Andrews, D, 2000: *An Introduction to Atmospheric Physics.* Cambridge University Press, Cambridge, 228 pp.

Andrews, D, Holton, J, and C Leovy, 1987: *Middle Atmosphere Dynamics.* Academic Press, San Diego, 489 pp.

Antonov, J, Locarnini, R, Boyer, T, Mishonov, A, and H Garcia, 2006: *World Ocean Atlas 2005*, vol 2: Salinity, S Levitus, Ed. NOAA Atlas NESDIS 62, US Govt Printing Office, Washington, DC, 182 pp.

Araneda, A, Torrejon, F, Aguayo, M, Torres, L, Crueces, F, Cisternas, M, and R Urritia, 2007: Historical records of San Juan glacier advances: another clue to Little Ice Age timing in Southern Chile. *The Holocene*, **17**, 987–998.

Atmospheric Aerosols: Their Formation, Optical Properties, and Effects, 1982: A Deepak, Ed., Spectrum Press, Hampton, VA, 480 pp.

Aris, R, 1962: *Vectors, Tensors, and the Basic Equations of Fluid Mechanics.* Prentice Hall, Englewood Cliffs, NJ, 286 pp.

Arrhenius, S, 1896: On the influence of carbonic acid in the air upon the temperature of the ground. *Phil Mag*, **41**, 237–276.

Arrhenius, S, 1908: Das Werden der Welten. Academic Publishing House, Leipzig, 208 pp.

Bader, D, Covey, C, Gutowski, W, Held, I, Kunkel, K, Miller, R, Tokmakian, R, and M Zhang, 2008: *Climate Models: An Assessment of Strengths and Limitations.* Dept of Energy, Office of Biological and Environmental Research, Washington, DC, 124 pp.

Baldwin, M and T Dunkerton, 1999: Propagation of the Arctic Oscillation from the stratosphere to the troposphere. *J Geophys Res*, **104**, 30,937–30,946.

Baldwin, M and T Dunkerton, 2001: Stratospheric Harbingers of Anomalous Weather Regimes. *Science*, **294**, 581–584.

Battan, L, 1984: *Fundamentals of Meteorology*. Prentice Hall, Englewood Cliffs, NJ, 304 pp.

Banks, P and G Kocharts, 1973: *Aeronomy*. Academic Press, New York, 430 pp.

Barnola J, Raynaud, D, Korotkevitch, Y, and C Lorius, 1987: Vostok ice core: A 160,000 year record of atmospheric CO_2. *Nature*, **329**, 408–414.

Batchelor, G, 1977: *An Introduction to Fluid Dynamics*. Cambridge University Press, Cambridge, 615 pp.

Bauer, J, 2010: Molecular epidemiology of melanoma. *Melanoma Res*, **20**, doi: 10.1097/01.cmr.0000382758.93495.d6.

Berlage, H, 1957: Fluctuations in the general atmospheric circulation of more than one year: their nature and prognostic value. *Korte Ned Met Inst Meded Verh*, **69**, 1–152.

Bednarz, Z and J Ptak, 1990: Influence of temperature and precipitation on ring widths of oak in the Niepolomice forest near Cracow. *Tree Ring Bull*, **50**, 1–10.

Bithell, M, Gray, L, Harries, J, Russell, J, and A Tuck, 1994: Synoptic interpretation of measurements from HALOE. *J Atmos Sci*, **51**, 2942–2956.

Bleck, R, 1978a: Finite difference equations in generalized vertical coordinates. Part I: Total energy conservation. *Beiträge zur Physik der Atmosphäre*, **51**, 360–372.

Bleck, R, 1978b: Finite difference equations in generalized vertical coordinates. Part II: Potential vorticity conservation. *Beiträge zur Physik der Atmosphäre*, **52**, 95–105.

Bourke, W, 1974: A multi-level spectral model. I. Formulation and hemispheric integrations. *Mon Wea Rev*, **102**, 687–701.

Boyce, D, Lewis, M, and B Worm, 2010: Global phytoplankton decline over the past century. *Nature*, **466**, 591–596.

Branstator, G, 2002: Circumpolar teleconnections, the jet stream waveguide, and the north atlantic oscillation. *J Climate*, **15**, 1893–1910.

Brasseur, G and S Solomon, 1986: *Aeronomy of the Middle Atmosphere*. Reidel, Dordrecht, 2nd ed. 452 pp.

Brewer, A, 1949: Evidence for a world circulation provided by the measurements of helium and water vapor distributions in the stratosphere. *Quart J Roy Met Soc*, **75**, 351.

Briffa, K, 2000: Annual climate variability in the holocene: Interpreting the message of ancient trees. *Quaternary Sci Revs*, **19**, 87–105.

Brillouin, L, 1926: Remarques sur la mecanique ondulatoire. *J Phys Radium*, **7**, 353–368.

Broecker, W, 2000: Was a change in the thermohaline circulation responsible for the Little Ice Age? *Proc NAS*, 97, 1339–1342.

Callaghan, P, Fusco, A, Francis, G, and Salby, M, 1999: A Hough spectral model for 3-dimensional studies of the middle atmosphere. *J Atmos Sci*, **56** 1461–1480.

Carlson, T and S Benjamin, 1982: Radiative heating rates for a desert aerosol (Saharan dust). In *Atmospheric Aerosols: Their Formation, Optical Properties and Effects*, A. Deepak, Ed., Spectrum Press, Hampton, VA, pp. 435–457.

Cascinelu, N and R Marchesini, 2008: Increasing incidence of cutaneous melanoma, ultraviolet radiation, and the clnincian. *Photochem and Photobiol*, doi: 10.1111/1751-1097.1989tb05555.

Cess, R, 1976: Climate change: An appraisal of atmospheric feedback mechanism employing zonal climatology. *J Atmos Sci*, **33**, 1831–1843.

Chapman, S, 1930: On ozone and atomic oxygen in the upper atmosphere. *Phil Mag*, **10**, 369–383.

Charney, J, 1947: The dynamics of long waves in a baroclinic westerly current. *J Meteorol*, **4**, 135–163.

Charney, J, Fjortoft, R, and J von Neumann, 1950: Numerical integration of the barotropic vorticity equation. *Tellus*, **2**, 237–254.

Charney, J, 1973: Planetary fluid mechanics. In *Dynamical Meteorology*, P. Morel ed., Reidel, Dordrecht, 97–351.

Charney J and P Drazin, 1961: Propagation of planetary scale disturbances from the lower into the upper atmosphere. *J Geophys Res*, **66**, 83–109.

Charney J and M Stern, 1962: On the stability of internal baroclinic jets in a rotating atmosphere. *J Atmos Sci*, **19**, 159–172.

Christy, J Spencer, R, and D Braswell, 2000: MSU tropospheric temperatures: Dataset construction and radiosonde comparisons. *J Atmos Ocean Tech*, **17**, 1153–1170.

Cook, E, Palmer, J, and R D'Arrigo, 2002: Evidence for a 'Medieval Warm Period' in a 1100 year tree-ring reconstruction of past austral summer temperatures in New Zealand. *Geophys Res Lett*, **29**, doi: 10.1029/2001GL014580.

Collmore, C, Martin, D, and M Hitchman, 2003: On the relationship between the QBO and tropical deep convection. *J Climate*, **16**, 2552–2568.

Coughlin, K, and KK Tung, 2001: QBO signal found at the extratropical surface through northern annular modes. *Geophys Res Lett*, **28**, 4563–4566.

Coulson, K, 1975: *Solar and Terrestrial Radiation.* Academic Press, New York, 322 pp.

Cox, S, 1981: Radiation characteristics of clouds in the solar spectrum. In *Clouds: Their formation, Optical Properties, and Effects*, P Hobbs and A Deepak, Eds., Academic Press, New York, 241–280.

Crooks, S and L Gray, 2005: Characteristics of the 11-yr solar signal using a multiple regression analysis of the ERA-40 dataset. *J Clim*, **18**, 996–1015.

Danielsen, E, 1982: A dehydration mechanism for the stratosphere. *Geophys Res Lett*, **9**, 605–608.

Denbigh, K, 1971: *The Principles of Chemical Equilibrium.* Cambridge University Press, London, 494 pp.

Deser, C, 2000: On the teleconnectivity of the "Arctic Oscillation." *Geophys Res Lett*, **27**, 779–782.

DeWeaver E and S Nigam, 2004: On the forcing of ENSO teleconnections by anomalous heating and cooling. *J Clim*, **17**, 3225–3235.

Dickinson, R, 1968: Planetary Rossby waves propagating through weak westerly wind wave guides. *J Atmos Sci*, **25**, 984–1002.

Dickinson, R, 1970: Development of a Rossby wave critical level. *J Atmos Sci*, **27**, 627–633.

Dickinson, RE, 1973: Baroclinic instability of an unbounded zonal shear flow in a compressible atmosphere. *J Atmos Sci*, **30**, 1520–1527.

Dietrich, G, Kalle, K, Krauss, W, and G Siedler, 1980: *General Oceanography*, 2nd ed, Wiley-Interscience, New York.

Dikii, L, 1968: The terrestrial atmosphere as an oscillating system. *Izv Acad Sci USSR Atmos Oceanic Phys*, Engl. Transl., **1**, 469–489.

Dobson, G, 1930: Observations of the amount of ozone in the Earth's atmosphere and its relation to other geophysical conditions. *Proc Roy Soc London, Sec A*, **129**, 411–433.

Donner, L, Schubert, W, and R Somerville, 2010: *The Development of Atmospheric General Circulation Models.* Donner, L, Schubert, W, and R Somerville, Eds. Cambridge University Press, Cambridge, UK, 255 pp.

Douglas, B, 1997: Global sea rise: A redetermination. *Surveys in Geophysics*, **18**, 279–292.

Dowling, D, Radke, RR, and F Lawrence, 1990: A summary of the physical properties of cirrus clouds. *J Applied Meteorology*, **29** 970–978.

Drazin, P and W Reid, 1985: *Hydrodynamic Instability.* Cambridge University Press, Cambridge, 527 pp.

Dutton, J, 1986: *The Ceaseless Wind.* Dover, New York, 617 pp.

Eady, E, 1949: Long waves and cyclone waves. *Tellus*, **1**, 33–52.

Easterling, D, Horton, B, Jones, P, Peterson, T, Karl, T, Parker, D, Salinger, MJ, Raxuvayev, V, Plummer, N, Jamason, P, and C Folland, 1997: Maximum and minimum temperature trends for the globe. *Science*, **277**, 364–367.

Eckart, C, 1960: *Hydrodynamics of Oceans and Atmospheres.* Pergamon, New York, 290 pp.

Eisberg, R, 1967: *Fundamentals of Modern Physics.* John Wiley, New York, 729 pp.

Elsasser, W, 1938: Mean absorption and equivalent absorption coefficient of a band spectrum. *Phys Rev*, **54**, 126–129.

Ertel, 1942: Ein neuer hydrodynamischer Wirbelsatz. *Meteorol Z*, **59**, 271–281.

Etheridge, D, Steele, L, Langenfelds, R, Francey, R, Barnola, J, and V Morgan, 1996: Natural and anthropogenic changes in atmospheric CO_2 over the last 1000 years from air in Antarctic ice and firn. *J Geophys Res*, **101**, 4115–4128.

Fels, S, 1982: A parameterization of scale-dependent radiative damping rates in the middle atmosphere. *J Atmos Sci*, **39**, 1141–1152.

Fels, S, 1985: Radiative-dynamical interactions in the middle atmosphere. *Adv Geophys*, **28A**, 277–300.

Fischer, H, Wahlen, M, Smith, J, Mastrioianm̀, D, and B Deck, 1999: Ice core records of atmospheric CO_2 arouind the last three glacial terminations. *Science*, **283**, 1712–1714.

Fleming, E, Chandra, S, Schoeberl, M, and J Barnett, 1988: Montly-Mean Climatology of Temperature, Wind, Geopotential Height, and Pressure for 0–120 km. NASA TM-100697. Available from NASA Goddard Space Flight Center, Greenbelt, MD.

Friedli, H, Lotscher, H, Oeschger, H, Siegenthaler, U, and B Stauffer, 1986: Ice core record of the $^{13}C/^{12}C$ ratiio of atmospheric CO_2 in the past two centuries. *Nature*, **324**, 237–238.

Fujita, T, 1992: *The Mystery of Severe Storms*. WRL Research Paper No. 239, NTIS No. PB 92-182021, 298 pp.

Frederiksen, J, 2006: Instability of waves and zonal flows in two-layer models on a sphere. *Quart J Roy Meteoral Soc*, **104**, 841–872.

Francis, G and M Salby, 2001: Radiative influence of Antarctica on the polar night vortex. *J Atmos Sci*, **58**, 1300–1309.

Francois, R, Altabet, M, and R Goericke, 1993: Changes in the $\delta^{13}C$ of surface water particulate organic matter across the subtropical convergence inthe SW Indian Ocean. *Global Biological Cycles*, **7**, 627–644.

Fusco, A and M Salby, 1994: Relationship between horizontal eddy motions and mean meridional motions in the stratosphere. *J Geophys Res*, **99**, 20,633–20,695.

Gage, K, McAfee, J, Carter, D, Ecklund, W, Riddle, A, Reid, G, and B Balsley, 1991: Long-term vertical motion over the tropical Pacific: Wind profiling Doppler measurements. *Science*, **254**, 1771–1773.

Garcia, R, 1994: Causes of ozone depletion. *Physics World*, **7**, 49–55.

Garcia, R and M Salby, 1987: Transient response to localized episodic heating in the tropics. Part II: Far-field behavior. *J Atmos Sci*, **44**, 499–530.

Garcia, R and S Solomon, 1983: A numerical model of zonally-averaged dynamical and chemical structure of the middle atmosphere. *J Geophys Res*, **88**, 1379–1400.

Garcia, R and S Solomon, 1987: A possible interaction between interannual variability in Antarctic ozone and the quasi-biennial oscillation. *Geophys Res Lett*, **14**, 848–851.

Garrison, T, 2007: *Oceanography: Invitation to Marine Science*, 6th ed. Brooks Cole, Belmont, CA, 588 pp.

Geisler, J and R Dickinson, 1974: A numerical study of an interacting Rossby wave and barotropic zonal flow near a critical level. *J Atmos Sci*, **31**, 946–955.

Gill, A, 1980: Some simple solutions for heat-induced tropical circulation. *Quart J Roy Meteorol Soc*, **106**, 447–462.

Gill, A, 1982: *Atmosphere-Ocean Dynamics*. Academic Press, San Diego, 662 pp.

Goericke, R and B Fry, 1994: Variations of marine plankton $\delta^{13}C$ with latitude, temperature, and dissolved CO_2 in the world ocean. *Global Biol Cycles*, **8**, 85–90.

Gong, D and S Wang, 1999: Definition of the Antarctic Oscillaton. *Geophys Res Lett*, **26**, 459–462.

Goodridge, J, 1996: Comments on "Regional simulations of greenhouse warming including natural variability." *Bull Am Meteorol Soc*, **77**, 1588–1589.

Goody, R., 1952: A statistical model for water vapor absorption. *Quart Roy Meteorol Soc*, **78**, 165–169.

Goody, R and Y Yung, 1995: *Atmospheric Radiation: Theoretical Basis.* Oxford U Press, 544 pp.

Goody, R, West, R, Chen, L, and D Crisp, 1989: The correlated-k method for radiation calculations in nonhomogeneous atmospheres. *J Quant Spectroscopy and Radiative Transfer*, **42**, 539–550.

Gray, L, S Crooks, Pascoe, C, and S Sparrow, 2004: Solar and QBO influences on the timings of stratosphseric sudden warmings. *J Atmos Sci*, **61**, 2777–2796.

Grove, J and R Switsur, 1994: Glacial geological evidence for the medieval warm period. *Climate Change*, **26**, 143–169.

Gossard, E, and W Hooke, 1975: *Waves in the Atmosphere.* Elsevier, Amsterdam, 456 pp.

Green, G, 1838: On the motion of waves in variable canal of small depth and width. *Trans Cambridge Philos Soc*, in Mathematical Papers (1871), Macmillan, London, 223–230.

Greenspan, H, 1968: *Theory of Rotating Fluids.* Cambridge University Press, London, 327 pp.

Gruber, C and L Haimberger, 2008: On the homogeneity of radiosonde wind time series. *Meteorol Zeit*, **17**, 631–643.

Hall, B and G Denton, 2002: Holocene history of the Wilson Piedmont Glacier along the southern Scott Coast, Antarctica. *The Holocene*, **12**, 619–627.

Haltiner, G and R Williams, 1980: *Numerical Prediction and Dynamic Meteorology.* Wiley, New York, 477 pp.

Handbook of Geophysics and Space Environment, 1965: S. Valley, Ed., Air Force Cambridge Research Laboratory, Hanscom AFB, Mass., 692 pp.

Hansen, J and L Travis, 1974: Light scattering in planetary atmospheres. *Space Sci Rev*, **16**, 527–610.

Hartmann, D, 1993: The radiative effect of clouds on climate. In *Aerosol-Cloud-Climate Interactions*, P Hobbs, Ed., Academic Press, New York, 151–170.

Hartmann, D, 1994: *Global Physical Climatology.* Academic Press, San Diego, 408 pp.

Hartmann, D, Ramanathan, V, Berroir, A, and G Hunt, 1986: Earth radiation budget data and climate research. *Rev Geophys*, **24**, 439–468.

Hartmann, D and D Doelling, 1991: On the net radiative effectiveness of clouds. *J Geophys Res*, **96**, 869–891.

Hasebe, F, 1983: Interannual variations of global total ozone revealed from Nimbus 4 BUV and ground based observations. *J Geophys Res*, **88**, 6819–6834.

Hendon, H and M Salby, 1994: The life cycle of the Madden-Julian Oscillation. *J Atmos Sci*, **51**, 2225–2237.

Hendon, H and K Woodberry, 1993: The diurnal cycle of tropical convection. *J Geophys Res*, **98**, 16623–16637.

Hendon, H, Thompson, D, and M Wheeler, 2007: Australian rainfall and surface temperature variations associated with the southern annular mode. *J Clim*, **20**, 2452–2467.

Herzberg, G, 1945: *Molecular Spectra and Molecular Structure. II: Infrared and Raman Spectra of Polyatomic Molecules.* Nan Nostrand, New York, 616 pp.

Herzberg, L, 1965: In *Physics of the Earth's Upper Atmosphere*, C Hines, I Paghis, T Hartz, and J Fejer, Eds. Prentice Hall, Englewood Cliffs, 31–45.

Hering, W and T Borden, 1965: Ozone sonde observations over North America, vol. 3, AFCRL Report AFCRL-64-30. Air Force Cambridge Research Laboratories, Bedford, MA.

Hess, P and J Holton, 1985: The origin of temporal variance in long-lived trace constituents in the summer stratosphere. *J Atmos Sci*, **42**, 1455–1463.

Hide, R, 1966: On the dynamics of rotating fluids and related topics in geophysical fluid dynamics. *Bull Amer Meteorol Soc*, **47**, 873–885.

Holton, 1984: Troposphere-stratosphere exchange of trace constituents: The water vapor puzzle. In *Dynamics of the Middle Atmosphere*, J. Holton and T. Matsuno, Eds., Terrapub, Tokyo, 369–385.

Holton, J, 1986: Meridional distribution of stratospheric trace species. *J Atmos Sci*, **43**, 1238–1242.

Holton, J, 1990: On the global exchange of mass between the stratosphere and troposphere. *J Atmos Sci*, **47**, 392–395.

Holton, J, 2004: *An Introduction to Dynamic Meteorology*, 4th ed. Academic Press, San Diego, 535 pp.

Holton, J and R Lindzen, 1972: An updated theory for the quasi-bienmial cycle of the tropical stratosphere. *J Atmos Sci*, **29**, 1076–1080.

Holton, J, Haynes, P, McIntyre, M, Douglass, A, Rood, R, and L Pfister, 1995: Stratosphere-troposphere exchange. *Rev Geophys*, **33**, 403–439.

Holton, J and HC Tan, 1980: The influence of the equatorial quasi-biennial oscillation on the global circulation at 50 mb. *J Atmos Sci*, **37**, 2200–2208.

Hoffman, D, 1988: Aerosols from past and present volcanic emissions. In *Aerosol and Climate*, P Hobbs and P McCormick, Eds., A Deepak Publishing, Hampton, VA, 195–214.

Hoffman, D and S Solomon, 1989: Ozone destruction through heterogeneous chemistry following the eruption of El Chichon. *J Geophys Res*, **94**, 5029–5041.

Horel, J and J Wallace, 1981: Planetary scale atmospheric phenomena associated with the inter-annual variability of sea-surface temperature in the equatorial Pacific. *Mon Wea Rev*, **109**, 813–829.

Horowitz, L, Walters, S, Mauzerall, D, Emmons, L, Rasch, P, Granier, C, Tie, X, Lamarque, J, Schultz, M, Tyndall, G, Orlando, J, and G Brasseur, 2003: A global simulation of tropospheric ozone and related tracers: Description and evaluation of Mozart version 2. *J Geophys Res*, **208**, 4784 doi:10.1029/2002JD002853.

Hoskins, B, 1982: A mathematical theory of frontogenesis. *Annu Rev Fluid Mech*, **14**, 131–151.

Hoskins, B, McIntyre, M, and A Robertson, 1985: On the use and significance of isentropic potential vorticity maps. *Quart J Roy Meteorol Soc*, **111**, 877–946.

Hoskins, B and D Karoly, 1981: The steady linear response of a spherical atmosphere to thermal and orographic forcing. *J Atmos Sci*, **38**, 1179–1196.

Houze, RA, 1982: Cloud clusters and large-scale vertical motions in the tropics. *J Meteorol Soc Jpn*, **60**, 396–410.

Houze, R, 1993: *Cloud Dynamics*. Academic Press, San Diego, 573 pp.

Huang, S and H Pollack, 1997: Late quaternary temperature changes seen in world-wide continental heat flow measurements. *Geophys Res Lett*, **24**, 1947–1950.

Huck, P, McDonald, A, Bodeker, G, and H Struthers, 2005: Interannaual variability in Antarctic ozone depletion controlled by planetary waves and polar temperature. *Geophys Res Lett*, **32**, L13819, doi:10.1029/2005GL022943.

Huesmann, A and M Hitchmann, 2003: Th 1978 shift in the NCEP reanalysis stratospheric quasi-biennial oscillation. *Geophys Res Lett*, **30**, 1048. doi:10.1029/2002GL016323.

Humphreys, W, 1964: *Physics of the Air*. Dover, New York, 661 pp.

Hurrell, J, Kushnir, Y, Ottersen, G, and M Visbeck, 1996: An overview of the North Atlantic Oscillation. In *The North Atlantic Oscillation: Climatic Signficance and Environmental Impact*. Geophysical Monograph 134, American Geophysical Union, 10.1029/134GM01.

Indemuhle, A, Monnin, E, Stauffer, B, and T Stocker, 2000: Atmospheric CO_2 concentration from 60 to 20 kyr BP fromthe Taylor Dome ice core, Antarctica. *Geophys Res Lett*, **27**, 735–738.

IPCC, 1990: *Climate Change. Intergovernmental Panel on Climate Change*. J Houghton, G Jenkins, and J Ephraums, Eds. Cambridge University Press, Cambridge, 365 pp.

IPCC, 2007: *Intergovernmental Panel on Climate Change. Climate Change 2007: The Physical Science Basis*. Cambridge University Press, Cambridge, 1008. pp.

Iribarne, J and W Godson, 1981: *Atmospheric Thermodynamics*. Reidel, Dordrecht, 259 pp.

Jackson, J, 1975: *Classical Electrodynamics*. Wiley, New York, 848 pp.

James, I, 1993: *Introduction to Circulating Atmospheres*. Cambridge University Press, New York, 422 pp.

Jensen et al, 2004: Ice supersaturations exceeding 100% at the cold tropical tropopause: Implications for cirrus formation and deydration. *Atmos Chem Phys*, **4**, 7433–7462.

Jin, F and B Hoskins, 1995: The direct response to tropical heating in a baroclinic atmosphere. *J Atmos Sci*, **52**, 307–319.

Johnson, R and D Kriete, 1982: Thermodynamic circulation characteristics of winter monsoon tropical mesoscale convection. *Mon Wea Rev*, **110**, 1898–1911.

Jones J and M Widman, 2004: Early peak in Antarctic oscillation index. *Nature*, **432**, 290–291.

Jouzel, J, Waelbroeck, B, Malaize, M, Bender, J, Petit, M, Stievenard, N, Barkov, J, Barnola, T, Kink, V, Kotlyakov, V, Lipenkov, V, Lorius, C, Raynaud,D, Ritz, Z, and T Sowers, 1995: Climatic interpretation of the recently extended Vostok ice records. *Climate Dynamics*, **12**, 513–521.

Kallberg, P, Berrisford, P, Hoskins, B, Simmons, A, Uppala, S, Lamy-Th'epaut, S, and R Hine, 2005: ERA-40 Atlas ERA-40 Project Report Series No 17. European Centre for Medium Range Weather Forcasting, Reading.

Keigwin, L, 1996: The Little Ice Age and Medieval Warm Period in the Sargasso Sea. *Science*, **274**, 1504–1508.

Kelly, K, Proffitt, M, Chan, K, Lowenstein, M, Podolske, J, Strahan, S, Wilson, J, and D Kley, 1993: Water vapor and cloud water measurements over Darwin during the STEP 1987 tropical mission. *J Geophys Res*, **98**, 8713–8723.

Kent, G and P McCormick, 1984: SAGE and SAM II measurements of global stratospheric aerosol optical depth and mass loading. *J Geophys Res*, **89**, 5303–5314.

Kiehl, J, and S Solomon, 1986: On the radiative balance of the stratosphere. *J Atmos Sci*, *43*, 1525–1534.

Kiehl, J, 1993: Atmospheric general circulation modeling. In *Climate System Modeling*. Cambridge University Press, Cambridge, 818 pp.

Kocharts, G, 1971: Penetration of solar radiation in the Schumann-Runge bands of molecular oxygen. In *Mesospheric Models and Related Experiments*, G Fiocco, Ed., Reidel, Dordrecht, 160–176.

Kodera, K and Y Kuroda, 2002: Dynamical response to the solar cycle: Winter stratopause and lower stratosphere. *J Geophys Res*, **107**, 4749.

Koschmieder, E and S Pallas, 1974: Heat transfer through a shallow horizontal convecting fluid layer. *Int J Heat Mass Transfer*, **17**, 991–1002.

Keeling, C, Bacastow, R, Carter, A, Piper, S, Whorf, T, Heimann, M, Mook, W, and H Rheloffzen, 1989: A three dimensional model of atmospheric *CO*2 based on observed winds: 1. Analysis of observational data. *Aspects of Climate Variability in the Western Pacific and Western Americas*, D Peterson, Ed., *Geophysical Monographs*, **55**, American Geophysical Union, Washington, DC, 165–236.

Keenan, J, 1970: *Thermodynamics*. MIT Press, Cambridge, 507 pp.

Kelvin, Lord, 1880: On a disturbing infinity in Lord Rayleigh's solution for waves in a plane vortex stratum. *Nature*, **23**, 45–46.

Knollenberg, RG, K Kelly, and JC Wilson, 1993: Measurements of measurements of number densities of ice crystals in the tops of tropical cumulonimbus. *J Geophys Res*, **98**, 8639–8664.

Kramer, H, 1926: Wellenmechanik und halbzhalige Quantisierung. *Z Phys*, **39**, 828–840.

Kramer et al, 2009: Ice supersaturations and cirrus cloud crystal numbers. *Atmos Chem Phys*, **9**, 3505–3522.

Kreutz, K, Mayewski, P, Meeker, L, Twickler, M, Whitlow, S, and I Pittalwala, 1997: Bipolar changes in atmospheric circulation during the Little Ice Age. *Science*, **277**, 1294–1296.

Krueger, A, 1973: The mean ozone distributions from several series of rocket soundings to 52 km at latitudes from 58 S to 64 N. *Pure Appl Geophys*, **106–108**, 1272–1280.

Lamb, H, 1965: Paleogeography, Paleoclimatology, Paleoecology. 1, 13–37.

Labitzke, K, 1982: On interannual variability of the middle stratosphere during northern winters. *J Meteorol Soc Japan*, **60**, 124–139.

Labitzke, K and H van Loon, 1988: Association between the 11-yr solar cycle, the QBO, and the atmosphere. *J Atmos Terr Phys*, **50**, 197–206.

Labitzke K, 2005: On the solar cycle - QBO relationship: A summary. *J Atmos Sol Terr Phys*, **67**, 45-54.

Lait, L, Schoeberl, M, and P Newman, 1989: Quasi-biennial modulation of Antarctic ozone depletion. *J Geophys Res*, **94**, 11559-11571.

Landau, X and Y Lifshitz, 1980: *Statistical Physics*, 3rd ed., Part 1. Buttenworth-Heinamann, Oxford, 544 pp.

Lamb, H, 1910: On atmospheric oscillations. *Proc Roy Soc London*, **84**, 551-572.

Lejenas, H and Okland, 1983: Characteristics of Northern Hemisphere blocking as determined from a ong time series of observational data. *Tellus*, **35A**, 350-362.

Lejenas, H and R Madden, 1992: Travelling planetary-scale waves and blocking. *Mon Wea Rev*, **120**, 2821-2830.

Lorius, et al, 1985: A 150,000 year climatic record from Antarctic ice. *Nature*, **316**, 591-596.

Lau, N, 1984: *Circulation Statistics Based on FGGE Level III-B Analyses.* NOAA Data Report ERL GFDL-5. NOAA Environmental Research Laboratories, Boulder CO.

Lee, J, Sears, F, and D Turcotte, 1973: *Statistical Thermodynamics.* Addison-Wesley, Reading, 371 pp.

Lighthill, J, 1978: *Waves in Fluids.* Cambridge University Press, Cambridge, 504 pp.

Lindzen, R and J Holton, 1968: A theory of the quasi-biennial oscillation. *J Atmos Sci*, **25**, 1095-1107.

Lindzen, R and Y Choi, 2009: On the determination of climate feedbacks from ERBE data. *Geophys Res Lett*, **36**, doi: 10.1029/2009GL039628.

Lilly, D, 1978: A severe downslope windstorm and aircraft turbulence event induced by a mountain wave. *J Atmos Sci*, **35**, 59-77.

Liou, K, 1980: *An Introduction to Atmospheric Radiation.* Academic Press, San Diego, 392 pp.

Liou, K, 1990: *Radiation and Cloud Processes in the Atmosphere.* Oxford University Press, New York, 487 pp.

Lincoln, C, 1972: *On Quiet Wings: A Soaring Anthology.* Northland Press, Flagstaff, AZ, 397 pp.

Liouville, J, 1837: Sur le développment des fonctions ou parties de fonctions en séries... *J Math Pure Apl*, **2**, 16-35.

List, R, 1958: *Smithsonian Meteorological Tables*, 6th ed. Random House, Smithsonian Institute Press, New York.

Loehle, C, 2007: A 2000-yr global temperature reconstruction based on non-tree ring proxies. *Energy & Env*, **18**, 1049-1058.

Loehle, C and J McCulloch, 2008: Correction to: A 2000-yr global temperature reconstruction based on non-tree ring proxies. *Energy & Env*, **19**, 93-100.

Logan, J, 1999: An analysis of ozonesonde data for the troposphere: Recommendations for testing 3D models and development of a gridded climatology for tropospheric ozone. *J Geophys Res*, **104**, 16115-16149.

London, J, 1980: Radiative energy sources and sinks in the stratosphere and mesosphere. *Proceedings of the NATA Advanced Study Institute on Atmospheric Ozone: Its Variation and Human Influences.* Rep. FAA-EE-80-20, A Aiken, Ed., 703-721.

London, J. (1985), The observed distribution of atmospheric ozone and its variations. In *Ozone in the Free Atmosphere*, R Whitten and S Prasad, Eds., van Nostrant-Reinhold, Princeton, 11-80.

Lorenz, E, 1955: Available potential energy and the maintenance of the general circulation. *Tellus*, **7**, 157-167.

Lynn, R and J Reid, 1968: Characteristics and circulation of the deep and abyssal waters. *Deep-Sea Res*, **15**, 577-598.

Madden, R and P Julian, 1971: Description of a 40-50 day oscillation in the zonal wind in the tropical Pacific. *J Atmos Sci*, **28**, 702-708.

Madden, R and P Julian, 1972: Description of global-scale circulation cells in the tropics with a 40-50 day period. *J Atmos Sci*, **29**, 1109-1123.

Madden, R, 1986: Seasonal variations of the 40-50 day oscillation in the tropics. *J Atmos Sci*, **43**, 3138-3158.

Madden, R and G Meehl, 1993: Bias in the global mean temperature estimated from sampling a greenhouse warming pattern with the current surface observing network. *J Clim*, **6**, 2486-2489.

Maloney, E and D Hartmann, 1998: Frictional moisture convergence in a composite life cycle of the Madden-Julian Oscillation. *J Clim*, **11**, 2387-2403.

Maloney, E and J Kiehl, 2002: MJO-related SST variations over the tropical eastern Pacific during Northern Hemisphere summer. *J Clim*, **15**, 675-689.

Manabe S and R Strickler, 1964: Thermal equilibrium of the atmosphere with convective adjustment. *J Atmos Sci*, **21**, 361-385.

Manabe, S and R Wetherald, 1967: Thermal equilibrium of the atmosphere with a given distribution of relative humidity. *J Atmos Sci*, **24**, 241.

Mantua, N and S Hare, 2002: The Pacific decadal oscillation. *J Oceanography*, **58**, 35-44.

Margules, M, 1903: Über die energie der sturme. *Jahrb Zentralanst Meteorol Wien*, **40**, 1-26.

Marland, G, Boden, T, and R Andres, 2008: Global, regional, and national fossil fuel CO_2 emissions. In *Trends: A Compendium of Data on Global Change*. Carbon Dioxide Information Analysis Center, Oak Ridge National Laboratory, US Dept of Energy, Oak Ridge, TN.

Marshall, J, 2003: Trends in the southern annular mode from observations and reanlyses. *J Clim*, **16**, 4134-4143.

Mastepanov et al, 2008: Large tundra methane burst during onset of freezing. *Nature*, **456**, 628-631.

Matveev, L, 1967: *Physics of the Atmosphere*. Israel Program for Scientific Translations. Jerusalem, 699 pp.

McBride, J and N Nichols, 1983: Seasonal relationships between Australian rainfall and the Southern Oscillation. *Mon Wea Rev*, **111**, 1998-2004.

McClatchey, R and J Selby, 1972: Atmospheric transmittance, 7-30 μm: Attenuation of CO_2 laser radiation. *Env Res*, Paper No. 419, AFCRL-72-0611.

McGann, M, 2008: High-resolution, forimaniferal, isotopic and trace element records from Holocene estuarine deposits of San Francisco Bay. *J Coastal Res*, **24**, 1092-1109.

McIntyre, M and T Palmer, 1983: Breaking planetary waves in the stratosphere. *Nature*, **305**, 593-600.

Mears, C, Schabel, M, and F Wentz, 2003: A reanalysis of the MSU channel 2 tropospheric temperature record. *J Clim*, **16**, 3650-3664.

Mie, 1908: Beigrade zur optik trüber medienspeziell kolloidaler metallösungen. *Ann Physik*, **25**, 377-445.

Miles, T and W Grose, 1986: Transient medium-scale wave activity in the summer stratosphere. *Bull Amer Meteor Soc*, **67**, 674-686.

Minnis, P and E Harrison, 1984: Diurnal variability of regional cloud and clear-sky radiative parameters derived from GOES data. III. November 1978 radiative parameters. *J Clim and Appl Meteor*, **23**, 1032-1051.

Mlawer, E, Taubman, S, Brown, P, Iacono, M, and S Clough, 1997: Radiative transfer for inhomogenous atmospheres: RRTM, a validated correlated-k model for the longwave. *J Geophys Res*, **102**, 16663-16682.

Moberg, A, Sonechkin, D, Holmgren, K, Datsenko, N, and W Karlen, 2005: Highly variable Northern Hemisphere temperatures reconstructed from low- and high-resolution proxy data. *Nature*, **433**, 613-617.

Monahan, A, Fyfe, J, Ambaum, M, Stephenson, D, and G North, 2009: Empirical orthogonal functions: The medium is the message. *J Clim*, **22**, 6501-6514.

Monin, A and A Yaglom, 1973: *Statistical Fluid Mechanics*. MIT Press, Cambridge, 769 pp.

Monnin, E, Indermühle, A, Dällenbach, A, Flückiger, J, Stauffer, B, Stocker, T, Raynaud, D, and J-M Barnola, 2001: Atmospheric CO_2 concentrations over the last glacial termination. *Science*, **291**, 112-114.

Morse, P and H Feschbach, 1953: *Methods of Theoretical Physics*, vols. I and II. McGraw Hill, New York, 1978 pp.

Muller et al, 2003: Chlorine activation and chemical ozone loss deduced from HALOE and balloon measurements in the Arctic during the winter of 1999-2000. *J Geophys Res*, **108**, 8302.

Murgatroyd, R and F Singleton, 1961: Possible meridional circulations in the stratosphere and mesosphere. *Quart J Roy Meteorol Soc*, **87**, 125-135.

Naito, Y and I Hirota, 1997: Interannual variability of the northern winter stratosphere circulation related to the QBOand solar cycle. *J Meteor Soc Japan*, **75**, 925-937.

Naujokat, B, 1986: An update of the observed quasi-biennial oscillation of he stratospheric winds over the tropics. *J Atmos Sci*, **43**, 1873-1877.

Nicolet, M, 1980: The chemical equations of stratospheric and mesospheric ozone. *Proceedings of the NATO Advanced Study Institute on Atmospheric Ozone (Portugal)*. US Dept. of Transportation, FAA, Washington, DC, Report No. FAA-EE-80-20.

Nigam, S, 2003: *Teleconnections*. In *Encyclopedia of Atmospheric Sciences*. Academic Press, San Diego, pp. 2243-2269.

Norris, J and M Wild, 2009: Trends in aerosol radiative effects over China and Japan inferred from observed cloud cover, solar dimming, and solar brightening. *J Geophys Res*, **114** doi: 10.1029/2008JD011378.

North, G, 1975: Theory of energy balance models. *J Atmos Sci*, **32**, 2033-2043.

Oort, A and J Peixoto, 1983: Global angular momentum and energy balance requirements from observations. *Adv Geophys*, **25**, 355-490.

Osterlind, A, Tucker, M, Stone, B, and Jensen, O, 2006: The Danish case control study of cutaneous malignant melanoma. II. Importance of UV-light exposure. *Int J Cancer*, **42**, 319-324.

O'Sullivan, D and M Salby, 1990: Coupling of the quasi-biennial oscillation and the extratropical circulation in the stratosphere through planetary wave transport. *J Atmos Sci*, **47**, 650-673.

Paeschke, W, 1937: Experimentelle Untersuchungen zum Rauhigkeits-und Stabilitaets-problem in der freien Atmosphaere. *Beitr Phys Atmos*, **24**, 163-189.

Paltridge, G and C Platt, 1981: Aircraft measurements of solar and infrared radiation and the microphysics of cirrus clouds. *Quart J Roy Meteorol Soc*, **107**, 367-380.

Parrenin et al, 2007: The EDC3 chrolonology for the EPICA Dome C ice core. *Clim Past Disc*, **3**, 575-606.

Patterson, E, 1982: Size distributions, concentrations, and composition of continental and marine aerosols. In *Atmospheric Aerosols: Their Formation, Optical Properties, and Effects*, A. Deepak, Ed., Spectrum Press, Hampton, VA, 1-23.

Pedlosky, J, 1979: *Geophysical Fluid Dynamics*. Springer-Verlag, New York, 624 pp.

Peixoto, J, and A Oort, 1992: *Physics of Climate*. American Institute of Physics, New York, 520 pp.

Peterson, T and R Vose, 1997: Overview of the global historical climatology network temperature data base. *Bull Am Meteorol Soc*, **78**, 2837-2849.

Petit et al, 1999: Climate and atmospheric history of the past 420,000 yrs from the Vostok ice core, Antarctica. *Nature*, **399**, 429-436.

Phillips, H and T Joyce, 2007: Bermuda's tale of two time series: Hydrostation S and BATS. *J Phys. Oceanography*, **37**, 554-571.

Platt, C, Dilley, A, Scott, J, Barton, I, and GL Stephens, 1984a: Remote sounding of high clouds. V: Infrared properties and structures of tropical thunderstorm anvils. *J Clim Appl Meteor*, **23**, 1296-1308.

Platt, C, Scott, J, and A Dilley, 1984b: Remote sounding of high clouds. IV: Optical properties of midlatitude and tropical cirrus. *J Atmos Sci*, **44**, 729-747.

Philander, S, 1983: El Nino Southern Oscillation phenomena. *Nature*, **302**, 295-301.

Phillips, N, 1966: The equations of motion for a shallow rotating atmosphere and the "Traditional Approximation." *J Atmos Sci*, **23**, 626-628.

Plumb, R, 1982: The circulation of the middle atmosphere. *Aust Meteorol Mag*, **30**, 107-121.

Pope, F, Hansen, J, Bayes, K, Friedl, R, and S Sander, 2007: UV absorption spectrum of chlorine peroxide, ClOOCl. *J Phys Chem A*, **111**, 4322-4332.

Pruppacher, H, 1981: The microstructure of atmospheric clouds and precipitation. In *Clouds: Their Formation, Optical Properties, and Effects*. P Hobbs and A Deepak, Eds., Academic Press, San Diego, pp. 93–186.

Pruppacher, H and J Klett, 1978: *Microphysics of Clouds and Precipitation*. Reidel, Dordrecht, 714 pp.

Queney, P, 1948: The problem of air flow over mountains: A summary of theoretical studies. *Bull Am Meteorol Soc*, **29**, 16–26.

Rayleigh, Lord, 1871: On the light from the sky, its polarization and colour *Phil Mag*, **41**, 107–120.

Rayleigh, Lord, 1880: On the stability or instability of certain fluid motions. *Proc London Math Soc*, **9**, 57–70.

Ramanathan, V, 1987: Atmospheric general circulation and its low frequency variance: Radiative influences. *J Meteorol Soc Jpn*, **65**, 151–175.

Rasmusson, E and T Carpenter, 1982: Variation of tropical sea surface temperature and surface wind fields associated with the Southern Oscillation/El Nino. *Mon Wea Rev*, **110**, 354–384.

Rektorys, K, 1969: *Survey of Applicable Mathematics*. MIT Press, Cambridge, 1369 pp.

Remsberg, E, Russell, J, Gordley, L, Gille, J, and P Bailey, 1984: Implications of the stratospheric water vapor distribution as determined from the Nimbus-7 LIMS experiment. *J Atmos Sci*, **41**, 2934–2945.

Rex, M, Salawitch, R, von der Gathen, P, Harris, N, Chpperfield, M, and B Naujoka, 2004: Arctic ozone loss and climate change. *Geophys Res Lett*, **31**, doi: 10.1029/2003GL018844.

Reynolds, D, Vonder Haar, T, and S Cox, 1975: The effect of solar radiation absorption in the tropical troposphere. *J Appl Meteor*, **14**, 433–443.

Robinson, A, Balliunas, S, Soon, W, and Z Robinson, 1998: Environmental effects of increased atmospheric carbon dioxide. *Med Sent*, **3**, 171–178.

Rodgers, C and C Walshaw, 1966: The computation of infrared cooling rate in planetary atmospheres. *Quart J Roy Meteor Soc*, **92**, 67–92.

Roper, R, 1977: Turbulence in the lower thermosphere, Chapter 7 in *The Upper Atmosphere and Magnetosphere*, F Johnson, Ed., U.S. National Academy of Science, Washington, DC, pp. 117–129.

Rosenfeld, D, 2006: Aerosol-cloud interactions control of Earth radiation and latent heat release budgets. *Space Science Revs*, **125**, 149–157.

Rossby, C, et al. 1939: Relations between variations in the intensity of the zonal circulation of the atmosphere and the displacements of the semipermanent centers of action. *J Mar Res*, **2**, 38–55.

Rotty, R, 1987: Estimates of seasonal variation in fossil fuel CO_2 emissions. *Tellus*, **39B**, 184–202.

Ruddiman, W and M Raymo, 2003: A methane based time scale for Vostok ice. *Quaternary Sci Rev*, **22**, 141–155.

Ruth, S, Remedios, J, Lawrence, B, and F Taylor, 1994: Measurements of N_2O by the Improved Stratospheric and Mesospheric Sounder during early northern winter 1991/92. *J Atmos Sci*, **51**, 2818–2833.

Saji, N, Goswami, B, Vinayachandran, P, and T Yamagata, 1999: A dipole mode in the tropical Indian Ocean. *Nature*, **401**, 360–363.

Salby, M, D O'Sullivan, R Garcia, and P Callaghan, 1990: Air motions accompanying the development of a planetary wave critical layer. *J Atmos Sci*, **47**, 1179–1204.

Salby M and P Callaghan, 1993: Fluctuations in total ozone and their relationship to stratospheric air motions. *J Geophys Res*, **98**, 2716–2727.

Salby, M and H Hendon, 1994: Intraseasonal behavior of clouds, temperature, and motion in the tropics. *J Atmos Sci*, **51**, 2207–2224.

Salby, M and P Callaghan, 2000: Connection between the solar cycle and the QBO: The missing link. *J Climate*, **13**, 2652–2662.

Salby, M and P Callaghan, 2002: Interannual changes of the stratospheric circulation: Relationship to ozone and tropospheric structure. *J Climate*, **15**, 3673–3685.

Salby, M, Sassi, F, Callaghan, P, Read, W, and H Pumphrey, 2003: Fluctuations of cloud, humidity, and thermal structure near the tropical tropopause. *J Climate*, **15**, 3428–3446.

Salby, M and P Callaghan, 2004a: Control of the tropical tropopause and vertical transport across it. *J Climate*, **17**, 965–985.

Salby, M, and P Callaghan, 2004b: Systematic changes of Northern Hemisphere ozone and their relationship to random interannual changes. *J Climate*, **17**, 4512–4521.

Salby, M and P Callaghan, 2005: Interaction between the Brewer-Dobson circulation and the Hadley circulation. *J Climate*, **18**, 4303–4316.

Salby, M and P Callaghan, 2006: Relationship of the QBO to the stratospheric signature of the solar cycle. *J Geophys Res*, **111**, D06110, doi: 10.1029/2005JD006012.

Salby, M, 2007: Influence of the solar cycle on the general circulation of the stratosphere and upper tropoposphere. *Solar Variability and Planetary Climates*, 287–303, Springer Verlag.

Salby, M and P Callaghan, 2007: On the wintertime increase of Arctic ozone: Relationship to changes of the polar-night vortex. *J Geophys Res* **112**, D06116, doi: 10.1029/2006JD007948.

Salby, M, 2011: Interannual changes of stratospheric temperatures and ozone: Forcing by anomalous wave driving and the QBO. *J Atmos Sci*, **68**, 1513–1525.

Salby, M, Titova, E, and L Deschamps, 2011: Rebound of Antarctic ozone. *Geophys Res Lett* (38, L09702, doi:10.1029/2011GL047266.).

Schiermeier, Q, 2007: Chemists poke holes in ozone theory. *Nature*, **449**, 382–383.

Schlicting, H, 1968: *Boundary Layer Theory*. McGraw Hill, New York, 744 pp.

Scorer, R, 1978: *Environmental Aerodynamics*. Ellis Horwood Ltd., West Sussex, 488 pp.

Scorer, R, 1986: *Cloud Investigation by Satellite*. Ellis Horwood Ltd., West Sussex, 23 chaps.

Shabbar, Huang, J, and K Higachi, 2001: The relationship between the wintertime north Atlantic oscillation and blocking episodes in the north Atlantic. *Int J Climatol*, **21**, 355–369.

Shapiro, L, 1989: The relationship of the quasi-biennial oscillation to Atlantic tropical storm activity. *Mon Wea Rev*, **117**, 1545–1552.

Shapiro, M, 1982: Nowcasting the position and intensity of jet streams using a satellite-borne total ozone mapping spectrometer. In *Nowcasting*, K. A. Browning, ed. Academic Press, 256 pp.

Shapiro, M and J Hastings, 1973: Objective cross-section analysis by Hermite polynomial interpolation on isentropic surfaces. *J Appl Meteorol*, **12**, 753–762.

Shea, D, K Trenberth, and R Reynolds, 1990: *A Global Monthly Sea Surface Temperature Climatology*. Tech Note TN 345+STR, National Center for Atmospheric Research, Boulder, CO, 167 pp.

Shinoda, T and H Hendon, 1998: Mixed layer modeling of intraseasonal variability in the tropical western Pacific and Indian Oceans. *J Clim*, **11**, 2668–2685.

Siddall et al, 2003: Sea level fluctuations during the last glacial cycle. *Nature*, **423**, 853–858.

Simmons, A, Wallace, J, and G Branstator, 1983: Barotropic wave propagation and instability and atmospheric telleconnection pattern. *J Atmos Sci*, **40**, 1363–1392.

Slingo, A, 1989: A GCM parameterization for the SW radiative properties of water clouds. *J Atmos Sci*, **46**, 1419–1427.

Slinn, W, 1975: Atmospheric aerosol particles in surface-level air. *Atmos Env*, **9**, 763–764.

Smith, W and D Gottlieb, 1974: Solar flux and its variations. *Space Sci Rev*, **16**, 771–802.

Soden, B, Wetherald, G, Stenchikov, G, and A Robock, 2002: Global cooling after the eruption of Mount Pinatubok: a test of climate feedback by water vapor. *Science*, **296**, 727–730.

Solomon, S, 1990: Progress towards a quantitative understanding of Antarctic ozone depletion. *Nature*, **347**, 347–354.

Sorbjan, Z, 1989: *The Structure of the Atmospheric Boundary Layer*. Prentice Hall, Englewood Cliffs, NJ, 317 pp.

Sowers et al, 1993: 135,000 year Vostok – SPECMAP common temporal framework. *Paleoceanogr*, **8**, 737–766.

Spichtinger, P, Gierens, K, and W Read, 2006: The global distribution of ice-supersaturated regions as seen by the Microwave Limb Sounder. *Q J Roy Meteorol Soc*, **129**, 3391–3410.

Stanford et al, 2006: Timing of the meltwater pulse 1A and climate responses to meltwater injections. *Paleoceanogr*, **21**, 4103.

Stein, O, 2008: The variability of Atlantic-European blocking as derived from long SLP time series. *Tellus*, **52**, 225–236.

Stewart, R, 2008: *Introduction to Physical Oceanography.* http://oceanworld.tamu.edu/ocng_textbook.

Stommel, H and A Arons, 1960: On the abyssal circulation of the world ocean (I). Stationary planetary flow patterns on a sphere. *Deep Sea Res*, **6**, 140–154.

Strub, P, Mesias, J, Montecino, V, Rutlant, J, and S Salinas, 1998: Coastal ocean circulation off western South America coastal segment. *The Sea*, **11**, 273–308.

Stull, R, 1988: *An Introduction to Boundary Layer Meteorology.* Kluwer, Boston, 666 pp.

Sun, W, and C Chang, 1986: Diffusion model for a convective layer. *J Clim Appl Meteorol*, **25**, 1445–1453.

Sverdrup, H, 1947: Wind-driven currents in a baroclinic ocean; with application to the equatorial currents of the eastern Pacific. *Proc Nat Acad Sci*, **33**, 318–326.

Taylor, G, 1929: Waves and tides in the atmosphere. *Proc Roy Soc London Ser A*, **126**, 169–183.

Tennekes, H and J Lumley, 1972: *A First Course in Turbulence.* MIT Press, Cambridge, 300 pp.

Thompson, D and J Wallace, 2000: Annular modes in the extratropical circulation. Part I: Month to month variability. *J Clim*, **13**, 1000–1016.

Thompson, D, Wallace, J, and C Hegerl, 2000: Annular modes in the extratropical circulation. Part II: Trends. *J Clim*, **13**, 1018–1036.

Thorpe, S, 1969: Experiments on the instability of stratified flows: Immiscible fluids. *J Fluid Mech*, **39**, 25–48.

Thorpe, S, 1971: Experiments on the instability of stratified flows: Miscible fluids. *J Fluid Mech*, **46**, 299–319.

Thuburn, J and G Craig, 2000: Stratospheric influence on tropopause height: The radiative constraint. *J Atmos Sci*, **57**, 17–28.

Tilmes, S, Muller, R, Groos, J, McKenna, D, Russel, J, and Y Sasano, 2003: Calculation of chemical ozone loss in the Arctic winter 1996–1997 using ozone tracer correlations. Comparison of ILAS and HALOE results. *J Geophys Res*, **108**, 4045.

Tsushima, Y and S Manabe, 2001: Influence of cloud feedback on annual variation of global mean surface temperature. *J Geophys Res*, **106**, 22635–22646.

Tung, KK and H Yang, 1994: Global QBO in circulation and ozone. II: A simple mechanistic model. *J Atmos Sci*, **51**, 2708.

Turco, R, Drdla, K, A Tabazadeh, and P Hamill, 1993: Heterogeneous chemistry of polar stratospheric clouds and volcanic aerosols. *The Role of the Stratosphere in Global Change*, NATO ASI Series I, **8**, M Chanin, Ed., Springer Verlag, Heidelberg.

Twomey, S, 1977: *Atmospheric Aerosols.* Elsevier, Amsterdam, 302 pp.

Understanding Climate Change, 1975: U.S. National Academy of Sciences, Washington, DC, 239 pp.

U.S. Standard Atmosphere, 1976: National Oceanic and Atmospheric Administration, National Aeronautics and Space Administration, United States Air Force. U.S. Govt. Printing Office, NOAA-S/T 76-1562, Washington, DC, 228 pp.

Vallis, G, 2006: *Atmospheric and Oceanic Fluid Dynamics.* Cambridge University Press, Cambridge, 745 pp.

Van Dyke, M, 1982: *An Album of Fluid Motion.* Parabolic Press, Stanford, 174 pp.

Vinnichenko, N, 1970: The kinetic energy spectrum in the free atmosphere – 1 second to 5 years. *Tellus*, **22**, 158–166.

Waliser, D, 1996: Formation and limiting mechanisms for very high sea surface temperatures: Linking the dynamics and thermodynamics. *J Clim*, **9**, 161–188.

Wallace, J, 1967: A note on the role of radiation in the biennial oscillation. *J. Atmos. Sci.*, **24**, 598–599.

Wallace, J and P Hobbs, 1977: *Atmospheric Science: An Introductory Survey.* Academic Press, San Diego, 467 pp.

Wallace, J and P Hobbs, 2006: *Atmospheric Science: An Introductory Survey*, 2nd ed. Academic Press, San Diego, 483 pp.

Wang, B and H Rui, 1990: Dynamics of the coupled moist Kelvin-Rossby wave on an equatorial beta plane. *J Atmos Sci*, **47**, 397–413.

Wang, B and X Xie, 1998: Coupled modes of the warm pool climate system. I: The role of air-sea interaction in maintaining the MJO. *J Clim*, **11**, 2116–2135.

Warner, J, 1969: The microstructure of cumulus cloud. Part I. General features of the droplet spectrum. *J Atmos Sci*, **26**, 1049–1059.

Warren, S and S Schneider, 1979: Seasonal simulation as a test for uncertainties in the parameterizations of a Budyko-Sellers zonal climate model. *J Atmos Sci*, **36**, 1377–1391.

Webster et al, 2004: Drowning of the -150m reef off Hawaii: A causality of global meltwater pulse 1A? *Geology and GSA Today*, 249–252.

Welander, P, 1955: Studies of the general development of motion in a two-dimensional ideal fluid. *Tellus*, **7**, 141–156.

Welander, P, 1959: On the vertically integrated mass transport in the oceans. *The Atmosphere and the Sea in Motion*. B Bolin, Ed. Rockefeller Institute Press, Albany, 75–101.

Wentzel, G, 1926: Eine Verallgemeinerung der Quantenbedingung fur die Zwecke der Wellenmechanik. *Z Phys*, **38**, 518–529.

Whipple, 1930: The great Siberian meteor, and the waves, seismic and aerial, which it produced. *Quart J Roy Meteorol Soc*, **56**, 287–298.

Wilson, A, Hency, C, and C Reynolds, 1979: Short-term climate change and New Zealand temperatures during the last millenium. *Nature*, **279**, 315–317.

Williams, M, Aydin, M, Tatum, C, and E Saltzman, 2007: A 2000 year atmospheric history of methyl chloride from a south pole ice core: Evidence for climate-controlled variability. *Geophys Res Lett*, **34**, doi:10.1029/2006GL029142.

Williamson, D, Kiehl, J, Ramanathan, V, Dickinson, R, and J Hack, 1987: *Description of the NCAR Community Climate Model*. NCAR/TN-285/STR. Available from NCAR, Boulder, CO.

Willson, RC, Hudson, HS, Frohlich, C, and RW Brusa, 1986: Long-term downward trend in total solar irradiance, *Science*, **234**, 1114–1117.

WMO, 1969: *International Cloud Atlas*. World Meteorological Organization, Geneva, 62 pp.

WMO, 1986: *Atmospheric Ozone: Assessment of our Understanding of the Processes Controlling its Present Distribution and Change*. Report No. 16, World Meteorological Organization, Global Ozone Research and Monitoring Project, Washington, DC.

WMO, 1988: *Report of the International Ozone Trends Panel 1988*. Report No. 18, World Meteorological Organization, Global Ozone Research and Monitoring Project, NASA, Washington, DC.

WMO, 1991: *Scientific Assessment of Ozone Depletion: 1991*. Global Ozone Research and Monitoring Project Report 25, World Meteorological Organization, NASA, Washington, DC.

WMO, 1995: *Observed Chages in Ozone and Source Gases. Scientific Assessment of Ozone Depletion: 1994*. Rep 37. Available from NASA, Washington DC.

WMO, 2006: *Scientific Assessment of Ozone Depletion: 2006*. Global Ozone Research and Monitoring Project, Report No. 50, Geneva.

Wu, D, Read, W, Dessler, A, Sherwood, S, and J Jiang, 2005: UARS/MLS cloud ice measurements: Implications for H_2O transport near the tropopause. *J Atmos Sci*, **62**, 518–530.

Wunsch, C, 2005: The total meridional heat flux and its oceanic and atmospheric partition. *J Clim*, **18**, 4374–4380.

Yanai, M, Esbensen, S, and J Chu, 1973: Determination of the bulk properties of tropical cloud clusters from large-scale heat and moisture budgets. *J Atmos Sci*, **30**, 11–27.

Young, K, 1993: *Microphysical Processes in Clouds*. Oxford University Press, New York, 427 pp.

Yulaeva, E, Holton, J, and J Wallace, 1994: On the cause of the annual cycle in tropical lower-stratospheric temperature. *J Atmos Sci*, **51**, 169–174.

Zhang, C, 1996: Intraseasonal perturbations in sea surface temperatures of the equatorial eastern Pacific and their association with the Madden-Julian oscillation. *J Clim*, **14**, 1309–1322.

Index

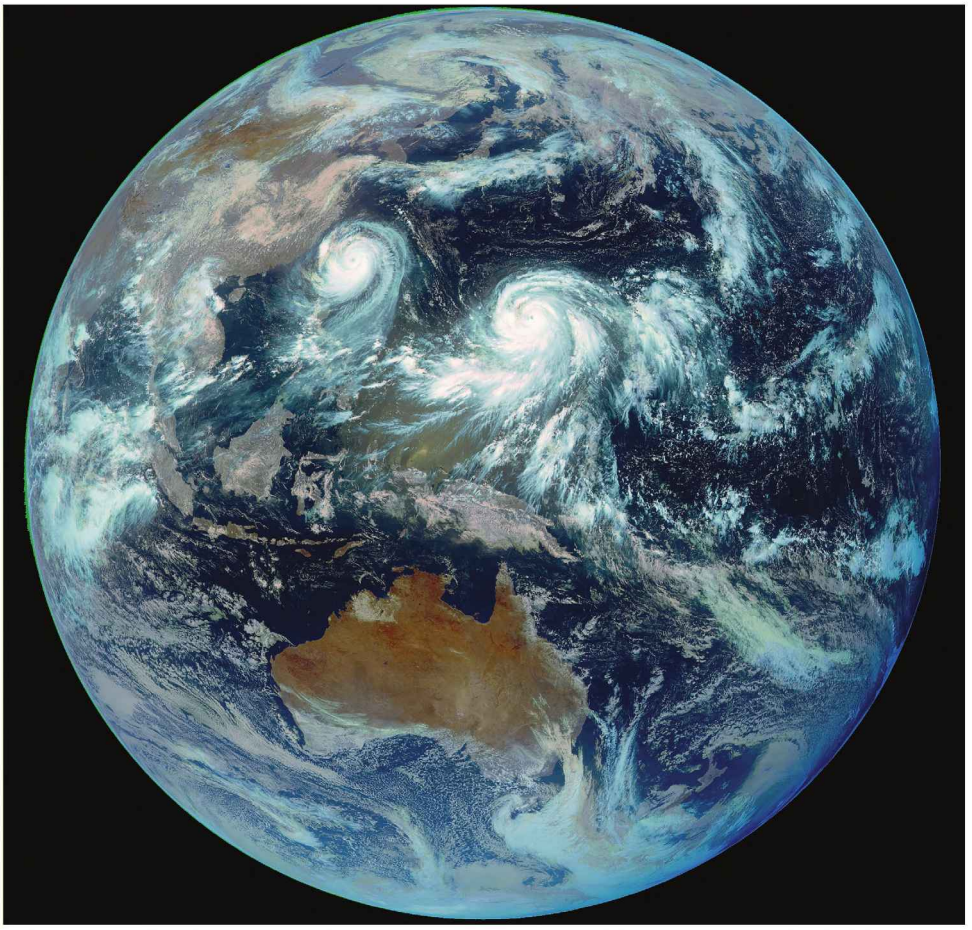

Plate 0 Visible imagery during August 2005, revealing twin cyclones that formed in the equatorial Pacific. Being entrained into them is haze from Indonesian forest fires, which developed during prolonged drought under El Nino conditions (negative phase of the Southern Oscillation). While it prevailed over SE Asia, the dense aerosol that was mantained by those fires led to widespread health restrictions and public closures. Courtesy of Australian Bureau of Meteorology and Japan Meterological Agency.

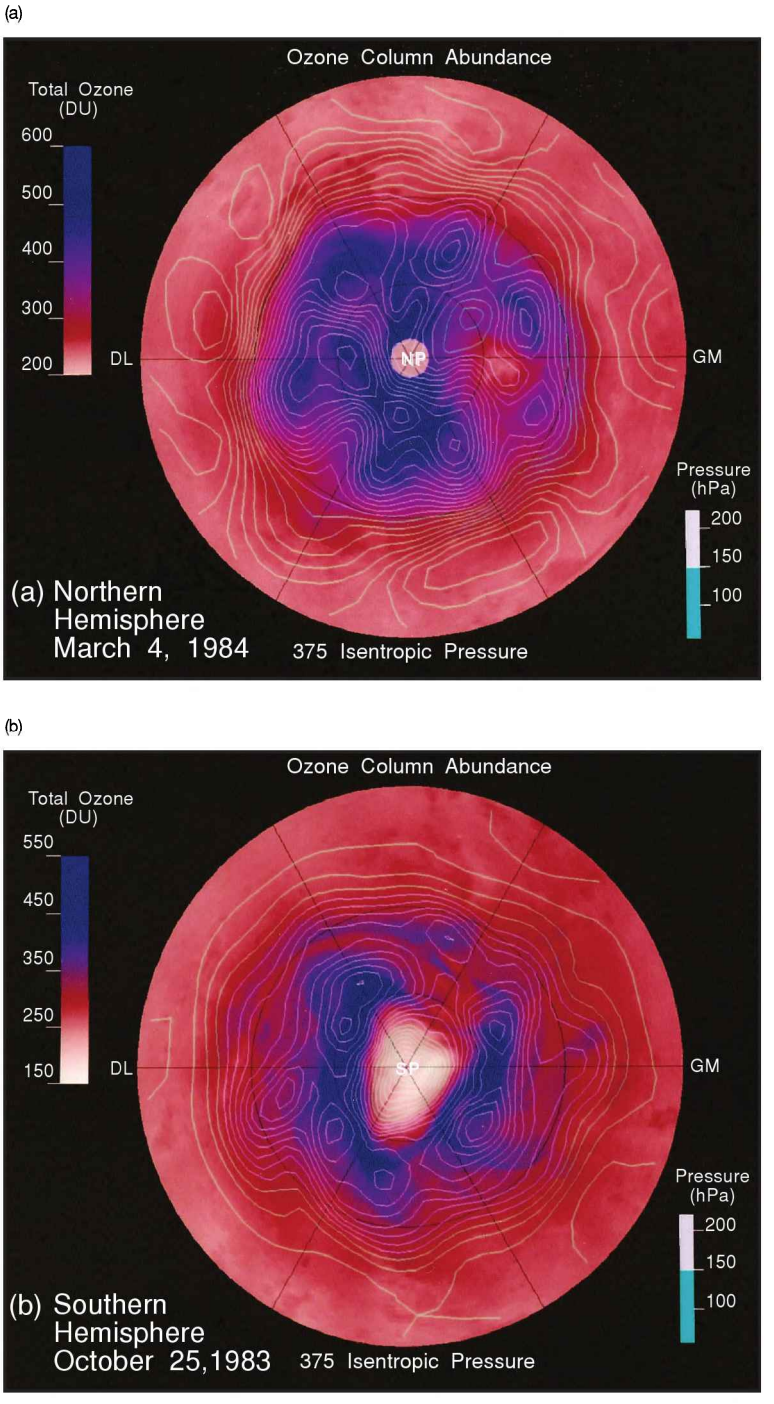

Plate 1 Distribution of total ozone (color) from the Total Ozone Mapping Spectrometer (TOMS) on board Nimbus-7 and pressure (contours) on the 375°K isentropic surface (see Sec. 2.4.1) over (a) the Northern Hemisphere on March 4, 1984 and (b) the Southern Hemisphere on October 25, 1983.

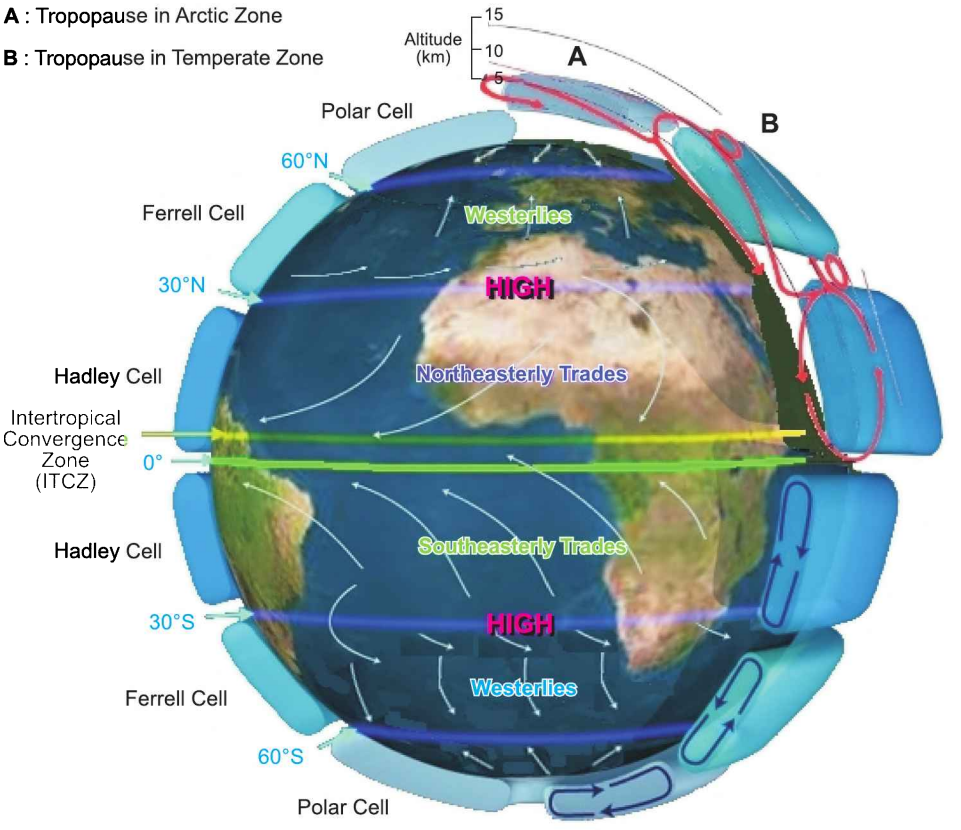

Plate 2 Schematic of the mean circulation, which is comprised of Hadley cells equatorward of 30°, Ferrell cells at mid-latitudes, and polar cells at higher latitude. The lower branch of the Hadley cell involves northeasterly and southeasterly Trade Winds, which meet in the InterTropical Convergence Zone (ITCZ), where air rises to form deep cumulus convection and heavy rainfall. *Source*: sealevel.jpl.nasa.gov.

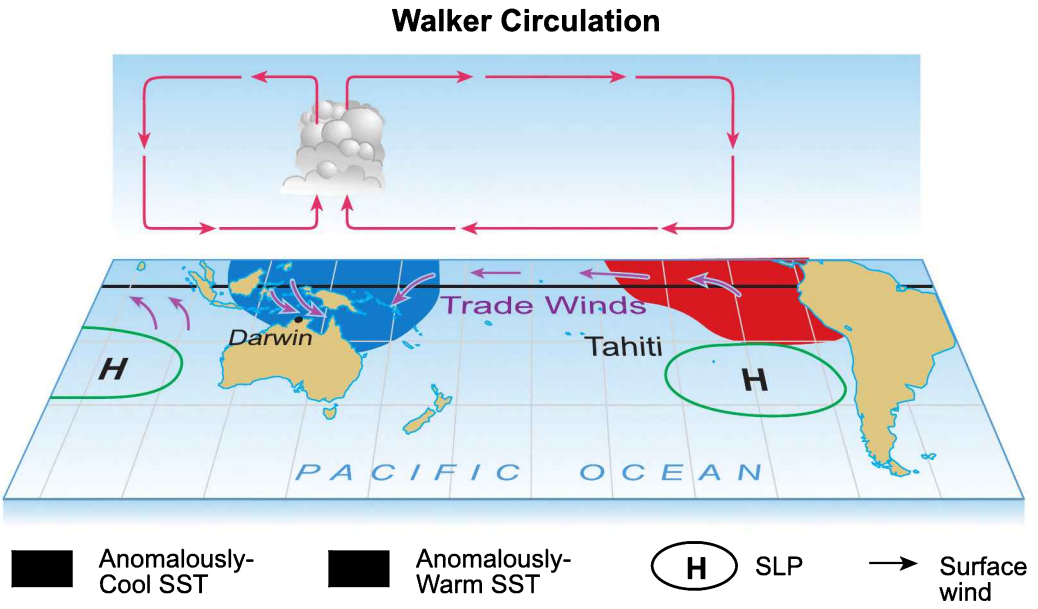

Plate 3 Schematic of the Pacific Walker circulation. *Source*: http://www.bom.gov.au/lam/climate/levelthree/analclim.

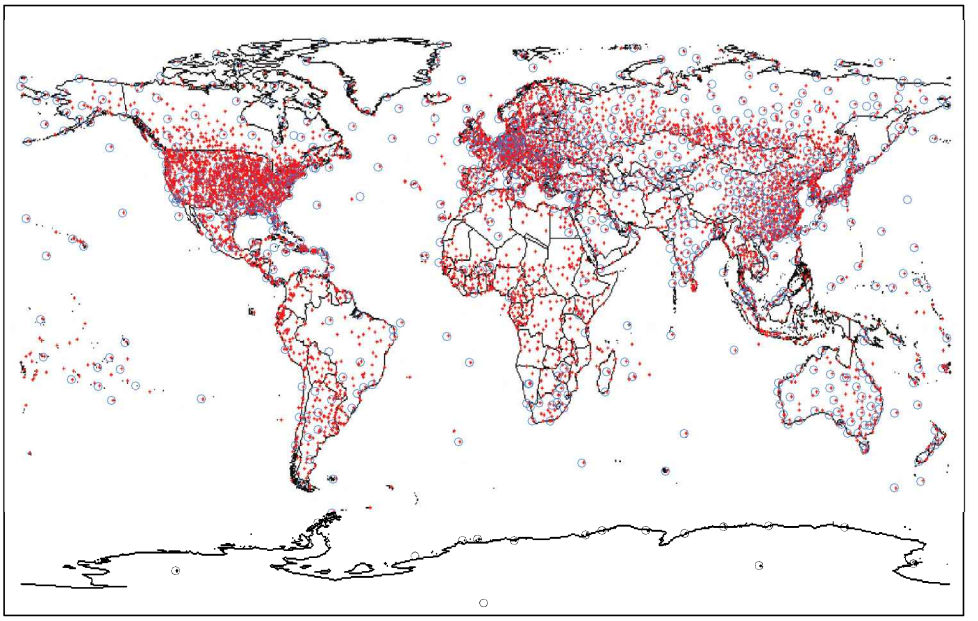

Plate 4 Stations comprising the global radiosonde network, where vertical profiles of atmospheric structure are measured twice daily at 0000 and 1200 UT (open circles), and the ground network of surface temperature measurements (dots). *Sources:* Gruber and Haimberger (2008), Peterson and Vose (1997).

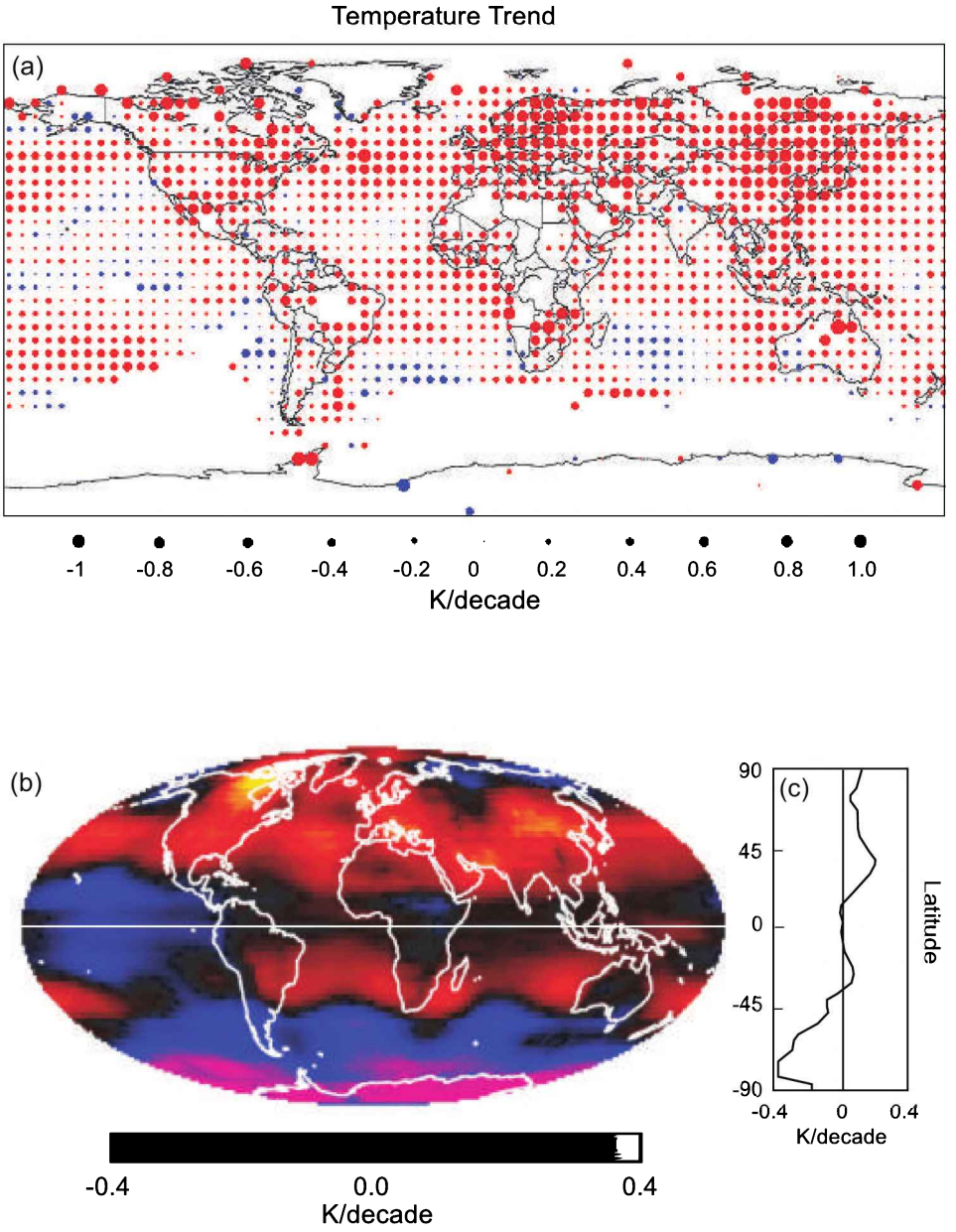

Plate 5 Temperature trend during the satellite era, as function of geographical position, derived from (a) the surface record and (b) the satellite record. (c) Zonal-mean trend in the sattellite record, which has global coverage. *Sources:* IPCC (2007), Mears et al. (2003).

Plate 6 (a) Schematic of the mountain wave that develops leeward of an elongated range. *Lenticular clouds* are fixed with respect to orography, while air flows through them. The positions of *rotor clouds* are also fixed, but those fragmented features are highly unsteady, with turbulent ascent (descent) along their leading (trailing) edges. Westward tilt with height (e.g., of wave crests) corresponds to upward propagation of energy (Chap. 14), a feature that is often visible in the structure of lenticular clouds. (b) Longitudinal view through the mountain wave. Smooth lenticular clouds form in a stack, separated by clear regions, due to stratification of moisture. These laminar features contrast sharply with turbulent rotor clouds below. (c) Transverse view from the ground. Vorticity and severe turbulence are made visible by looping cloud matter that comprises rotor. Courtesy of V. Haynes and L. Feierabend (Soaring Society of Boulder).

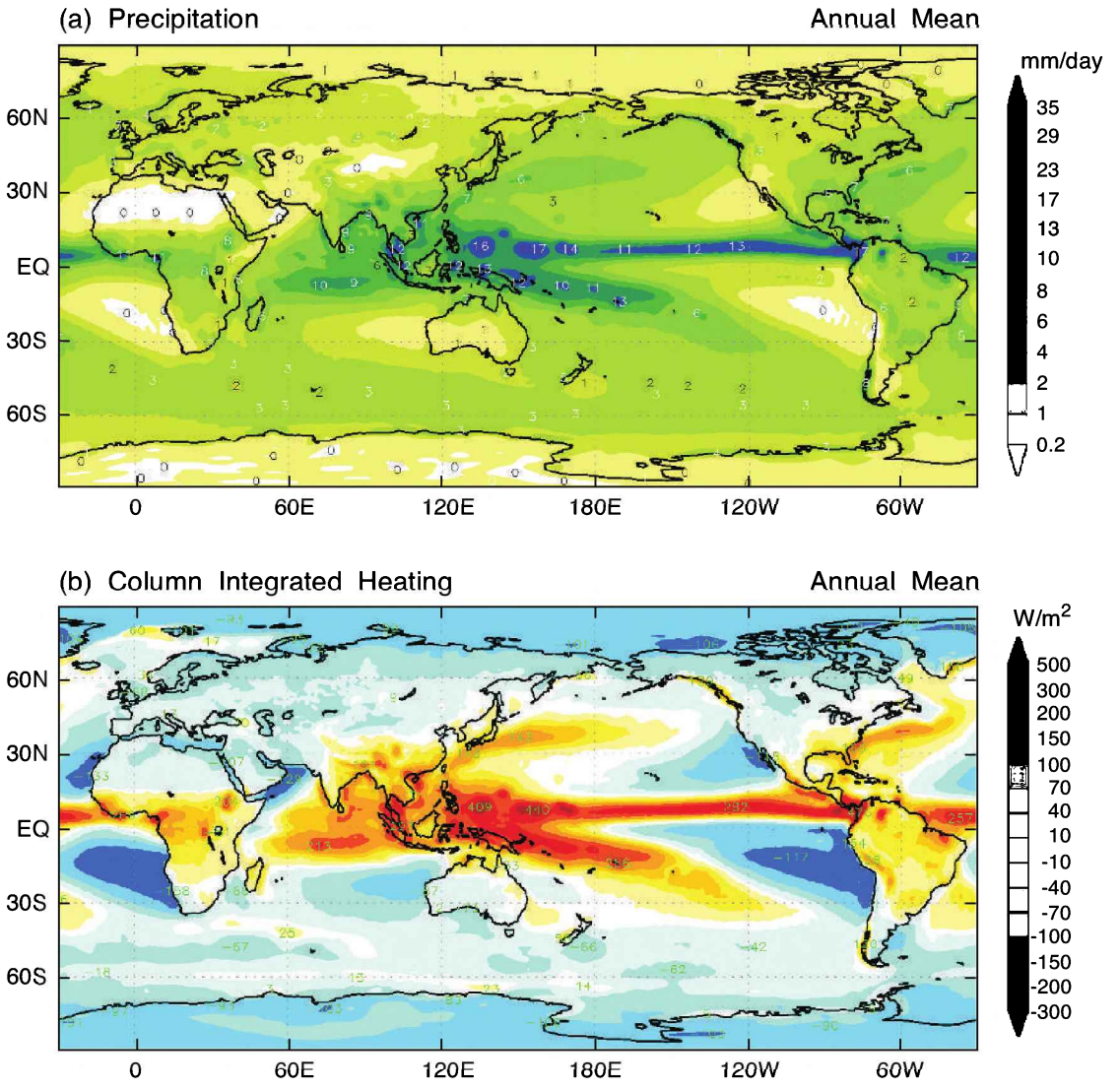

Plate 7 (a) Annual-mean precipitation rate (mm/day). (b) Column-integrated atmospheric heating (W m^{-2}). Both are concentrated inside the ITCZ, where precipitation and atmospheric heating exceed 10 mm/day and 250 W m^{-2}, respectively. Support comes from the South Pacific Convergence Zone (SPCZ), the South Atlantic Convergence Zone (SACZ), and the North Atlantic and North Pacific storm tracks. *Source:* Japanese 25-yr Climatology, cooperative project of Japan Meteorological Agency (JMA) and Central Research Institute of Electric Power Industry (CRIEPI) (http://ds.data.jma.go.jp).

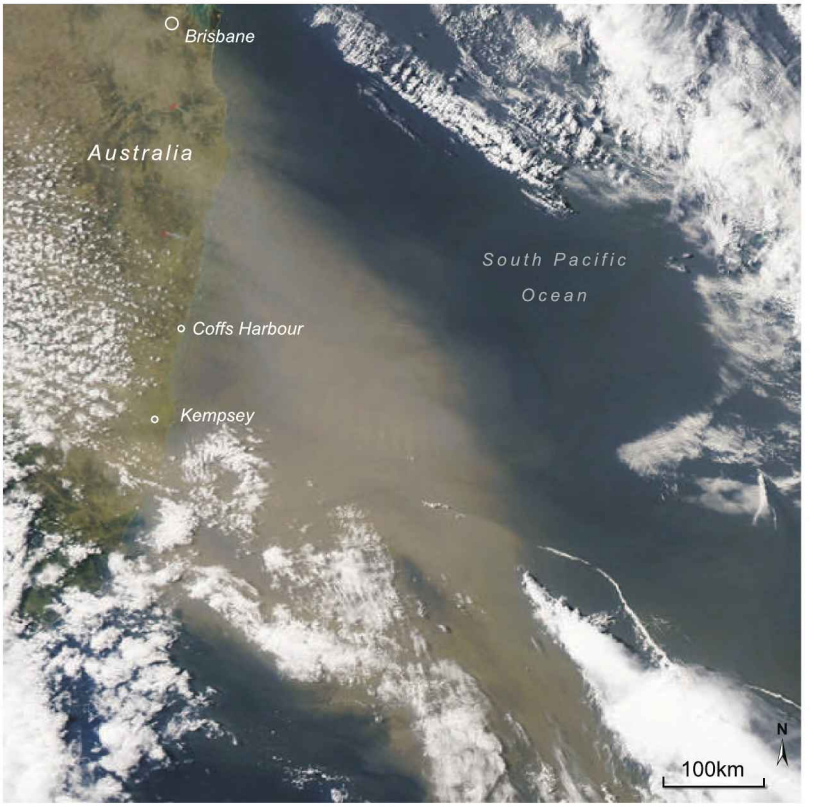

Plate 8 Visible imagery during September 2009, when the eastern seaboard of Australia was blanketed by red dust that originated 1000 km to the west. Notice the change of albedo relative to neighboring ocean.

Plate 9 Field of view across Sydney Harbor (a) under normal conditions and (b) during the dust storm of September 2009. With permission, copyright 2010 Fairfax Digital.

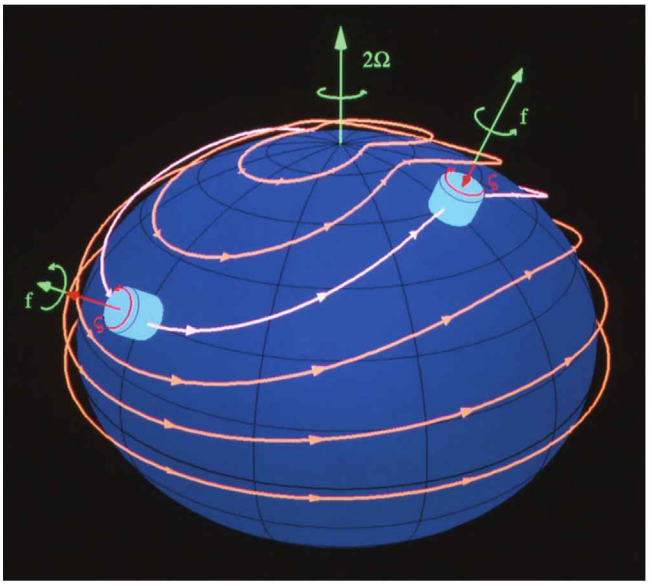

Plate 10 Schematic illustrating the reaction of an air parcel to meridional displacement. Displaced equatorward, an eastward-moving parcel spins up cyclonically to conserve absolute vorticity. Northward motion induced ahead of it then deflects the parcel's trajectory poleward back toward its undisturbed latitude. The reverse process occurs when the parcel overshoots and is displaced poleward of its undisturbed latitude.

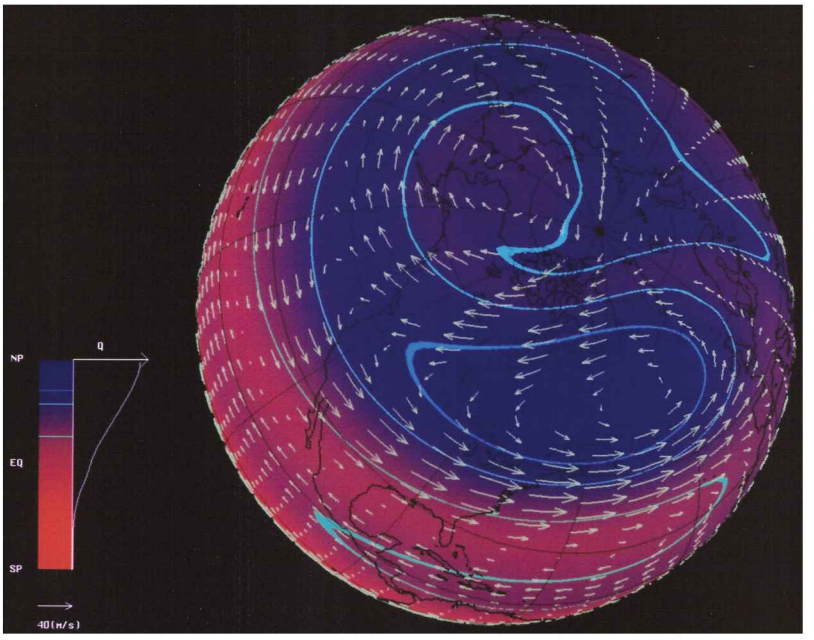

Plate 11 Distribution of potential vorticity Q and horizontal motion in a 2-dimensional calculation representative of the stratospheric circulation at 10 hPa under disturbed conditions. Color and velocity scales shown at left. High-Q polar air (blue), which marks the polar-night vortex, has been displaced well off the pole and distorted by an amplified planetary wave. Replacing it is low-Q air from equatorward (red), which has been advected into the polar cap. It spins up anticyclonically, forming a reversed circulation with easterly circumpolar flow at high latitude. These features are characteristic of a *stratospheric sudden warming* (cf. Fig. 18.13).

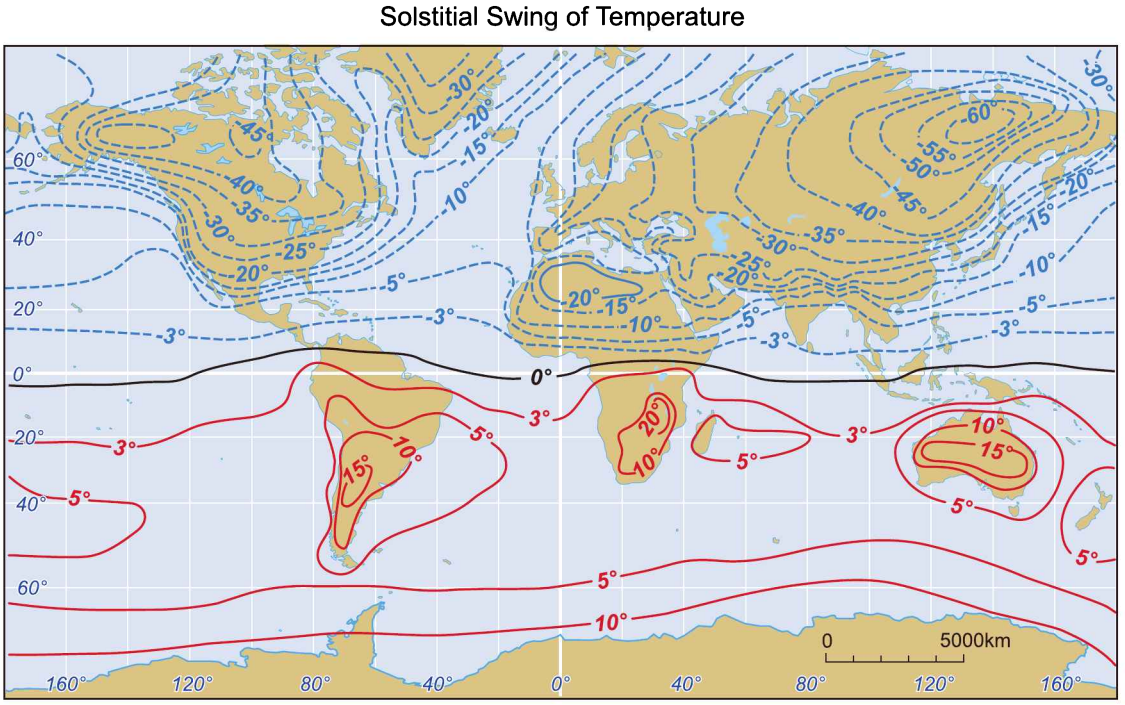

Plate 12 Annual swing of surface temperature: January–July.

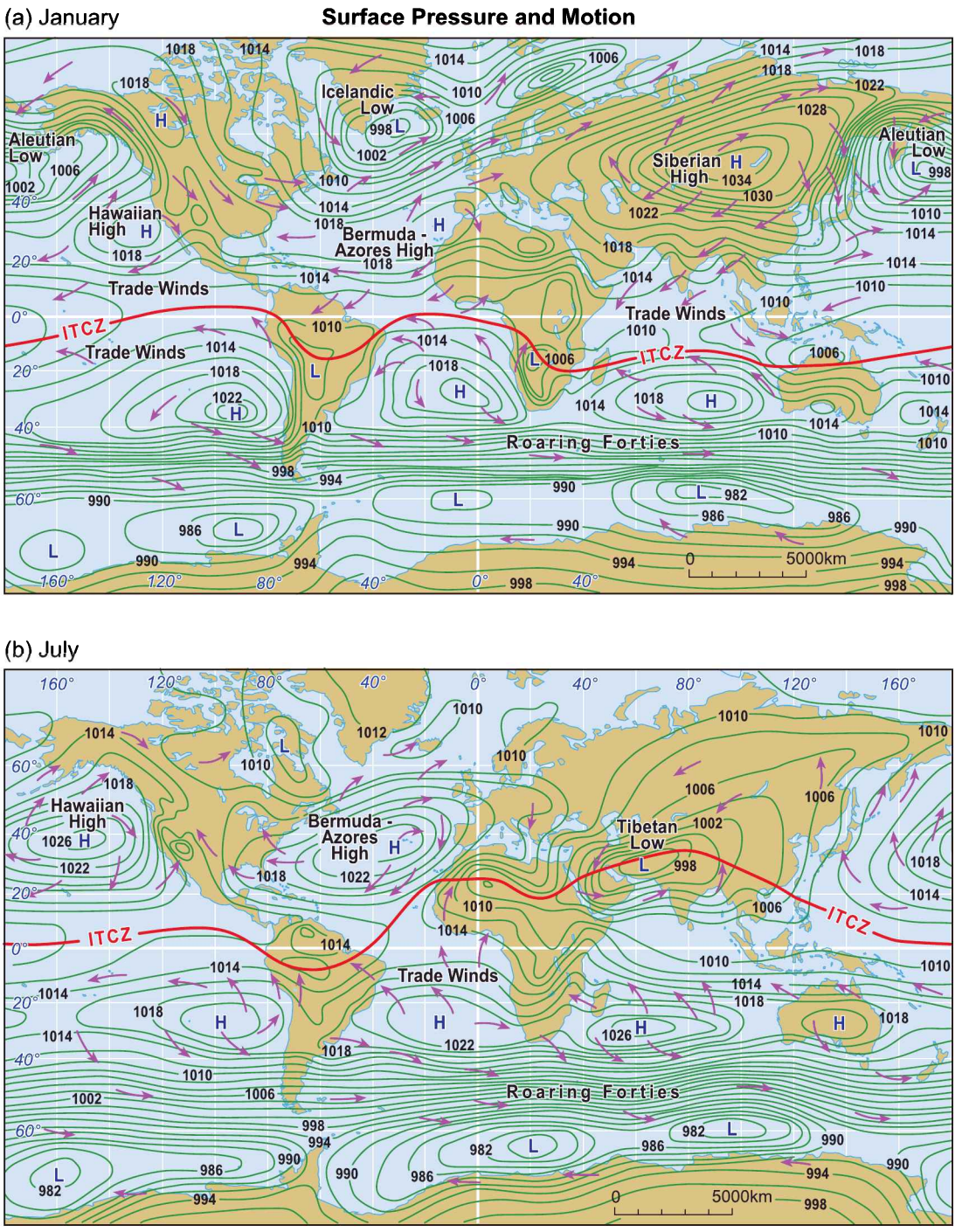

Plate 13 Climatological-mean SLP and surface motion for (a) January and (b) July.

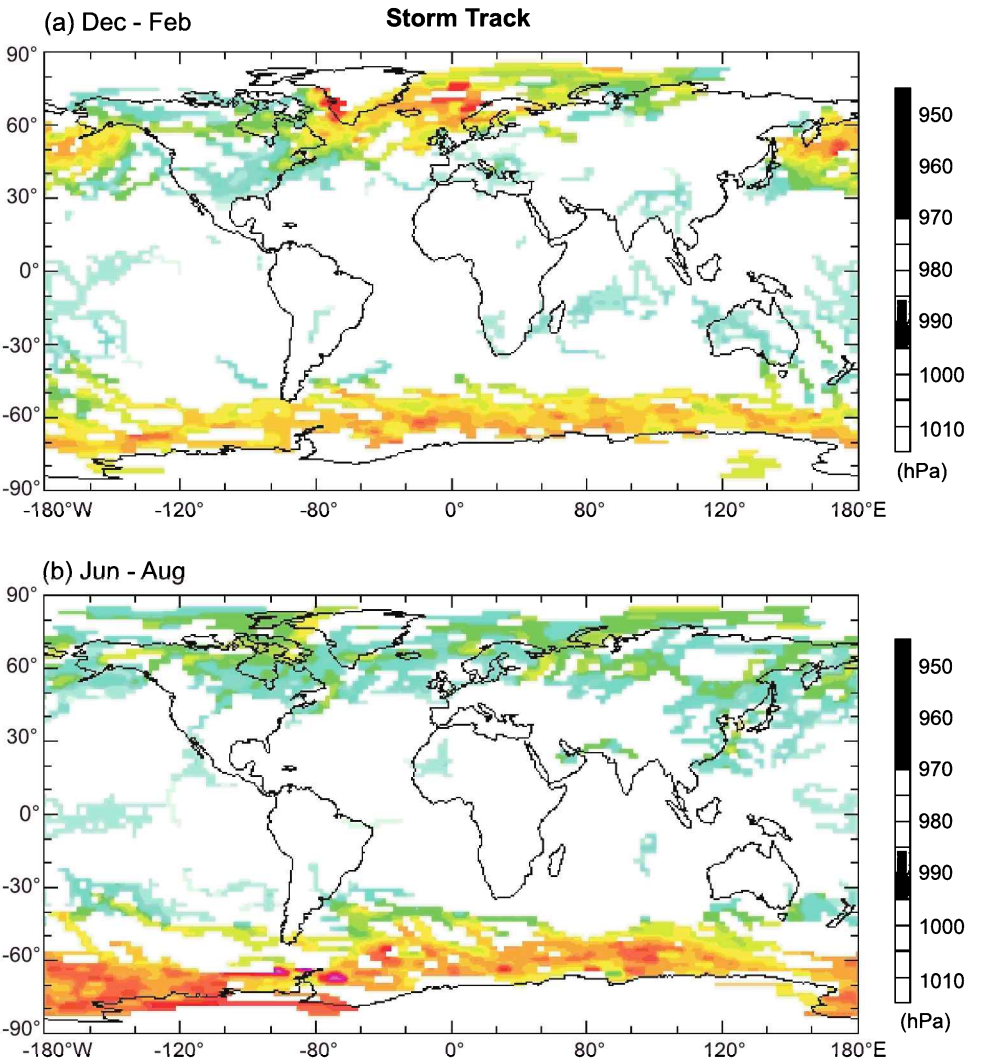

Plate 14 Mean intensity of cyclonic disturbances, measured by their depression of SLP, during (a) December–February 1984 and (b) June–August 1984. *Source:* http://data.giss.nasa.gov (10.07.10).

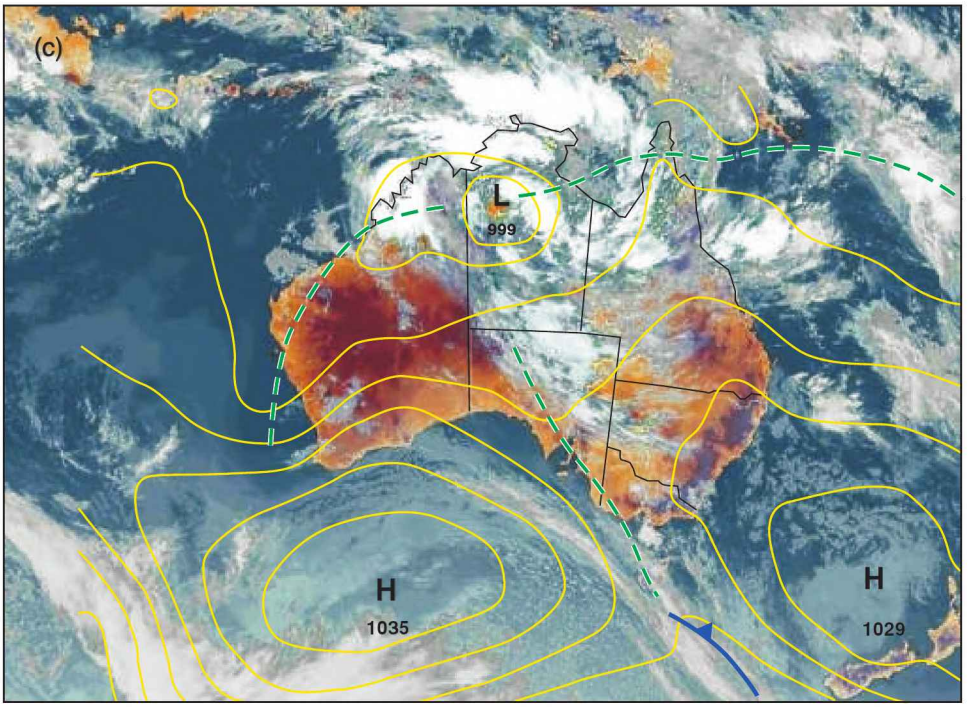

Plate 15 Instantaneous SLP and IR imagery under conditions typical of the Australian monsoon. Deep convection is organized by the monsoon low, as well as trough axes that emanate from it. Cirrus blow off at upper levels spirals outward anticyclonically.

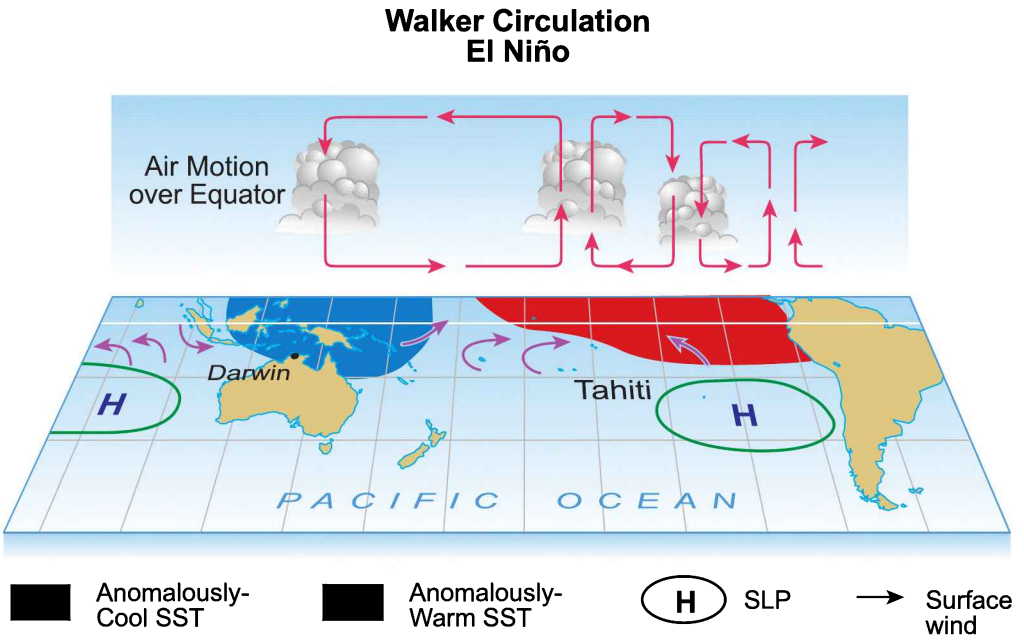

Plate 16 Disturbed Walker circulation during El Nino. Adapted from http://www.bom.gov.au (11.07.10).

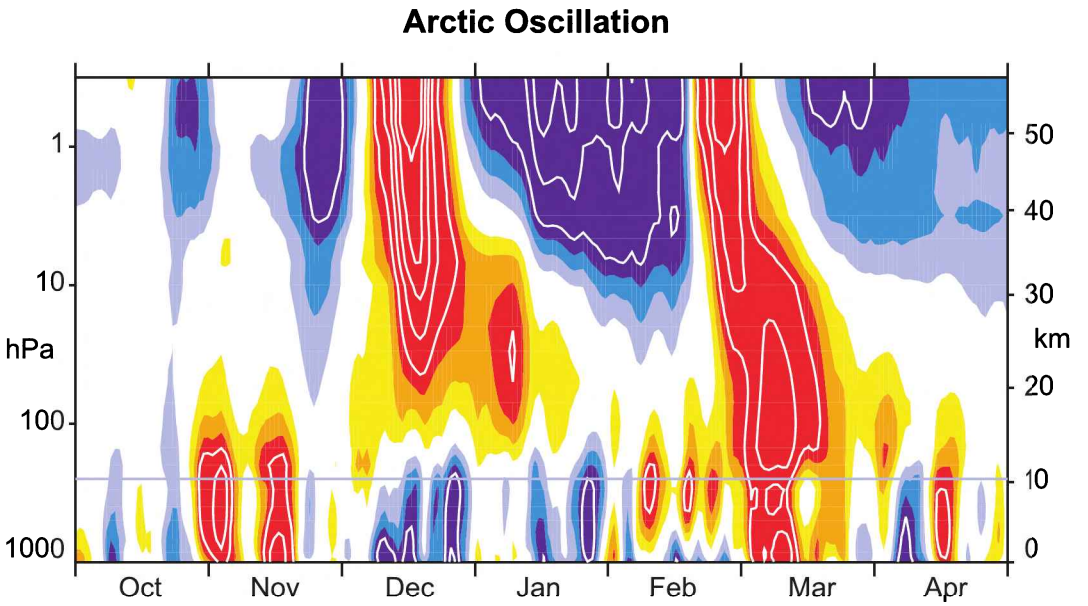

Plate 17 Time-height section of dimensionless AO index during 1998–1999. AO index represents the intensity of the leading EOF of geopotential height. After Baldwin and Dunkerton (2001).

(a)

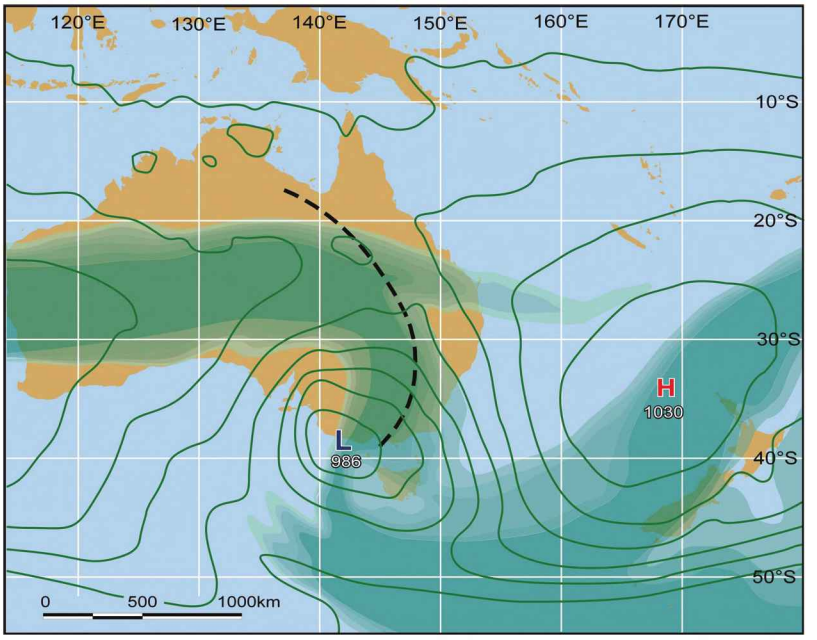

(b)

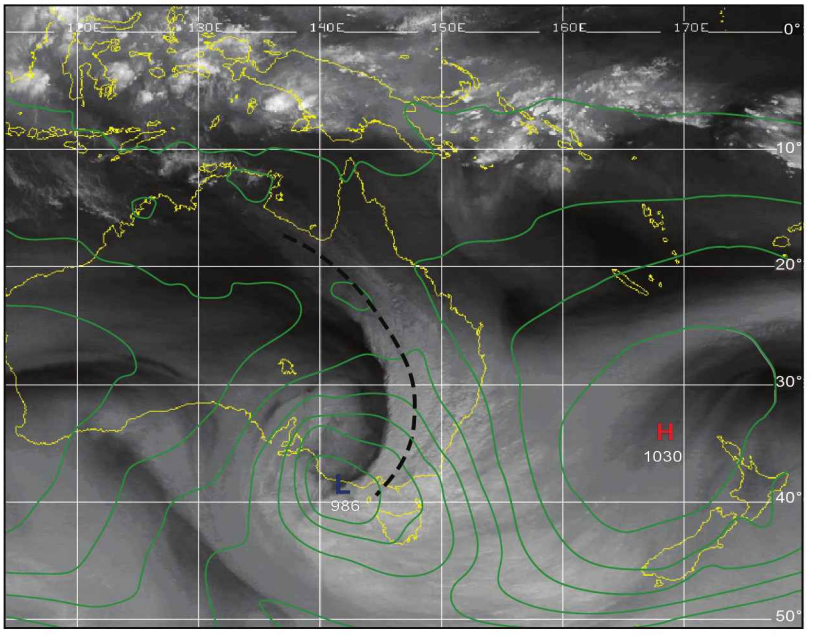

Plate 18 Conditions accompanying an amplifying baroclinic system that has reached maturity. (a) Distribution of SLP (contoured) and 300-hPa isotachs stronger than 20 m/s, which delineate the jet stream (shaded). (b) Contemporaneous water vapor image from MTSAT, representing humid air (light) and dry air (dark).

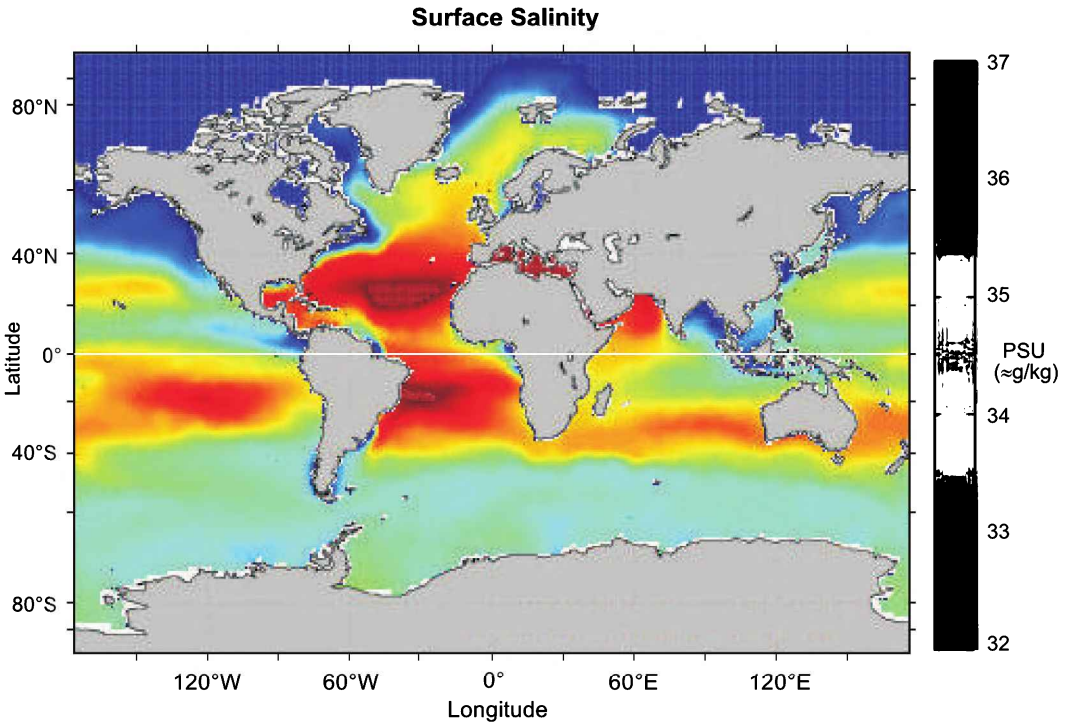

Plate 19 Annual-mean surface salinity, in Practical Salinity Units (PSU), approximately equal to g/kg. *Source:* Antonov et al. (2006).

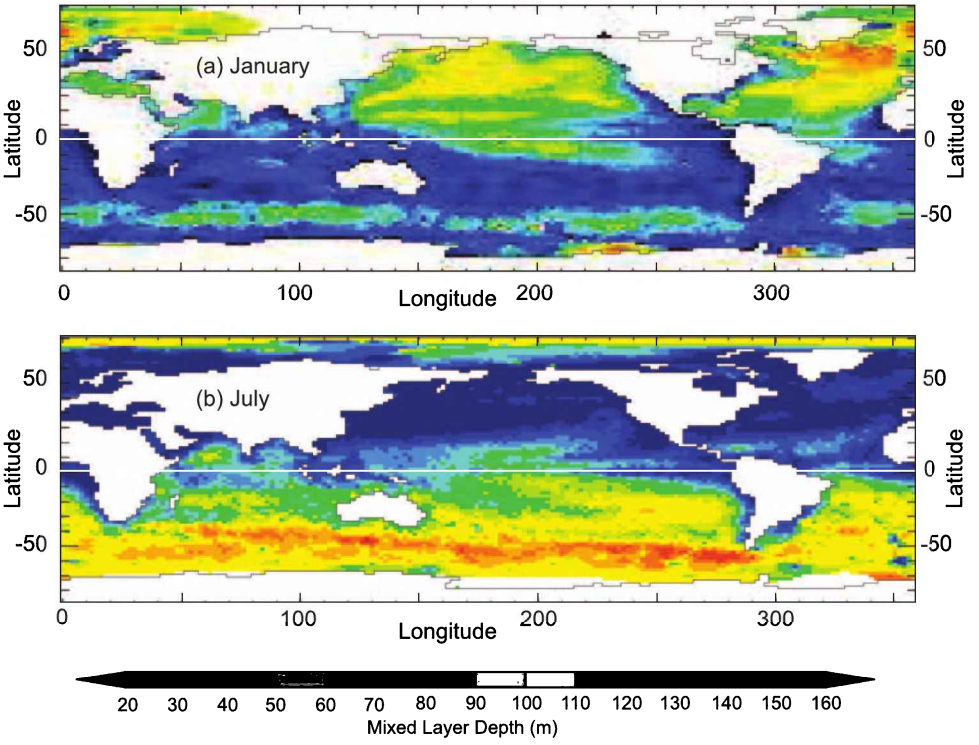

Plate 20 Depth of the mixed layer, as function of geographical position, during (a) January and (b) July. *Source:* http:/www./locean-ipsl.upmc.fr.

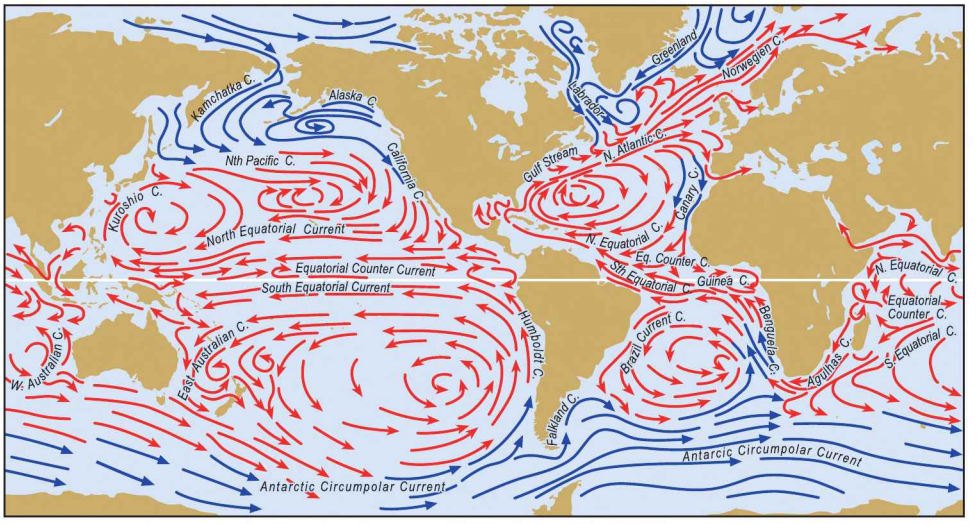

Plate 21 Surface circulation during January, illustrating water that is comparatively warm (red) and cold (blue). *Source:* US Navy Oceanographic Office.

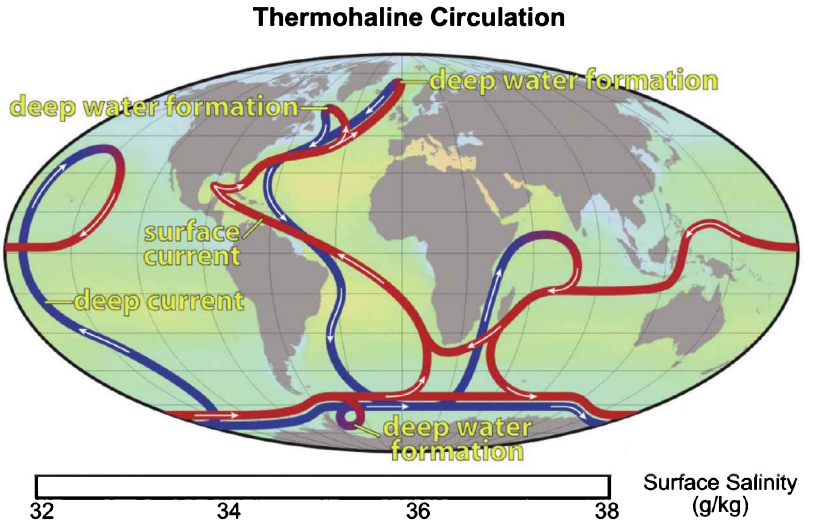

Plate 22 Schematic of the thermohaline circulation, along with surface salinity (shaded). Deep water (blue) forms in the far north Atlantic, near Greenland, and in the Weddell Sea, near Antarctica. After meandering through the global ocean, it eventually percolates upward, forming surface water (red). The time for the entire circuit to be completed is 1000–2000 years. *Source:* http://earthobservatory.nasa.gov.

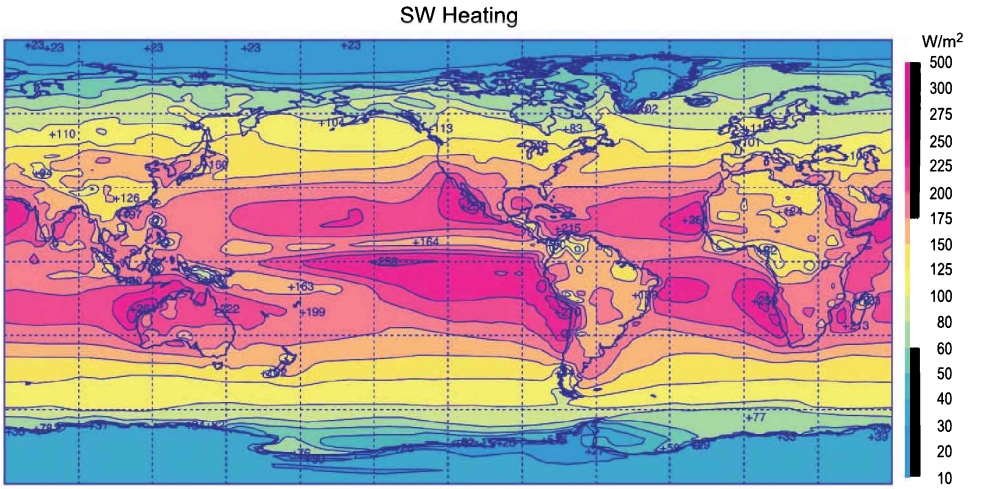

Plate 23 Annual-mean absorption of SW radiation at the Earth's surface. SW heating maximizes in the subtropics, especially in the eastern oceans, which are comparatively free of cloud and have large albedo. Derived from ERA-40 reanalysis. *Source:* Kallberg et al. (2005).

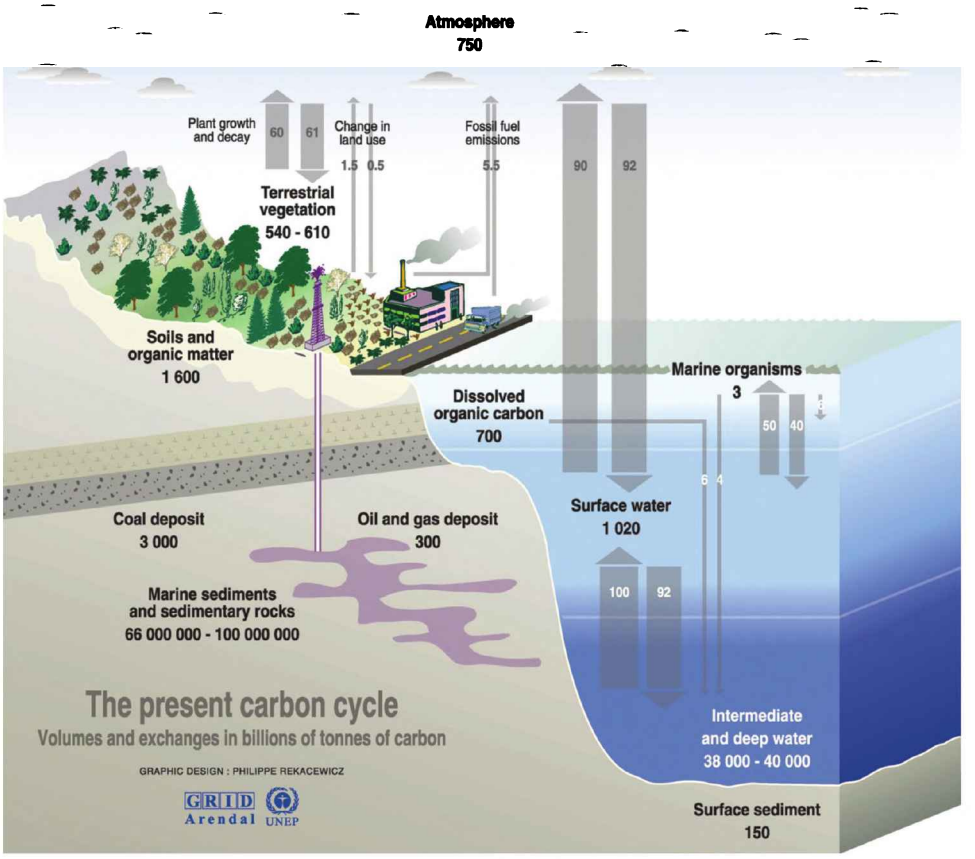

Plate 24 Estimated global carbon cycle, illustrating stores of carbon, in GtC, and transfers in GtC/yr, where 1 GtC = 10^9 tons of carbon. *Source:* http://maps.grida.no/go/graphic/the-carbon-cycle, design by Philippe Rekacewicz, UNEP/GRID-Arendal (11.07.10).

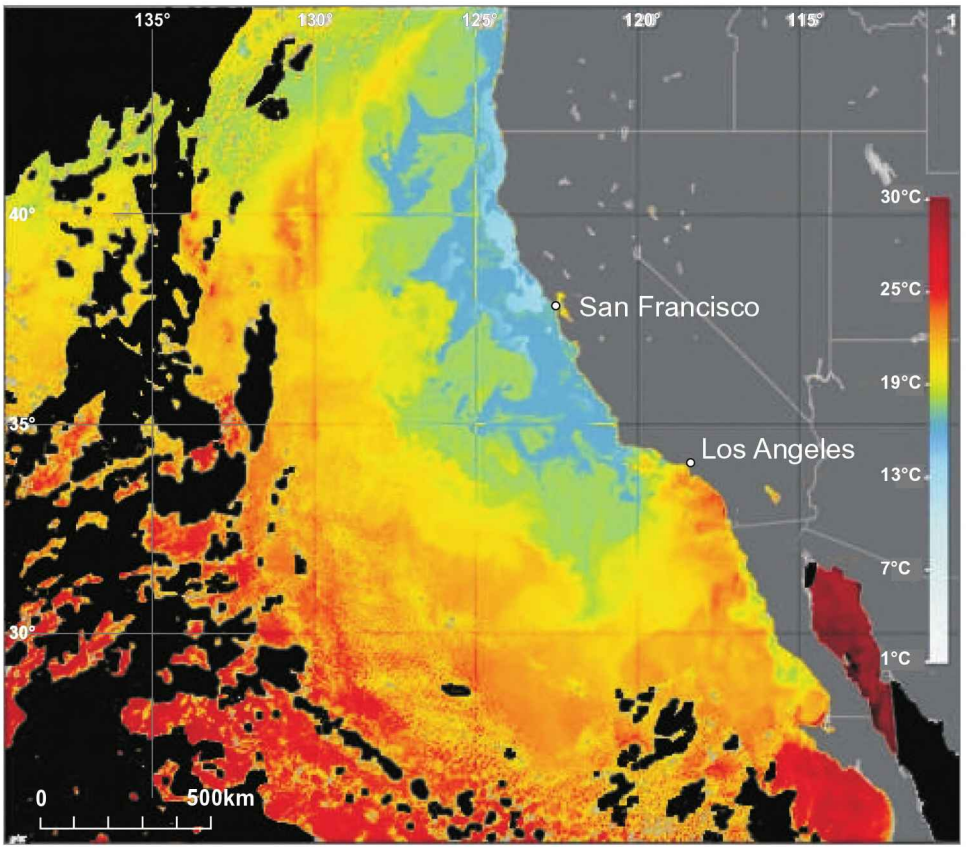

Plate 25 Surface temperature off the California coast. Temperature decreases shoreward, attaining values 10–15°C colder than in the open ocean. Black shading represents sites that are overcast, where data is unavailable. *Source:* http://oceanmotion.org.

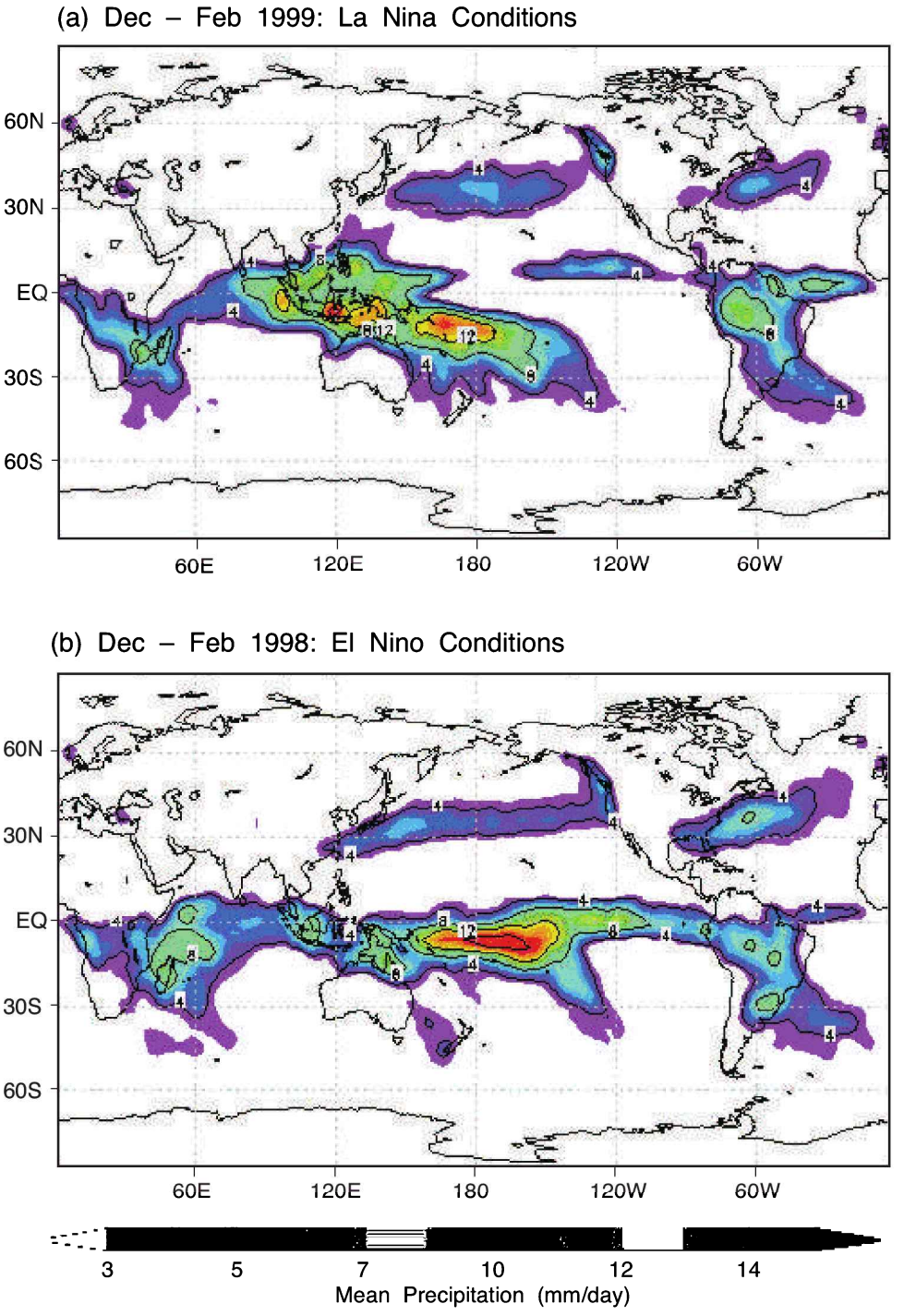

Plate 26 Global distribution of precipitation (a) during Dec–Feb 1999, under La Nina conditions, when rainfall was concentrated in the western Pacific, and (b) during Dec–Feb 1998, under El Nino conditions, when rainfall was displaced eastward into the central Pacific. Also evident during northern winter are the storm tracks over the north Atlantic and north Pacific, where precipitation is organized by amplifying synoptic weather systems. *Source:* http://www.esrl.noaa.gov (15.07.10).

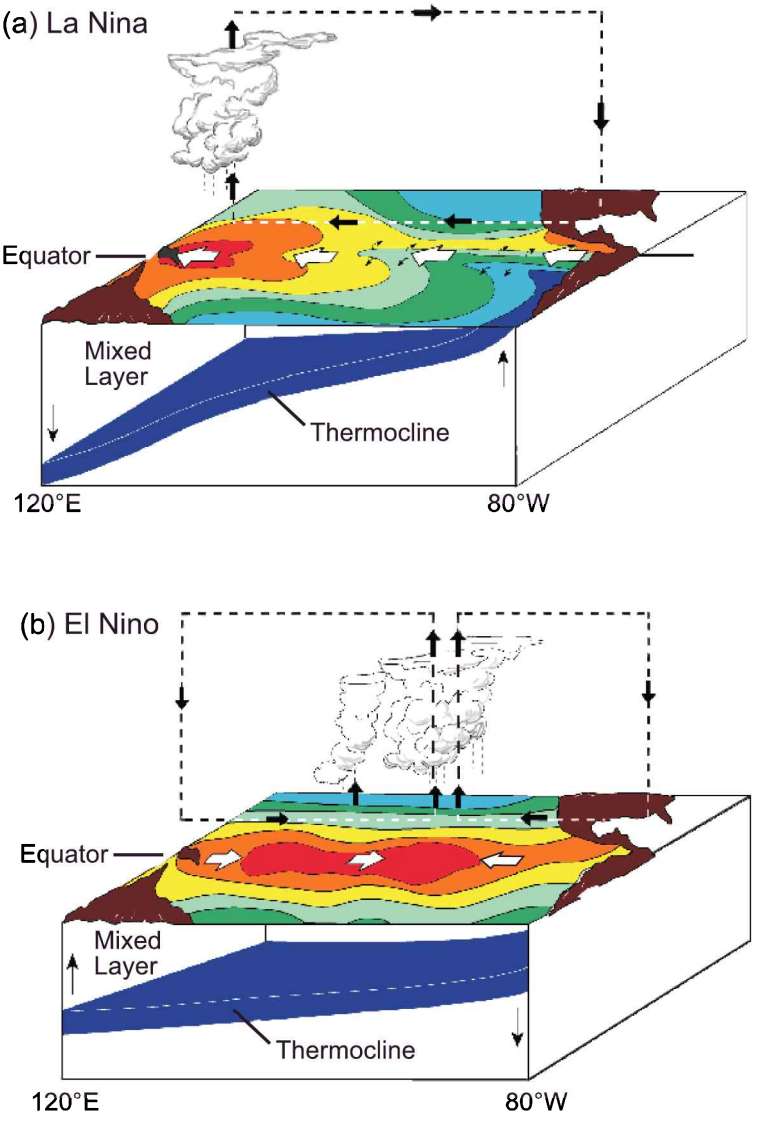

Plate 27 Ocean thermal structure, surface wind, SST (contoured, with red warmest), and Walker circulation under (a) La Nina conditions and (b) El Nino conditions. *Source:* http://www.pmel.noaa.gov.

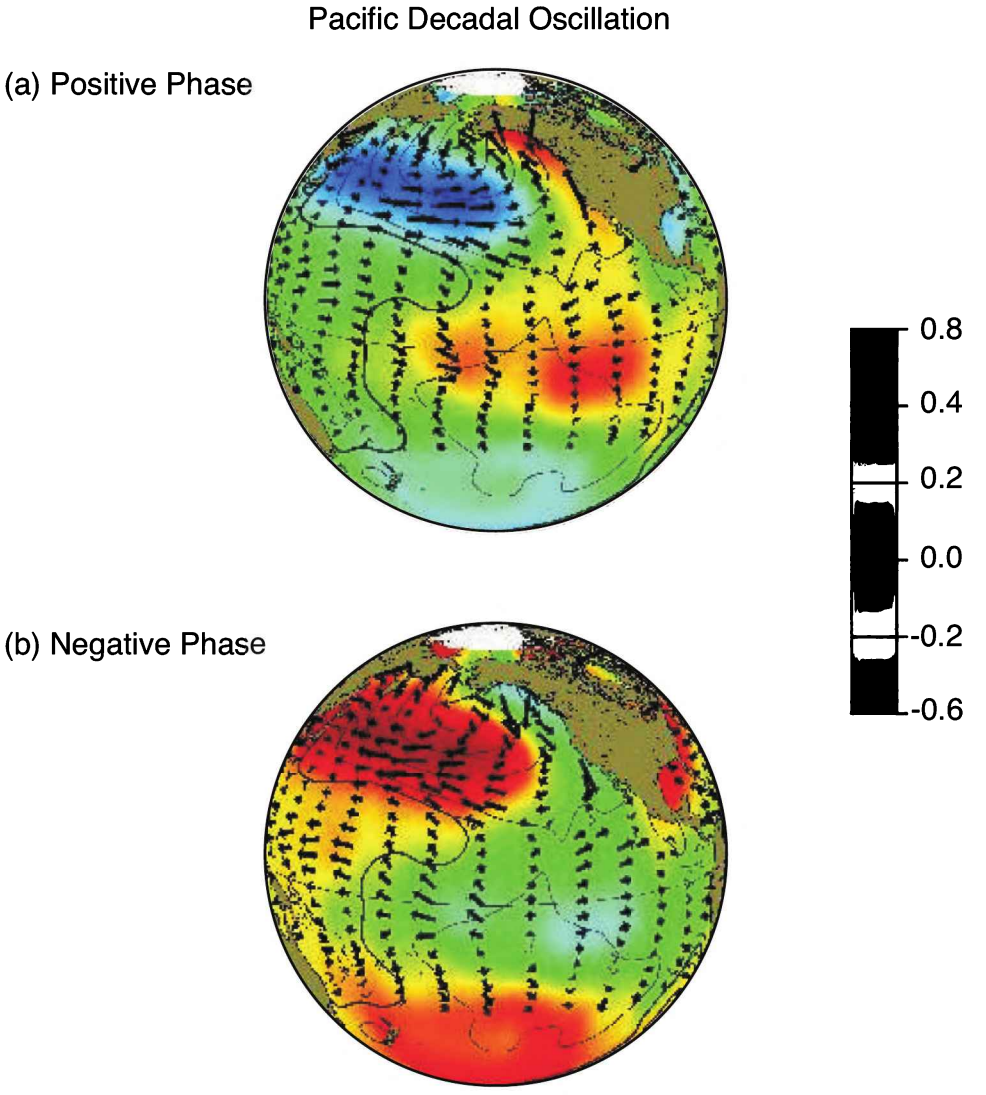

Plate 28 Anomalous SST (shaded), SLP (contoured), and surface wind associated with the Pacific Decadal Oscillation (PDO) during its (a) positive phase, when SST in the equatorial eastern Pacific is anomalously warm, and (b) negative phase, when SST in the equatorial eastern Pacific is anomalously cool. *Source:* http://jisao.washington.edu.

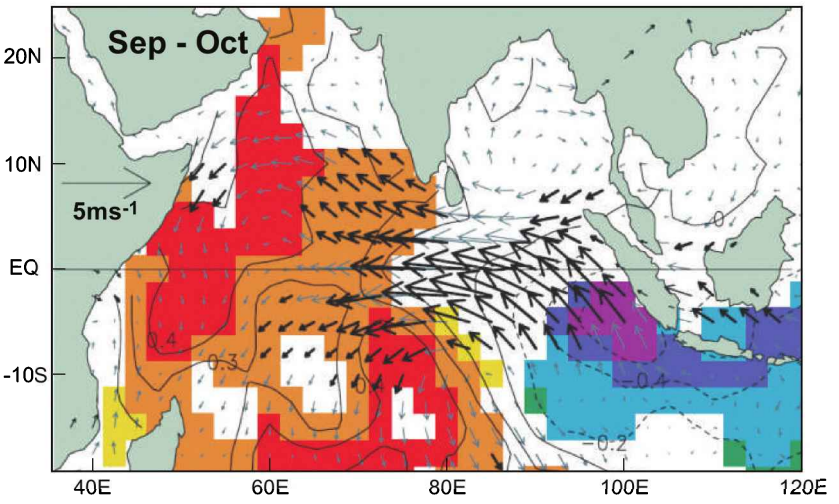

Plate 29 Anomalous SST (contoured), regions of >90% significance shaded with red significant and warm and blue significant and cold, and surface wind associated with Indian Ocean dipole (IOD). After Saji et al. (1999). Reprinted by permission of Macmillan Publishers Ltd: Nature (Saji et al., 1999), Copyright (1999).

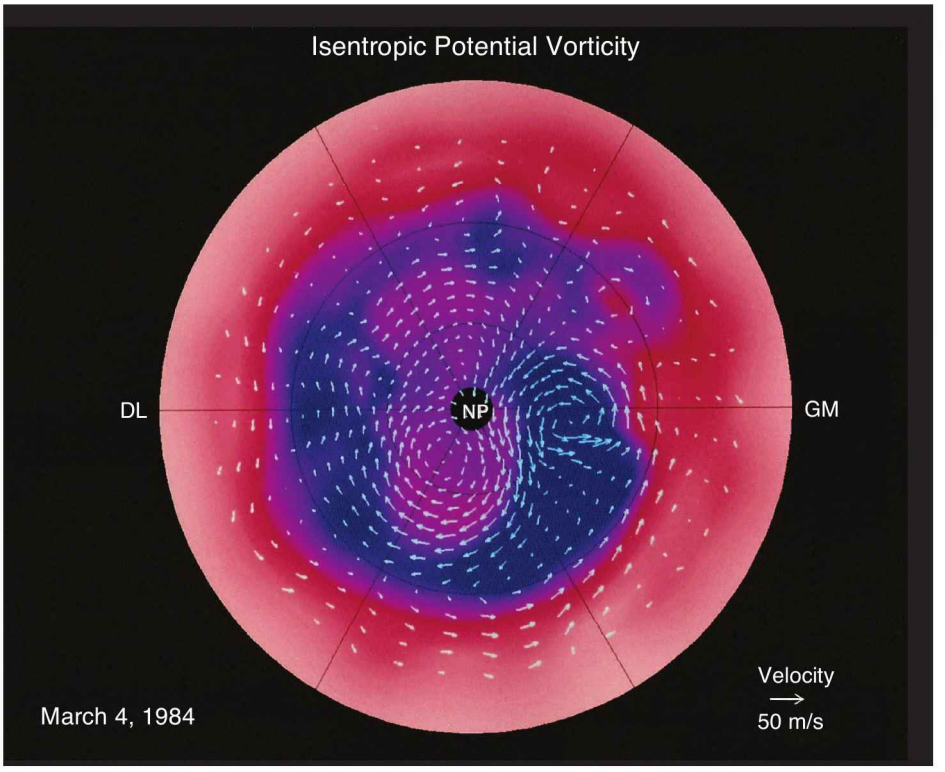

Plate 30 Distributions of potential vorticity *Q* and horizontal motion on the 850°K isentropic surface (near 10 hPa) for March 4, 1984. High-Q polar air (blue), which marks the polar-night vortex, has been displaced off the pole and distorted by a large amplitude planetary wave, with secondary eddies appearing along its tail. Low-Q air from equatorward (red) that is advected into the polar cap spins up anticyclonically, forming a reversed circulation with easterly circumpolar flow at high latitude (cf. 14.26).

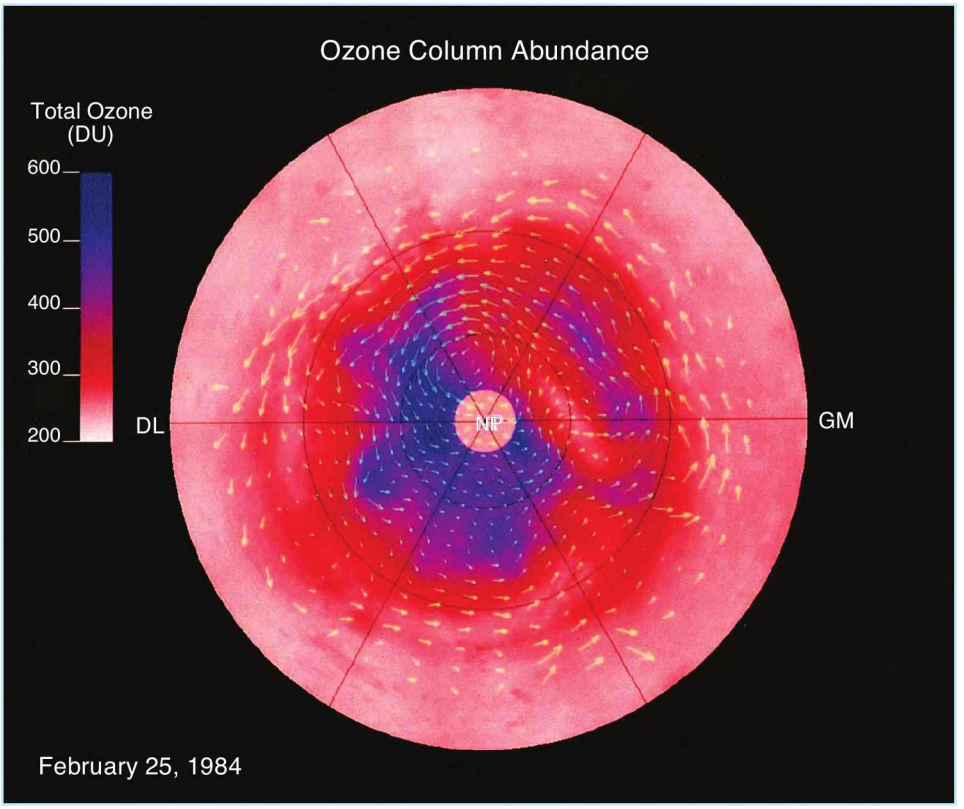

Plate 31 Total ozone Σ_{O_3} and horizontal motion on the 400°K isentropic surface in the Northern Hemisphere on February 25, 1984, during a stratospheric warming when zonal flow was disturbed down to 70 hPa. A tongue of enhanced Σ_{O_3} coincides with cross-polar flow between longitudes of 150 E and 30 W, where air descends along isentropic surfaces and undergoes compression. Air displaced equatorward in the Eastern Hemisphere ascends isentropically and undergoes expansion, introducing anomalously low Σ_{O_3}.

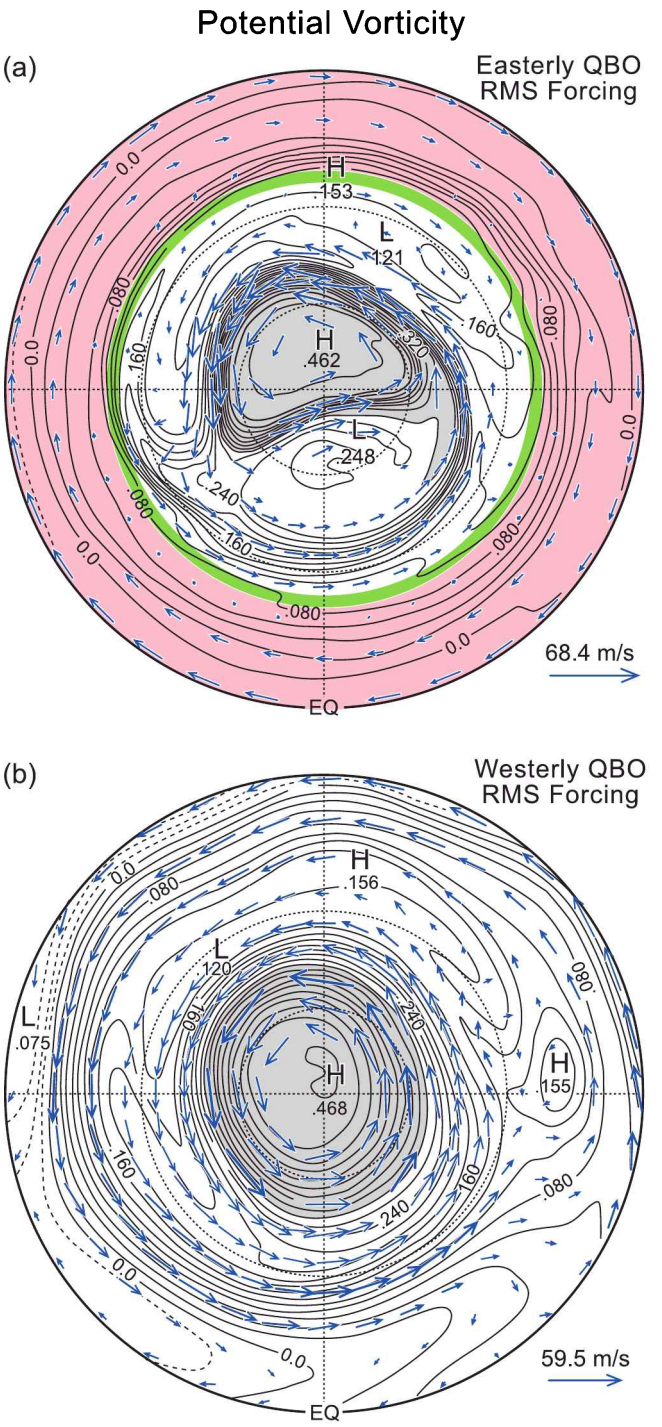

Plate 32 Distributions of potential vorticity and motion in a 2-dimensional calculation representative of the polar-night vortex (a) during the QBO easterlies (red), when the zero-wind line (green), which is the critical line for stationary planetary waves, invades the winter subtropics, and (b) during the QBO westerlies, when the critical line for stationary planetary waves recedes into the summer subtropics. Adapted from O'Sullivan and Salby (1990).

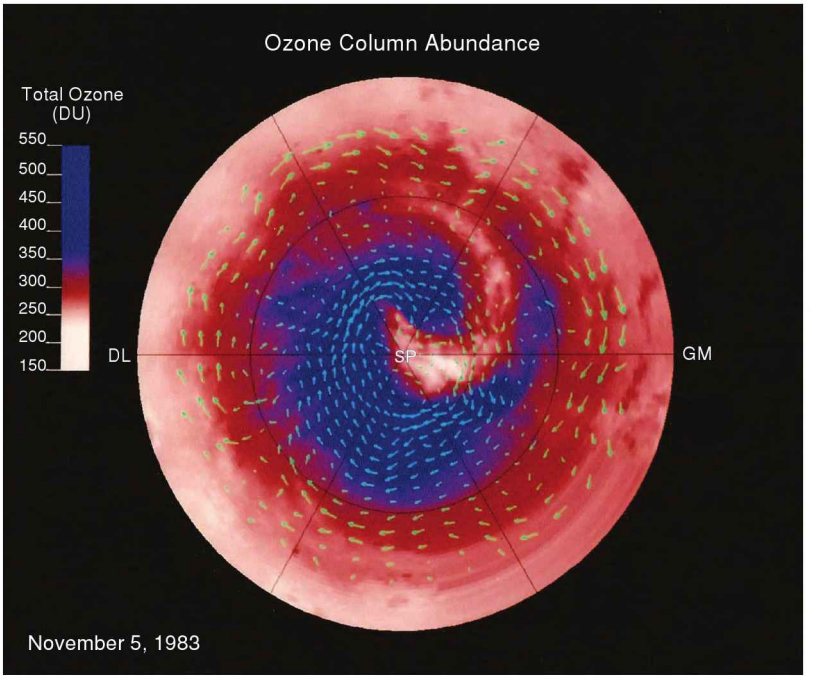

Plate 33 Distributions of total ozone and horizontal motion on the 325°K isentropic surface over the Southern Hemisphere on November 5, 1983, during the final warming. Ozone-depleted air (white), which had previously been confined inside the polar-night vortex, escapes in a tongue of anomalously-lean values (white) that spirals anticyclonically into mid-latitudes to conserve potential vorticity.

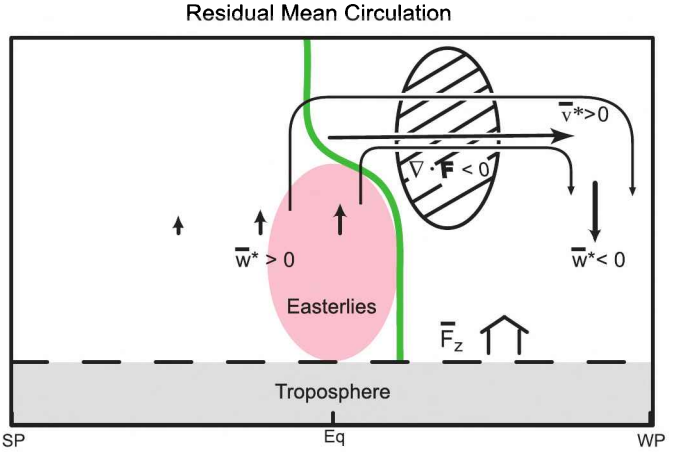

Plate 34 Schematic representation of the residual mean circulation $(\overline{v}^*, \overline{w}^*)$. Driven by absorption of EP flux $(\nabla \cdot \boldsymbol{F})$ that is transmitted upward by planetary waves (18.27). The latter is measured by the upward EP flux at 100 hPa, integrated over latitude $\overline{F}_z$ (18.32). During QBO easterlies (red), the zero-wind line (green), which is the critical line for stationary planetary waves, invades the winter hemisphere (cf. Fig. 18.17a).

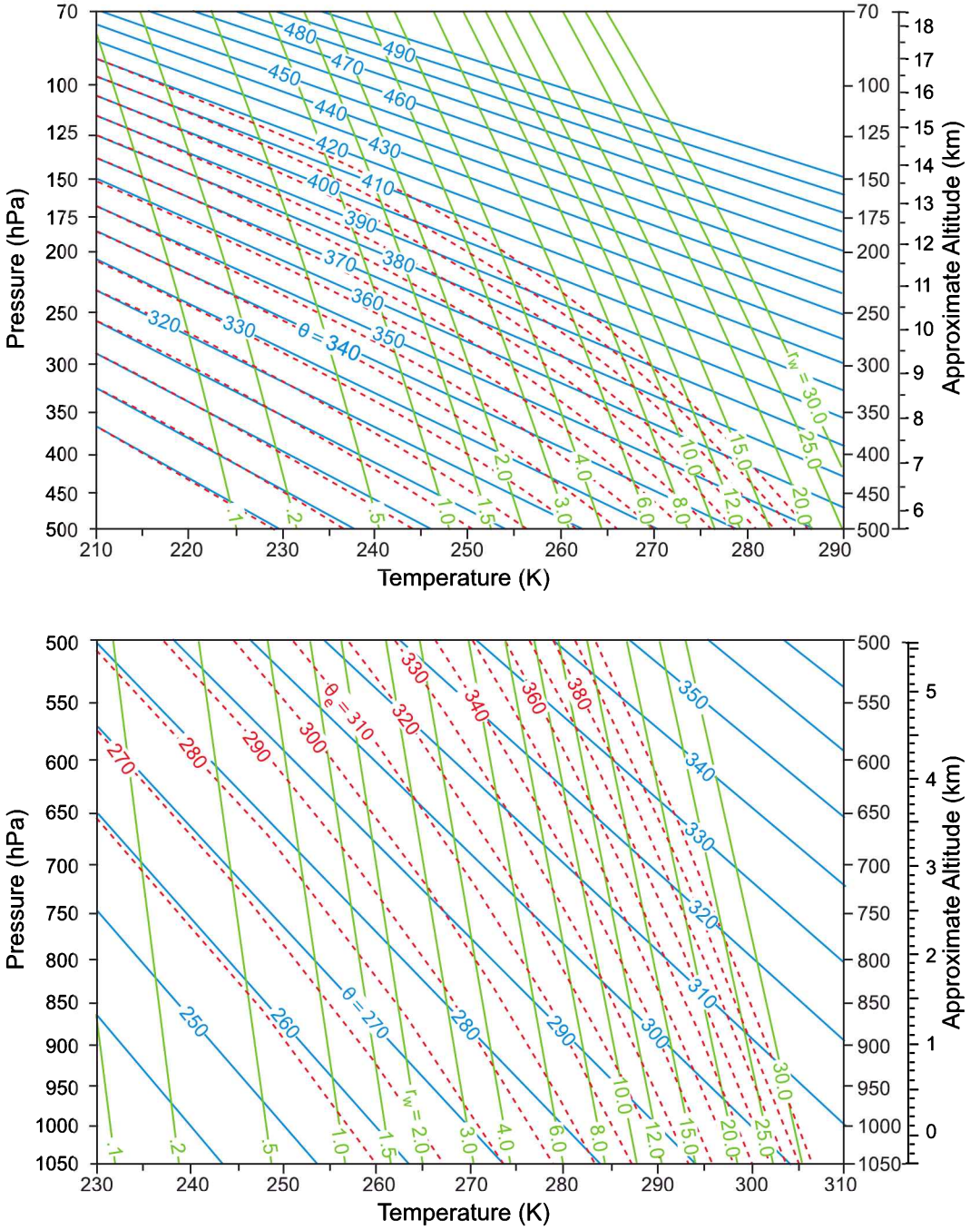

Plate 35 Pseudo-Adiabatic Chart: Adiabats (blue-solid), which are characterized by constant values of potential temperature θ; pseudo-adiabats (red-dashed), which are characterized by constant values of equivalent potential temperature θ_e; and isopleths of saturation mixing ratio with respect to water r_w (green), all as functions of temperature and pressure with the ordinate proportional to $\left(\frac{p_0}{p}\right)^{\kappa}$.